

Development of Novel Catalysts for Bio-Oil Upgradation

by

Sagar Bathla

A thesis submitted in partial fulfillment of the requirements for the degree of

Doctor of Philosophy

in

Chemical Engineering

Department of Chemical and Materials Engineering

University of Alberta

© Sagar Bathla, 2024

Abstract

Transition metal carbide catalysts (TMCs), particularly Molybdenum carbide (Mo_2C), have emerged as a cost-effective and promising alternative to precious-metal-based catalysts (Pt, Ru) for the hydrodeoxygenation (HDO) of biomass-derived species, including bio-oil. However, low selectivity towards deoxygenation and stability against oxygen poisoning are major limitations of monometallic carbide catalysts. This work primarily focuses on developing Mo_2C -based bimetallic carbide catalysts and provides structural and mechanistic insights into HDO mechanism, as these insights are pivotal in developing more selective and stable catalysts for HDO.

Understanding the atomic/molecular structure of the catalyst is crucial, hence, using a combination of density functional theory (DFT) calculations of mixing energies and relative stabilities with experimental characterization data, we predicted the most stable microstructure with a Tungsten to Molybdenum ratio (W/Mo) of 5:3, a mixed metal carbide bulk with overlayers of metallic tungsten (MoWC) is the most stable microstructure. Further investigation into the reaction mechanisms and pathways for the HDO of guaiacol revealed that the presence of tungsten overlayers on bulk MoWC catalyst creates a step-like structure which selectively favors direct deoxygenation (DDO) pathway in comparison to its monometallic counterpart Mo_2C on which both DDO and hydrogenation (HYD) pathways are competitive. These results explain the experimentally observed higher selectivity towards benzene on MoWC, as opposed to the monometallic Mo_2C .

Bio-oils from lignocellulosic biomass are complex mixtures of oxygenated organic compounds, making catalyst performance crucial for effective hydrodeoxygenation (HDO). We compared monometallic Mo_2C with W-doped Mo_2C (MoWC) using DFT calculations and bio-oil components. Our study found that MoWC, due to tungsten's enhanced oxophilicity, is more

effective for HDO than Mo₂C. MoWC can cleave both single and double C–O/C=O bonds, while Mo₂C only cleaves single C–O bonds. MoWC also outperforms Mo₂C in HDO of aromatic and carbohydrate components.

While MoWC bimetallic carbide catalysts show improved activity and selectivity, stability against oxygen poisoning remains a challenge. We screened 45 Mo₂C-based bimetallic carbides (Co, Cr, Fe, Mn, Nb, Ni, Ti, and Zr) using phenol as a model compound and evaluating three key reactions: C–O dissociation, oxygen removal, and ring hydrogenation. Among these, optimal candidates for direct deoxygenation (DDO) include Mo-terminated Fe₃Mo₃C, Mn-terminated Mn₃Mo₃C, and Ni-terminated Ni₃Mo₃C, while triclinic Mo-terminated Fe₁₁MoC₄ and Ni-terminated Ni₆Mo₆C excel in hydrogenation (HYD). We identified an optimal oxygen binding energy (OBE) range of -100 to -200 kJ/mol for effective DDO, balancing oxygen binding with removal. This OBE descriptor and the proposed parameter combining activity, stability, and selectivity offer a basis for preliminary screening of catalysts in large databases for DDO and HYD processes.

We investigated solvent effects on HDO reactions of bio-oil using a combination of catalytic experiments, advanced characterization, and quantum mechanical simulations. Ruthenium (Ru), known for its high catalytic activity, served as a benchmark to compare noble-metal TMCs. We found that Ru's selectivity shifts from deoxygenation in the gas phase to ring hydrogenation in the condensed phase. In aqueous conditions, water partially dissociates into hydroxyl fragments and H atoms, which are critical for this shift. Experiments showed >99% conversion and >75% selectivity towards hydrogenated products in the presence of water. Computational results supported these findings, showing reduced kinetic barriers for hydrogenation (70 kJ/mol) and increased barriers for dehydroxylation (63 kJ/mol to 202 kJ/mol). Water not only provides H for

hydrogenation but also regenerates with external hydrogen supply, acting as a hydrogen shuttle.
This study highlights how solvent effects can tune Ru catalyst selectivity towards hydrogenation.

Preface

Chapters 2,3 and 5 of this thesis have been published or submitted for publication. I performed all the computational research under the direct supervision of Prof. Samir H. Mushrif. In Chapter 2, the experimental work was conducted by Dr. Chi Cong Tran under the supervision of Prof. Serge Kaliaguine at the University of Laval. In Chapter 5, Dr. Bhanu Priya and Dr. Ankit Kumar conducted the experimental work under the supervision of Prof. Sanjay Kumar Singh at the Indian Institute of Technology, Indore.

A comprehensive version of literature review presented in Chapter 1 of this thesis has been published, as Sagar Bathla, Dahi Akmach, Chi-Cong Tran, Serge Kaliaguine, and Samir H. Mushrif, *Transition metal carbide catalysts for Upgrading lignocellulosic biomass-derived oxygenates: A review of the experimental and computational investigations into structure-property relationships*, *Catalysis Today*, Volume 423, 2023, 114285. <https://doi.org/10.1016/j.cattod.2023.114285> © 2024 Elsevier

Chapter 2 and Appendix B of this thesis has been published, with minor changes, as Sagar Bathla, Chi-Cong Tran, Serge Kaliaguine, and Samir H. Mushrif, *Doping an Oxophilic Metal into a Metal Carbide: Unravelling the Synergy between the Microstructure of the Catalyst and Its Activity and Selectivity for Hydrodeoxygenation*, *ACS Catalysis*, 12, 22, 13980–13998. <https://doi.org/10.1021/acscatal.2c03500> © 2022 American Chemical Society.

Chapter 3 and Appendix C of this thesis have been submitted for publication, as Sagar Bathla, and Samir H. Mushrif, *"Revealing the Potential of Bimetallic Carbide Catalysts for Upgrading Biomass-derived Bio-Oil: A First Principles-Based Investigation Using Representative Bio-oil Constituents"*.

Chapter 5 and Appendix E of this thesis have been published, with major changes, Sagar Bathla, Bhanu Priya, Ankit Kumar, Sanjay K. Singh, Samir H. Mushrif, *"Water-assisted hydrogenation of aromatics under ambient conditions over Ru catalyst: A combined experimental and computational investigation"*, *Journal of Catalysis*, Volume 434, 2024, 115522, <https://doi.org/10.1016/j.jcat.2024.115522> © 2024 Elsevier

Acknowledgements

First and foremost, I would like to express my deepest gratitude to my advisor, Dr. Samir H. Mushrif, for their unwavering support, guidance, and patience throughout my research. His expertise and insightful feedback have been invaluable in shaping this work and also to develop fundamental thinking and improve my scientific communication skills.

Special thanks go to my friends at the University of Alberta. Their camaraderie, stimulating discussions, and willingness to help have made my time here both productive and enjoyable. In particular, I would like to acknowledge Dr. Sanjula Kammammettu, Dr. Anuja Tripathi, Dr. Hikmat Binyaminov, Mr. Faraz Amjad, Mr. Aadil Khan, and Ms. Aishwarya Pawar for their support and friendship.

I extend my gratitude to Prof. Serge Kaliaguine and Dr. Chi Cong Tran for their collaboration in the first project of my Ph.D. degree and their guidance in the interpretation of critical results. I thank Dr. Ojus Mohan for the help in performing simulations during the initial stage of my Ph.D and his availability for innumerable discussions throughout my Ph.D. I also thank Prof. Sanjay Singh, Dr. Bhanu Priya and Dr. Ankit Kumar for their collaboration in one project. I thank my current and previous fellow colleagues: Mr. Shang Jiang, Dr. Arul Padmanathan, Dr. José Carlos Velasco Calderón, Mr. Seth Beck, Mr. Nilesh Orupattur, Mr. Sourav Paul, Dr. Eduardo Romero Montalvo for the constructive discussions and for all the fun we have had. A special shout out to Mr. Ryan Wei Jie Tan for his significant contribution to one of the projects!

I am deeply appreciative of the financial support provided by Canada First Research Excellence Fund as part of the University of Alberta's Future Energy Systems Research Initiative, the Natural Sciences and Engineering Research Council of Canada (NSERC) via their Discovery Grants program and the Digital Research Alliance of Canada for providing computational resources, without which this research would not have been possible.

On a personal note, I am eternally grateful to my family for their unconditional love and encouragement. To my parents, Charanjeet Bathla and Asha Bathla, thank you for your sacrifices and for always believing in me. To my siblings, Hardik and Ishan, your support means the world

to me. Finally, to my wife, Himanshi, your patience, understanding, and unwavering support have been amazing in the final year of this incredible Ph.D. journey.

Table of Contents

Abstract	ii
Preface	v
Acknowledgements	vi
List of Figures	xv
List of Tables	xxv
Chapter 1: Introduction	1
1.1 Background.....	1
1.1.1 Classification of Biomass	1
1.1.2 Lignocellulosic Biomass – A viable substitute to petroleum	2
1.1.3 Thermochemical conversion – Pyrolysis and Liquefaction.....	2
1.1.4 Bio-oil and Need for Hydro-processing.....	3
1.1.5 Bio-oil Upgradation	4
1.1.5.1 Types of Catalysts.....	6
1.2 Literature Review.....	7
1.2.1 Hydrodeoxygenation (HDO) of real Bio-oil.....	7
1.2.2 Hydrodeoxygenation (HDO) of model compounds.....	8
1.2.2.1 HDO of linear chain carbonyl and carboxyl groups derived from bio-oil (aldehydes, ketones, and carboxylic acids).....	9
▪ Experimental Studies	9
▪ Computational Studies	13
1.2.2.2 HDO of carbohydrate fractions (levoglucosan, Glucose) and furanic units (HMF, Furfural).....	17
▪ Experimental Studies	17
▪ Computational Studies.....	18
1.2.2.3 HDO of oxygenated aromatic rings (lignin components).....	22

▪	Experimental Studies	22
▪	Computational Studies	28
1.3	Aqueous phase processing of bio-oil	31
1.4	Motivation of the thesis	33
1.5	Objectives	36
1.5.1	Key objectives of Chapter 2.....	36
1.5.2	Key objectives of Chapter 3.....	37
1.5.3	Key objectives of Chapter 4.....	37
1.5.4	Key objectives of Chapter 5.....	37
1.6	Dissertation overview	37
Chapter 2: Doping an Oxophilic Metal into a Metal Carbide: Unravelling the Synergy Between the Microstructure of the Catalyst and its Activity and Selectivity for Hydrodeoxygenation		40
Abstract	40
2.1	Introduction.....	41
2.2	Methods.....	45
2.2.1	Computational methodology.....	45
2.2.2	Mixing and Cohesive Energies	47
2.3	Results and Discussion	48
2.3.1	Model Structures/configurations of the Bimetallic Carbide (MoWC) catalyst	48
2.3.2	Relative Stability of modelled Structures of Bimetallic carbide (MoWC).....	50
2.3.3	Comparison of Experimentally Measured and DFT computed XPS Shifts	52
2.3.4	Correlation between Surface Core-level shifts and D-band Center (ϵd)	53
2.3.5	CO adsorption studies	55
2.3.6	HDO Reaction network of Guaiacol on Mo ₂ C	56
2.3.6.1	Guaiacol adsorption configuration on Mo ₂ C	57
2.3.6.2	Benzene Formation	58
2.3.6.3	Ring Hydrogenated Products (Cyclohexene and Cyclohexane).....	60

▪	Direct Ring Hydrogenation of Guaiacol	61
▪	Guaiacol → Catechol → Cyclohexene Pathway	62
▪	Guaiacol → Phenol/Anisole → Cyclohexene Pathway	63
▪	Guaiacol → Benzene → Cyclohexane Pathway.....	64
	2.3.6.4 Linear chain Products (Hexene Formation).....	65
	2.3.6.5 Proposed Reaction Pathways	66
	2.3.7 Tungsten doped Molybdenum Carbide Catalyst (MoWC) for guaiacol HDO	69
	2.3.7.1 Guaiacol Adsorption configuration on Tungsten-doped Mo ₂ C	69
	2.3.7.2 Guaiacol Activation on Tungsten doped Mo ₂ C (MoWC) surface.....	70
	2.3.7.3 Ring Hydrogenation pathways.....	72
	2.3.8 Comparison with Experimental Results for Guaiacol HDO.....	74
	2.4 Conclusions.....	76
	Chapter 3: Revealing the Potential of Bimetallic Carbide Catalysts for Upgrading Biomass-derived Bio-Oil: A First Principles-Based Investigation Using Representative Bio-oil Constituents	78
	Abstract.....	78
	3.1 Introduction.....	79
	3.2 Computational Methodology	83
	3.3 Results and Discussion	84
	3.3.1 5 – Hydroxymethyl furfural (Furanics).....	86
	3.3.1.1 Adsorption Configuration	86
	3.3.1.2 Reaction Energetics of 5-HMF on Mo ₂ C and MoWC.....	86
	3.3.2 Methyl Glyoxal (MG).....	92
	3.3.2.1 Adsorption Configuration on Mo ₂ C and MoWC.....	92
	3.3.2.2 First activation of MG on Mo ₂ C and MoWC	92
	3.3.3 Acetic Acid (AA).....	95
	3.3.3.1 Adsorption Configuration on Mo ₂ C and MoWC.....	95

3.3.3.2 Reaction Pathways on Mo ₂ C and MoWC.....	95
3.3.4 Levoglucosan (LGA).....	98
3.3.4.1 Adsorption Configuration.....	98
3.3.4.2 Reaction Mechanism of LGA on Mo ₂ C and MoWC.....	98
3.3.5 Vanillin.....	104
3.3.5.1 Adsorption Configuration.....	104
3.3.5.2 Reaction Pathways.....	104
3.3.6 Eugenol.....	107
3.3.6.1 Adsorption Configuration.....	107
3.3.6.2 Reaction Pathways.....	108
3.3.7 Phenol and Cresol.....	110
3.4 Conclusions.....	112
Chapter 4: Predicting Active, Selective and Stable Mo₂C–Based Bimetallic Carbides for Direct Deoxygenation and Hydrogenation Reactions: A Computational Screening.....	113
Abstract.....	113
4.1 Introduction.....	114
4.2 Models and Computational Methods.....	117
4.2.1 Model Structures.....	117
4.2.2 Methodology.....	119
4.2.3 Screening Strategy.....	120
4.3 Results and Discussion.....	121
4.3.1 Hydrogen and Oxygen Adsorption.....	121
4.3.2 Preliminary Screening of 45 bimetallic carbides for HDO.....	123
4.3.3 C – O Scission (Direct Deoxygenation).....	125
4.3.4 Oxygen Removal ($OH^* + H^* \rightarrow H_2O$).....	127
4.3.5 C=C Hydrogenation.....	129

4.3.6 Selective and Stable DDO and HYD Candidates	132
4.3.6.1 DDO Candidates	132
4.3.6.2 Selective Hydrogenation (HYD) Candidates	135
4.3.7 Search for a Descriptor	136
4.4 Conclusions.....	139
Chapter 5: Water-Assisted Hydrogenation of Aromatics under Ambient Conditions over Ru Catalyst: A Combined Experimental and Computational Investigation	140
Abstract.....	140
5.1 Introduction.....	141
5.2 Experimental and computational methods.....	144
5.2.1 Chemical Reagents.....	144
5.2.2 Catalyst synthesis.....	144
5.2.3 Characterization	144
5.2.4 General procedure for catalytic hydrogenation reactions	145
5.2.5 Computational methods	146
5.3 Results and discussion	147
5.3.1 Catalyst characterization.....	147
5.3.2 Optimization of reaction conditions.....	148
5.3.2.1 Hydrogenation of phenol	148
5.3.3 Effect of the solvent.....	152
5.3.4 DFT investigation	157
5.3.4.1 Reaction pathways and energetics in the absence and presence of water.....	157
5.4 Conclusions.....	170
Chapter 6: Conclusions and Outlook.....	172
Bibliography	177
Appendices	203
Appendix A Computational Methods.....	204

A.1 Overview of Electronic Structure Calculations	204
A.2 Density Functional Theory (DFT)	206
Appendix B Supplementary Information to Chapter 2	212
B.1 Estimating Gibbs energy for elementary reaction steps.....	212
B.2 Electronic Energy of All Reactions.....	214
B.3 Transition State Configurations on Mo ₂ C	216
B.4 Transition State Configurations on MoWC	221
B.5 Experimental Characterization Results	224
Appendix C Supplementary Information to Chapter 3	228
C.1 Energy Barriers of All Reactions on Six Model Compounds	228
C.2 Adsorption Characteristics of model compounds on Mo ₂ C and MoWC	230
C.3 Transition state Configurations of 5-HMF.....	231
C.4 Transition state Configurations of Methyl Glyoxal	234
C.5 Transition state Configurations of Acetic Acid.....	235
C.6 Transition state Configurations of LGA.....	236
C.7 Transition state Configurations of Vanillin.....	238
C.8 Transition state Configurations of Eugenol	239
Appendix D Supplementary Information to Chapter 4.....	242
D.1 Surface Energy Calculations.....	242
D.2 Lattice Parameter Optimization	243
D.3 Surface energy tables	245
D.4 Catalyst Models.....	247
D.5 Optimized stable adsorption configuration of H adatom on catalyst surfaces.....	252
D.6 Optimized stable adsorption configuration of OH fragment on catalyst surfaces ...	259
D.7 Hydrogen Binding Energy (HBE) and Oxygen Binding Energy (OBE) Plots	265

D.8 Adsorption configurations of Phenol	268
D.9 Transition State Configurations of C-O dissociation (R1) reaction.....	274
D.10 Transition State Configurations for O* removal (R3) Reaction	280
D.11 Transition State Configurations for Ring Hydrogenation (R3) Reaction	286
Appendix E Supplementary Information to Chapter 5	293
E.1 Experimental Results.....	293
E.2 Leaching experiment.	296
E.3 Hg poisoning experiment.	297
E.4 Catalyst stability and reusability.	298
E.5 Computational Data – Transition State and Adsorption Configurations.....	309
Bibliography	320

List of Figures

Figure 1.1 Typical reactions which occur in the bio-oil upgrading process.	5
Figure 1.2 a) Conversion of propanal at 573 K with and without co-feed H ₂ (atmospheric pressure of H ₂), b) selectivity of C ₃ + at 573 K with H ₂ , and c) comparison of the yields of C ₃ hydrocarbons and water from propanal with H ₂ . The products from propanal include C ₂ species (ethylene and ethane from the cleavage of one of the C – C bonds), C ₃ products (propylene and propane) from C-O scission, C ₆ (2-methyl-3-pentanone) from the coupling of oxygenates, and H ₂ O from the removal of oxygen (Reproduced with permission from Wiley from ref. [31])	10
Figure 1.3 HREELS spectra from WC surface exposed to propanol or propanal.(Reproduced with permission from RSC from ref [32])	11
Figure 1.4 A schematic of proposed Acetone HDO Reaction Pathway (Reproduced with permission from ACS from ref. [34])	12
Figure 1.5 Acetone HDO rate, defined as combined rate of formation of (propylene + propane), normalized by catalyst loading, with T = 369 K, 0.53 kPa of IPA or acetone feed, 54 kPa of H ₂ , 4 kPa of CH ₄ as an internal standard, 0.29 gcat loading, and ~1.83 cm ³ s ⁻¹ total flow. Activated catalyst was treated with 13 kPa O ₂ cofeed with no H ₂ cofeed at T = 369 K for ~4 h preceding t = 0 shown above; total pressure 1 atm. (Reproduced with permission from ACS from ref. [34])	12
Figure 1.6 (a) Schematic of the possible reaction pathway for propanol and propanal decomposition on the WC (0001) surface. The activation barrier (and the corresponding reaction energy in parenthesis) is in eV. The energetically favorable pathway is highlighted in green. (b) Energy profile of the most favorable reaction pathway for propanol decomposition on the WC (0001) surface. (Adapted from ref: [31])	13
Figure 1.7 Schematic of the key reaction pathways for propanal decomposition and hydrogenation on a Mo ₂ C (0001) surface. The most facile pathway is highlighted in green and the activation barriers shown above the arrows are in eV. (Adapted from ref: [33]).....	15
Figure 1.8 Schematic illustration of the proposed reaction pathway for furfural activation on Ru (001) surfaces. Bold arrows – preferred pathway. The activation barrier and the corresponding reaction energy (in parenthesis) are in kJ/mol. (Adapted from ref:[67]).....	19
Figure 1.9 Cyclohexane production rate measured from either benzene hydrogenation reaction (■, shaded areas) or vapor-phase anisole HDO reaction (■) on a Mo ₂ C catalyst. Benzene synthesis	

rate \odot indicates deoxygenation activity. The catalyst was first tested for benzene hydrogenation for ~ 10 ks (feed composition : benzene/H₂ = 0.23%/bal with total flow rate ~ 1.67 cm³ s⁻¹) and then switched to vapor-phase anisole HDO reaction (feed composition: anisole/H₂ = 0.14%/bal with total flow rate ~ 1.67 cm³ s⁻¹), followed by restoring the reaction conditions to benzene hydrogenation. The reaction temperature was maintained at ~ 423 K under ambient pressure during the switch of the aforementioned two reactions. Catalyst loading was ~ 150 mg. (Reproduced with permission from Elsevier from ref [65])..... 24

Figure 1.10 HDO of anisole. Reaction selectivity of MoC_x/FAU, pristine Mo₂C, parent FAU, and Mo₂C+FAU catalysts at the final point of reaction run (TOS = 1200 min). The conversions of these catalysts were 97% (MoC_x/ FAU), 49% (Mo₂C), 31% (FAU), and 61% (Mo₂C+FAU). (Reproduced with permission from ACS from ref [63]) 26

Figure 1.11 Pulse chemisorption of metallic tungsten and metal carbides. (Reproduced with permission from ACS from ref [70]). 28

Figure 1.12 The reaction profile for the most favorable pathway of HDO of guaiacol over β -Mo₂C. The activation barrier for each step is given in red, in eV, and the rate constant of the conversion at 500 K is given in purple, in s⁻¹ (Adapted from ref [71]). 29

Figure 1.13 Proposed reaction pathways with the calculated barrier for guaiacol conversion at 350 °C, 450 psig. Solid line: kinetically favored route. Dashed line: kinetically nonfavored route. Electronic barriers (kJ mol⁻¹) are in green color for Mo₂C and violet color for MoWC. DDO: direct deoxygenation. HYD: hydrogenation–dehydration. (Reproduced with permission from ACS from ref [70]). 30

Figure 2.1 2-D Schematic of different possible structures (side view) for mixed metal carbide catalyst (MoWC). Molybdenum and tungsten atoms are shown in green and blue color respectively. The stoichiometric ratio in all the structures is different. Case – 1 to case – 5 represent bulk alloys with increasing tungsten proportion, and cases - 6, 7 represent models with adlayers of metallic tungsten and tungsten carbide, respectively..... 49

Figure 2.2 (a) Mixing energies (Δ /eV) calculated using equation (3), and (b) Cohesive energies (ΔC /eV) calculated using equation (5) for different structures of MoWC with reference to Mo₂C. The most stable (most negative Δ) cases are highlighted in the red circle. 51

Figure 2.3 Comparison of the theoretical layer-projected d-band center with the experimental core level binding energy shifts in the W 4f and Mo 3d core-level components. The physical system under comparison is depicted schematically in the insets on the left and right. 55

Figure 2.4 Optimized geometries and corresponding free energies of guaiacol adsorption on the Mo₂C surface (a) Top view of $\eta^2(\text{C} - \text{O})$ configuration, (b) Side view of $\eta^2(\text{C} - \text{O})$ configuration, (c) Top view of $\eta^1(\text{C} - \text{O})$ configuration, (d) Side view of $\eta^1(\text{C} - \text{O})$ configuration. Color coding for atoms is same as in Figure 2.1..... 57

Figure 2.5 Schematic showing probable end products that can be obtained from guaiacol and potential mechanisms for the initial activation of guaiacol. The five potential routes via which guaiacol can activate are presented: *C7 - O scission*, *C2 - O scission*, *C1 - O scission*, *Cring hydrogenation*, *Cring - Cring scission*. *Cring* includes the carbon atoms of the benzene ring which are labelled as *C2 - C6*. The nomenclature for carbon atoms is shown in the central guaiacol molecule. Free energy barriers and reaction free energies (in parenthesis) at 623 K and 1 bar are shown above the arrow for each pathway. Green and red color are used for favorable and unfavorable reaction steps, and products, respectively. 58

Figure 2.6 Comparison of free energy profiles for benzene formation on Mo₂C (1 0 0) surface at 623 K and 1 bar via two pathways (a) Anisole formation (in red), and (b) Phenol formation (in blue). Free energy barriers are also shown in red and blue color for the respective pathways in kJ/mol..... 60

Figure 2.7 Free energy profiles of direct ring hydrogenation of guaiacol pathway and catechol ring hydrogenation pathway in blue and red color, respectively. Calculated barriers are shown in kJ/mol..... 62

Figure 2.8 Comparison of free energy profile of Anisole and Phenol ring hydrogenation pathways on Mo₂C surface in red and blue color, respectively. Barriers are shown in kJ/mol..... 64

Figure 2.9 Free energy profile for benzene ring hydrogenation on Mo₂C at 623 K and 1 bar. 65

Figure 2.10 (a) First activation free energy barrier of possible pathways after ring-opening is shown. (b) Free energy profiles for hexane formation via two competitive pathways is shown for guaiacol HDO on Mo₂C surface at 623 K and 1 bar. Kinetically favored pathways are highlighted for the formation of the dominant product (hexene). Above the arrow lines, free energy barriers and reaction free energies (in parentheses) in kJ/mol are indicated. 66

Figure 2.11 Proposed reaction pathway for Guaiacol activation on Mo₂C (100) surface. Kinetically favored pathways for the formation of Benzene, Anisole, Cyclohexene, Cyclohexane and Phenol are shown here. Indicated above the arrows are free energy barriers and reaction free energies (in parentheses) in kJ/mol. According to our calculations, the surface of Mo₂C kinetically and thermodynamically favours benzene and cyclohexene. Green and red colour are used for favourable and unfavourable reaction steps, and products, respectively..... 68

Figure 2.12 Top and side view of the optimized geometry of the most stable guaiacol adsorption configuration over MoWC surface in (a) and (b), respectively. The Mo and W atoms in the carbides are represented as dark cyan and blue spheres, respectively. The atoms in the adsorbed guaiacol is represented by white, red, and grey spheres for H, O, and C, respectively. 69

Figure 2.13 Comparison of free energy barriers of (a) Direct dehydroxylation reaction (b) Ring hydrogenation of cresol among Mo₂C (Green), MoWC (Blue), and MoWC_bulk (Red) catalyst surface. 71

Figure 2.14 Comparison of free energy barriers of (a) Direct dehydroxylation reaction (b) Ring hydrogenation of Phenol among Mo₂C, MoWC, and MoWC_bulk catalyst surface. 72

Figure 2.15 Comparison of ring hydrogen pathway for Benzene and Phenol between Mo₂C and MoWC. Free energy barriers and reaction free energies (in parenthesis) calculated at 623 K and 1 bar with units kJ/mol are shown for Mo₂C (blue) and MoWC (red), respectively..... 73

Figure 2.16 Comparison of ring hydrogen pathway for Benzene and Phenol between Mo₂C and MoWC. Free energy barriers and reaction free energies (in parenthesis) calculated at 623 K and 1 bar with units kJ/mol are shown for Mo₂C (blue) and MoWC (Red), respectively..... 74

Figure 3.1. Schematic of six representative constituents (a) 5-hydroxymethylfurfural, (b) Methyl Glyoxal, (c) Vanillin, (d) Acetic Acid, (e) Levoglucosan, and (f) Eugenol, with different types of functionalities in the real bio-oil. Carbon and oxygen atom numbering in the compounds are also shown. 83

Figure 3.2. Optimized geometries of a) MoWC surface (top view and side view) (b) Mo₂C surface (top view and side view). Dark cyan, blue, and gray spheres represent Mo, W, and C atoms in the carbides, respectively¹²⁵. 84

Figure 3.3 Top view and side view of optimized adsorption configurations of six bio-oil constituents considered in this study on Mo₂C surface (a, c, e, g, i, and k), *and* MoWC surface (b,d,f,h,j, and l). Dark cyan and blue spheres represent Mo and W atoms in the carbides,

respectively. White, red, and gray spheres represent H, O, and C in the adsorbed guaiacol, respectively 85

Figure 3.4 Schematic showing potential reaction paths for the initial activation of 5-HMF and their resulting end products. The eight potential pathways via which 5-HMF can activate are presented: C¹ – O, (ii) C⁶ – O, (iii) C² – O, (iv) C⁵ – O scission, (v) C⁵ – C⁶, (vi) C¹ – C² scission, (vii) C¹ – O hydrogenation, and (viii) C^{ring} hydrogenation. The nomenclature for carbon atoms is shown in the central 5-HMF molecule. 87

Figure 3.5 (a) Electronic energy barriers and (b) reaction energies in the bar graphs are shown below the schematic and each reaction pathway is shown using same color scheme as depicted in figure 4. 89

Figure 3.6 (a) Schematic showing potential reaction paths for the initial activation of 5-MF on Mo₂C surface. The six considered pathways via which 5-MF can activate are presented: C¹ – O, (ii) C² – O, (iii) C⁵ – O scission, (iv) C⁵ – C⁶, (v) C¹ – C² scission, (vi) C¹ – O hydrogenation. The nomenclature for carbon atoms in is shown in the central 5-MF molecule. (b) Comparison of electronic energy barriers and (c) reaction energies in the bar graphs are shown below the schematic for Mo₂C and MoWC and each reaction pathway is shown using distinct colors. 90

Figure 3.7 (a) Schematic for reaction pathways for methyl glyoxal activation on Mo₂C and MoWC surface. (b) Electronic energy barriers and (c) reaction energies for different first activation routes. The six considered pathways via which MG can activate are presented: C¹ – O, (ii) C² – O, (iii) C¹ – C² scission, (iv) C² – C³ scission, (v) C¹ – O hydrogenation, and (vi) C² – O hydrogenation. The nomenclature for carbon atoms is shown in the central MG molecule. (b) Comparison of electronic energy barriers and (c) reaction energies in the bar graphs are shown below the schematic for Mo₂C and MoWC and each reaction pathway is shown using distinct colors. 94

Figure 3.8 (a) Schematic for reaction pathways for acetic acid activation on Mo₂C and MoWC surfaces. (b) Electronic energy barriers and (c) reaction energies for different first activation routes. The four considered pathways via which AA can activate are presented: C¹ – OH, (ii) C¹ – O, (iii) C¹ – C² scission, (iv) C¹ – O hydrogenation. The nomenclature for carbon atoms is shown in the central AA molecule. (b) Comparison of electronic energy barriers and (c) reaction energies in the bar graphs are shown below the schematic for Mo₂C and MoWC and each reaction pathway is shown using distinct colors. 96

Figure 3.9 (a) Schematic showing probable end products that can be produced and demonstrating potential reaction paths for the initial activation of LGA on Mo₂C(left) and MoWC(right) surfaces. All considered pathways via which LGA can activate on both catalysts are presented. The nomenclature for carbon atoms is shown in the central LGA molecule. (a) Comparison of energy barriers and (b) reaction energies in the bar graphs for Mo₂C. (c) Comparison of energy barriers and (d) reaction energies in the bar graphs for MoWC (right side) and each reaction pathway is shown using distinct colors..... 100

Figure 3.10 Schematic of intermediates formed on (a) Mo₂C and (b) MoWC surface. 102

Figure 3.11 (a) and (d) Schematics showing probable end products that can be produced and demonstrating potential reaction paths for the initial activation of intermediate 1 and 2 on Mo₂C (on the left) and MoWC (on the right) surfaces, respectively. All considered pathways via which intermediates can activate on both catalysts are presented. The nomenclature for carbon atoms is shown in the central intermediates. Comparison of energy barriers (b and e) and reaction energies (c and f) in the bar graphs are shown below the schematic for Mo₂C (on the left) and MoWC (on the right) and each reaction pathway is shown using distinct colors..... 103

Figure 3.12 (a) Schematic showing probable end products that can be produced and demonstrating potential reaction paths for the initial activation of vanillin on Mo₂C and MoWC surfaces. The six considered pathways via which vanillin can activate are presented: (i) C¹ – O scission, (ii) C² – O scission, (iii) C⁵ – O scission, (iv) C⁷ – O scission, (v) C⁴ – C⁵ scission, and (vi) C⁵ – O hydrogenation. The nomenclature for carbon atoms is shown in the central intermediate 2 molecule. Comparison of (b) energy barriers and (c) reaction energies in the bar graphs are shown below the schematic for Mo₂C and MoWC and each reaction pathway is shown using distinct colors..... 106

Figure 3.13 (a) Schematic showing probable end products that can be produced and demonstrating potential reaction paths for the initial activation of eugenol on Mo₂C and MoWC surfaces. The five considered pathways via which eugenol can activate are presented: (i) C² – O, (ii) C⁷ – O dissociation, (iii) C⁹ hydrogenation, (iv) C¹⁰ hydrogenation, and (v) Ring hydrogenation. The nomenclature for carbon atoms is shown in the central eugenol molecule. Comparison of (b) energy barriers and (c) reaction energies in the bar graphs are shown below the schematic for Mo₂C and MoWC and each reaction pathway is shown using distinct colors..... 109

Figure 3.14 (a) Schematics showing for the Phenol and Cresol first activation. The two considered pathways via which phenol and cresol can activate are presented: (i) C – O dissociation, (ii) Ring hydrogenation. Comparison of (b) energy barriers and (c) reaction energies in the bar graphs are shown below the schematic for Mo₂C and MoWC and each reaction pathway is shown using distinct colors..... 111

Figure 4.1. Schematic of all the considered catalysts with different compositions and possible terminations. A, B and C represents the respective dopant termination, molybdenum termination and mix of dopant and molybdenum termination, respectively..... 119

Figure 4.2. Schematic of the screening strategy adopted in this work for screening the catalysts with different compositions and possible terminations (A, B and C)..... 121

Figure 4.3 Comparison of mean oxygen binding energy (OBE) for each termination (A, B, C) across all catalysts (with the exception of Zr-doped catalysts) with one standard deviation. The blue and brown colors represent the cases in which $\Theta_{\text{dopant}} < \Theta_{\text{Mo}}$ and $\Theta_{\text{dopant}} > \Theta_{\text{Mo}}$ respectively. The standard deviation for the rightmost dataset is not shown as there is only one value in that dataset (NbMo₃C)..... 122

Figure 4.4 Reaction energies of $OH^* + H^* \rightarrow H_2O$, OR for all 45 catalysts investigated in this work. The green, red, and brown colors represent the selected, eliminated, and reference candidates (Mo₂C and MoWC) respectively. 124

Figure 4.5 Potential energy profiles for the C–OH scission reaction, DDO, on (a) Co-doped Mo₂C, (b) Cr-doped Mo₂C, (c) Fe-doped Mo₂C with low Fe/Mo ratio (d) Fe-doped Mo₂C with high Fe/Mo ratio, (e) Mn-doped Mo₂C, (f) Nb-doped Mo₂C, (g) Ni-doped Mo₂C and (h) Miscellaneous (Mo₂C, MoWC, BMoWC, ZrA). 125

Figure 4.6 Potential energy profiles for the oxygen removal reaction ($OH^* + H^* \rightarrow H_2O$), OR, on (a) Co-doped Mo₂C, (b) Cr-doped Mo₂C, (c) Fe-doped Mo₂C with lower composition, (d) Fe-doped Mo₂C with higher composition, (e) Mn-doped Mo₂C, (f) Nb-doped Mo₂C, (g) Ni-doped Mo₂C and (h) Miscellaneous (Mo₂C, MoWC, BMoWC, ZrA). 128

Figure 4.7 Potential energy profiles for the ring hydrogenation, HYD, on (a) Co-doped Mo₂C, (b) Cr-doped Mo₂C, (c) Fe-doped Mo₂C with lower composition, (d) Fe-doped Mo₂C with higher composition, (e) Mn-doped Mo₂C, (f) Nb-doped Mo₂C, (g) Ni-doped Mo₂C and (h) Miscellaneous (Mo₂C, MoWC, BMoWC, ZrA). 130

Figure 4.8 Variation of C – O dissociation (DDO) barriers with hydrogenation (HYD) barriers for all 35 catalyst surfaces. Color gradient is used to highlight the difference between DDO and oxygen removal (OR) barriers with olive color representing a small difference of < -80 kJ/mol and maroon color representing a large difference > 240 kJ/mol. Markers are shown on the right side to differentiate among catalysts. Plot area is also divided into four regions of high/low selectivity towards HYD/DDO.	133
Figure 4.9 Variation of proposed parameter, $\eta = \Delta\text{HYD} - \text{DDOOR}$, as a function of OBE for all catalysts. Two qualitative trendlines are drawn. The line on the left (low η and strong binding) and right (low η and weak binding) sides are indicated. Region of optimal OBE between -200 kJ/mol to -100 kJ/mol is shaded in blue. Color gradient is used to highlight the difference between DDO and OR barriers with olive color representing a small difference of < -80 kJ/mol and maroon color representing a large difference > 240 kJ/mol. Markers are shown on the right side to differentiate among catalysts.	138
Figure 5.1 (a) P-XRD pattern, and (b) XPS spectra of 3p core levels (c) TEM image, and (d) particle size distribution curve for fresh Ru nanoparticles.	148
Figure 5.2 Schematic of catalytic hydrogenation of phenol over ruthenium catalyst at room temperature in water.	149
Figure 5.3 Schematic of a potential Reaction pathway for the hydrogenation of phenol to cyclohexanol over Ru surface.	151
Figure 5.4 Time dependent reaction profile for hydrogenation of (a) phenol and (b) guaiacol. Reaction conditions: Ru catalyst (0.04 mmol), phenol (1 mmol) or guaiacol (1 mmol), H ₂ (1 bar), water (10 mL), room temperature.	151
Figure 5.5 Products obtained from catalytic hydrogenation reaction of guaiacol over the Ru catalyst at room temperature in water.	152
Figure 5.6 (a) GC-MS of reaction performed in H ₂ O. (b) GC-MS of reaction performed in D ₂ O. Reaction conditions: Ru catalyst (0.04 mmol), phenol (1 mmol), solvent (5 mL), H ₂ (1 bar), room temperature, 75 min.	154
Figure 5.7 (a) Schematic illustrating possible reaction pathways for the first activation of guaiacol. The three considered pathways by which guaiacol can activate are shown: C ⁷ -O scission, C ² -O scission, C ^{ring} hydrogenation. C ^{ring} includes the carbon atoms of the benzene ring which are labelled as C ² – C ⁷ . Free energy barriers and reaction free energies (in parenthesis) at 298 K and 1 bar are	

shown above the arrow for each pathway in gas phase. (b) Comparison of free energy profiles on Ru (101) surface at room temperature and 1 bar for 3 considered pathways: C²-O scission (in orange), C⁷-O scission (in red), and direct C^{ring} hydrogenation (in green). Free energy barriers are also shown in orange, red and green color for the respective pathways in kJ/mol..... 159

Figure 5.8 (a) Schematic illustrating possible reaction pathways for the first activation of phenol. The two considered pathways by which phenol can activate are shown: C¹-O scission, and C^{ring} hydrogenation. C^{ring} includes the carbon atoms of the benzene ring which are labelled as C¹-C⁶. Free energy barriers and reaction free energies (in parenthesis) at 298 K and 1 bar are shown above the arrow for each pathway in the gas phase. (b) Comparison of free energy profiles on Ru (101) surface at room temperature and 1 bar for 2 considered pathways: C¹-O scission (in red), and direct C^{ring} hydrogenation at C³ carbon (shown in green). Free energy barriers are also shown in red and green color for the respective pathways in kJ/mol..... 160

Figure 5.9 (a) Top and side view of the optimized geometry of 18 intact water molecules on the Ru (101) surface (b) Top view and side view of the optimized geometry of 2:1 water-hydroxyl and H* fragments mixture on the Ru (101) surface. The atoms in the adsorbed water molecules are represented by white, red spheres for H, O, and Ru atoms are shown in green spheres, respectively. Relative energies are also reported. 161

Figure 5.10 Optimized geometries and corresponding free energies of guaiacol and phenol adsorption on the Ru (101) surface in the presence of co-adsorbed partially dissociated water molecules (a) Top view and side view guaiacol adsorption in $\eta^2(\text{C}-\text{O})$ configuration, (b) Top view and side view phenol adsorption in $\eta^2(\text{C}-\text{O})$ configuration. The atoms in the adsorbed guaiacol and phenol is represented by white, red, and grey spheres for H, O, and C, respectively and Ru atoms are shown in green color. 162

Figure 5.11 (a) Schematic illustrating possible reaction pathways for the first activation of guaiacol in the presence of water. The three considered pathways by which guaiacol can activate are shown: C⁷-O scission, C²-O scission, C^{ring} hydrogenation. C^{ring} includes the carbon atoms of the aromatic ring which are labelled as C²- C⁶. Free energy barriers and reaction free energies (in parenthesis) at 298 K and 1 bar are shown above the arrow for each pathway. (b) Comparison of free energy profiles on Ru (101) surface in presence of partially dissociated water molecules at room temperature and 1 bar for 3 considered pathways: C²-O scission (in orange), C⁷-O scission (in

red), and direct C^{ring} hydrogenation (in green). Free energy barriers are also shown in red, orange and green color for the respective pathways in kJ/mol. 163

Figure 5.12 (a) Schematic illustrating possible reaction pathways for the first activation of phenol in the presence of water. The two considered pathways by which phenol can activate are shown: C¹-O scission, and C^{ring} hydrogenation. C^{ring} includes the carbon atoms of the benzene ring which are labelled as C¹-C⁶. Free energy barriers and reaction free energies (in parenthesis) at 298 K and 1 bar are shown above the arrow for each pathway. (b) Comparison of free energy profiles on Ru (101) surface in the presence of partially dissociated water molecules at room temperature and 1 bar for 2 considered pathways: C¹-O scission (in red), and direct C^{ring} hydrogenation (in green). Free energy barriers are also shown in red and green color for the respective pathways in kJ/mol. 165

Figure 5.13 Proposed reaction pathway for Guaiacol and Phenol activation on Ru (101) surface. Free energy barriers and reaction free energies (in parenthesis) in kJ/mol for vapor phase (Red) and condensed phase (Green) are indicated above and below the arrows, respectively. Our calculations suggest that 1-methoxy cyclohexanol and cyclohexanol are kinetically and thermodynamically favoured on Ru surface in the presence of water, whereas, benzene, and anisole are kinetically and thermodynamically favoured in gas phase. 167

List of Tables

Table 1.1 Comparison of elemental composition between petroleum crude oil and bio-oil. Adapted from ref:[30].....	4
Table 1.2 Energy Barrier, E_a (kJ/mol), Reaction Energy, E_r (kJ/mol), and Rate Constant, k (423 K) of Furfural Hydrodeoxygenation on the Clean and H-pre-covered Mo_2C (101) Surface. (Adapted from ref: [56])	20
Table 1.3 Comparison of Energy Barrier, E_a (kJ/mol), Reaction Energy, E_r (kJ/mol), of Furfural Hydrodeoxygenation on the Mo_2C (101) and Ru (001) Surface. (Adapted from ref [56])	21
Table 1.4 Comparison of the bond lengths (\AA) and binding energies (eV) of furfural on Mo_2C (0001), Co/ Mo_2C (0001). (Adapted from ref:[63]).....	22
Table 1.5 HDO of lignin model compounds over transition metal carbides	22
Table 2.1. Mo 3d and W 4f Core Level Binding Energy (CLBE) Shifts for different surface atoms on MoWC surface relative to the Mo_2C and W surface, respectively	53
Table 2.2 Calculated d-band center and CO binding energies on Mo_2C and MoWC surfaces projected on the atom highlighted in yellow color.	56
Table 2.3 Comparison of DFT Calculated Free Energy barriers (in kJ/mol) for Ring hydrogenation of Guaiacol Pathways on Mo_2C (100) surface at 623 K and 1 bar.	61
Table 2.4 Comparison of DFT Calculated Free Energy barriers (in kJ/mol) for Ring-Opening of Guaiacol Pathway at 623 K and 1 bar.....	66
Table 2.5 Product distribution observed in two cases over Mo_2C and MoWC catalysts in the HDO of Guaiacol at 623 K, and $P = 400$ psig.	75
Table 4.1 DDO barriers, OR barriers and $\Delta_{\text{HYD-DDO}}$ (kJ/mol) are tabulated for top 10 screened catalysts. The top 4 candidates with optimum balance between DDO and oxygen removal barriers are highlighted in bold.	134
Table 4.2 HYD barriers and $\Delta_{\text{HYD-DDO}}$ (kJ/mol) are tabulated for best screened catalysts. Three most active and selective candidates are highlighted in bold.	135
Table 5.1 Optimization of reaction conditions for hydrogenation of phenol. ^a	150
Table 5.2 Effect of solvent on hydrogenation of phenol over the Ru catalyst. ^a	153
Table 5.3 Hydrogenation of different lignin-derived substrates over the Ru catalyst under optimized reaction conditions ^a	156

Chapter 1: Introduction

1.1 Background

Energy is the basic need for technological and economic development. The economic progress marked with the onset of the industrial revolution in the mid-eighteenth century has seen a noteworthy surge in energy demand. Since then, each year fossil fuels are being consumed in even greater quantities which makes it unsustainable, owing to population growth and development. Now with dwindling reserves of fossil fuels, combined with increased demand for petroleum by emerging economies, and political and environmental concerns, it is imperative to develop economical and energy-efficient processes for the sustainable production of fuels and chemicals. Particularly, in the transportation sector, biomass could provide viable solutions as an abundant carbon source for producing biofuels.¹ The implementation of biofuels derived from biomass would not require extensive changes to the industrial infrastructure and to the internal combustion engines.² The biorefinery concept has some similarities with the petrochemical refinery which would be notably beneficial as the current infrastructures would transform a sustainable source of organic carbon not only into fuels but also valuable chemical products.³

1.1.1 Classification of Biomass

Biomass can be classified into three general classes including: (i) starch- and sugar-based feedstocks; (ii) triglyceride-based feedstocks; and (iii) lignocellulosic feedstocks. The first and the second feedstocks are derived primarily from food crops (e.g. grains, oilseeds, and sugar beet).^{4,5} Increasing production of these biofuels on a larger scale raises concerns about food and energy because of the limited land available for cultivation. On the other hand, lignocellulose, which contributes to the structural integrity of plants, is non-edible by humans and can provide a solution for the food-versus-fuel debate. Lignocellulosic biomass is the most abundant carbon source on the planet. This feedstock can be found in almost all plant-derived materials, while starch and triglycerides are only available in a few parts of plants (for example seeds). Based on these advantages, the utilization of lignocellulosic biomass could avoid the concerns of first-generation biofuels and provide a promising approach for the long-term alternative of crude oil.⁶

1.1.2 Lignocellulosic Biomass – A viable substitute to petroleum

The three major components of lignocellulose biomass, cellulose (40-50%), hemicellulose (25-35%), and lignin (15-20%), are natural organic polymers, in which the monomers are linked together by strong covalent linkages such as β -1-4 glycosidic bonds, β -O-4, 5-5, β -5, and β -1 bonds.⁷ These linkages make them more difficult to be decomposed in comparison to the starch- and sugar-based biomass, hence efficient fractionation is required. As the most bountiful polymer in nature, lignocellulosic biomass is produced on an estimated scale of 200 billion metric tons per year worldwide.⁸ According to an EIA report in 2015, a dry tonne of biomass is estimated to have an energy content of 15 – 19 *Gigajoules (GJ)*, in contrast, a barrel of oil has an energy content of 6.1 GJ and a cubic meter of natural gas has an energy content of 0.0373 *GJ*.^{9,10,11} A review study by Brendes et al.¹² estimated that contribution of biomass in the global energy supply will be in the range of 100 *EJ yr⁻¹* – 400 *EJ yr⁻¹* (*EJ = Exajoules = 10¹⁸ Joules*) by 2050. In Canada, the proportion of biomass in total energy supply was ~7 % in 2024 and continuously increasing from 6.1 % in 2015 and 5.9 % in 2014.¹³ Despite high potential and availability of biomass, the challenge lies in its efficient conversion to biofuels and chemicals.

Biomass can be transformed into specialized chemicals and fuels mainly via three primary routes - Bio-chemical,¹⁴ Physio-chemical, and Thermo-chemical¹⁵. Biochemical conversion involves the use of enzymes of bacteria or other microorganisms to break down biomass through the processes of anaerobic digestion¹⁶, fermentation¹⁷, or composting. Physio-chemical consists of extraction, and thermochemical treatment includes gasification, pyrolysis, combustion, and liquefaction. Among these routes, pyrolysis integrated with upgrading is the simplest and the most cost-effective.¹⁸ In addition, it can be employed in a decentralized manner. Therefore, the resulting bio-oils (pyrolysis oils) have been identified as the cheapest renewable liquid fuels.¹⁹

1.1.3 Thermochemical conversion – Pyrolysis and Liquefaction

Two primary routes to produce bio-oils are Pyrolysis and Liquefaction. Pyrolysis is thermal degradation of biomass by heat (673 K – 1073 K) in the absence of oxygen, which results in the production of charcoal (solid), bio-oil (liquid), and fuel gas products. The main pyrolysis reaction is



The condensable gases, resulting from the pyrolysis of biomass, condense at room temperature to form a corrosive and acidic liquid, bio-oil. While light gases like H₂, CO, CO₂ are non-condensable. Depending on the operating conditions, the pyrolysis process can be divided into 3 subclasses: conventional pyrolysis (carbonization), fast pyrolysis, and flash pyrolysis. The end product mainly consists of char in slow pyrolysis which is usually executed at a low reaction temperature, heating rate, and long residence times. To produce bio-oil (liquid), fast-pyrolysis is preferred.^{20,21} Fast pyrolysis has gained significant attention in the recent past because liquids can be stored and transported more easily and at a lower cost than solid biomass. Moreover, techno-economic studies show that fast pyrolysis is competitive despite the low product value because of significantly low capital cost, high process efficiency, and yields when compared to gasification or biochemical techniques.¹⁸

Hydrothermal liquefaction (HTL) is another technique which can be used to convert biomass into bio-oil, which involves the reaction of biomass in the water at elevated temperatures (573 K – 673 K) and pressures (5–20 MPa) with or without the presence of a catalyst.²² Bio-oil production from the pyrolysis of biomass is considered to have superior economics than that from the high-pressure liquefaction process. Despite the relatively high oxygen content (~50 %), pyrolysis derived bio-oil gives higher yield of bio-oil (~ up to 80 %) as compared to HTL (20 – 60 %), which makes it cost-effective.²³ Additionally, HTL requires high-pressure operating conditions that add to capital investment. Although bio-oil can be produced simply and efficiently, its properties result in multiple significant problems during its utilization as transportation fuels in standard equipments such as combustion boilers, engines, and turbines constructed for use of oil-derived fuels.²⁴

1.1.4 Bio-oil and Need for Hydro-processing

Elemental analysis reveals that bio-oil comprises of more than 400 different types of oxygenated compounds generated from the degradation of biopolymer units (cellulose, hemicellulose, and lignin) during pyrolysis.^{25,26} These compounds are present in a variety of functionalities, including acids, aldehydes, esters, alcohols, ethers, ketones, phenolics, sugars, and furans.²⁷ Bio-oil holds numerous advantages over petroleum crude oil attributing to the properties of sustainability and carbon neutrality. A comparison between the properties of pyrolysis oil and crude oil is shown in Table 1.1.^{28,29} Notably, pyrolysis oil contains insignificant amounts of sulphur and nitrogen, hence, negligible SO_x emissions and >50% lower NO_x emissions than petroleum are generated.

Unfortunately, raw bio-oil has undesirable properties of (i) low heating value, (ii) incompatibility with conventional fuels due to high oxygen content, (iii) high solids content, (iv) high viscosity, (v) chemical instability, and (vi) high acidity and corrosiveness.¹⁹ Therefore, it is imperative to upgrade the bio-oil. The substantial presence of oxygen in nearly every component of bio-oil, and consequently the overall high oxygen content, is the primary difference between bio-oil and petroleum-derived oils. It is reported that the removal of oxygen would have the following effects: (i) heating value increases, (ii) more compatible with crude oil, (iii) reduction in viscosity, (iv) chemically more stable. Therefore, in recent years, significant attention has been paid towards the deoxygenation of bio-oils to produce chemicals and fuels.

Table 1.1 Comparison of elemental composition between petroleum crude oil and bio-oil. Adapted from ref :[30]

Elements	Petroleum crude oil (wt %)	Bio-oil (wt %)
C	83 – 86	55 – 65
H	11 – 14	5 – 7
O	< 1	30 – 50
N	< 4	< 0.1
S	< 1	< 0.05
Water	< 0.1	20 – 30

1.1.5 Bio-oil Upgradation

The purpose of bio-oil upgrading is to convert crude bio-oil into hydrocarbons or other intermediates that can be directly dropped into an existing petroleum refinery for production of “green” gasoline, diesel, or other industrial chemicals. Two general routes for the upgrading of bio-oil are (i) Zeolite cracking, (ii) Catalytic hydrodeoxygenation (HDO). In zeolite cracking, zeolites, like HZSM-5, are used as catalysts for the deoxygenation reactions. In this process, hydrocarbons are converted to smaller fragments through general cracking reactions. The actual oxygen elimination is associated with decarbonylation, decarboxylation, and dehydration, with dehydration being the main route.³¹ Despite the advantage of performing this operation at atmospheric pressure as there is no requirement of hydrogen, bio-oil results in a low H/C ratio of the oil product. Furthermore, extensive carbon deposition results in very short catalyst lifetimes.

Overall, oil from zeolite cracking is of a low grade, with heating values approximately 25% lower than that of crude oil.¹

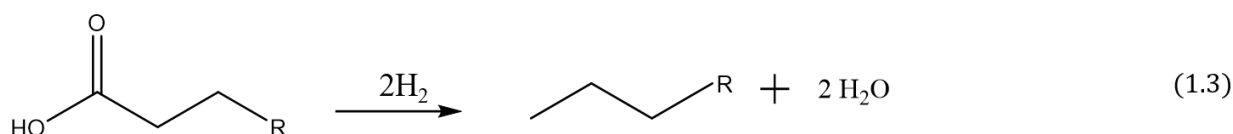
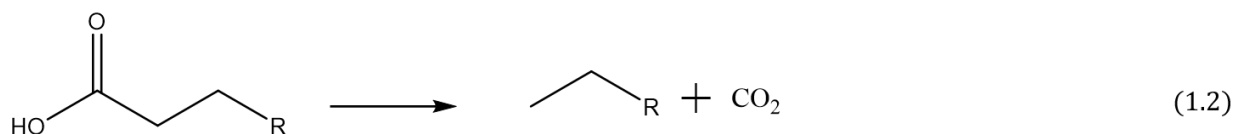
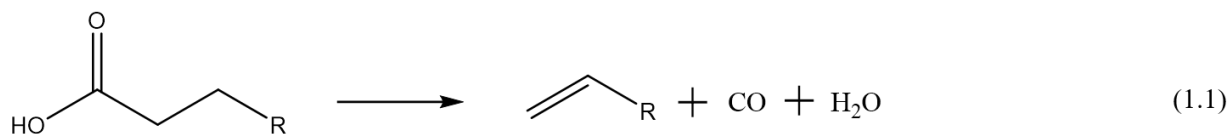


Figure 1.1 Typical reactions which occur in the bio-oil upgrading process.

Catalytic hydrodeoxygenation (HDO) is an efficient method in which hydrogen is used to extract chemically-bound oxygen from the bio-oil, giving a high-grade oil product. In this method, unsaturated compounds in the bio-oil are hydrogenated and oxygen is removed in the form of water as shown in equation 1.3 in Figure 1.1. Oxygen removal in the form of water and saturation of double bonds are the effects of using hydrogen resulting in decreased O/C ratios and increased H/C ratios, both of which increase the fuel grade of the oil by increasing the heating value (HV).³² In 1989, Elliott et al.³³ first proposed the concept of upgrading of bio-oil and since then catalytic HDO has emerged as a key area of research in the scientific community.

The HDO upgrading stage can be integrated into the fast pyrolysis process by few different approaches: (1) Catalytic fast pyrolysis (CFP) which is further divided into two categories: (a) “in-situ” CFP in which catalyst is present in the pyrolysis reactor (b) “ex-situ” CFP, where the vapors formed in the biomass pyrolysis are subsequently passed through a separate catalyst bed, and (2) Aqueous phase processing that refers to down-stream treatment of bio-oil in separate catalytic units/processes using the condensed/collected organic phase of the bio-oil. “In-situ” CFP offers the advantage of both HDO and cracking reactions during bio-oil upgrading at atmospheric pressure, without the requirements of expensive hydrogen or other reactive agents and/or other expenses (heating, high pressure, transfer costs, etc.). However, simultaneous or tandem multiple reactions of catalytic cracking, hydrodeoxygenation, decarbonylation, decarboxylation,

hydrocracking, or hydrogenation occur in one reactor. As a result, various intermediates and products are generated simultaneously and many of them could react further with products from other components in the presence of alkali and alkali earth metals which can also act as catalysts. It can deactivate the catalysts as well leading to low carbon efficiency and high processing costs. Additionally, the optimum pyrolysis temperature may not be ideal for upgrading. On the other hand, ex-situ CFP with catalysts separated from the pyrolyzer, has attracted more and more attention due to its unique advantages of individually optimizing the pyrolysis conditions and catalyst performances. Moreover, the pyrolysis vapor would be of high partial pressure and the residence time will be much higher than that in its ex-situ counterpart. Aqueous phase processing suffers a major drawback as it requires high hydrogen pressure which further increases the hydrotreating cost. Accounting all the factors, ex-situ CFP seems to have an upper hand in the hydrotreating process as it favors the high carbon selectivity to aromatics due to low H₂ consumption. It has its own advantages in terms of high target product selectivity and minimizing undesirable thermal degradation.

1.1.5.1 Types of Catalysts

Till now, three major categories of catalysts have been utilized for hydrotreating bio-oils: (i) transition metal sulfides (TMS), (ii) supported noble metals, and (iii) the more recent catalysts including transition metal carbides (TMC), nitrides, and phosphides.^{30,34} TMS have been employed over decades for the hydrotreatment of petroleum (i.e. hydrodesulfurization and hydrodenitrogenation). The distinct properties of petroleum and bio-oils, with petroleum having around 3000 ppm of oxygen and bio-oils containing up to 500,000 ppm of oxygen, pose a major challenge for TMS catalysts.³⁰ In addition, crude oil contains about 0.1-5 wt% of sulfur while sulfur in bio-oils is at ppm-level, thus the addition of sulphur reagents during the HDO of bio-oils is required to retain TMSs' activity. Alternatively, noble metal catalysts that don't require the addition of sulfur to maintain their activity are less attractive due to their high expense and limited availability. The critical challenge for developing HDO catalysts is to make the upgraded biofuels financially competitive with the current well-established petroleum-based fuels. One solution could be to find inexpensive catalysts which are active, selective and stable under the reaction conditions. Moreover, a selective catalyst can also reduce excessive H₂ consumption which can further reduce the cost. Typically, about 35-420 moles H₂ are used to convert 1 kg bio-oil in HDO processes, while 25 mol/kg is theoretically needed to obtain completely deoxygenated biooil.³⁵

Development of novel hydrotreating catalysts that can work under low-pressure hydrogen near stoichiometric requirement and selectively favor cleavage of C – O bond over C – C and C – H bonds is highly desirable. Since Levy and Boudart discovered that TMCs exhibit characteristics similar to those of platinum group metals, these noble metal-like catalysts have attracted a lot of interest and are now being investigated as alternate, less expensive catalysts for HDO of bio-oil.³⁶ Mo₂C-based catalysts are now known to be bifunctional, with both hydrogen-active and acid-site functionalities^{37–39}, and that this bifunctionality is essential to hydrodeoxygenation.³⁰ Since then TMCs, nitrides, and phosphides have gained great attention over the past decade, with metal carbides showing their potential in catalytic hydrotreatment of bio-oils. TMCs have been reported to possess bifunctional properties and favour direct deoxygenation (DDO) and/or HDO routes. Moreover, they possess catalytic properties similar to noble metal-based materials with much lower cost of preparation.⁴⁰

1.2 Literature Review

In this literature review, section 1.2.1 and 1.2.2 provide a comprehensive account of experimental and computational studies undertaken to analyze transition metal carbides (TMCs) tested to upgrade the pyrolysis derived bio-oil via catalytic fast pyrolysis (CFP) method. Section 1.2.3 will focus on the aqueous phase processing of the bio-oil.

This section is broadly divided into two categories:

1. Hydrodeoxygenation (HDO) of real bio-oil
2. Hydrodeoxygenation (HDO) of model compounds
3. Aqueous phase processing of bio-oil

1.2.1 Hydrodeoxygenation (HDO) of real Bio-oil

The first attempt was from Oak Ridge national laboratory (ORNL) and Pacific Northwest National Laboratory (PNNL) in the United States.⁴¹ Choi and co-workers carried out the HDO of pine-derived bio-oils over various metals doped-Mo carbides in the 2-stage fix bed reactor designed at PNNL. More specifically, the 2-stage reactor contains two different heating zones operating at low temperature (< 200°C) and at moderate temperature (350-400°C), in which the glass beads were

inserted in the middle for separating the two zones and for preventing heat transfer. It should be noted that, this design is critical for stabilizing the HDO process in the long time on stream (TOS). Indeed, the active species such as carbonyl and carboxyl groups in pyrolysis bio-oil were partially hydrogenated in the first stage at mild temperature, and then were introduced to the second stage at a higher temperature for deep-HDO. The hydrogenation-stabilization step at a mild temperature reduces the chances of oligomerization and further polymerization of the active species at a higher temperature which often induces the coke formation.⁴²

Among the catalysts studied, the authors reported that Ni-doped Mo carbides outperformed with a residual oxygen content of 1.29 wt% and a total acid number less than 0.01 mg KOH g⁻¹. Moreover, the stability of the metal-doped Mo carbides was verified over a TOS of 240h, in which no bulk oxidation, significant structural changes, and bed plugging were observed. More recently, Remón and co-workers carried out the HDO of the fast pyrolysis bio-oil derived from pine sawdust over Mo₂C/CNF catalysts in batch reactor for producing biofuels and chemicals.⁴³ The optimal product they obtained had a residual oxygen content of 13 wt% and a heating value of 35 MJ/kg, in contrast to the raw bio-oil, which had 47 wt% oxygen and a heating value of 19 MJ/kg. Nonetheless, the authors observed that solid yield increased from 19% to 41% upon the increasing temperature from 250 to 350°C, respectively, resulting from the polymerisation of phenolic compounds and lignin oligomers. Lopez and colleagues looked at the use of Mo₂C and sulfided NiMo catalyst for upgrading bio-oil derived from acacia wood at 623 K.⁴⁴ Both catalysts exhibited a tendency to boost the concentrations of carbon and hydrogen in the samples while dramatically lowering the levels of oxygen, which improved the heating value of bio-oil. Moreover, the upgrading procedure utilizing Mo₂C was observed to be more effective since it raised the carbon percentage from 63.8 to 85.4 and the hydrogen percentage from 8.1 to 9.7, while lowering the oxygen percentage from 28.1 to 4.9. To sum up, the TMCs have shown their promising catalytic performance not only in model HDO reactions but also in the practical hydro processing of pyrolysis derived bio-oil. Furthermore, for the HDO of the fast pyrolysis bio-oil, the multi-stage process is essential to optimize the catalytic activity and stability, allowing this approach to be more feasible in industry.

1.2.2 Hydrodeoxygenation (HDO) of model compounds

Considering the complex composition of lignin-derived bio-oil and the difficulty in deconvoluting possible reaction pathways during deoxygenation process, most HDO investigations employ

model compounds to obtain fundamental mechanistic understanding of the role and interaction of metal, promoter, support, and operating conditions in HDO process. Moreover, using model compounds helps in evaluating the performance and selectivity of catalysts under controlled conditions, facilitating the identification of the most effective catalysts for the HDO process. The insights gained from studying model compounds can be used to improve the selectivity and stability of TMCs which is still a critical issue. Knowledge of the underlying chemistry and mechanisms of model compounds can allow for better control over the desired products, reducing unwanted side reactions and it can be further applied to the more complex bio-oil mixtures. The following subsections will cover the model compound based HDO studies.

1.2.2.1 HDO of linear chain carbonyl and carboxyl groups derived from bio-oil (aldehydes, ketones, and carboxylic acids)

▪ *Experimental Studies*

Since pyrolysis bio-oil comprises of 20-30% of organic compounds with carboxylic acid, aldehyde, and ketone functionalities, the investigation of TMCs' HDO activity over these compounds is necessary. Ren et al. studied the HDO activity of porous β - Mo_2C over propanal and found unprecedented selectivity to propylene as shown in Figure 1.2.⁴⁵ The low selectivity towards C_2 products suggests that the catalyst primarily facilitates the cleavage of $\text{C}=\text{O}$ bonds rather than $\text{C}-\text{C}$ bond scission. Hydrogenation of propylene to propane wasn't observed even under excess hydrogen supply which explains the crucial role of hydrogen feed to keep the catalyst activity during the reaction. In fact, the strong oxygen binding to Mo_2C surface during HDO induces the poisoning of the catalyst active sites and thus its rapid deactivation as confirmed by the HDO reaction in absence of hydrogen feed. Thus, hydrogen plays two important roles, oxygen removal from the reactant and simultaneous regeneration of the catalyst active sites. Similar explanations were further provided by Schaidle et al. where they also observed a noticeable production of H_2O during the HDO of acetic acid.⁴⁶ It was attributed not only to removal of oxygens from acetic acid but also to the removal of surface hydroxyl groups to regenerate the catalyst deoxygenation active sites. Ren et al. also studied the deoxygenation of propanal and propanol using WC.⁴⁷ Similar to Mo_2C , WC showed high selectivity to produce propylene by the scission of $\text{C}=\text{O}$ bonds. The authors modified the WC surface by Ni and noticed switched selectivity to $\text{C}-\text{C}$ bond scission, producing ethylene. It can be correlated to the suppression of oxygenates adsorption sites by doped Ni atoms. HREELS experiments revealed that propanol adsorption on WC led to the dissociation

of the O-H bond as no O-H mode was observed in the spectra (Figure 1.3). Thus, maintaining the carbide selective catalytic activity for longer reaction time requires high hydrogen pressure as this inhibits the hindering of catalyst active sites by oxygen.

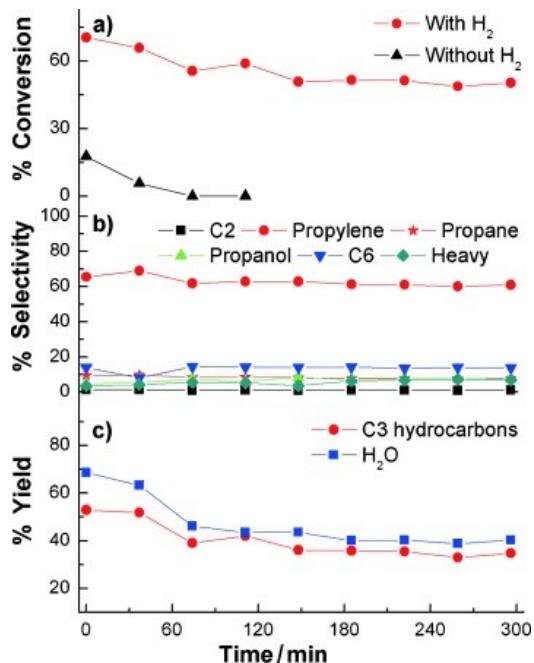


Figure 1.2 a) Conversion of propanal at 573 K with and without co-feed H₂ (atmospheric pressure of H₂), b) selectivity of C₃ + at 573 K with H₂, and c) comparison of the yields of C₃ hydrocarbons and water from propanal with H₂. The products from propanal include C₂ species (ethylene and ethane from the cleavage of one of the C – C bonds), C₃ products (propylene and propane) from C-O scission, C₆ (2-methyl-3-pentanone) from the coupling of oxygenates, and H₂O from the removal of oxygen (Reproduced with permission from Wiley from ref. [45])

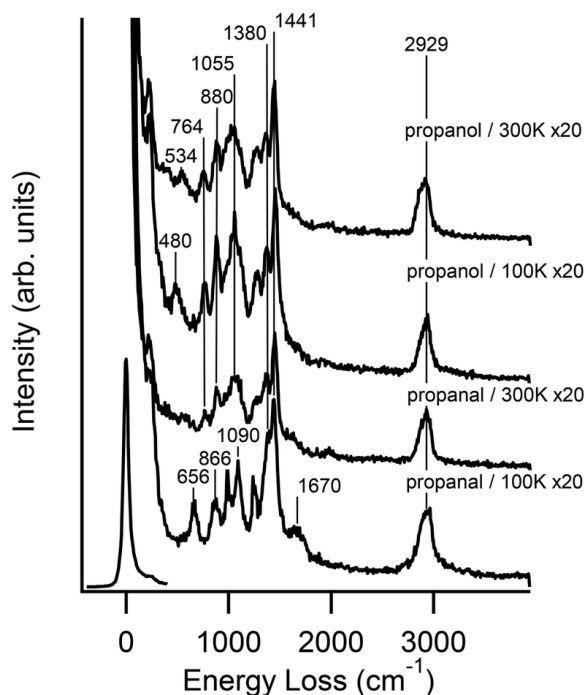


Figure 1.3 HREELS spectra from WC surface exposed to propanol or propanal. (Reproduced with permission from RSC from ref [47])

Sullivan et al. confirmed the bifunctionality of Mo_2C during acetone deoxygenation by modifying the molybdenum carbide surface.³⁷ The catalysts underwent pre-treatment under oxygen and hydrogen, separately. In oxidizing conditions, there is an increase in the oxy-carbide phase, leading to enhanced Brønsted acidity of the catalyst. Conversely, treatment under hydrogen reduces this acidity by reducing oxy-carbide functionalities, thereby increasing the exposure of metal sites on the catalyst's surface. It was confirmed that the hydrogenation of the $\text{C}=\text{O}$ of acetone occurs on the metal sites (catalyst treated under hydrogen) giving isopropyl alcohol (IPA), while the dehydration of the latter occurs over acidic Brønsted sites of the transition metal carbides (Figure 1.4). The authors used IPA as a reactant with oxidized molybdenum carbide and found that the catalyst was active to the production of (propylene and propane). However, upon introducing acetone to the oxidized catalyst, the (propylene and propane) formation rate decreased drastically (Figure 1.5). This result suggests that excessive oxidation of the catalyst induces the suppression of the hydrogenation functionality and thus blocks the first step of the HDO of acetone to isopropyl alcohol. Thus, successful HDO of acetone to a mixture of propylene and propane requires controlled bifunctional molybdenum carbide with adjusted acidity while preserving the hydrogenation functionality.

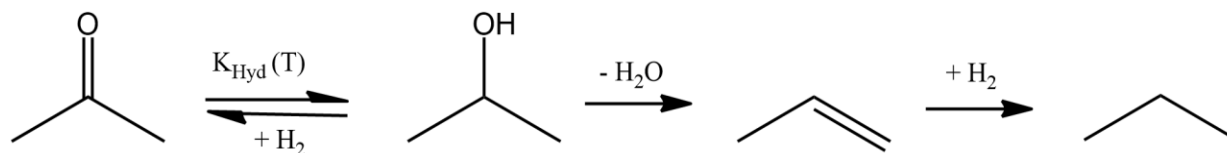


Figure 1.4 A schematic of proposed Acetone HDO Reaction Pathway (Reproduced with permission from ACS from ref. [37])

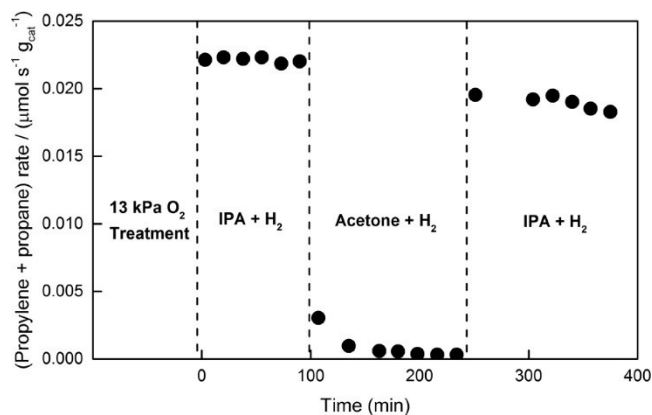


Figure 1.5 Acetone HDO rate, defined as combined rate of formation of (propylene + propane), normalized by catalyst loading, with $T = 369 \text{ K}$, 0.53 kPa of IPA or acetone feed, 54 kPa of H_2 , 4 kPa of CH_4 as an internal standard, $0.29 \text{ g}_{\text{cat}}$ loading, and $\sim 1.83 \text{ cm}^3 \text{ s}^{-1}$ total flow. Activated catalyst was treated with $13 \text{ kPa } O_2$ cofeed with no H_2 cofeed at $T = 369 \text{ K}$ for $\sim 4 \text{ h}$ preceding $t = 0$ shown above; total pressure 1 atm . (Reproduced with permission from ACS from ref. [37])

Baddour et al. reported that different acid to H-sites ratios in $\alpha\text{-Mo}_2\text{C}$ changed the deoxygenation reaction pathway of acetic acid. Indeed, low acid site to H-site ratio of 8.1 led to higher HDO selectivity by producing C_2 hydrocarbons whereas a higher acid-site to H-site ratio shifts the product selectivity to C_1 hydrocarbon through decarboxylation.⁴⁸ Schaidle et al. studied the HDO of acetic acid over Mo_2C and reported acetaldehyde and ethylene as the major products at reaction temperature below 400°C .⁴⁶ On the other hand, temperatures ranging from $400\text{-}550^\circ\text{C}$ shifted the catalyst selectivity to C—C bond scission by decarboxylation and/or decarbonylation. The hydrogenation active sites were reported to be on exposed Mo or C sites and their availability was proposed to be an indicator of the catalyst activity. Indeed, during the HDO of acetic acid to ethylene, acetaldehyde and ethanol were formed as intermediates. The authors found that ethylene formation from the dehydration of ethanol was relatively facile in comparison to the hydrogenation

of acetaldehyde to ethanol due to the high surface coverage of acidic site (40%) against only 5% for H₂ chemisorption sites.

▪ *Computational Studies*

At times, it can be challenging to investigate the 1) Nature and active sites on the catalyst, 2) Accurate atomic configuration/molecular structure of the catalyst, and 3) Interaction of the reactants and the products with the catalyst material, and 4) Investigation of elementary reactions and their energetics using experiments alone. Computational methods may offer a solution in this situation for understanding the mechanistic pathways and identifying the intermediates involved in HDO. The understanding of catalytic reaction pathways enables researchers in catalysis to modify the catalyst's properties at a molecular level to enhance its performance for a specific reaction. Additionally, understanding of the electronic properties of catalysts and reactants can substantially aid in the selection of suitable catalysts.

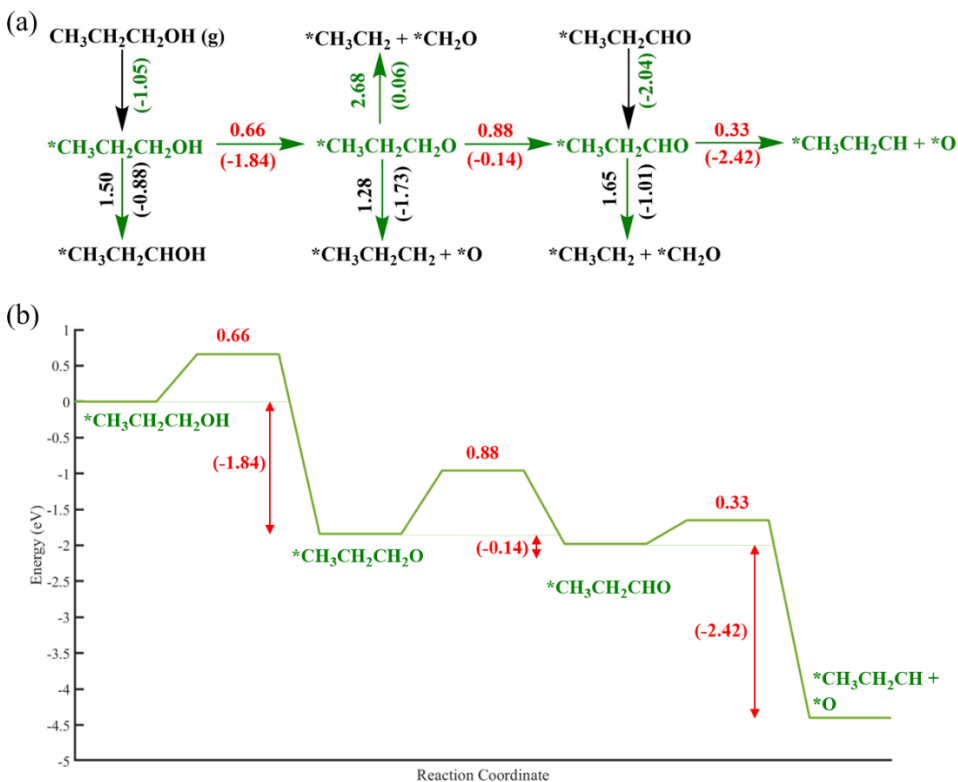


Figure 1.6 (a) Schematic of the possible reaction pathway for propanol and propanal decomposition on the WC (0001) surface. The activation barrier (and the corresponding reaction energy in parenthesis) is in eV. The energetically favorable pathway is highlighted in green. (b)

Energy profile of the most favorable reaction pathway for propanol decomposition on the WC (0001) surface. (Adapted from ref: [45])

Several authors have employed density functional theory (DFT) to investigate the underlying reaction energetics of HDO chemistry using model compounds. As discussed previously, Ren et. al. investigated tungsten carbide, (WC (0001)), and molybdenum carbide (Mo_2C (0001)) catalysts for the HDO mechanism of propanol and propanal.^{45,47} These compounds were selected due to their simple structures which allow the detailed DFT investigation of reaction energetics for pathways including C – C and C=O/C – O bond scission. Furthermore, it also reveals if and how the deoxygenation activity differs between C–O and C=O bonds, which frequently occur in biomass-derived compounds. On closed-packed WC (0001) surface, propanol and propanal molecules strongly chemisorbed with high adsorption energies of -1.05 eV, and -2.04 eV, respectively. A complete schematic of the considered reaction pathways is shown in Figure 1.6a. For propanol, C – H dissociation leading to propanal formation is calculated to be the feasible pathway over C – C or direct C – O cleavage with the lowest barrier of 0.88 eV. Upon propanal formation, direct C – O bond dissociation becomes more facile showing a barrier of 0.33 eV, as shown in the energy profile in Figure 1.6b. In another study, the authors investigated propanal HDO on Mo_2C (0001) surface demonstrating high selectivity towards C – O bond scission with the lowest barrier of 0.61 eV in comparison to the C – C cleavage which requires much higher energy of 1.21 eV as shown in Figure 1.7. Both of these aforementioned studies indicate that both metal carbides are selective towards direct C – O/C = O bond scission leading towards the formation of propane after hydrogenation reaction steps. It is to be noted here that C – O bond cleavage is relatively more facile on WC (0001) in comparison to Mo_2C (0001). It could be attributed to the high oxophilic nature of WC.

Schaidle and coworkers performed a combined experimental and computational investigation of acetic acid deoxygenation over partially oxidized Mo_2C catalyst ($\text{O}^*\text{-Mo}_2\text{C}$) to elucidate the role of Brønsted acidic sites which has been reported to play a key role in dehydration.⁴⁶ These acidic sites form as a result of the interaction between oxygen and the Mo_2C surface and they propose that two distinct types of sites (metallic sites and acidic sites) are required in the HDO chemistry. However, it was observed that when oxygen coverage increased, the number of active sites available on the Mo_2C surface decreased (either from oxygen treatment or oxygenated reactants). It was found out that 0.75 ML and 0.5 ML of oxygen is the most favourable on Mo-terminated

Mo₂C, and C-terminated Mo₂C, respectively. Regarding the favourable pathway, cleavage of C – O bonds were computed to be more facile than C – C bonds producing primarily acetaldehyde and ethylene likely proceeding through a pathway including an ethoxy intermediate. It was proposed that these C – O cleavage steps proceed over either the acidic hydroxyl sites or oxygen vacancy (exposed Mo) sites. The hydrogenation of surface-bound intermediates was limited due to the low density of metallic-like H-adsorption sites on the Mo₂C surface, thus resulting in a product mixture favoring acetaldehyde instead of ethylene/ethane. In a similar comparison of both Mo- and C-terminations based on Mo₂C (0001) catalyst, Martinez and co-workers investigated the direct deoxygenation of carbonyl bonds (C = O) found in ketone and aldehydes.⁴⁹ The authors employed three typical oxygenates: formaldehyde, acetaldehyde, and cyclopentanone. Reaction energy profile calculations indicated that the rate of direct deoxygenation would be different on the C- and M-terminated polymorphs. Additionally, the Mo-terminated polymorphs' projected lower reaction barriers (0.12 and 0.15 eV) for cyclopentanone demonstrating a more feasible dissociation step. According to the computed transition state geometries for both Mo- and C-terminated Mo₂C, the C = O bond-breaking step occurs on Mo atoms, making their placement on the carbide surface vital.

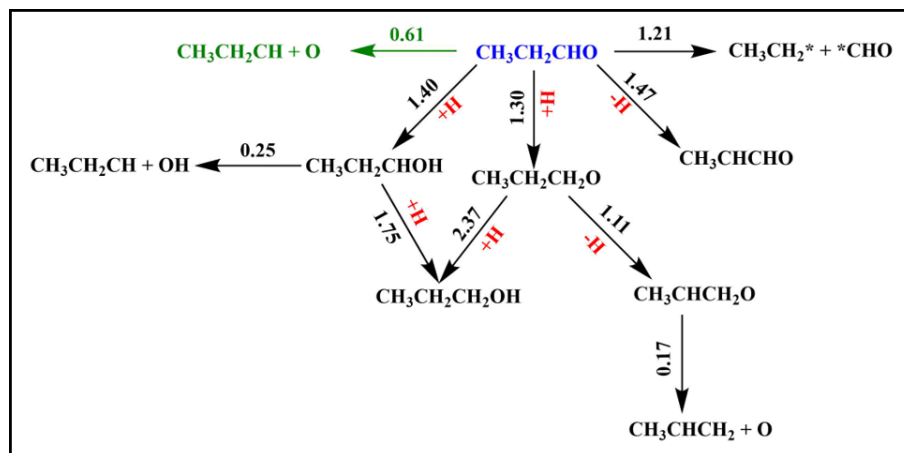


Figure 1.7 Schematic of the key reaction pathways for propanal decomposition and hydrogenation on a Mo₂C (0001) surface. The most facile pathway is highlighted in green and the activation barriers shown above the arrows are in eV. (Adapted from ref: [47])

The research described above suggests promising catalytic activity of TMCs, particularly molybdenum and tungsten carbides in HDO chemistry. In the case of Mo₂C, although it is highly

active towards C – O hydrogenolysis, it is prone to deactivation due to retainment of O atoms on the catalyst surface during HDO, resulting in the formation of molybdenum oxycarbide and hence, blocking the available active sites. DFT calculations performed by Rodriguez and co-workers also suggest that O atoms resulting from the deoxygenation reactions can bind very strongly to both C and Mo sites of molybdenum carbides with adsorption energies of ~520, and ~786 kJ/mol.⁵⁰ Therefore, high hydrogen pressure is required to avoid the retainment of O atoms on the catalyst's surface, by removing them in the form of H₂O. Lee et. al. investigated a spent Mo₂C catalyst after vapor phase anisole HDO using transient kinetic measurements combined with temperature-programmed surface reaction with H₂ (TPSR).⁵¹ They observed oxygen accumulation in/on Mo₂C catalysts even at high H₂-to-anisole molar ratio (~110) in the reactant feed at 423 K under ambient pressure. However, it changes the catalyst's selectivity because, when hydrogen pressure is high, it prefers ring hydrogenated products, which increases H₂ consumption. Furthermore, high temperatures might cause carbon to build up on the catalyst surface.^{52,53}

In the quest of further optimizing the catalytic activity of transition metal (TM) carbides and tune the ratio of two distinct active sites to enhance the HDO performance, it has been shown that the mere presence of other TMs such as iron and nickel into either tungsten or molybdenum carbide lattice can improve the catalytic activity of these materials.^{54,55} Therefore, several bimetallic carbide catalysts (i.e. Ni–Mo, Co–Mo, Ni–W, Nb–Mo, and Pt–Mo) have been further investigated till now for the HDO process owing to their superior hydrotreating performance compared to their corresponding single components.^{56–59}

Yu et. al. explored Ni-modified WC catalyst using a combination of DFT calculations and experiments for the selective bond scission of the C – OH and C = O functionalities using glycolaldehyde as a model substrate.⁶⁰ Additionally, they investigated Ni/WC system to explore the possibility of replacing Ni/Pt with Ni/WC as an active catalytic system with higher stability and lower cost. They observed that glycolaldehyde binds more strongly to bimetallic carbide (1ML NiWC) in comparison to bimetallic (NiPtPt) catalyst (-31.14 kcal/mol vs. -30.63 kcal/mol). It demonstrates that WC could be a viable replacement for expensive platinum as 1ML Ni/WC and NiPtPt (111) surfaces exhibit very similar glycolaldehyde binding energies, and the surface d-band center values. In another study, the authors extended this study to three C₂ oxygenates with different combinations of –OH, –C=O, and –COOH functional groups, namely, ethylene glycol,

acetaldehyde, and acetic acid on clean WC and Ni-modified WC surfaces.⁶¹ A reduction in binding energy was observed on Ni-doped WC catalyst for all three substrates. It could be attributed to the insertion of Ni into WC lattice, which decreases its oxophilicity as Ni is known to be active towards the hydrogenation reactions. This also suggests that different reaction pathways may be favored on the WC surface. Temperature Programmed Desorption (TPD) measurements confirmed that all the three C₂ oxygenates prefer deoxygenation pathway to produce ethylene on clean WC surface, resulting from the C–O bond scission with the C–C bond remaining intact. On the contrary, C₂ oxygenates follow the reaction pathways involving C–C bond cleavage on Ni–WC surfaces converting C₂ oxygenates to syngas. To corroborate the reported product distribution, a comprehensive investigation of reaction energetics incorporating all of the elementary reaction steps is extremely desired. It can compare the performance of different active sites for C–C or C–O bond cleavages which ultimately can help in designing better catalysts.

From a computational standpoint, only a few mechanistic investigations employing TMCs, particularly Mo₂C and WC, for the HDO of bio-oil derived model compounds have been reported. These studies provide valuable insights about the efficacy of these carbides towards the selective C–O bond scission in comparison to other competitive pathways (C–C scission, C–H scission etc.). Nevertheless, these are confined to small C₂-C₃ model compounds, which do not accurately represent the composition of bio-oil, which is much more diverse. Hence, more detailed investigation of reaction energetics using complex model compounds is highly desirable which will surely aid in the design of HDO catalysts. Although metal carbides demonstrate high activity and selectivity, there are concerns about high hydrogen consumption, and their stability. One possible solution to suppress the hydrogen consumption could be to add other TMs into the parent monometallic carbide which can alter its catalytic activity. Studies investigating bimetallic carbides exist but very limited information is available about their microstructure and catalytic activity in HDO chemistry.

1.2.2.2 HDO of carbohydrate fractions (levoglucosan, Glucose) and furanic units (HMF, Furfural)

▪ *Experimental Studies*

Cellulose and hemicellulose comprising more than 55% of lignocellulosic biomass are converted into anhydrosugars and further dehydrated to furanic compounds during pyrolysis, and hence

furfural is a major component of biooils derived from cellulosic fraction in biomass.⁶² Furfural can be upgraded via HDO or hydrogenation to different high-value products that are commercially viable, such as furfuryl alcohol (FA), methyl furan (MF), methyl tetrahydrofuran (MTHF), tetrahydrofurfuryl alcohol (THFA), levulinic acid (LA), and maleic acid. The selective removal of oxygen in the carbonyl group $-C(H)=O$ while leaving the C₅ ring intact via catalytic HDO is an appealing pathway for fuel production. To carry out this task, Mo₂C and Co/Mo₂C were reported to be highly selective for facilitating the C=O bond cleavage in the aldehyde group of furfural to produce 2-MF as the major product with a selectivity of 60%.^{63,64} It should be noted that those works were carried out in the vapor-phase at atmospheric pressure and low temperature ($\leq 250^\circ\text{C}$), in which furfural reactant was introduced in the vapor phase with H₂ into a tubular quartz reactor containing the activated metal carbides. To get insight into the reaction mechanism, temperature-programmed desorption (TPD) equipped mass spectrometer and high-resolution electron energy loss spectroscopy (HREELS) techniques were used to investigate the HDO of furfural over the Mo₂C surface. These techniques allow monitoring the intermediates formed during the hydrotreating reactions. To verify if FA is an intermediate for the conversion of furfural to 2-MF, FA was injected over the hydrogen-pre-covered surface of Mo₂C. The observed HREELS and TPD spectra indicated the presence of methylfuran-like intermediates in the HDO of FA, which is similar to those in the HDO of furfural.⁶⁴

This observation suggests that during the HDO reaction, furfural tends to adsorb on the carbides via its carbonyl group resulting in the hydrogenation of the $-C(H)=O$ to form FA, followed by HDO of $-CH_2-OH$ group to produce 2-MF as the main product. The selectivity of furfural HDO can be modified by doping different promoters onto the transition metal carbides. While Co was reported to stabilize the catalyst activity by facilitating the removal of surface oxygen, Ni was found to enhance the rate of hydrogenation of both the aldehyde group and the furan ring.^{65,66} More specifically, the rate constant of furfuran hydrogenation to FA was shown to increase linearly with increasing atomic ratio of Ni/Mo from 1 to 6.⁶⁵

▪ *Computational Studies*

As mentioned before, furfural is one of the key components present in bio-oil, and is a precursor to the formation of methylfuran (MF), which is an excellent gasoline additive. Noble metals, particularly, Ru-based catalysts have been proposed as potential candidates for the condensed-

CH₂O) whereas, the dissociation pathway includes the removal of hydrogen from the carbon of C = O group (F-CHO → F-CO+H). The former leads to 2-methylfuran formation through furfural hydrogenation into furfuryl oxide, followed by the dissociation of C=O bond and finally converted to 2-methylfuran after hydrogenation at the carbon atom. The latter results in the formation of furan which is initiated after the C–H dissociation of furfural, followed by the C-C scission from the F–CO intermediate. Results based on the computed minimum energy path on the clean surface, both reaction pathways are found to be kinetically and thermodynamically competitive with similar energy barriers and reaction energies of 111(12) and 97(7) kJ/mol, respectively as tabulated in Table 1.2. In contrast, furfural hydrogenation route becomes more favourable on hydrogen pre-covered Mo₂C (101) as the barrier for dissociation pathway (F – CHO → F – CO + H) significantly increased to 152 kJ/mol in comparison to 121 kJ/mol for the hydrogenation step (F-CHO+H → F-CH₂O) and it also becomes highly endothermic with a reaction energy of 105 kJ/mol. Moreover, surface micro-kinetics also shows that high H₂ partial pressure can promote 2-methylfuran formation and suppress furan formation as the calculated rate constant for the hydrogenation reaction steps was computed to be 10⁴ times higher than the competitive dissociation pathway on hydrogen pre-covered Mo₂C surface. It doesn't commensurate well with experimental findings reported by Lee and co-workers, where they observed a high selectivity of ~50 – 60 % towards 2-MF formation on clean Mo₂C surface at 423 K under ambient pressure conditions. Moreover, furan selectivity was found to be even less than 1%.

Table 1.2 Energy Barrier, E_a (kJ/mol), Reaction Energy, E_r (kJ/mol), and Rate Constant, k (423 K) of Furfural Hydrodeoxygenation on the Clean and H-pre-covered Mo₂C (101) Surface. (Adapted from ref: [69])

Reaction	Clean Mo ₂ C (101) surface			H- precovered Mo ₂ C surface		
	E_a	E_r	k	E_a	E_r	k
1. F-CHO + H → F-CH ₂ O	111	12	3.95×10^{-1}	121	-7	2.39×10^{-2}
2. F-CHO + H → F-CHOH	129	50	2.72×10^{-3}	135	34	4.84×10^{-4}
3. F-CHO + H → F-CO + 2H	97	7	2.14×10^1	152	105	7.09×10^{-6}
4. F-CHO + H → F-CH + O + H	160	-16	6.60×10^{-7}	172	2	2.75×10^{-8}
5. F-CHO + H → F + CHO + H	142	16	1.12×10^{-4}	151	68	1.14×10^{-5}
6. F-CH ₂ O + H → F-CH ₂ OH	91	46	1.05×10^2	104	28	3.27×10^0

7.	$\text{F-CH}_2\text{O} + \text{H} \rightarrow \text{F-CH}_2 + \text{O} + \text{H}$	63	-119	2.42×10^5	71	-49	3.08×10^4
8.	$\text{F-CH}_2 + \text{O} + \text{H} \rightarrow \text{F-CH}_3 + \text{O}$	95	17	3.34×10^1	110	-75	5.00×10^{-1}

On comparing the common pathways between the two aforementioned studies, it can be clearly seen that both Ru and Mo₂C catalysts showed similar barriers for the same reaction as tabulated in Table 1.3. For instance, R1, R4, and R5 which involve 3 different types of reaction namely C – O hydrogenation, C–O cleavage, C–C cleavage, respectively. Both catalysts showed relatively similar barriers and reaction energies which confirms that both Ru and Mo₂C exhibit similar HDO activity owing to their excellent hydrogenation and deoxygenation capabilities. However, high selectivity was calculated towards the formation of furfuryl alcohol which further confirms that Ru and TMCs behave similarly in the HDO process.

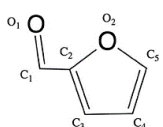
Table 1.3 Comparison of Energy Barrier, E_a (kJ/mol), Reaction Energy, E_r (kJ/mol), of Furfural Hydrodeoxygenation on the Mo₂C (101) and Ru (001) Surface. (Adapted from ref [69])

Reaction	Mo ₂ C (101) surface		Ru (001) surface	
	E_a	E_r	E_a	E_r
1. $\text{F-CHO} + \text{H} \rightarrow \text{F-CH}_2\text{O}$	111	12	121	-7
2. $\text{F-CHO} + \text{H} \rightarrow \text{F-CHOH}$	129	50	135	34
3. $\text{F-CHO} + \text{H} \rightarrow \text{F-CO} + 2\text{H}$	97	7	152	105
4. $\text{F-CHO} + \text{H} \rightarrow \text{F-CH} + \text{O} + \text{H}$	160	-16	172	2
5. $\text{F-CHO} + \text{H} \rightarrow \text{F} + \text{CHO} + \text{H}$	142	16	151	68
6. $\text{F-CH}_2\text{O} + \text{H} \rightarrow \text{F-CH}_2\text{OH}$	91	46	104	28
7. $\text{F-CH}_2\text{O} + \text{H} \rightarrow \text{F-CH}_2 + \text{O} + \text{H}$	63	-119	71	-49
8. $\text{F-CH}_2 + \text{O} + \text{H} \rightarrow \text{F-CH}_3 + \text{O}$	95	17	110	-75

Recently, transition metal doped Mo₂C catalysts have also been tested for furfural HDO. Lin and co-workers performed DFT calculations to investigate the adsorption configuration of furfural on Mo₂C(0001) and Co/Mo₂C(0001) surfaces.⁶³ They used Co overlayer to modify Mo₂C and investigated its effect on the binding energies and adsorption configuration. Table 1.4 summarizes the bond lengths and the binding energies of furfural on the two surfaces. Compared to gas phase furfural, the bonds of adsorbed furfural on the Co/Mo₂C (0001) and Mo₂C (0001) surfaces are both

elongated, consistent with a η^2 -(C, O) bonding configuration via the carbonyl group. The elongated C₁–O₁ bonds should facilitate the bond scission and the subsequent 2-MF formation on both surfaces. In addition, C₁–C₂ bond is shortened on both surfaces, indicating that the C–C bond scission pathway to form furan is not preferred. Moreover, the oxygen and furfural binding energies are both stronger on Mo₂C (0001) than on Co/Mo₂C (0001). This difference suggests that the surface oxygen and furfural can be more easily removed from Co/Mo₂C (0001) during the reaction, leaving the active sites open for the subsequent reaction.

Table 1.4 Comparison of the bond lengths (Å) and binding energies (eV) of furfural on Mo₂C (0001), Co/Mo₂C (0001). (Adapted from ref:[63])

	C ₁ – O ₁ (Å)	C ₁ – C ₂ (Å)	Furfural binding energy (eV)	Oxygen binding energy (eV)
Gas phase	1.23	1.45		
Mo ₂ C (0001)	1.36	1.43	-3.62	-9.47
Co/Mo ₂ C (0001)	1.35	1.42	-2.08	-7.96

1.2.2.3 HDO of oxygenated aromatic rings (lignin components)

▪ Experimental Studies

Lignin is the most abundant source of aromatics on earth. Lignin valorisation ideally consists of its depolymerization to highly functionalized aromatics followed by their upgrading via HDO to produce BTX-like monomers (benzene, toluene and xylene). Table 1.5 summarizes HDO activity of TMCs for various lignin-derived oxygenates. From the table, we can clearly see that the reaction depends on several parameters that affects the conversion of oxygenated aromatics including the type of reactor, reaction temperature and pressure, weight hourly space velocity (WHSV) for continuous reactor and reaction time for batch reactor. However, varying the catalyst components (metal and support) is the key factor in shifting reaction selectivity from partially oxygenated aromatics (phenol) to fully deoxygenated (benzene) or hydrogenated (cyclohexane) compounds. In this section, the HDO activity of TMCs over several oxygenated aromatics will be discussed.

Table 1.5 HDO of lignin model compounds over transition metal carbides

No	Feedstock	Reactor	Catalyst	Reaction conditions (T, P, and t)	Conversion (%)	Main product	Ref
1	Guaiacol	Batch	Mo ₂ C/CNF	300°C, 290 psig and 2h	66	phenol	70
2	Guaiacol	Batch	ReC/AC	350°C, 725 psig, and 4h	~ 90	phenol	71
3	Anisole	Batch	MoC/SiO ₂	320°C, 870 psig, and 4h	100	benzene	72
			Ni ₂ MoC/SiO ₂		100	cyclohexane	
4	Guaiacol	Batch	Mo ₂ C/AC	300 °C, 435 psig, and 3h	~97	Phenol	73
5	Guaiacol	Continuous flow	Mo ₂ C	350 °C, P= 400 psig	78	cyclohexene	74
			WC	vapor-phase reaction	27	phenol	
			MoWC	WHSV 1.8 h ⁻¹	93	benzene	
6	Guaiacol	Continuous flow	WC/CNT	300°C, 435 psig vapor-phase reaction WLHSV 3 h ⁻¹	~ 58	phenol	75
7	Anisole	Continuous flow	Mo ₂ C/Faujasite	250°C, P= 14.5 psig vapor-phase reaction anisole flow: 150 µl/h	~97	Phenol/alkylated phenol	76

Liu et al. made a comparison of carbon supported Pd, Ru, and Mo₂C for the HDO of 2-methoxyphenol (guaiacol) in a liquid phase batch reactor.⁷⁷ The idea was based on the comparison of the catalyst behaviour under high hydrogen pressures. The authors observed that Pd/C and Ru/C promoted the hydrogenation of the aromatic ring of guaiacol at low temperature (240°C), whereas direct deoxygenation occurred for Mo₂C/C and the methoxy group was removed. At temperatures above 300°C, molybdenum carbide yielded benzene as the major product while noble metal catalysts produced cyclohexane. This shows that Mo₂C/C is more efficient for oxygen removal than for hydrogenation of the aromatic ring. Lee et al. noticed that β-Mo₂C affinity to saturate the benzene ring was altered by the presence of oxygen.⁷⁸ These authors conducted benzene hydrogenation over Mo₂C followed by the introduction of anisole to the reaction system. As shown

in Figure 1.9, Mo₂C was very active for benzene ring hydrogenation but upon anisole injection, the selectivity to cyclohexane was significantly hindered. Similar results were found after the introduction of methanol or water. These results were explained by the modification of Mo₂C hydrogenation functionality by the presence of oxygenated compounds. The same authors conducted vapor phase HDO of anisole over Mo₂C at relatively low temperatures (420-520K) and observed high selectivity toward benzene (>90%). They noticed that as anisole conversion increased, methane selectivity decreased. This result suggested that the strong aryl – O bond (422 kJ. mol⁻¹) was selectively cleaved by Mo₂C rather than the weaker aliphatic C – O bond (399 kJ. mol⁻¹). Moreover, they reported that the rate of benzene synthesis has no dependence on anisole pressure and near half-order dependence for H₂ pressure. These results were considered as a proof of the existence of two distinct sites on Mo₂C surface that are responsible for hydrogen and anisole activation.

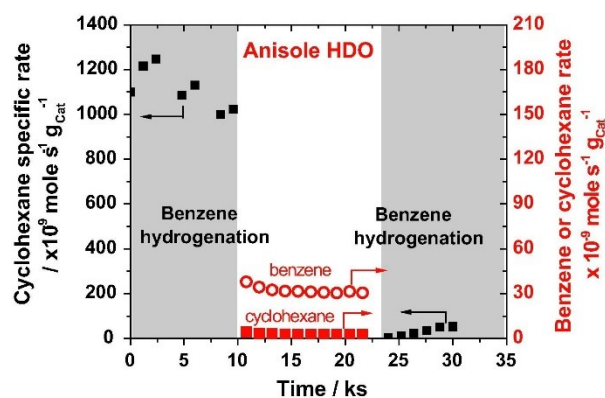


Figure 1.9 Cyclohexane production rate measured from either benzene hydrogenation reaction (■, shaded areas) or vapor-phase anisole HDO reaction (■) on a Mo₂C catalyst. Benzene synthesis rate (○) indicates deoxygenation activity. The catalyst was first tested for benzene hydrogenation for ~10 ks (feed composition : benzene/H₂ = 0.23%/bal with total flow rate ~1.67 cm³ s⁻¹) and then switched to vapor-phase anisole HDO reaction (feed composition: anisole/H₂ = 0.14%/bal with total flow rate ~1.67 cm³ s⁻¹), followed by restoring the reaction conditions to benzene hydrogenation. The reaction temperature was maintained at ~423 K under ambient pressure during the switch of the aforementioned two reactions. Catalyst loading was ~150 mg. (Reproduced with permission from Elsevier from ref [78])

Zhu et al. compared the catalytic activity of oxycarbide and molybdenum carbide catalysts.⁷⁹ The selectivity shifted from a mixture of benzene and phenol to the production of benzene as a major product. To understand the catalyst's properties, authors titrated the catalyst active sites by CO

and N_2O chemisorption respectively. They claimed that carbidic Mo sites effectively chemisorb CO while the oxophilic Mo sites chemisorb N_2O . It was concluded that the benzene synthesis rate from anisole HDO correlates with the amount of carbidic Mo sites on the catalyst whereas the presence of oxygen in the oxycarbide phase alters the selectivity to phenol. It is important to mention that a noticeable amount of methyl-anisole was obtained using the oxycarbide catalyst suggesting that isomerization of anisole occurred. This result indicates the acidic nature of the oxycarbide phase. Iglesia et al. reported that chemisorbed oxygen on the surface of tungsten carbide promoted the isomerization of neopentane by introducing Brønsted acid sites.⁸⁰ Thus, the catalyst acidity should be investigated in works aiming to gain more insights into the catalyst surfaces in relation with their HDO performance.

Iida et al confined molybdenum carbide inside zeolite faujasite (FAU) and obtained a bifunctional catalyst that combines HDO functionality provided by Mo_2C and Brønsted acid sites from the zeolite support.⁷⁶ However, it was noticed that a small percentage of benzene was formed with $\text{Mo}_2\text{C}/\text{FAU}$ in comparison to Mo_2C and the physically mixed $\text{Mo}_2\text{C} + \text{FAU}$ from the vapor phase HDO of anisole as shown in Figure 1.10. This result suggests that anisole deoxygenation occurs mainly in the Mo_2C surface and not over the acidic support. On the other hand, the $\text{Mo}_2\text{C}/\text{FAU}$ shows high activity towards the formation of a mixture of phenol and alkylated phenol during the vapor phase HDO of anisole. It was proposed that the catalyst activity was attributed to the transalkylation of methoxy groups from one anisole molecule to another promoted by Brønsted acid sites. The proximity of molybdenum carbide species to Brønsted acid sites favors the deoxygenation of alkylated anisole to form a higher percentage of alkylated phenol in comparison to the physically mixed $\text{Mo}_2\text{C} + \text{FAU}$; whereas around 20% selectivity of alkylated anisole was obtained. This result was explained by the desorption of these intermediates before their subsequent deoxygenation. Moreover, the authors found a remarkable selectivity to light hydrocarbons $\text{C}_2 - \text{C}_5$ instead of commonly obtained CH_4 derived from methanol through aryl- OCH_3 cleavage.

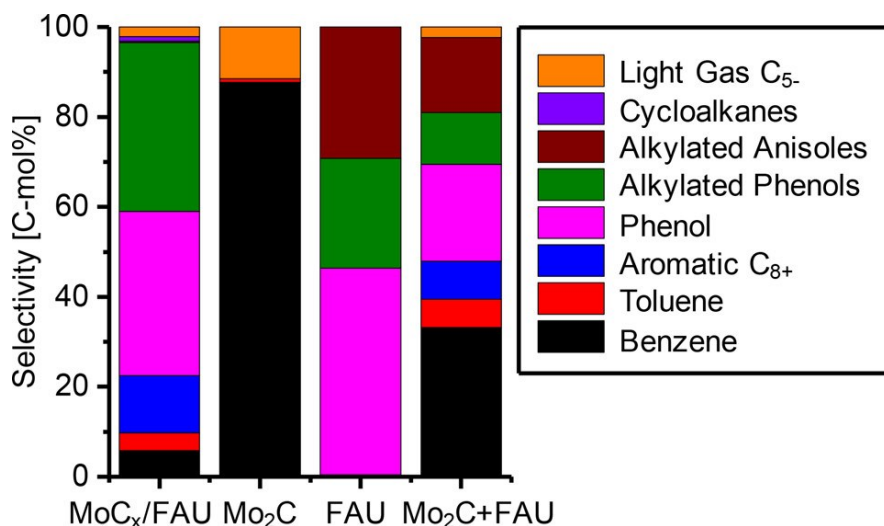


Figure 1.10 HDO of anisole. Reaction selectivity of MoC_x/FAU, pristine Mo₂C, parent FAU, and Mo₂C+FAU catalysts at the final point of reaction run (TOS = 1200 min). The conversions of these catalysts were 97% (MoC_x/FAU), 49% (Mo₂C), 31% (FAU), and 61% (Mo₂C+FAU). (Reproduced with permission from ACS from ref [76])

Mortensen et al. investigated the HDO activity of Mo₂C over simulated bio-oil containing a mixture of phenol+octanol.⁸¹ The reaction was performed in a fixed bed-continuous flow reactor. The authors observed that at low temperatures 280°C and 340°C, high ratios of octene and benzene were formed respectively. Interestingly, at 380°C, the ratio of octene/octane and benzene/cyclohexane became 0.001 and 2.4 respectively. After 76 h of TOS, the conversion of both phenol and octanol and the selectivity to HDO products dropped by almost half. The catalyst deactivation was correlated to the oxidation of the carbide phase by water formed during the HDO process. To confirm this hypothesis, co-feed of water effect was monitored during the HDO reaction and using an in-situ XRD analysis. As expected, a drastic decrease in catalyst activity was found, and the molybdenum carbide was converted to its oxide phase. Jongerius et al. reported the preparation of Mo₂C and W₂C supported on carbon nanofiber by the carbothermal reduction method.⁸² The catalysts were employed for the HDO of guaiacol in a batch reaction system at 350°C, 55 bar H₂ pressure for 4 hours. Both catalysts were selective to the demethoxylation of guaiacol yielding mostly phenol. However, recycling tests of the catalysts showed that W₂C was more sensitive to oxidation. On the other hand, Fang et al. reported the enhancement of W_xC/CNT stability during the HDO of guaiacol with a catalyst lifespan of 150 h.⁷⁵ Indeed, the metal precursor-CNT support was wrapped by a thin polymeric layer and it was found that wrapping the metal precursor-CNT support with a thin polymeric layer significantly enhanced the activity and

stability of the catalyst during the HDO of guaiacol. This result underlines the need for innovative carbide synthesis methods.

Tran et al. reported the efficient deoxygenation of guaiacol to benzene using bimetallic MoWC.⁷⁴ The catalyst displayed impressive catalytic activity with 93% conversion and 70% selectivity to benzene. Characterizations of the catalyst revealed that the presence of a mixture of tungsten phases (metallic + carburized) and molybdenum (carburized + oxy-carbide) enriched the surface properties of the bimetallic catalyst. Indeed, the introduction of tungsten into the molybdenum carbide changed the surface properties of the carbide and resulted in an electron transfer from W to Mo.

The alteration of surface properties consequently increases the density of active sites on the surface. To better understand the nature of the active sites, present in MoWC bimetallic carbide, authors studied the chemisorption of O₂, H₂, and CO for orthorhombic β -Mo₂C, MoWC, and tungsten metal W prepared under the same reaction conditions (Figure 1.11).⁸³ A notable increment was observed in the density of CO adsorption sites compared to Mo₂C with the presence of metallic tungsten on molybdenum carbide indicating the superior oxophilicity of the bimetallic carbide. Moreover, hydrogen chemisorption revealed that bimetallic carbide has a higher density of hydrogen adsorption sites (29 $\mu\text{mol.m}^{-2}$) in comparison to Mo₂C (12 $\mu\text{mol.m}^{-2}$). Typically, hydrogen active sites are recognized to possess noble metal-like characteristics for the activation of hydrogen and hydrogenolysis of C–O bonds. The high density of hydrogen sites, combined with the enhanced oxophilicity of the mixed carbides, resulted in the highest rate of hydrodeoxygenation (HDO) among all the catalysts investigated.

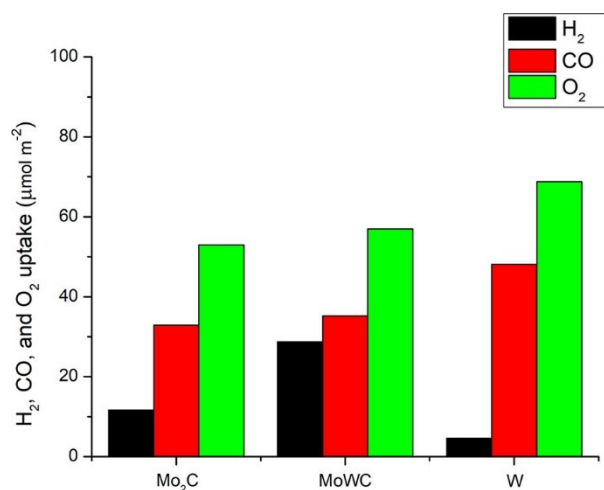


Figure 1.11 Pulse chemisorption of metallic tungsten and metal carbides. (Reproduced with permission from ACS from ref [83]).

▪ *Computational Studies*

Several DFT studies have also been reported particularly on Mo₂C using guaiacol as a model compound. Agrawal et. al. performed a combined DFT and microkinetic study for the HDO of guaiacol over the orthorhombic Mo₂C surface.⁸⁴ For the first activation, they observed demethoxylation would be facile with the least free energy barrier of 0.9 eV in comparison to dehydroxylation and direct ring hydrogenation reaction steps which showed relatively high barriers of 1.02 and 1.15 eV. The authors also extended the study to determine the effect of temperature on the energetics of HDO of guaiacol. The highest rate constant was observed for the demethoxylation step with the value of $9.65 \times 10^7 \text{ s}^{-1}$ in contrast to dehydroxylation ($4.82 \times 10^6 \text{ s}^{-1}$) and ring hydrogenation ($1.78 \times 10^5 \text{ s}^{-1}$), suggesting demethoxylation will be much faster than the other reactions at 500 K, which agrees with kinetic barriers for first activation.

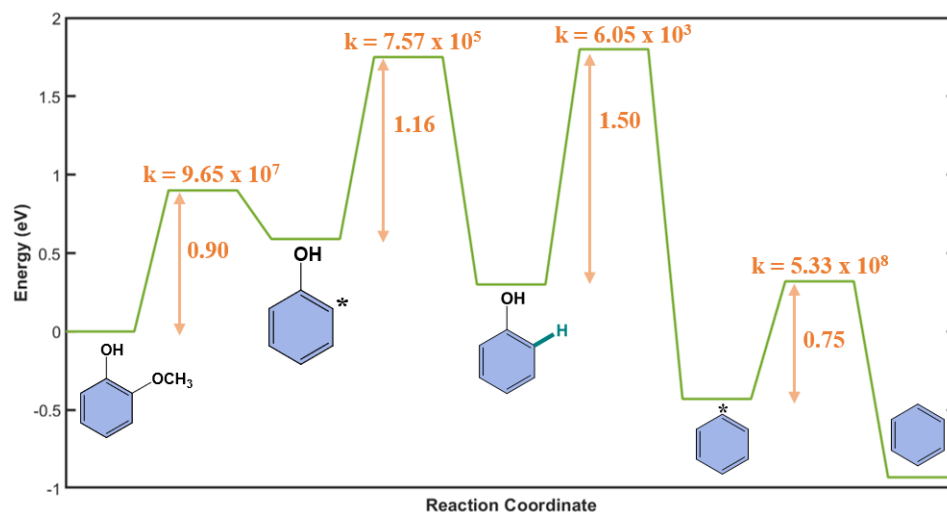


Figure 1.12 The reaction profile for the most favorable pathway of HDO of guaiacol over β -Mo₂C. The activation barrier for each step is given in red, in eV, and the rate constant of the conversion at 500 K is given in purple, in s⁻¹ (Adapted from ref [84]).

Results show that the most likely pathway to form benzene initiates with the cleavage of methoxyl group followed by subsequent hydrogenation to give phenol. It continues with the dissociation of the hydroxyl group, followed by the hydrogenation step to produce benzene, as shown in Figure 1.12. The rate-determining step for the pathway was observed to be the dehydroxylation from phenol with the highest barrier of 1.50 eV. Overall, the Mo₂C catalyst demonstrated good selectivity towards aromatic products like benzene and suppressed the undesired H₂ consumption, which increased its efficiency. However, this study was limited to the formation of benzene and hasn't included all the possibilities like ring-saturated products such as cyclohexanol, cyclohexane, and 1-methoxycyclohexanol.

Tran and coworkers also investigated of HDO of guaiacol over orthorhombic monometallic and bimetallic carbides based on Mo₂C using a combined experimental and DFT approach.⁸³ The DFT calculations were used to establish the mechanism and energetics of the catalytic conversion of guaiacol via two pathways i.e., Direct dissociation (DDO) vs Hydrogenation (HYD). Calculations indicated that the two reactions have similar activation barriers (i.e., 106 and 113 kJ/mol) showing that both DDO and HYD pathways are favored over the monometallic carbide, Mo₂C as shown in Figure 1.13. It suggests that Mo₂C favors the formation of both ring-saturated and aromatic products such as cyclohexene and benzene, respectively. Furthermore, they also studied a W-modified Mo₂C (MoWC), bimetallic carbide catalyst, to explore the effect of an oxophilic dopant

on reaction energetics. From the binding energy results, it was observed that oxygen bonded ~ 100 kJ/mol stronger on the bimetallic carbide (MoWC) than on the monometallic molybdenum carbide surface, confirming the enhanced oxophilicity of the carbide in the presence of W. Regarding the deoxygenation reactions, guaiacol activates via demethoxylation with a high barrier of 270 kJ/mol in comparison to 112 kJ/mol on Mo₂C followed by hydrogenation to produce phenol on both catalyst surfaces. The phenol intermediate can lead to the aforementioned two competitive pathways, either DDO or HYD. The authors observed that the barrier for dehydroxylation calculated to be 123 kJ/mol is lower than for the ring hydrogenation, computed as 162 kJ/mol. By contrast, for Mo₂C, the barriers of both reactions are relatively similar to 106 and 113 kJ/mol. These calculations indicate why the bimetallic carbide MoWC kinetically favors the DDO route to yield benzene as the major product, as observed experimentally. This study presented some indications of the two competing pathways (HYD or DDO) on Mo₂C, however only the initial activation was taken into consideration. A complete reaction pathway is necessary to evaluate the selectivity towards end products.

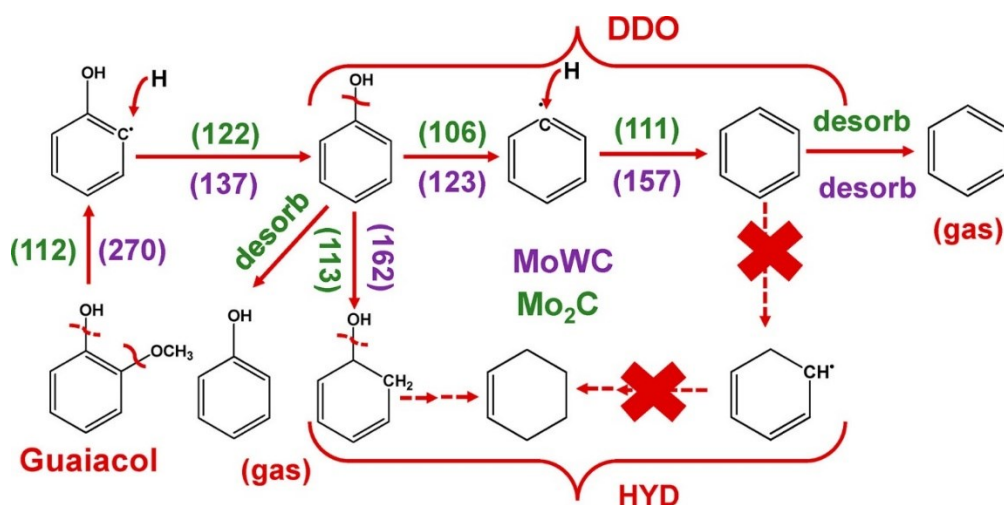


Figure 1.13 Proposed reaction pathways with the calculated barrier for guaiacol conversion at 350 °C, 450 psig. Solid line: kinetically favored route. Dashed line: kinetically nonfavored route. Electronic barriers (kJ mol⁻¹) are in green color for Mo₂C and violet color for MoWC. DDO: direct deoxygenation. HYD: hydrogenation–dehydration. (Reproduced with permission from ACS from ref [83]).

Zhou et al. provided some insights on the effect of Ni dopant in molybdenum carbide (Orthorhombic - Mo₂C (001)) catalyst on its oxygen removal capability.⁸⁵ They demonstrated the promoting effect of Ni which facilitates the removal of oxygen from various considered Mo₂C

surfaces by decreasing the binding energy of O* and OH* species. The authors further extended the research on this catalyst by employing first-principles-based microkinetic modeling (MKM) to evaluate the HDO performance using furans as a surrogate compound.⁸⁶ Calculations show that the surface modification caused by the Ni dopant increases the catalyst's activity by energetically disrupting the adsorption of CHCHCHCHO* species. This facilitates the formation of butadiene and propyne and lowers the selectivity for the synthesis of butadiene.

Based on reported literature on lignin-based model compounds, it is evident that Mo₂C has performed well in selectively removing oxygen from oxygenated compounds. It has also been demonstrated to favour ring hydrogenation, which consumes unwanted H₂ and produces ring-saturated compounds.

1.3 Aqueous phase processing of bio-oil

In this section, the focus will be on liquid phase processing of bio-oil as it holds its own merits in terms of providing higher target product selectivity and minimizing undesirable thermal degradation.^{32,87} Using this technique, lignin-derived aromatic monomers can be converted into cyclohexanol, cyclohexanone, alkyl cyclohexanol, cyclohexane, and other ring saturated hydrocarbons. These valuable intermediates can be further used as building blocks for the synthesis of different polymers, resins, dyes, and fine chemicals, and these substitutions can help in tuning the physical properties, such as melting points, elasticity, and crystallinity of these materials.^{88,89} Till date, hydrogenation of various lignin-derived monomers (phenol, guaiacol, eugenol etc.) to corresponding substituted cyclohexanols is studied extensively over non-noble and noble metal based heterogeneous catalysts. Among non-noble metals Ni⁹⁰⁻⁹², and Co⁹³⁻⁹⁵ have been reported for selective hydrogenation reactions. Schutyser et al. tested Ni/SiO₂-Al₂O₃ catalyst for the selective hydrogenation of 4-propylguaiacol (PG) to 4-propylcyclohexanol (PCol) at 300 °C under 40 bar H₂ and observed a PCol selectivity of ~70% in hexadecane.⁹¹ Bykova and co-workers studied guaiacol HDO using Ni-containing catalysts at 320 °C and under a high hydrogen pressure of 170 bar.⁹⁶ They observed a mixture of deoxygenated and ring-saturated products (cyclohexane, 1-methylcyclohexane-1,2-diol, cyclohexanone). Zhou et al. observed maximum conversion (96%) of guaiacol HDO in the presence of water over the NiCo/γ-Al₂O₃ bimetallic catalyst, whereas methanol and ethanol yielded 40% and 48%, respectively.⁹⁷ Lately, Natte et al. also reported a pine needle biomass-derived nitrogen-doped carbon-supported

Co₃O₄ nanoparticles (Co₃O₄/PNC), a Co – based heterogenous catalyst, for the selective ring hydrogenation of various arenes at 120 °C and 30 bar H₂ using t-BuOH as the solvent.⁹⁸ Moderate to excellent yields (> 55%) of different products were obtained. Non-noble metal catalysts are cost-effective; however, harsher reaction conditions are required for their use. It could lead to increased energy consumption and operational costs. Furthermore, these catalysts may exhibit lower selectivity owing to the occurrence of competing side reactions, making the overall process less efficient.⁹⁹ To overcome the limitations of non-noble metal-based catalysts, various noble metal-based catalysts mainly Pd, Pt or Ru in liquid phase were explored. For instance, Lercher et al. used phenol hydrogenation as a model reaction to compare three solvents viz. water, methanol, and hexadecane over Pd/C catalyst at 200 °C and 40 bar H₂ and observed highest phenol hydrogenation rate while using water as the solvent.¹⁰⁰ Hensen et al. also studied Pt/C and Ru/C catalysts to selectively hydrogenate guaiacol, employing water as a solvent at a temperature of 150°C and 20 bar of H₂ pressure. They achieved a selectivity of 100% for cyclohexanol with the Pt/C catalyst and 84% with the Ru/C catalyst within a reaction time of 2 hours.¹⁰¹ Various other Ru based catalytic systems comprising of Ru/C, Ru/Nb₂O₅, Ru-RuO₂-Nb₂O₅/H β , Ru/NC (NC is nitrogen doped carbon) and different solvents such as acetic acid, isopropanol, or decahydronaphthalene were also explored for hydrogenation of lignin derived aromatics.^{102,103} Numerous studies noted that the hydrogenation capability of ruthenium (Ru) is significantly influenced by the solvation environment. Consequently, when compared to palladium (Pd) or platinum (Pt) in aqueous solutions, Ru demonstrated higher activity for hydrogenation reactions.^{104–109} Overall, it can be inferred that Ru is significantly more active in aqueous environments, making it a common choice for the hydrogenation of aromatics in aqueous phases. Moreover, among all the solvents available, the interest in water stems from its significant economic and ecological benefits, as well as its many functions, which include solvation effects i.e., its influence on chemical reactivity, carbon removal, and surface restoration.^{110–112} For instance, Tomishige et al. investigated the production of cyclohexanol from guaiacol and discovered that a combination of Ru/C and MgO in water at 160 °C and 15 bar H₂ pressure results in a high cyclohexanol yield of 78%.¹¹³ In a subsequent study, the authors reported a higher cyclohexanol yield of 81% on a bimetallic Ru-MnOx/C catalyst from guaiacol in water at 160 °C and 15 bar H₂.¹¹⁴ On the contrary, over Ru/C catalyst, guaiacol produced a considerably lower yield of cyclohexanol (72%). In the conversion of eugenol, over Ru supported on carbon nanotubes

in a biphasic water-dodecane mixture at 160-180 °C and 50 bar H₂ pressure, Fu et al. achieved extremely PCol yields (up to 90%).¹¹⁵ In a different study, the researchers also found that a metal-solid base bifunctional catalyst, Ru/ZrO₂-La(OH)₃, is highly selective in the conversion of different 4-alkylguaiacols and 4-alkylsyringols to the corresponding 4-alkylcyclohexanols (RCols) in the aqueous phase at 200 °C and 40 bar H₂, with RCol yields exceeding 87%.¹¹⁶

All these aforementioned studies suggest that a synergistic combination of an effective catalyst and choice of solvent is vital for the selective hydrogenation of lignin-derived aromatics. One such combination could be Ru-water system which has also been studied using DFT simulations suggesting possible hydrogenation in the aqueous phase.^{109,117} For instance, Michel et al. performed DFT calculations on Ru (0001) surface with only one explicit water molecule using acetone as model carbonyl compound. They observed that the alkoxy intermediate forms an H-bond with the chemisorbed water molecule which makes the hydrogenation route more feasible by reducing the barrier by 41 kJ/mol.¹⁰⁹ Akpa et al. also carried out DFT calculations to understand the beneficial role of water on Ru (0001) surface in the hydrogenation of 2-butanone. They showed the water molecules interact with the intermediate species such as hydroxy butyl due to which the energy barrier decreases for hydrogenation.¹¹⁷ Later, Chin et al. shed light on the role of hydrides and protons in the catalytic hydrogenolysis of guaiacol at Ru-water interface.¹¹⁸ They found the enol intermediate undergoes an intramolecular proton transfer assisted by a vicinal water molecule, during which its hydroxyl proton transfers to its methoxy leaving group during the C–O bond cleavage. Moreover, they reported that the promotional effect of water on the hydrogenation cycle remains small. In the three investigations discussed above, they did not consider the possible dissociation of water molecules adsorbed on the ruthenium surface, as suggested from theoretical and experimental investigations which could have a potential role to play in the selective hydrogenation.^{119–123}

1.4 Motivation of the thesis

Transition metal carbides (TMCs), particularly, molybdenum carbide (Mo₂C) gained significant attention in HDO process due to their availability, low cost and similar activity as of noble metals.¹²⁴ It is well established that two types of sites (metallic and acidic sites) are needed for the HDO process³⁰ and TMCs are bifunctional which possess both sites.^{37,38,59} However, selectivity still remains a challenge over Mo₂C.^{74,125} Moreover, the retainment of oxygenated species results

in poisoning the surface.^{51,126,127} It has been conjectured that tuning the ratio of these two active sites by doping Mo₂C with oxophilic or hydrogen activating transition metals (such as Ni, Co, Cu, W, Fe, and Mn) could enhance its stability and selectivity.^{57,128} Therefore, it becomes pertinent to modify Mo₂C to improve its selectivity for C–O bond scission and suppress O* poisoning kinetically and thermodynamically for an efficient and effective HDO process.

For a rational catalyst design, it is imperative to acquire fundamental understanding of 1) the nature and types of active sites, 2) Interaction of the reactants and the products with the catalyst material, and 3) Investigation of elementary reactions and their energetics. In order to do so, a reasonable atomic configuration/molecular structure of the catalyst must be considered as any change in the assumed structure would affect the reaction pathways and energetics significantly and could lead to different inferences.^{129,130} For instance, Chen et. al.¹²⁹ investigated three Mo-doped Ni based alloys with different Mo/Ni ratio. The potential energy surfaces reveal that the single-atom alloy results in furfural (FAL) conversion to 2-MF by the OH path (Hydrogenation due to H₂O dissociation), while the bulk alloy favored the H path (Hydrogenation due to H₂ dissociation) for the same reaction. With the advent in computing power in the past few decades, computational tools like density functional theory can provide fundamental insights at nanoscale. However, there is still a wide gap between nanoscale insights gained by computations and the macroscale reaction kinetics data collected in experiments. For bimetallic carbides, reported modelled microstructures are based on assumptions of either a single atom alloy or metal overlayers over the monometallic carbide surface. As a result, these findings about the role of doped metal remain questionable due to the limited understanding of their microstructure. Therefore, computational studies employing catalysts which are an accurate representation of the experimentally synthesized catalyst are highly desired. This is the background for the present investigation on effect of tungsten (W) dopant on Mo₂C carbide catalyst.

Even though metal carbides are heavily studied for the HDO of bio-oil. However, majority of the studies are limited to model compounds due to the convoluted nature of bio-oil.³⁴ As discussed in Section 1.2.2., bio-oils are multicomponent mixtures of a large number of oxygenated compounds derived from lignocellulosic biomass feedstocks. Therefore, it is critical to assess how each compound or family of compounds will behave over a catalyst to perform effectively for the HDO of real bio-oil derived from pyrolysis of biomass. There is a notable research gap, particularly in the case of bimetallic carbides, as they have not been tested for multiple representative bio-oil

components originating from carbohydrate and lignin fractions of native biomass. Model compound studies have been invaluable to identify catalysts and reaction conditions that are favorable for the desired reactions. Model compound studies have also been crucial for understanding catalyst behavior. The knowledge gained from the model compound studies can be applied to convoluted bio-oil mixtures and actual pyrolysis oil vapors to produce gasoline range components.

As mentioned above, another concern regarding the stability of Mo_2C is that it is prone to deactivation due to the retainment of O atoms on the catalyst surface during HDO which further requires higher H_2 pressures to maintain its activity.^{126,127} However, reaction pathway gets altered as ring hydrogenation becomes competitive at higher H_2 pressures.^{69,128} We identified that activity and selectivity could be enhanced by adding tungsten dopant. However, removal of O^* species after C – O dissociation still remains a challenge. Hence, for an active, selective and durable HDO catalyst, a fine tuning between C-O dissociation activity and O^* removal activity is imperative. In addition, bimetallic carbides for selective catalysis are now gaining traction to develop catalysts with high stability and activity. In this context, a systematic screening of these catalysts is lacking to identify suitable Mo_2C -based bimetallic carbides that can improve catalyst stability without compromising activity and selectivity.

Solvent environment is also believed to play a critical role in the HDO of bio-oil. Catalysts can interact strongly with solvents which can alter their structure, catalytic activity, and selectivity due to interfacial adsorption and/or reactions with solvent molecules. Ru exhibit high hydrogenolysis activity in gas phase.^{67,131} However, selective hydrogenation can also be favored on Ru in the presence of solvents, particularly, water as discussed in Section 1.3. It suggests that a synergistic combination of an effective catalyst and choice of solvent is vital for the selective hydrogenation of lignin-derived aromatics. Optimizing the reaction conditions still pose a stern challenge as majority of studies are either reported at higher temperature or at higher H_2 pressure. Moreover, mechanistic role of the catalyst and water is still unclear in the selective hydrogenation reaction. Therefore, it is crucial to comprehend how the catalyst itself may be affected by the solvent environment, as well as how the solvent-catalyst, solvent-reactant, and catalyst-reactant interactions are altered. As a first step, we employed ruthenium (Ru) catalyst owing to its high catalytic activity towards HDO and it is used as benchmark to compare catalytic activity of noble-

metal like TMCs. All these motivate the investigation of selective hydrogenation on Ru-water interface.

From the above discussion, it is clear that there is lack of fundamental understanding in designing of molybdenum carbide based bimetallic carbide catalysts and mechanistic understanding of reaction energetics of HDO process on bimetallic carbides. Moreover, investigation of catalytic phenomena at solid-liquid interfaces remains a key challenge in catalysis science due to limited knowledge of the synergistic role of solvent and catalysts. Accordingly, computational tools need to be implemented to gain fundamental, molecular level insights. Molecular modeling techniques such as Density Functional Theory (DFT) can be employed as a predictive tool to understand the reaction mechanism. Such fundamental understanding of the nature of active sites within the catalyst microstructure will aid in the design and development of superior catalysts. The knowledge of reaction pathways and corresponding energetics will enable the selection of an efficient and effective HDO catalyst to improve yields and selectivity of desired products. Lastly, it will also provide guidance for the rationale choice of solvent in the hydrotreatment of bio-oil.

1.5 Objectives

The theme of the thesis to investigate the catalytic conversion of bio-oil constituents in vapor phase followed by the investigating solvent effects using DFT based computational studies by employing an accurate functional choice. The primary objectives of the present thesis are 1) to identify a correct atomic structure of W – doped Mo_2C (MoWC) catalyst followed by a comprehensive investigation of reaction energetics on Mo_2C and MoWC using guaiacol as a model compound 2) to perform a detailed mechanistic analysis of Mo_2C and MoWC surfaces for six bio-oil constituents derived from different component of biomass 3) to perform a computational catalyst screening and predict novel catalyst (more active and stable) for the HDO process 4) to perform a combined experimental and computational study elucidating the synergistic role of Ru-water system in selective hydrogenation. The specific objectives for each chapter are given below:

1.5.1 Key objectives of Chapter 2

- To find out the most stable configuration of W-doped molybdenum carbide (MoWC) catalyst.
- To validate the computationally predicted microstructure using experimental characterization data.

- A comprehensive thermodynamic and kinetic evaluation of multiple competitive pathways for guaiacol HDO on the Mo₂C catalyst.
- To compare reaction pathways for guaiacol HDO on the novel MoWC catalyst with those on the monometallic Mo₂C.

1.5.2 Key objectives of Chapter 3

- A comprehensive thermodynamic and kinetic evaluation of multiple competitive pathways for HDO of six key bio-oil constituents on the W-doped Mo₂C (MoWC) bimetallic carbide catalyst.
- To compare reaction energetics for HDO of the model compounds on the novel MoWC catalyst with those on the monometallic Mo₂C

1.5.3 Key objectives of Chapter 4

- A comprehensive computational screening to identify Mo₂C based bimetallic carbide catalysts that are more active, selective and stable against oxygen poisoning for C-O dissociation and hydrogenation reactions.
- To explore/determine a descriptor to screen catalysts for hydrogenation and C-O dissociation reactions involved in HDO of bio-oil.

1.5.4 Key objectives of Chapter 5

- To perform a detailed experimental and computational analysis to provide molecular level understanding of the solvent effect on the catalyst activity and selectivity.
- To explain the direct and indirect roles of water in the selective hydrogenation of aromatics. Also, to reveal the vital role of external hydrogen for selective hydrogenation.
- A comprehensive thermodynamic and kinetic evaluation of multiple competitive pathways for guaiacol and phenol hydrogenation on the Ru catalyst in the absence and presence of water.

1.6 Dissertation overview

The main findings of the thesis are organized into 4 chapters. Each of these chapters has a brief introduction covering the background, challenges, and relevant literature on the topic addressed in the chapter. In each of these chapters, following the introduction, a brief discussion on the computational system and methodology employed is presented. Afterward, the results are

presented and discussed in detail. Subsequently, each chapter is concluded with a summary of the key findings. The organization of the subsequent chapters is as follows:

Chapter 2 identifies the most stable microstructure of W-doped bimetallic carbide catalyst with tungsten to molybdenum ratio of 5:3, a mixed metal carbide bulk with overlayers of metallic tungsten (MoWC) is predicted. Subsequently, it delves into the comprehensive hydrodeoxygenation (HDO) reaction mechanism on Mo₂C using guaiacol as a model compound. Lastly, the reaction energetics of key reactions in the HDO process are performed over bimetallic carbide, MoWC, catalyst and a systematic comparison to its metallic counterpart is drawn to compare their activity. It was shown how the inclusion of W in Mo₂C significantly reduces the direct deoxygenation barrier from 60 kJ/mol on Mo₂C to only 18 kJ/mol on MoWC. Moreover, reaction energetics of ring hydrogenation of benzene and other intermediates to ring saturated products was also analyzed and shown that it is not favored on MoWC unlike Mo₂C which explains the experimentally observed higher selectivity towards benzene on MoWC, as compared to that on the monometallic Mo₂C.

Chapter 3 presents a comprehensive quantum mechanical investigation to reveal that the W-doped Mo₂C carbide (MoWC) catalyst with increased oxophilicity, owing to tungsten, can perform HDO of real bio-oil more effectively in comparison to its monometallic counterpart (Mo₂C) using six substrates representing different components of bio-oil. These six key constituents: 5-Hydroxymethyl furfural (5-HMF), Acetic acid, Eugenol, Levoglucosan (LGA), Methylglyoxal (MG), and Vanillin were selected to represent different oxygen functionalities present in the complex mixture of bio-oil. All six bio-oil constituents were tested on both Mo₂C and MoWC catalysts in detail and their reaction energetics for all possible elementary reaction steps is computed and compared.

Chapter 4 focuses on the screening of bimetallic carbide catalysts for HDO reactions. Based on the ability to dissociate C – O bond and hydrogenate the ring of ring-containing molecules, 45 Mo₂C-based catalysts were considered. Moreover, the feasibility of removal of adsorbed O* species in the form of water was also tested and systematically compared by calculating the reaction energetics of the water formation reaction ($OH^* + H^* \rightarrow H_2O$). Overall, the most active, selective and stable bimetallic carbide catalysts based on Mo₂C are proposed for selective hydrogenation and selective deoxygenation reactions.

Chapter 5 investigates a catalytic system comprising of Ru with water as a solvent to attain selective hydrogenation at ambient conditions using a combination of experiments and first-principles calculations. The activity and selectivity of the Ru catalyst for selective hydrogenation in the presence and absence of water molecules was assessed. Furthermore, the explicit role of water in the hydrogenation process is revealed. Using isotope-labelling experiments and DFT based mechanistic investigations, the active role of water on Ru catalyst as H-donor (after water dissociation) was confirmed. The activity and selectivity of the Ru catalyst for selective hydrogenation in the presence and absence of water molecules was assessed.

Chapter 6 summarises the conclusions drawn from this thesis and perspectives on these. A comprehensive description of computational methods is presented in Appendix A and additional supporting data pertaining to each chapter is also listed as appendices to different chapters.

Chapter 2: Doping an Oxophilic Metal into a Metal Carbide: Unravelling the Synergy Between the Microstructure of the Catalyst and its Activity and Selectivity for Hydrodeoxygenation¹

Abstract

Transition metal carbide catalysts (Mo_2C , W_2C) have emerged as promising alternatives to precious-metal-based catalysts like Pt, Pd and Ru for the hydrodeoxygenation (HDO) of biomass derived species, including bio-oil. However, low selectivity towards deoxygenation and excessive hydrogenation are major limitations of monometallic carbide catalysts. Hence, using the popular molybdenum carbide as an example, this work demonstrates how the doping of an oxophilic metal like Tungsten (W) into it can alter its structure, activity, and selectivity. Combining density functional theory (DFT) calculations of mixing energies and relative stabilities with experimental characterization data (X-ray diffraction, X-ray photoelectron spectroscopy), we confirmed that for a Tungsten to Molybdenum ratio of 5:3, a mixed metal carbide bulk with overlayers of metallic tungsten (MoWC) is the most stable microstructure. We also computed core-level shifts in the binding energy of Mo and W, validating the experimentally observed XPS shifts of +0.3 eV and -0.1 eV in the W 4f and Mo 3d spectra respectively, which correspond to a decrease in the electron density of W atom. In addition, a linear correlation was confirmed between the shifts in the d-band center and core-level shifts in binding energies to further validate the suggested MoWC structure. Furthermore, stronger CO adsorption on MoWC agrees well with the experimental findings. Investigations into the reaction mechanisms and pathways for the HDO of guaiacol revealed that the presence of tungsten overlayers on bulk MoWC catalyst creates a step-like structure and significantly brings down the direct deoxygenation barrier from 60 kJ/mol on Mo_2C to only 18 kJ/mol on MoWC. The subsequent dehydroxylation of the cresol intermediate is also kinetically

¹ Reproduced, with minor modifications, with permission from Sagar Bathla, Chi-Cong Tran, Serge Kaliaguine, and Samir H. Mushrif, *Doping an Oxophilic Metal into a Metal Carbide: Unravelling the Synergy between the Microstructure of the Catalyst and Its Activity and Selectivity for Hydrodeoxygenation*, ACS Catalysis, 12, 22, 13980–13998. <https://doi.org/10.1021/acscatal.2c03500> © 2022 American Chemical Society.

and thermodynamically more facile on MoWC in comparison to Mo₂C. Unlike Mo₂C, ring hydrogenation of benzene and other intermediates to ring saturated products is not favored on MoWC; explaining the experimentally observed higher selectivity towards benzene on MoWC, as compared to that on the monometallic Mo₂C.

Keywords: metal Carbides, Hydrodeoxygenation (HDO), Hydrogenation-Dehydration (HYD), Direct Deoxygenation (DDO), C-O scission, Selectivity, density functional theory.

2.1 Introduction

The development of cost-effective and energy-efficient technologies for the sustainable production of fuels and chemicals from alternate resources is essential due to the rising demand for chemicals and energy globally. In the current scenario, lignocellulosic biomass offers a possible solution for replacing/complementing petroleum based fuels and lowering carbon emissions.^{32,132} Among thermochemical conversion methods, bio-oil production from the pyrolysis of biomass is considered to have superior economics and efficacy^{20,21} However, due to undesired properties of bio-oil, such as high oxygen content and low heating value, bio-oil cannot be utilized directly as an alternative fuel. To achieve the desired properties of bio-oil, catalytic hydrodeoxygenation (HDO) is one of the most efficient methods through which hydrogen is used to extract chemically bound oxygen from the bio-oil, giving a higher-grade oil product. Transition metal sulfides (Co/NiMoS)^{133–136}, the most popular hydrotreating catalysts in the conventional hydroprocessing of petroleum, are among the catalysts that have been reported in the literature. However, the use of a toxic sulfur reagent added during the process is necessary but highly unfavorable. To overcome the limitations of transition metals sulfides, researchers turned to noble metals (Ru, Pt)^{137–139}. Despite their promising results in the bio-oil HDO process, high cost and limited availability of these catalysts make them uneconomical on an industrial scale.

Since Levy and Boudart discovered the platinum-like properties of transition metal carbides (e.g., Mo₂C, W₂C)³⁶, these noble metal-like catalysts have gained considerable attention and are considered alternate inexpensive candidate catalysts for HDO of bio-oil due to their excellent selective C-O scission capabilities.^{140,141} It is now proven that *Mo – C* catalysts are bifunctional, exhibiting both acid-site and hydrogen-active site functionalities^{37,38,59}, and this bifunctionality is essential for hydrodeoxygenation.³⁰ The most widely recognized explanation is that the addition of carbon to the metal lattice causes the d-electron density of state of carbides to move closer to

the Fermi level, which is similar to that of noble metals.⁵⁹ Kitchin and coworkers¹⁴² performed theoretical studies to understand the electronic modification of molybdenum atom (Mo) by carbidic carbon. The d-band of Mo was significantly widened and gave rise to a number of unique features as a result of the intercalation of carbidic C into the Mo lattice. It was ascribed to hybridization between the sp-orbitals of interstitial C atoms and the d-orbitals of Mo atoms. Several studies have been reported on the HDO performance of molybdenum carbide (Mo₂C) in the literature. For instance, Shi et al.¹⁴³ compared reaction pathways for furfural HDO on clean and H₂ pre-covered Mo₂C surface. Results revealed that, unlike clean Mo₂C surface, hydrogen pre-covered Mo₂C (101) kinetically and thermodynamically favors furfural hydrogenation into furfuryl alcohol (F-CH₂O) over furfural dissociation into F-CO + H, which leads to furan formation. Tran et al.¹²⁸ also observed a mixture of hydrogenated and completely deoxygenated products i.e., Cyclohexene and Benzene, respectively, in the guaiacol HDO process, suggesting both direct deoxygenation and hydrogenation pathways are favorable on Mo₂C. This can lead towards excessive hydrogen consumption via sequential hydrogenation resulting in undesirable ring saturated products. Bhan et. al.^{64,144} also manifested the potential of transition metal carbides (TMC), especially Mo₂C, in the vapor phase hydrodeoxygenation process at low temperatures (423 K) and ambient pressure conditions. They observed high aromatics yield (>90%) for mixtures containing m-cresol, anisole, 1,2-dimethoxybenzene, and guaiacol with high hydrogen efficiency. The different operating conditions between the two investigations may be the reason of the discrepancy in selectivity. In the former, experiments were conducted in the aqueous phase with high hydrogen pressure, whereas in the later, they were conducted in the vapor phase at low temperatures and low hydrogen pressure. Based on the aforementioned research, Mo₂C may function as a potential catalyst for the HDO of compounds derived from lignin. It needs to be underlined that there are three important factors on which a catalyst's performance is assessed, viz., 1. Activity, 2. Selectivity, and 3. Stability. In the case of Mo₂C, although it is highly active towards C – O hydrogenolysis, it is prone to deactivation due to retainment of O atoms on the catalyst surface during HDO, resulting in the formation of molybdenum oxycarbide and hence, blocking the available active sites. Therefore, high hydrogen pressure is required to avoid the retainment of O atoms on the catalyst's surface, by removing them in the form H₂O. However, it alters the selectivity of the catalyst as it favors ring hydrogenated products under high hydrogen

pressure which results in higher consumption of H₂.¹⁴³ In addition, carbon can accumulate on the catalyst surface at high temperatures.^{145,146}

Bimetallic carbide catalysts, (Ni-Mo, Co-Mo, Ni-W, Nb-Mo, and Pt-Mo) have recently attracted more attention because of their improved hydrotreating abilities, in comparison to their corresponding single metal counterparts.^{57,59,147,148} For example, Ruddy and co-workers⁵⁷ demonstrated that the modification of β -Mo₂C with Pt and Ni can tune the acid-/H*-site ratio, which improves the selectivity towards aromatic products for the bimetallic carbide catalyst. Modified bimetallic carbide catalyst displayed high conversions (>94%) and high selectivity to oxygen-free products like benzene (>80%) in guaiacol deoxygenation under ex-situ catalytic fast pyrolysis (CFP) conditions (623 K and 0.44 MPa H₂). Furthermore, Pt/Mo₂C catalyst showed the highest hydrogenation activity with 98.8% conversion of guaiacol and 99% nonoxygen-containing products whereas Ni/Mo₂C showed even better conversion of 99.8% and 90 % selectivity towards deoxygenated products. Tran et al.¹²⁸ observed enhanced activity (conversion = 93%) and selectivity (Benzene = 70%) of Tungsten (W) doped molybdenum carbide using guaiacol as a model compound at 623 K and 2.75 MPa. It was attributed to the synergistic effect between Mo and W atoms, which led to increased density of H₂-activating sites. Moreover, it was proposed that the presence of metallic W would enhance the oxophilicity of the catalyst to facilitate the adsorption of oxygen containing functional groups, thereby achieving improved deoxygenation activity.

Apart from their enhanced HDO performances than their mono-metal counterparts, with the advancements in characterization techniques such as XRD, XPS, HREELS, XAFS, several experimental studies provided insights into the microstructure of bimetallic transition metal carbides. For instance, Baddour et al.⁵⁷ shed light on the Ni, Pd and Pt-doped molybdenum carbide surfaces. Firstly, they confirmed that all considered bimetallic carbide (M/Mo₂C) catalysts retained the orthorhombic β -Mo₂C structure upon deposition and reduction of the metals. Moreover, they also reported the different phases in which these metals are present in modified bimetallic carbide (M/Mo₂C). Smirnov et al.¹⁴⁷ compared Ni-Mo carbides having different Ni/Mo compositions and showed that bimetallic systems contain β -Mo₂C and Mo₃Ni₂C and an alloy Ni_xMo_{1-x} with a high nickel content. Tran et al.¹²⁸ investigated the effect of W-dopant on Mo₂C and it was confirmed, via XRD and XPS characterization, that W was present both in metallic phase (W⁰) and in the

tungsten carbide phase (W_2C). Although these experimental studies provide some insights about the structure of the bimetallic carbide catalyst, theoretical investigations that aimed to characterize the microstructure are rare. Zhou et al.¹⁴⁹ demonstrated the promoting effect of Ni on a molybdenum carbide (Mo_2C) catalyst in its oxygen removal capability using DFT calculations. They showed that Ni, present as a single atom on Mo_2C , assists in the oxygen removal by destabilizing the adsorption of O^* and OH^* species. Lin et al.⁶³ reported an improved HDO performance on cobalt (Co)-modified molybdenum carbide where cobalt, present as overlayers, alters the oxygen and furfural binding energies preventing the poisoning by these adsorbates to increase the catalyst's stability. Kelly et al.¹⁵⁰⁻¹⁵² compared various bimetallic carbides where monometallic carbides (Mo_2C , W_2C) are modified with metal overlayers (Ni, Cu, Au, Rh, Pt) assumed to be epitaxial with the slab. They demonstrated that the bare Mo_2C surface was active for C-O cleavage, while Ni and Cu surface modifications resulted in preferential C-C bond scission and C-H scission, respectively. Wannakao et al.^{153,154} probed tungsten carbide surfaces with monolayer and sub-monolayers metal films for the CO_2 reduction to methane. Overall, it is to be noted that the modelled microstructures for bimetallic carbides are based on assumptions of either a single atom alloy or metal overlayers over the monometallic carbide surface. Any change in the assumed microstructure would affect the reaction pathways and energetics significantly and could lead to different inferences. For instance, Chen et al.¹²⁹ investigated three Mo – doped Ni based alloys with different Mo/Ni ratio. The potential energy surfaces reveal that the single-atom alloy results in furfural (FAL) conversion to 2-MF by the OH path (Hydrogenation due to H_2O dissociation), while the bulk alloy favored the H path (Hydrogenation due to H_2 dissociation) for the same reaction. As a result, these findings about the role of doped metal remain questionable unless the microstructure is confirmed and is an accurate representation of the experimentally synthesized catalyst. Additionally, the fundamental understanding of the nature of active sites within the catalyst microstructure will aid in the design and development of superior catalysts.

In this context, we combined experiments and computations, to screen and predict the most stable microstructure of W-doped Mo_2C ($MoWC$), which was also an accurate representation of the experimentally synthesized catalyst. To the best of our knowledge, this is also the first detailed study demonstrating the contribution of W-dopant in boosting the HDO performance of Mo_2C using guaiacol as a model compound, elucidating multiple competitive pathways of guaiacol HDO to aromatics, and explaining the selectivity towards benzene on the bimetallic carbide catalyst. In

addition to explaining trends in guaiacol conversion and product selectivity on these catalysts, these molecular mechanistic insights also provide guidance for the rational design and development of better catalysts and processes. The paper is organized as follows.

Section 2.2 describes the details of the computational techniques used in this work. Moreover, details of experimental catalyst synthesis methods and catalytic HDO experiments' procedure can be found elsewhere.¹²⁸ Rationale behind the selection of model catalyst configurations and their screening based on computations and experimental characterization data are presented in Sections 2.3.1 and 2.3.2. Reaction pathways, mechanisms and energetics of the hydrodeoxygenation of guaiacol on the Mo₂C catalyst to form benzene and cyclohexene are presented and discussed in section 2.3.6. The key reactions steps and their energetics on Mo₂C are compared and contrasted with those on MoWC in section 2.3.7. DFT findings about the differences in activity and selectivity of Mo₂C and MoWC are validated using experimental data in section 2.3.8. In section 2.4, the findings are summarized and conclusions are drawn.

2.2 Methods

2.2.1 Computational methodology

Plane-wave pseudopotential implementation of Kohn-Sham DFT using periodic boundary conditions are used to perform the First-principles calculations. To determine the electronic ground state and the core level binding energy shifts, Vienna ab initio simulation package (VASP)^{155,156} developed at the Fakultät für Physik of the Universität Wien^{157,158} is used. With a plane wave cut-off energy of 450 eV, the interaction between valence electrons and ions is described using the projector augmented wave (PAW)¹⁵⁹ method. The weak, long-range dispersion interactions between CO, H, and aromatic compounds (such as guaiacol and furfural) and the catalyst surface were taken into account using the vdW-DF functional. The vdW-DF functional has been previously used and worked well to investigate HDO reaction mechanisms on transition metals based catalysts.¹³⁹ Energy convergence criteria of 10⁻⁶ eV per unit cell and a maximum force tolerance of 0.05 eV/Å are used to ensure high accuracy. We used k-points sampling of 3 3 1 with the Monkhorst-pack approach for integration across the Brillouin zone in the reciprocal space. Spin polarization was enabled for all simulations. To prevent interaction in the z-direction with the periodic image, a 15 Å vacuum was inserted above the top layer. Adsorption energies were converged with respect to the number of slab layers and the density of k-points. All reactants and

products' vibrational frequencies were carefully examined as well, and no imaginary frequencies were observed. The Nudged Elastic Band (NEB) approach with climbing images was used to estimate transition state structures. In NEB, a total of 5 - 10 images were employed, and the force was minimized to $0.05 \text{ eV } \text{\AA}^{-1}$. In order to confirm the transition state, vibrational frequency analysis was performed with a displacement criterion of 0.01 \AA on the NEB image that was closest to the transition state after its optimization, using the quasi-Newton algorithm. At relevant experimental conditions, we estimated thermodynamic and zero-point energy corrections. The enthalpy corrections for molecules in the gas phase were obtained using thermodynamic tables, and for the adsorbed system, statistical thermodynamics using vibrational partition function was used. The Gibbs free energy change is reported for all reaction energies and activation barriers. The supplementary information includes a description of all the equations used as well as the change in Gibbs free energy calculation method. All reaction energies, G_r , are calculated as $G_r = G_{tot}(FS) - G_{tot}(IS)$, with FS and IS referring to final and initial state structures. The corresponding activation barriers, G_a , are calculated as $G_a = G_{tot}(TS) - G_{tot}(IS)$, with TS referring to transition state structure. All the energies calculated using DFT have an uncertainty of 5-10 kJ/mol.

Using the final-state approximation,¹⁶⁰ we estimated core-level shifts as the total energy difference between two separate calculations.¹⁶¹ The first one uses the completely relaxed system to do a conventional DFT calculation. In the second calculation, one electron is excited to the lowest conduction band state from the selected core level of a particular atom, enabling only the valence electronic structure to relax at a fixed atomic configuration. Without taking into consideration the impact of core-electron screening, the difference in total energy between the two computations provides an estimate of the core-level binding energy (although screening by valence electrons is included). Absolute values for the core-level binding energies cannot be obtained using the procedure,¹⁶¹ and in any case, it is basically challenging to calculate such absolute values using DFT.¹⁶² Thus, it is necessary to take into account core-level shifts (ECLS), which are known as variations in the binding energies of certain core electrons (ECL) of atoms in comparison to reference atoms (ECL_{ref}):

$$ECLS = ECL - ECL_{ref} \quad (2.1)$$

The density of states (DOS), which is projected on the d-band for the surface Mo site that coordinates with the adsorbed CO molecule, is used to examine the electronic interaction between various surfaces and CO. The two-step VASP algorithm is used to carry out the DOS computations: The charge density is generated in the first step using a self-consistent calculation, and the charge density from the first step is used in the second step's non-self-consistent calculation. Next, p4vasp is used to evaluate and display the observed DOS data. In the literature, projected DOS analysis is frequently used to compare the activities of several sites on the metal surface.^{163,164} This is based on the band model that Hammer and Nørskov proposed^{165,166}. If the d-band centre (ϵ_d) is closer to the Fermi level, the adsorption will be stronger, according to this model. Finally, we determined the following valence d-band parameters: the first moment of the d-projected density of states, $g_d(E)$ with respect to the Fermi level (E_F) yields the position of the center (E_d),

$$\epsilon_d = \frac{\int_{-\infty}^{\infty} \rho E dE}{\int_{-\infty}^{\infty} \rho dE} \quad (2.2)$$

2.2.2 Mixing and Cohesive Energies

To compare the relative stabilities of different possible configurations of the bimetallic carbide catalyst, excess/mixing energy was calculated as follows^{167,168}

$$\text{Mixing Energy} = E_{tot}(Mo_xW_yC_z) - x * \frac{E_{tot}(Mo_{x+y+z})}{x+y+z} - y * \frac{E_{tot}(W_{x+y+z})}{x+y+z} - z * \frac{E_{tot}(C_{x+y+z})}{x+y+z} \quad (2.3)$$

where $E_{tot}(Mo_xW_yC_z)$ denotes the the energy of $Mo_xW_yC_z$ alloys, $E_{tot}(Mo_{x+y+z})$, $E_{tot}(W_{x+y+z})$, and $E_{tot}(C_{x+y+z})$ are the energies of pure Mo, W, and C slabs with the same size ($x+y+z$) as $Mo_xW_yC_z$. x, y, z are the numbers of atoms of Mo, W, and C, respectively. To model the C slab, crystal structure of graphite was assumed. Lower mixing energy (Δ) suggests favorable mixing, whereas higher values indicate a higher segregation tendency. Previously, Fan et al.¹⁶⁷ explored the stability of Pd–Ir nano-alloys on the basis of their mixing energies. Ferrando et al.¹⁶⁸ also investigated the transition metal doped Ag/Au – X bimetallic nano-alloys and compared their relative stabilities among several modelled structures with different compositions.

An alternative method using cohesive energies of individual metal atoms is also used.^{167,168} The cohesive energies of individual atoms are given by equation (2.4)

$$E_{coh}^i = E_{unitcell} - N * E_{isolated}^i \quad (2.4)$$

Where, E_{coh}^i is the cohesive energy of individual atom, $E_{unitcell}$ is the energy of the unitcell of that atom, N is the total number of atoms in the unit cell, and $E_{isolated}^i$ is the energy of an isolated atom in vacuum

The Cohesive energy is given by

$$Cohesive\ Energy = E_{tot}(Mo_xW_yC_z) - x * E_{coh}^{Mo} - y * E_{coh}^W - z * E_{coh}^C \quad (2.5)$$

Where, $E_{tot}(Mo_xW_yC_z)$ denotes the total energy of $Mo_xW_yC_z$ alloys, x, y, z is the number of atoms of metal Mo, W, and C, respectively, E_{coh}^i is the cohesive energy of individual atoms.

2.3 Results and Discussion

2.3.1 Model Structures/configurations of the Bimetallic Carbide (MoWC) catalyst

Mo_2C mainly has two crystalline structures, the orthorhombic Mo_2C phase¹⁶⁹ and the hexagonal Mo_2C phase^{170,171}. Moreover, Mo_2C can be modelled with both C-termination and Mo-termination.⁸³ In this work, we used the orthorhombic Mo_2C phase with (100) facet and Mo termination. Tran and coworkers⁸³ compared the binding energies of guaiacol and its HDO products i.e., phenol and benzene on both terminations of Mo_2C . It was found that these species adsorb more strongly on $Mo_2C - Mo$ than C- termination. Additionally, they also investigated the interaction between the active sites on both terminations ($Mo_2C - Mo$, and $Mo_2C - C$) using probe molecules (hydrogen, CO, and O_2) both computationally and experimentally. The DFT computed energies on Mo-terminated Mo_2C were able to explain experimental observations effectively. Therefore, we considered $Mo_2C - Mo$ termination in this study. The rationale to adopt the orthorhombic phase is because it was observed in the experimental XRD characterization.¹²⁸ Optimized lattice constants of $a = 4.79 \text{ \AA}$, $b = 5.28 \text{ \AA}$, $c = 6.12 \text{ \AA}$ were also in reasonable agreement with the experimental values.¹⁷² To find the most stable microstructure for W-doped Mo_2C , 7

different configurations for the bimetallic carbide catalyst have been considered as shown in Figure 2.1. The stoichiometric ratio in all configurations is different to maintain the constraint of 176 atoms in each structure.

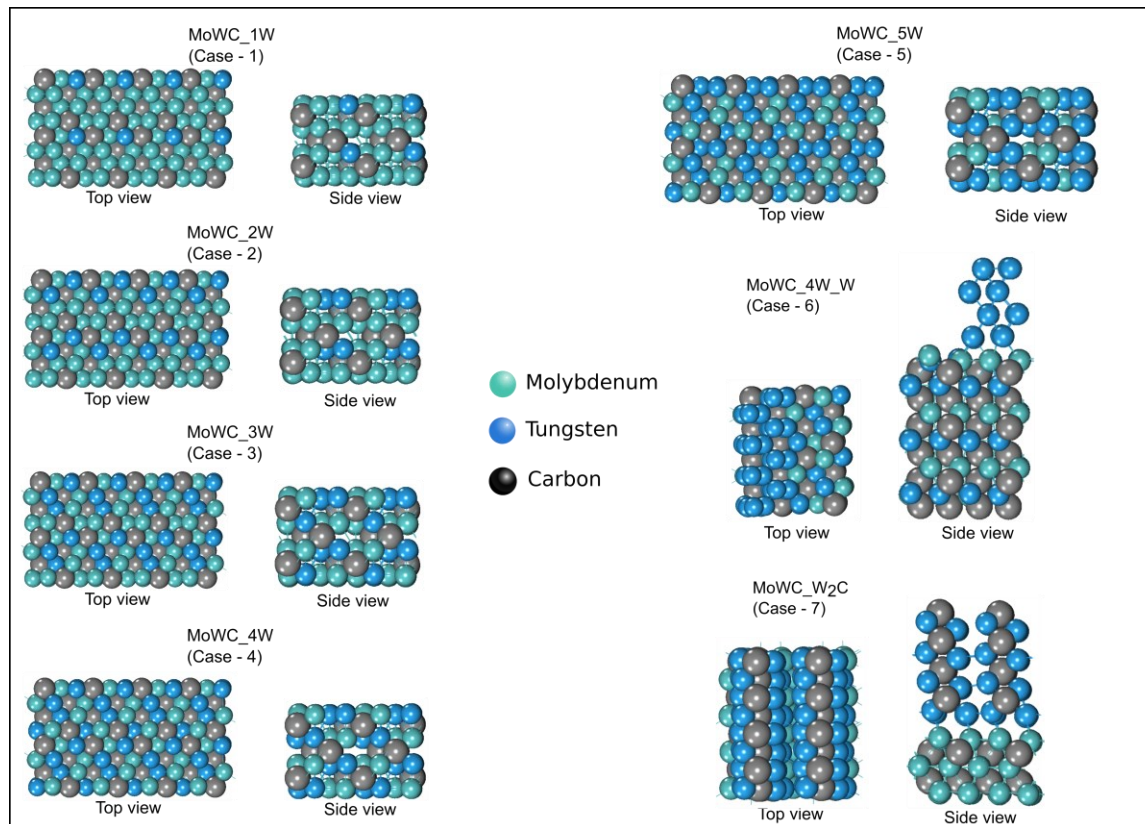


Figure 2.1 2-D Schematic of different possible structures (side view) for mixed metal carbide catalyst (MoWC). Molybdenum and tungsten atoms are shown in green and blue color respectively. The stoichiometric ratio in all the structures is different. Case – 1 to case – 5 represent bulk alloys with increasing tungsten proportion, and cases - 6, 7 represent models with adlayers of metallic tungsten and tungsten carbide, respectively.

To identify the location of tungsten dopant in the bimetallic carbide, we considered the possibility of bulk alloys, bulk alloy with metallic tungsten (W) overlayers (Case 6), and tungsten carbide (W_2C) overlayer (Case 7) on Mo_2C such that the active sites are present at the interface of the adlayer and slab, as shown in Figure 2.1. Moreover, Case 6 could also manifest the effect of metallic tungsten in the bimetallic carbide. For a systematic comparison among bulk alloys, five cases (Case 1 to Case 5) were considered for bimetallic carbide MoWC as bulk alloys in which molybdenum atoms are replaced by tungsten atoms in the unit cell, as shown in the Figure 2.1. In the orthorhombic unit cell of Mo_2C , there are 8 Mo atoms and 4 C atoms. Tungsten proportion is

increased stepwise from case 1 to case 5 by replacing Mo atoms from the unit cell. Other possible cases with higher W concentration in the bulk were not considered as the Mo/W atomic ratio in the experimentally synthesized catalyst was reported to be 0.6.¹²⁸ Some amount of tungsten could also be present as metallic tungsten, as suggested by the XRD and XPS characterization results (also presented later in the paper and in the SI).²⁰ We have also observed both metallic W⁰ and W₂C phases for W dopant in molybdenum tungsten carbide. To incorporate that, metallic tungsten overlayers are placed in MoWC bulk alloy (Case 6) with Mo/W = 1:1 in bulk. Moreover, this model is consistent with the experimental observations where the Mo/W ratio was found to be 0.6. The only constraint to use this criterion is to keep the total number of atoms equal in all the possible structures. In order to achieve that, 176 atoms are used to model all the structures with different compositions.

2.3.2 Relative Stability of modelled Structures of Bimetallic carbide (MoWC)

Mixing energies for all configurations shown in Figure 2.1, relative to Mo₂C, are calculated using equation -3, and are shown in Figure 2.2a. Results indicate that cases 6 and 7 are the two most stable structures for the bimetallic carbide (MoWC) with similar mixing energies of **-34.68 eV** and **-31.62 eV**, respectively. On the other hand, it was found that bulk alloy structures from Case 1 to Case 5 with different Mo to W ratio become unstable as the relative mixing energy increases with a decrease in the Mo/W ratio from 7 to 0.6 as shown in Figure 2.2a.

Cases 5 and 6 have a notable similarity that they comprise the same Mo/W atomic ratio of 0.6. However, the two also have a distinct difference that all the W atoms are present in the bulk in Case 5 while in Case 6, W is distributed in both carbide and metallic phase. A significant drop in mixing energy from +8.62 eV in case 5 to -31.62 eV in case 6 can be seen in Figure 2.2a. These results clearly demonstrate that W prefers to distribute itself in both metallic and carbide phases. It corroborates well with the experimental observations reported by Tran et. al.¹²⁸, in which they confirmed the presence of W in metallic phase and in the form of carbide as well. The results obtained from XRD characterization unveil the presence of metallic tungsten (W⁰) with three sharp peaks at 2θ values of 40.4, 58.3 and 73.2° along with the peak characteristics of an orthorhombic β – Mo₂C phase (Figure B.16). On the surface of the samples, X-ray photoelectron spectroscopy (XPS) was also employed to characterize the chemical states of each element. The core-level spectra of Mo 3d and W 4f of MoWC suggested that the bimetallic carbide sample possesses both,

molybdenum and tungsten carbide states (Figure B.17). Furthermore, W^0 phase was also observed on the surface of MoWC in XPS analysis with characteristic peaks at 31.4 and 33.6 eV. Therefore, Case 6 becomes a suitable candidate for the microstructure of the W-doped molybdenum carbide catalyst.

Cases 6 and 7 show relatively similar mixing energies values, however, Case 7 does not correlate well with experimental results. Because W_2C overlayers are present on the surface, the elemental composition in model Case 7 (W - 16, C - 8 atoms) does not contain Mo on the surface, which disagrees with the experimental results (Table B.3), which showed that the Mo/W atomic ratio was 0.6 in the XPS analysis. Secondly, metallic tungsten phase is completely absent in this case as all the W atoms exist in the form of tungsten carbide which contradicts with the XPS and XRD results, where tungsten was observed in W^0 oxidation state along with the carbidic phase in the bimetallic carbide (MoWC) sample, respectively.

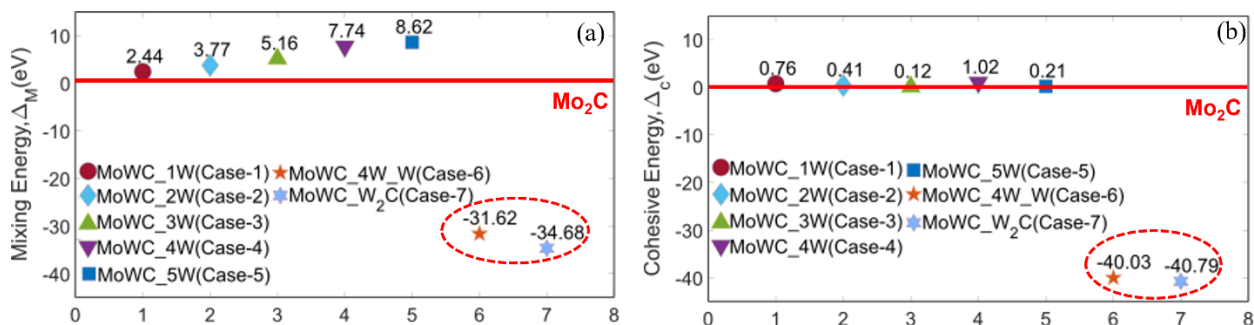


Figure 2.2 (a) Mixing energies (Δ/eV) calculated using equation (3), and (b) Cohesive energies (Δ_C/eV) calculated using equation (5) for different structures of MoWC with reference to Mo_2C . The most stable (most negative Δ) cases are highlighted in the red circle.

To further test the relative stabilities, cohesive energies were also calculated using equation – 5 and presented in Figure 2.2b. It is the absolute measure of the average interaction among the atoms when they are arranged in a crystalline state, as compared with the gas state. Overall, cohesive energies follow the same trend as mixing energies. In this case as well, Case 7 was found to be marginally more stable but the difference is very small (0.76 eV) and Case 7 can be ruled out due to the same reasons as explained above. Hence, it can be established from the results that Case 6 is the most appropriate and realistic configuration for the bimetallic carbide (MoWC) catalyst, as its extremely close in energy to the most stable configuration and has characteristics that agree very well with the experimental XRD and XPS data.

2.3.3 Comparison of Experimentally Measured and DFT computed XPS Shifts

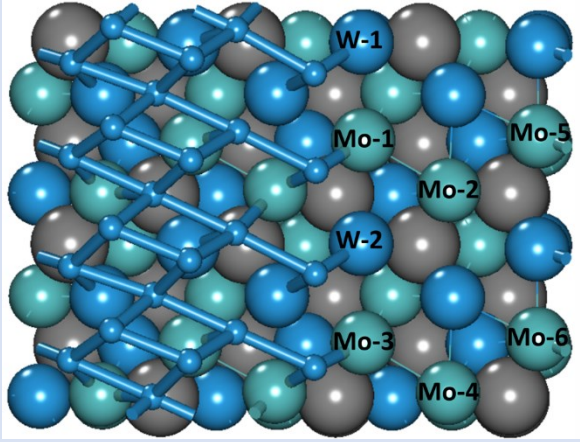
An effective and widely used method for characterizing surfaces is X-ray photoelectron spectroscopy (XPS). Detected shifts in the core electron binding energies are sensitive to the chemical composition and local environment of the surface species.^{173,174} The structure and binding locations of the surface species are frequently identified using the chemical shift in the core level binding energies (CLBEs). Recently, DFT has become a key tool in calculating the chemical shifts in binding energies.^{175–181} For instance, Trinh et al.¹⁷⁵ illustrated the accuracy of DFT with final state approximation method by calculating CLBE's with a maximum deviation of 85 meV in predicting the C 1s and B 1s BEs on Co and Pt surfaces which can be compared to the 0.1 eV resolution of synchrotron-based XPS. Moreover, they were able to distinguish chemical shifts in the case of multiple types of carbon atoms present on the surface. Kresse and Kohler¹⁶¹ confirmed the CO adsorption site on Rh(111) surface by comparing Rh 3d_{5/2} surface core-level shifts with experimental values. Artyushkova and coworkers¹⁸¹ validated the use of independent DFT predictions of BE shifts for defect identification and confirming XPS observations for Me-N_x moieties in pyrolyzed carbon-based ORR electrocatalysts. Trinh. et al.¹⁷⁹ applied DFT and XPS synergistically to determine the Hubbard-U correction (in DFT) and for the identification of adsorbates on the surface (and their XPS shifts) using CuO as a model transition metal oxide surface. Aforementioned studies indicate that DFT computed BE shifts provide reasonable correlation with experimentally observed XPS shifts, and those can be used to confirm the experimentally measured BE shifts in XPS.

To reaffirm the structure of W – doped molybdenum carbide (MoWC), we also calculated the chemical shifts in binding energy and compared them with the XPS shifts observed in the experiments (experimental XPS spectra shown in Figure B.18). A shift of - 0.1 and + 0.3 eV in core level binding energies of Mo 3d and W 4f XPS spectra, respectively, was observed in the experimental XPS characterization¹²⁸. We also calculated the core level shifts in the binding energy of Mo 3d and W 4f spectra for Case 6.

According to the DFT calculated XPS shifts, a positive shift of +0.38 for tungsten atoms on the step sites/edges of the mixed metal carbide (MoWC) surface, as shown in Table 2.1, was found with respect to tungsten atom on a metallic tungsten slab. Metallic tungsten was adopted as a baseline for comparing chemical shifts in core level binding energy, similar to the experimental

study. The XPS shift calculated by DFT agrees reasonably well with the experimentally observed XPS shift of +0.3 eV in the W 4f spectra. A reduction in the electron density on the W atom is correlated with this upward shift in the binding energy. The change in the electron density caused by the interaction between Mo and W atoms, which is responsible for the positive and negative chemical shifts, is attributed to the charge transfer from W to Mo. The consistency between experimentally determined and estimated CLSs is clear evidence of the sensitivity of measurements of core-level shifts to local electronic structural changes. On the other hand, In the case of Mo 3d spectra, the calculated shifts fluctuate between 0 – 0.3 eV as shown in Table 2.1. Hence, a negative shift of -0.1 eV could not be confirmed from DFT. It could also be attributed the error margin of DFT in calculating core level binding energies, which is 0.1 – 0.15 eV.

Table 2.1. Mo 3d and W 4f Core Level Binding Energy (CLBE) Shifts for different surface atoms on MoWC surface relative to the Mo₂C and W surface, respectively

<p style="text-align: center;">MoWC Surface (Case 6)</p> 	<p style="text-align: center;">DFT calculated Mo 3d and W4f XPS shifts (Experimental: Mo = - 0.1 eV, W = +0.3 eV)</p>
Mo – 1	+0.26
Mo – 2	+0.06
Mo – 3	+0.20
Mo – 4	+0.06
Mo – 5	+0.22
Mo – 6	+0.20
W – 1	+0.38
W – 2	+0.38

2.3.4 Correlation between Surface Core-level shifts and d-band Center (ϵ_d)

Modern synchrotron radiation facilities' high-resolution X-ray photoemission spectroscopy (HRPES) experiments have more recently demonstrated a linear relationship between surface core-level shifts (SCLS) changes and the theoretically determined ϵ_d shifts, thus indicating that, in these cases, the screening correction magnitude is rather small compared with the overall trend of initial-

state shifts. The correlation between core- and valence-level shifts of a metal surface and adlayers has been discussed before by several authors.^{182,183} A remarkable linear correlation was found between core-level shifts and d-band center, which makes core-level shifts reliable experimental descriptors of the chemical reactivity.¹⁸² Moreover, from a theoretical point of view, it offers to confirm the core-level shifts observed in experiments by DFT calculations. Hence, we calculated the d-band center for various surface atoms of the Case 6 model structure of MoWC, to confirm the core-level shifts observed in the experimental study.

In Figure 2.3, it can be seen that the projected d-band center of surface molybdenum (Mo) atoms lies at -1.07 eV and for Mo atoms on mixed metal carbide surface lies at -0.97 eV, which confirms the negative shift of -0.1 eV. Moreover, in the case of W (4f orbital), the d-band center for W atoms in metallic tungsten slab lies at -0.78 eV whereas, in the case of mixed metal carbide (MoWC), the d-band center for different types of W atoms lies in the range ((-0.9) – (-1.3)) eV. This is in excellent agreement with the experimental observations where a negative shift of -0.1 eV and +0.3 eV was observed in core-level binding energies for Mo (3d) and W(4f) XPS spectra. These results align well with the reported studies in the literature, confirming a linear correlation between core-level shifts and d-band center shifts, as shown in Figure 2.3. Golfetto et. al.¹⁸² reported a similar linear correlation between the d-band center and experimental core-level shifts in binding energy for Pd/Ru (0001) Pseudomorphic Overlayers. A similar comparison was also reported by Baraldi et. al.¹⁸³ on Pt – Rh bimetallic surfaces. This further confirms that the proposed structure for the bimetallic carbide (MoWC) modeled as case 6 would be the most likely microstructure of the experimentally synthesized MoWC.

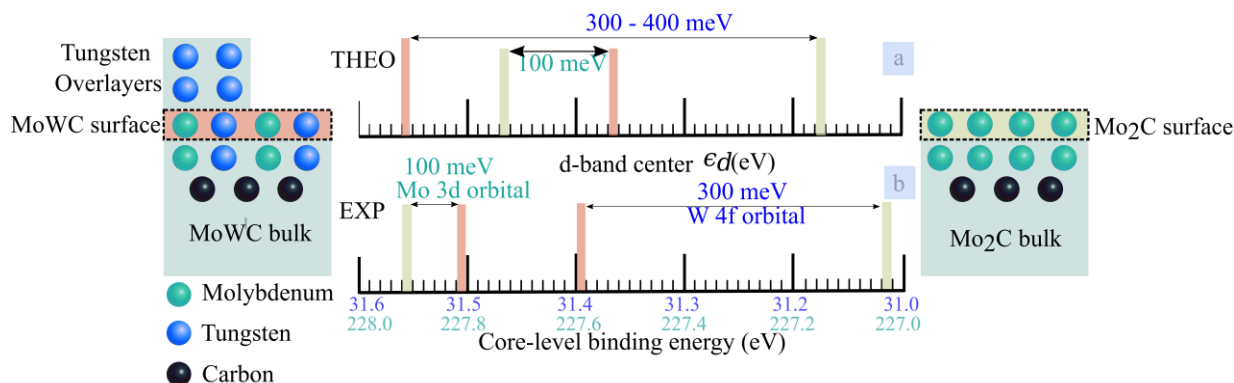


Figure 2.3 Comparison of the theoretical layer-projected d-band center with the experimental core level binding energy shifts in the W 4f and Mo 3d core-level components. The physical system under comparison is depicted schematically in the insets on the left and right.

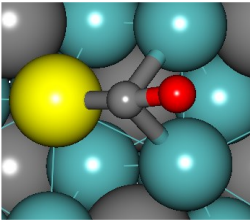
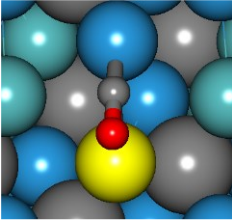
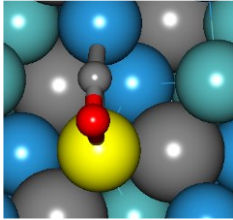
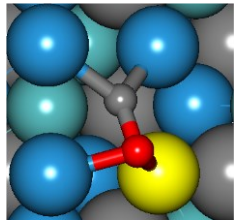
2.3.5 CO adsorption studies

We also performed CO pulse chemisorption as CO has been extensively employed to quantify the density of active sites.¹⁸⁴ The amounts of CO uptake over the as-prepared monometallic (Mo_2C) and bimetallic (MoWC) carbides are $230 \mu\text{mol g}^{-1}$ and $317 \mu\text{mol g}^{-1}$, respectively. This observation is not surprising due to the higher oxophilicity of metallic W present in MoWC , in contrast to monometallic carbide. Using DFT, we computed CO binding energies and calculated the projected density of states on the Mo sites on which CO preferred to adsorb on carbide surfaces, as reported in Table 2.2.

It can be seen that CO adsorbs stronger on the microstructure of Case 6 of MoWC (263 kJ/mol) as compared to Mo_2C (203 kJ/mol). Moreover, this calculation was extended for two other cases as well, i.e., Case 5, Case 4, and the binding energies for CO adsorption on these cases were found to be nearly equal to pure molybdenum carbide surface. It is to be noted here that there is no metallic tungsten present in cases 4 and 5, which further indicates that metallic tungsten contributes significantly towards strong adsorption of CO on MoWC . This is in agreement with the experimental observation where the highest adsorption capacity ($345 \mu\text{mol g}^{-1}$) was reported for metallic tungsten W case. It was ascribed to the high oxophilicity of metallic tungsten atoms as CO binds via both C and O atoms to surface of Case 6, in contrast to Mo_2C where it only adsorbs via the C atom. Regarding the active sites for CO adsorption, CO prefers to adsorb on 3-fold hollow

sites on Mo₂C, whereas it prefers bridge sites between Mo and W surface atoms for cases 4 and 5. However, with metallic tungsten present in Case 6, the most stable adsorption configuration was found on the corner/step sites bonding with metallic tungsten atoms and surface Mo and W atoms, as shown in Table 2.2.

Table 2.2 Calculated d-band center and CO binding energies on Mo₂C and MoWC surfaces projected on the atom highlighted in yellow color.

Surface	Mo ₂ C	MoWC_4W (Case 4)	MoWC_5W (Case 5)	MoWC_4W_W (Case 6)
Configuration				
E_{ads} ($\frac{kJ}{mol}$)	-203	-206	-200	-263
d-band center ϵ_d (eV)	-1.94	-1.30	-1.36	-1.00

D-band center was also calculated to understand the changes in the electronic structure during CO chemisorption. According to the definition of the d-band model, an upshift in the d-band center towards the Fermi level is expected to correspond to stronger CO adsorption. To put these data into perspective, we observed an upward shift of the d-band centers for MoWC which can be clearly observed from the data in Table 2.2. The d-band center for Case 6 (-1.00) shifted upwards towards the Fermi-level as compared to the Mo₂C (-1.94). These results are consistent with the experimental observation of higher CO uptake on MoWC than Mo₂C.

2.3.6 HDO Reaction network of Guaiacol on Mo₂C

One of the most typically employed model substrates in the research of lignin valorization is guaiacol (2-methoxyphenol).^{185–187} It has functional groups, such as methoxy and hydroxyl groups, that are comparable to those found in aromatic oxygenates obtained from the pyrolysis of lignin. In comparison to the simpler phenol, where only dehydroxylation may occur, demethylation and

demethoxylation reactions can also play a role in guaiacol HDO. Hence, a comprehensive reaction mechanism is computed here for guaiacol HDO and different competitive pathways are compared. All energies are reported as Gibbs free energies in this study and the electronic energies are provided in the supplementary information.

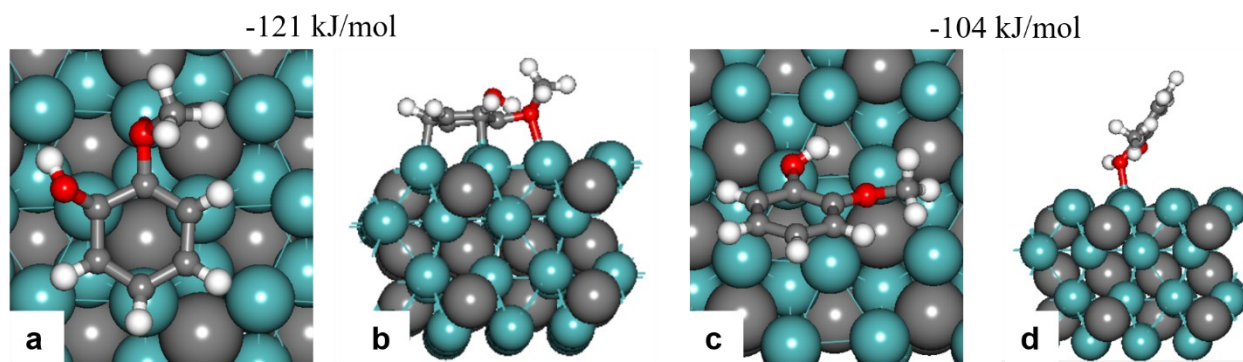


Figure 2.4 Optimized geometries and corresponding free energies of guaiacol adsorption on the Mo₂C surface (a) Top view of $\eta^2(\text{C} - \text{O})$ configuration, (b) Side view of $\eta^2(\text{C} - \text{O})$ configuration, (c) Top view of $\eta^1(\text{C} - \text{O})$ configuration, (d) Side view of $\eta^1(\text{C} - \text{O})$ configuration. Color coding for atoms is same as in Figure 2.1.

2.3.6.1 Guaiacol adsorption configuration on Mo₂C

Guaiacol ($\text{C}_6\text{H}_4(\text{OH})(\text{OCH}_3)$) can adsorb on the Mo₂C (100) surface in two possible configurations: i) a flat parallel configuration in which both, the ring and the methoxy group, ($\text{O} - \text{CH}_3$) interact with the metal carbide surface, $\eta^2(\text{C} - \text{O})$, and ii) a vertical configuration in which the aromatic benzene ring does not interact with the surface, $\eta^1(\text{C} - \text{O})$. Figure 2.4 shows these adsorption configurations. Configuration $\eta^2(\text{C} - \text{O})$, is the more stable configuration (Figure 2.4a, b) with adsorption free energy of -121 kJ/mol, as compared to -104 kJ/mol for the $\eta^1(\text{C} - \text{O})$ configuration (Figure 2.4c, d). The hollow face-centered cubic (fcc) site is preferred for the benzene ring to adsorb. Noticeably, in this arrangement, the oxygen and ring hydrogen atoms bend out of the plane. Guaiacol activation can take place through five possible pathways, namely (i) $\text{C}^1 - \text{O}$ and (ii) $\text{C}^2 - \text{O}$ (iii) $\text{C}^7 - \text{O}$ cleavage, and (iv) $\text{C}^{\text{ring}} -$ scission, (v) $\text{C}^{\text{ring}} -$ Hydrogenation, (see Figure 2.5 for the nomenclature of carbon atoms). Each of these pathways can further lead to the formation of several platform chemicals, as depicted in Figure 2.5 along with the first activation and reaction free energies for these five pathways. Direct cleavage of $\text{C}^2 - \text{O}$ and $\text{C}^7 - \text{O}$ bond are the most facile pathways in guaiacol activation, with free energy barriers of 62 and 60 kJ/mol, respectively. They can lead to the formation of Anisole, Phenol, Benzene, Cyclohexene,

Cyclohexane. However, the initial activation step may not be the rate-determining step, therefore determining Mo₂C selectivity for any of these products would need a thorough investigation of the entire reaction network.

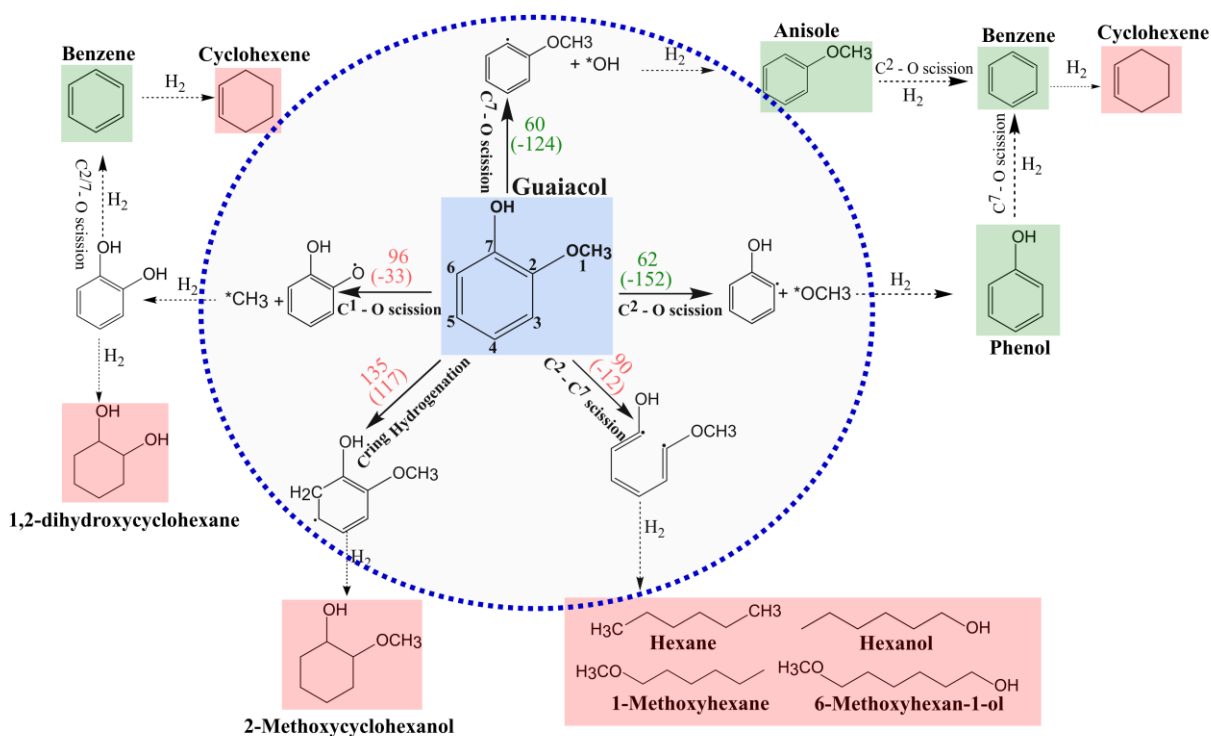


Figure 2.5 Schematic showing probable end products that can be obtained from guaiacol and potential mechanisms for the initial activation of guaiacol. The five potential routes via which guaiacol can activate are presented: $C^7 - O$ scission, $C^2 - O$ scission, $C^1 - O$ scission, C^{ring} hydrogenation, $C^{ring} - C^{ring}$ scission. C^{ring} includes the carbon atoms of the benzene ring which are labelled as $C^2 - C^6$. The nomenclature for carbon atoms is shown in the central guaiacol molecule. Free energy barriers and reaction free energies (in parenthesis) at 623 K and 1 bar are shown above the arrow for each pathway. Green and red color are used for favorable and unfavorable reaction steps, and products, respectively.

2.3.6.2 Benzene Formation

Guaiacol could be activated via direct cleavage of C – O bond leading towards the formation of aromatic products such as benzene which can form by three pathways: a) via an anisole intermediate in which $C^7 - O$ scission precedes $C^2 - O$ scission or b), via a phenol intermediate in

which $C^2 - O$ dissociation is followed by $C^7 - O$ dissociation or c) via a catechol intermediate which initiates via $C^1 - O$ cleavage and continues with either $C^{2/7} - O$ cleavage. Reaction energies and free energy barriers for pathways (a) and (b), going via anisole and phenol, are compared in Figure 2.6. With respect to the activation barriers, both direct deoxygenation pathways are favorable as both reaction steps showed competitive free energy barriers of 60 and 62 (kJ/mol) leading to the formation of 2 - methoxy phenyl ($C^7 - O$ cleavage) and 2 - hydroxy phenyl ($C^2 - O$ cleavage), respectively. It is followed by the hydrogenation at the corresponding C^7 and C^2 carbon atoms to form anisole and phenol intermediates, respectively. The energy barrier for the hydrogenation at C^2 carbon is calculated to be 126 kJ/mol which is 27 kJ/mol higher than the hydrogenation barrier at C^7 carbon (99 kJ/mol). However, thermodynamically, phenol formation seems more facile with its reaction free energy of -154 kJ/mol, in comparison to the -124 kJ/mol for anisole formation. Agrawal et al.¹⁸⁸ also reported comparable free energy barriers of 81 and 95 kJ/mol for methoxy and hydroxyl dissociation from guaiacol reaction steps on Mo_2C at 600 K. Moreover, they have also observed identical results in gas phase bond dissociation of guaiacol with activation barriers of 92 and 108 kJ/mol for $C^7 - O$ and $C^2 - O$ bond. The small difference in energy barriers from our results could be due to the different density functional incorporated in the two studies. Phenol and Anisole could undergo further direct deoxygenation via $C^7 - O$ and $C^2 - O$ cleavage, respectively, followed by the hydrogenation at the corresponding C^7 and C^2 carbon atom. On comparing the energy barriers, both dehydroxylation and demethoxylation are found to be competitive with similar barriers of 75 and 67 kJ/mol, correspondingly. Moreover, the methoxy dissociation reaction step from anisole is 55 kJ/mol more exergonic than the hydroxyl dissociation from phenol. However, slightly more exergonic nature of the phenol pathway could possibly make it a more favorable pathway for benzene formation. These results align well with the experimental observations¹²⁸ (provided in SI) in which only phenol was observed at 623 K. It was also noted that desorption of phenol is 89 kJ/mol more favorable on Mo_2C than anisole (84 kJ/mol vs. 173 kJ/mol), which suggests that anisole would likely undergo reaction over desorption. In comparison with metal catalysts like Cu and Pt, Mo_2C has shown better deoxygenation ability. Recently, Konadu et. al.¹⁸⁹ reported a high electronic energy barrier of 200 kJ/mol for the dehydroxylation step from guaiacol whereas, it is more feasible on Mo_2C with a low barrier of 78 kJ/mol (provided in Table B.1). On Pt (111) surface as well, high barriers of 240 and 244 kJ/mol for dehydroxylation and demethoxylation reaction steps, respectively were observed.¹⁹⁰ Moreover, even in the case of

a bimetallic catalyst with a combination of hydrogen active metal (Pt/Ni) and oxophilic metal (Fe), for instance, PtFe and NiFe have shown much higher barrier for the direct $C_{aryl} - OH$ bond with the values of 205 and 142 kJ/mol.¹⁹¹ It implies that Mo_2C possesses both acid sites which are essential for dehydration and metallic sites favorable for hydrogenation reaction steps.

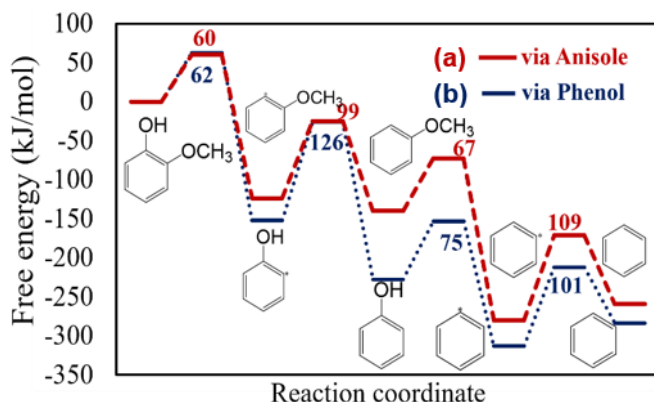


Figure 2.6 Comparison of free energy profiles for benzene formation on Mo_2C (1 0 0) surface at 623 K and 1 bar via two pathways (a) Anisole formation (in red), and (b) Phenol formation (in blue). Free energy barriers are also shown in red and blue color for the respective pathways in kJ/mol.

Another important intermediate compound catechol can also be formed from guaiacol via $C^1 - O$ cleavage followed by the hydrogenation step. As shown in Figure 2.5, the energy barrier for guaiacol initiation via $C^1 - O$ cleavage is 96 kJ/mol, which is ~ 37 kJ/mol higher than the direct $C^{2/7} - O$ bond dissociation which makes this pathway relatively unfavorable on the Mo_2C surface. Moreover, catechol formation via $C^1 - O$ cleavage is more endergonic than the direct deoxygenation pathway. A recent study by Agrawal et. al.¹⁸⁸ on Mo_2C (1 0 0) surface reported a free energy barrier of 122 kJ/mol for the demethylation step of guaiacol. Similarly, Zhou and coworkers¹⁹² also reported high electronic energy barriers of 160 and 120 for the demethylation reaction step on Ni (111) and Ni - Fe (111) alloys, respectively. It suggests that catechol formation is unlikely in the HDO of guaiacol on Mo_2C . However, catechol was observed as a primary intermediate over Ru/C catalyst at 673 K and 4.0 MPa.¹⁹³

2.3.6.3 Ring Hydrogenated Products (Cyclohexene and Cyclohexane)

Guaiacol hydrogenation to cyclohexene and cyclohexane can proceed through five pathways: (a) Direct ring hydrogenation of guaiacol followed by the $C^2 - O$ and $C^7 - O$ cleavage, (b) $C^2 - O$ dissociation precedes the ring hydrogenation of phenol followed by $C^7 - O$ dissociation, (c) $C^7 -$

O dissociation precedes the ring hydrogenation of anisole followed by C² – O dissociation, (d) C¹ – O cleavage of guaiacol to catechol followed by ring hydrogenation of catechol and terminates with C^{2/7} – O cleavage, (e) ring hydrogenation of benzene. We have explored and discussed all the pathways in the following subsections.

Table 2.3 Comparison of DFT Calculated Free Energy barriers (in kJ/mol) for Ring hydrogenation of Guaiacol Pathways on Mo₂C (100) surface at 623 K and 1 bar.

<i>Bond Type</i>	$\Delta G_{barrier}(kJ/mol)$	$\Delta G_{rxn}(kJ/mol)$
C ³ – H	151	119
C ⁴ – H	143	128
C ⁵ – H	135	117
C ⁶ – H	146	123

- *Direct Ring Hydrogenation of Guaiacol*

Ring hydrogenation would initiate at the C⁵ carbon atom of the aromatic ring as energy barrier for the hydrogenation at C⁵ has a lower barrier than at other carbon atoms, *i.e.*, 135 kJ/mol on C⁵ vs. 151, 143, and 146 on C³, C⁴, C⁶ carbons, respectively, as reported in Table 2.3. Free energy profile for the ring hydrogenation of guaiacol is shown in Figure 2.7. Guaiacol ring hydrogenation proceeds with the barriers of 135, 169, 160, 153 kJ/mol for the addition of 1st, 2nd, 3rd, 4th hydrogen atom at C⁵, C⁶, C³, and C⁴, respectively to form methoxycyclohexen-1-ol intermediate. Upon the formation of 2-methoxycyclohexen-1-ol, it proceeds with the dissociation of methoxy group with a very low barrier of 14 kJ/mol, followed by the hydrogenation at C² carbon producing 2 – cyclohexen-1-ol ((C₆H₉)OH). It would further undergo dehydroxylation reaction followed by hydrogenation at C⁷ carbon to produce cyclohexene with barriers of 19 and 104 kJ/mol, respectively. However, the formation of 2-methoxycyclohexen-1-ol would be inhibited due to relatively higher barriers for the direct hydrogenation of guaiacol in comparison to the direct deoxygenation (DDO) pathways discussed in the previous subsection 3.6.2. The guaiacol direct ring hydrogenation pathway continues with another spontaneous deoxygenation step with a negative reaction free energy of -129 kJ/mol and a small kinetic barrier of 19 kJ/mol with subsequent hydrogenation at C⁷ carbon leading to the formation of cyclohexene. The interesting

point to be highlighted from the ring hydrogenation of all the intermediate compounds is that ring hydrogenation lowers the free energy barriers of the subsequent deoxygenation steps.

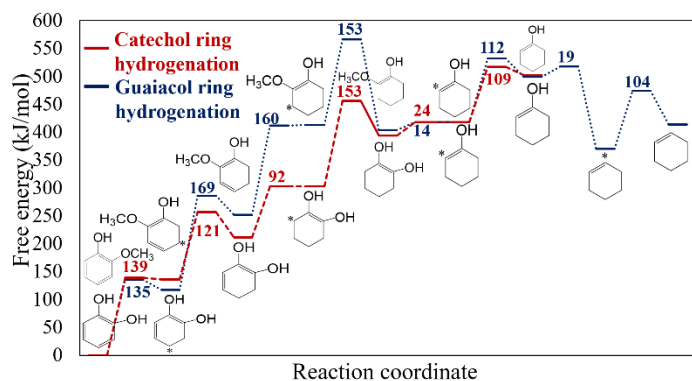


Figure 2.7 Free energy profiles of direct ring hydrogenation of guaiacol pathway and catechol ring hydrogenation pathway in blue and red color, respectively. Calculated barriers are shown in kJ/mol.

- *Guaiacol* → *Catechol* → *Cyclohexene Pathway*

This pathway initiates with first activation of guaiacol via $C^1 - O$ cleavage ($(C_6H_4)(OCH_3)(OH) \rightarrow C_6H_4(OH)(O) + CH_3$) followed by the hydrogenation at the oxygen center at C^2 carbon leading to form catechol as an intermediate. From Figure 2.5, it can be noted that demethylation is not kinetically favorable in comparison to DDO pathways due to relatively high barrier of 96 kJ/mol but it is thermodynamically favored with reaction free energy of -33 kJ/mol. For the cyclohexene formation, it continues with the ring hydrogenation of the aromatic ring via C^3 carbon atom with a higher energy barrier of 139 kJ/mol. Further ring hydrogenation at C^4 , C^5 , and C^6 carbons occur with the energy barriers of 121, 92, 153 kJ/mol, respectively as shown in Figure 2.7 (Red color). For the formation of cyclohexene, it undergoes dehydroxylation which could be possible via $C^2 / C^7 - O$ cleavage ($(C_6H_4)(OH)(OH) \rightarrow C_6H_4(OH) + OH$) with an energy barrier of 24 kJ/mol to form C_6H_4OH . It is followed by the hydrogenation step which produces 2-Cyclohexen-ol. Subsequently, 2nd dehydroxylation followed by hydrogenation at $C^{2/7}$ carbon to form cyclohexene with barrier of 19 and 104 kJ/mol, respectively. Similar to ring hydrogenation of guaiacol, the $C^{2/7} - O$ cleavage (DDO routes) becomes kinetically facile after the ring saturation as the bond dissociation barriers are reduced to only 24 kJ/mol and 19 kJ/mol for 1st and 2nd dehydroxylation steps, in comparison to DDO route *i.e.*, 60 kJ/mol. Overall, the 4th ring hydrogen addition reaction

was observed to be the rate-limiting step in the conversion of catechol to cyclohexene with the highest energy barrier of 153 kJ/mol.

▪ *Guaiacol* → *Phenol/Anisole* → *Cyclohexene Pathway*

As mentioned above, cyclohexene can also form as a result of the ring hydrogenation of the intermediates including phenol and anisole, which are formed in the DDO pathway. It initiates after the formation of phenol or anisole, where ring hydrogenation precedes dehydroxylation of phenol and demethoxylation of anisole. A comparison of energy profiles of this pathway for phenol (Blue color) and anisole (Red color) is shown in Figure 2.8. In the case of phenol, hydrogenation of the aromatic ring exhibits energy barriers of 113, 104, 131, 145 kJ/mol for the addition of 1st, 2nd, 3rd, and 4th hydrogen, respectively. However, the energy barrier for direct hydroxyl cleavage is lower than the 1st hydrogenation reaction step *i.e.*, (75 vs. 113 kJ/mol). The hydrogenation step after the hydroxyl cleavage to form benzene and 1st hydrogenation step of phenol has relatively similar energy barriers of 101 kJ/mol and 113 kJ/mol, respectively. The hydrogenation reaction step of phenol is 72 kJ/mol more endergonic than the benzene formation. It suggests that hydrogenation of aromatic ring of phenol is kinetically feasible on Mo₂C surface. Furthermore, it is to be noted that the energy barrier for C⁷ – OH dissociation after the 4th hydrogenation step has decreased significantly to 25 kJ/mol in comparison to 62 kJ/mol for direct C⁷ – O cleavage. It is thermodynamically more feasible with the reaction free energy of -170 kJ/mol. We also explored the possibility of cyclohexanol formation and results suggest that it is not favorable after the 4th hydrogenation step due to high kinetic barrier of 131 kJ/mol, as compared to dehydroxylation.

On the other hand, anisole ring hydrogenation initiation has an activation barrier which is 22 kJ/mol higher than phenol ring hydrogenation. Further hydrogenation of the anisole ring exhibits energy barriers of 119, 146, 135 kJ/mol for the addition of 2nd, 3rd, 4th hydrogen, respectively to form 1-methoxycyclohexene. It is followed by demethoxylation and subsequent hydrogenation with the energy barriers of, 49, and 118 kJ/mol, respectively. Similar to phenol, after the ring hydrogenation the energy barrier for C_{aryl} – O cleavage has reduced to 49 kJ/mol, as compared to 60 kJ/mol for the DDO pathway. Moreover, this step becomes 16 kJ/mol more exergonic as well. Based on the overall kinetics, anisole hydrogenation seems to be less favorable than phenol hydrogenation. Bhan and coworkers⁷⁸ have also provided experimental evidence for this

observation, as only 9% selectivity was reported for ring-saturated products in anisole HDO over Mo₂C under ambient pressure conditions at 423 K.

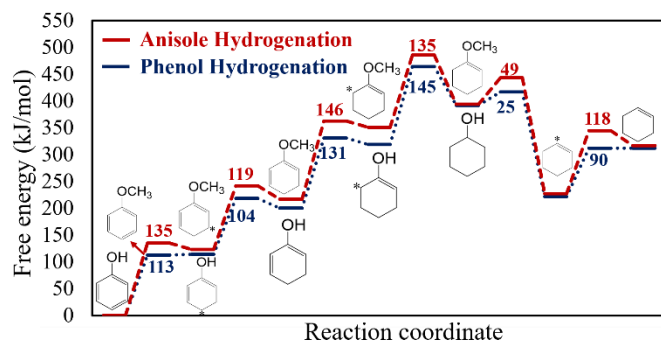


Figure 2.8 Comparison of free energy profile of Anisole and Phenol ring hydrogenation pathways on Mo₂C surface in red and blue color, respectively. Barriers are shown in kJ/mol.

- *Guaiacol* → *Benzene* → *Cyclohexane* Pathway

Benzene can form via DDO pathway as discussed in subsection 3.6.2 via anisole and phenol intermediates. We also investigated the possibility of cyclohexene and cyclohexane formation by hydrogenation of the benzene ring. Free energy profile of benzene ring hydrogenation is shown in Figure 2.9. This pathway includes six hydrogenation steps. Our calculations reveal that the sequential hydrogenation of the benzene ring has energy barriers of 109, 98, 124, and 83 kJ/mol for the addition of 1st, 2nd, 3rd, and 4th hydrogen atom, respectively. Further hydrogenation results in cyclohexane with free energy barriers of 109, 176 kJ/mol for the 5th, and 6th hydrogenation steps. Cyclohexane formation is 72 kJ/mol endergonic. It has to be noted that free energy barrier for the cyclohexene formation (4th step) is the lowest among the six hydrogenation reaction steps of benzene. This suggests that cyclohexene formation via benzene is more viable on Mo₂C surface than complete hydrogenation to cyclohexane. These findings are in agreement with experimental product distribution observed over Mo₂C catalyst 623 K (refer Table 2.5).¹²⁸ Higher selectivity of 59.1% towards cyclohexene as compared to only 2.2% for cyclohexane was observed in experiments. The high barrier of 176 kJ/mol for the last ring hydrogenation step would inhibit the formation of cyclohexane.

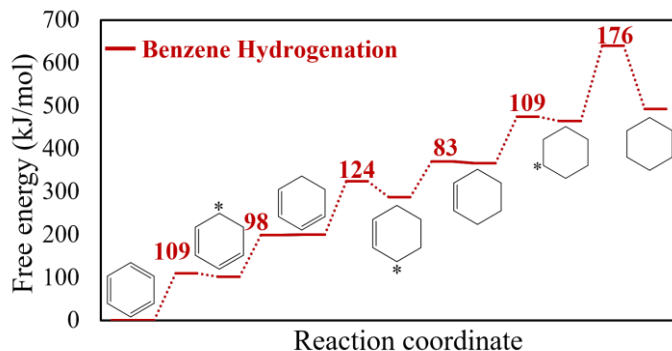


Figure 2.9 Free energy profile for benzene ring hydrogenation on Mo₂C at 623 K and 1 bar.

2.3.6.4 Linear chain Products (Hexene Formation)

In order to complete the reaction mechanism of guaiacol HDO over Mo₂C surface, we also investigated the possibility of ring opening resulting into the formation of linear chain alcohols, alkanes and alkenes. There are six prospective C – C bonds which could dissociate in order to open the aromatic ring of guaiacol. We compared the free energy barriers of all the six possibilities and our results predict that the ring opening at C² – C⁷ exhibits the minimum barrier of 97 kJ/mol, as shown in Table 2.4. This could be due to the steric hinderance of two functional groups i.e., methoxy and hydroxyl attached at C² and C⁷ carbon atom of guaiacol, respectively, which makes the bond dissociation relatively more facile in comparison to the other possibilities. Moreover, it is thermodynamically feasible as well with reaction free energy of -16 kJ/mol. Calculations revealed that after the ring-opening step, hydrogenation at C² or C⁷ carbon is nether kinetically nor thermodynamically favored, with a high barrier of 149 and 142 kJ/mol, respectively as shown in Figure 2.10a. According to the considered reactions, the most kinetically feasible and spontaneous reaction turns out to be demethoxylation with a very low barrier of 15 kJ/mol. On comparison with demethoxylation, dehydroxylation reaction showed a relatively higher barrier of 44 kJ/mol and both reactions are highly exergonic with -205 and -183 kJ/mol of reaction free energy, respectively. One other possibility is the demethylation, however, the rate limiting step in the demethylation pathway is hydrogenation at O atom at C² carbon with a barrier of 205 kJ/mol, leading to open chain diol products. Therefore, the demethylation pathway was not further explored. The energetics of two DDO pathways are compared in Figure 2.10b. It can be noted that both pathways are competitive. Interestingly, the ring opening also has a significant effect on the deoxygenation reaction steps, especially on demethoxylation. The barrier is reduced by 45 kJ/mol in comparison to the direct C² – O cleavage of guaiacol.

Table 2.4 Comparison of DFT Calculated Free Energy barriers (in kJ/mol) for Ring-Opening of Guaiacol Pathway at 623 K and 1 bar.

Bond Type	$G_{\text{barrier}}(\text{kJ/mol})$	$\Delta G_{\text{rxn}}(\text{kJ/mol})$
C ² -C ⁷	97	-13
C ³ -C ⁴	134	128
C ² -C ³	155	21
C ⁴ -C ⁵	119	65
C ⁵ -C ⁶	108	-1
C ⁶ -C ⁷	130	64

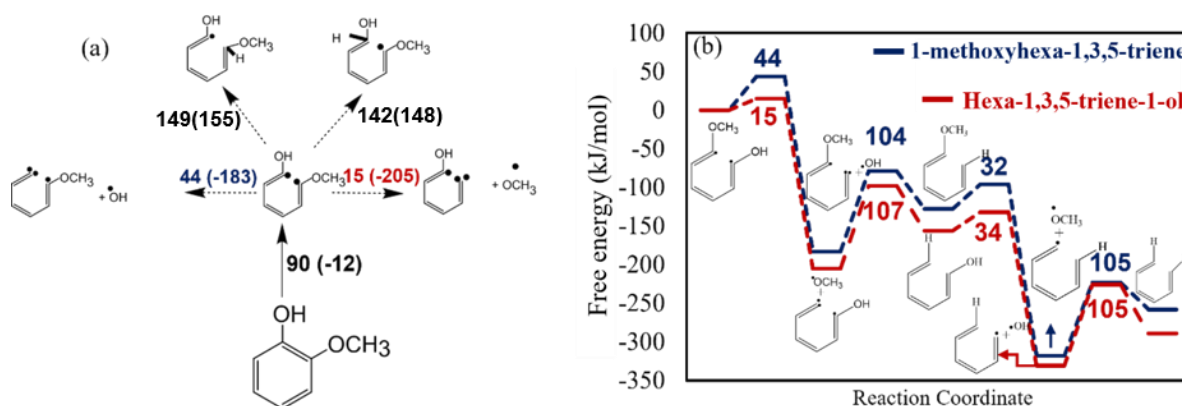


Figure 2.10 (a) First activation free energy barrier of possible pathways after ring-opening is shown. (b) Free energy profiles for hexane formation via two competitive pathways is shown for guaiacol HDO on Mo₂C surface at 623 K and 1 bar. Kinetically favored pathways are highlighted for the formation of the dominant product (hexene). Above the arrow lines, free energy barriers and reaction free energies (in parentheses) in kJ/mol are indicated.

2.3.6.5 Proposed Reaction Pathways

We now summarize the complete reaction mechanism and energetics for different guaiacol conversion pathways on the molybdenum carbide (Mo₂C (100)) surface, as shown in Figure 2.11. Thermodynamically, benzene via phenol (from C² - O scission) and benzene via anisole (from C⁷ - O scission) are favoured over Mo₂C surfaces. The two pathways mentioned above also have the lowest initial activation barriers (62 and 60 kJ/mol, respectively). Among all the pathways studied, benzene via anisole (C⁷ - O cleavage), benzene via phenol (C² - O cleavage), and cyclohexene formation via benzene ring hydrogenation have the lowest barriers for the rate determining step of only 99, 126 and 123 kJ/mol: thus, suggesting them to be the favoured products of guaiacol HDO

on Mo₂C. The low C² – O scission and C⁷ – O scission barriers of 62 and 60 kJ/mol for guaiacol suggest that both the pathways are kinetically competitive. Next, we focus on the potential reaction pathways originating from a C² – O scission and C⁷ – O scission. After their formation, phenol and anisole can either further undergo hydrodeoxygenation to benzene or hydrogenate to form cyclohexene. As discussed in earlier sections, the former is both thermodynamically and kinetically favoured. On the other hand, only the hydrogenation of phenol formed after C² – O scission followed by hydrogenation is kinetically feasible in comparison to anisole hydrogenation. Direct deoxygenation (C² – O or C⁷ – O scission) would lead to benzene formation, whereas phenol hydrogenation would form cyclohexene. Thus, mixture of benzene and cyclohexene are suggested to be the major products from guaiacol.

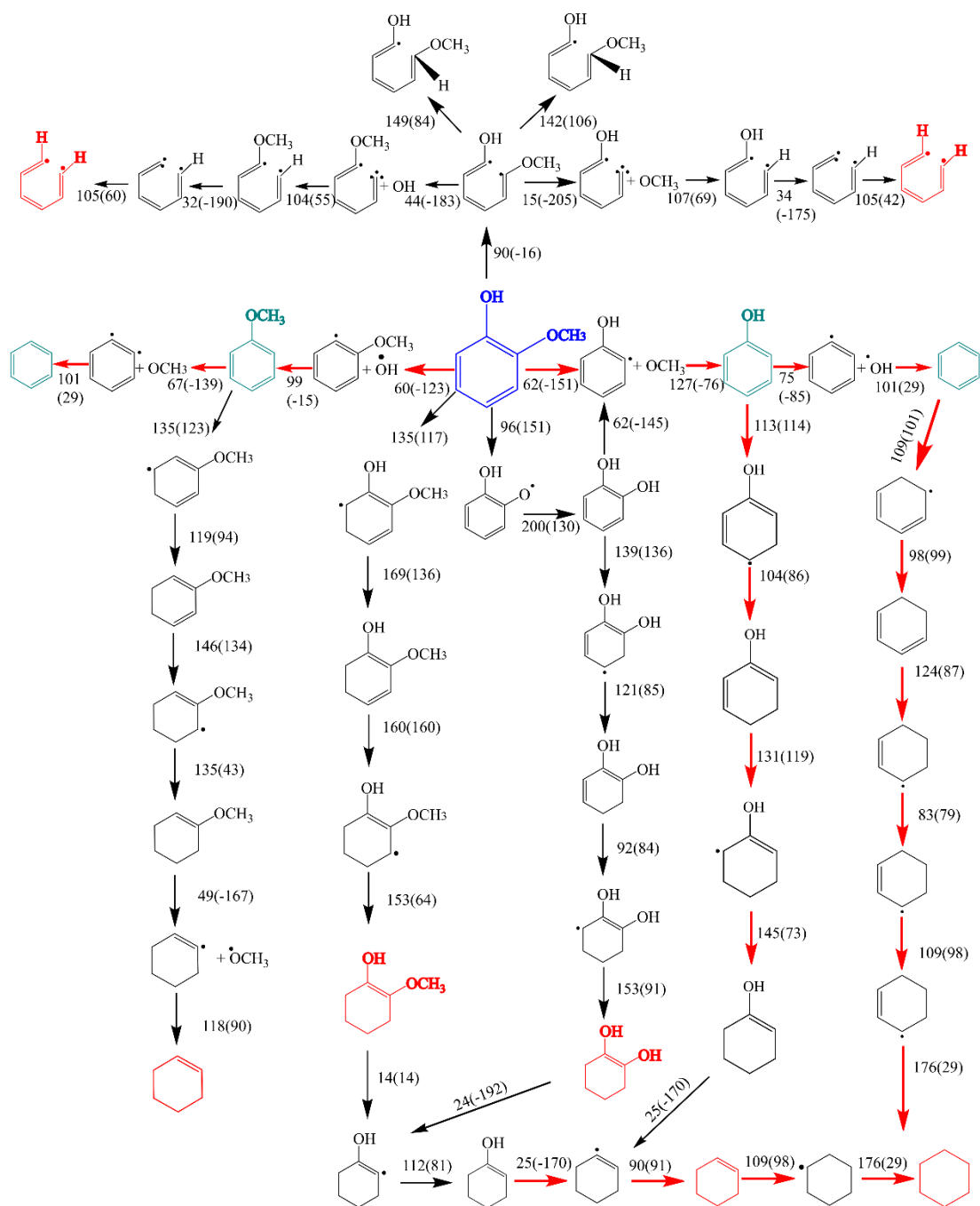


Figure 2.11 Proposed reaction pathway for Guaiacol activation on Mo₂C (100) surface. Kinetically favored pathways for the formation of Benzene, Anisole, Cyclohexene, Cyclohexane and Phenol are highlighted in red color. Indicated above the arrows are free energy barriers and reaction free energies (in parentheses) in kJ/mol. According to our calculations, the surface of Mo₂C kinetically

and thermodynamically favours benzene and cyclohexene. Green and red colour are used for favourable and unfavourable reaction steps, and products, respectively.

2.3.7 Tungsten doped Molybdenum Carbide Catalyst (MoWC) for guaiacol HDO

2.3.7.1 Guaiacol Adsorption configuration on Tungsten-doped Mo₂C

The most stable MoWC model, Case 6, was used to study guaiacol HDO. Adsorption of guaiacol at different sites was considered on the MoWC surface, and the most stable adsorption configuration is shown in Figure 2.12. The presence of metallic tungsten enhances the guaiacol adsorption free energy significantly. In this case, it adsorbs in the most stable $\eta^1(-C-O)$ configuration with the free energy of adsorption of -169 kJ/mol at 623 K, which is 48 kJ/mol stronger than the most stable configuration on the Mo₂C surface. It suggests oxophilic tungsten metal facilitates the adsorption of guaiacol via the oxygen atom either of hydroxyl or methoxy functional group. One peculiar observation about the adsorption of guaiacol is the transfer of methyl group from the oxygen atom to C² carbon as it adsorbs via the oxygen atom to tungsten atom present on the catalyst surface, as shown in Figure 2.12. It indicates the possibility of the formation toluene on MoWC surface which is in contrast with Mo₂C surface. Along with the binding energies, C – O (d_{C-O}) distances are also shown in Table B.2. It can be seen that C – O bond length stretches to 1.49 Å for the adsorbed guaiacol configuration on MoWC whereas, C – O bond length is 1.43 Å on the Mo₂C surface. It can be inferred that dissociation of C – O would be easier on MoWC, as compared to that on Mo₂C.

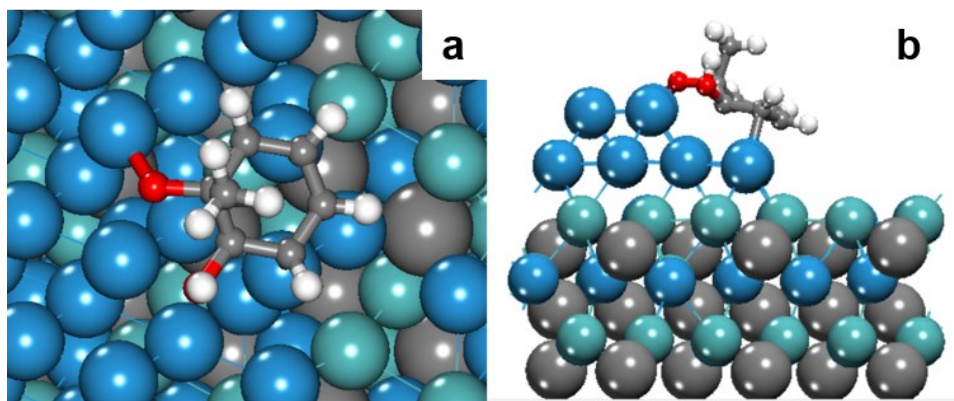


Figure 2.12 Top and side view of the optimized geometry of the most stable guaiacol adsorption configuration over MoWC surface in (a) and (b), respectively. The Mo and W atoms in the carbides

are represented as dark cyan and blue spheres, respectively. The atoms in the adsorbed guaiacol is represented by white, red, and grey spheres for H, O, and C, respectively.

2.3.7.2 Guaiacol Activation on Tungsten doped Mo_2C (MoWC) surface

Direct deoxygenation (DDO) and hydrogenation-dehydration (HYD) are the two main routes involved in the broadly perceived mechanism for the HDO of guaiacol.^{30,186} In this section, direct deoxygenation (DDO) pathways and hydrogenation (HYD) pathways for guaiacol HDO are evaluated on MoWC surface and are compared with monometallic Mo_2C . On MoWC, $\text{C}^2 - \text{O}$ cleavage is facile with a very low barrier of 18 kJ/mol and with a reaction free energy of -180 kJ/mol which leads to the formation of cresol after subsequent hydrogenation at C^2 carbon. It could be due to the presence of Oxophilic tungsten overlayers on MoWC that facilitates the adsorption of guaiacol via oxygen atoms in the hydroxyl or methoxy groups. Due to high oxygen affinity of tungsten, it forms a strong metal – oxygen bond resulting in a stretched C – O bond which makes the C – O dissociation more facile on MoWC in comparison to Mo_2C . As mentioned previously, transfer of methyl group is observed from O^1 to C^2 carbon atom of guaiacol. The transfer of methyl group leads to intermediates like cresol which were absent on Mo_2C surface. To provide an exact comparison, we used cresol and phenol as intermediates to compare the energetics of dehydroxylation and hydrogenation in each individual reaction step on Mo_2C and MoWC. We also added bulk MoWC_4W (Case 4) catalyst for comparison to confirm the involvement of metallic tungsten overlayers in the reduction of direct deoxygenation barriers. The comparison of free

energy barriers of cresol's direct dehydroxylation and direct ring hydrogenation steps is shown in Figure 2.13.

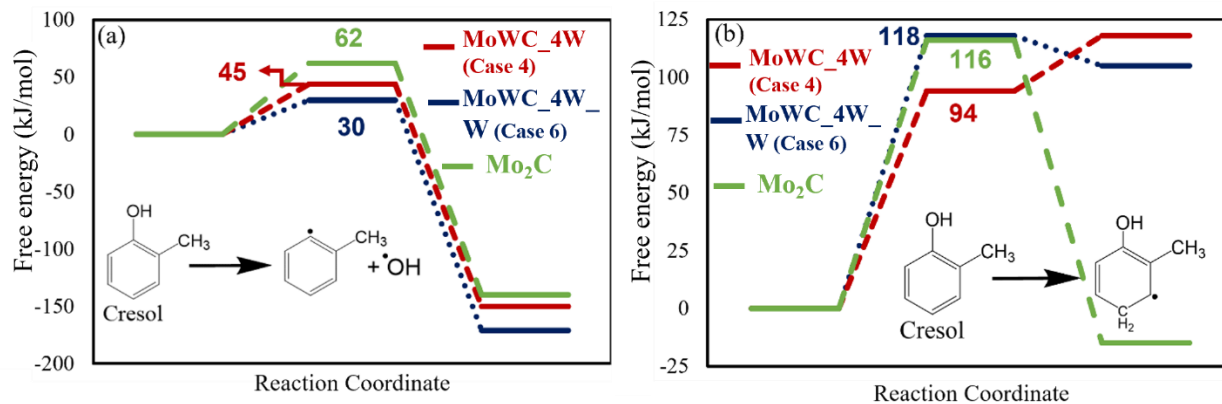


Figure 2.13 Comparison of free energy barriers of (a) Direct dehydroxylation reaction (b) Ring hydrogenation of cresol among Mo₂C (Green), MoWC (Blue), and MoWC_bulk (Red) catalyst surface.

It should be highlighted that MoWC catalyst showed a lower free energy barrier of 30 kJ/mol for dehydroxylation in comparison to 62 kJ/mol on Mo₂C. Moreover, it is also lower than the barrier of 44 kJ/mol on Case 4 which doesn't contain metallic tungsten overlayers, confirming the role oxophilic tungsten overlayers. In addition, the dissociation of hydroxyl group is 31 and 21 kJ/mol more exergonic on MoWC surface than Mo₂C and MoWC_bulk catalyst, respectively. On the other hand, ring hydrogenation reaction step is competitive on MoWC and Mo₂C with barrier of 118 and 116 kJ/mol, whereas MoWC_bulk showed the least barrier of 94 for the same. The difference between the DDO and HYD pathways is observed to be highest of 88 kJ/mol on MoWC in comparison to 54, and 50 kJ/mol on Mo₂C, and MoWC_bulk correspondingly. This confirms that bimetallic carbide MoWC catalyst favors DDO pathways in cresol HDO leading to the formation of aromatic products and is relatively less facile for the hydrogenation of aromatic ring.

Another prominent intermediate is phenol which is common between Mo₂C and MoWC surface. On MoWC, phenol could be formed via demethylation step of cresol followed by the hydrogenation at C² carbon. The comparison of hydroxyl dissociation and ring hydrogenation energy barriers of phenol on MoWC, Mo₂C, and MoWC_bulk is shown in Figure 2.14. Similar to cresol, dehydroxylation reaction from phenol is more favorable on MoWC surface with the lowest barrier of 26 kJ/mol as compared to that on Mo₂C (60 kJ/mol), and MoWC_bulk (101 kJ/mol). In

contrast to cresol, MoWC_bulk showed the highest barrier of 101 kJ/mol in the phenol dehydroxylation. Thermodynamically, removal of hydroxyl group from phenol is feasible on all the three catalysts, however, it is more exergonic on MoWC surface than MoWC_bulk, and Mo₂C by 77, and 83 kJ/mol, respectively. Ring hydrogenation of phenol follows the same trend on MoWC and Mo₂C with competitive barriers of 113, and 112 kJ/mol. Also, in the case of phenol, MoWC manifested the highest difference between the barriers for DDO and HYD pathways i.e., 86 kJ/mol. Overall, the comparison of DDO and HYD pathways on these catalysts confirms that metallic tungsten overlayers play a vital role in reducing direct deoxygenation energy barrier. For the deoxygenation of phenolics, direct dehydroxylation (C⁷ - OH) is known as the most effective but also the most challenging elementary reaction because it necessitates the direct cleavage of the C (sp²) - OH bond before the hydrogenation of the phenyl ring. According to the results, MoWC manifested a superior HDO performance with least energy barriers for DDO pathways.

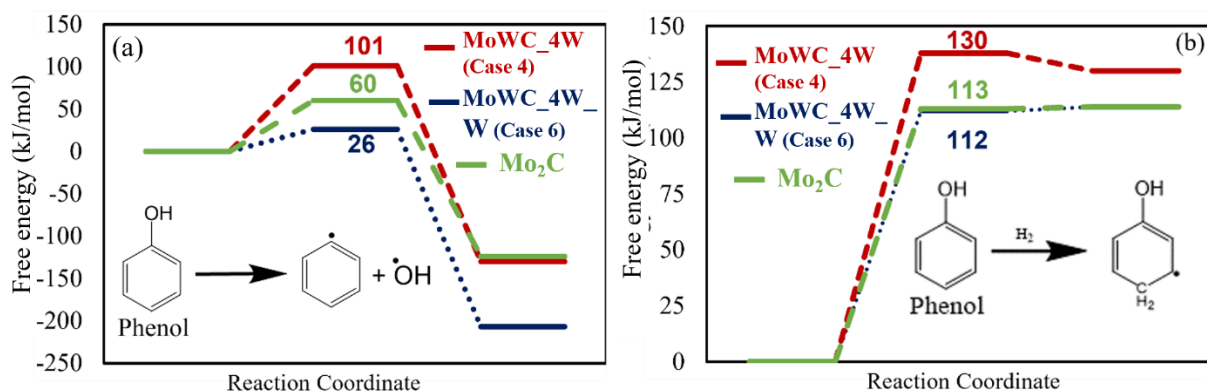


Figure 2.14 Comparison of free energy barriers of (a) Direct dehydroxylation reaction (b) Ring hydrogenation of Phenol among Mo₂C, MoWC, and MoWC_bulk catalyst surface.

2.3.7.3 Ring Hydrogenation pathways

We investigated the ring hydrogenation of intermediates like phenol and benzene on MoWC in order to corroborate the experimental results that showed Mo₂C to have higher selectivity towards ring hydrogenated products like cyclohexene and cyclohexane than MoWC. The comparison of free energy profiles of benzene ring hydrogenation and phenol ring hydrogenation between Mo₂C and MoWC is shown in Figure 2.15. Benzene ring hydrogenation is initiated with relatively high activation barrier of 142 kJ/mol in comparison to 109 kJ/mol on Mo₂C. Further ring hydrogenation of benzene leads to cyclohexane with barriers of 96, 209, 50, 34, and 122 kJ/mol for the addition

of 2nd, 3rd, 4th, 5th, and 6th hydrogen atom, respectively on MoWC. On comparing the highest energy barrier in the conversion of benzene to cyclohexene (MoWC (209kJ/mol) vs. Mo₂C (124kJ/mol)), it was found to be 85 kJ/mol higher on MoWC. It clearly suggests that benzene hydrogenation is unfavorable on MoWC, relative to Mo₂C, due to which it would not promote the formation of ring saturated products i.e., cyclohexene, and cyclohexane. On the contrary, cyclohexene formation seems to be relatively favorable on Mo₂C as the highest barriers in the benzene formation and cyclohexene formation are 101, and 124 kJ/mol, respectively. Furthermore, benzene desorption energies on both surfaces were also estimated and compared, and it was found that benzene desorption is 20 kJ/mol easier on MoWC (90 kJ/mol) than Mo₂C (110 kJ/mol).

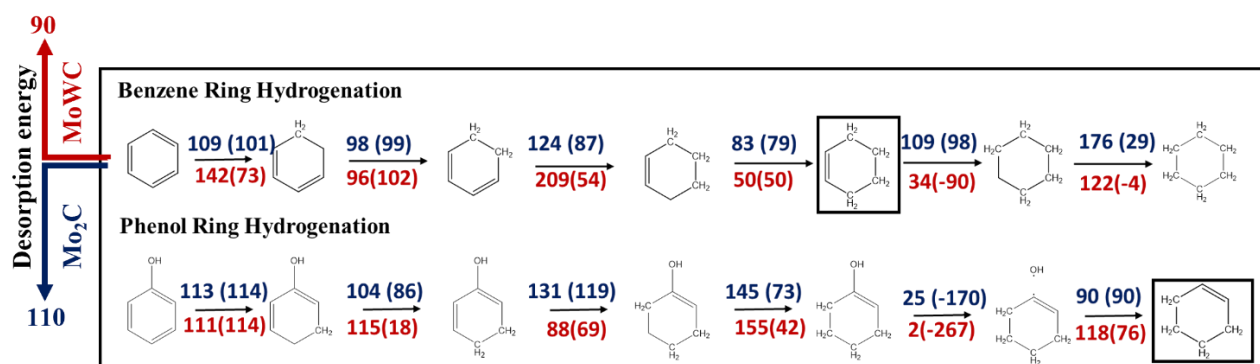


Figure 2.15 Comparison of ring hydrogen pathway for Benzene and Phenol between Mo₂C and MoWC. Free energy barriers and reaction free energies (in parenthesis) calculated at 623 K and 1 bar with units kJ/mol are shown for Mo₂C (blue) and MoWC (red), respectively.

The hydrogenation of the phenol ring follows a similar pattern to that of benzene. On Mo₂C and MoWC, the activation barriers for ring hydrogenation of the phenol ring are similar, with values of 113 and 111 kJ/mol, respectively. Further hydrogen additions lead to the formation of cyclohexen-1-ol, with energy barriers of 115, 88, and 155 for the second, third, and fourth hydrogen additions to the aromatic ring, respectively. It can now either proceed to the synthesis of cyclohexanol with one more hydrogen addition or to the formation of cyclohexene by dehydroxylation followed by hydrogenation pathway. The calculated free energy profile reveals that the dehydroxylation pathway is facile with a barrierless reaction step than the cyclohexanol formation pathway, which has a higher barrier of 143 kJ/mol. Furthermore, as demonstrated in Figure 2.16, cyclohexanol synthesis is 370 kJ/mol more endergonic than dehydroxylation. It confirms that the synthesis of cyclohexene is more favorable on Mo₂C. Deoxygenation barriers

are lowered followed by ring hydrogenation, and the barrier for dehydroxylation on MoWC is reduced even further to only 2 kJ/mol, compared to 30 kJ/mol for the direct dehydroxylation step.

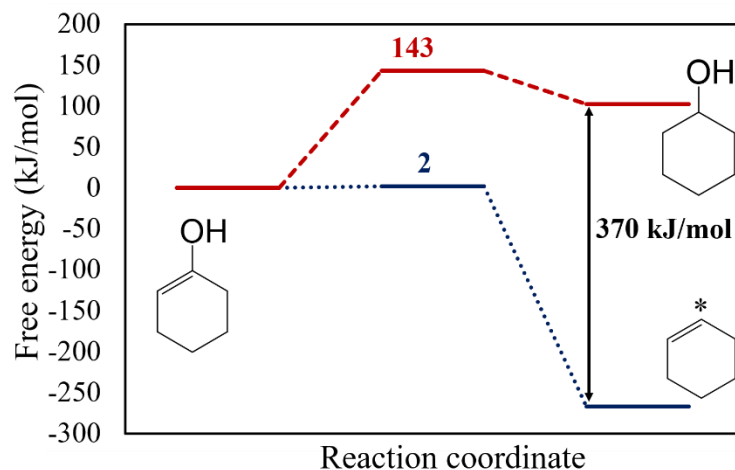


Figure 2.16 Comparison of ring hydrogen pathway for Benzene and Phenol between Mo₂C and MoWC. Free energy barriers and reaction free energies (in parenthesis) calculated at 623 K and 1 bar with units kJ/mol are shown for Mo₂C (blue) and MoWC (Red), respectively.

2.3.8 Comparison with Experimental Results for Guaiacol HDO

The HDO experiments were conducted at 623 K and 400 psig H₂ pressure on Mo₂C and MoWC catalysts to compare the performance of monometallic (Mo₂C) and bimetallic carbide (MoWC) catalysts.¹²⁸ The product distribution of the guaiacol HDO over carbides at 623 K is shown in Table 2.5(Case –1). It was observed that MoWC facilitates the formation of aromatic deoxygenated products *i.e.*, Benzene with 70% selectivity. On the contrary, the HDO reaction over Mo₂C produced cyclohexene as the dominant product at 59.1 mol%. It could be due to hydrogenation and dehydration reactions of intermediates formed in the DDO pathway (phenol and benzene). Moreover, we also compared the product selectivity at similar conversions (48% and 50% for Mo₂C and MoWC, respectively) as shown in Table 2.5 (Case – 2). For MoWC, benzene accounts for 63.5 mol% of the final product, whereas cycloalkanes get a lower fraction (8.9 mol% for cyclohexene, for example). For Mo₂C, however, the ratio of benzene selectivity to cycloalkane selectivity is 1:1, which suggests that the HDO of guaiacol occurred via both DDO and HYD pathways.

Table 2.5 Product distribution observed in two cases over Mo₂C and MoWC catalysts in the HDO of Guaiacol at 623 K, and P = 400 psig.

Catalyst (Case -1)	Conversion (%)	Product Selectivity (mol %)				
		Phenol	Benzene	Toluene	Cyclohexene	Cyclohexane
Mo₂C	78	15.1	22.1	–	59.1	2.2
MoWC	93	7.8	70	6.4	–	15.8

Catalyst (Case -2)	Conversion (%)	Product Selectivity at similar conversions (mol %)				
		Phenol	Benzene	Toluene	Cyclohexene	Cyclohexane
Mo₂C	48	30	38	–	29	3
MoWC	50	11.5	63.5	15	8.9	2.1

Our DFT findings correspond very well with the experimentally observed product distribution over Mo₂C and MoWC catalysts. Comparison of energy barriers for DDO pathways (Figure 2.13 & 2.14) on both catalysts shows that the barriers have significantly reduced for the direct dissociation of C^{aryl} – O bond on MoWC due to the oxophilic tungsten overlayers on which the oxygen atom of the hydroxyl or methoxy group gets adsorbed. For instance, barriers for direct dehydroxylation of cresol and phenol on MoWC dropped down to 30 and 26 kJ/mol, respectively in comparison to 62 and 60 kJ/mol on Mo₂C. It confirms that MoWC favours DDO pathways. For the hydrogenation-dehydration (HYD) pathways leading to the formation of cyclohexene or cyclohexane, increase in the barriers of ring hydrogenation of benzene and phenol on MoWC are observed, in comparison to Mo₂C, as shown in Figure 2.15. The energy barrier for 1st hydrogen addition to benzene ring is increased by 33 kJ/mol on MoWC as compared to Mo₂C. Moreover, the difference in energy barriers between DDO and HYD pathways is increased on MoWC to 88 and 86 kJ/mol in comparison to Mo₂C (64 and 63 kJ/mol) in case cresol and phenol, respectively.

As mentioned previously, the barrier of the rate limiting step in the benzene formation is relatively similar for phenol and benzene (Table 2.5 (case -2)) ring hydrogenation, suggesting both HYD and DDO pathways are equally facile on Mo₂C. It explains the relatively higher selectivity towards cyclohexene on Mo₂C surface.

2.4 Conclusions

In this work, the structure, activity, and selectivity of a novel tungsten doped molybdenum carbide catalyst (MoWC) were investigated and compared to its monometallic carbide counterpart Mo₂C. Firstly, different model structures of the bimetallic carbide (MoWC) catalyst were screened to identify the location of tungsten in the mixed metal carbide based on their relative stabilities. The configuration that exhibited highest stability and agreed with the experimental characterization data was revealed. Bulk MoWC, (W/Mo atomic ratio 1:1) with metallic tungsten overlayers was found to be the microstructure that represented the experimentally synthesized bimetallic carbide most accurately and was thermodynamically stable. Theoretically calculated positive XPS shift of +0.38 eV in W 4f spectra for surface W atoms was consistent with the experimental observation of +0.3 eV shift in the W 4f XPS spectra. Additionally, shifts in d-band center of the mono- and bi-metallic carbides showed a linear correlation with experimentally observed shifts in core-level binding energies. This further validated the suggested microstructure for the bimetallic carbide catalyst. The presence of metallic tungsten overlayers induces a step-like structure on the top surface layer of bulk MoWC. A comprehensive reaction map of guaiacol HDO was investigated on Mo₂C and among all the pathways studied, benzene via anisole (C⁷ – O cleavage), benzene via phenol (C² – O cleavage), and cyclohexene formation via benzene ring hydrogenation have the lowest barriers for the rate determining step of only 99, 126 and 123 kJ/mol. It confirms that both HYD and DDO pathways are competitive on Mo₂C resulting in a mixture of deoxygenated and ring saturated products. However, On MoWC, presence of metallic tungsten facilitates the adsorption of guaiacol via the oxygen atom either via hydroxyl or methoxy functional group. As a result, direct deoxygenation of guaiacol on MoWC becomes facile with a very low barrier of 18, and 30 kJ/mol for demethoxylation and dehydroxylation steps, in comparison to 60, and 62 kJ/mol on Mo₂C. Moreover, generated surface adsorbed species like phenol, benzene would not preferentially ring hydrogenate on MoWC due to higher activation barriers, resulting into the formation of aromatic products with higher selectivity. It demonstrates that the MoWC catalyst, which inhibits the formation of cycloalkenes and cycloalkanes, causes the difference between HYD and DDO to widen. These findings perfectly fit the experimental data, which demonstrated higher selectivity for the DDO route on MoWC and higher selectivity for the HYD pathway on Mo₂C. The promotional effect of the tungsten overlayers in enhancing the activity of Mo₂C is due to the oxophilic nature of tungsten and charge transfer from W to Mo, contributing synergistically

the bifunctionality of the bimetallic MoWC carbide. This study emphasizes the importance of using both theory and experiments to comprehend the nature/morphology of the bimetallic catalyst. The fundamental distinctions between mono- and bimetallic carbide catalysts in HDO reaction energetics were also made clear. Finding the correct and stable site of dopants, like W in this instance, is crucial since it can alter the product selectivity and adsorption characteristics. According to the mechanistic findings of this work, the search for alternative catalysts for the hydrodeoxygenation of oxygenated substances may be restricted to metal carbides that possess both acid-site and hydrogen-active site capabilities. However, for the HDO process to work synergistically, optimization of both capabilities with the suitable dopants is essential, especially with high oxophilicity.

Chapter 3: Revealing the Potential of Bimetallic Carbide Catalysts for Upgrading Biomass-derived Bio-Oil: A First Principles-Based Investigation Using Representative Bio-oil Constituents²

Abstract

Bimetallic carbides, especially based on molybdenum carbide, proved to be a promising hydrodeoxygenation (HDO) catalyst, with enhanced selectivity towards C – O bonds cleavage. However, catalysts are generally investigated using limited model components derived from only one of the biopolymers in biomass (either lignin or carbohydrates), therefore, HDO of raw biomass-derived bio-oil still remains a challenge, as it contains molecules of different functionalities. This paper presents a systematic comparison of the monometallic carbide, Mo₂C, with the novel bimetallic carbide incorporating W using representative bio-oil components of different functionalities and derived from different bio-polymers components of biomass. We employed quantum mechanical investigation to reveal that the W-doped Mo₂C carbide (MoWC) catalyst with increased oxophilicity, owing to tungsten incorporation, can perform HDO of real bio-oil more effectively in comparison to its monometallic counterpart (Mo₂C) using six substrates representing different components of bio-oil. We showed MoWC can selectively cleave both single/double (C – O/C = O) bonds with similar barriers in comparison to Mo₂C which can only selectively cleave single C – O bonds. This observation was consistent for 5-HMF, Acetic acid, and Methyl Glyoxal. We also showed that MoWC outperforms its metallic counterpart Mo₂C in the HDO for aromatic and carbohydrates components.

² This Chapter and Appendix C of this thesis have been submitted for publication, as Sagar Bathla, and Samir H. Mushrif, "Revealing the Potential of Bimetallic Carbide Catalysts for Upgrading Biomass-derived Bio-Oil: A First Principles-Based Investigation Using Representative Bio-oil Constituents."

3.1 Introduction

Lignocellulose biomass has the potential to meet the rising fuel demand due to its vast abundance and capability to support the sustainable production of liquid and gaseous biofuels.¹⁹⁴ However, the raw bio-oil, produced from the valorization of biomass, contains more than 400 oxygenated constituents¹, which leads to some of its undesirable characteristics like 1) Reduced heating value, 2) Chemical instability, and 3) Corrosive nature. These characteristics restrict its direct use as a transportation fuel and also poses major challenges in its storage and transportation. Therefore, selective removal of oxygen is necessary to improve its quality. Catalytic upgrading is one of the possible ways by which it can be upgraded to useful chemicals and fuels. In particular, Hydrodeoxygenation (HDO), in which hydrogen is supplied and oxygen is removed as water (H₂O) by a catalytic reaction, while keeping the other types of chemical bonds (C – H and C – C) intact, is a sustainable and viable way to upgrade the bio-oil.⁶² Till now, a plethora of studies have been reported on different types of catalysts for HDO of bio-oil including CoMo, and NiMo sulphided catalysts^{136,195–197}, noble metals^{77,198,199} such as Ru, Pt, and Pd, and non-noble metals^{139,200}. However, the use of a toxic sulfur reagent added during the process is necessary for sulphided catalysts which is highly unfavorable. Noble metals especially Ru displayed promising results, but high cost and limited availability of these catalysts make them uneconomical on an industrial scale.

In the ground-breaking discovery by Levy and Boudart³⁶ they elucidated noble metal like behavior shown by transition metal carbides (TMCs). Since then, TMCs especially, molybdenum carbide (Mo₂C) and tungsten carbide (WC, W₂C) have been drawing attention for their application in different processes including hydrogen evolution reactions^{201–203}, CO₂ conversion^{204–206}, and methane dry reforming^{207,208}. Hydrodeoxygenation (HDO) of bio-oil represents an emerging field where these catalysts have demonstrated promising results. Researchers are actively engaged in extensive investigations to unlock their potential for enhancing and upgrading bio-oil.^{64,74,125,209} It is now proven that Mo – C catalysts are bifunctional, exhibiting both acid-site and hydrogen-active site functionalities^{37–39}, and this bifunctionality is essential for HDO³⁰. To date, numerous researchers have examined the HDO capability of Mo₂C using isolated model constituents. For instance, smaller linear oxygenates like propanal, propanol, acetic acid etc were used as probe molecules to test catalysts for HDO process as they form a significant portion of the bio-oil.¹ Ren et. al. examined both tungsten and molybdenum carbide (WC/Mo₂C) catalysts using propanol and

observed that it gets converted to propanal first which is followed by the C = O cleavage with low barriers of 66 kJ/mol, and 33 kJ/mol on WC (0001) surface. Similarly, on Mo₂C too, C – O dissociation was found to be facile with a barrier of 61 kJ/mol. Similar results for acetic acid were reported by Schaidle and workers where the cleavage of C – O bonds was computed to be more favorable than C – C bonds, producing acetaldehyde and ethylene.⁴⁶ Bhan and co-workers noted that Mo₂C exhibited exceptional selectivity in the vapor-phase HDO of anisole, yielding benzene as the primary product (>90%) among the C₆⁺ products. These favorable results were achieved at relatively low temperatures (420 – 520 K) and standard atmospheric pressure. Additionally, they reported that the catalyst displayed good stability, remaining effective for a duration of approximately 50 hours. Mo₂C catalyst also had been tested for a mixture of phenolic constituents in the vapor phase HDO and manifested a high aromatic yield (>90%, benzene and toluene) under atmospheric pressure at 533 – 553 K.²¹⁰ Xiong et. al. reported high selective deoxygenation ability of Mo₂C for converting Furfural to 2-Methylfuran.⁶⁴ In their findings, they identified 2-methylfuran as the primary product, exhibiting the selectivity of around 60% at 423 K and it was attributed to the strong interaction between the carbonyl (C=O) bond of furfural and the Mo₂C surface. Shi et. al. elucidated the pivotal influence of H₂ partial pressure in the HDO process of furfural (F – CHO). They achieved this by contrasting crucial reaction pathways on a clean Mo₂C surface with that of a Mo₂C surface pre-covered with H₂. According to their findings, when Mo₂C is pre-covered with hydrogen, it exhibits a preference for the hydrogenation of furfural into furfuryl alcohol (F - CH₂O) as opposed to the dissociation of furfural into F – CO + H, which leads to furan formation. This preference is observed both from kinetic and thermodynamic perspectives, indicating that under elevated hydrogen pressure, Mo₂C tends to favor the hydrogenation pathway. Tran et al. also obtained comparable findings in the HDO of guaiacol on Mo₂C. Their research revealed a mixture of cyclohexene and benzene as the primary products, with benzene being a minor product, at a temperature of 623 K and a pressure of 2.75 MPa. Nevertheless, the utilization of high hydrogen pressure presents two significant challenges: 1) Hydrogen is a costly resource, and high consumption of hydrogen can render the HDO process economically unfavorable, and 2) High hydrogen pressure may induce sequential hydrogenation reactions, leading to the undesirable formation of ring-saturated products, which may not align with the desired product profile. Aforementioned investigations suggest Mo₂C to be a potential catalyst for the HDO of bio-oil derived constituents but desired selectivity remains a challenge.

To enhance the catalytic performance of monometallic carbides, researchers have explored the strategy of introducing heteroatoms into the lattice of tungsten or molybdenum carbides. This approach has shown the potential to enhance the HDO capabilities of these materials.^{21,32} Therefore several bimetallic carbide catalysts have been investigated till now for the HDO process owing to their superior hydrotreating performance towards selective deoxygenation compared to their corresponding monometallic counterparts.^{56,57,211,212} For instance, Baddour et al. conducted a study involving Pt/Ni-modified Mo₂C catalysts for the deoxygenation of guaiacol. Their investigation revealed an increase in the density of active sites (H*-sites), leading to high conversion rates (>94%) and selectivity (>80%) towards the completely deoxygenated products at 623 K and 0.44 MPa.⁵⁷ Furthermore, it has been documented that the introduction of Ni into the Mo₂C surface reduces the binding energy of crucial reactive intermediates (such as O* and OH*) in comparison to the undoped Mo₂C. This reduction in binding energy makes it more favorable to remove these fragments from the catalyst surface, contributing to the catalyst's improved performance.⁸⁵ Tran and workers investigated the effect of tungsten (W) dopant on Mo₂C catalyst and interestingly, they observed enhanced activity (conversion = 93%, Selectivity = 70%) of bimetallic carbide (MoWC) for guaiacol HDO at 623 K and 2.75 MPa.⁷⁴ Later, the preferential selectivity towards aromatic products in HDO of guaiacol on MoWC was further explained by the mechanistic investigation of key reaction pathways using DFT simulations.²⁰⁹ The precise microstructure of bimetallic W-doped molybdenum carbide (MoWC) catalysts was elucidated. It was found that tungsten (W) existed in both metallic and carbidic forms.¹²⁵ The metallic tungsten formed overlayers, creating a step-like structure on the catalyst surface. Additionally, a comprehensive reaction map was constructed, encompassing elementary reactions in guaiacol HDO, and compared the reaction pathways and energetics with its monometallic counterpart. Results demonstrated the promotional effect of W-dopant is to significantly reduce the activation barriers for direct deoxygenation owing to its oxophilic nature resulting in strong binding of the adsorbate to the surface.

All these aforementioned studies collectively indicate that bifunctional Mo₂C holds significant promise as an HDO catalyst. Moreover, the introduction of suitable elements through doping can further enhance the catalytic performance of monometallic carbides. However, for an HDO catalyst to be optimal, it's crucial that it performs effectively for the HDO of real bio-oil derived from native biomass. So far, the evidence is partial because most reported studies have focused on

a specific model compound that represents only a small portion of the bio-oil. There is a notable research gap, particularly in the case of bimetallic carbides, as they have not been tested for multiple representative bio-oil components originating from carbohydrate and lignin fractions of native biomass. As mentioned earlier, bio-oil is known to comprise of more than 400 oxygenated constituents²¹³; therefore, selecting key constituents is crucial for mimicking its complex nature. Herein, we selected six key constituents: 5-Hydroxymethyl furfural (5-HMF), Acetic acid, Eugenol, Levoglucosan (LGA), Methylglyoxal (MG), and Vanillin to represent different oxygen functionalities present in the complex mixture of bio-oil. These are also major components of bio-oil, collectively making almost 30-50 % of bio-oil, encompassing most of the functionalities present in bio-oil components. A schematic of these constituents is shown in Figure 3.1. Among these, 5 – HMF represents the furanics class derived from the carbohydrate fraction which make up a significant portion of the bio-oil^{214,215} and is also a precursor to the formation of methylfuran (MF), which is an excellent gasoline additive. Methyl glyoxal, and Acetic acid are two major constituents representing small oxygenates with yield of 2.5 wt% and 5.33 wt% in bio-oil, respectively.²¹⁶ They are comprised of three types of carbonyl groups i.e., ketone, aldehyde and carboxylic acid which are predominantly present in the bio-oil.²¹⁶ Levoglucosan (LGA), an anhydrosugar, representing the cellulose component containing a ketal functional group in pyrolyzed bio-oil.²¹⁴ It makes up a significant portion of bio-oil which varies between 20 – 40% depending on the reactor type and conditions.^{216,217} Lastly, Vanillin and Eugenol were chosen to represent the phenolic or lignin components of biomass, encompassing multiple oxygenated functionalities such as hydroxyl, methoxyl, and aldehyde. Collectively, these constituents mimic the diverse bio-oil mixture and assist in evaluating HDO performance of different catalysts for real bio-oil. In this study, we investigated HDO performance of the W-doped Mo₂C bimetallic carbide (MoWC) catalyst and its metallic counterpart (Mo₂C) using these six representative constituents. Moreover, investigating the reaction pathways of all these diverse oxygenates will not only provide valuable mechanistic insights into these catalysts but, more importantly, it will offer a better assessment of the catalyst's suitability for processing real bio-oil mixtures, which contain a complex mixture of constituents from different biomass components. This research is crucial for advancing the development of practical and efficient HDO catalysts for the bio-oil upgrading process.

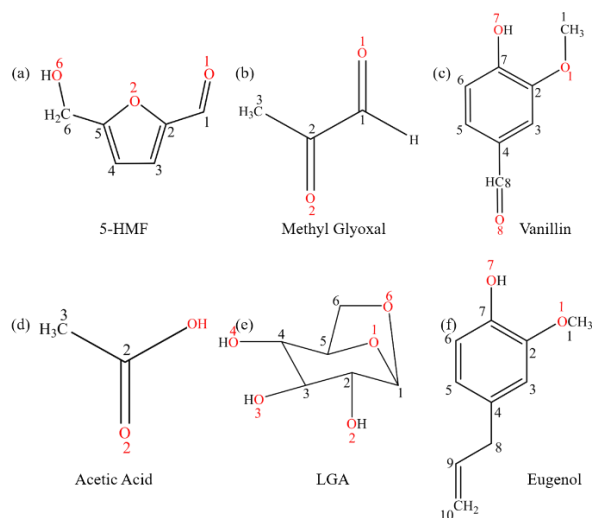


Figure 3.1. Schematic of six representative constituents (a) 5-hydroxymethylfurfural, (b) Methyl Glyoxal, (c) Vanillin, (d) Acetic Acid, (e) Levoglucosan, and (f) Eugenol, with different types of functionalities in the real bio-oil. Carbon and oxygen atom numbering in the compounds are also shown.

3.2 Computational Methodology

All First-principles simulations were performed using plane-wave pseudopotential implementation of Kohn-Sham DFT with periodic boundary conditions. The projector augmented wave (PAW) method was used to describe the interaction between valence electrons and ions.²¹⁸ The weak long-range dispersion interactions between adsorbates and the catalyst surface was also incorporated using vdW-DF functional as this functional has been previously reported and worked well to investigate HDO reaction mechanism on transition metals based catalysts.²¹⁹ Energy convergence criteria of 10^{-5} eV per unit cell and a maximum force tolerance of $0.05 \text{ eV}/\text{\AA}$ are used to ensure high accuracy. We used a k-points sample of $3 \times 3 \times 1$ with the Monkhorst-pack approach for integration across the Brillouin zone in reciprocal space, and spin polarization was enabled for all simulations. To prevent interaction in the z-direction with the subsequent unit cell, a 15 vacuum gap is inserted above the top layer. In order to guarantee that the adsorption energies are properly converged with regard to the computational setup mentioned here, the number of slab layers and the density of k-point grids are selected. All reactants and products' vibrational frequencies were carefully examined as well, and no imaginary frequencies were observed. The Nudged Elastic Band (NEB) approach with climbing images was used to estimate transition state structures. In NEB, a total of 5-10 images were employed, and the force was minimized to $0.05 \text{ eV } \text{\AA}^{-1}$. In order to confirm the transition state, vibrational frequency analysis was performed with a displacement

criterion of 0.02 Å on the NEB image that was closest to the transition state after its optimization using the quasi-Newton algorithm.

3.3 Results and Discussion

As mentioned earlier, we mimicked the real bio-oil sample using six key representative constituents on monometallic molybdenum carbide (Mo_2C) and bimetallic W-doped molybdenum carbide (MoWC) catalysts. Mo_2C mainly has two crystalline structures, the orthorhombic Mo_2C phase¹⁶⁹ and the hexagonal Mo_2C phase^{170,171}. Moreover, Mo_2C can be modelled with both C-termination and Mo-termination.⁸³ In this work, we opted for the orthorhombic Mo_2C phase with (100) facet and Mo termination. For bimetallic carbide (MoWC), we used the previously validated (using both theory and experiments) microstructure of MoWC catalyst¹²⁵ in which it was revealed that W dopant prefers to be present in both metallic form (W^0) and carbidic form (W^{2+}). The structures of both MoWC and Mo_2C catalysts are shown in Figure 3.2a and 2b, respectively.

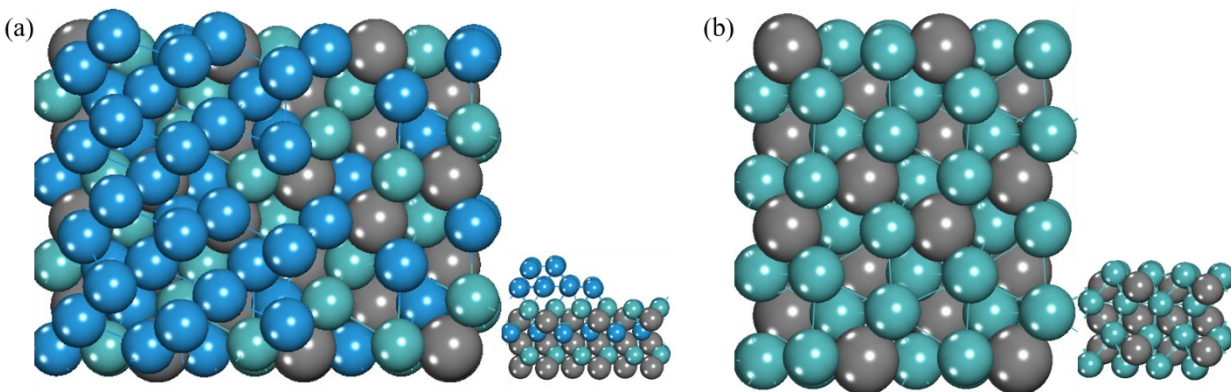


Figure 3.2. Optimized geometries of a) MoWC surface (top view and side view) b) Mo_2C surface (top view and side view). Dark cyan, blue, and gray spheres represent Mo, W, and C atoms in the carbides, respectively¹²⁵.

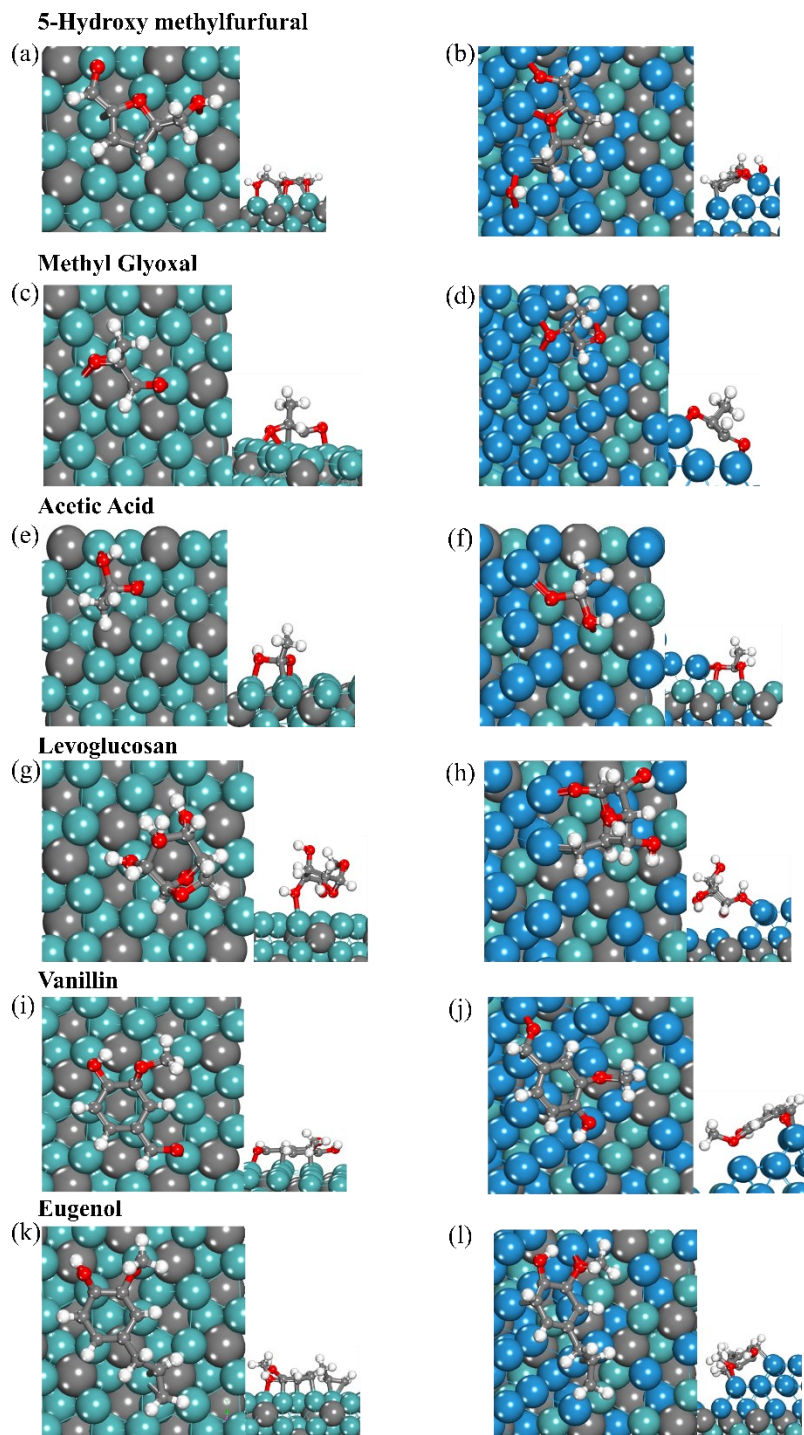


Figure 3.3 Top view and side view of optimized adsorption configurations of six bio-oil constituents considered in this study on Mo₂C surface (a, c, e, g, i, and k), and MoWC surface (b,d,f,h,j, and l). Dark cyan and blue spheres represent Mo and W atoms in the carbides, respectively. White, red, and gray spheres represent H, O, and C in the adsorbed guaiacol, respectively

3.3.1 5 – Hydroxymethyl furfural (Furanics)

3.3.1.1 Adsorption Configuration

In terms of the adsorption configuration, on Mo₂C, it prefers a flat parallel configuration ($\eta^2(C - O)$) in which the furanic ring prefers to adsorb parallelly over 3-fold hollow site while the carbonyl (C=O) group interact with the catalyst surface by occupying the top site on Mo atom, with the binding energy of -364 kJ/mol, as shown in Figure 3.3a. Interestingly, on MoWC, dissociative chemisorption at the C⁶ carbon was found to be facile with the binding energy of -478 kJ/mol shown in Figure 3.3b. It is attributed to the existence of oxophilic tungsten overlayers. These overlayers serve as anchors for the adsorption of 5-HMF molecules, specifically through their oxygen atoms within the molecule. Due to high affinity of W towards oxygen, it binds with oxygen strongly resulting in the stretching of carbonyl (C = O) bond to 1.39 Å in comparison to 1.23 Å in the gas phase (tabulated in Table C.2.).

3.3.1.2 Reaction Energetics of 5-HMF on Mo₂C and MoWC

A systematic comparison of catalytic activities of Mo₂C and MoWC for the first activation reaction steps are presented in Figure 3.5 for 5-HMF. It is clearly seen in Figure 3.5a and b that C–O dissociations have the lowest barriers for the first activation. A schematic of 5-HMF with its numbering scheme is already presented in Figure 3.1.

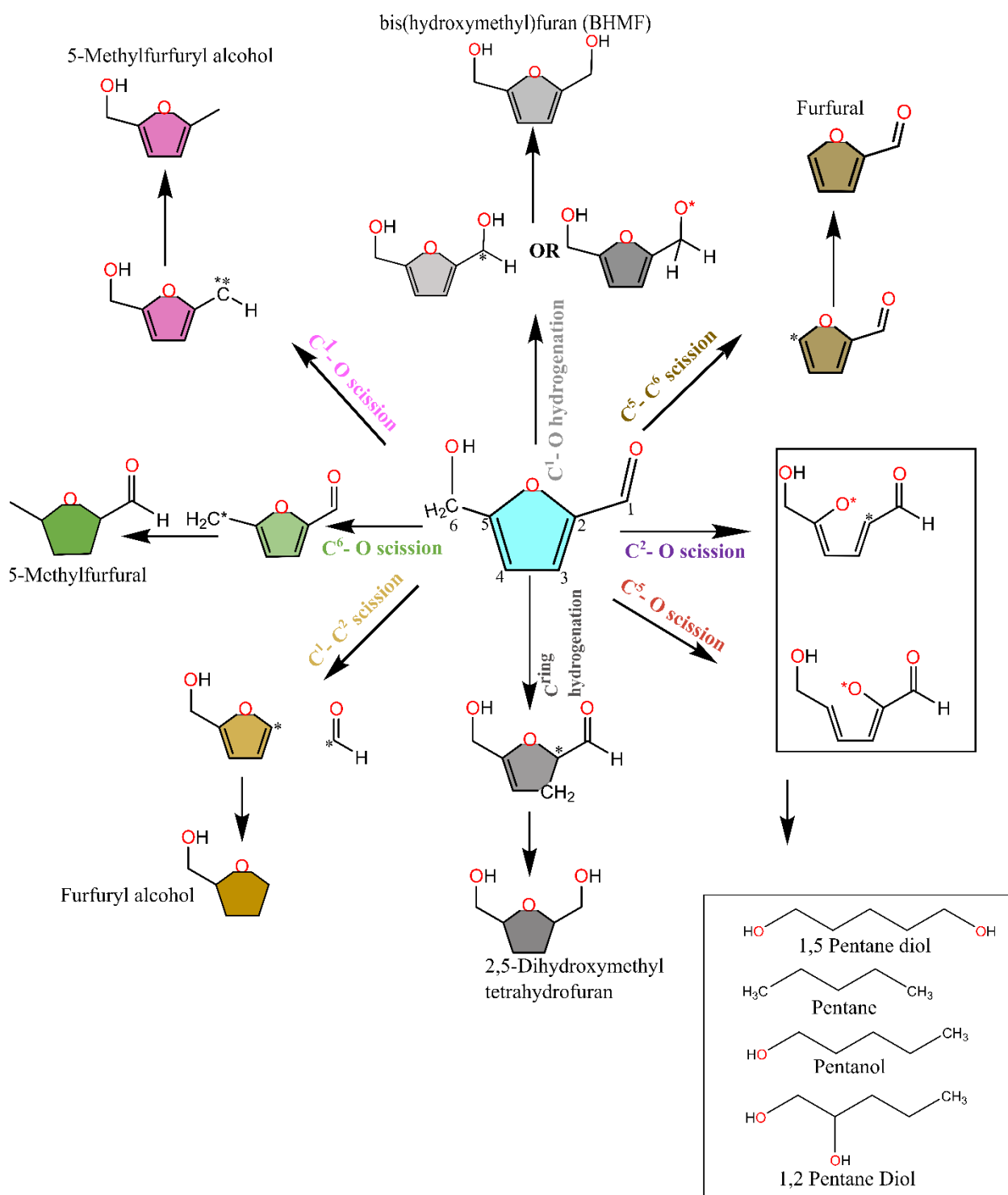


Figure 3.4 Schematic showing potential reaction paths for the initial activation of 5-HMF and their resulting end products. The eight potential pathways via which 5-HMF can activate are presented: C¹ – O, (ii) C⁶ – O, (iii) C² – O, (iv) C⁵ – O scission, (v) C⁵ – C⁶, (vi) C¹ – C² scission, (vii) C¹ – O hydrogenation, and (viii) C^{ring} hydrogenation. The nomenclature for carbon atoms is shown in the central 5-HMF molecule.

5-HMF could be activated through eight possible pathways, namely (i) $C^1 - O$, (ii) $C^6 - O$, (iii) $C^2 - O$, (iv) $C^5 - O$ scission, (v) $C^5 - C^6$, (vi) $C^1 - C^2$ scission, (vii) $C^1 - O$ hydrogenation, and (viii) C^{ring} hydrogenation. These pathways have the potential to further branch out, resulting in the formation of a variety of platform chemicals, as illustrated in Figure 3.4. The first activation and reaction energies for these eight pathways are reported in Figure 3.5a and 3.5b, respectively on both Mo_2C and $MoWC$ catalysts. On Mo_2C , $C^6 - OH$ scission and ring opening via $C^5 - O$ dissociation are observed to be two competitive pathways with energy barriers of 39, and 34 kJ/mol, respectively. Thermodynamically, $C^6 - OH$ dissociation was more favorable with a more favorable reaction energy of -149 kJ/mol, in comparison to -20 kJ/mol for $C^5 - O$ dissociation. The two favorable pathways ($C^6 - O$, and $C^5 - O$ scission) lead to the formation of 5-methyl furfural (5-MF) and linear chain pentanols or pentanes, respectively after the hydrogenation steps. On the contrary, $C^6 - O$ bond scission occurs spontaneously upon chemisorption on the bimetallic carbide catalyst ($MoWC$) which results in the formation of 5-MF after the hydrogenation at C^6 carbon atom. Hydrogenation reactions including that of ring and of the $C^1 = O$ double bond were not feasible kinetically, since they exhibited higher barriers on both catalysts, as shown in Figure 3.5a and 3.5b. Moreover, $C - C$ cleavage which includes $C^1 - C^2$ and $C^5 - C^6$ bond scissions is also limited by high kinetic barriers of 180 and 191 kJ/mol on Mo_2C and of 200 and 117 kJ/mol on $MoWC$. From the first activation results, it can be concluded that both Mo_2C and $MoWC$ catalysts selectively favor the $C - O$ bond scission over $C - C$ bond scission and hydrogenation reactions, with $MoWC$ being the more selective catalyst as W improves the deoxygenation ability. We also investigated further pathways using 5-MF as an intermediate on both catalysts.

Upon 5-MF (I - 1) formation, it can be activated primarily via (i) $C^1 - O$ scission, (ii) $C^1 - C^2$ dissociation, (iii) $C^1 - O$ hydrogenation, (iv) $C^5 - O$ dissociation, and (v) $C^2 - O$ dissociation. On both catalysts, ring-opening via $C^5 - O$ dissociation was found to be the kinetically favorable pathway with similar activation barriers of only 8 and 18 kJ/mol on Mo_2C , and $MoWC$, respectively. An interesting observation is that ring opening can occur via either $C^2 - O$ or $C^5 - O$ dissociation. However, the calculated barrier for $C^2 - O$ dissociation is relatively higher, i.e., 44 kJ/mol and 58 kJ/mol on Mo_2C and $MoWC$, respectively. This disparity can be attributed to the distinct functional groups present at the C^2 (-CHO) and C^5 (-CH₃) carbon positions. The -CHO group tends to withdraw electrons, leading to a partial positive charge on the C^2 carbon, while the electron-donating methyl group induces a partial negative charge on the C^5 carbon. This charge

distribution results in a more stable transition state for $C^5 - O$ dissociation, leading to the observed lower barrier on both catalysts. Similar findings were reported for furfural hydrodeoxygenation on Ru catalysts, where ring opening via $C^5 - O$ dissociation was found to have a lower barrier (64 kJ/mol) compared to $C^2 - O$ dissociation (116 kJ/mol).¹⁹⁸ Conversely, alternative routes exhibit significantly higher barriers of 107, 200, and 320 kJ/mol for $C^1 - O$ scission, $C^1 - C^2$ dissociation, and $C^1 - O$ hydrogenation, respectively on MoWC and as well as on Mo_2C (105, 176, and 213 kJ/mol), as shown in Figure 3.6b(I-1). These barriers suggest that the formation of linear chain pentanols or pentanes is likely to occur on both Mo_2C and MoWC catalysts. Following the most favorable pathway, the resulting open-chain product undergoes hydrogenation at both the oxygen and carbon ends, leading to the formation of the intermediate 2, (I - 2, $C_6H_8O_2$, shown in Figure 3.6b).

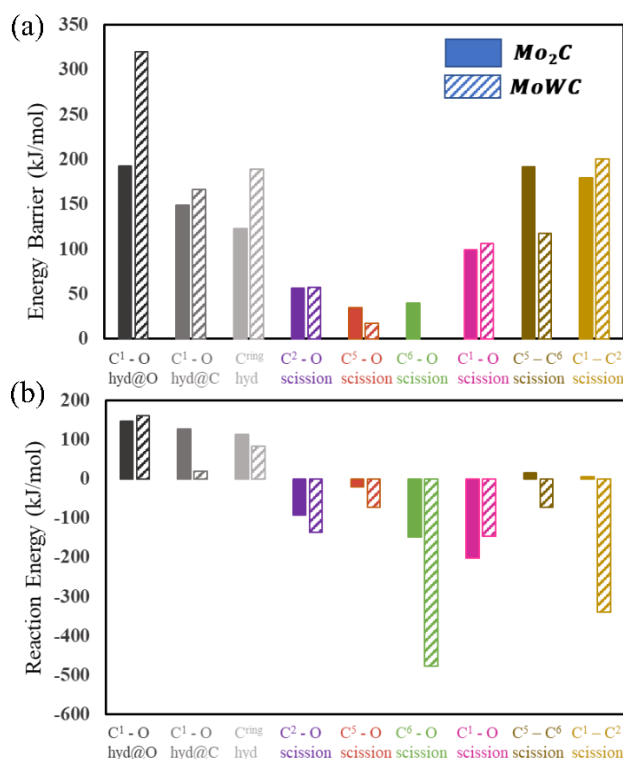


Figure 3.5 (a) Electronic energy barriers and (b) reaction energies in the bar graphs are shown below the schematic and each reaction pathway is shown using same color scheme as depicted in figure 4.

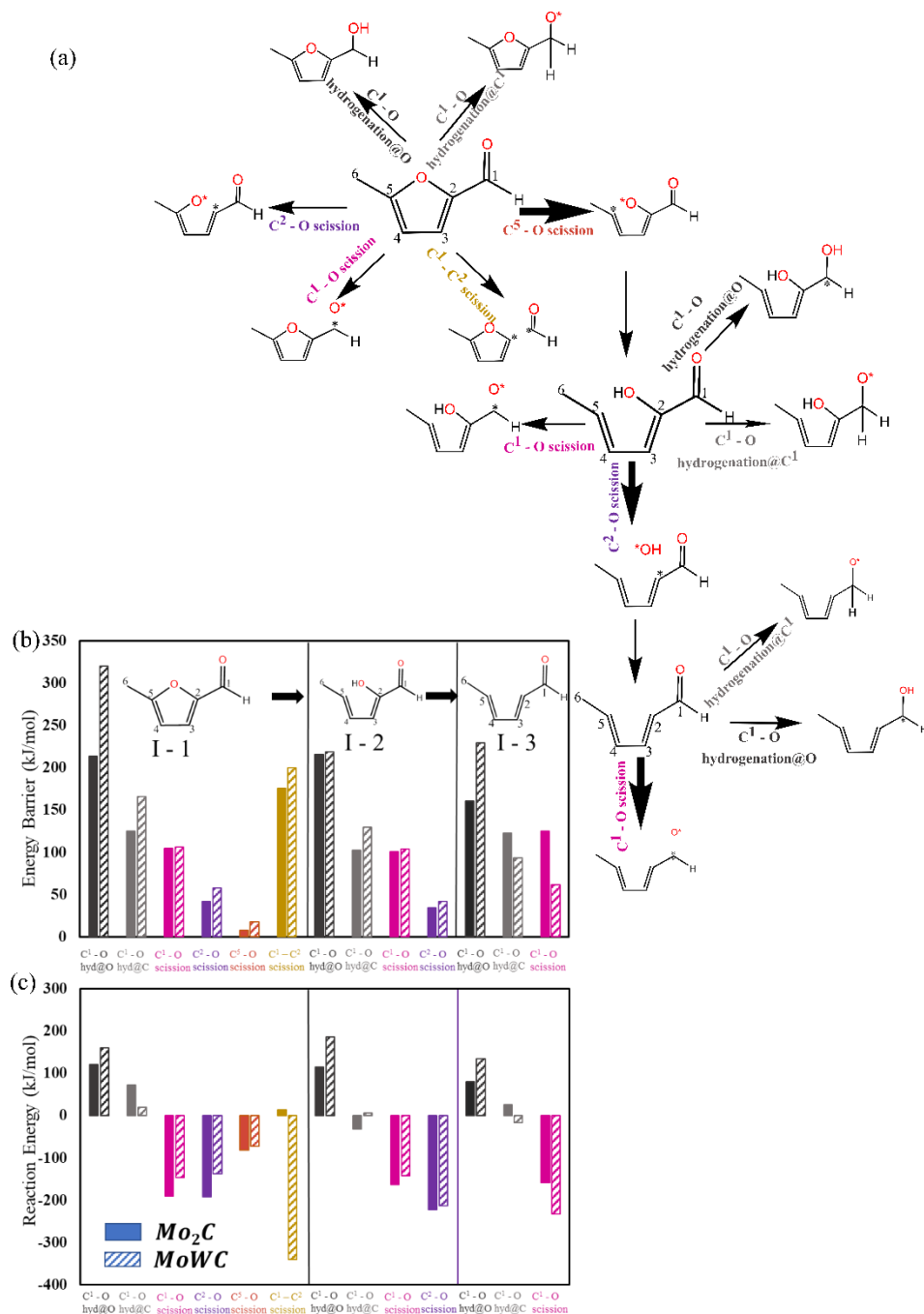


Figure 3.6 (a) Schematic showing potential reaction paths for the initial activation of 5-MF on Mo₂C surface. The six considered pathways via which 5-MF can activate are presented: C¹ – O, (ii) C² – O, (iii) C⁵ – O scission, (iv) C⁵ – C⁶, (v) C¹ – C² scission, (vi) C¹ – O hydrogenation. The nomenclature for carbon atoms in is shown in the central 5-MF molecule. (b) Comparison of electronic energy barriers and (c) reaction energies in the bar graphs are shown below the schematic for Mo₂C and MoWC and each reaction pathway is shown using distinct colors.

I-2 could further undergo reaction via 3 routes (i) direct deoxygenation at C¹ – O, and C² – O, and (ii) hydrogenation of C¹- O bond which will produce linear chain diols. On comparing these three

routes, C^2-OH scission is the most favorable pathway kinetically with the lowest energy barriers, i.e., 34 kJ/mol on Mo_2C in comparison to 42 kJ/mol on the MoWC surface. Moreover, C^2-OH scission is also highly exothermic with reaction energies -223 and -214 kJ/mol on Mo_2C and MoWC, respectively. Other considered routes involving C^1-O dissociation and C^1-O hydrogenation showed high barriers of 101, and 103 kJ/mol on Mo_2C as compared to 104 and 130 kJ/mol on MoWC. Although C^1-O dissociation is highly exothermic (-142 kJ/mol on MoWC vs. -164 on Mo_2C), relatively higher barriers for direct C^1-O dissociation can be explained by the fact that C^1 carbon atom is aldehydic carbon which forms a carbonyl bond with O which requires higher energy to break in comparison to single C^2-OH bond.^{143,198} It can be seen that both catalysts showed similar results for intermediate 2 where C^2-OH is the most facile pathway which leads to the intermediate 3(I-3) i.e., 2,4-Hexadienal (C_6H_8O) after the hydrogenation at C^2 carbon end.

Upon 2,4-Hexadienal formation, we investigated only two key reactions, (i) C^1-O hydrogenation, leading to the formation of pentanols, and (ii) direct C^1-O scission, leading to an alkene, viz, 2,4-Hexadiene formation. Results for the final activation showed that the latter pathway becomes facile on MoWC as the barrier for C^1-O significantly reduced to 61 kJ/mol in comparison to hydrogenation pathway with high barriers of 93 and 229 kJ/mol on the carbon and oxygen end, respectively. On the contrary, both pathways are competitive on Mo_2C with similar barriers of 125 and 123 kJ/mol for C^1-O scission, and hydrogenation at the carbon end, correspondingly. The lower barrier observed on MoWC can be attributed to a change in the adsorption configuration. Specifically, the 2,4-Hexadienal appears to adsorb in an $\eta^1-(C-O)$ configuration (Figure C.22c) on the bridge site of the tungsten overlayers, anchored via an oxygen atom. This differs from the adsorption configuration of intermediate 2 (Figure C.22b), which binds to the top site. This altered adsorption configuration, likely due to the presence of the tungsten overlayers, is a crucial factor contributing to the reduced activation barrier for the reaction involving intermediate 3 on the MoWC catalyst. As a result, the C^1-O bond is stretched to 1.44 Å (Table C.2) for intermediate 3 which makes it easier to cleave as compared to 1.34 Å which still possesses the double bond characteristics.

To summarize, ring opening via C^5-O dissociation is feasible on both Mo_2C , and MoWC surfaces compared to other steps. Final activation results confirmed that MoWC catalyst is more active towards $C-O$ bond scission including both single and double bonds, as compared to monometallic

Mo₂C catalyst which only favors cleavage of the saturated C – O bond. Moreover, dissociative chemisorption was observed on MoWC in which C⁶ – OH bond dissociates spontaneously and hence, requiring one less reaction step in order to achieve completely deoxygenated products. This will possibly result in the formation of completely deoxygenated 2,4-Hexadiene on MoWC in comparison to a mixture of 2,4-Hexadiene and partial deoxygenated 2,4-Hexadien-1-ol products on Mo₂C. In terms of deoxygenation catalytic ability, bimetallic carbide (MoWC) acts similar to Ru catalyst on which pentene/pentane was observed as favorable product for furfural HDO.¹⁹⁸

3.3.2 Methyl Glyoxal (MG)

3.3.2.1 Adsorption Configuration on Mo₂C and MoWC

MG binds to the surface of Mo₂C where O² oxygen (refer to Figure 3.1 for atom numbering) atom occupies the bridge site and O¹ occupies the top site of Mo atom and methyl group buckles out of the plane with the binding energy of -323 kJ/mol. However, both, O¹ and O² bind to bridge site on metallic tungsten overlayers present in MoWC with much stronger binding energy of -333 kJ/mol, owing to oxophilic nature of tungsten. The adsorption configurations of MG on Mo₂C, and MoWC surfaces are shown in Figs. 3c and 3d.

3.3.2.2 First activation of MG on Mo₂C and MoWC

The first activation of MG via different bond activations is shown in Figure 3.7. It is evident that C – C and C – O bond dissociations are competitive on Mo₂C, in contrast with MoWC on which selectively C – O bond dissociation is favored.

HDO of MG could possibly take place via six main competitive routes (i) C¹ – C² scission, (ii) C² – C³ scission, (iii) C¹ – O scission, (iv) C² – O scission, (v) C¹ – O hydrogenation, and (vi) C² – O hydrogenation. The cleavage of the carbon-carbon bond in the (i) and (ii) routes results in the production of acetaldehyde and glyoxal, respectively. For the (iii) and (iv) pathways, when hydrogenation occurs at the C¹ and C² carbon positions, it would form acetone and propionaldehyde, respectively. Additionally, hydrogenation at the C¹ – O bond leads to the formation of either hydroxy acetone or acetol. These reactions were investigated on Mo₂C and MoWC, and the associated energy profiles are shown in Figure 3.7b and 7c.

On Mo₂C, the direct dissociation of the carbonyl C² – O bond has a relatively low energy barrier of 33 kJ/mol, while the dissociation of the other carbonyl C¹ – O bond has a higher barrier of 76

kJ/mol. Both reactions are highly exothermic, with reaction energies of -129 kJ/mol and -64 kJ/mol, respectively. The lower barrier for the $C^2 - O$ bond dissociation can be attributed to the longer bond length (1.43 Å) caused by oxygen binding to the bridge site, compared to the $C^1 - O$ bond (1.37 Å), where oxygen binds to the top site on the Mo atom (Table C.2). Furthermore, the dissociation of the $C^1 - C^2$ bond exhibits a barrier of 61 kJ/mol, which is lower than that of $C^1 - O$ dissociation. Both reactions result in similar reaction energies of -64 kJ/mol and -72 kJ/mol for $C^1 - O$ dissociation and $C^1 - C^2$, respectively as shown in Figure 3.7c. This suggests that the dissociation of the carbon-carbon (C - C) bond and the carbon-oxygen (C=O) bond are competitive on the Mo_2C surface, potentially producing a mixture of formaldehyde, acetaldehyde and propionaldehyde. However, the hydrogenation of the carbonyl ($C^1=O$) bond on Mo_2C is kinetically not favorable due to the high energy barrier of 157 kJ/mol. Additionally, this reaction is highly endothermic with a reaction energy of 93 kJ/mol, making it unfavorable thermodynamically too. On MoWC, the direct dissociation of both $C^2 - O$ and $C^1 - O$ bonds are kinetically and thermodynamically favorable, with relatively low energy barriers of 34 kJ/mol and 28 kJ/mol, respectively. The reaction energies for these steps are -113 kJ/mol and -177 kJ/mol. Interestingly, MoWC not only promotes the direct dissociation of the carbonyl C=O bond but also makes the dissociation of the C - C bond unfavorable. The barriers for $C^1 - C^2$ and $C^2 - C^3$ bond dissociation on MoWC are calculated to be 96 kJ/mol and 174 kJ/mol, respectively, compared to the Mo_2C surface, which had barriers of 61 kJ/mol for $C^1 - C^2$ and 127 kJ/mol for $C^2 - C^3$ dissociation. This suggests that MoWC is less conducive to C - C bond cleavage reactions compared to Mo_2C . Lastly, the hydrogenation of the carbonyl ($C^1=O$) bond on MoWC has the highest energy barrier of 271 kJ/mol, which is notably higher than the corresponding reaction on Mo_2C (157 kJ/mol). This significant increase in barrier makes the hydrogenation of the $C^1=O$ bond on MoWC even less favorable kinetically.

In summary, MoWC promotes the selective dissociation of $C^2 - O$ and $C^1 - O$ bonds, while hindering C - C bond dissociation reactions unlike Mo_2C , which shows little or no selectivity. Additionally, the hydrogenation of the carbonyl bond is kinetically less favorable on MoWC.

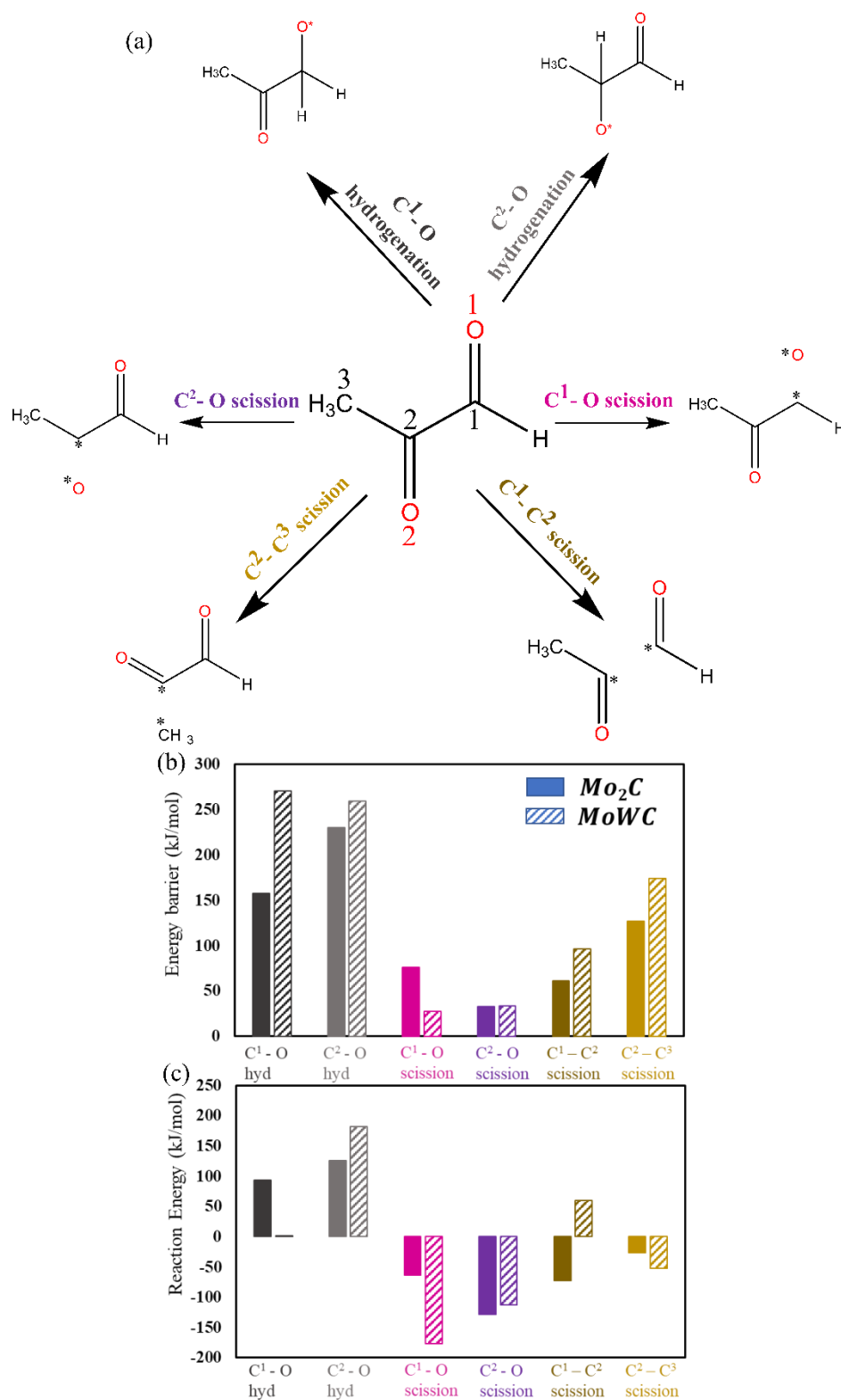


Figure 3.7 (a) Schematic for reaction pathways for methyl glyoxal activation on Mo_2C and MoWC surface. (b) Electronic energy barriers and (c) reaction energies for different first activation routes. The six considered pathways via which MG can activate are presented: $\text{C}^1\text{-O}$, (ii) $\text{C}^2\text{-O}$, (iii) C^1

– C² scission, (iv) C² – C³ scission, (v) C¹ – O hydrogenation, and (vi) C² – O hydrogenation. The nomenclature for carbon atoms is shown in the central MG molecule. (b) Comparison of electronic energy barriers and (c) reaction energies in the bar graphs are shown below the schematic for Mo₂C and MoWC and each reaction pathway is shown using distinct colors.

3.3.3 Acetic Acid (AA)

3.3.3.1 Adsorption Configuration on Mo₂C and MoWC

Acetic acid adsorbs weakly on Mo₂C surface where both oxygen atoms at C¹ carbon bind to top sites of Mo atom with a binding energy of -143 kJ/mol. On the other hand, on MoWC, AA adopts a similar configuration but the only difference is that the ketonic O at C¹ also binds to metallic tungsten due to step like structure of MoWC. Moreover, it binds very strongly with a binding energy of – 170 kJ/mol. The most stable adsorption configuration of AA on Mo₂C and MoWC are shown in Figure 3.3e and 3f.

3.3.3.2 Reaction Pathways on Mo₂C and MoWC

Four key pathways for the first activation of acetic acid are shown in Figure 3.8a. Similar to MG, C – C and C – O dissociations are calculated to be competitive on Mo₂C and only C – O dissociation is preferred over MoWC surface.

AA can be activated via four key pathways (i) direct C¹ = O dissociation, (ii) C¹ – OH dissociation, (iii) C¹ – C² cleavage, and (iv) C¹ = O hydrogenation. Pathway (i) leads to the formation of ethanol, whereas, the pathway (ii) will form acetaldehyde. Pathway (iii) involves C – C scission forming either methane and carbon dioxide or methane, carbon monoxide, and water in the absence and presence of H₂, respectively. Pathway (iv) will result in the conversion of aldehyde to its corresponding alcohol and will form a geminal alcohol namely 1,1-ethanediol which is considered as unstable. We analyzed the first activation of AA on Mo₂C and MoWC surfaces and the corresponding energy profile is shown in Figure 3.8b and 3.8c.

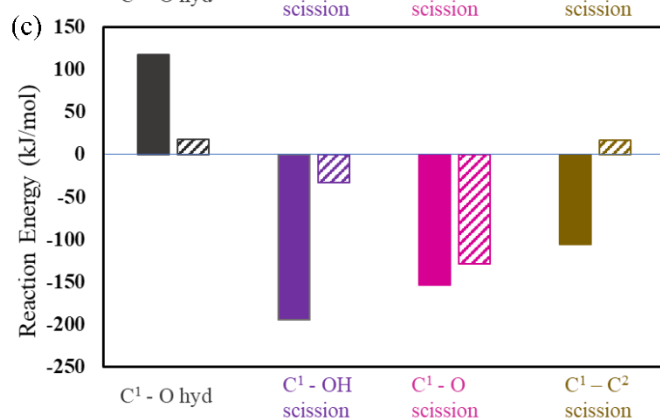
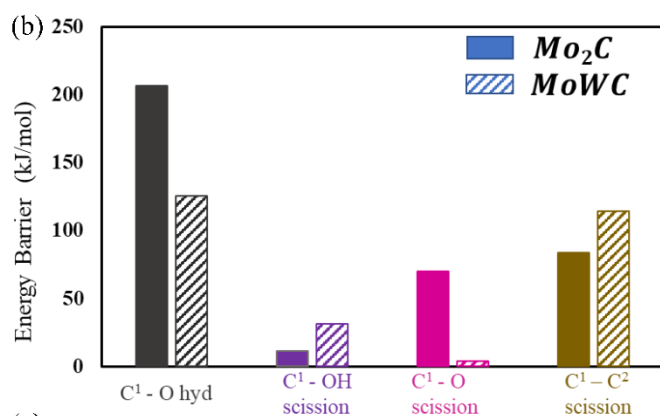
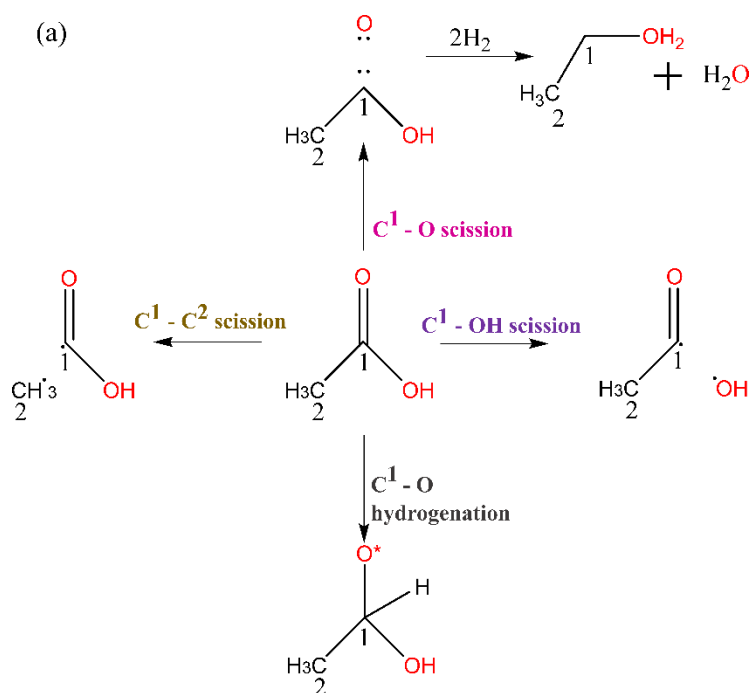


Figure 3.8 (a) Schematic for reaction pathways for acetic acid activation on Mo_2C and MoWC surfaces. (b) Electronic energy barriers and (c) reaction energies for different first activation routes. The four considered pathways via which AA can activate are presented: $\text{C}^1 - \text{OH}$, (ii) $\text{C}^1 - \text{O}$, (iii) $\text{C}^1 - \text{C}^2$ scission, (iv) $\text{C}^1 - \text{O}$ hydrogenation. The nomenclature for carbon atoms is shown in the

central AA molecule. (b) Comparison of electronic energy barriers and (c) reaction energies in the bar graphs are shown below the schematic for Mo₂C and MoWC and each reaction pathway is shown using distinct colors

Looking at the reaction energetics in Figure 3.8b and 3.8c, dehydroxylation or C¹ – OH dissociation showed the least barrier of 12 kJ/mol on Mo₂C and the reaction is highly exothermic with reaction energy of -194 kJ/mol. It agrees well with previously reported study by Bhan and coworkers in which they also observed acetaldehyde intermediately after the dehydroxylation of acetic acid on Mo₂C.²²⁰ However, Mo₂C showed relatively similar barriers of 84, and 70 kJ/mol for C¹ – C² and C¹ = O bond dissociation, respectively. Although C¹ = O bond dissociation is 48 kJ/mol more thermodynamically favorable than C¹ – C² dissociation, similar kinetic barriers indicate that the Mo₂C surface may lead to a mixture of C¹ and C² products. On the contrary, barriers for C¹ – OH and C¹ = O bond dissociation on MoWC are 32, and only 4 kJ/mol and both reactions have reaction energies of -33, and -129 kJ/mol, respectively. Feasibility of C¹ = O dissociation on MoWC could be due to the stretching of C¹ = O bond to 1.52 Å (Table C.2) as it is bonded to both metallic tungsten and molybdenum atom, in comparison to Mo₂C surface, where it occupies top site on Mo atom and the bond length is 1.39 Å (Table C.2). Moreover, C¹ – C² dissociation showed a higher barrier of 114 kJ/mol on MoWC, indicating higher preference towards direct deoxygenation on the bimetallic carbide. Lastly, the hydrogenation pathway was found to be kinetically and thermodynamically less favorable on both Mo₂C and MoWC surfaces. This pathway presented high energy barriers of 206 kJ/mol on Mo₂C and 125 kJ/mol on MoWC, along with reaction energies of 117 kJ/mol and 18 kJ/mol, respectively.

In short, comparing the activation barriers and reaction energies of acetic acid HDO pathways, Mo₂C showed relatively similar barriers of 84, and 70 kJ/mol for C¹ – C² and C¹ = O bond dissociation, respectively. In contrast, MoWC is highly selective towards direct deoxygenation (DDO) with low barriers in comparison to C – C dissociation. Consequently, Mo₂C could lead to a mixture of C₁ and C₂ products, whereas, MoWC can selectively form completely deoxygenated C₂ products.

3.3.4 Levoglucosan (LGA)

3.3.4.1 Adsorption Configuration

LGA consists of three vicinal hydroxyl groups at C², C³, and C⁴ carbons, respectively (shown in Figure 3.1) and it also has a bicyclic structure consisting of a 5-membered and a 6-membered ring. On Mo₂C, it binds weakly in a $\eta^1(C - O)$ configuration in which hydroxyl group at C⁴ carbon occupies the Mo top site and the 6-membered ring hovers over the 3-fold hollow site with a binding energy of -230 kJ/mol. However, on MoWC, dissociative chemisorption is observed, in which the 5-membered ring opens up via C⁶ – O bond resulting in $\eta^2(C - O)$ geometry in which C⁶ and O atoms bind to the metallic tungsten atom strongly with a binding energy of -281 kJ/mol. The most stable adsorption configuration is shown in Figure 3.3g and 3.3h for Mo₂C and MoWC, respectively.

3.3.4.2 Reaction Mechanism of LGA on Mo₂C and MoWC

Reaction energetics of LGA molecule are computed for key elementary reaction steps in the first and second activation on Mo₂C and MoWC surfaces and are shown Figure 3.9 and Figure 3.11 respectively. Overall, C – O dissociation is observed to be more favorable on MoWC than Mo₂C. There are several HDO routes via which LGA can be activated namely, (i) C¹ – O⁶ scission (5-membered ring opening), (ii) C¹ – O¹ scission, (iii) C⁶ – O⁶ scission, (iv) C⁵ – O¹ scission, (v) C² – OH, (vi) C³ – OH, and (vii) C⁴ – OH scission. We have investigated and compared each pathway on Mo₂C and MoWC, except C³ – OH dissociation. As mentioned before, there are three vicinal hydroxyl groups and we only included two of them as they possess same bond type with similar bonding configuration. Ring opening is possible via four routes, namely, (i) C¹ – O⁶, (ii) C⁶ – O⁶, (iii) C¹ – O¹, and (iv) C⁵ – O¹. The first two pathways lead to the opening of the 5-membered ring whereas the pathways (ii) and (iii) lead to the 6-member ring opening. C¹ – O⁶ bond scission on Mo₂C has a barrier of 45 kJ/mol and this reaction is exothermic with reaction energy of -112 kJ/mol, making it kinetically and thermodynamically feasible. C⁶ – O⁶ bond scission showed a barrier of 116 kJ/mol and it is even more exothermic than C¹ – O⁶ bond scission with a reaction energy of -207 kJ/mol. On the other hand, both C¹ – O¹ and C⁵ – O¹ bond scissions in which 6-membered ring could open showed relatively high barriers of 108 and 98 kJ/mol, as shown in Figure 3.9. Higher kinetic barriers for pathways (iii) and (iv) could be explained by the fact that

$C^1 - O - C^6$ angle is 104.82° degrees which is more strained than $C^1 - O - C^5$ angle (102.28° degrees) as the molecule adsorbs in η^1 configuration in which O^6 is bonded to Mo atom on Mo_2C surface. Hence, the $C^1 - O$ or $C^5 - O$ bond scission would require relatively higher energy to cleave. It can be pointed out that all considered reactions are thermodynamically feasible on Mo_2C . LGA also has three OH groups, and it has been reported that regioselective derivation of isomers is not easy.^{221,222} According to the results of first activation of LGA on Mo_2C , dehydroxylation at both C^2 and C^4 carbon showed identical energy barriers of 79 kJ/mol and thermodynamically also they have similar reaction energies of -175 and -178 kJ/mol. It perfectly agrees with the reported literature that formation of regioselective isomers is difficult.^{221,222}

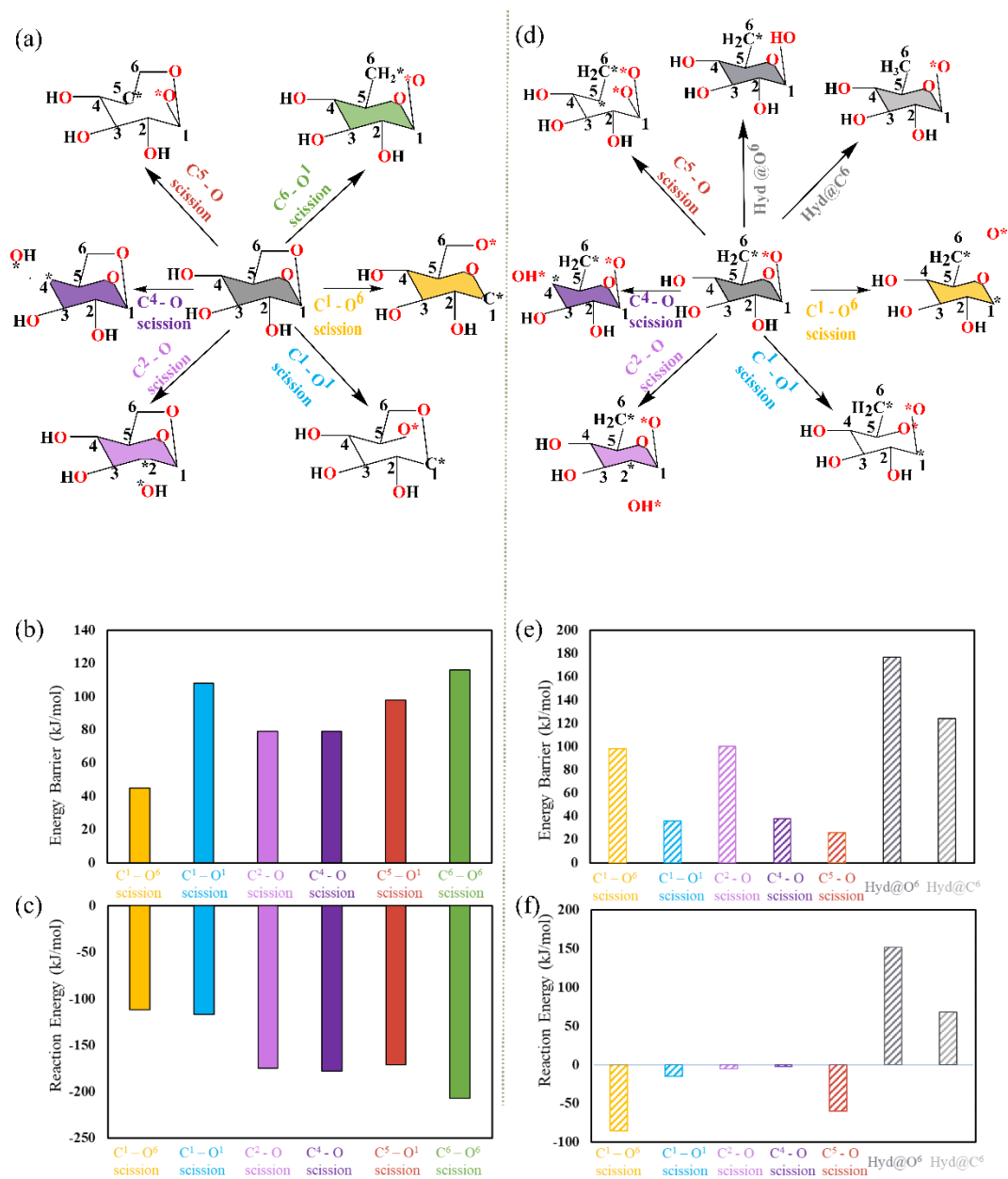


Figure 3.9 (a) Schematic showing probable end products that can be produced and demonstrating potential reaction paths for the initial activation of LGA on Mo₂C(left) and MoWC(right) surfaces. All considered pathways via which LGA can activate on both catalysts are presented. The nomenclature for carbon atoms is shown in the central LGA molecule. (a) Comparison of energy barriers and (b) reaction energies in the bar graphs for Mo₂C. (c) Comparison of energy barriers and (d) reaction energies in the bar graphs for MoWC (right side) and each reaction pathway is shown using distinct colors

On MoWC, as mentioned earlier, C⁶ – O⁶ dissociation occurs spontaneously upon chemisorption requiring one less reaction step to get the deoxygenated product. Hence, we used the intermediate obtained after C⁶ – O⁶ dissociation reaction step to evaluate further activation possibilities. After

the 5-membered ring-opening via $C^6 - O^6$ scission, we considered seven key HDO routes namely, (i) $C^1 - O^6$, (ii) $C^1 - O^1$, (iii) $C^5 - O^1$ dissociation, (iv) $C^2 - OH$, (v) $C^4 - OH$ dissociation, (vi) hydrogenation@ C^6 , and (vii) hydrogenation@ O^6 atom. Reaction energetics of all the routes have been compared on MoWC in Figure 3.9e and 3.9f. Among the considered routes, $C^5 - O^1$ dissociation is the most facile with the least barrier of only 26 kJ/mol, clearly indicating the formation of linear chain alcohols or alkanes formation after the opening of both rings. Additionally, this reaction step ($C^5 - O^1$ dissociation) is exothermic, demonstrating its thermodynamic feasibility with the reaction energy of - 60 kJ/mol. Calculations suggest that the 6-membered ring opening via $C^1 - O^1$ dissociation is also a competitive route with similar barrier of merely 36 kJ/mol. Interestingly, $C^2 - OH$ and $C^4 - OH$ have a significant difference of 62 kJ/mol in their barriers owing to the adsorption configuration as $C^4 - OH$ is more favorable due to stabilization of its transition state (shown in Figure C13f and C13g). Methylene group is known to exhibit positive inductive effect (+I).²²³ Methylene functional group ($-CH_2$) is present at C^5 carbon which is relatively closer to C^4 carbon than C^2 carbon (refer to Figure 3.1). As a result, it exerts a positive induction effect (+I) effect to the resulting carbocation in the transition state of $C^4 - OH$ dissociation which makes it more stable. Unlike Mo_2C , this difference between similar reactions on MoWC indicate the possibility of formation of regioselective isomers by selectively cleaving hydroxyl group from specific carbon. Coming to the hydrogenation route, it is not favorable kinetically on the C^6 carbon and on the O^6 end with high barriers of 124 and 177 kJ/mol. It can be clearly noted from Figure 3.9e and 3.9f that hydrogenations are not preferred with reaction energies of +68 and +152 kJ/mol.

In summary, $C^1 - O$ dissociation, opening of the 5-membered ring, is the most facile route on Mo_2C both thermodynamically and kinetically with a barrier of 45 kJ/mol and a reaction energy of -112 kJ/mol. This leads to the formation of intermediate 1 shown in Figure 3.10a. On MoWC, $C^6 - O$ dissociation occurs spontaneously upon chemisorption followed by 6-membered ring as well via $C^5 - O$ dissociation with a barrier of only 26 kJ/mol leading to intermediate 2 (shown in Figure 3.10b) indicating the formation of linear chain products.

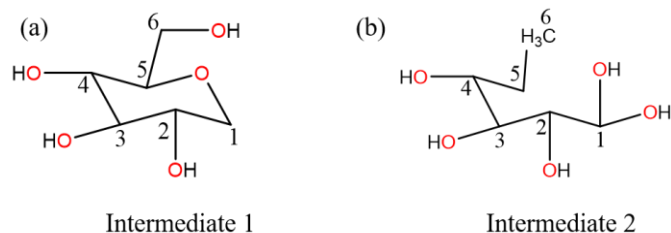


Figure 3.10 Schematic of intermediates formed on (a) Mo_2C and (b) MoWC surface.

In the second activation for HDO of intermediate 1 on Mo_2C , there are mainly three types of bond scissions that could occur, namely, (1) dehydroxylation, which can occur via (i) $\text{C}^2 - \text{OH}$, (ii) $\text{C}^3 - \text{OH}$, and (iv) $\text{C}^6 - \text{OH}$, (2) ring – opening, that can occur via (i) $\text{C}^1 - \text{O}^1$ or (ii) $\text{C}^5 - \text{O}^1$ scission, (3) $\text{C} - \text{C}$ bond scission via $\text{C}^5 - \text{C}^6$ bond scission (Figure 3.11a). The reaction energetics of all the routes on Mo_2C are shown in Figure 3.11b and 3.11c. The least barrier of 47 kJ/mol was calculated for $\text{C}^2 - \text{OH}$ bond dissociation, making it the kinetically most favorable route on Mo_2C . This reaction step ($\text{C}^2 - \text{OH}$ dissociation) is exothermic with the reaction energy of -98 kJ/mol. $\text{C}^3 - \text{OH}$ and ring – opening via $\text{C}^5 - \text{O}^1$ bond dissociation are next two competitive routes with similar barriers of 84 and 68 kJ/mol. Thermodynamically, all reaction steps are feasible with negative reaction energies as shown in Figure 3.11c. As there is no possibility for hydrogenation, the competition is between $\text{C} - \text{C}$ and $\text{C} - \text{O}$ bond scission. However, $\text{C}^5 - \text{C}^6$ bond dissociation is highly unfavorable with a very high barrier of 385 kJ/mol, which suggests that the resulting HDO product on Mo_2C will have same number of carbon atoms as the reactant. To be noted, ring – opening via $\text{C}^1 - \text{O}^1$ bond dissociation shows a higher barrier of 135 kJ/mol in comparison to $\text{C}^5 - \text{O}^1$ bond dissociation, owing to the formation of secondary carbocation at C^5 due to the presence of CH_2OH group which is relatively more stable in comparison to primary carbocation at C^1 .

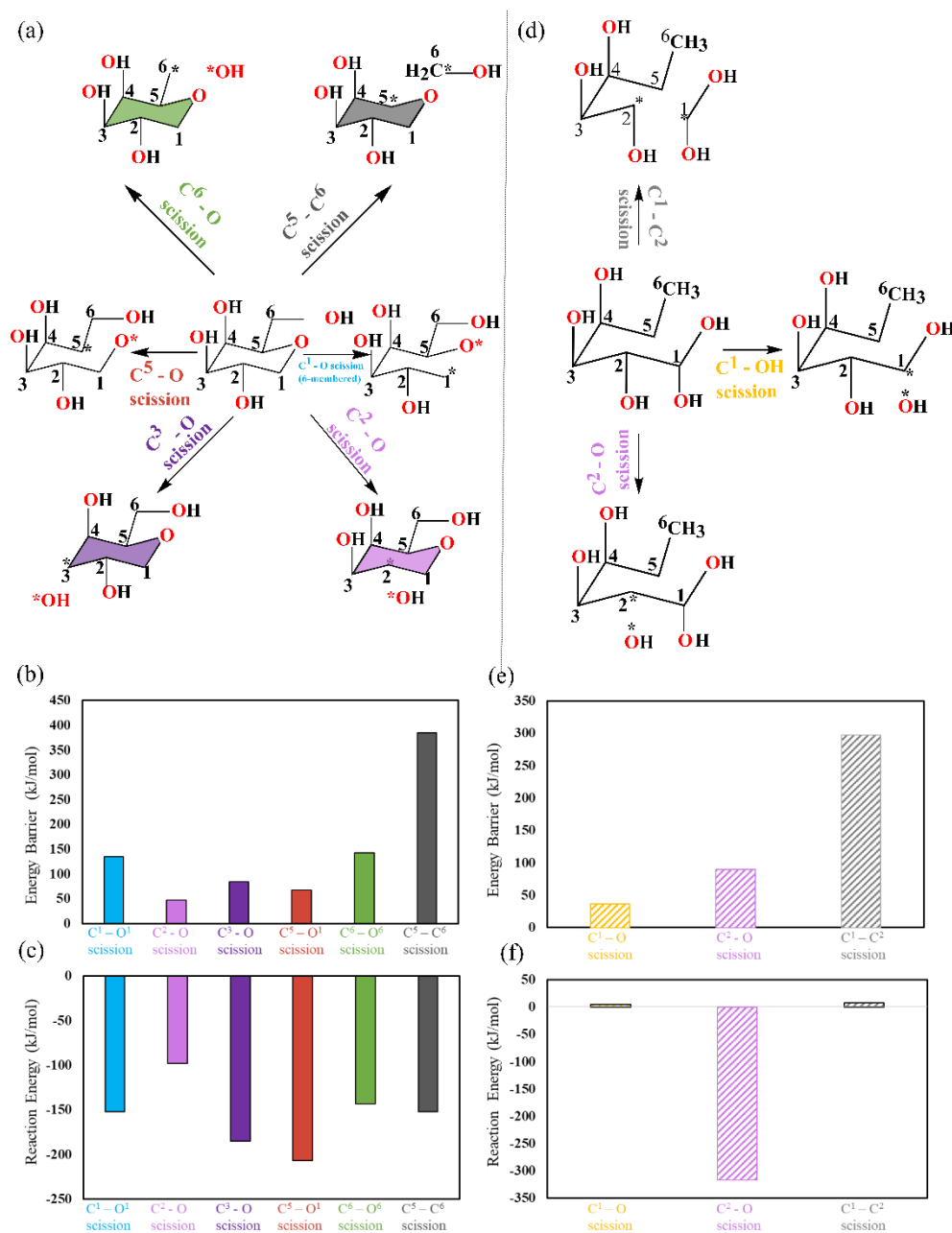


Figure 3.11 (a) and (d) Schematics showing probable end products that can be produced and demonstrating potential reaction paths for the initial activation of intermediate 1 and 2 on Mo₂C (on the left) and MoWC (on the right) surfaces, respectively. All considered pathways via which intermediates can activate on both catalysts are presented. The nomenclature for carbon atoms is shown in the central intermediates. Comparison of energy barriers (b and e) and reaction energies (c and f) in the bar graphs are shown below the schematic for Mo₂C (on the left) and MoWC (on the right) and each reaction pathway is shown using distinct colors.

On MoWC, C¹ – OH is computed to be the most facile pathway with the least energy barrier of only 37 kJ/mol in comparison to C² – OH dissociation which shows a barrier of 90 kJ/mol. This is

because the C¹ carbon atom has two hydroxyl groups which makes it geminal diol, whereas, C² – OH only has one hydroxyl group and geminal diols are unstable in nature because of the repulsion between electron pairs of two oxygen atoms. Thermodynamically, C² – OH dissociation is 320 kJ/mol more exothermic than C¹ – OH dissociation. It adopts a more stable adsorption configuration, binding to W and Mo atoms on the MoWC surface. In contrast, C¹ – OH dissociation is relatively less stable as it is physisorbed on MoWC. Similar to Mo₂C, C – C dissociation is not favorable on MoWC with very high barrier of 297 kJ/mol.

In summary, dehydroxylation at geminal diol at C¹ carbon is feasible on MoWC indicating the formation of linear chain alcohol or alkane. On the contrary, 6-membered ring opening via C⁵ – O dissociation is relatively unfavorable on Mo₂C in comparison to dehydroxylation at C² – OH indicating that it is not activated enough to open the second ring potentially retaining the ring and could lead to the formation of tetrahydropyran as the final HDO product.

▪ Lignin-derived bio-oil components (Eugenol, Vanillin, Phenol, Cresol)

3.3.5 Vanillin

3.3.5.1 Adsorption Configuration

On Mo₂C, Vanillin binds in η^2 (C – O) configuration with the aromatic ring parallel to the catalyst's surface over a 3- fold hollow site. In this configuration, the C², C⁴, and C⁶ carbon atoms (numbering shown in Figure 3.1) bind to Mo sites present in the top layer, forming Mo–C bonds. Additionally, the oxygen atom present at the C⁸ carbon also binds to the Mo atom, with a binding energy of -357 kJ/mol. In comparison to Mo₂C, Vanillin adsorbs more strongly on MoWC in the η^1 (C – O) configuration, with a binding energy of – 402 kJ/mol. This strong adsorption is due to the strong affinity of tungsten (W) towards oxygen and it facilitates the adsorption of vanillin by binding via O at C⁸ carbon. Moreover, due to the presence of tungsten in MoWC, it leads to a step-like structure which is more active than flat geometry of Mo₂C. Adsorption configurations of vanillin on Mo₂C and MoWC are shown in Figure 3.3i and 3.3j, respectively.

3.3.5.2 Reaction Pathways

The first activation of Vanillin and Eugenol and their corresponding reaction energetics are shown in Figure 3.12 and Figure 3.13. In both cases, dehydroxylation and demethoxylation showed least

energy barriers suggesting direct deoxygenation to be preferred on both Mo₂C and MoWC surfaces.

We considered six key HDO routes for Vanillin on both Mo₂C and MoWC namely, (i) C¹ – O scission, (ii) C² – O scission, (iii) C⁸ – O scission, (iv) C⁷ – O scission, (v) C⁴ – C⁸ scission, and (vi) C⁸ – O hydrogenation. Results of the first activation are shown in Figure 3.12. On Mo₂C, C² – O and C⁷ – O dissociation are found to be two kinetically competitive pathways with similar barriers of 93 and 84 kJ/mol. However, C² – O dissociation is 48 kJ/mol more exothermic than C⁷ – O dissociation, which makes it thermodynamically more feasible. Direct deoxygenation is also possible at C⁸ – O bond in the aldehyde group but it has a higher barrier of 128 kJ/mol. However, the reaction is highly exothermic with a reaction energy of -171 kJ/mol.

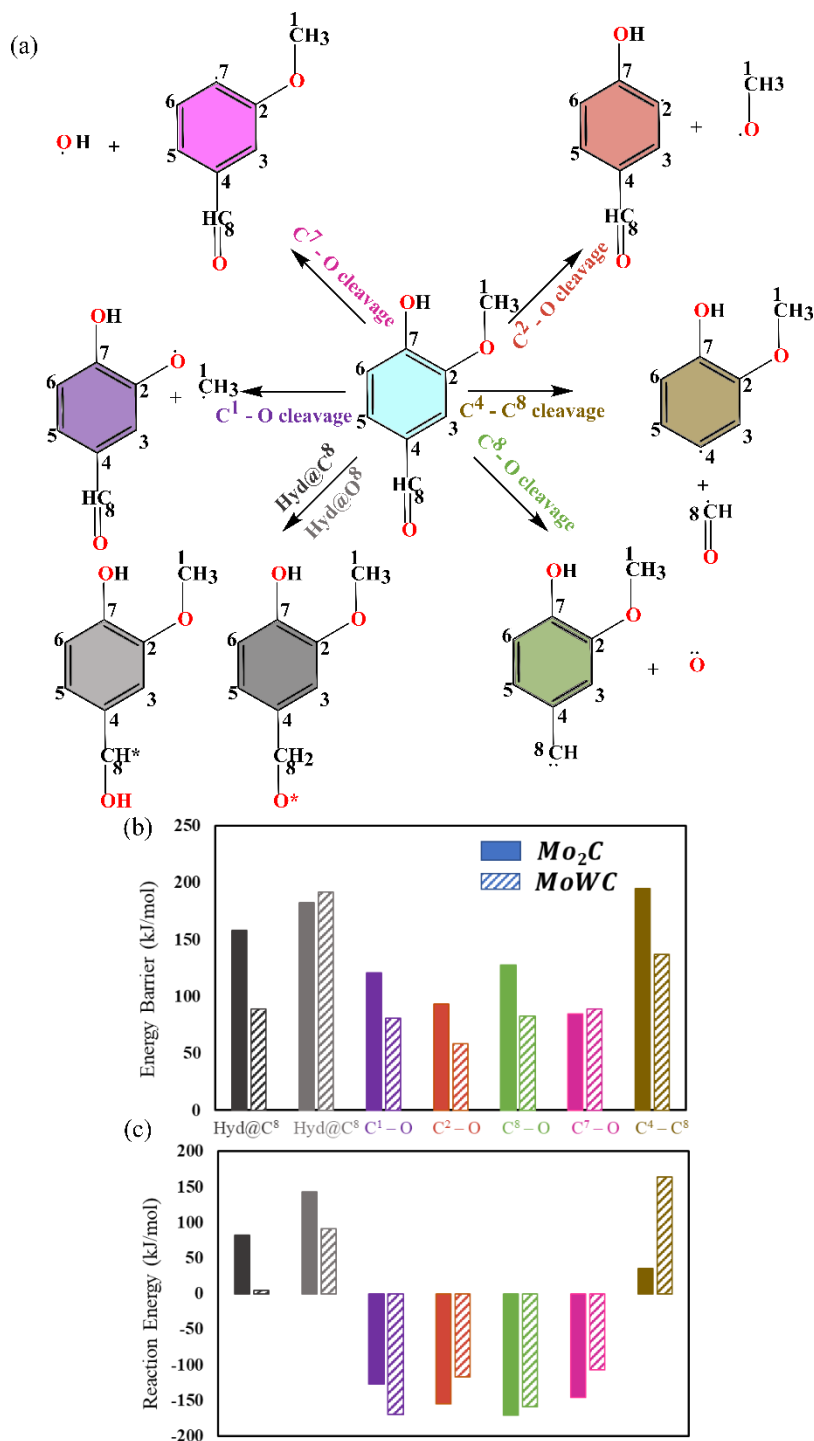


Figure 3.12 (a) Schematic showing probable end products that can be produced and demonstrating potential reaction paths for the initial activation of vanillin on Mo₂C and MoWC surfaces. The six considered pathways via which vanillin can activate are presented: (i) C¹ – O scission, (ii) C² – O scission, (iii) C⁵ – O scission, (iv) C⁷ – O scission, (v) C⁴ – C⁵ scission, and (vi) C⁵ – O hydrogenation. The nomenclature for carbon atoms is shown in the central intermediate 2 molecule. Comparison of (b) energy barriers and (c) reaction energies in the bar graphs are shown

below the schematic for Mo₂C and MoWC and each reaction pathway is shown using distinct colors.

Oxygen removal via decarbonylation could happen via C⁴ – C⁸ cleavage and it exhibited a high barrier of 195 kJ/mol with the reaction energy of 36 kJ/mol making it unfavorable both kinetically and thermodynamically. In addition, hydrogenation of C⁵ – O bond resulting in the formation of vanillyl alcohol has a barrier of 158 and 182 kJ/mol at the carbon and oxygen end, respectively. Moreover, it is endothermic in nature with reaction energies of 82 and 143 kJ/mol.

On MoWC, C² – O dissociation is the most facile pathway both kinetically and thermodynamically with the least barrier of 59 kJ/mol and the reaction energy of -117 kJ/mol. Alternate direct deoxygenation routes including C¹ – O, C⁷ – O, C⁸ – O dissociation are competitive with similar barriers of 81, 90, and 83 kJ/mol, unlike Mo₂C, where C¹ – O, and C⁸ – O showed high barriers (121 and 128 kJ/mol). This indicates that bimetallic carbide (MoWC) can break C – O bonds, regardless of whether they are single or double, similar to observations made with methyl glyoxal and acetic acid. Interestingly, hydrogenation of C⁸ – O at the carbon end seems plausible with a competitive barrier of 89 kJ/mol, however, hydrogenation initiation at oxygen end is unfavorable with a high barrier of 192 kJ/mol. In addition, this reaction was 86 kJ/mol more endothermic on oxygen end suggesting it might form vanillyl alcohol in which hydrogenation starts at the carbon end.

3.3.6 Eugenol

3.3.6.1 Adsorption Configuration

On Mo₂C, Eugenol adopts the similar configuration as guaiacol and vanillin in which it adsorbs in a $\eta^2(C - O)$ geometry with aromatic ring parallel to the surface and it is bonded via C³, C⁵, and C⁷ carbon atom. Moreover, the propyl chain consisting of an unsaturated bond between C⁹ and C¹⁰ atom also binds to the top site on Mo atom and the oxygen atom of the methoxy group occupies the top site, as shown in Figure 3.3k. On the contrary, due to the step-like structure of MoWC, it adsorbs in a tilted geometry due to the presence of metallic tungsten overlayers as shown in Figure 3.3l. In this case, the adsorption configuration is anchored via oxygen atom present in the methoxy group which binds to the tungsten atom with a relatively weaker binding energy of -266 kJ/mol in comparison to Mo₂C (-351 kJ/mol). This could be due to the propyl chain present in eugenol molecule which prefers to adsorb on Mo surface in comparison to metallic tungsten.

3.3.6.2 Reaction Pathways

In this case, we investigated the key reactions involving (i) $C^2 - O$, (ii) $C^7 - O$ dissociation, (iii) C^9 hydrogenation, (iv) C^{10} hydrogenation, and (v) Ring hydrogenation. Reaction energetics of these reactions are shown in Figure 3.13b and 3.13c.

Results clearly suggest that, on Mo_2C , hydrogenation of the allyl group has the highest barriers of 140 and 153 kJ/mol at C^9 and C^{10} carbon end indicating that 4-Propyl guaiacol formation won't be feasible kinetically. In addition, direct ring hydrogenation showed a similar barrier of 126 kJ/mol and it is also highly endothermic with a reaction energy of +103 kJ/mol. This reduces the possibility of ring saturated alcohols as major products. It contrasts with the reported literature on Ru catalysts where hydrogenation of the allyl group is reported to be the most feasible route resulting in 4-Propyl guaiacol as major product.²²⁴⁻²²⁶ Similar to vanillin, direct deoxygenation via $C^2 - O$ or $C^7 - O$ dissociation were calculated to be the two feasible and competitive pathways with relatively similar barriers of 97 and 80 kJ/mol, respectively. On top of that, both reactions are highly exothermic with reaction energies of -156 and -118 kJ/mol.

On $MoWC$ as well, similar trend was observed where direct deoxygenation is favorable over direct hydrogenation. However, $C^2 - O$ dissociation has the least barrier of only 6 kJ/mol (almost a barrier less step) leading to the formation of 4-allyl phenol after the hydrogenation reaction step. This could be attributed to the high affinity of tungsten atom for oxygen which facilitates the adsorption of eugenol anchored via the oxygen atom, resulting in stretching of the $C^2 - O$ bond to 1.49 Å in comparison to Mo_2C surface where the $C^2 - O$ bond length is 1.42 Å (Table C.2). In addition, barrier for $C^7 - O$ dissociation has reduced to 66 kJ/mol on $MoWC$ in comparison to Mo_2C (97 kJ/mol) which confirms the promotional effect of W on Mo_2C for the direct deoxygenation. Hydrogenation of the allyl group exhibited very high barriers of 135 and 164 kJ/mol similar to what we observed on Mo_2C indicating these metallic carbides won't prefer hydrogenation.

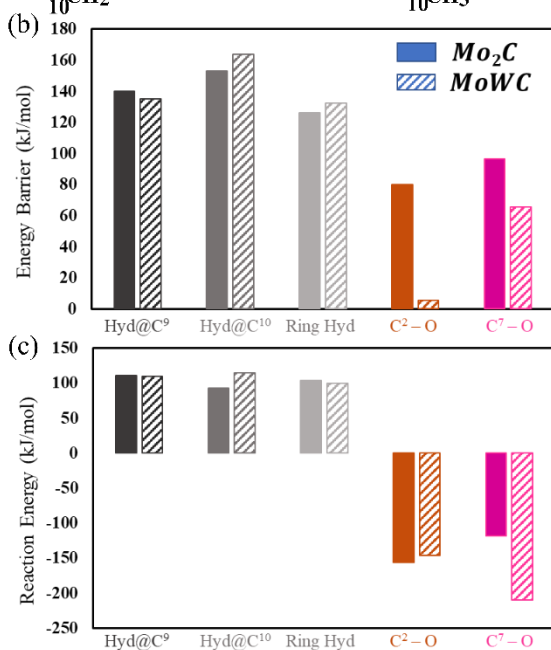
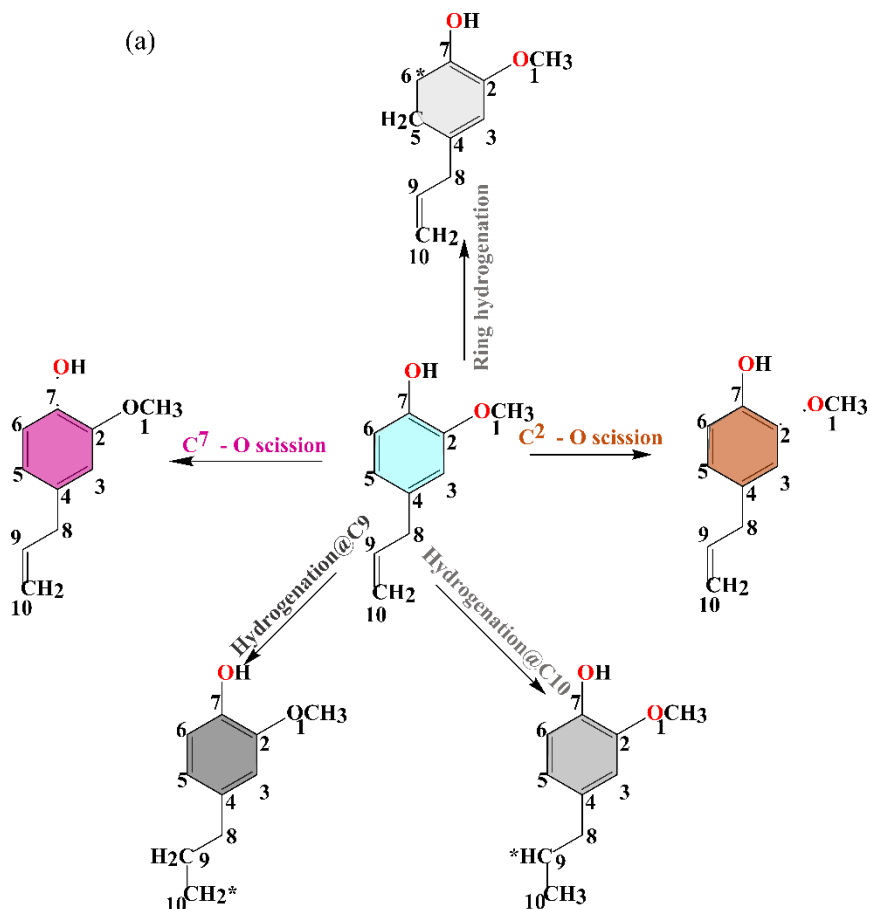


Figure 3.13 (a) Schematic showing probable end products that can be produced and demonstrating potential reaction paths for the initial activation of eugenol on Mo_2C and MoWC surfaces. The five considered pathways via which eugenol can activate are presented: (i) $\text{C}^2 - \text{O}$, (ii) $\text{C}^7 - \text{O}$ dissociation, (iii) C^9 hydrogenation, (iv) C^{10} hydrogenation, and (v) Ring hydrogenation. The

nomenclature for carbon atoms is shown in the central eugenol molecule. Comparison of (b) energy barriers and (c) reaction energies in the bar graphs are shown below the schematic for Mo₂C and MoWC and each reaction pathway is shown using distinct colors.

Based on the first activation results presented above for vanillin and eugenol, it is evident that both Mo₂C and MoWC would favor the deoxygenation pathway in comparison to hydrogenation and C – C bond scissions. To point out, W – doped Mo₂C significantly further brings down the barrier for C – O dissociation. In addition, the difference between the direct deoxygenation (DDO) and hydrogenation (HYD) pathways is widened up in the case of bimetallic carbide (MoWC). This suggests higher selectivity of MoWC towards DDO pathway resulting in deoxygenated aromatic products.

3.3.7 Phenol and Cresol

The comparison of reaction pathways of cresol and phenol's direct dehydroxylation (C – O dissociation) and direct ring hydrogenation steps is shown in Figure 3.14. For cresol, MoWC catalyst showed a lower energy barrier of 52 kJ/mol for dehydroxylation in comparison to 78 kJ/mol on Mo₂C. In addition, the dissociation of hydroxyl group is 38 kJ/mol more exothermic on MoWC surface than Mo₂C. Similar to cresol, dehydroxylation reaction from phenol is more favorable on MoWC surface with the lowest barrier of 35 kJ/mol, as compared to that on Mo₂C (80 kJ/mol). Ring hydrogenation of phenol follows the same trend as cresol on MoWC and Mo₂C with competitive barriers of 115, and 110 kJ/mol. Overall, MoWC manifested the highest difference between the barriers for DDO and HYD pathways i.e., 66 and 75 kJ/mol, in both cresol and phenol, respectively. Hence, ring hydrogenation and C – O dissociation becomes competitive on Mo₂C in contrast to MoWC which selectively favors the direct deoxygenation pathway. Detailed ring hydrogenation results for phenol and cresol are also presented in our previous study.¹²⁵ Overall, the comparison of DDO and HYD pathways on these catalysts confirms that metallic tungsten overlayers play a vital role in reducing direct deoxygenation energy barrier.

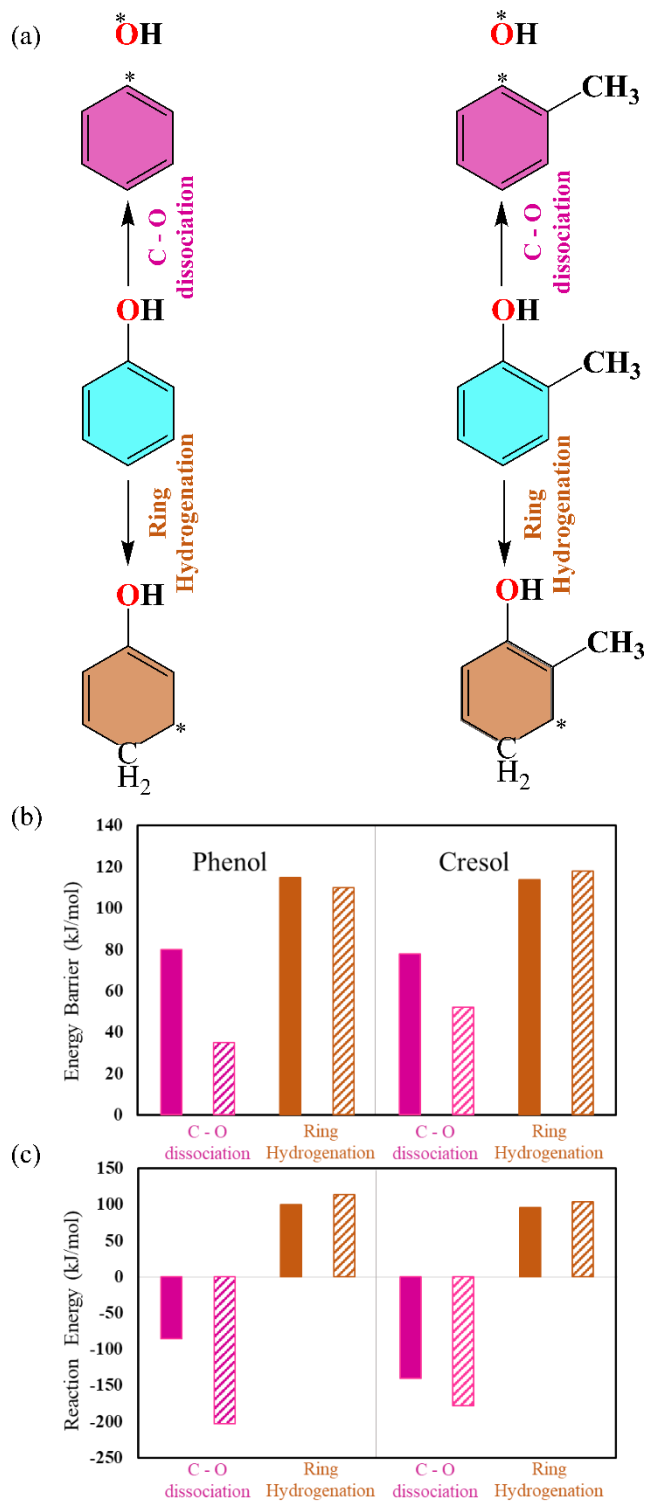


Figure 3.14 (a) Schematics showing for the Phenol and Cresol first activation. The two considered pathways via which phenol and cresol can activate are presented: (i) C – O dissociation, (ii) Ring hydrogenation. Comparison of (b) energy barriers and (c) reaction energies in the bar graphs are shown below the schematic for Mo₂C and MoWC and each reaction pathway is shown using distinct colors.

3.4 Conclusions

In this work, we investigated Molybdenum-based mono and bimetallic carbide catalysts for their ability to hydrodeoxygenate biomass-derived bio-oil, using six key, representative components in bio-oil, namely, 5-HMF, Acetic acid, Eugenol, Levoglucosan, Methylglyoxal, Guaiacol and Vanillin. We predicted that single C – O bond dissociation is feasible on both monometallic Mo₂C and bimetallic MoWC. However, in comparison with Mo₂C, the direct dissociation of carbonyl double bonds present in acetic acid and methyl glyoxal are only feasible on MoWC with low barriers of 3 and 29 kJ/mol, respectively. Therefore, Mo₂C could lead to a mixture of C₁ and C₂ products for acetic acid, and a mixture of C₁, C₂, and C₃ products for methyl glyoxal. On the other hand, MoWC can selectively form completely deoxygenated C₂ products for acetic acid and C₃ products for methyl glyoxal. Reaction energetics of 5-HMF manifested spontaneous dissociation of C–OH bond in furan ring upon chemisorption on MoWC. Moreover, in the HDO of 5-HMF, carbonyl C = O bond cleavage becomes kinetically feasible on MoWC in comparison to Mo₂C which favors both hydrogenation and deoxygenation with competitive barriers indicating to formation of a mixture of alcohols and alkenes. In the case of LGA, results indicate the formation of linear chain alkanes on MoWC as it favors both ring-opening reactions, however, Mo₂C shows competitive barriers of 68 kJ/mol for ring-opening in comparison to dehydroxylation (47 kJ/mol) suggesting it might lead to the formation of partially deoxygenated tetrahydropyran as the major product. Lignin-derived constituents follow the same trend where MoWC significantly reduces the barrier for direct deoxygenation to only 18 kJ/mol, in comparison to Mo₂C (60 kJ/mol) and similar trend can be seen for Eugenol and Vanillin where C²/ C⁷ – O cleavage is favorable, leading to aromatic products, whereas, Mo₂C favors both hydrogenation and direct deoxygenation leading to a mixture of ring-saturated and aromatic products. Overall, as a result of its enhanced activity and selectivity towards direct deoxygenation for all oxygenated constituents, MoWC could be an effective and efficient catalyst for the real bio-oil mixture. The present study provides mechanistic understanding into the overall energy landscape for HDO of different representative constituents of biooil on monometallic (Mo₂C) and bimetallic carbide (MoWC) surfaces for the first time and will stimulate further experimental studies for the vapor-phase upgrading of bio-oil.

Chapter 4: Predicting Active, Selective and Stable Mo₂C–Based Bimetallic Carbides for Direct Deoxygenation and Hydrogenation Reactions: A Computational Screening

Abstract

Transition metal carbides (TMCs), especially molybdenum carbide (Mo₂C), represent an economical and attractive alternative to precious noble metal catalysts for processes involving hydrogenation (HYD) and direct deoxygenation (DDO) reactions such as hydrodeoxygenation (HDO). Although Mo₂C has good activity for DDO, it is not selective as it displays similar activity towards HYD as well. Moreover, stability against oxygen poisoning is a critical issue as it is the major reason of catalyst deactivation. Herein, using phenol as a model compound, we employed density functional theory (DFT) calculations to investigate three key reactions (C-O dissociation, oxygen removal and ring hydrogenation) representing activity, stability and selectivity which are critical to the HDO process on 45 Mo₂C-based bimetallic carbide catalysts (Co, Cr, Fe, Mn, Nb, Ni, Ti and Zr) obtained from the Materials Project database. Among these catalysts, different dopants, stoichiometric ratios and terminations were considered. First, reaction energies of oxygen removal were used to identify stable catalysts. Subsequently, with the energy barriers of DDO and HYD for activity and their differences for selectivity, best candidates for DDO (Mo-terminated Fe₃Mo₃C, Mn-terminated Mn₃Mo₃C and Ni-terminated Ni₃Mo₃C) and HYD (triclinic Mo-terminated Fe₁₁MoC₄ and Ni-terminated Ni₆Mo₆C) were identified. Since strong oxygen binding favors DDO but hinders oxygen removal, an optimal range of oxygen binding energy (OBE) between -100 kJ/mol to -200 kJ/mol has been proposed. In addition, a parameter encompassing three critical aspects (activity, stability, and selectivity) of a catalyst was proposed. Using OBE as a descriptor and the proposed parameter, a qualitative trend was obtained which can be used for preliminary screening of large databases of catalysts, including TMCs other than Mo₂C, for processes involving DDO and HYD reactions.

4.1 Introduction

The quest of finding an optimal catalyst for biomass conversion has picked up momentum as it is a sustainable way of producing biofuels and specialized chemicals.^{1,25,227,228} Moreover, it can complement the petroleum-based fuels to meet ever-rising energy demands globally. Biomass can be utilized to produce bio-oil, mainly by two processes: fast pyrolysis and hydrothermal liquefaction.^{15,23} However, high oxygen content in the bio-oil due to the presence of more than 400 oxygenated compounds presents a critical hurdle in its direct use.^{1,25} Transition metal carbides (TMCs), represent a cost-effective alternative to traditional noble-metal-based catalysts since their discovery by Levy and Boudart.³⁶ TMCs, particularly Mo₂C (molybdenum carbide), have gained significant attention for the hydrodeoxygenation (HDO) of bio-oil^{64,140,141,229} due to the coexistence of metallic and acidic functionalities on their surfaces.³⁰ Direct deoxygenation (DDO) of oxygenated functional groups and C=C hydrogenation (HYD) are the two competitive routes in the process of HDO. In the former, oxygen is selectively cleaved (C-O/C=O bond scission) followed by O removal in the form of water without successive hydrogenation and/or undesired C-C scission, whereas the latter favors selective hydrogenation of unsaturated C=C/C=O bonds. DDO leads to the formation of aromatics, alkenes and alkanes, but HYD produces ring-saturated compounds, alkanes and alcohols. Depending on the desired target products, catalysts are required that are highly selective towards either the DDO or HYD pathway as each has its own applications. For instance, the DDO pathway is preferred for producing aromatics used in fuels, while the HYD pathway is suitable for generating ring-saturated compounds used in specialized chemicals.^{89,230} Mo₂C has shown similar activity for both DDO and HYD²³¹⁻²³⁴, leading to the formation of a mixture of hydrogenated and unsaturated deoxygenated products, which are difficult to separate.^{74,125}

Another concern regarding the stability of Mo₂C is that it is prone to deactivation due to the retainment of O atoms on the catalyst surface during HDO. Consequently, oxygen poisoning on Mo₂C surface leads to the formation of oxycarbides, which can suppress the catalytic activity and/or selectivity.^{37,51,126,127,235,236} It has been confirmed that these residual oxygen species suppress the metallic sites significantly.^{78,234} Above 800 K, surface oxygen species migrate into the bulk (at least down to the interrogation depth (~6 nm) of X-ray photoelectron spectroscopy (XPS)),²³⁷ explained by an observed change in the oxidation states of the Mo atoms. Therefore, high H₂ pressure is required to avoid the retainment of O atoms on the catalyst's surface by removing them

in the form of H₂O. However, it compromises the selectivity of the catalyst as the high H₂ pressure results in hydrogenated products along with higher consumption of H₂.¹⁴³ Therefore, hydrogen consumption during HDO needs to be minimized since H₂ is an expensive commodity, and the conditions at which O removal occurs without over hydrogenation needs to be determined.

Doping of a hetero-metal in to the monometallic carbide, has been investigated to enhance their selectivity towards DDO/HYD and its stability. Several authors have investigated the effect of different dopants on the HDO performance of Mo₂C-based bimetallic carbide catalysts.^{57,58,65,85,152,238} Ruddy et al. demonstrated that the modification of β-Mo₂C with Pt and Ni can tune the acid-/H*-site ratio, which improved the selectivity towards aromatic products for the bimetallic carbide catalyst.⁵⁷ The modified bimetallic carbide catalyst displayed high conversions (>94%) and high selectivity towards oxygen-free products like benzene (>80%) in guaiacol deoxygenation under ex-situ catalytic fast pyrolysis (CFP) conditions (623 K and 0.44 MPa H₂). Tran et al.¹²⁸ observed enhanced activity (conversion = 93%) and selectivity for benzene (70%) on tungsten-doped molybdenum carbide (MoWC) using guaiacol as a model compound at 623 K and 2.75 MPa. It was attributed to the synergistic effect between Mo and W atoms, which led to increased density of H₂-activating sites. It was proposed that the presence of metallic W would enhance the oxophilicity of the catalyst to facilitate the adsorption of oxygen containing functional groups, thereby achieving improved deoxygenation activity. Zhou et al.¹⁴⁹ demonstrated that the doping of Ni in Mo₂C catalyst promotes its oxygen removal capability by reducing the adsorption strength of O* and OH* species. Lin et al.⁶³ reported a combined experimental and computational study on Co-modified Mo₂C in which cobalt, present as overlayers, reduces both oxygen and furfural binding energies by approximately 150 kJ/mol, hence, preventing the poisoning by these adsorbates and increasing the catalyst's stability. Kelly et al.¹⁵⁰⁻¹⁵² compared various bimetallic carbides in which monometallic carbides (Mo₂C, W₂C) were modified with metal overlayers (Ni, Cu, Au, Rh, Pt) assumed to be epitaxial with the slab. They showed bare Mo₂C surface was active for C–O cleavage while surface modification with Ni and Cu resulted in the selective scission of C–C and C–H bond scission, respectively. Wannakao et al.^{153,154} probed tungsten carbide surfaces with monolayer and sub-monolayers metal films for the reduction of CO₂ to methane. In the majority of these computational studies the modelled microstructures for bimetallic carbides were chosen arbitrarily without any understanding or rationale, hence, the results explaining the effect of the metal on activity and selectivity remain questionable. Moreover, our fundamental

understanding of mixed-metal carbides^{239,240} is currently much less developed in comparison to our knowledge of other mixed metal materials like single/mixed-metal oxides.^{241,242} A systematic comparison of the effect of doping different metals on the activity, selectivity and stability of Mo₂C has yet to be explored, especially with different compositions and structures. This has potential industrial applications beyond biomass conversion.^{204,243,244} For example, Mo₂C and cobalt-modified Mo₂C were both reported to be effective catalysts for CO₂ conversion.²⁰⁶ Pt-decorated α -MoC has been used to produce H₂ at low temperature via the water-gas shift (WGS) reaction.²⁴⁵

The multitude of investigations from the literature into the HDO performance of Mo₂C allows us to conclude that, despite its high activity, Mo₂C is prone to form molybdenum oxycarbide which further requires higher H₂ pressures to maintain its activity.^{126,127} However, reaction pathway gets altered as hydrogenation becomes competitive at higher H₂ pressures.^{69,128} In Chapter 2, we revealed that the presence of tungsten overlayers on bulk W-doped molybdenum carbide (MoWC) catalyst creates a step-like structure and significantly reduces the DDO barrier from 60 kJ/mol on Mo₂C to only 18 kJ/mol on MoWC.¹²⁵ However, removal of oxygen species after C-O dissociation still remains a challenge for Mo₂C-based catalysts. Based on the above discussion, novel catalysts based on Mo₂C should have following abilities in order to favor the DDO pathway: i) high adsorbate binding energy, ii) low C – O activation barriers, iii) low oxygen removal barriers and iv) high hydrogenation barriers. For HYD pathway, low hydrogenation barriers and high DDO barriers are required. These characteristics will extend the application of bimetallic carbides to CO₂ reduction and reverse water-gas shift reaction (RWGSR). Additionally, the vast library of metal-doped bimetallic carbides based on Mo₂C has never been explored²⁴⁶, but that would be difficult to do with experiments alone. In this context, computational tools such as density functional theory (DFT) can be useful in performing efficient screening of catalysts for HDO, which will provide critical insights regarding the active sites and underlying reaction mechanism. Additionally, proposing a descriptor to refine the search for suitable HDO catalysts through preliminary screening would be highly beneficial. For transition metals (TM), effective descriptors like the d-band model have already been established, linking atomic structure with the activity of TM catalysts. This has also led to simple descriptors, such as the adsorption energy of oxygen and CO for the WGSR reaction, which can elucidate experimental data on TM surfaces. However, such universal descriptors have not been proposed in the context of TMCs and it is highly desired.

In this work, we performed a computational screening of 45 Mo₂C-based bimetallic carbide catalysts (M-Mo₂C) obtained from the Materials Project database.²⁴⁶ Among these 45 available candidates, 20 catalysts are experimentally observed as well.²⁴⁷ In this database, other bimetallic carbides (e.g., M-WC) are also available. However, this work is limited to Mo₂C-based bimetallic carbides. We systematically investigated the effect of doped transition metals on Mo₂C's catalytic performance using 3 key reactions (C-O dissociation, oxygen removal and ring hydrogenation) for phenol, representing DDO activity, stability against oxygen poisoning and hydrogenation activity. The addition of partner metal alters the adsorption characteristics, and further changes the energetics of the considered reaction. Utilizing the reaction energetics of probe reactions, active, selective and stable catalysts for both DDO and HYD pathways are identified. Lastly, η , defined as the difference between the barriers of DDO and HYD ($\Delta_{DDO-HYD}$) divided by that of water formation, was identified as the parameter that encompasses all three critical aspects for a catalyst, viz. activity, selectivity, and stability. Using oxygen binding energy (OBE) as a descriptor and η , a qualitative trend was observed which will aid in screening bimetallic carbide catalysts for HDO. Lastly, an optimal range for the OBE value of -200 kJ/mol to -100 kJ/mol was proposed for HDO, since strong oxygen binding favors DDO but hinders oxygen removal.

Modelled structures and computational methods are discussed in Sections 4.2.1 and 4.2.2, respectively. Screening strategy of M- Mo₂C catalysts is presented in Section 4.2.3. Adsorption characteristics of small adsorbates (H and OH) on all catalysts is discussed in Section 4.3.1 followed by the preliminary screening of stable candidates in Section 4.3.2. In Sections 4.3.3 to 4.3.5, energy barriers and reaction energies are reported for C – O dissociation, oxygen removal and ring hydrogenation reactions respectively for M-Mo₂C catalysts. Subsequently, selective and stable DDO and HYD are identified in Section 4.3.6.1 and 4.3.6.2, respectively. In Section 4.3.7, a descriptor-based approach is presented. The key findings from the study are summarized in Section 4.4.

4.2 Models and Computational Methods

4.2.1 Model Structures

All Mo₂C – based bimetallic carbides (M-Mo₂C) structures were adapted from the Materials Project (MP) Database.²⁴⁶ A total of 20 models for bimetallic carbide catalysts with different compositions spread across 8 dopants, namely, cobalt (Co), manganese (Mn), iron (Fe), nickel

(Ni), chromium (Cr), niobium (Nb), titanium (Ti), zirconium (Zr) were available. To point out, 8/20 catalysts ($\text{Fe/Ni/Co}_2\text{Mo}_4\text{C}$, $\text{Fe/Ni/Co}_3(\text{Mo})_3\text{C}$ and $\text{Fe/Ni/Co}_6\text{Mo}_6\text{C}$) are reported to be experimentally synthesized as well.²⁴⁷ In our previous work, we elucidated the enhanced effect of tungsten (W) dopant on the HDO performance of Mo_2C . However, oxygen removal is difficult on this catalyst with a high barrier of 238 kJ/mol. We also considered a boron-doped molybdenum tungsten trimetallic carbide (BMoWC). The rationale of selecting BMoWC was to investigate the effect of boron in reducing the oxygen removal barrier while maintaining its activity. Moreover, BMoWC has been synthesized experimentally²⁴⁸. With 20 modelled catalysts, the most stable facet was first identified based on surface energies as shown in Table D.1-Table D.7 in Appendix D. Computational methodology to calculate surface energy is also presented in detail in Section D1. We also investigated the effect of different terminations with different stoichiometry/compositions on the surface which increased the total number of candidates to 45. A schematic showing all the catalysts with their possible compositions and different terminations is shown in Figure 4.1. The structures of all catalysts considered in this work are presented in Figure D5-D13 in Appendix D.

In order to name and identify each catalyst surface in a systematic yet convenient manner, we have assigned shorthand names to every catalyst surface in the general form M_{XY} . ‘M’ denotes the dopant metal present in the catalyst. The subscript ‘X’ denotes the stoichiometric coefficient of dopant atoms in the formula of the bimetallic carbide. The subscript ‘Y’, where $\text{Y} = \text{A, B, C}$, corresponds to a surface termination of dopant metal, molybdenum, and a mixture of both respectively. For example, $\text{Co}_2\text{Mo}_4\text{C}$ terminated with dopant Co atoms is named $\text{Co}_{2\text{A}}$, and $\text{Cr}_{22}\text{MoC}_6$ terminated with Mo atoms is named $\text{Cr}_{22\text{B}}$. For the same X values across different compositions, the stoichiometric coefficient of Mo is used instead. For example, NbMoC_2 and NbMo_3C_4 are referred to as NbMo and NbMo₃ respectively. The only exceptions are the orthorhombic and triclinic $\text{Fe}_{11}\text{MoC}_4$ structures as they have the same composition, thus, an additional ‘O’ or ‘T’ tag denotes the orthorhombic and triclinic structures. For example, $\text{Fe}_{11}\text{O}_\text{A}$ and $\text{Fe}_{11}\text{T}_\text{A}$ corresponds to the orthorhombic and triclinic $\text{Fe}_{11}\text{MoC}_4$ structures with A-termination respectively.

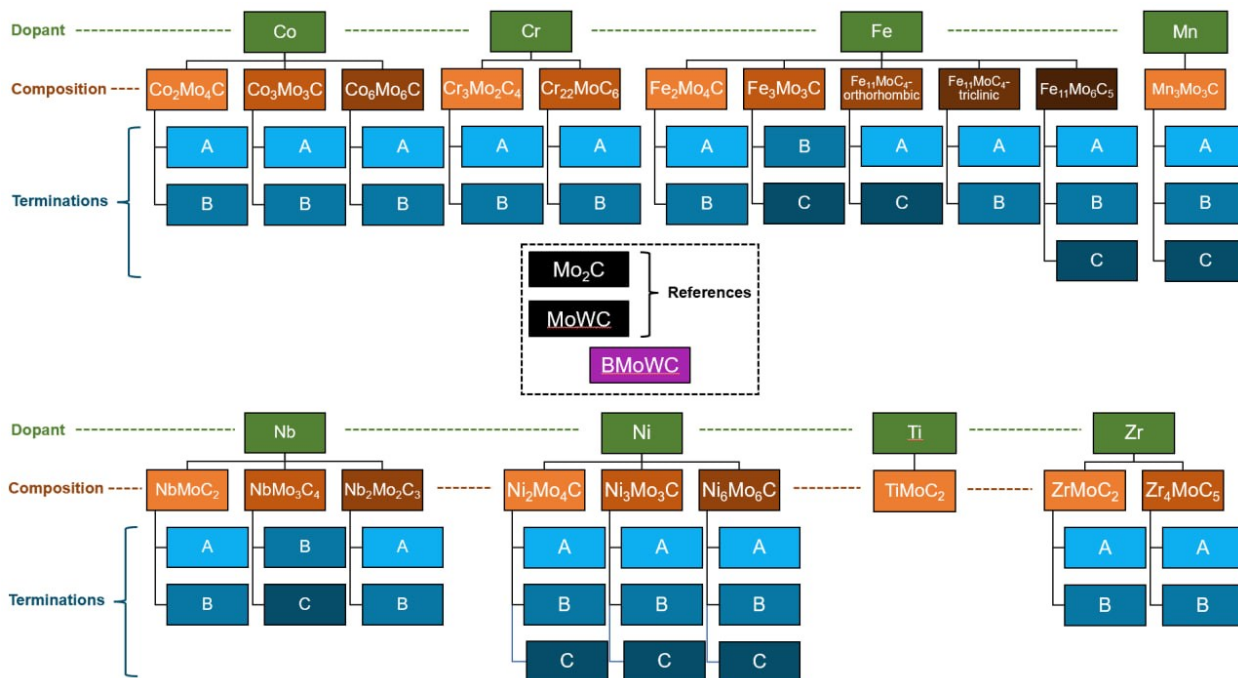


Figure 4.1. Schematic of all the considered catalysts with different compositions and possible terminations. A, B and C represents the respective dopant termination, molybdenum termination and mix of dopant and molybdenum termination, respectively.

4.2.2 Methodology

DFT simulations were performed using the Vienna ab initio Simulation Package (VASP)^{157,158}. All calculations were done using the projector augmented wave (PAW) method¹⁵⁹ employing a plane with cut-off energy of 450 eV and a Monkhorst-Pack scheme k-point sampling of 3x3x1. Spin-polarized calculations were performed, and a high level of accuracy is ensured with force convergence criteria of 10⁻⁵ eV/Å per unit cell and force tolerance of 0.05 eV/Å. Generalized gradient approximation (GGA) based rPBE-vdW exchange-correlation functional was employed. The catalyst was modeled using 5-layer, p(4x4) unit cell with an inter-slab distance of 12 Å. The transition state (TS) for all reactions was identified using the Nudged Elastic Band (NEB) method (with 8 to 12 images)²⁴⁹. Using the quasi-Newton algorithm, the image closest to the TS was optimized and the TS was confirmed by performing vibrational frequency analysis²⁵⁰. The reaction energies and activation barriers of all elementary reactions in this study are reported as electronic energy changes. The adsorption energy of H adatom and phenol is defined as,

$$\Delta E_{\text{ads}} = E_{\text{slab}} - E_{\text{slab}} - E_{\text{adsorbate}}(g) \quad (4.1)$$

where $E_{\text{Slab/adsorbate}}$ represents DFT total energy of the adsorbed system (H/phenol adsorbed on catalyst surface), E_{Slab} represents DFT total energy of the catalyst surface, and $E_{\text{adsorbate}}$ represents DFT total energy of the adsorbate in gas phase.

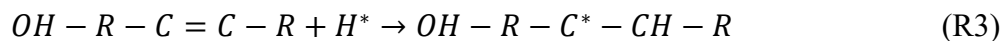
The adsorption energy of oxygen is defined as,

$$\Delta E_{\text{ads}} = \frac{E_{\text{Slab}}}{\text{OH}} - E_{\text{Slab}} - E_{\text{H}_2\text{O}}(g) + \frac{1}{2}E_{\text{H}_2}(g) \quad (4.2)$$

where $E_{\text{Slab/OH}}$ represents DFT total energy of the adsorbed system (OH adsorbed on catalyst surface), E_{Slab} represents DFT total energy of the catalyst surface, and $E_{\text{H}_2\text{O}}$, E_{H_2} represents DFT total energy of H_2O and H_2 molecules in gas phase.

4.2.3 Screening Strategy

To explore the pool of 45 candidates to identify active, selective and stable catalysts for direct deoxygenation and hydrogenation, we employed three probe reactions; 1) C-OH dissociation (DDO), 2) oxygen removal (OR), and 3) C=C hydrogenation (HYD) as shown below:



In DDO process, R1 and R2 take place in tandem as hydrogenation of oxygen species and removal in the form of water is critical for the stability of a catalyst surface. Therefore, the reaction energy of water formation constitutes the first screening criterion. Catalysts showing reaction energy of greater than 175 kJ/mol for water formation were not considered further in the screening process. Following the first screening, the activity, stability and selectivity aspects were then assessed in parallel by considering the barriers and reaction energies of DDO (R1), OR (R2) and HYD (R3). This enabled us to first identify selective DDO catalysts based on the following criteria:

- The tradeoff between R1 activity and R2 activity (since strong oxygen binding generally results in low DDO barriers, but also makes oxygen removal from the surface difficult). Hence, energy barriers of both R1 and R2 must be low.
- The selectivity which is determined by difference in energy barriers of R1 and R3 reactions.

Using the 2nd criteria, we also identified selective HYD catalysts as well. An overview of the screening process is shown in Figure 4.2.

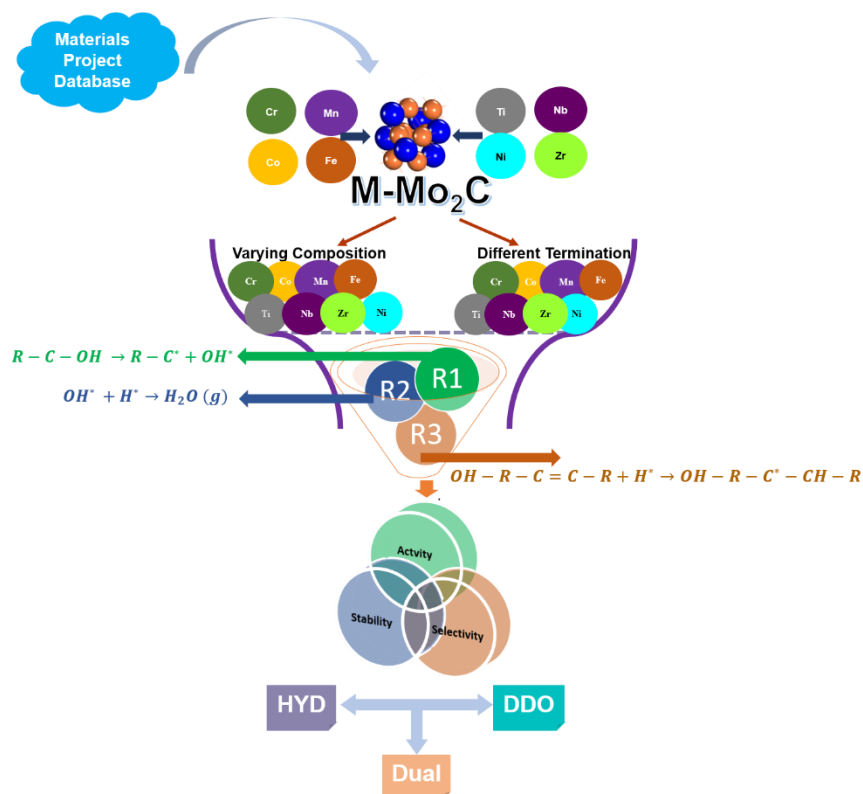


Figure 4.2. Schematic of the screening strategy adopted in this work for screening the catalysts with different compositions and possible terminations (A, B and C).

4.3 Results and Discussion

4.3.1 Hydrogen and Oxygen Adsorption

In the HDO process, oxygen is removed via C – O dissociation by the catalytic reaction with hydrogen. The first step involves the breaking of the C – O bond followed by the hydrogenation of the oxygen species and its desorption from the catalyst's surface. Therefore, oxygen binding characteristics on the catalysts will govern their ability to cleave C – O bonds, while hydrogen binding is crucial for hydrogen diffusion, which is essential for hydrogenation. Hence, we first studied the chemisorption of H* and OH* species on all 45 candidates and we also included Mo₂C and MoWC catalysts for reference. Computed hydrogen (HBE) and oxygen binding energies (OBE) on all catalysts are shown in Figure D32-33 and Table D.8 in Appendix D. For OBE, there is a notable difference in binding energy for A and B terminations as shown in Figure 4.3. It can

be attributed to the oxophilicity difference between the respective dopant and Mo atoms. Oxophilicity (Θ) describes the tendency to form oxides and there exists an oxophilicity scale proposed by Kepp, which can provide more accurate measures for rationalization and improvement of catalyst design.²⁵¹ According to this scale, Mo has an oxophilicity of 0.6.

For dopants that are less oxophilic than Mo, which are Co (0.4), Ni (0.2), Cr (0.6), Fe (0.4), and Mn (0.4), it follows that the catalyst surfaces in these dopant categories with a B-termination will exhibit a stronger OBE than those with an A-termination because the A- and B- terminations correspond to the dopant metal and Mo respectively. Correspondingly, for the dopants that are more oxophilic than Mo, which are Nb (0.8), Zr (0.8) and Ti (1), the opposite trend is observed, and surfaces with an A-termination will show a stronger OBE instead. The variations in OBE values on catalyst surfaces with a C-termination can also be correlated with the relative proportions of Mo atoms on the surface – OBE values increase with increasing Mo proportions in the cases of less oxophilic dopants, and vice versa. Although Cr and Mo have the same oxophilicity (0.6), the B-termination still showed a higher OBE value due to the high bond dissociation energy (BDE) of Mo – O bond of 502 kJ/mol in comparison to Cr which has a BDE of 461 kJ/mol.²⁵¹ One exception was found in the case Fe_3C , which contained an equal proportion of Fe and Mo atoms on the surface. An OBE value of -362 kJ/mol was reported on Fe_3C due to the presence of undercoordinated sites on the surface, which tend to bind the adsorbates stronger than on the pure surface.

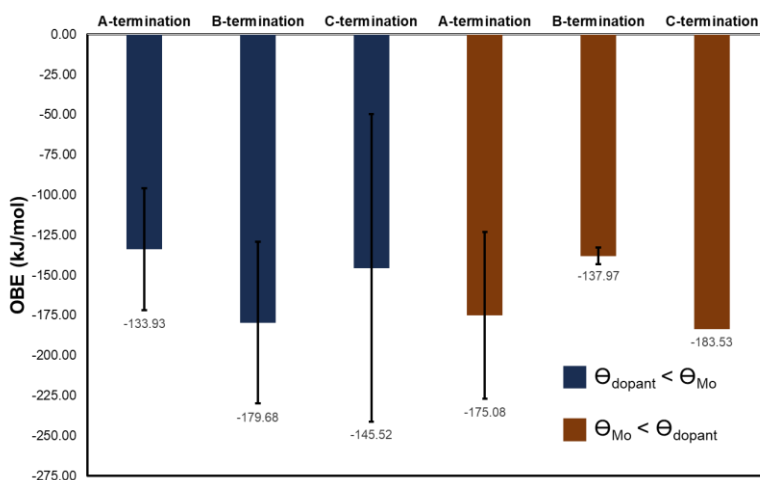


Figure 4.3 Comparison of mean oxygen binding energy (OBE) for each termination (A, B, C) across all catalysts (with the exception of Zr-doped catalysts) with one standard deviation. The blue and brown colors represent the cases in which $\Theta_{\text{dopant}} < \Theta_{\text{Mo}}$ and $\Theta_{\text{dopant}} > \Theta_{\text{Mo}}$

respectively. The standard deviation for the rightmost dataset is not shown as there is only one value in that dataset (NbMo₃C).

On the other hand, for dopants having $\Theta > 0.6$, which are Nb (0.8), Zr (0.8), Ti (1), the A-termination will exhibit stronger OBE. For example, Nb-terminated surfaces displayed stronger OBE for all three compositions for Nb-doped bimetallic carbides as shown in Figure D33b. It perfectly corroborates with the oxophilicity scale, since Nb with higher oxophilicity binds strongly with OH* species. The only Ti-doped surface we considered showed a very strong OBE of -235 kJ/mol in comparison to the parent Mo₂C (-155 kJ/mol), in correspondence with its high oxophilicity of 1. However, Zr, with the same oxophilicity as Nb, did not follow any trend as the OBE was stronger on B-terminated surfaces instead.

For HBE, one key observation was that it followed the same trend as OBE on all the catalysts except Zr. It can be explained by the occupancy of similar active sites on the catalyst's surface. The most stable adsorption site was calculated to be 3-fold hollow sites for both H* and OH* (Figure D13-31). To highlight, Zr_A was the only surface on which the HBE (-64 kJ/mol) was stronger than the OBE (-46 kJ/mol).

Overall, it gives a clear understanding of how various terminations and compositions of a catalyst can alter the adsorption characteristics of hydrogen adatoms and OH* fragments.

4.3.2 Preliminary Screening of 45 bimetallic carbides for HDO

As mentioned in Section 2.3, the reaction energies of the oxygen removal reaction (OH* + H* → H₂O, OR) was the first screening criterion for the 45 candidate surfaces. Importantly, all reaction energies were observed to be positive, which indicates that oxygen removal is endothermic and it would be thermodynamically favored at higher temperatures.

Catalyst surfaces on which reaction energy for OR was higher than +175 kJ/mol were screened out from the initial set of candidates. This limit was chosen for two reasons. Firstly, the parent Mo₂C showed a reaction energy of +196 kJ/mol, demonstrating that the catalyst surface would get poisoned. Shi et. al also reported a similar reaction energy of +187 kJ/mol.²⁵² Experimental studies also confirmed the oxygen poisoning with the formation of molybdenum oxidic/oxycarbide surface even at elevated temperatures of 423 K and 1 kPa H₂ pressure.^{126,127} Both theory and experimental studies suggest that an optimal bimetallic carbide should have a reaction energy less

than that of Mo₂C.²⁵³ Secondly, a high reaction energy of +175 kJ/mol would imply that the kinetic barrier is higher than +175 kJ/mol, which is highly energy intensive. Therefore, we set a limit of 175 kJ/mol for the first screening of the candidates which is 20 kJ/mol lower than the Mo₂C. Reaction energies of OR for the set of 45 candidates are shown in Figure 4.4.

13 candidates showed a reaction energy above +175 kJ/mol. One common thing among those catalysts is the fact that surfaces with terminations exposing more oxophilic metal (Nb and Ti) than Mo showed higher reaction energies, except in the case of Ni₂A. As discussed in Section 3.1, terminations with more oxophilic atoms lead to a stronger OBE, which also translates into a higher OR reaction energy, as the OH* will not be readily hydrogenated. High reaction energy for Ni₂A (Ni₂Mo₄C) could also be explained by the low Ni/Mo ratio of ~ 0.5. Other factors could be the type of site preferred by OH* and H* fragments and the local environment of the adsorbate. Generally, both OH* and H* species prefer 3-fold hollow sites, particularly on a carbide catalyst surface, which are typically more stable than the top sites due to higher coordination number.

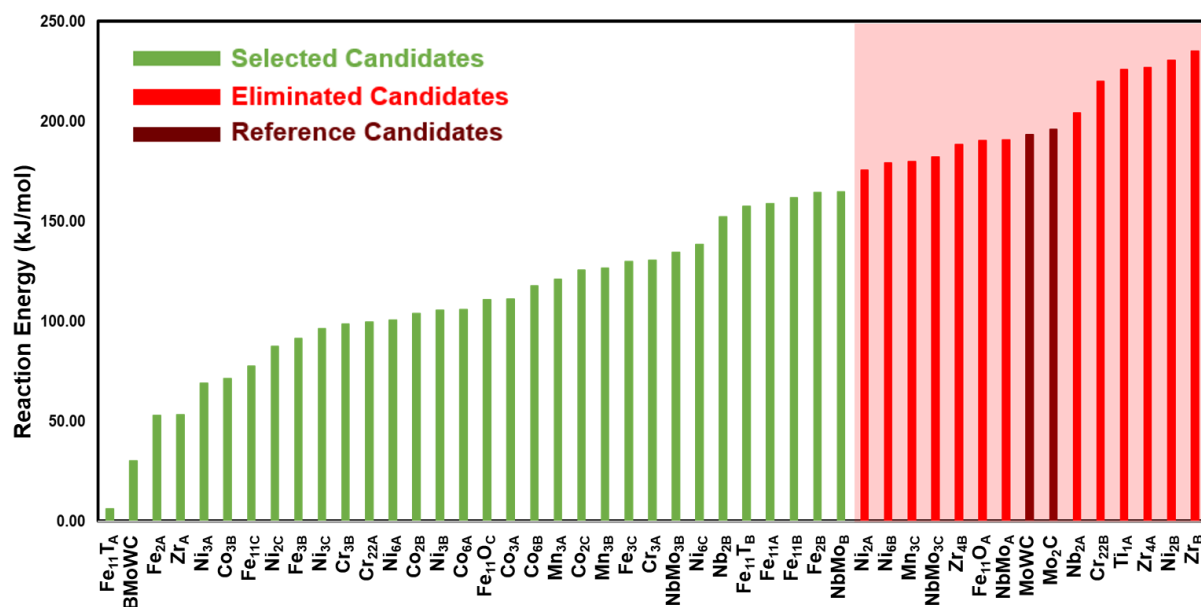


Figure 4.4 Reaction energies of $OH^* + H^* \rightarrow H_2O$, OR for all 45 catalysts investigated in this work. The green, red, and brown colors represent the selected, eliminated, and reference candidates (Mo₂C and MoWC) respectively.

Figure 4.4 also shows Mo₂C and MoWC (in brown) as references. Both Mo₂C and MoWC showed high reaction energies of 196 kJ/mol and 193 kJ/mol respectively, indicating that oxygen removal is difficult on these surfaces. Notably, the reaction energy on BMoWC was merely +30 kJ/mol,

showing the effect of boron doping in improving the thermodynamic feasibility of OR compared to MoWC. It is primarily because the binding strength of the OH* fragment reduced from -191 kJ/mol to -93 kJ/mol on its surfaces which makes the desorption of water more facile.

4.3.3 C – O Scission (Direct Deoxygenation)

We investigated DDO using phenol as a model compound where aryl–OH bond scission represents the C-O bond scission. Phenol has been employed as a model compound for numerous experimental investigations for studying DDO reaction as it is the most persistent, yet fairly abundant, compound in bio-oil.^{81,254–256} The potential energy profiles of DDO on all 34 candidates are shown in Figure 4.5.

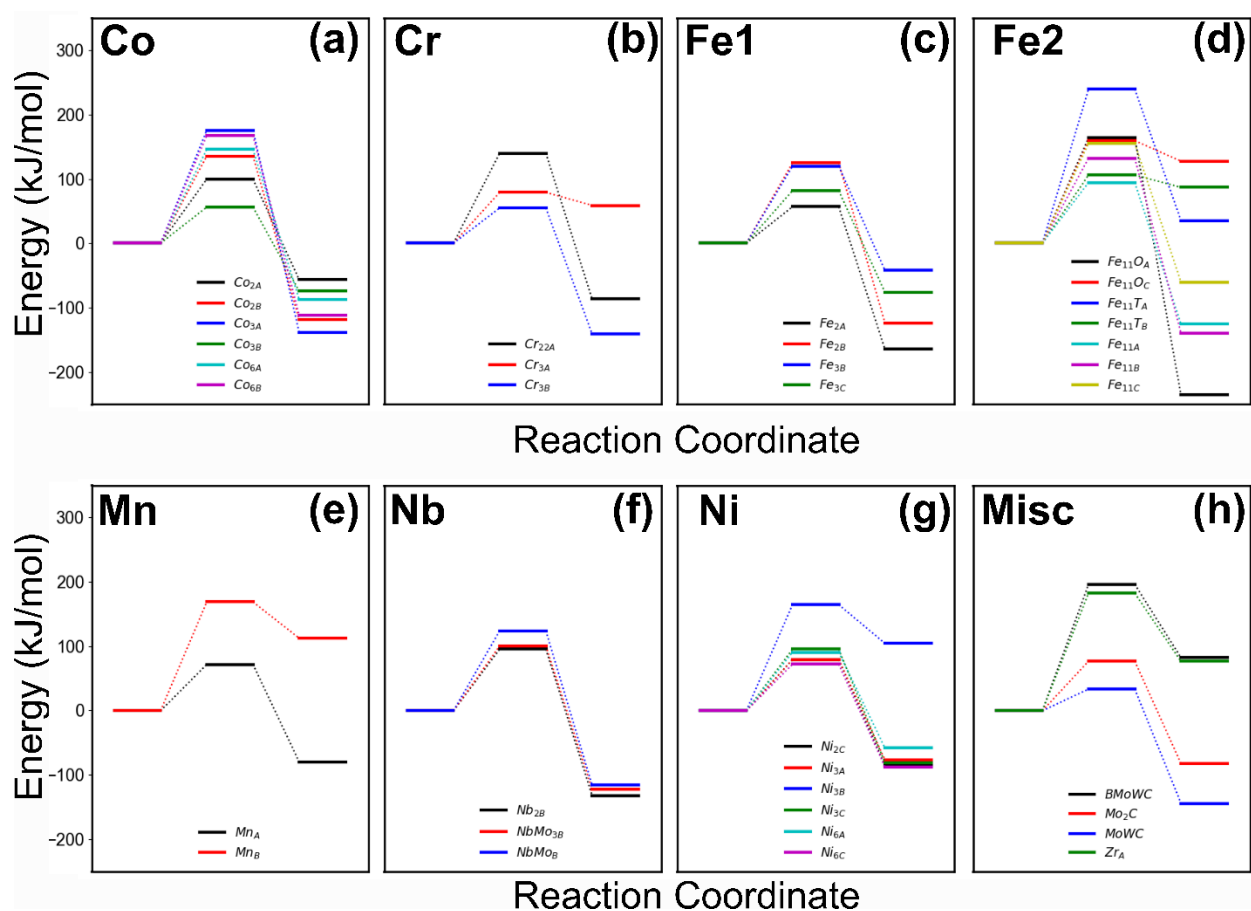


Figure 4.5 Potential energy profiles for the C–OH scission reaction, DDO, on (a) Co-doped Mo₂C, (b) Cr-doped Mo₂C, (c) Fe-doped Mo₂C with low Fe/Mo ratio (d) Fe-doped Mo₂C with high Fe/Mo ratio, (e) Mn-doped Mo₂C, (f) Nb-doped Mo₂C, (g) Ni-doped Mo₂C and (h) Miscellaneous (Mo₂C, MoWC, BMoWC, ZrA).

Figure 4.5a show the energy profiles of DDO for the 6 Co-doped catalysts. Co_{3B} displayed the lowest barrier of only 56 kJ/mol with a reaction energy of -74 kJ/mol, demonstrating the kinetic and thermodynamic feasibility of DDO on this surface. Overall, surfaces showing a lower energy barrier, such as Co_{3B} and Co_{2A} (with barriers of 56 kJ/mol and 100 kJ/mol respectively), are more suitable for this reaction. For Cr-doped catalysts (shown in Figure 4.5b), DDO has a low barrier of 55 kJ/mol on Cr_{3B} in comparison to Cr_{3A} (80 kJ/mol) attributing to the stronger binding energy on B-termination. On the other hand, DDO barrier increases to 140 kJ/mol for Cr_{22A}. It implies that a higher proportion of Cr/Mo suppresses the C–O scission activity of the resulting bimetallic carbide.

The energy profiles for Fe-doped bimetallic carbides are presented in Figure 4.5c and 5d. For lower stoichiometric ratios of Fe/Mo ($0 < \text{Fe/Mo} < 1$), Fe_{2A} and Fe_{3C} are active catalysts for DDO, which have barriers of only 57 kJ/mol and 82 kJ/mol respectively. This is because phenol binds very strongly with binding energies of -227 kJ/mol and -426 kJ/mol for Fe_{2A} and Fe_{3C} respectively (shown in Table D.9). The exceptionally high binding energy of Fe_{3C} is attributed to the presence of undercoordinated sites on its surface (Figure D26). DDO is more exothermic on Fe_{2A} (-165 kJ/mol) than Fe_{3C} (-76 kJ/mol). For higher ratios ($\text{Fe/Mo} > 1$), the lowest barrier of 94 kJ/mol was observed on Fe_{11A}. Moreover, Fe_{11TB} also showed a competitive barrier of 106 kJ/mol. However, C–O dissociation was not favorable on Fe_{11TB} with a reaction energy of 87 kJ/mol. On comparing low and high Fe/Mo ratios, the energy barrier of DDO increases with an increasing ratio of Fe/Mo. A similar effect was observed in the case of Cr-doped catalysts.

In the cases of Mn-doped catalysts (Figure 4.5e), DDO is both kinetically and thermodynamically facile on Mn_{3A} with a barrier of only 72 kJ/mol and a reaction energy of -80 kJ/mol. In comparison, Mn_{3B} displayed a huge barrier of 169 kJ/mol and is endothermic by +113 kJ/mol. The enhanced C–O dissociation activity of Mn also has been reported earlier for CO₂ activation in the context of bimetallic alloys.²⁵⁷ For Nb-based candidates, all 3 surfaces exhibited competitive barriers ranging from 96 kJ/mol to 124 kJ/mol. (Figure 4.5f). The Ni-doped catalyst surfaces (Figure 4.5g) also showed similar barriers in the range of 72 kJ/mol to 96 kJ/mol and reaction energies in the range of -87 kJ/mol to +58 kJ/mol, with the lowest barrier and reaction energy reported on Ni_{6C}. A clear exception is Ni_{3B}, which has a higher barrier of 165 kJ/mol; furthermore, DDO is endothermic by +105 kJ/mol. Figure 4.5h shows that the BMoWC and Zr_A catalyst surfaces perform significantly

poorly, with DDO barriers of 197 kJ/mol and 183 kJ/mol respectively, and reaction energies of 83 kJ/mol and 77 kJ/mol respectively. In contrast, of the two reference catalyst surfaces, the MoWC surface showed outstanding activity towards DDO in comparison with the other catalyst surfaces. It had the lowest energy barrier of 34 kJ/mol, and a reaction energy of -144 kJ/mol. Meanwhile, the Mo₂C surface showed a barrier of 77 kJ/mol and reaction energy of -82 kJ/mol.

Based on their activity for DDO, none of the candidates showed barriers lower than MoWC (34 kJ/mol). However, Cr_{3B} (55 kJ/mol) < Co_{3B} (56 kJ/mol) < Fe_{2A} (57 kJ/mol) < Mn_{3A} (72 kJ/mol) = Ni_{6C} (72 kJ/mol) < Ni_{3A} (80 kJ/mol) = Ni_{2C} (80 kJ/mol) < Fe_{3C} (82 kJ/mol) < Ni_{6A} (91 kJ/mol) < Fe_{11A} (94 kJ/mol) < Ni_{3C} (96 kJ/mol) = Nb_{2B} (96 kJ/mol) are twelve candidates which showed enhanced or similar activity as compared to the monometallic carbide Mo₂C (77 kJ/mol). All the barriers and reaction energies are tabulated in Table D.9 in Appendix D.

4.3.4 Oxygen Removal ($OH^* + H^* \rightarrow H_2O$)

Water is formed by the hydrogenation of the OH* fragment left over from the DDO reaction step, and the energy barrier of its formation directly correlates with the stability of the catalyst surface, as a low barrier implies that water is readily formed after the DDO reaction, and that the catalyst surface is less likely to be poisoned by the OH* fragments. The potential energy profiles of water formation on all 34 catalyst surfaces are shown in Figure 4.6.

Overall, all candidates showed positive reaction energies for OR. Figure 4.6a presents the comparison of Co-based catalysts, and among them, Co_{2B} and Co_{3B} were found to be most active, showing similar barriers of 142 kJ/mol and 143 kJ/mol respectively. Surprisingly, Co_{3A} showed a barrier of 295 kJ/mol, indicating high probability of getting poisoned even at higher temperatures and thus could become unstable under operating conditions. On Cr-doped surfaces (Figure 4.6b),

hydrogenation of OH* becomes more difficult since Cr_{3A}, Cr_{3B} and Cr_{22A} showed barriers of 204 kJ/mol, 163 kJ/mol and 172 kJ/mol respectively.

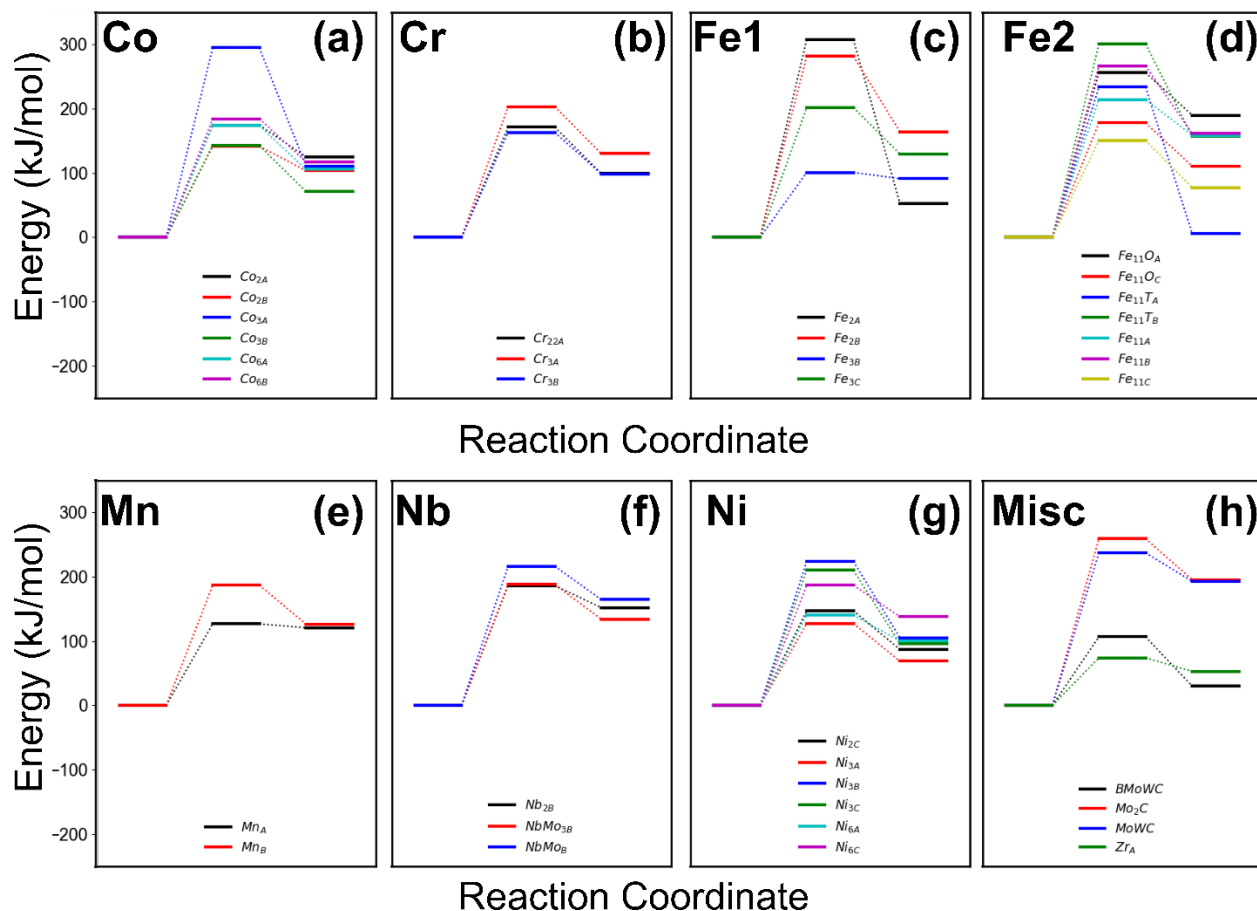


Figure 4.6 Potential energy profiles for the oxygen removal reaction ($OH^* + H^* \rightarrow H_2O$), OR, on (a) Co-doped Mo₂C, (b) Cr-doped Mo₂C, (c) Fe-doped Mo₂C with lower composition, (d) Fe-doped Mo₂C with higher composition, (e) Mn-doped Mo₂C, (f) Nb-doped Mo₂C, (g) Ni-doped Mo₂C and (h) Miscellaneous (Mo₂C, MoWC, BMoWC, ZrA).

The energy profiles for Fe-doped catalysts are presented in Figure 4.6c and 6d. For lower stoichiometric ratios ($0 < Fe/Mo < 1$), Fe_{3B} has the lowest barrier of 101 kJ/mol. Notably, both Fe_{3B} and Fe_{3C} showed lower barriers than Fe_{2A} and Fe_{2B}, indicating OR is relatively more facile on catalysts with Fe/Mo ratio of 1 rather than 0.5. For Fe/Mo > 1, the lowest barrier of 151 kJ/mol was observed on Fe_{11C}. From Figure 4.6c and 6d, we see that the lowest energy barriers of OR are observed on catalysts where Fe/Mo = 1. Meanwhile, from Figure 4.6e, OR has a moderate barrier of 127 kJ/mol on Mn_{3A} as compared to 187 kJ/mol on Mn_{3B}. This difference can be explained by the weaker OBE for Mn_{3A} (-155 kJ/mol) compared to Mn_{3B} (-219 kJ/mol). All three Nb-based

catalysts showed very high barriers ranging from 187 kJ/mol to 217 kJ/mol (Figure 4.6f). Meanwhile, among the Ni-based catalysts (Figure 4.6g), we observe notable differences in reaction barriers for different terminations within the same composition. For example, among Ni_{3A/B/C}, the energy barriers increase: Ni_{3A} (128 kJ/mol) < Ni_{3C} (210 kJ/mol) < Ni_{3B} (224 kJ/mol). A similar trend is observed for the Ni₆Mo₆C catalysts: Ni_{6A} (141 kJ/mol) < Ni_{6C} (187 kJ/mol). Since Ni is less oxophilic than Mo (0.2 < 0.6)²⁵¹, an increasing proportion of surface Mo atoms leads to stronger OH* binding and a higher barrier for oxygen removal.

Lastly, from Figure 4.6h, while the Mo₂C and MoWC surfaces were seen to be very active towards DDO, as discussed in the previous subsection, they unfortunately have very high barriers for water formation of 260 kJ/mol and 238 kJ/mol respectively, indicating oxygen accumulation on the catalyst's surface during HDO. It is also confirmed by experiments that oxygen accumulation occurs even at a high H₂-to-anisole molar ratio (~110) in the reactant feed during HDO at 423 K under ambient pressure.⁵¹ On the other hand, doping boron in MoWC significantly reduces the barrier to 107 kJ/mol from 238 kJ/mol. Notably, Zr_A showed the least barrier of only 74 kJ/mol among all the 34 candidates as it is the only catalyst on which hydrogen binds strongly (-64 kJ/mol) in comparison to oxygen (-46 kJ/mol).

Overall, the best candidates in decreasing order of their oxygen removal activity are Zr_A (74 kJ/mol) > Fe_{3B} (101 kJ/mol) > BMoWC (107 kJ/mol) > Mn_{3A} (127 kJ/mol) > Ni_{3A} (128 kJ/mol) > Ni_{6A} (141 kJ/mol) > Co_{2B} (142 kJ/mol) > Co_{3B} (143 kJ/mol) > Ni_{2C} (148 kJ/mol) > Fe_{11C} (151 kJ/mol).

4.3.5 C=C Hydrogenation

For a selective HDO catalyst, selective C-O scission is vital while maintaining the other C-C and C-H bonds intact. In this context of phenol, ring hydrogenation is a key competitive reaction^{83,125,128}, hence, HYD is investigated on all the candidates to assess their selectivity for DDO. Moreover, there are some applications where selective HYD is desired to produce some specialty chemicals. For example, it can form alkyl or alkoxy-substituted cyclohexanols, which are used as building blocks for the synthesis of different polymers, resins, dyes, and fine chemicals, and these substitutions can help in tuning the physical properties, such as melting points, elasticity, and crystallinity of these materials.^{89,99} Several experimental studies used ring hydrogenation of phenol as a probe reaction to investigate selective HYD in which cyclohexane and cyclohexanol

were observed as major products.^{95,116,258} In contrast to DDO, the ring hydrogenation of phenol at the para position is a largely endothermic process, given that the reaction involves a disruption of the aromaticity in phenol. Similarly, Figure 4.7 shows the potential energy profiles for the HYD reaction on all 34 catalyst surfaces.

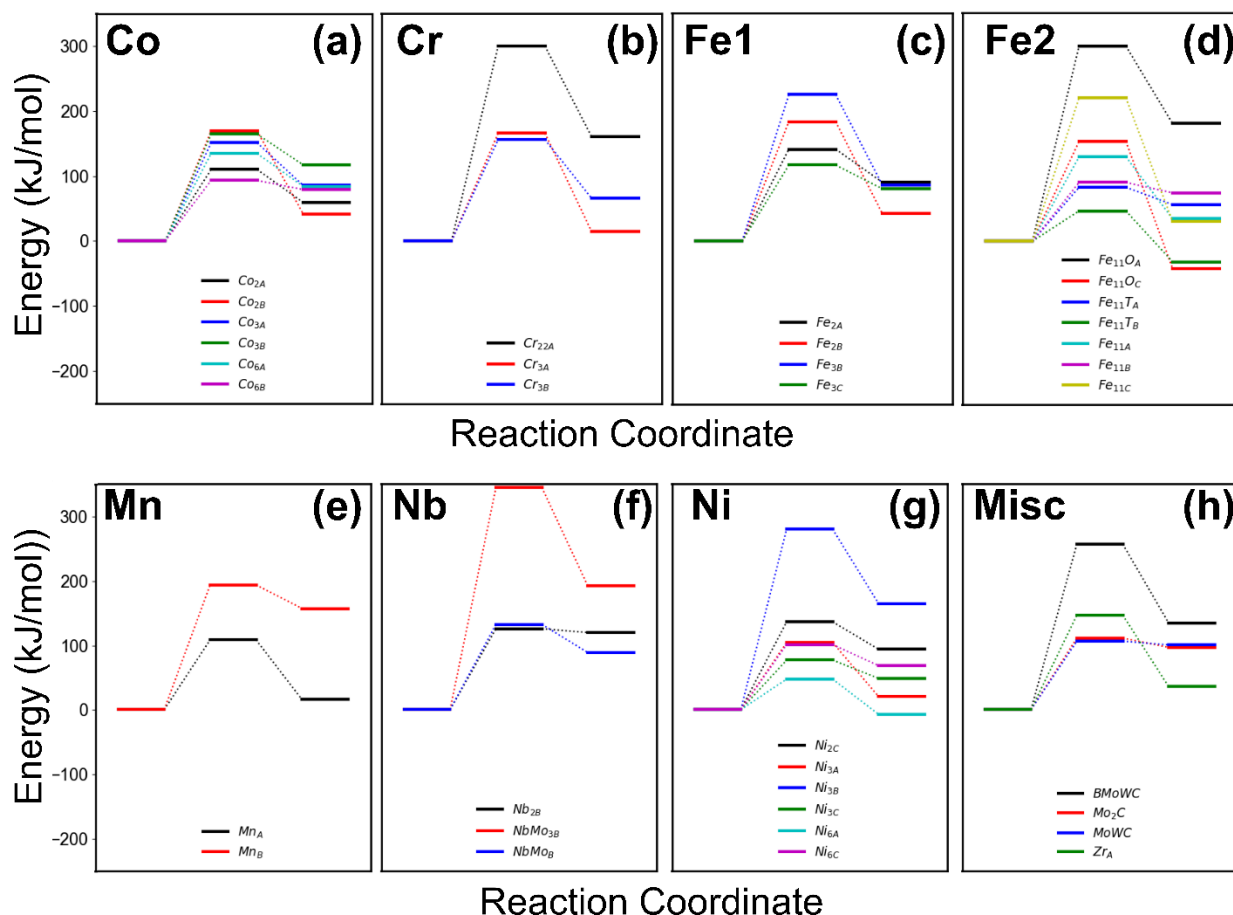


Figure 4.7 Potential energy profiles for the ring hydrogenation, HYD, on (a) Co-doped Mo₂C, (b) Cr-doped Mo₂C, (c) Fe-doped Mo₂C with lower composition, (d) Fe-doped Mo₂C with higher composition, (e) Mn-doped Mo₂C, (f) Nb-doped Mo₂C, (g) Ni-doped Mo₂C and (h) Miscellaneous (Mo₂C, MoWC, BMoWC, Zr_A).

The potential energy profiles of HYD for the Co-doped catalysts, shown in Figure 4.7a, show noticeable differences from the energy profiles for DDO in Figure 4.5a and this difference in activity is critical for the selectivity of a catalyst. For example, Co_{3B}, which reported the lowest barrier of 56 kJ/mol for DDO, now has a barrier of 165 kJ/mol for HYD, the second-highest of all Co-doped catalysts. Conversely, Co_{6B}, having the highest DDO barrier of 167 kJ/mol, now shows the lowest barrier of 93 kJ/mol for HYD; this suggests that these catalysts may be both active and

highly selective towards a particular ($\text{Co}_{3\text{B}}$ for DDO and $\text{Co}_{6\text{B}}$ for HYD) reaction. For A-terminations, energy barriers increased from 110 kJ/mol to 151 kJ/mol with an increase in Co/Mo ratio from 0.5 to 1, whereas no change was observed in B-termination. For B-terminations, energy barriers decreased from 169 kJ/mol to 93 kJ/mol with a decrease in $\frac{C}{\text{Co}+\text{Mo}}$ ratio from 1/7 to 1/13. Qualitatively, it can be inferred that reduction in carbon content of the carbide results in enhancement of metallic character which is necessary for hydrogenation. Upon observing Figure 4.5d, Figure 4.7d, Figure 4.5f and Figure 4.7f, similar conclusions can be drawn about $\text{Fe}_{11}\text{T}_\text{A}$, $\text{Fe}_{11}\text{T}_\text{B}$ and NbMo_3B . For instance, $\text{Fe}_{11}\text{T}_\text{A}$, $\text{Fe}_{11}\text{T}_\text{B}$ which showed highest DDO barrier in their category, now show remarkably low HYD barriers of 83 kJ/mol and 47 kJ/mol respectively and similarly NbMo_3B shows a drastically high HYD barrier of 344 kJ/mol compared to its moderate DDO barrier of 101 kJ/mol.

Moving to Cr- and Mn-doped surfaces which are shown in Figure 4.7b and Figure 4.7e respectively, catalysts in both categories show similar trends in performance for the HYD and DDO reactions. In the case of Cr, HYD shows similar barriers on $\text{Cr}_{3\text{A}}$ (166 kJ/mol) and $\text{Cr}_{3\text{B}}$ (156 kJ/mol) which is lower than $\text{Cr}_{22\text{A}}$ (300 kJ/mol), demonstrating a large difference in HYD activity. For Mn-doped cases, $\text{Mn}_{3\text{A}}$ shows a lower barrier of 108 kJ/mol in contrast to 193 kJ/mol on $\text{Mn}_{3\text{B}}$ as the trend remains the same as DDO. Meanwhile, Figure 4.7g presents the potential energy profiles for Ni-doped catalyst surfaces. HYD was kinetically and thermodynamically feasible only on the $\text{Ni}_{6\text{A}}$ surface, with a low barrier of only 47 kJ/mol and a reaction energy of -7 kJ/mol. Moreover, it also binds weakly to hydrogen with an HBE of -30 kJ/mol, which makes hydrogen diffusion facile on its surface. On the other hand, $\text{Ni}_{6\text{C}}$ binds relatively strongly with hydrogen with an HBE of -53 kJ/mol, and consequently, the barrier also increased to 101 kJ/mol. Finally, in Figure 4.7h, we note that the BMoWC and Zr_A surfaces, again, performed worse for HYD than the references. The BMoWC catalyst, for example, is particularly inactive towards both DDO and HYD, having barriers of 197 kJ/mol and 256 kJ/mol respectively. The reference Mo_2C and MoWC catalyst surfaces displayed relatively moderate reaction energies of +96 kJ/mol and +100 kJ/mol respectively, with barriers of 111 kJ/mol and 106 kJ/mol respectively for HYD reaction. Overall, ten catalysts showed enhanced or similar activity than Mo_2C . Four of these belong to the set of Ni-doped catalysts, demonstrating their promise as highly active HYD catalysts. Notably, HYD was found to be exothermic only on two out of the 34 catalyst surfaces investigated, namely $\text{Fe}_{11}\text{T}_\text{B}$ and $\text{Ni}_{6\text{A}}$. Incidentally, these two catalysts, the most kinetically active within their dopant

categories, also displayed the equal and the lowest energy barrier out of all 34 catalysts of only 47 kJ/mol.

The best candidates in decreasing order of their ring hydrogenation activity are Fe₁₁T_B (47 kJ/mol) = Ni_{6A} (47 kJ/mol) > Ni_{3C} (77 kJ/mol) > Fe₁₁T_A (83 kJ/mol) > Fe_{11B} (90 kJ/mol) > Co_{6B} (93 kJ/mol) > Ni_{6C} (101 kJ/mol) > Ni_{3A} (104 kJ/mol) > MoWC (106 kJ/mol) > Mn_{3A} (108 kJ/mol) > Co_{2A} (110 kJ/mol).

4.3.6 Selective and Stable DDO and HYD Candidates

4.3.6.1 DDO Candidates

The DDO pathway necessitates a kinetically and thermodynamically feasible DDO reaction ($R_{aryl} - OH \rightarrow R^* + OH^*$, R1) followed by the OR reaction ($OH^* + H^* \rightarrow H_2O$, R2). One of the primary challenges is to identify a catalyst that not only exhibits high activity for DDO but also makes OR facile to prevent oxygen poisoning. Hence, DDO and OR must take place simultaneously, otherwise more OH* fragments will form, and these species may poison the active sites and deactivate the catalyst. Hence, for an active and stable DDO catalyst, a fine tuning between DDO activity and OR activity is imperative. In other words, an optimal catalyst should possess low energy barriers for both DDO and OR. For selectivity, the difference between the HYD and DDO barriers, $\Delta_{HYD-DDO}$, must be high. Variation of the DDO barrier with HYD barrier for all 35 candidates is shown in Figure 4.8. A color gradient bar (shown at the right side of Figure 4.8) is used to show the difference between OR and DDO barriers going from olive (low) to maroon (high). A small difference between the OR and DDO barriers indicates similar activity towards both reactions, while a large difference suggests that the catalyst is only effective for one of the reactions.

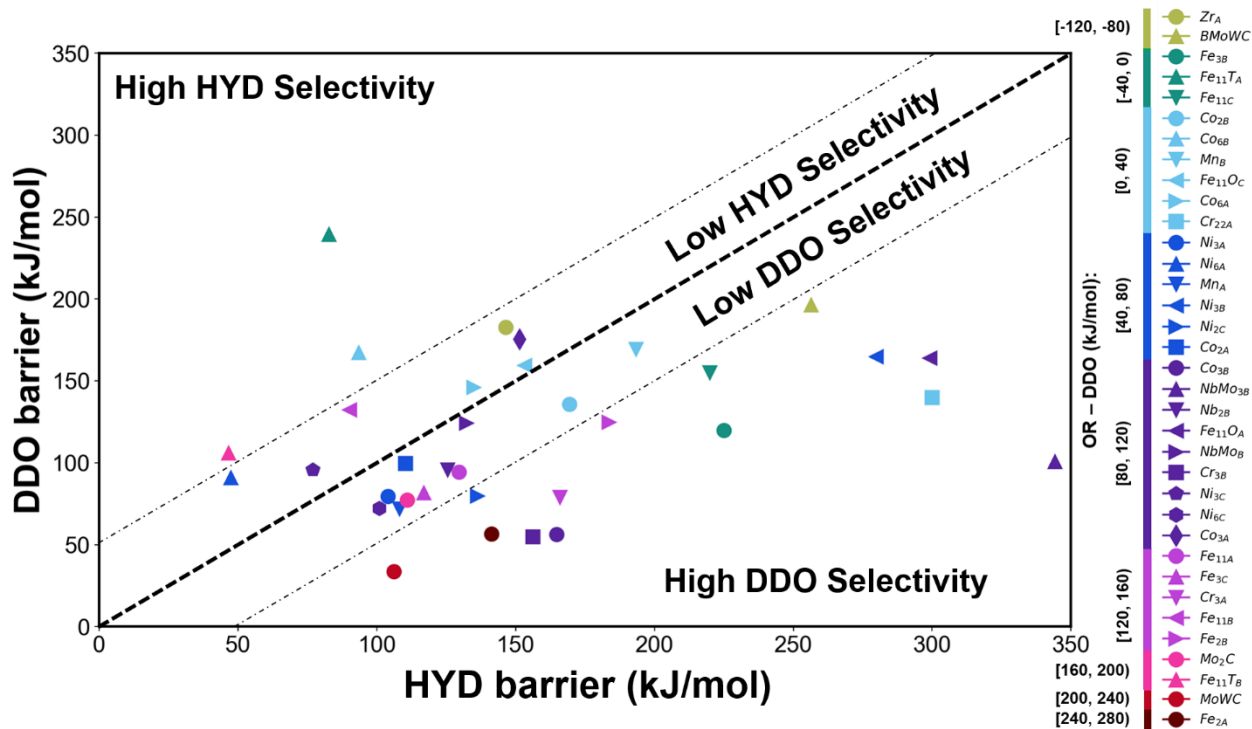


Figure 4.8 Variation of C – O dissociation (DDO) barriers with hydrogenation (HYD) barriers for all 35 catalyst surfaces. Color gradient is used to highlight the difference between DDO and oxygen removal (OR) barriers with olive color representing a small difference of < -80 kJ/mol and maroon color representing a large difference > 240 kJ/mol. Markers are shown on the right side to differentiate among catalysts. Plot area is also divided into four regions of high/low selectivity towards HYD/DDO.

The reference catalyst, MoWC displayed highest activity and good selectivity towards DDO with the lowest energy barrier of 34 kJ/mol, and a $\Delta_{\text{HYD-DDO}}$ of 72 kJ/mol. The parent monometallic carbide, Mo₂C, showed a DDO barrier of 77 kJ/mol with a moderate $\Delta_{\text{HYD-DDO}}$ of 34 kJ/mol.¹²⁵ However, both Mo₂C and MoWC (pink and red circles in Figure 4.8) displayed extremely high OR barriers of 260 kJ/mol and 238 kJ/mol respectively. Consequently, oxygen poisoning has been observed on Mo₂C surfaces leading to the formation of oxycarbides, which impacts catalytic activity or selectivity.^{37,51,126,127,235,236} It confirms the inevitable tradeoff between DDO and OR barriers to maintain the catalyst’s activity and stability. This is worth noting that doping with B dramatically improves the stability by reducing the barrier for oxygen removal decreased

significantly to 107 kJ/mol in comparison to MoWC (238 kJ/mol). However, the DDO barrier increased to 197 kJ/mol.

In terms of activity and selectivity for DDO, Cr_{3B}, Co_{3B}, Fe_{3B} and NbMo_{3B} exhibited remarkable selectivity with $\Delta_{\text{HYD-DDO}}$ above 100 kJ/mol while maintaining good activity (Figure 4.8 and Table 4.1). As far as stability is concerned, Fe_{3B}, Cr_{3B}, Co_{3B} and NbMo_{3B} show activation barriers of 101 kJ/mol, 163 kJ/mol, 143 kJ/mol and 188 kJ/mol for OR. To highlight, Fe_{3B} is identified as the best DDO candidate as the maximum reduction in OR barrier from 260 kJ/mol on Mo₂C to 101 kJ/mol was observed. However, the DDO barrier is increased to 120 kJ/mol as a result of the aforementioned trade-off. It can be attributed to the relatively weaker OBE of -125 kJ/mol on Fe_{3B} compared to -155 kJ/mol on Mo₂C. A similar effect has been observed by Lin et al.⁶³, who observed weaker binding energies for oxygen and the model compound, furfural, on a Co-modified Mo₂C surface. The modification allows the facile removal of surface oxygen and furfural to improve the stability of the catalyst. Improvement in product selectivity from destabilization of intermediates by reduction in binding energies was also reported for Ni-doped Mo₂C catalyst.⁸⁶ The next best catalysts for selective DDO are Mn_{3A} and Ni_{3A} which both showed similar barrier of 127 kJ/mol and 128 kJ/mol respectively, followed by Co_{2B} with a barrier of 142 kJ/mol for OR (Table 4.1). However, selectivity is compromised as $\Delta_{\text{HYD-DDO}}$ decreased significantly to 36 kJ/mol, 25 kJ/mol and 34 kJ/mol for Mn_{3A}, Ni_{3A} and Co_{2B} respectively.

In summary, the best DDO candidates comprise dopant and Mo atoms in equal stoichiometric proportions (i.e., M₃Mo₃C where M = Fe, Ni, Co, Cr, Mn). Moreover, Fe₃Mo₃C, Co₃Mo₃C and Ni₃Mo₃C have been synthesized experimentally as well.²⁴⁷ This suggests that these catalysts accurately represent the experimentally tested catalysts, as any alteration in the modeled microstructure would notably impact reaction pathways and energetics, potentially resulting in different conclusions.

Table 4.1 DDO barriers, OR barriers and $\Delta_{\text{HYD-DDO}}$ (kJ/mol) are tabulated for top 10 screened catalysts. The top 4 candidates with optimum balance between DDO and oxygen removal barriers are highlighted in bold.

Catalyst	DDO barrier (kJ/mol)	OR barrier (kJ/mol)	$\Delta_{\text{HYD-DDO}}$ (kJ/mol)
Fe_{3B}	120	101	105

Cr ₃ B	55	163	101
Co ₃ B	56	143	108
Ni ₂ C	80	148	56
Fe ₁₁ C	155	151	65
NbMo ₃ B	101	188	243
Cr ₂₂ A	140	172	160
Mn₃A	72	127	36
Co ₂ B	136	142	34
Ni₃A	80	128	25

4.3.6.2 Selective Hydrogenation (HYD) Candidates

In this subsection, we will focus on the candidates which selectively favor ring hydrogenation (HYD). We already discussed in detail the activity for HYD on all 35 candidates in Section 3.5. To combine the activity and selectivity aspects, variation of DDO barriers with HYD barriers is shown in Figure 4.8. It can be clearly seen that only 10/35 candidates (Figure 4.8 and Table 4.2) are selective for HYD.

Table 4.2 HYD barriers and $\Delta_{\text{HYD-DDO}}$ (kJ/mol) are tabulated for best screened catalysts. Three most active and selective candidates are highlighted in bold.

Catalyst	HYD barrier (kJ/mol)	$\Delta_{\text{HYD-DDO}}$ (kJ/mol)
Fe₁₁T_B	47	-59
Co₆B	93	-74
Ni ₆ A	47	-44
Fe ₁₁ B	90	-42
Fe₁₁T_A	83	-157
Ni ₃ C	77	-19
Zr _A	146	-36
Co ₃ A	151	-24
Co ₆ A	135	-11

Fe ₁₁ O _C	153	-6
---------------------------------	-----	----

Fe₁₁T_A is the only candidate which showed remarkable selectivity with a high $\Delta_{\text{HYD-DDO}}$ of -157 kJ/mol as more negative $\Delta_{\text{HYD-DDO}}$ means more selective for HYD. Moreover, it also showed high activity with an energy barrier of 83 kJ/mol. In terms of activity, Fe₁₁T_B and Ni_{6A} showed equal and the lowest energy barriers of 47 kJ/mol, albeit with a relatively lower selectivity with $\Delta_{\text{HYD-DDO}}$ values of -59 kJ/mol and -44 kJ/mol respectively. Other competitive candidates with similar selectivity are Co_{6B}, Fe_{11B} and Zr_A with corresponding $\Delta_{\text{HYD-DDO}}$ values of -74 kJ/mol, -42 kJ/mol, and -36 kJ/mol respectively. We note that although Zr_A showed $\Delta_{\text{HYD-DDO}}$ of -36 kJ/mol, it however possesses a high energy barrier of 146 kJ/mol for HYD, which is approximately 100 kJ/mol higher than that for Fe₁₁T_B and Ni_{6A}. The remaining four candidates (Ni_{3C}, Co_{3A}, Co_{6A}, Fe₁₁O_C) had a low $\Delta_{\text{HYD-DDO}}$ value greater than -25 kJ/mol. Moreover, with the exception of Ni_{3C}, the other candidates showed high HYD barriers (151 kJ/mol for Co_{3A}, 135 kJ/mol for Co_{6A}, 153 kJ/mol for Fe₁₁O_C) confirming their low activity as well. Therefore, these four candidates are neither selective nor active towards HYD.

Overall, there are only 6 screened candidates which favor the HYD pathway and follow a decreasing order of activity as follows: Fe₁₁T_B (47 kJ/mol) = Ni_{6A} (47 kJ/mol) > Fe₁₁T_A (83 kJ/mol) > Fe_{11B} (90 kJ/mol) > Co_{6B} (93 kJ/mol) > Zr_A (146 kJ/mol) for HYD barriers. On the basis of selectivity, the order changes to Fe₁₁T_A (-157 kJ/mol) > Co_{6B} (-74 kJ/mol) > Fe₁₁T_B (-59 kJ/mol) > Ni_{6A} (-44 kJ/mol) > Fe_{11B} (-42 kJ/mol) > Zr_A (-36 kJ/mol) for $\Delta_{\text{HYD-DDO}}$ values.

4.3.7 Search for a Descriptor

The second objective of this work is to propose a reactivity descriptor for screening of metal carbide catalysts for selective DDO and HYD. Performing comprehensive DFT analyses and experiments for a large number of candidate catalysts is time-consuming and thus not efficient for catalyst screening purposes. Previously, descriptors such as binding energy of adsorbate and key intermediates (H*, OH*) have been reported to assess catalytic activity of metals and metal alloys for HDO and CO₂ conversion processes.^{191,259–261} For example, Chen et al.²⁵⁹ employed oxygen binding energy to systematically evaluate 17 Ni-based bimetallic alloys for HDO. Jia and coworkers²⁶¹ also confirmed that the usage of OH* binding energy can be used as a good descriptor

for deoxygenation activity for Pt-based bimetallic alloys. With growing interest in TMCs due to their similar activity as of noble metals for several types of reactions, such as hydrogenation, deoxygenation reactions, a theoretical approach extended to more complex materials than transition metals is of high interest. However, to the best of our knowledge, it has not been proposed for metal carbides. Herein, we will use the insights gained from investigating our 34 bimetallic carbide catalysts to propose a parameter which can account for the interplay between a catalyst's activity, selectivity and stability. The idea is to combine the activation barriers of three critical reactions involved in HDO and come up with a single parameter to assess catalytic performance. This lone parameter can encompass the activity, selectivity, and stability of a catalyst, thereby eliminating the necessity of evaluating several parameters to assess each aspect individually. In Section 3.6, we saw that an optimal DDO catalyst must be active towards both DDO (C – O scission) and OR ($\text{OH}^* + \text{H}^* \rightarrow \text{H}_2\text{O}$). For selectivity towards DDO, the difference of barriers, $\Delta_{\text{HYD-DDO}}$, must be maximized. Connecting these two aspects, we proposed that the ratio of $\Delta_{\text{HYD-DDO}}$ and OR barrier ($\frac{\Delta(\text{HYD-DDO})}{\text{OR}} = \eta$) can measure overall catalytic performance and a correlation is obtained between η and OBE as shown in Figure 4.9. OBE affects the energetics of both DDO and HYD as stronger OBE results in stretching the C-O bond which facilitates C-OH scission, but also hinders the removal of OH^* . It is imperative to find a compromise between C-OH scission and oxygen removal. Thus, an optimal range of OBE needs to be estimated which can be used as a screening criterion for finding the optimal catalyst for HDO.

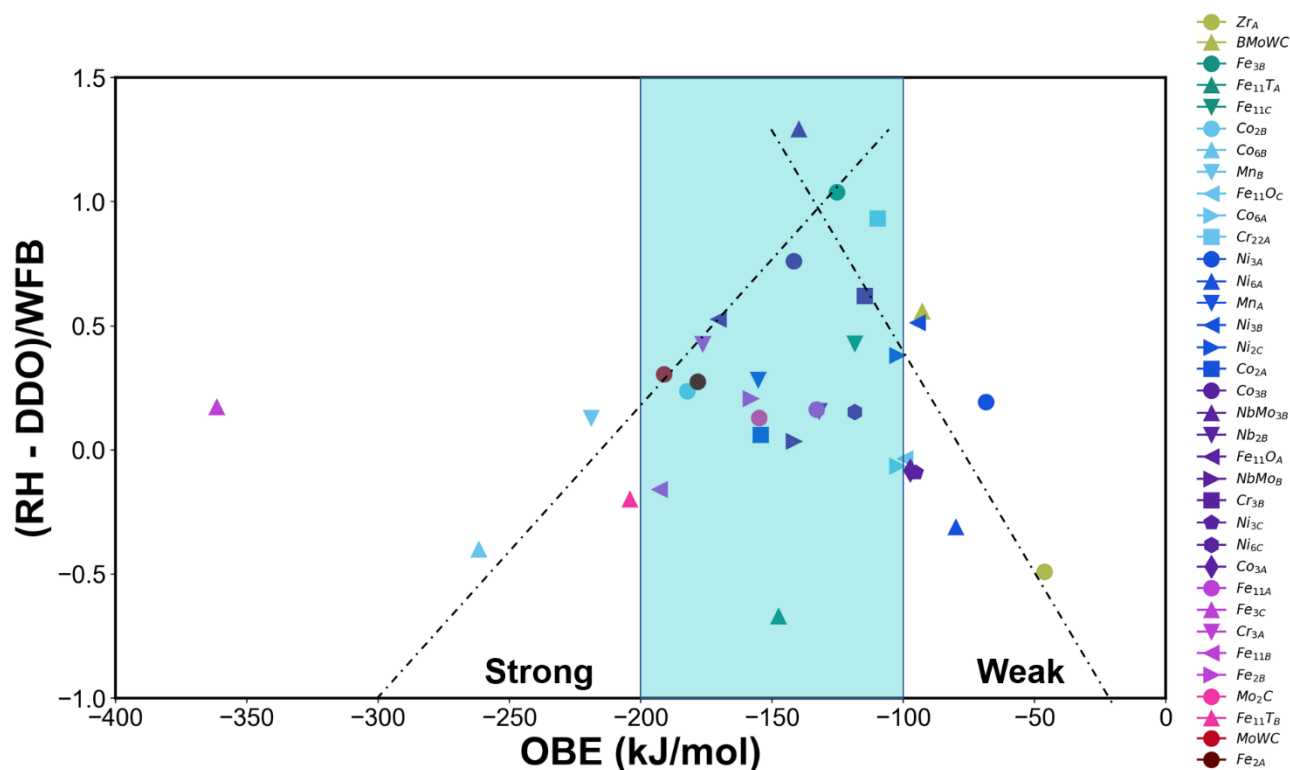


Figure 4.9 Variation of proposed parameter, $\eta = \frac{\Delta(\text{HYD}-\text{DDO})}{\text{OR}}$, as a function of OBE for all catalysts. Two qualitative trendlines are drawn. The line on the left (low η and strong binding) and right (low η and weak binding) sides are indicated. Region of optimal OBE between -200 kJ/mol to -100 kJ/mol is shaded in blue. Color gradient is used to highlight the difference between DDO and OR barriers with olive color representing a small difference of < -80 kJ/mol and maroon color representing a large difference > 240 kJ/mol. Markers are shown on the right side to differentiate among catalysts.

A majority of the candidates lie in the OBE range between -100 kJ/mol and -200 kJ/mol (highlighted region in Figure 4.9). Qualitatively, it can be seen that η first increases with increasing OBE (from 0 to -150 kJ/mol) and reaches a maximum value of 1.4 for NbMo_{3B} at an OBE value of -150 kJ/mol. Afterwards, η decreases with increasing OBE (from -150 kJ/mol to -300 kJ/mol). To specify what value of OBE corresponds to the optimal catalyst, we propose that it lies between an approximate range of -100 kJ/mol to -200 kJ/mol for the set of bimetallic carbides for HDO process. Similarly, an OBE range of -200 kJ/mol to -400 kJ/mol was predicted for Ni-based bimetallic catalysts for HDO of furfural to 2-methylfuran.²⁵⁹ Interestingly, the incorporation of C into the metal lattice can significantly reduce the OBE. Utilizing this plot, we can find potential candidates for selective DDO and HYD. For DDO, η should be maximized. Notably, NbMo_{3B}, Fe_{3B}, Co_{3B}, Cr_{3B} and Cr_{22B} are predicted from the OBE vs. η plot for DDO, and they were also

present in the preliminary top candidates in selective DDO as discussed in Section 3.6.1. Similarly, for selective HYD, Fe_{11}T_A , Fe_{11}T_B , Co_{6B} , Ni_{6A} , and Fe_{11B} were suggested based on our earlier detailed analysis discussed in Section 3.6.2, and we can identify them using the plot (Figure 4.9). Overall, this plot can be used to preliminarily screen a large dataset of bimetallic carbide catalysts to identify potential candidates for HDO process.

4.4 Conclusions

In summary, 45 Mo_2C -based bimetallic carbide catalysts ($\text{M-Mo}_2\text{C}$) with different compositions (M/Mo ratios) and terminations (A/B/C) were systematically studied and screened for the HDO process employing periodic density functional theory (DFT) calculations using phenol as a model compound. The adsorption characteristics of both H adatom and OH fragment were investigated as they are directly involved in the HDO process. Both hydrogen (HBE) and oxygen binding energies (OBE) showed similar trend owing to the occupancy of similar 3-fold active sites. Additionally, OBE trend can be explained with the oxophilicity scale (tendency to form oxides), and stronger OBE values were observed on surfaces terminated with more oxophilic atoms except Zr-doped catalysts. For the screening strategy, three probe reactions, namely C-O dissociation, oxygen removal and ring hydrogenation, were used to represent direct deoxygenation (DDO), stability against oxygen poisoning and hydrogenation (HYD). Consequently, active, selective and stable candidates were proposed for respective DDO and HYD. For DDO, Mo-terminated $\text{Fe}_3\text{Mo}_3\text{C}$ (Fe_{3B}), Mn-terminated $\text{Mn}_3\text{Mo}_3\text{C}$ (Mn_{3A}) and Ni-terminated $\text{Ni}_3\text{Mo}_3\text{C}$ (Ni_{3A}) catalysts displayed an optimal balance between C-O scission and oxygen removal aspect of the HDO process. For HYD, Mo-terminated $\text{Fe}_{11}\text{MoC}_4$ (Fe_{11}T_B) and Ni-terminated $\text{Ni}_6\text{Mo}_6\text{C}$ (Ni_{6A}) showed remarkable activity and selectivity for this reaction with the lowest and equal barrier of 47 kJ/mol respectively. Lastly, using the energy barriers of the probe reactions, a parameter, η , is proposed, which encompasses the activity, selectivity and stability aspects of a catalyst. Utilizing OBE as a descriptor and the proposed parameter, η , a qualitative trend was observed which can be used to screen catalysts for the HDO process. Using this trend, an optimal range for the OBE value of -100 kJ/mol to -200 kJ/mol is proposed for HDO catalysts. Moreover, the insights gained from this work can provide guidance for rational design of bimetallic carbide catalysts and it can be further extended for other processes involving C-O activation, water formation and hydrogenation, such as CO_2 conversion, oxygen reduction, and reverse water gas shift reactions.

Chapter 5: Water-Assisted Hydrogenation of Aromatics under Ambient Conditions over Ru Catalyst: A Combined Experimental and Computational Investigation³

Abstract

Conventional hydrogenation of lignin-derived compounds requires high H₂ pressures and temperatures, and yet, achieving the desired conversion and selectivity remains a challenge. Herein, a novel reaction system with a ruthenium catalyst and water as a solvent is developed for the selective hydrogenation of lignin-derived aromatics to corresponding ring-saturated products under ambient conditions (room temperature, and 1 bar H₂ pressure). Using a synergistic combination of catalysis experiments, advanced characterization techniques and quantum mechanical simulations, we elucidate that Ru catalyst switches its selectivity from deoxygenation in gas phase to ring hydrogenation in the condensed phase. Water partially dissociates and adsorbs on the catalyst surface as a combination of hydroxyl fragments, H atoms, and physisorbed molecules, and this is critical for Ru to flip its selectivity in the aqueous phase. Experimental results demonstrate a high conversion (>99%) and >75% selectivity towards the total hydrogenated products in the presence of water, corroborating the computational results in which kinetic free energy barriers for direct hydrogenation steps reduced to 70 kJ/mol and barrier for direct dehydroxylation increased from 63 kJ/mol to 202 kJ/mol in the case of phenol. Furthermore, H from dissociated water molecules is utilized in the hydrogenation and water also gets regenerated utilizing external hydrogen supply, thus acting as a shuttler for the external hydrogen.

Keywords: Phenol, Guaiacol, Water, Hydrogenation, Ruthenium, DFT.

³ Reproduced, with minor modifications, with permission from Sagar Bathla, Bhanu Priya, Ankit Kumar, Sanjay K. Singh, Samir H. Mushrif, “*Water-assisted hydrogenation of aromatics under ambient conditions over Ru catalyst: A combined experimental and computational investigation*”, *Journal of Catalysis*, Volume 434, 2024, 115522, <https://doi.org/10.1016/j.jcat.2024.115522> © 2024 Elsevier

5.1 Introduction

Environmental concerns and the depletion of non-renewable fossil resources compel the search for alternate renewable feedstocks.^{32,262,263} In this regard, lignocellulosic biomass has great potential to substitute petroleum-based feedstocks to produce chemicals and fuel components.²⁶⁴ Lignocellulosic biomass comprises of cellulose, hemicellulose, and lignin, and lignin is the most prevalent source of aromatics in nature.^{265,266} But direct usage of lignin is not viable due to its complex polymeric structure, comprising of various phenylpropanoid subunits held together by C-C or C-O bonds in random order.²⁶⁷ To convert lignin into various value-added chemicals and fuel components, it should be first depolymerized into monomer units by hydrogenolysis,²⁶⁸ pyrolysis,²⁶⁹ oxidation,²⁷⁰ and hydrolysis²⁷¹ processes and then these monomer units can be upgraded to target products. However, depolymerization results in the formation of monomeric oxygen containing aromatics, and their hydrodeoxygenation (HDO) or hydrogenation is an essential way for the upgradation of these monomers into cyclohexanol, cyclohexanone, alkyl cyclohexanol, cyclohexane, and other ring saturated hydrocarbons.^{144,272} Selective hydrogenation results in the alkyl or alkoxy-substituted cyclohexanols, which can be used as building blocks for the synthesis of different polymers, resins, dyes, and fine chemicals, and these substitutions can help in tuning the physical properties, such as melting points, elasticity, and crystallinity of these materials.^{99,89}

Till date, hydrogenation of various lignin-derived monomers (phenol, guaiacol, eugenol etc.) to corresponding substituted cyclohexanols is studied extensively over non-noble and noble metal based heterogeneous catalysts in both, gas and liquid, phases. However, liquid phase processes can provide higher target product selectivity.^{32,87} Non-noble metal based catalysts such as Ni,^{90–92,96} and Co^{93–95} have also been reported for selective hydrogenation reactions. Jiang et al. investigated the effect of solvents in guaiacol HDO over NiCo/ γ -Al₂O₃ bimetallic catalyst and observed the highest conversion (96%) in the presence of water, in comparison to 40%, and 48% with methanol and ethanol, respectively.⁹⁷ Very recently, Natte et al. also reported a Co based heterogeneous catalyst for the selective ring hydrogenation of various arenes at 120 °C and 30 bar H₂ using t-BuOH as the solvent.⁹⁸ Schutyser et al. studied Ni/SiO₂-Al₂O₃ catalysts for the selective hydrogenation of 4-propylguaiacol (PG) to 4-propylcyclohexanol (PCol) at 300 °C under 40 bar H₂ and catalyst displayed a PCol selectivity of ~70%.⁸⁹

While non-noble metal catalysts are cost-effective, their use often requires harsher reaction conditions, leading to higher energy consumption and operating costs. Additionally, these catalysts sometimes exhibit poor product selectivity due to various side reactions, making the overall process less efficient.⁹⁹ To overcome the limitations of non-noble metal-based catalysts, various noble metal-based catalysts mainly Pd, Pt or Ru in liquid phase were explored. For instance, Lercher et al. systematically compared phenol hydrogenation among three solvents viz. water, methanol, and hexadecane over Pd/C catalyst at 200 °C and 40 bar H₂ and observed highest phenol hydrogenation rate while using water as the solvent.¹⁰⁰ Hensen and colleagues also employed Pt/C and Ru/C catalysts for the conversion of guaiacol using water as a solvent at 150 °C and 20 bar H₂ pressure and obtained a selectivity of 100% and 84% for cyclohexanol respectively in 2 h.¹⁰¹ Various other Ru based catalytic systems comprising of Ru/C, Ru/Nb₂O₅, Ru-RuO₂-Nb₂O₅/H β , Ru/NC (NC is nitrogen doped carbon) and different solvents such as acetic acid, isopropanol, or decahydronaphthalene were also explored for hydrogenation of lignin derived aromatics.^{102,103,273,274} Many researchers reported that the hydrogenation capability of Ru is more strongly affected by the solvation medium and thus, in comparison to Pd or Pt in aqueous solution, Ru has displayed higher activity for the hydrogenation reactions.^{104–109} Therefore, Ru is significantly more active in aqueous environments, making it a common choice for the hydrogenation of aromatics in aqueous phases. For instance, Tomishige et al. investigated the production of cyclohexanol from guaiacol and discovered that a combination of Ru/C and MgO in water at 160 °C and 15 bar H₂ pressure resulted in a high cyclohexanol yield of 78%.¹¹³ In a subsequent study, the authors reported a higher cyclohexanol yield of 81% on a bimetallic Ru-MnO_x/C catalyst from guaiacol in water at 160 °C and 15 bar H₂.¹¹⁴ On the contrary, over Ru/C catalyst, guaiacol produced a considerably lower yield of cyclohexanol (72%).¹¹⁴ In the conversion of eugenol, over Ru supported on carbon nanotubes in a biphasic water-dodecane mixture at 160-180 °C and 50 bar H₂ pressure, Fu et al. achieved extremely PCol yields (up to 90%).¹¹⁵ In a different study, the researchers also found that a metal-solid base bifunctional catalyst, Ru/ZrO₂-La(OH)₃, is highly selective in the conversion of different 4-alkylguaiacols and 4-alkylsyringols to the corresponding 4-alkylcyclohexanols (RCols) in the aqueous phase at 200 °C and 40 bar H₂, with RCol yields exceeding 87%.¹¹⁶ Boronoev et al., delves into the examination of Ru nanoparticles supported on nanosized spherical polymers for guaiacol hydrogenation.²⁷⁵ The primary emphasis lies in investigating the impact of support

size. An increase in conversion with a reduction in the size of support particles was observed due to the improved stabilization of Ru nanoparticles.

Ru-water system has also been studied using DFT simulations suggesting possible hydrogenation in the aqueous phase.^{109,117} For instance, Michel et al. performed DFT calculations on Ru (0001) surface with only one explicit water molecule using acetone as model carbonyl compound. They observed that the alkoxy intermediate forms an H-bond with the chemisorbed water molecule which makes the hydrogenation route more feasible by reducing the barrier by 41 kJ/mol.¹⁰⁹ Akpa et al. also carried out DFT calculations to understand the beneficial role of water on Ru (0001) surface in the hydrogenation of 2-butanone. They showed the water molecules interact with the intermediate species such as hydroxy butyl due to which the energy barrier decreases for hydrogenation.¹¹⁷ Later, Chin et al. shed light on the role of hydrides and protons in the catalytic hydrogenolysis of guaiacol at Ru-water interface.¹¹⁸ They found the enol intermediate undergoes an intramolecular proton transfer assisted by a vicinal water molecule, during which its hydroxyl proton transfers to its methoxy leaving group during the C–O bond cleavage. Moreover, they reported that the promotional effect of water on the hydrogenation cycle remains small. In the three investigations discussed above, they did not consider the possible dissociation of water molecules adsorbed on the ruthenium surface, as suggested from theoretical and experimental investigations.^{119–123}

All these aforementioned studies suggest that a synergistic combination of an effective catalyst and choice of solvent is vital for the selective hydrogenation of lignin-derived aromatics. One such combination could be ruthenium catalyst and water as a solvent on which partial dissociation of water has been observed which could possibly play a critical role in the hydrogenation process. However, mechanistic role of the catalyst and water is still unclear in the selective hydrogenation reaction. Therefore, it is crucial to comprehend how the catalyst itself may be affected by the solvent environment, as well as how the solvent-catalyst, solvent-reactant, and catalyst-reactant interactions are altered. Therefore, herein, we investigated Ru catalyst in the absence and presence of water molecules by combining both experimental and computational methods, elucidating the underlying mechanism for the selective hydrogenation of lignin-derived aromatics. To the best of our knowledge, this is also the first extensive study which shows that the selective hydrogenation of lignin derived aromatics in water can be achieved at ambient conditions at 1 bar H₂ pressure and room temperature. This work offers not only insights about the role of water in the

hydrogenation process but also provides guidance for the rationale choice of solvent in the hydrotreatment of bio-oil.

5.2 Experimental and computational methods

5.2.1 Chemical Reagents

All the chemical reagents and metal salts were available commercially and were used as such without any further purification. $\text{RuCl}_3 \cdot 3\text{H}_2\text{O}$, sodium borohydride, cetyltrimethylammonium bromide (CTAB), Phenol, Guaiacol, diphenyl methane and Benzyl phenyl ether were purchased from Sigma Aldrich, India. Benzyl alcohol, Cinnamyl alcohol, and Eugenol were purchased from TCI analytics, India. High purity hydrogen gas was procured from Sigma gases, India.

5.2.2 Catalyst synthesis

Ruthenium catalyst was synthesized using our previously reported chemical reduction method.^{276,277} Typically, an aqueous solution of sodium borohydride (25 mg in 5 mL water) was added dropwise to a solution of 50 mg CTAB and 0.04 mmol (10.4 mg) $\text{RuCl}_3 \cdot 3\text{H}_2\text{O}$ in 5 mL water. The contents of the flask were sonicated for 15 minutes. Ru nanoparticles were centrifuged, washed several times with distilled water, dried under vacuum overnight and then used for catalytic reactions. Similarly, catalysts with different Ru loadings were synthesized using different amounts of $\text{RuCl}_3 \cdot 3\text{H}_2\text{O}$.

5.2.3 Characterization

Synthesized catalysts were dried under vacuum overnight prior to the catalyst characterization. Powder X-ray Diffraction (P-XRD) measurements were performed using Rigaku Smart Lab, an Automated Multipurpose X-ray diffractometer at 40 kV and 30 mA ($\text{Cu}_\alpha \lambda = 1.5418 \text{ \AA}$). Scanning Electron Microscopic (SEM) images and elemental mapping data were collected with a JOEL-7610 F Plus equipped with an EDS detector. X-Ray Photoelectron Spectroscopy (XPS) was performed using Omricon ESCA (Electron Spectroscopy for Chemical Analysis), Oxford Instrument, Germany. Aluminum (Al) anode was used as a monochromatic X-ray source (1486.7 eV) for XPS measurements. Transmission electron microscopic (TEM) imaging energy dispersive X-ray spectroscopy (EDS) were performed on the Tecnai G2, Spirit Twin microscope with an operating voltage of 120 kV. High resolution transmission electron microscopic (HR-TEM) imaging was performed on FEI Tecnai G2, F30 HR-TEM with operating voltage of 300 kV. For TEM and HR-TEM analysis, the catalyst was suspended in ethanol, and a few drops of the suspension were

deposited over the amorphous carbon coated 400 mesh Cu grid and dried at room temperature. Inductively Coupled Plasma Atomic Emission Spectroscopic (ICP-AES) analyses were performed using ARCOS, a simultaneous spectrometer of SPECTRO analytical instruments. ^1H NMR (500 MHz) and ^{13}C NMR (125 MHz) were recorded in deuterated solvents using Bruker Ascend 500 spectrometers. Chemical shifts were referenced to the internal solvent resonances and were reported relative to tetramethylsilane. GC-MS analysis was performed using Shimadzu GC-MS, QP2010 Mass Spectrometer and RTX-5MS tubular 5% diphenyl/95% dimethyl polysiloxane capillary column, 30 m long, 0.25 mm inner diameter with a df value of 1.0 μm . The oven temperature was varied from 40 to 280 $^\circ\text{C}$ at a heating rate of 20 $^\circ\text{C min}^{-1}$ and the detector temperature were set at 350 $^\circ\text{C}$.

5.2.4 General procedure for catalytic hydrogenation reactions

Catalytic tests were performed in a 100 mL stainless-steel high-pressure reactor equipped with a magnetic stirrer. Typically, 1 mmol substrate [phenol (94 mg), guaiacol (124 mg), benzyl alcohol (108 mg), cinnamyl alcohol (134 mg) diphenyl methane (168 mg), benzyl phenyl ether (184 mg), diphenyl ether (170 mg), eugenol (164 mg)], was added to the reaction vessel. For catalytic reactions, these Ru nanoparticles (0.04 mmol, 4 mg) were transferred to reactor in a suspension form. To make the suspension, we added 2 mL water to the centrifuge tube containing Ru nanoparticles, sonicated it for 5 minutes and transferred to reactor with the help of pipette. This process was repeated two times to make sure that all the nanoparticles were transferred to the reactor. Then substrate and remaining volume of water was added, and reaction was carried out in the presence of H_2 . For catalyst recovery process, after reaction completion, the reaction solution was centrifuged at 8500 rpm for 15 minutes using REMI-24 centrifuge machine. The reactor was washed 2-3 times with water to recover all the catalyst. Product is extracted from water portion using dichloromethane (5 \times 10 mL) and the combined organic portions were dried over the anhydrous Na_2SO_4 and all the volatiles were removed under reduced pressure. For the catalyst recycling experiments, the catalyst was separated by centrifugation, washed thoroughly with distilled water, dried overnight under vacuum, and then used for next catalytic run. Isolated products were identified by ^1H NMR, ^{13}C NMR, and GC-MS. Conversion was calculated using the following formula.

$$\text{Conversion} = \frac{(nR_i - nR_f)}{nR_i} \times 100 \%$$

where, nR_i is the initial amount of reactant (mmol) at the beginning of the reaction, and nR_f is the final amount of reactant (mmol) after the reaction.

5.2.5 Computational methods

First-principles calculations are performed using periodic boundary conditions and plane-wave pseudopotential implementation of Kohn-Sham DFT. Vienna ab initio simulation package (VASP)^{155,156} developed at the Fakultät für Physik of the Universität Wien^{157,158} is used to determine the electronic ground state and the core level binding energy shifts. The projector augmented wave (PAW)¹⁵⁹ method is used to describe the interaction between valence electrons and ions with a plane wave cut-off energy of 450 eV. The vdW-DF functional was employed to account for the weak long-range dispersion interactions between CO, H, and aromatic compounds (e.g. guaiacol, furfural) and the catalyst surface. The vdW-DF functional was used and worked well to investigate HDO reaction mechanisms on transition metal-based catalysts.²⁷⁸ A high level of accuracy is ensured by employing energy convergence criteria of 10^{-5} eV per unit cell and a maximum force tolerance of 0.05 eV/Å. For integration across the Brillouin zone in reciprocal space, we employed a k-points sampling of 3x3x1 with the Monkhorst-pack strategy, and spin polarization was disabled for all simulations. A vacuum space of 15 Å is added above the top layer to avoid interaction with the adjacent unit cell in the z-direction. The number of slab layers and the density of k-point grids are chosen to ensure that the adsorption energies are well converged with respect to the computational set-up discussed here. Vibrational frequencies of all reactants and products were also carefully analysed, and no imaginary frequencies were observed. Transition state structures were estimated using the climbing image Nudged Elastic Band (NEB) method. A total of 5-10 images were used in NEB, and the force was minimized to 0.05 eV Å⁻¹. The NEB image closest to the transition state was further optimized using the quasi-Newton algorithm, and vibrational frequency analysis was done with a displacement criterion of 0.02 Å to confirm the transition state. We calculated zero-point energy and thermodynamic corrections at pertinent experimental conditions. The enthalpy corrections for gas-phase molecules are taken from thermodynamic tables while we employed statistical thermodynamics using vibrational partition function for the adsorbed system. All the reaction energies and activation barriers are reported as Gibbs free energy change. The estimation method for Gibbs free energy changes along with all the equations employed are given in the supplementary information. All reaction energies,

G_r are calculated as $G_r = G_{tot} (FS) - G_{tot} (IS)$, with FS and IS referring to final and initial state structures, respectively. The corresponding activation barriers, G_a , are calculated as $G_a = G_{tot} (TS) - G_{tot} (IS)$, with TS referring to transition state structure.

5.3 Results and discussion

5.3.1 Catalyst characterization

Ru catalyst was synthesized by chemical reduction method and is characterized by P-XRD and FE-SEM analysis. P-XRD spectra (Figure 5.1a) exhibited a major peak at 2θ degrees 43.43° corresponding to the (101) major plane for hexagonal-close packed Ru catalyst (JCPDS 01-077-3315).²⁷⁷ Broad nature of peaks is indicative of the small crystallite size of Ru nanoparticles. FE-SEM images and EDS mapping revealed the presence of Ru nanoparticles (Figure. E1). Further, X-ray photoelectron spectroscopy (XPS) measurements were performed to know the chemical state of Ru. In the high resolution XPS spectra, two peaks at the binding energies of 462.37 eV and 484.69 eV in Ru 3p region can be assigned to Ru 3p_{3/2} and Ru 3p_{1/2} respectively corresponding to the metallic Ru(0) (Figure 5.1b).^{279,280} However, we could not eliminate the possibility of the formation of a thin layer of metal oxide on the catalyst surface. This oxide layer, which is known to form on Ru catalysts under ambient conditions, forms after the synthesis process.^{115,281–286} So, the binding energies of 465.23 eV and 487.89 eV were ascribed to the Ru (IV) state. The ratio of Ru (0) to Ru (IV) was found to be 75:25 for fresh Ru catalyst.

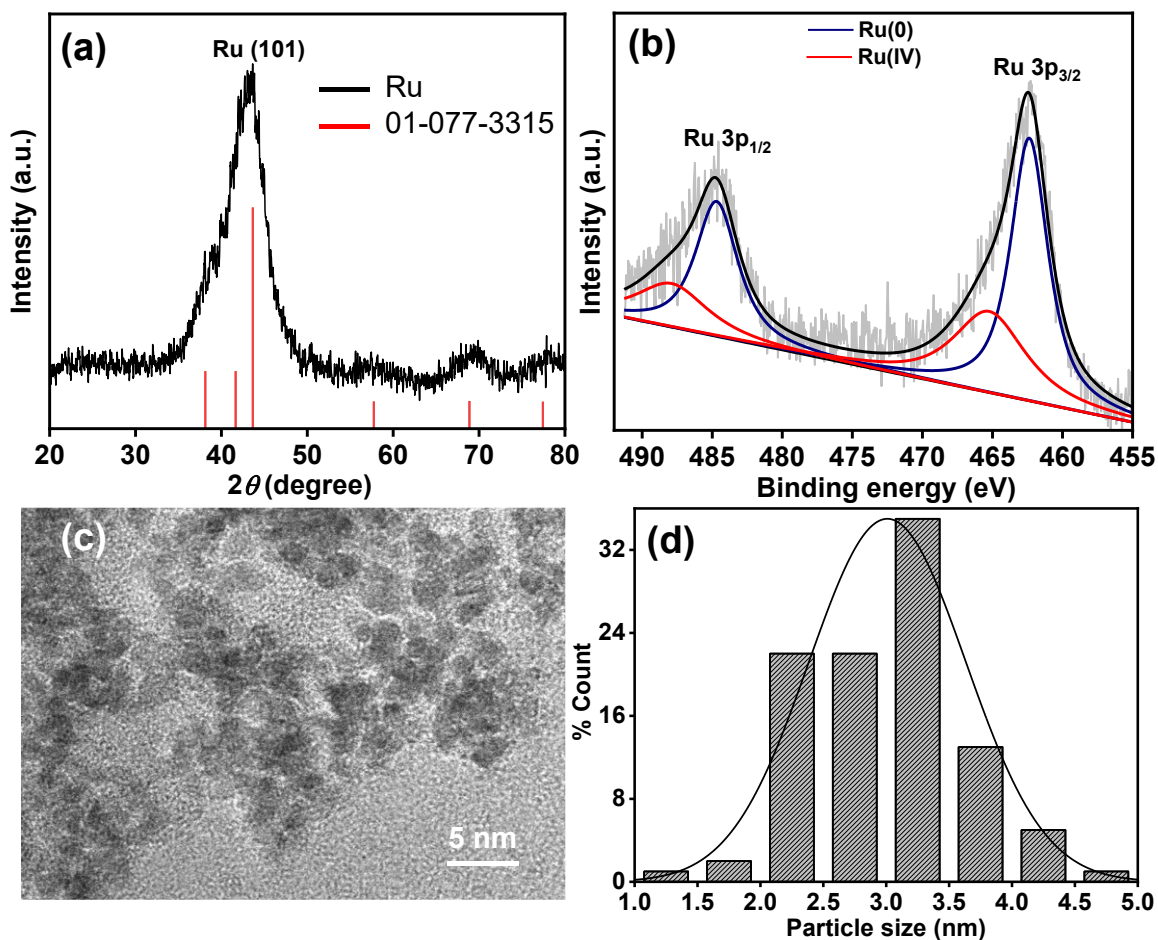


Figure 5.1 (a) P-XRD pattern, and (b) XPS spectra of 3p core levels (c) TEM image, and (d) particle size distribution curve for fresh Ru nanoparticles.

Transmission electron microscopy (TEM) images revealed the presence of well dispersed Ru nanoparticles with an average particle size of ~ 3.0 nm (Figure 5.1c-d). The d -spacing as calculated from TEM is found to be 0.20 nm also confirming the presence of (101) plane of Ru (Figure. E2). Further, the BET surface area of the synthesized Ru nanoparticles was found to be 36 m²/g (Figure. E3).

5.3.2 Optimization of reaction conditions

5.3.2.1 Hydrogenation of phenol

At an outset, phenol (**1**) hydrogenation was selected as a benchmark reaction to evaluate the catalytic efficiency of Ru nanoparticles under mild conditions i.e., at room temperature and 1 bar H₂. Water is used as a solvent to carry out these reactions.

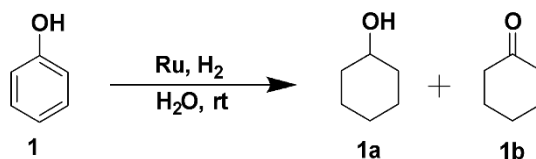


Figure 5.2 Schematic of catalytic hydrogenation of phenol over ruthenium catalyst at room temperature in water.

Initially for 5 min, there was no conversion of phenol (Table 5.1, entry 1) which might be attributed to the induction time required for the catalyst activation. As indicated by density functional theory (DFT) calculations, discussed in detail in Section 4, the activation energy barrier for water dissociation on an H-precovered surface is 83 kJ/mol. In comparison, the activation energy barrier for the hydrogenation of phenol is 70 kJ/mol. Since the hydrogen required for the hydrogenation reaction is initiated from the dissociation of water molecules, the observed longer induction period could be attributed to the time required for water dissociation on the Ru surface. Moreover, in Ru catalysts, it is generally observed that there is a formation of an oxide layer on the catalyst surface while handling under ambient conditions.^{115,281–286} In our study, we also noticed the formation of an oxide layer on the Ru catalyst, which increased the induction time needed to activate the catalyst for hydrogenation reactions. Similar findings have been reported by Koopman et al. and others regarding the activation of Ru catalysts in water.^{285,287–289} These researchers reported an induction time of up to 1 hour. Additionally, it has been noted that Ru catalysts can be activated at 30°C in water, whereas higher temperatures are required for activation in other non-polar solvents.²⁸⁷ These observations help explain the longer induction times required for catalytic evaluation in our study. On increasing the reaction time to 15 min, the conversion increased to 32% and cyclohexanol (**1a**) was formed as a major product (sel. 81%) and cyclohexanone (**1b**) as a minor product (sel. 19%) (Table 5.1, entry 2). On further increasing the reaction time, the conversion of phenol increased, and complete conversion was achieved in 75 min with 95% yield of cyclohexanol (Table 5.1, entries 3-6). Furthermore, the hydrogenation of phenol using RuO₂ as the catalyst under ambient conditions (1 bar H₂ and room temperature) resulted in <5% conversion after 75 minutes of reaction time. This observation suggests that RuO₂ alone is not efficient in catalyzing hydrogenation reactions under these conditions. These results support the hypothesis that Ru(0) species are the active form of the catalyst for hydrogenation reactions.

Table 5.1 Optimization of reaction conditions for hydrogenation of phenol.^a

Entry	Time (min)	Conv. (%)	Selectivity for 1a (%)	Selectivity for 1b (%)
1	5	n.r.	-	-
2	15	32	81	19
3	30	55	89	11
4	45	76	93	7
5	60	90	97	3
6	75	>99	>99 (95) ^b	-
7 ^c	75	n.r.	-	-
8 ^d	75	n.r.	-	-
9 ^e	960	>99	>99	-
10 ^f	480	>99	>99	-
11 ^g	60	>99	>99	-

^aReaction conditions: Ru catalyst (0.04 mmol), phenol (1 mmol), water (10 mL), H₂ (1 bar), room temperature, t h. ^bisolated yield, ^creaction performed without catalyst, ^dreaction performed without H₂, ^eRu catalyst (0.004 mmol), ^fRu catalyst (0.01 mmol), ^gRu catalyst (0.05 mmol), n.r.- no reaction.

Reaction performed without the Ru catalyst (Table 5.1, entry 7) or in absence of hydrogen gas (Table 5.1, entry 8) unsurprisingly, showed no conversion, suggesting the crucial role of catalyst and hydrogen in carrying out the hydrogenation reaction. To optimize the catalyst loading, reactions with varying amounts of Ru were performed. On decreasing the catalyst loading by 10 times (0.004 mmol) reaction took 960 min (16 h) (Table 5.1, entry 9), whereas a catalyst loading of 0.01 mmol resulted in complete conversion after 480 min (8 h) (Table 5.1, entry 10). On increasing the catalyst loading to 0.05 mmol, reaction completed in 60 min with complete selectivity to cyclohexanol (Table 5.1, entry 11). Time dependent studies revealed that cyclohexanone is formed as an intermediate while carrying out the phenol hydrogenation (Figure 5.4a). In the presence of water, on Ru (101) surface, phenol is adsorbed dissociatively as revealed by DFT calculations (explained in detail in section 4.1). At Ru surface water molecules are in partially dissociated form and when there is an OH* near phenol, there is the formation of H₂O and phenol is adsorbed as phenoxy on Ru surface. Further, phenoxy hydrogenation follows a

sequential hydrogenation pathway, with the least hydrogenation barrier at C-4 (for nomenclature of carbon atoms in phenol see Figure 5.11), followed by the subsequent hydrogenation at other carbon atoms resulting in the formation of cyclohexanone intermediate as observed experimentally as well (Figure 5.3). This cyclohexanone is then further hydrogenated to cyclohexanol in aqueous solutions.^{290–292}

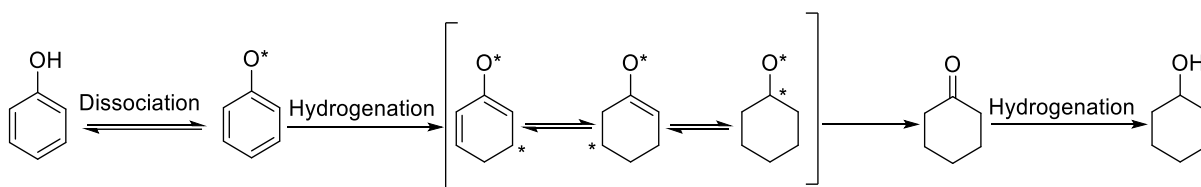


Figure 5.3 Schematic of a potential Reaction pathway for the hydrogenation of phenol to cyclohexanol over Ru surface.

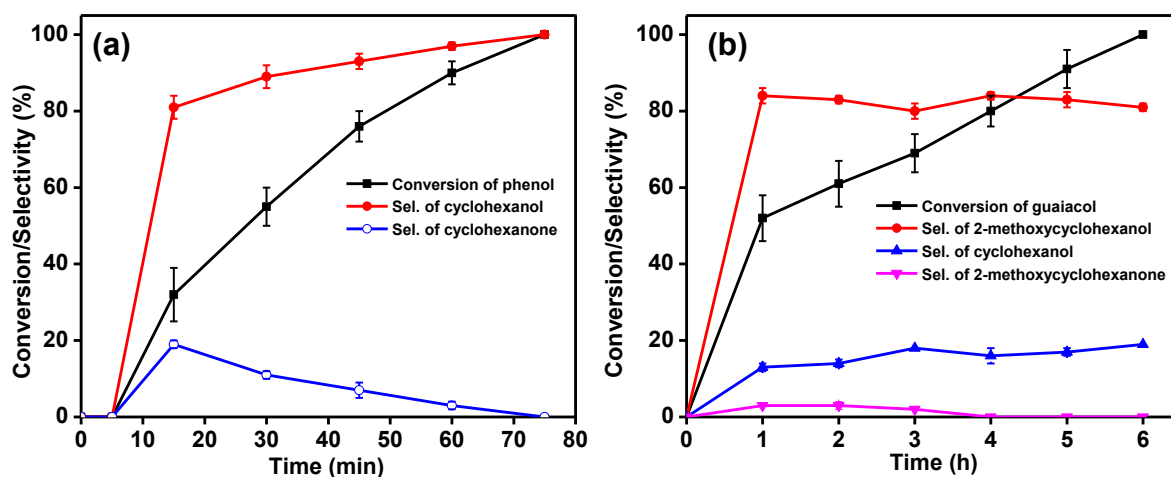


Figure 5.4 Time dependent reaction profile for hydrogenation of (a) phenol and (b) guaiacol. Reaction conditions: Ru catalyst (0.04 mmol), phenol (1 mmol) or guaiacol (1 mmol), H₂ (1 bar), water (10 mL), room temperature.

Further, we carried out the hydrogenation of guaiacol (2-methoxyphenol) as it is directly accessible from depolymerization of lignin under the optimized reaction conditions i.e., at room temperature and 1 bar H₂ in water (Table E.1). With increase in the time from 1 to 6 h, the conversion of guaiacol increased and reached maximum in 6 h (Figure 5.4b). Along with the major hydrogenated product, 2-methoxy cyclohexanol (**2a**), small amount of hydrodeoxygenated product cyclohexanol (**1a**) was also observed. In the initial hours, 2-methoxy cyclohexanone (**2b**) was also observed indicating that hydrogenation reaction proceeds via the formation of this intermediate (Figure 5.4b). Product distribution suggests that there is a competitive hydrodeoxygenation (HDO)

pathway leading to the formation of cyclohexanol from guaiacol which is almost independent of time. Noticeably, we did not observe any dehydroxylation of guaiacol. Reaction performed using 2-methoxy cyclohexanol as a substrate under the optimized reaction conditions resulted in no formation of cyclohexanol, which further evidenced the fact that C-O bond hydrogenolysis (scissoring of methoxy group) of guaiacol is more favourable than 2-methoxycyclohexanol (Table E.1).

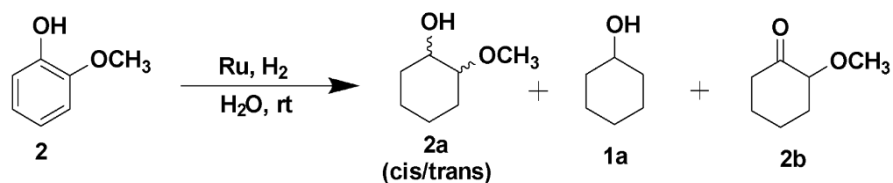


Figure 5.5 Products obtained from catalytic hydrogenation reaction of guaiacol over the Ru catalyst at room temperature in water.

5.3.3 Effect of the solvent

Effect of solvents on the catalytic activity and product distribution for selective hydrogenation of phenol (**1**) is shown in Table 5.2. We screened polar protic solvents such as methanol and ethanol, polar aprotic solvent such as acetone and most polar water for the Ru catalysed hydrogenation of phenol under optimized reaction conditions (1 bar H₂ and room temperature). When reaction was carried out using methanol or ethanol as solvent, 22% and 29% conversion was observed respectively (Table 5.2, entries 1, 2). Also, in case of methanol the selectivity for our desired product cyclohexanol (**1a**) was 78% whereas in case of ethanol it was observed as 69%. Notably, methanol and ethanol are commonly used as hydrogen donor solvents,²⁸⁵ but when reaction was carried out in the absence of external H₂, there was no conversion of phenol, suggesting that under our optimized reaction conditions, these solvents are not acting as hydrogen source. In case of acetone, we observed 38% conversion of phenol with 73% selectivity for cyclohexanol (**1a**) in 75 min over Ru catalyst (Table 5.2, entry 3). But highest conversion (>99%) was observed using water as solvent at room temperature with complete selectivity towards cyclohexanol in 75 min (Table 5.1, entry 6). Therefore, to check the effect of solvent, further, we used acetone (as it does not have any protic proton like methanol, ethanol and water) as a solvent and added water in small quantities and observed a drastic change in the catalytic activity (Table 5.2, entries 4-7). As we varied the amount of water from 0 to 100 μ L, the conversion of phenol increased from 37% to

94%. These results clearly suggest that water has an obvious positive impact on the activity of Ru catalyst in the hydrogenation of phenol to cyclohexanol, which agreed well with the studies done by Lercher, Rinaldi, and Lou.^{100,293,294} Lercher et al. reported that water could give the highest phenol hydrogenation rate, while acetal reactions would happen between methanol and other intermediates (such as cyclohexanone, etc.) when methanol was used as a solvent.¹⁰⁰ Rinaldi et al. and Lou et al. also reported that methanol and ethanol would adsorb on the active sites, hindering chemisorption of reactant on the active sites, which would lead to low conversion rate.^{293,294}

Table 5.2 Effect of solvent on hydrogenation of phenol over the Ru catalyst.^a

Entry	Solvent	Conv. (%)	Selectivity for 1a (%)	Selectivity for 1b (%)
1	methanol	22	78	22
2	ethanol	29	69	31
3	acetone	38	73	27
4	acetone + water ^b	49	78	22
5	acetone + water ^c	67	81	19
6	acetone + water ^d	83	86	14
7	acetone + water ^e	94	82	12

^aReaction conditions: Ru catalyst (0.04 mmol), phenol (1 mmol), solvent (10 mL), H₂ (1 bar), room temperature, 75 min, ^bwater 20 μL, ^cwater 40 μL, ^dwater 60 μL, ^ewater 100 μL.

A breakthrough study undertaken by Davis and co-workers shed light on the reactivity of gold/water interface during selective oxidation of alcohols.²⁹⁵ They elucidated the direct role of H₂O in the oxidation and indirect role of O₂ in generating more hydroxide species which were confirmed by isotope-labelling experiments and DFT calculations. Therefore, to get more insights into the effect of water during selective hydrogenation of phenol, we performed the isotope labelling experiment with D₂O. The products of experiments were analyzed by GC-MS and ¹³C

NMR (Figure 5.6 and Figure E.4). We observed a shift of 7-8 amu in GC-MS spectrum of the product showing the formation of deuterated cyclohexanol. Also, in the ^{13}C NMR spectrum, we observed the splitting of peaks presumably due to the D attached to C atoms.²⁹⁶ As the D atom is not from H_2 , the D atom from D_2O was likely added to the C of phenol during hydrogenation reaction, indicating that D_2O is participating in the reaction. It is presumed that H_2 interacts with Ru active sites, dissociates into H atoms, and forms Ru-H species and D_2O splits into D and OD. These adsorbed H atoms (Ru-H) undergoes H/D exchange to form Ru-D species. These D atoms may be then further transferred to phenol to form deuterated cyclohexanol as a product. Similar observation was made by Jiang et al. in the aqueous phase hydrodeoxygenation of lignin phenolics over Nb_2O_5 supported Ni catalyst, where they observed H/D exchange over the catalyst surface.²⁹⁷ Further, the reaction using CD_3OD as a solvent in the absence of H_2 also did not result in the formation of any deuterium-incorporated products. From the above discussion, it is clear that water

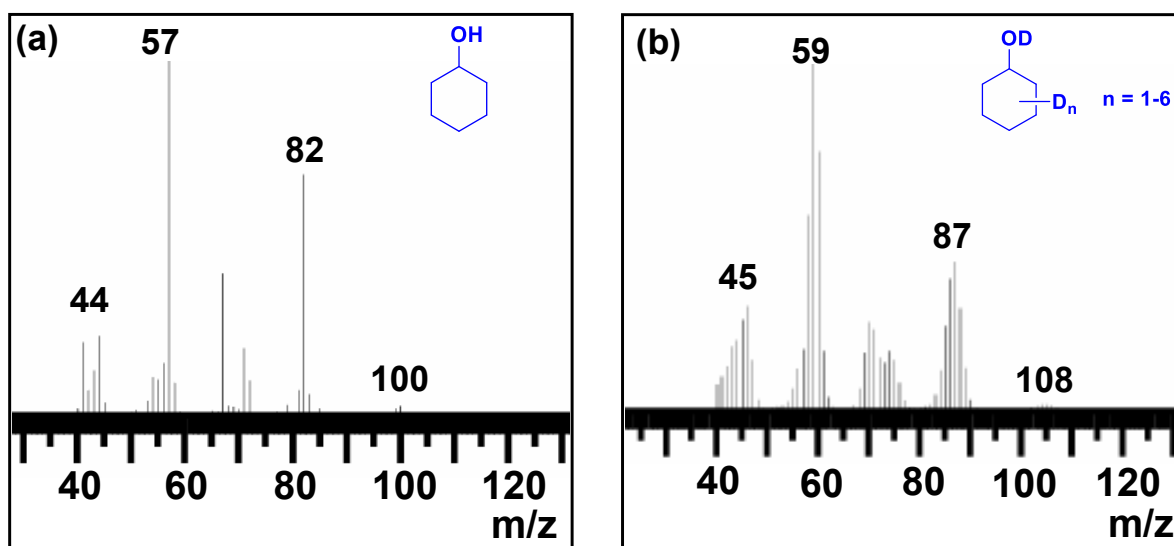


Figure 5.6 (a) GC-MS of reaction performed in H_2O . (b) GC-MS of reaction performed in D_2O . Reaction conditions: Ru catalyst (0.04 mmol), phenol (1 mmol), solvent (5 mL), H_2 (1 bar), room temperature, 75 min.

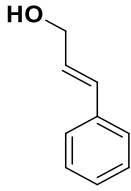
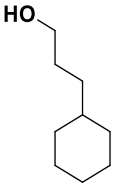
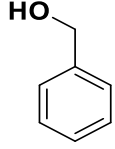
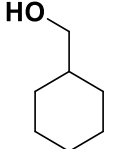
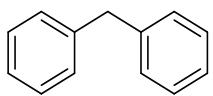
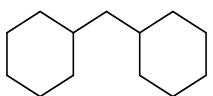
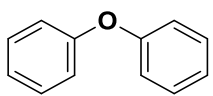
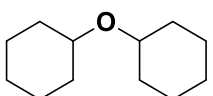
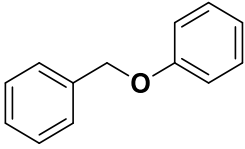
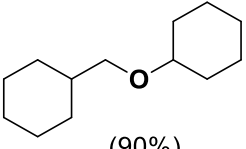
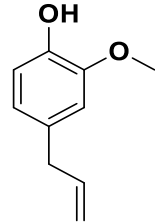
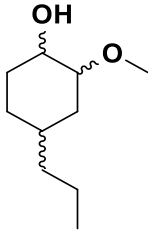
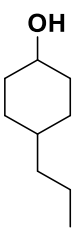
participates in the hydrogenation reaction of lignin-derived phenols to corresponding alcohols. In addition, the presence of water in the reaction medium significantly reduced the activation barrier for hydrogenation and enhanced the hydrogenation activity, as discussed later in section 4.

3.4. Scope of Ru catalyst for the selective hydrogenation of arenes

Monomeric phenols with alkyl and/or methoxy groups are the major components of lignin bio-oil. So, we carried out the hydrogenation reactions with the substrates that closely resembles to the

structural motifs in lignin. Cinnamyl alcohol is first hydrogenated to 3-phenylpropanol and then to 3-cyclohexylpropanol (86% yield) in 12 h under the optimized reaction conditions (1 bar H₂ and room temperature) (Table 5.3, entry 1). Similarly, benzyl alcohol is also hydrogenated to corresponding alicyclic alcohol (cyclohexylmethanol) with 84% yield in 4 h (Table 5.3, entry 2). Further, more complicated dimers were explored to evaluate the scope of Ru catalyst. Diphenylmethane is converted to dicyclohexylmethane in 8 h with appreciably good yields (Table 5.3, entry 3). Generally, when hydrogenation of phenylic ethers is carried out, C-O bond cleavage occurs readily resulting in the mixture of products.²⁹⁸ We observed only selective ring hydrogenation with no C-O bond cleavage in case of diphenyl ether and benzyl phenyl ether (Table 5.3, entries 4,5). Moreover, successful hydrogenation of eugenol was also carried out and total hydrogenated product i.e., 2-methoxy-4-propylcyclohexanol was obtained in 67% yield in 24 h (Table 5.3, entry 6). Along with the desired hydrogenation product of eugenol, some C-O bond cleavage of methoxy group was observed resulting in the formation of 4-propylcyclohexanol (25% yield). The experimental conditions were the same for all substituents, except that longer reaction time was required for the substrates containing alkyl or methoxy substituents. As shown in Table 5.3, a broad range of lignin-derived aromatics were hydrogenated to corresponding alicyclic compounds in good yields. Aromatics with the methoxy substituents provided slightly lower yields of total hydrogenated products as along with the hydrogenation some C-O bond cleavage was also observed.

Table 5.3 Hydrogenation of different lignin-derived substrates over the Ru catalyst under optimized reaction conditions^a

Entry	Substrate	Time (h)	Product (yield%)	
1		12	 (86%)	
2		4	 (84%)	
3		8	 (91%)	
4		12	 (83%)	
5		8	 (90%)	
6		24	 (67%)	 (25%)

^aReaction conditions: Ru catalyst (0.04 mmol), substrate (1 mmol) water (10 mL), H₂ (1 bar), room temperature, t h.

5.3.4 DFT investigation

Experimental findings inferred the crucial role of water in the hydrogenation of phenol, where using water as a solvent significantly enhanced the complete and selective hydrogenation of phenol to cyclohexanol. Moreover, the hydrogenation of phenol performed in D₂O suggested that D₂O splits into D and OD over the Ru surface to facilitate H/D exchange. To further investigate the mechanism at the molecular level, we performed a detailed DFT study for the hydrogenation of phenol and guaiacol, over Ru (101) facet, as it was observed in the P-XRD (Figure 5.1a). We used guaiacol (2-methoxyphenol) and phenol as model substrates for our simulations since they are the most common model substrates in lignin valorisation research^{185,186} and are also used in the experiments in this work. They contain methoxy and hydroxyl functional groups that are similar to those found in aromatic oxygenates derived from lignin.

First, we studied the adsorption characteristics of guaiacol and phenol over the Ru surface. In both cases, configuration $\eta^2(\text{C-O})$ is the more stable configuration where the benzene ring prefers the hollow face-centered cubic (fcc) site for adsorption (Figure E.20). Next, we investigated reaction energetics of guaiacol activation which can take place via multiple possible pathways, namely (i) C¹-O, (ii) C²-O, (iii) C⁷-O cleavage, (iv) ring - opening, and (v) C^{ring}-hydrogenation, (see Figure 5.7 for the nomenclature of carbon atoms). Since higher selectivity was observed towards ring-saturated products (over HDO) in experiments. Therefore, in this study, we investigated and compared deoxygenation (i) C²-O, (ii) C⁷-O cleavage, and (iii) C^{ring}-hydrogenation to distinguish between hydrodeoxygenation (C^{2/7}-O cleavage) and direct ring hydrogenation (C^{ring}-hydrogenation). Similarly, we also included phenol, and compared the HDO pathway (C¹-O cleavage) and the hydrogenation pathway (C^{ring}-hydrogenation).

5.3.4.1 Reaction pathways and energetics in the absence and presence of water

Previous studies have shown that Ru prefers deoxygenation over hydrogenation in the gas phase.^{68,198,299} For instance, Mironenko et al. reported that over Ru (001) surface, the C-O scission of the formyl group (-CHO) of furfural is more facile, with barriers of 65 kJ/mol, compared to the hydrogenation of furfural to furfuryl alcohol.²⁹⁹ Banerjee et al. observed that ring opening of furfural is facile on Ru surface in the gas phase, and that alkane formation (64 kJ/mol) is kinetically

and thermodynamically favoured during furfural HDO.¹⁹⁸ Hence, to elucidate the synergistic effect of the catalyst and the solvent water in this case, we performed calculations with and without water molecules present on the Ru surface for a systematic comparison.

We investigated the aforementioned three pathways for guaiacol activation on Ru (101) surface in the absence of water. It was observed that the ring hydrogenation can be initiated at six different carbon atoms of the aromatic ring. Therefore, we explored all possible activations via direct ring hydrogenation. Results revealed that direct cleavage of C²-O and C⁷-O bond are the most facile pathways in guaiacol activation, with free energy barriers of 87 and 63 kJ/mol, respectively, as shown in Figure 5.7a. Lu et al. also observed a similar activation barrier of 87 kJ/mol for C² - O dissociation, however, they observed that C⁷ - O dissociation is energetically and kinetically unfavorable.³⁰⁰ On the other hand, direct hydrogenation of the aromatic ring has relatively higher barriers of 118, 112, 116, 116, 130, 145 kJ/mol at C³, C⁴, C⁵, C⁶, C², and C⁷ carbons, respectively. Moreover, the reaction free energies for deoxygenation pathway are negative (-78 to -90 kJ/mol) in comparison to hydrogenation pathway (+40 to 79 kJ/mol), further confirming the feasibility of HDO pathway in the absence of water. Coming to hydrogenation pathway, the hydrogenation barriers for all the six possibilities except C⁷ were calculated to be similar, in the range of 112 – 130 kJ/mol. For subsequent hydrogenation steps, we started with C⁴ carbon which displayed a free energy barrier of 112 kJ/mol. Noticeably, direct hydrogenation barriers at C² and C⁷ carbon were observed to be much higher than the other carbon atoms which could be attributed to the presence of the methoxy and hydroxyl functional groups at those corresponding carbon atoms. As a result, hydrogen faces more steric hinderance in the presence of these groups while attacking the carbon atoms. On comparing the least hydrogenation activation barrier with HDO barriers in Figure 5.7b, it can be clearly noticed that C⁷-O dissociation is the kinetically and thermodynamically favourable route, implying that ring hydrogenation is not preferred in the absence of water. The first activation via dehydroxylation will probably lead to the formation of anisole, benzene. However, the initial activation step may not be the rate-determining step, therefore determining Ru selectivity without the participation of water for any of these products would need an investigation of the entire reaction network. The subsequent hydrogenation steps leading to the formation of ring-saturated products are presented and discussed later in Figure 5.13.

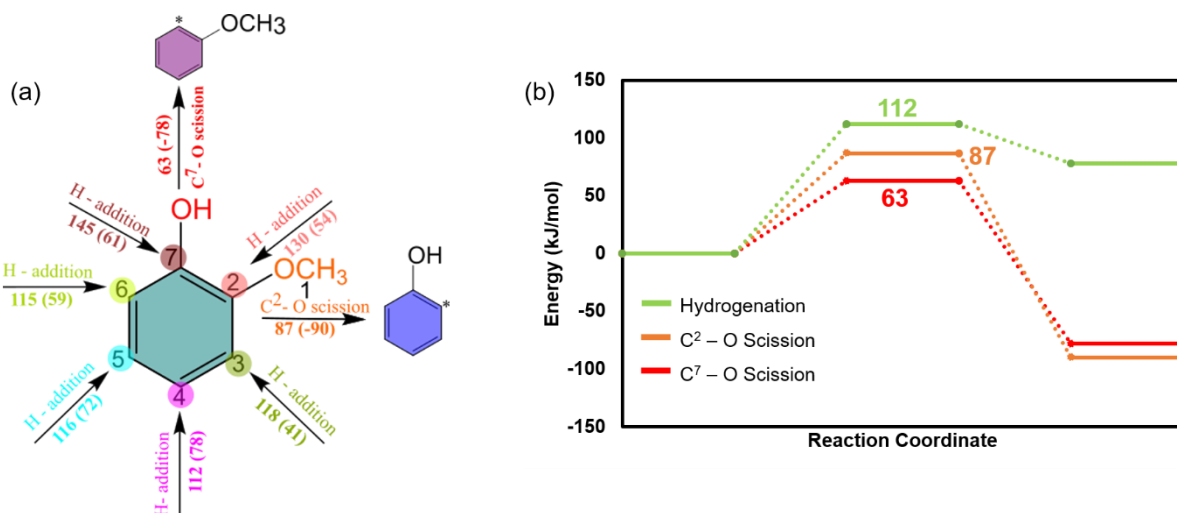


Figure 5.7 (a) Schematic illustrating possible reaction pathways for the first activation of guaiacol. The three considered pathways by which guaiacol can activate are shown: C⁷-O scission, C²-O scission, C^{ring} hydrogenation. C^{ring} includes the carbon atoms of the benzene ring which are labelled as C²– C⁷. Free energy barriers and reaction free energies (in parenthesis) at 298 K and 1 bar are shown above the arrow for each pathway in gas phase. (b) Comparison of free energy profiles on Ru (101) surface at room temperature and 1 bar for 3 considered pathways: C²-O scission (in orange), C⁷- O scission (in red), and direct C^{ring} hydrogenation (in green). Free energy barriers are also shown in orange, red and green color for the respective pathways in kJ/mol.

Similar to guaiacol, we compared activation barriers and reaction energies for the first activation mechanisms for phenol too. It includes (i) direct C¹ – O scission, and (ii) C^{ring}–hydrogenation. However, in this case, ring hydrogenation can initiate at five possible sites by the attack of hydrogen at different carbon atoms of the aromatic ring. The comparison is shown in Figure 5.8. Similar trend in the activation barriers was observed in the case of phenol. Direct dissociation of the C–O bond is kinetically more facile here too, with a free energy barrier of 63 kJ/mol, compared to the lowest ring hydrogenation barrier calculated to be at C⁵ carbon, which was 107 kJ/mol. Similar energy barrier (104 kJ/mol) for first hydrogenation step of phenol was reported on Ru (0001) surface.³⁰¹ Moreover, the hydrogenation barriers at other carbon atoms are much higher, i.e., 146, 124, 110, and 118 kJ/mol at C², C³, C⁴, and C⁶ carbons, respectively, as shown in Figure 5.8a. We also explored the subsequent hydrogenation steps required to reach cyclohexanol from phenol. Results indicate that even the sequential hydrogenation steps show relatively higher kinetic barriers with the values of 102, 101, 99, 80, and 96 kJ/mol at C⁴, C³, C², C⁶, and C¹ carbon atoms, respectively (presented and discussed later in Figure 5.13).

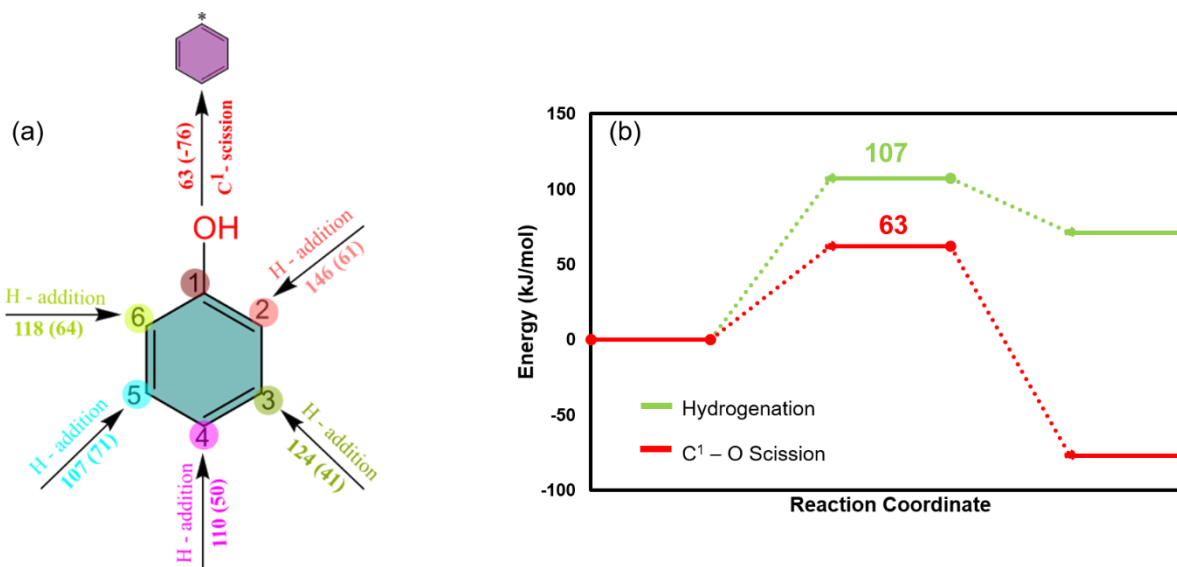


Figure 5.8 (a) Schematic illustrating possible reaction pathways for the first activation of phenol. The two considered pathways by which phenol can activate are shown: C¹-O scission, and C^{ring} hydrogenation. C^{ring} includes the carbon atoms of the benzene ring which are labelled as C¹-C⁶. Free energy barriers and reaction free energies (in parenthesis) at 298 K and 1 bar are shown above the arrow for each pathway in the gas phase. (b) Comparison of free energy profiles on Ru (101) surface at room temperature and 1 bar for 2 considered pathways: C¹-O scission (in red), and direct C^{ring} hydrogenation at C³ carbon (shown in green). Free energy barriers are also shown in red and green color for the respective pathways in kJ/mol.

Overall, it can be noted that HDO pathway is facile on Ru (101), in comparison to the hydrogenation pathway for both guaiacol and phenol, in the absence of water, which is in line with the earlier reported studies in gas phase.¹⁹⁸ However, it does not agree with the experimental observation where ring saturated products were observed as major products in the condensed aqueous phase, i.e., 2-methoxy cyclohexanol, and cyclohexanol, correspondingly for guaiacol and phenol. This suggests the vital role of solvent in reversing the product distribution/selectivity and consequently, ring hydrogenation becoming a more feasible pathway. Moreover, isotope labelling experiments with D₂O confirmed the participation of water in the selective hydrogenation (as presented in section 3.3). Results confirmed that hydrogen involved in the hydrogenation of aromatic ring is partly coming from water. As a result, we investigated the same set of reactions for guaiacol and phenol in the presence of water, to investigate the role of the solvent.

Studies in the literature have pointed out that water molecules exist on the surface of Ru (0001) in their intact state or in a partially dissociated form.^{119-123,302} According to the reported studies, water can form hexamer rings of almost flat molecules by a network of hydrogen bonds (HBs), where each molecule donates two hydrogen bonds and accepts one, while interacting with the metal

substrate through an O-lone pair. Partially dissociated water on Ru (0001) is composed of intact water molecules, hydroxyl fragments and hydrogen atoms that form elongated stripes of 2.5 to 6 ruthenium lattice distances wide with a honeycomb interior structure.¹²³ A recent study by Maier et al. also unveiled the mechanism of water partial dissociation on Ru (0001) surface, and it was demonstrated that, instead of purely physisorbed state, water prefers to be present as a mixture of intact water molecules and dissociated hydroxyl fragments and hydrogen atoms on the Ru surface.³⁰²

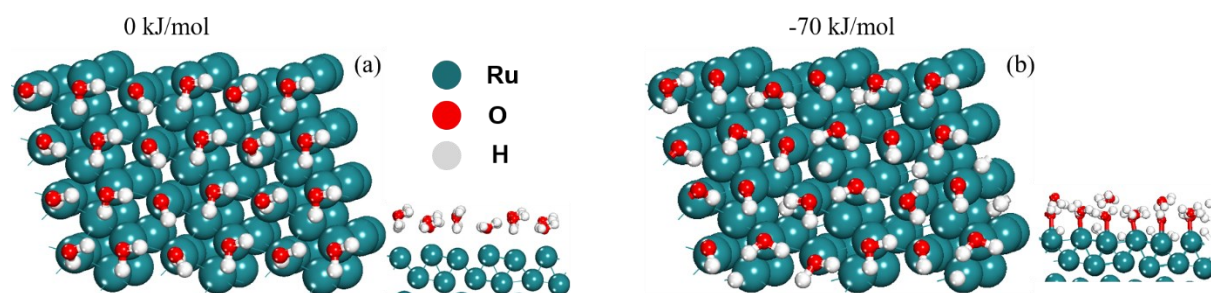


Figure 5.9 (a) Top and side view of the optimized geometry of 18 intact water molecules on the Ru (101) surface (b) Top view and side view of the optimized geometry of 2:1 water-hydroxyl and H* fragments mixture on the Ru (101) surface. The atoms in the adsorbed water molecules are represented by white, red spheres for H, O, and Ru atoms are shown in green spheres, respectively. Relative energies are also reported.

To determine the relative stability of intact and partially dissociated water molecules on Ru (101) surface, we compared five configurations with different ratios of intact and partially dissociated water molecules on the Ru surface. We selected 18 water molecules as it is the optimum number of water molecules to occupy all the active sites on the catalyst's surface. In the partially dissociated case, we considered 1:1, 2:1, 3:1, 17:1 mixtures of intact and partially dissociated water molecules i.e., hydroxyl fragments and hydrogen atoms (OH, H₂O, and H). On comparing the energies of all optimized configurations (refer to Figure E.24), the partially dissociated water with a ratio of 2:1 is found to be the most stable on the Ru (101) surface by 70 kJ/mol, as shown in Figure 5.9. It agrees with the previously reported studies confirming that water tends to dissociate partially on the Ru catalyst surface with optimal ratio of intact to partially dissociated water molecules in range of 2 – 2.5:1.³⁰⁰ In order to understand the impact of solvent molecules on the reaction mechanism, we adopted this configuration in which water is present in partially dissociated form as an interfacial water on the Ru catalyst's surface with ratio of 2:1.

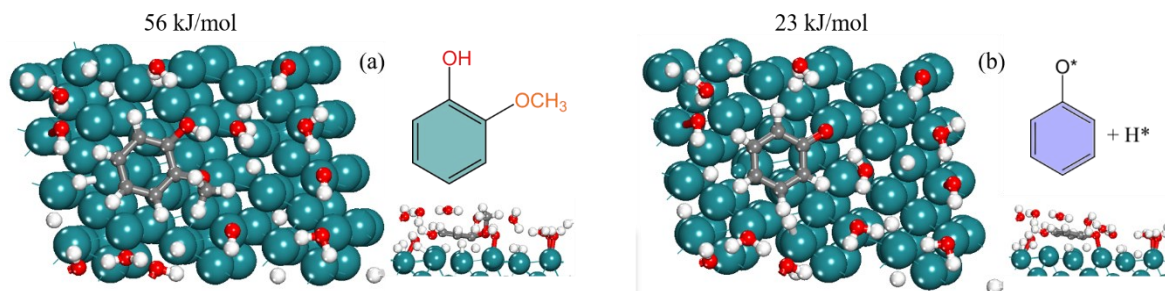


Figure 5.10 Optimized geometries and corresponding free energies of guaiacol and phenol adsorption on the Ru (101) surface in the presence of co-adsorbed partially dissociated water molecules (a) Top view and side view guaiacol adsorption in $\eta^2(\text{C}-\text{O})$ configuration, (b) Top view and side view phenol adsorption in $\eta^2(\text{C}-\text{O})$ configuration. The atoms in the adsorbed guaiacol and phenol is represented by white, red, and grey spheres for H, O, and C, respectively and Ru atoms are shown in green color.

We determine the adsorption characteristics of the adsorbates, guaiacol and phenol, in the presence of partially dissociated water molecules on Ru surface. To incorporate these adsorbates on the surface along with water molecules, we eliminated six water molecules, leaving only twelve, of which eight were intact and four were dissociated into OH and H fragments to keep the ratio of intact to dissociated water molecules to be 2:1. The most stable adsorption configurations of both guaiacol and phenol are shown in Figure 5.10. Interestingly, the most stable adsorption configurations of guaiacol and phenol remain the same as those in the absence of water i.e., $\eta^2(\text{C}-\text{O})$. However, the adsorption free energies decrease to 56, and 23 kJ/mol (gas phase: 63, and 49 kJ/mol) for guaiacol and phenol, respectively. It can be attributed to hydrogen bonding with partially dissociated water molecules that better stabilizes the adsorbates, resulting in stronger adsorption. Additionally, OH fragments assist in activating the O–H bond of the hydroxyl functional group present in phenol as dissociative chemisorption is observed in the case of phenol, where $[(\text{CH})_5\text{CO}^*]$ is formed when the O–H bond of the hydroxyl group spontaneously dissociates and creates water after bonding to the closest adsorbed OH* species. It can lead towards the formation of cyclohexanone after ring saturation which aligns with the experimental observations as cyclohexanone was observed as the key intermediate. Similar to the gas phase, same set of reactions were simulated in the presence of water, to confirm the direct participation of solvent molecules in the reaction mechanism.

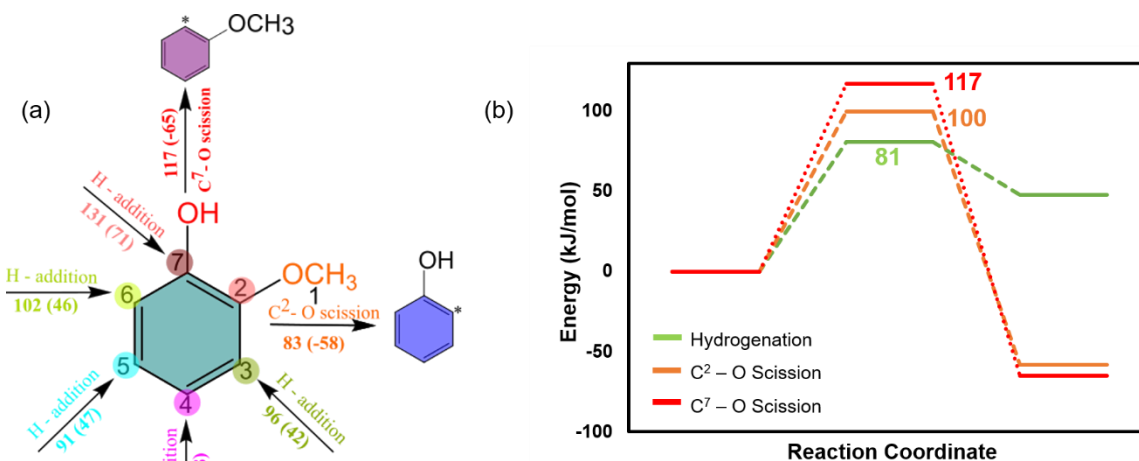


Figure 5.11 (a) Schematic illustrating possible reaction pathways for the first activation of guaiacol in the presence of water. The three considered pathways by which guaiacol can activate are shown: C⁷-O scission, C²-O scission, C^{ring} hydrogenation. C^{ring} includes the carbon atoms of the aromatic ring which are labelled as C²- C⁶. Free energy barriers and reaction free energies (in parenthesis) at 298 K and 1 bar are shown above the arrow for each pathway. (b) Comparison of free energy profiles on Ru (101) surface in presence of partially dissociated water molecules at room temperature and 1 bar for 3 considered pathways: C²-O scission (in orange), C⁷-O scission (in red), and direct C^{ring} hydrogenation (in green). Free energy barriers are also shown in red, orange and green color for the respective pathways in kJ/mol.

For guaiacol, we investigated the same pathways which were considered in the absence of water molecules for its first activation on Ru (101) surface, including six possibilities at different carbon atoms of the aromatic ring for hydrogenation (Figure 5.11). Results for the first activation reveal that hydrodeoxygenation pathways via C^{2/7}-O cleavage exhibit higher kinetic barriers of 100, and 117 kJ/mol for demethoxylation (C²-O scission), and dehydroxylation (C⁷-O scission), respectively. In the hydrogenation pathway, the lowest activation barrier among all the six possibilities was observed to be at C⁴ carbon atom of 81 kJ/mol. The hydrogenation barriers at other carbon atoms are calculated to be 96, 91, 102, and 131 kJ/mol for C³, C⁵, C⁶, and C⁷, respectively. Overall, demethoxylation and ring hydrogenation are two kinetically competitive pathways with similar barriers of 100 and 81 kJ/mol. It explains the experimental product distribution for guaiacol where a mixture of cyclohexanol and 2-methoxycyclohexanol was obtained (Table E.1). The detailed comparison of guaiacol first activation with and without the presence of water on the Ru surface is later shown and discussed in Figure 5.13. The point to be noted is that activation barriers for dehydroxylation have increased while those for direct hydrogenation decreased, making ring hydrogenation kinetically more facile in the presence of

water. Reduction in direct hydrogenation barrier at C⁴ carbon atom can be explained by the stabilization of the hydrogen atom by Ru surface atom in the transition state (shown in Figure E.18e). However, reaction free energy almost remains the same for hydrogenation case in the absence and presence of water, as addition reaction of hydrogen on aromatic ring breaks the resonance in the ring, resulting in reduced stability. Increase in deoxygenation barriers is due to the improved stabilization of the co-adsorbed guaiacol (the reactant) in the presence of water due to the hydrogen bonding network. The distances of dissociated OH fragments and intact water molecules from the oxygen atom of the methoxy group lie in the range of 1.8–2.3 Å, which confirms hydrogen bonding. This suggests that ring hydrogenation would initiate the reaction and will result in ring-saturated products. However, because the first activation step may not be the rate-determining step, evaluating Ru selectivity for any of these products would need investigating subsequent reaction steps. A systematic and comprehensive reaction network for both model compounds, in the absence and presence of water is shown in Figure 5.13. Notably, subsequent hydrogenation stages involving the addition of 2nd, 3rd, 4th, 5th, and 6th hydrogen to the aromatic ring at C⁵, C³, C², C⁶, and C⁷ exhibit considerably lower barriers with values of 75, 56, 56, 107, and 103 kJ/mol, respectively in comparison to the corresponding barriers observed in the absence of water for guaiacol (93, 110, 86, 97, and 116 kJ/mol). It validates that ring hydrogenation becomes kinetically more facile in the presence of water, in contrast to the gas phase, where hydrodeoxygenation was more favorable. Although, from a thermodynamic point of view, C²–O dissociation happens to be 116 kJ/mol more exergonic than the first step in hydrogenation pathway. It is ascribed to the hydrogen addition to the aromatic ring, which would break the stable delocalized electronic structure in the cyclic aromatic ring. Once the aromatic ring's stability is disturbed, subsequent hydrogenation steps become thermodynamically favorable as well, especially for the 2nd, 4th, and 6th hydrogenation steps as it gets reduced to (CH)₂(CH₂)₂(COCH₃)CO* then to (CH₂)₄(COCH₃)CO* and finally to the 2-methoxy cyclohexanol [(CH₂)₄(CHOCH₃)COH] product, respectively which are relatively more stable. Similar trend was also observed in the gas phase that with successive hydrogenation steps, pathway becomes thermodynamically more feasible.

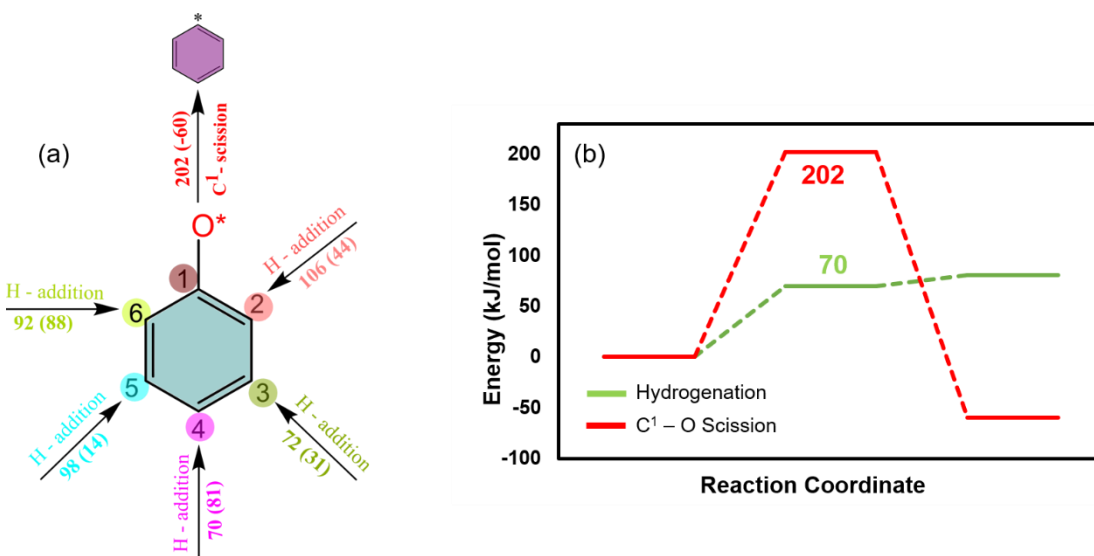


Figure 5.12 (a) Schematic illustrating possible reaction pathways for the first activation of phenol in the presence of water. The two considered pathways by which phenol can activate are shown: C¹-O scission, and C^{ring} hydrogenation. C^{ring} includes the carbon atoms of the benzene ring which are labelled as C¹-C⁶. Free energy barriers and reaction free energies (in parenthesis) at 298 K and 1 bar are shown above the arrow for each pathway. (b) Comparison of free energy profiles on Ru (101) surface in the presence of partially dissociated water molecules at room temperature and 1 bar for 2 considered pathways: C¹-O scission (in red), and direct C^{ring} hydrogenation (in green). Free energy barriers are also shown in red and green color for the respective pathways in kJ/mol.

Similar sets of reactions were simulated for phenol in the presence of partially dissociated water molecules (Figure 5.12). As mentioned earlier, the O-H bond of the hydroxyl group dissociates spontaneously during dissociative chemisorption, suggesting the formation of cyclohexanone after hydrogenation. It was also observed in experiments that mixture of both cyclohexanol and cyclohexanone was formed in the initial period of the reaction. On comparing the HDO and hydrogenation pathway, the free energy barrier for C¹-O dissociation is calculated to be 202 kJ/mol in comparison to merely 70 kJ/mol for the hydrogenation at C⁴ carbon which was calculated to be the lowest among the possibilities for first activation. Other possible first hydrogenation activation pathways showed higher barriers of 106, 72, 98, and 92 kJ/mol at C², C³, C⁵, and C⁶, respectively. Moreover, the hydrodeoxygenation barrier is found to be increased to 202 kJ/mol from 63 kJ/mol in the gas phase. It could be the consequence of keto-enol tautomerization (of phenol to generate cyclohexadienone of the (CH)₅CO* resulting from the breaking of the O-H bond, making the C-O bond stronger and shorter as the C-O bond length decreased to 1.32 from 1.42 Å in the gas phase). Furthermore, reaction proceeds with subsequent stepwise hydrogenation of neighboring carbon atoms with the barriers of 63, 87, 67, 79, and 25 kJ/mol leading to the

formation of intermediate $(\text{CH}_2)_5\text{CHO}^*$. Finally, cyclohexanol formation takes place with an addition of hydrogen at the oxygen atom with a barrier of 128 kJ/mol and the reaction free energy of -45 kJ/mol, which confirms that it is thermodynamically feasible as well.

thermodynamically favoured on Ru surface in the presence of water, whereas, benzene, and anisole are kinetically and thermodynamically favoured in gas phase.

*Note – Deprotonation of phenol is only observed in the presence of water molecules.

The complete hydrogenation pathway of guaiacol and phenol, in the presence and absence of water, is shown in Figure 5.13. For guaiacol, it can be seen that the subsequent hydrogenation steps after the activation at C³ carbon also show relatively high barriers of 95, 102, 79, 97, and 103 kJ/mol for the hydrogenation at C⁴, C⁵, C⁶, C², and C⁷ respectively in comparison to C^{2/7}–O dissociation in the absence of water. It confirms that direct dissociations of C–O bonds in the case of guaiacol are more favorable on Ru (101) surface in the absence of water molecules. It is important to note that hydrogen solubility is very little in water under our operating conditions and hence it would limit the amount of hydrogen that might potentially adsorb on Ru and undergo dissociation. So, it is expected that H fragments from partially dissociated water would serve as a hydrogen source. Hence, the hydrogen participating in the hydrogenation processes of the aromatic ring would partially come from dissociated water molecules on the Ru surface. To investigate that, we calculated the free energy barrier for water dissociation on the Ru surface, and it was found to be 96 kJ/mol, and it gets reduced to 83 kJ/mol on hydrogen pre-covered Ru surface. Moreover, it's a thermoneutral step which suggests that it is thermodynamically feasible. This is in perfect agreement with the experimental results from the D₂O based isotope labeling tests. In accordance with the findings, the D atom in phenol was added from deuterated water, as illustrated in Figure 5.6, and not necessarily only from H₂. Moreover, a slightly higher barrier of H₂O dissociation than the first hydrogenation step also explains the time-dependent reaction profile where an induction period was observed for the activation of catalyst for hydrogenation. As it can be seen in Figure 5.4(a), selectivity of cyclohexanol or cyclohexanone starts increasing from 0 to 81% and 19%, respectively after 15 minutes from the start of the reaction. It indicates that hydrogenation starts after water dissociation on Ru surface and then the dissociated hydrogen gets added to the one of the carbon atoms of the aromatic ring. Demir et al. provided insights on the effects of the presence of water in acetone hydrogenation on Ru/C catalyst.³⁰³ They demonstrated that the presence of water molecules on the surface of oxophilic metal catalysts reduces the energy barrier for acetone hydrogenation, resulting in higher rates of acetone hydrogenation. Similar effect was observed in the case of butanal hydrogenation as well in which water promotes the hydrogenation of two steps in the alkoxy pathway.³⁰⁴ On the contrary, dissociation of H₂ will initiate the reaction in the absence

of water molecules, but it requires high hydrogen pressure for partial hydrogenation which perfectly aligns with the literature.^{305–307} Fan et al. investigated the elementary hydrogenation reactions on benzene and resulting important intermediates under different H coverage conditions.³⁰⁸ It was reported that high hydrogen coverage reduces the reaction barriers to 32–114 kJ/mol from 68–97 kJ/mol at low hydrogen coverage. Moreover, hydrogenation under low coverage was found to be endergonic by more than 200 kJ/mol in comparison to high coverage of hydrogen.

From the above discussion, it is evident that Ru catalyst prefers the selective hydrogenation route in the presence of water as water also acts as a hydrogen source making the hydrogenation feasible at mild conditions (room temperature and 1 bar H₂ pressure) which is validated through isotope-labelling experiments. Additionally, water enhances the adsorption of substrate on the Ru catalyst's surface by establishing hydrogen bonding between oxygenated functional groups (-OH and -OCH₃) and water/OH fragments. These OH fragments generated as a result of partial dissociation of water over Ru surface activate the O-H bond of the hydroxyl group present in phenol and H atom hops on to the OH fragment resulting in the formation of water and (CH)₅CO*. As a result, the C–O bond acquires a partial double bond character through keto-enol tautomerization. This renders the cleavage of the C–O bond challenging, with the free energy barrier increasing to 202 kJ/mol. Hence, the hydrogenation is favoured over direct dissociation in the presence of water. The isotope-labelling studies revealed partly deuterated cyclohexanol suggesting that water is participating as a reactant in reaction. It is likely that hydrogen fragments (H*) from water are consumed during the hydrogenation reaction. Hence, the equilibrium between intact and dissociated water molecules is disturbed. We hypothesize that these H* are replenished by the external hydrogen, converting the resulting OH fragments back to H₂O to maintain the ratio of intact water molecules to partially dissociated water molecules to be 2:1 on Ru. [85] To validate this, we compared the reaction energy of water formation (OH* + H* = H₂O*) between two configurations with 1:1 and 2:1 ratios of intact and partially dissociated water molecules. In the latter configuration, this reaction is 67 kJ/mol more exergonic which confirms the thermodynamic feasibility of water formation once the ratio of intact and partially dissociated water molecules is reduced below 2:1. One additional observation in the experiments was that there is no conversion in the absence of external hydrogen supply which indicate that water can't act as a hydrogen source alone. It can be explained by the fact that for Ru catalysts to remain active towards selective

hydrogenation, more water molecules need to dissociate to produce H*. Consequently, more OH* fragments will also form, and these species may contaminate the Ru surface by occupying the active sites and catalyst will get deactivated. If this is the case, then, either Ru surface would get oxidized, or the pH of the solvent medium would increase due to the presence of OH* fragments. However, in experiments, neither the pH is found to be increasing nor there is a very significant change in Ru²⁺ species on the surface (Figure E.7b) which further confirms that resulting OH fragments turn back to water to maintain the optimal ratio of 2:1 without increasing the pH of the system by dissolving in the water or oxidizing the Ru surface. In this way, solvent doesn't get sacrificed and external hydrogen complements the process by regenerating the solvent back. The solvent acts as a shuttler (via dissociation and regeneration, unlike just proton shuttling) of hydrogen. Although, external hydrogen is provided sufficiently enough to replenish the H* from water, water acting as an H-donor makes the selective hydrogenation feasible at room temperature and 1 bar pressure.

5.4 Conclusions

In this work, we employed experiments and theoretical DFT calculations to investigate the selective hydrogenation of lignin-derived aromatics over a stable Ru catalyst, under mild conditions (room temperature and 1 bar H₂ pressure), using water as the solvent. Under optimum reaction conditions, the catalyst showed complete conversion of phenol with a high yield (95%) towards cyclohexanol in 75 minutes and guaiacol conversion was completed in 6 h with 79% yield of 2-methoxy cyclohexanol. We revealed how selectivity flips from hydrodeoxygenation (HDO) in gas phase to hydrogenation in aqueous phase. Furthermore, DFT calculations reveal that water tends to partially dissociate on the Ru surface and the resulting OH fragments assist in activating the O–H bond of the hydroxyl functional group present in both, guaiacol and phenol. Consequently, free energy barriers for HDO pathway for guaiacol and phenol (C-OH dissociation) increases to 117 and 202 kJ/mol, respectively in the presence of water in comparison to 63 and 63 kJ/mol in the absence of water. Moreover, the energy barriers of initial hydrogenation steps reduce to 70, 87, 67 kJ/mol from 107, 102, and 101 kJ/mol. We also manifested that dissociated hydrogen from water is involved in the step wise hydrogenation reactions resulting in hydrogenation route being kinetically more facile. Isotope labelling experiments with D₂O confirmed water's participation in the reaction. As the dissociated hydrogen from the water is utilized, external

hydrogen combines with the leftover OH* fragments on the catalyst's surface to regenerate the solvent. In this way, solvent acts as a shuttler of hydrogen and ratio of intact to dissociated water molecules is maintained at 2:1 as well without contaminating the Ru surface. This catalytic system also showed high activity for the hydrogenation of other lignin-derived compounds such as cinnamyl alcohol, benzyl alcohol, biphenyl ether, benzyl phenyl ether, diphenyl methane and eugenol.

Chapter 6: Conclusions and Outlook

Chapter 2 - 4 of this thesis focus on the transition metal carbides (TMCs), particularly molybdenum carbide (Mo_2C), as a cheaper and suitable alternative to noble metals and how we can improve their catalytic performance for hydrodeoxygenation (HDO) of bio-oil in the vapor phase as it is considered a renewable feedstock to produce energy, fuels, chemicals and carbon materials. However, it is a multicomponent mixture of a large number of oxygenated compounds derived from lignocellulosic biomass feedstocks. In this context, we (i) identified stable and precise atomic structure of tungsten-doped molybdenum carbide (MoWC) catalyst, (ii) established the reaction mechanism for guaiacol HDO on MoWC and its comparison to its monometallic carbide counterpart Mo_2C , (iii) investigated MoWC for representative bio-oil compounds derived from different components of biomass (cellulose, hemi-cellulose and lignin) and (iv) performed computational screening on Mo_2C -based bimetallic carbide catalysts using key reactions involved in HDO and proposed an active, selective and stable catalyst. Chapter 5 includes the solvent effects in HDO process and using a combined experimental and computational approach, the synergistic role of Ru catalysts and water solvent in selective hydrogenation of aromatics is elucidated which could be difficult from a standalone approach.

Doping Mo_2C with another metal can significantly enhance its activity and selectivity, but existing studies often use arbitrary models for the resulting bimetallic carbide, leading to questionable conclusions about their microstructure. To address this, we focused on W-doped Mo_2C and evaluated various model structures of the MoWC catalyst to determine the most stable arrangement of tungsten atoms in the mixed metal carbide. Furthermore, we investigated HDO performance of MoWC catalysts and compared with its monometallic counterpart Mo_2C . Major conclusions are as follows:

- The presence of metallic tungsten on MoWC facilitates the adsorption of guaiacol via the oxygen atom of the hydroxyl or methoxy functional group. As a result, direct deoxygenation of guaiacol on MoWC becomes facile with a very low barrier of 18, and 30 kJ/mol for demethoxylation and dehydroxylation steps, in comparison to 60, and 62 kJ/mol on Mo_2C .

- Surface intermediates like phenol, benzene would not preferentially ring hydrogenate on MoWC due to higher activation barriers, resulting into the formation of aromatic products with higher selectivity.
- MoWC catalyst widens up the gap between two key pathways i.e., hydrogenation (HYD) and direct deoxygenation (DDO) as it inhibits the formation of cycloalkenes and cycloalkanes. In comparison, Mo₂C showed competitive barriers for C – O cleavage (99 kJ/mol) and ring hydrogenation (123 kJ/mol) confirming both HYD and DDO pathways are competitive on Mo₂C resulting in a mixture of deoxygenated and ring saturated products.
- These findings validated the experimental data, which demonstrated higher selectivity for the DDO route on MoWC in contrast to low selectivity on Mo₂C.

This study emphasizes the importance of using both theory and experiments to comprehend the nature/morphology of the bimetallic carbide catalyst. According to the mechanistic findings of this work, metal carbides can be cheap and viable alternative to noble-metals for hydrodeoxygenation of oxygenated substances due to the existence of both acid-site and hydrogen-active site capabilities. Moreover, for the HDO process to work synergistically, optimization of both capabilities with the suitable dopants is essential, especially with high oxophilicity.

It is critical to assess how the proposed MoWC catalyst perform for components derived cellulose and hemi-cellulose fraction of biomass to perform effectively for the HDO of real bio-oil. Therefore, we investigated Mo₂C and MoWC carbide catalysts for their ability to hydrodeoxygenate biomass-derived bio-oil, using six key, representative components in bio-oil, namely, 5-HMF, Acetic acid, Eugenol, Levoglucosan (LGA), Methylglyoxal, Guaiacol and Vanillin. Critical findings from our density functional theory (DFT) calculations are as follows:

- For small oxygenates (acetic acid and Methyl glyoxal), single C – O bond dissociation is favorable on both Mo₂C, however, carbonyl (C = O) bond and C – C dissociation is competitive on Mo₂C. MoWC selectively cleaves C – O /C = O bonds keeping the number of carbon atoms intact.
- Similarly, MoWC displayed lower barrier for carbonyl C = O bond cleavage in 5-HMF as well favoring direct deoxygenation in comparison to Mo₂C which favors both hydrogenation and deoxygenation with competitive barriers indicating to formation of a mixture of alcohols and alkenes.

- For LGA, results indicate the formation of linear chain alkanes on MoWC as it favors both ring-opening reactions, however, Mo₂C shows competitive barriers of 68 kJ/mol for ring-opening in comparison to dehydroxylation (47 kJ/mol) suggesting it might lead to the formation of partially deoxygenated tetrahydropyran as the major product.
- Lignin-derived constituents follow the same trend where MoWC significantly reduces the barrier for direct deoxygenation to only 18 kJ/mol, in comparison to Mo₂C (60 kJ/mol) and similar trend can be seen for Eugenol and Vanillin where C²/C⁷ – O cleavage is favorable, leading to aromatic products, whereas Mo₂C favors both hydrogenation and direct deoxygenation leading to a mixture of ring-saturated and aromatic products.

Overall, as a result of its enhanced activity and selectivity towards direct deoxygenation for all oxygenated constituents, MoWC could be an effective and efficient catalyst for the real bio-oil mixture suppressing H₂ consumption. This mechanistic study investigated a variety of different representative constituents of biooil on monometallic (Mo₂C) and bimetallic carbide (MoWC) surfaces to check the efficacy of these catalysts for a real bio-oil mixture unlike the reported literature where just one model compound is used.

Despite their enhanced HDO activity and selectivity, Mo₂C and MoWC face challenges with oxygen poisoning, leading to the need for higher H₂ pressures to maintain stability. Both catalysts have high barriers for water formation (260 kJ/mol for Mo₂C and 238 kJ/mol for MoWC), indicating susceptibility to poisoning. To address this,

- A comprehensive screening considering 45 Mo₂C-based bimetallic carbides from the Materials Project database, exploring various dopants, stoichiometries, and terminations is performed using three critical reactions (C–O dissociation, O* removal, and ring hydrogenation),
- we identified Fe₃Mo₃C (Mo-terminated), Mn₃Mo₃C (Mn-terminated), and Ni₃Mo₃C (Mo-terminated) as optimal catalysts for DDO: and triclinic Fe₁₁MoC₄ for selective hydrogenation (HYD).
- We developed a correlation between oxygen binding energy (OBE) and a parameter η , combining activity, selectivity, and stability, with an optimal OBE range of -100 to -200 kJ/mol for HDO.

This study aids in the rational design of bimetallic carbides and accelerates catalyst screening by improving understanding of metal-adsorbate interactions.

The low volatility of numerous biomass-derived compounds poses significant challenges for their vapor-phase transport; therefore, catalysts must be able to operate at moderately elevated temperatures in the presence of solvents. Heterogeneous catalysts can interact strongly with solvents which can alter their structure, activity, and selectivity due to interfacial adsorption and/or reactions with solvent molecules. For a rational catalyst design, it is imperative to identify, understand, and control the complex relationships between the structure of a catalyst and the behavior of its active sites in contact with the solvent molecules. In this context,

- we employed DFT calculations using experimental insights to investigate the selective hydrogenation of lignin-derived aromatics over a stable Ru catalyst, under mild conditions (room temperature and 1 bar H₂ pressure), using water as the solvent.
- We revealed how selectivity flips from DDO in gas phase to hydrogenation in aqueous phase.
- DFT calculations reveal that water tends to partially dissociate on the Ru surface with an optimal ratio of 2:1 of intact and partially dissociated water molecules and the resulting OH fragments assist in activating the O–H bond of the hydroxyl functional group present in both, guaiacol and phenol.
- Free energy barriers for HDO pathway for guaiacol and phenol (C-OH dissociation) increases to 117 and 202 kJ/mol, respectively in the presence of water in comparison to 63 and 63 kJ/mol in the absence of water.
- Isotope labelling experiments with D₂O confirmed water's participation in the reaction. The dissociated hydrogen from water participates in hydrogenation, regenerating the solvent and maintaining a 2:1 ratio of intact to dissociated water molecules.

This catalytic system also showed high activity for the hydrogenation of other lignin-derived compounds such as cinnamyl alcohol, benzyl alcohol, biphenyl ether, benzyl phenyl ether, diphenyl methane and eugenol. This study evaluated if these ring-saturated intermediates can be synthesized using an inexpensive and effective solvent like water at ambient conditions.

To sum up, this thesis presents how a precise microstructure of bimetallic carbide can be identified using a combination of DFT and experiments and their catalytic performance towards hydrodeoxygenation of bio-oil was also evaluated using multiple compounds derived from different components of biomass. A systematic and comprehensive computational screening of a vast database of bimetallic carbides was performed by which active, selective and stable catalysts

for DDO and also for HYD were identified. This thesis has also made significant contributions in developing solvent assisted, selective hydrogenation under extremely mild conditions. The various mechanisms of C-O bond activation and hydrogenation, the activation barriers for the dissociation along these pathways, factors influencing the activation barriers and measures of reactivity of the catalytic surfaces have been detailed.

Temperature and pressure effects plays a key role filling the gap between *in silico* models and the local catalyst environment, however, they are not reflected in this study. To incorporate these effects, microkinetic models such as mean-field microkinetic models (MF-MKMs) or kinetic Monte Carlo (KMC) simulations can be performed.^{309,310} In this method, (i) an initial catalyst is fed into the micro-kinetic model, (ii) reaction energetics are computed based on thermodynamics and kinetics and here the DFT data presented in this study can be used, (iii) Reactor mass-balance equations are written and model is solved to predict the corresponding catalyst performance.³¹¹ It can be used to compute reaction rates under realistic reaction conditions. With the advancement of computational power and recourses, novel schemes employing Machine learning (ML) tools have been developed which can capture the structure-property relationship of a catalyst and also predict the activity, selectivity and stability of catalysts with a much lower cost.³¹²⁻³¹⁴ Other future research directions from this thesis include (i) investigation of a mixture of model compounds on the screened Fe₃Mo₃C with Mo termination (Fe_{3B}) catalyst to understand the effect and interaction of these molecules, (ii) performing microkinetic analysis for HDO reactions on Fe_{3B} for predicting the reaction mechanism, coverage, and conversions under reaction conditions, (iii) synthesize and experimentally test the novel Fe_{3B} catalyst for DDO reactions, and (iv) investigate the solvents effects on metal carbides.

Bibliography

- (1) Mortensen, P. M.; Grunwaldt, J. D.; Jensen, P. A.; Knudsen, K. G.; Jensen, A. D. A Review of Catalytic Upgrading of Bio-Oil to Engine Fuels. *Applied Catalysis A: General*. 2011. <https://doi.org/10.1016/j.apcata.2011.08.046>.
- (2) Ali, A. A. M.; Mustafa, M. A.; Yassin, K. E. A Techno-Economic Evaluation of Bio-Oil Co-Processing within a Petroleum Refinery. *Biofuels* **2021**, *12* (6), 645–653. <https://doi.org/10.1080/17597269.2018.1519758>.
- (3) Maity, S. K. Opportunities, Recent Trends and Challenges of Integrated Biorefinery: Part I. *Renew. Sustain. Energy Rev.* **2015**, *43*, 1427–1445. <https://doi.org/10.1016/j.rser.2014.11.092>.
- (4) Martin, M. A. First Generation Biofuels Compete. *N. Biotechnol.* **2010**, *27* (5), 596–608. <https://doi.org/10.1016/j.nbt.2010.06.010>.
- (5) Abbaszaadeh, A.; Ghobadian, B.; Omidkhah, M. R.; Najafi, G. Current Biodiesel Production Technologies: A Comparative Review. *Energy Convers. Manag.* **2012**, *63*, 138–148. <https://doi.org/10.1016/j.enconman.2012.02.027>.
- (6) Valentine, J.; Clifton-Brown, J.; Hastings, A.; Robson, P.; Allison, G.; Smith, P. Food vs. Fuel: The Use of Land for Lignocellulosic “next Generation” Energy Crops That Minimize Competition with Primary Food Production. *GCB Bioenergy* **2012**, *4* (1), 1–19. <https://doi.org/10.1111/j.1757-1707.2011.01111.x>.
- (7) Ambursa, M. M.; Juan, J. C.; Yahaya, Y.; Taufiq-Yap, Y. H.; Lin, Y. C.; Lee, H. V. A Review on Catalytic Hydrodeoxygenation of Lignin to Transportation Fuels by Using Nickel-Based Catalysts. *Renew. Sustain. Energy Rev.* **2021**, *138* (December 2020), 110667. <https://doi.org/10.1016/j.rser.2020.110667>.
- (8) Kumar, G.; Bakonyi, P.; Periyasamy, S.; Kim, S. H.; Nemestóthy, N.; Bélafi-Bakó, K. Lignocellulose Biohydrogen: Practical Challenges and Recent Progress. *Renewable and Sustainable Energy Reviews*. Elsevier Ltd 2015, pp 728–737. <https://doi.org/10.1016/j.rser.2015.01.042>.
- (9) U.S. Energy Information, a. Annual Energy Outlook 2015 with Projections to 2040. *Off. Integr. Int. Energy Anal.* **2015**, *1*, 1–244. [https://doi.org/DOE/EIA-0383\(2013\)](https://doi.org/DOE/EIA-0383(2013)).
- (10) EIA, U. S. E. I. A. Appendix G-Conversion Factors - AEO 2016. **2016**, No. February, 32416.
- (11) Natural Gas: A Primer | Natural Resources Canada <https://www.nrcan.gc.ca/energy/energy-sources-distribution/natural-gas/natural-gas-primer/5641> (accessed 2020 -08 -24).
- (12) Berndes, G.; Hoogwijk, M.; Van Den Broek, R. The Contribution of Biomass in the Future Global Energy Supply: A Review of 17 Studies. *Biomass and Bioenergy*. Elsevier Ltd July 1, 2003, pp 1–28. [https://doi.org/10.1016/S0961-9534\(02\)00185-X](https://doi.org/10.1016/S0961-9534(02)00185-X).

- (13) Bioenergy and Bioproducts | Natural Resources Canada <https://www.nrcan.gc.ca/our-natural-resources/forests-forestry/forest-fact-book/bioenergy-bioproducts/21686> (accessed 2020 -08 -24).
- (14) Anwar, Z.; Gulfraz, M.; Irshad, M. Agro-Industrial Lignocellulosic Biomass a Key to Unlock the Future Bio-Energy: A Brief Review. *J. Radiat. Res. Appl. Sci.* **2014**, *7* (2), 163–173. <https://doi.org/10.1016/j.jrras.2014.02.003>.
- (15) McKendry, P. Energy Production from Biomass (Part 2): Conversion Technologies. *Bioresour. Technol.* **2002**, *83* (1), 47–54. [https://doi.org/10.1016/S0960-8524\(01\)00119-5](https://doi.org/10.1016/S0960-8524(01)00119-5).
- (16) Sawatdeenarunat, C.; Surendra, K. C.; Takara, D.; Oechsner, H.; Khanal, S. K. Anaerobic Digestion of Lignocellulosic Biomass: Challenges and Opportunities. *Bioresource Technology*. Elsevier Ltd February 1, 2015, pp 178–186. <https://doi.org/10.1016/j.biortech.2014.09.103>.
- (17) Fao. *FAO Forestry Department Wood Energy Programme FOOD AND AGRICULTURE ORGANIZATION OF THE UNITED NATIONS UNIFIED BIOENERGY TERMINOLOGY UBET*; 2004.
- (18) Anex, R. P.; Aden, A.; Kazi, F. K.; Fortman, J.; Swanson, R. M.; Wright, M. M.; Satrio, J. A.; Brown, R. C.; Daugaard, D. E.; Platon, A.; Kothandaraman, G.; Hsu, D. D.; Dutta, A. Techno-Economic Comparison of Biomass-to-Transportation Fuels via Pyrolysis, Gasification, and Biochemical Pathways. *Fuel* **2010**, *89* (SUPPL. 1), S29–S35. <https://doi.org/10.1016/j.fuel.2010.07.015>.
- (19) Czernik, S.; Bridgwater, A. V. Overview of Applications of Biomass Fast Pyrolysis Oil. *Energy and Fuels* **2004**, *18* (2), 590–598. <https://doi.org/10.1021/ef034067u>.
- (20) Bridgwater, T. Biomass for Energy. *Journal of the Science of Food and Agriculture*. John Wiley & Sons, Ltd September 12, 2006, pp 1755–1768. <https://doi.org/10.1002/jsfa.2605>.
- (21) Demirbas, A.; Arin, G. Energy Sources An Overview of Biomass Pyrolysis. *An Overv. Biomass Pyrolysis, Energy Sources* **2002**, *24* (5), 471–482. <https://doi.org/10.1080/00908310252889979>.
- (22) Ross, A. B.; Biller, P.; Kubacki, M. L.; Li, H.; Lea-Langton, A.; Jones, J. M. Hydrothermal Processing of Microalgae Using Alkali and Organic Acids. *Fuel* **2010**, *89*, 2234–2243. <https://doi.org/10.1016/j.fuel.2010.01.025>.
- (23) Xiu, S.; Shahbazi, A. Bio-Oil Production and Upgrading Research: A Review. *Renewable and Sustainable Energy Reviews*. Pergamon September 1, 2012, pp 4406–4414. <https://doi.org/10.1016/j.rser.2012.04.028>.
- (24) Czernik, S.; Bridgwater, A. V. Overview of Applications of Biomass Fast Pyrolysis Oil. *Energy and Fuels* **2004**, *18* (2), 590–598. <https://doi.org/10.1021/ef034067u>.
- (25) Milne, T.; Agblevor, F.; Davis, M.; Deutch, S.; Johnson, D. A Review of the Chemical Composition of Fast-Pyrolysis Oils from Biomass. In *Developments in Thermochemical Biomass Conversion*; Springer Netherlands, 1997; pp 409–424. https://doi.org/10.1007/978-94-009-1559-6_32.

- (26) Branca, C.; Giudicianni, P.; Di Blasi, C. GC/MS Characterization of Liquids Generated from Low-Temperature Pyrolysis of Wood. *Ind. Eng. Chem. Res.* **2003**, *42* (14), 3190–3202. <https://doi.org/10.1021/ie030066d>.
- (27) Mullen, C.; fuels, A. B.-E. &; 2008, undefined. Chemical Composition of Bio-Oils Produced by Fast Pyrolysis of Two Energy Crops. *ACS Publ.* **2008**, *22* (3), 2104–2109. <https://doi.org/10.1021/ef700776w>.
- (28) Maggi, R.; Delmon, B. Characterization and Upgrading of Bio-Oils Produced by Rapid Thermal Processing. *Biomass and Bioenergy* **1994**, *7* (1–6), 245–249. [https://doi.org/10.1016/0961-9534\(94\)00062-X](https://doi.org/10.1016/0961-9534(94)00062-X).
- (29) Bridgwater, A. V. Upgrading Biomass Fast Pyrolysis Liquids. *Environ. Prog. Sustain. Energy* **2012**, *31* (2), 261–268. <https://doi.org/10.1002/ep.11635>.
- (30) Ruddy, D. A.; Schaidle, J. A.; Ferrell, J. R.; Wang, J.; Moens, L.; Hensley, J. E. *Recent Advances in Heterogeneous Catalysts for Bio-Oil Upgrading via “Ex Situ Catalytic Fast Pyrolysis”*: Catalyst Development through the Study of Model Compounds; 2014; Vol. 16. <https://doi.org/10.1039/c3gc41354c>.
- (31) Corma, A.; Huber, G. W.; Sauvanaud, L.; O’Connor, P. Processing Biomass-Derived Oxygenates in the Oil Refinery: Catalytic Cracking (FCC) Reaction Pathways and Role of Catalyst. *J. Catal.* **2007**, *247* (2), 307–327. <https://doi.org/10.1016/j.jcat.2007.01.023>.
- (32) Huber, G. W.; Iborra, S.; Corma, A. Synthesis of Transportation Fuels from Biomass: Chemistry, Catalysts, and Engineering. *Chemical Reviews*. American Chemical Society September 2006, pp 4044–4098. <https://doi.org/10.1021/cr068360d>.
- (33) Elliott, D.; EG Baker - US Patent 4, 795,841; 1989, undefined. *Process for Upgrading Biomass Pyrolyzates*.
- (34) Wang, H.; Male, J.; Wang, Y. Recent Advances in Hydrotreating of Pyrolysis Bio-Oil and Its Oxygen-Containing Model Compounds. *ACS Catal.* **2013**, *3* (5), 1047–1070. <https://doi.org/10.1021/cs400069z>.
- (35) Venderbosch, R. H.; Ardiyanti, A. R.; Wildschut, J.; Oasmaa, A.; Heeres, H. J. Stabilization of Biomass-Derived Pyrolysis Oils. *J. Chem. Technol. Biotechnol.* **2010**, *85* (5), 674–686. <https://doi.org/10.1002/jctb.2354>.
- (36) Levy, R. B.; Boudart, M. Platinum-like Behavior of Tungsten Carbide in Surface Catalysis. *Science (80-.)*. **1973**, *181* (4099), 547–549. <https://doi.org/10.1126/science.181.4099.547>.
- (37) Sullivan, M. M.; Held, J. T.; Bhan, A. Structure and Site Evolution of Molybdenum Carbide Catalysts upon Exposure to Oxygen. *J. Catal.* **2015**, *326*, 82–91. <https://doi.org/10.1016/j.jcat.2015.03.011>.
- (38) Bej, S. K.; Thompson, L. T. Acetone Condensation over Molybdenum Nitride and Carbide Catalysts. *Appl. Catal. A Gen.* **2004**, *264* (2), 141–150. <https://doi.org/10.1016/j.apcata.2003.12.051>.
- (39) Zhang, W.; Zhang, Y.; Zhao, L.; Wei, W. Catalytic Activities of NiMo Carbide Supported on SiO₂ for the Hydrodeoxygenation of Ethyl Benzoate, Acetone, and Acetaldehyde.

- Energy and Fuels* **2010**, *24* (3), 2052–2059. <https://doi.org/10.1021/ef901222z>.
- (40) Lin, Z.; Chen, R.; Chen, J. G. Oxygenates over Metal Carbides : From Model. **2018**, 2679–2696. <https://doi.org/10.1039/c8gc00239h>.
- (41) Choi, J.-S.; Zacher, A. H.; Wang, H.; Olarte, M. V.; Armstrong, B. L.; Meyer, H. M.; Soykal, I. I.; Schwartz, V. Molybdenum Carbides, Active and In Situ Regenerable Catalysts in Hydroprocessing of Fast Pyrolysis Bio-Oil. *Energy & Fuels* **2016**, *30* (6), 5016–5026. <https://doi.org/10.1021/acs.energyfuels.6b00937>.
- (42) Zacher, A. H.; Elliott, D. C.; Olarte, M. V.; Santosa, D. M.; Preto, F.; Iisa, K. Pyrolysis of Woody Residue Feedstocks: Upgrading of Bio-Oils from Mountain-Pine-Beetle-Killed Trees and Hog Fuel. *Energy & Fuels* **2014**, *28* (12), 7510–7516. <https://doi.org/10.1021/ef5017945>.
- (43) Remón, J.; Casales, M.; Gracia, J.; Callén, M. S.; Pinilla, J. L.; Suelves, I. Sustainable Production of Liquid Biofuels and Value-Added Platform Chemicals by Hydrodeoxygenation of Lignocellulosic Bio-Oil over a Carbon-Neutral Mo₂C/CNF Catalyst. *Chem. Eng. J.* **2021**, *405*. <https://doi.org/10.1016/j.cej.2020.126705>.
- (44) López, M.; Hernández, D.; Laverde, J.; Pérez, S.; López, D. Catalytic Upgrading of Residual Biomass Derived Bio-Oil over Molybdenum Carbide. *Waste and Biomass Valorization* **2019**, *11* (6), 2849–2856. <https://doi.org/10.1007/s12649-019-00586-0>.
- (45) Ren, H.; Yu, W.; Saliccioli, M.; Chen, Y.; Huang, Y.; Xiong, K.; Vlachos, D. G.; Chen, J. G. Selective Hydrodeoxygenation of Biomass-Derived Oxygenates to Unsaturated Hydrocarbons Using Molybdenum Carbide Catalysts. *ChemSusChem* **2013**, *6* (5), 798–801. <https://doi.org/10.1002/cssc.201200991>.
- (46) Schaidle, J. A.; Blackburn, J.; Farberow, C. A.; Nash, C.; Steirer, K. X.; Clark, J.; Robichaud, D. J.; Ruddy, D. A. Experimental and Computational Investigation of Acetic Acid Deoxygenation over Oxophilic Molybdenum Carbide: Surface Chemistry and Active Site Identity. **2016**. <https://doi.org/10.1021/acscatal.5b01930>.
- (47) Ren, H.; Chen, Y.; Huang, Y.; Deng, W.; Vlachos, D. G.; Chen, J. G. Tungsten Carbides as Selective Deoxygenation Catalysts: Experimental and Computational Studies of Converting C₃ Oxygenates to Propene. *Green Chem.* **2014**, *16* (2), 761–769. <https://doi.org/10.1039/c3gc41256c>.
- (48) Baddour, F. G.; Nash, C. P.; Schaidle, J. A.; Ruddy, D. A. Synthesis of Alpha-MoC_{1-x} Nanoparticles with a Surface-Modified SBA-15 Hard Template: Determination of Structure-Function Relationships in Acetic Acid Deoxygenation. *Angew Chem Int Ed Engl* **2016**, *55* (31), 9026–9029. <https://doi.org/10.1002/anie.201602878>.
- (49) Martínez, B.; Viñes, F.; McBreen, P. H.; Illas, F. Insights on Alkylidene Formation on Mo₂C: A Potential Overlap between Direct Deoxygenation and Olefin Metathesis. *J. Catal.* **2021**, *393*, 381–389. <https://doi.org/10.1016/j.jcat.2020.11.037>.
- (50) Liu, P.; Rodriguez, J. A. Water-Gas-Shift Reaction on Molybdenum Carbide Surfaces: Essential Role of the Oxycarbide. *J. Phys. Chem. B* **2006**, *110* (39), 19418–19425. <https://doi.org/10.1021/JP0621629>.

- (51) Lee, W. S.; Kumar, A.; Wang, Z.; Bhan, A. Chemical Titration and Transient Kinetic Studies of Site Requirements in Mo₂C-Catalyzed Vapor Phase Anisole Hydrodeoxygenation. *ACS Catal.* **2015**, *5* (7), 4104–4114. <https://doi.org/10.1021/acscatal.5b00713>.
- (52) Liu, S.; Wang, H.; Kim, C. S.; Smith, K. J. Stability of Mo₂C/Carbon Catalysts during Dibenzofuran Hydrodeoxygenation. *Appl. Catal. A Gen.* **2020**, *600*, 117628.
- (53) Stottlemeyer, A. L.; Kelly, T. G.; Meng, Q.; Chen, J. G. Reactions of Oxygen-Containing Molecules on Transition Metal Carbides: Surface Science Insight into Potential Applications in Catalysis and Electrocatalysis. *Surf. Sci. Rep.* **2012**, *67* (9–10), 201–232.
- (54) Puello-Polo, E.; Brito, J. L. Effect of the Type of Precursor and the Synthesis Method on Thiophene Hydrodesulfurization Activity of Activated Carbon Supported Fe-Mo, Co-Mo and Ni-Mo Carbides. *J. Mol. Catal. A Chem.* **2008**, *281* (1), 85–92. <https://doi.org/https://doi.org/10.1016/j.molcata.2007.09.015>.
- (55) Xiao, T.; Wang, H.; York, A. P. E.; Williams, V. C.; Green, M. L. H. Preparation of Nickel–Tungsten Bimetallic Carbide Catalysts. *J. Catal.* **2002**, *209* (2), 318–330. <https://doi.org/https://doi.org/10.1006/jcat.2002.3651>.
- (56) Al-Megren, H. A.; González-Cortés, S. L.; Xiao, T.; Green, M. L. H. A Comparative Study of the Catalytic Performance of Co-Mo and Co(Ni)-W Carbide Catalysts in the Hydrodenitrogenation (HDN) Reaction of Pyridine. *Appl. Catal. A Gen.* **2007**, *329*, 36–45. <https://doi.org/10.1016/j.apcata.2007.06.013>.
- (57) Baddour, F. G.; Witte, V. A.; Nash, C. P.; Griffin, M. B.; Ruddy, D. A.; Schaidle, J. A. Late-Transition-Metal-Modified β -Mo₂C Catalysts for Enhanced Hydrogenation during Guaiacol Deoxygenation. *ACS Sustain. Chem. Eng.* **2017**, *5* (12), 11433–11439. <https://doi.org/10.1021/acssuschemeng.7b02544>.
- (58) Yu, C. C.; Ramanathan, S.; Dhandapani, B.; Chen, J. G.; Oyama, S. T. Bimetallic Nb- Mo Carbide Hydroprocessing Catalysts: Synthesis, Characterization, and Activity Studies. *J. Phys. Chem. B* **1997**, *101* (4), 512–518.
- (59) Zhang, W.; Zhang, Y.; Zhao, L.; Wei, W. Catalytic Activities of NiMo Carbide Supported on SiO₂ for the Hydrodeoxygenation of Ethyl Benzoate, Acetone, and Acetaldehyde. *Energy and Fuels* **2010**, *24* (3), 2052–2059. <https://doi.org/10.1021/ef901222z>.
- (60) Yu, W.; Barteau, M. A.; Chen, J. G. Glycolaldehyde as a Probe Molecule for Biomass Derivatives: Reaction of C–OH and C–O Functional Groups on Monolayer Ni Surfaces. *J. Am. Chem. Soc.* **2011**, *133* (50), 20528–20535.
- (61) Yu, W.; Mellinger, Z. J.; Barteau, M. A.; Chen, J. G. Comparison of Reaction Pathways of Ethylene Glycol, Acetaldehyde, and Acetic Acid on Tungsten Carbide and Ni-Modified Tungsten Carbide Surfaces. *J. Phys. Chem. C* **2012**, *116* (9), 5720–5729.
- (62) Han, Y.; Gholizadeh, M.; Tran, C. C.; Kaliaguine, S.; Li, C. Z.; Olarte, M.; Garcia-Perez, M. Hydrotreatment of Pyrolysis Bio-Oil: A Review. *Fuel Process. Technol.* **2019**, *195* (July). <https://doi.org/10.1016/j.fuproc.2019.106140>.
- (63) Lin, Z.; Wan, W.; Yao, S.; Chen, J. G. Cobalt-Modified Molybdenum Carbide as a Selective

- Catalyst for Hydrodeoxygenation of Furfural. *Appl. Catal. B Environ.* **2018**, *233*, 160–166. <https://doi.org/10.1016/J.APCATB.2018.03.113>.
- (64) Xiong, K.; Lee, W.-S.; Bhan, A.; Chen, J. G. Molybdenum Carbide as a Highly Selective Deoxygenation Catalyst for Converting Furfural to 2-Methylfuran. *ChemSusChem* **2014**, *7* (8), 2146–2149. <https://doi.org/10.1002/cssc.201402033>.
- (65) Shilov, I. N.; Smirnov, A. A.; Bulavchenko, O. A.; Yakovlev, V. A. Effect of Ni–Mo Carbide Catalyst Formation on Furfural Hydrogenation. *Catalysts* **2018**. <https://doi.org/10.3390/catal8110560>.
- (66) Bretzler, P.; Huber, M.; Nickl, S.; Köhler, K. Hydrogenation of Furfural by Noble Metal-Free Nickel Modified Tungsten Carbide Catalysts. *RSC Adv.* **2020**, *10* (46), 27323–27330. <https://doi.org/10.1039/d0ra02003f>.
- (67) Banerjee, A.; Mushrif, S. H. Reaction Pathways for the Deoxygenation of Biomass-Pyrolysis-Derived Bio-Oil on Ru: A DFT Study Using Furfural as a Model Compound. *ChemCatChem* **2017**, *9* (14), 2828–2838. <https://doi.org/10.1002/CCTC.201700036>.
- (68) Mironenko, A. V.; Gilkey, M. J.; Panagiotopoulou, P.; Facas, G.; Vlachos, D. G.; Xu, B. Ring Activation of Furanic Compounds on Ruthenium-Based Catalysts. *J. Phys. Chem. C* **2015**, *119* (11), 6075–6085.
- (69) Shi, Y.; Yang, Y.; Li, Y.-W.; Jiao, H. Mechanisms of Mo₂C (101)-Catalyzed Furfural Selective Hydrodeoxygenation to 2-Methylfuran from Computation. *ACS Catal.* **2016**, *6* (10), 6790–6803.
- (70) Ochoa, E.; Torres, D.; Moreira, R.; Pinilla, J. L.; Suelves, I. Carbon Nanofiber Supported Mo₂C Catalysts for Hydrodeoxygenation of Guaiacol: The Importance of the Carburization Process. *Appl. Catal. B Environ.* **2018**, *239*, 463–474. <https://doi.org/10.1016/j.apcatb.2018.08.043>.
- (71) Blanco, E.; Dongil, A. B.; Ghampson, I. T.; García-Fierro, J. L.; Escalona, N. Optimizing the Carburization Conditions of Supported Rhenium Carbide for Guaiacol Conversion. *Appl. Catal. A Gen.* **2021**, *623*. <https://doi.org/10.1016/j.apcata.2021.118267>.
- (72) Smirnov, A. A.; Geng, Z.; Khromova, S. A.; Zavarukhin, S. G.; Bulavchenko, O. A.; Saraev, A. A.; Kaichev, V. V.; Ermakov, D. Y.; Yakovlev, V. A. Nickel Molybdenum Carbides: Synthesis, Characterization, and Catalytic Activity in Hydrodeoxygenation of Anisole and Ethyl Caprate. *J. Catal.* **2017**, *354*, 61–77.
- (73) Cai, Z.; Wang, F.; Zhang, X.; Ahishakiye, R.; Xie, Y.; Shen, Y. Selective Hydrodeoxygenation of Guaiacol to Phenolics over Activated Carbon Supported Molybdenum Catalysts. *Mol. Catal.* **2017**, *441*. <https://doi.org/10.1016/j.mcat.2017.07.024>.
- (74) Tran, C.-C.; Han, Y.; Garcia-Perez, M.; Kaliaguine, S. Synergistic Effect of Mo–W Carbides on Selective Hydrodeoxygenation of Guaiacol to Oxygen-Free Aromatic Hydrocarbons. *Catal. Sci. & Technol.* **2019**, *9* (6), 1387–1397.
- (75) Fang, H.; Chen, W.; Wu, L.; Zhao, P.; Roldan, A.; Yuan, Y. Stable and Antisintering Tungsten Carbides with Controllable Active Phase for Selective Cleavage of Aryl Ether C–O Bonds. *ACS Appl. Mater. Interfaces.* **2021**, *13* (7), 8274–8284.

<https://doi.org/10.1021/acsami.0c19599>.

- (76) Iida, T.; Shetty, M.; Murugappan, K.; Wang, Z.; Ohara, K.; Wakihara, T.; Román-Leshkov, Y. Encapsulation of Molybdenum Carbide Nanoclusters inside Zeolite Micropores Enables Synergistic Bifunctional Catalysis for Anisole Hydrodeoxygenation. *ACS Catal.* **2017**, *7* (12), 8147–8151. <https://doi.org/10.1021/acscatal.7b03175>.
- (77) Liu, S.; Wang, H.; Smith, K. J.; Kim, C. S. Hydrodeoxygenation of 2-Methoxyphenol over Ru, Pd, and Mo₂C Catalysts Supported on Carbon. *Energy & Fuels* **2017**, *31* (6), 6378–6388.
- (78) Lee, W. S.; Wang, Z.; Wu, R. J.; Bhan, A. Selective Vapor-Phase Hydrodeoxygenation of Anisole to Benzene on Molybdenum Carbide Catalysts. *J. Catal.* **2014**, *319*, 44–53. <https://doi.org/10.1016/j.jcat.2014.07.025>.
- (79) Zhu, J.; Uslamin, E. A.; Kosinov, N.; Hensen, E. J. M. Tuning the Reactivity of Molybdenum (Oxy)Carbide Catalysts by the Carburization Degree: CO₂ Reduction and Anisole Hydrodeoxygenation. *Catal. Sci. Technol.* **2020**, *10* (11), 3635–3645. <https://doi.org/10.1039/d0cy00484g>.
- (80) Iglesia, E. Synthesis, Characterization, and Catalytic Properties of Clean and Oxygen-Modified Tungsten Carbides. *Catal. Today* **1992**, *15* (2), 307.
- (81) Mortensen, P. M.; de Carvalho, H. W. P.; Grunwaldt, J.-D.; Jensen, P. A.; Jensen, A. D. Activity and Stability of Mo₂C/ZrO₂ as Catalyst for Hydrodeoxygenation of Mixtures of Phenol and 1-Octanol. *J. Catal.* **2015**, *328*, 208–215. <https://doi.org/10.1016/j.jcat.2015.02.002>.
- (82) Jongorius, A. L.; Gosselink, R. W.; Dijkstra, J.; Bitter, J. H.; Bruijninx, P. C. A.; Weckhuysen, B. M. Carbon Nanofiber Supported Transition-Metal Carbide Catalysts for the Hydrodeoxygenation of Guaiacol. *ChemCatChem* **2013**, *5* (10), 2964–2972. <https://doi.org/10.1002/cctc.201300280>.
- (83) Tran, C. C.; Mohan, O.; Banerjee, A.; Mushrif, S. H.; Kaliaguine, S. A Combined Experimental and DFT Investigation of Selective Hydrodeoxygenation of Guaiacol over Bimetallic Carbides. *Energy and Fuels* **2020**, *34* (12), 16265–16273. <https://doi.org/10.1021/acs.energyfuels.0c03102>.
- (84) Agrawal, K.; Roldan, A.; Kishore, N.; Logsdail, A. J. Hydrodeoxygenation of Guaiacol over Orthorhombic Molybdenum Carbide: A DFT and Microkinetic Study. *Catal. Sci. Technol.* **2022**, *12* (3), 843–854. <https://doi.org/10.1039/D1CY01273H>.
- (85) Zhou, M.; Cheng, L.; Choi, J. S.; Liu, B.; Curtiss, L. A.; Assary, R. S. Ni-Doping Effects on Oxygen Removal from an Orthorhombic Mo₂C (001) Surface: A Density Functional Theory Study. *J. Phys. Chem. C* **2018**, *122* (3), 1595–1603. <https://doi.org/10.1021/acs.jpcc.7b09870>.
- (86) Zhou, M.; Doan, H. A.; Curtiss, L. A.; Assary, R. S. Effect of Ni Dopant on Furan Activation over Mo₂C Surface: Insights from First-Principles-Based Microkinetic Modeling. *J. Phys. Chem. C* **2020**, *124* (10), 5636–5646.
- (87) Corma Canos, A.; Iborra, S.; Velty, A. Chemical Routes for the Transformation of Biomass

- into Chemicals. *Chem. Rev.* **2007**, *107* (6), 2411–2502. <https://doi.org/10.1021/cr050989d>.
- (88) Xue, G.; Yin, L.; Shao, S.; Li, G. Recent Progress on Selective Hydrogenation of Phenol toward Cyclohexanone or Cyclohexanol.
- (89) Schutyser, W.; Van Den Bossche, G.; Raaffels, A.; Van Den Bosch, S.; Koelewijn, S. F.; Renders, T.; Sels, B. F. Selective Conversion of Lignin-Derivable 4-Alkylguaiacols to 4-Alkylcyclohexanols over Noble and Non-Noble-Metal Catalysts. *ACS Sustain. Chem. Eng.* **2016**, *4* (10), 5336–5346. <https://doi.org/10.1021/acssuschemeng.6b01580>.
- (90) Wang, X.; Rinaldi, R. Exploiting H-Transfer Reactions with RANEY® Ni for Upgrade of Phenolic and Aromatic Biorefinery Feeds under Unusual, Low-Severity Conditions. *Energy Environ. Sci.* **2012**, *5* (8), 8244–8260. <https://doi.org/10.1039/c2ee21855k>.
- (91) Schutyser, W.; Van Den Bosch, S.; Dijkmans, J.; Turner, S.; Meledina, M.; Van Tendeloo, G.; Debecker, D. P.; Sels, B. F. Selective Nickel-Catalyzed Conversion of Model and Lignin-Derived Phenolic Compounds to Cyclohexanone-Based Polymer Building Blocks. *ChemSusChem* **2015**, *8* (10), 1805–1818. <https://doi.org/10.1002/cssc.201403375>.
- (92) He, J.; Lu, X. H.; Shen, Y.; Jing, R.; Nie, R. F.; Zhou, D.; Xia, Q. H. Highly Selective Hydrogenation of Phenol to Cyclohexanol over Nano Silica Supported Ni Catalysts in Aqueous Medium. *Mol. Catal.* **2017**, *440*, 87–95. <https://doi.org/10.1016/j.mcat.2017.07.016>.
- (93) Wei, Z.; Li, Y.; Wang, J.; Li, H.; Wang, Y. Chemoselective Hydrogenation of Phenol to Cyclohexanol Using Heterogenized Cobalt Oxide Catalysts. *Chinese Chem. Lett.* **2018**, *29* (6), 815–818. <https://doi.org/10.1016/j.ccllet.2018.01.020>.
- (94) Lu, J.; Ma, Z.; Wei, X.; Zhang, Q.; Hu, B. Support Morphology-Dependent Catalytic Activity of the Co/CeO₂ catalyst for the Aqueous-Phase Hydrogenation of Phenol. *New J. Chem.* **2020**, *44* (22), 9298–9303. <https://doi.org/10.1039/c9nj06226b>.
- (95) Nie, Y.; Lin, W.; Zhang, Y.; Chen, Y.; Nie, R. Transfer Hydrogenation of Phenol over Co-CoO_x/N-Doped Carbon: Boosted Catalyst Performance Enabled by Synergistic Catalysis between Co⁰ and Co^{δ+}. *Dalt. Trans.* **2022**, *51* (41), 15983–15989. <https://doi.org/10.1039/d2dt02750j>.
- (96) Bykova, M. V.; Bulavchenko, O. A.; Ermakov, D. Y.; Lebedev, M. Y.; Yakovlev, V. A.; Parmon, V. N. Guaiacol Hydrodeoxygenation in the Presence of Ni-Containing Catalysts. *Catal. Ind. 2011 31* **2011**, *3* (1), 15–22. <https://doi.org/10.1134/S2070050411010028>.
- (97) Zhou, M.; Ye, J.; Liu, P.; Xu, J.; Jiang, J. Water-Assisted Selective Hydrodeoxygenation of Guaiacol to Cyclohexanol over Supported Ni and Co Bimetallic Catalysts. *ACS Sustain. Chem. Eng.* **2017**, *5* (10), 8824–8835. <https://doi.org/10.1021/acssuschemeng.7b01615>.
- (98) Singh, B.; Goyal, V.; Sarma, D.; Kumar, R.; Bhatt, T.; Mahata, A.; Raji Reddy, C.; Narani, A.; Natte, K. Earth-Abundant Heterogeneous Cobalt Catalyst for Selective Ring Hydrogenation of (Hetero)Arenes and Gram-Scale Synthesis of Pharmaceutical Intermediates. *ACS Catal.* **2023**, *13* (14), 9724–9744. <https://doi.org/10.1021/acscatal.3c02084>.
- (99) Xue, G.; Yin, L.; Shao, S.; Li, G. Recent Progress on Selective Hydrogenation of Phenol

- toward Cyclohexanone or Cyclohexanol. *Nanotechnology* **2022**, *33* (7). <https://doi.org/10.1088/1361-6528/ac385f>.
- (100) He, J.; Zhao, C.; Catalysis, J. L.-J. of; 2014, U. Impact of Solvent for Individual Steps of Phenol Hydrodeoxygenation with Pd/C and HZSM-5 as Catalysts. *Elsevier* **2014**, *309*, 362–375.
- (101) Güvenatam, B.; Kurs, O. Hydrodeoxygenation of Mono- and Dimeric Lignin Model Compounds on Noble Metal Catalysts. **2014**, *233*, 83–91. <https://doi.org/10.1016/j.cattod.2013.12.011>.
- (102) Vriamont, C. E. J. J.; Chen, T.; Romain, C.; Corbett, P.; Manageracharath, P.; Peet, J.; Conifer, C. M.; Hallett, J. P.; Britovsek, G. J. P. From Lignin to Chemicals: Hydrogenation of Lignin Models and Mechanistic Insights into Hydrodeoxygenation via Low-Temperature C-O Bond Cleavage. *ACS Catal.* **2019**, *9* (3), 2345–2354. <https://doi.org/10.1021/acscatal.8b04714>.
- (103) Jiang, W.; Cao, J.; Zhao, X.; Xie, T.; Zhu, C.; Xie, J.; Zhao, L. Highly Selective Aromatic Ring Hydrogenation of Lignin-Derived Compounds over Macroporous Ru / Nb 2 O 5 with the Lost Acidity at Room Temperature. *Fuel* **2020**, *282* (August), 118869. <https://doi.org/10.1016/j.fuel.2020.118869>.
- (104) Upare, P. P.; Lee, J. M.; Hwang, D. W.; Halligudi, S. B.; Hwang, Y. K.; Chang, J. S. Selective Hydrogenation of Levulinic Acid to γ -Valerolactone over Carbon-Supported Noble Metal Catalysts. *J. Ind. Eng. Chem.* **2011**, *17* (2), 287–292. <https://doi.org/10.1016/j.jiec.2011.02.025>.
- (105) Corbel-Demilly, L.; Ly, B. K.; Minh, D. P.; Tapin, B.; Especel, C.; Epron, F.; Cabiac, A.; Guillon, E.; Besson, M.; Pinel, C. Heterogeneous Catalytic Hydrogenation of Biobased Levulinic and Succinic Acids in Aqueous Solutions. *ChemSusChem* **2013**, *6* (12), 2388–2395. <https://doi.org/10.1002/cssc.201300608>.
- (106) Tukacs, J. M.; Jones, R. V.; Darvas, F.; Dibó, G.; Lezsák, G.; Mika, L. T. Synthesis of γ -Valerolactone Using a Continuous-Flow Reactor. *RSC Adv.* **2013**, *3* (37), 16283–16287. <https://doi.org/10.1039/c3ra43032d>.
- (107) Manzer, L. E. Catalytic Synthesis of α -Methylene- γ -Valerolactone: A Biomass-Derived Acrylic Monomer. *Appl. Catal. A Gen.* **2004**, *272* (1–2), 249–256. <https://doi.org/10.1016/J.APCATA.2004.05.048>.
- (108) Lee, J.; Xu, Y.; Huber, G. W. Applied Catalysis B: Environmental High-Throughput Screening of Monometallic Catalysts for Aqueous-Phase Hydrogenation of Biomass-Derived Oxygenates. **2013**, *141*, 98–107.
- (109) Michel, C.; Zaffran, J.; Ruppert, A. M.; Matras-Michalska, J.; Jędrzejczyk, M.; Grams, J.; Sautet, P. Role of Water in Metal Catalyst Performance for Ketone Hydrogenation: A Joint Experimental and Theoretical Study on Levulinic Acid Conversion into Gamma-Valerolactone. *Chem. Commun.* **2014**, *50* (83), 12450–12453. <https://doi.org/10.1039/c4cc04401k>.
- (110) Dai, Y.; Gao, X.; Chu, X.; Jiang, C.; Yao, Y.; Guo, Z.; Zhou, C.; Wang, C.; Wang, H.;

- Yang, Y. On the Role of Water in Selective Hydrogenation of Cinnamaldehyde to Cinnamyl Alcohol on PtFe Catalysts. *J. Catal.* **2018**, *364*, 192–203. <https://doi.org/10.1016/J.JCAT.2018.05.008>.
- (111) Chang, C. R.; Huang, Z. Q.; Li, J. The Promotional Role of Water in Heterogeneous Catalysis: Mechanism Insights from Computational Modeling. *Wiley Interdiscip. Rev. Comput. Mol. Sci.* **2016**, *6* (6), 679–693. <https://doi.org/10.1002/WCMS.1272>.
- (112) Hibbitts, D. D.; Loveless, B. T.; Neurock, M.; Iglesia, E. Mechanistic Role of Water on the Rate and Selectivity of Fischer–Tropsch Synthesis on Ruthenium Catalysts. *Angew. Chemie Int. Ed.* **2013**, *52* (47), 12273–12278. <https://doi.org/10.1002/ANIE.201304610>.
- (113) Nakagawa, Y.; Ishikawa, M.; Tamura, M.; Tomishige, K. Selective Production of Cyclohexanol and Methanol from Guaiacol over Ru Catalyst Combined with MgO. **2014**, 2197–2203. <https://doi.org/10.1039/c3gc42322k>.
- (114) Ishikawa, M.; Tamura, M.; Nakagawa, Y.; Tomishige, K. Applied Catalysis B : Environmental Demethoxylation of Guaiacol and Methoxybenzenes over Carbon-Supported Ru – Mn Catalyst. *Applied Catal. B, Environ.* **2016**, *182*, 193–203. <https://doi.org/10.1016/j.apcatb.2015.09.021>.
- (115) Chen, M.; Huang, Y.; Pang, H.; Liu, X.; Fu, Y. Ru Catalysts in Biphasic Systems †. **2015**, 1710–1717. <https://doi.org/10.1039/c4gc01992j>.
- (116) Xu, G. Y.; Guo, J. H.; Qu, Y. C.; Zhang, Y.; Fu, Y.; Guo, Q. X. Selective Hydrodeoxygenation of Lignin-Derived Phenols to Alkyl Cyclohexanols over a Ru-Solid Base Bifunctional Catalyst. *Green Chem.* **2016**, *18* (20), 5510–5517. <https://doi.org/10.1039/c6gc01097k>.
- (117) Akpa, B. S.; D’Agostino, C.; Gladden, L. F.; Hindle, K.; Manyar, H.; McGregor, J.; Li, R.; Neurock, M.; Sinha, N.; Stitt, E. H.; Weber, D.; Zeitler, J. A.; Rooney, D. W. Solvent Effects in the Hydrogenation of 2-Butanone. *J. Catal.* **2012**, *289*, 30–41. <https://doi.org/10.1016/j.jcat.2012.01.011>.
- (118) Shangguan, J.; Hensley, A. J. R.; Gradiski, M. V.; Pfriem, N.; McEwen, J. S.; Morris, R. H.; Chin, Y. H. C. The Role of Protons and Hydrides in the Catalytic Hydrogenolysis of Guaiacol at the Ruthenium Nanoparticle-Water Interface. *ACS Catal.* **2020**, *10* (20), 12310–12332. <https://doi.org/10.1021/acscatal.0c01963>.
- (119) Weissenrieder, J.; Mikkelsen, A.; Andersen, J. N.; Feibelman, P. J.; Held, G. Experimental Evidence for a Partially Dissociated Water Bilayer on Ru{0001}. *Phys. Rev. Lett.* **2004**, *93* (19), 196102. <https://doi.org/10.1103/PHYSREVLETT.93.196102/FIGURES/4/MEDIUM>.
- (120) Haq, S.; Clay, C.; Darling, G. R.; Zimbitas, G.; Hodgson, A. Growth of Intact Water Ice on Ru(0001) between 140 and 160 K: Experiment and Density-Functional Theory Calculations. *Phys. Rev. B - Condens. Matter Mater. Phys.* **2006**, *73* (11), 115414. <https://doi.org/10.1103/PHYSREVB.73.115414/FIGURES/10/MEDIUM>.
- (121) Clay, C.; Haq, S.; Hodgson, A. Intact and Dissociative Adsorption of Water on Ru(0 0 0 1). *Chem. Phys. Lett.* **2004**, *388* (1–3), 89–93. <https://doi.org/10.1016/J.CPLETT.2004.02.076>.

- (122) Gerda, J.; Michaelides, A.; Bocquet, M. L.; Feibelman, P. J.; Mitsui, T.; Rose, M.; Fomin, E.; Salmeron, M. Novel Water Overlayer Growth on Pd(111) Characterized with Scanning Tunneling Microscopy and Density Functional Theory. *Phys. Rev. Lett.* **2004**, *93* (11), 116101. <https://doi.org/10.1103/PHYSREVLETT.93.116101>. FIGURES/3/MEDIUM.
- (123) Tatarkhanov, M.; Fomin, E.; Salmeron, M.; Andersson, K.; Ogasawara, H.; Pettersson, L. G. M.; Nilsson, A.; Cerdá, J. I. The Structure of Mixed H₂O–OH Monolayer Films on Ru(0001). *J. Chem. Phys.* **2008**, *129* (15), 154109. <https://doi.org/10.1063/1.2988903>.
- (124) Sullivan, M. M.; Chen, C.-J.; Bhan, A. Catalytic Deoxygenation on Transition Metal Carbide Catalysts. *Catal. Sci. & Technol.* **2016**, *6* (3), 602–616.
- (125) Bathla, S.; Tran, C. C.; Kaliaguine, S.; Mushrif, S. H. Doping an Oxophilic Metal into a Metal Carbide: Unravelling the Synergy between the Microstructure of the Catalyst and Its Activity and Selectivity for Hydrodeoxygenation. *ACS Catal.* **2022**, *12* (22), 13980–13998. <https://doi.org/10.1021/acscatal.2c03500>.
- (126) Chen, C. J.; Bhan, A. Mo₂C Modification by CO₂, H₂O, and O₂: Effects of Oxygen Content and Oxygen Source on Rates and Selectivity of m-Cresol Hydrodeoxygenation. *ACS Catal.* **2017**, *7* (2), 1113–1122. <https://doi.org/10.1021/acscatal.6b02762>.
- (127) Kumar, A.; Bhan, A. Oxygen Content as a Variable to Control Product Selectivity in Hydrodeoxygenation Reactions on Molybdenum Carbide Catalysts. *Chem. Eng. Sci.* **2019**, *197*, 371–378. <https://doi.org/10.1016/j.ces.2018.12.027>.
- (128) Tran, C. C.; Han, Y.; Garcia-Perez, M.; Kaliaguine, S. Synergistic Effect of Mo-W Carbides on Selective Hydrodeoxygenation of Guaiacol to Oxygen-Free Aromatic Hydrocarbons. *Catal. Sci. Technol.* **2019**, *9* (6), 1387–1397. <https://doi.org/10.1039/c8cy02184h>.
- (129) Chen, L.; Shi, Y.; Chen, C.; Feng, H.; Wang, S.; Zhang, X.; Wei, M. Precise Control over Local Atomic Structures in Ni–Mo Bimetallic Alloys for the Hydrodeoxygenation Reaction: A Combination between Density Functional Theory and Microkinetic Modeling. *J. Phys. Chem. C* **2022**. <https://doi.org/10.1021/acs.jpcc.1c09172>.
- (130) Bandarenka, A. S.; Varela, A. S.; Karamad, M.; Calle-Vallejo, F.; Bech, L.; Perez-Alonso, F. J.; Rossmeisl, J.; Stephens, I. E. L.; Chorkendorff, I. Design of an Active Site towards Optimal Electrocatalysis: Overlayers, Surface Alloys and Near-Surface Alloys of Cu/Pt(111). *Angew. Chemie* **2012**, *124* (47), 12015–12018. <https://doi.org/10.1002/ange.201205314>.
- (131) Chiu, C. C.; Genest, A.; Borgna, A.; Rösch, N. Hydrodeoxygenation of Guaiacol over Ru(0001): A DFT Study. *ACS Catal.* **2014**, *4* (11), 4178–4188. <https://doi.org/10.1021/cs500911j>.
- (132) Serrano-Ruiz, J. C.; Dumesic, J. A. Catalytic Routes for the Conversion of Biomass into Liquid Hydrocarbon Transportation Fuels. *Energy Environ. Sci.* **2011**, *4* (1), 83–99. <https://doi.org/10.1039/c0ee00436g>.
- (133) Massoth, F. E.; Politzer, P.; Concha, M. C.; Murray, J. S.; Jakowski, J.; Simons, J. Catalytic Hydrodeoxygenation of Methyl-Substituted Phenols: Correlations of Kinetic Parameters with Molecular Properties. *J. Phys. Chem. B* **2006**, *110* (29), 14283–14291.

<https://doi.org/10.1021/jp057332g>.

- (134) Yoosuk, B.; Tumnantong, D.; Prasassarakich, P. Amorphous Unsupported Ni-Mo Sulfide Prepared by One Step Hydrothermal Method for Phenol Hydrodeoxygenation. *Fuel* **2012**, *91* (1), 246–252. <https://doi.org/10.1016/j.fuel.2011.08.001>.
- (135) Romero, Y.; Richard, F.; Brunet, S. Hydrodeoxygenation of 2-Ethylphenol as a Model Compound of Bio-Crude over Sulfided Mo-Based Catalysts: Promoting Effect and Reaction Mechanism. *Appl. Catal. B Environ.* **2010**, *98* (3–4), 213–223. <https://doi.org/10.1016/j.apcatb.2010.05.031>.
- (136) Şenol, O. I.; Viljava, T. R.; Krause, A. O. I. Hydrodeoxygenation of Aliphatic Esters on Sulphided NiMo/ γ -Al₂O₃ and CoMo/ γ -Al₂O₃ Catalyst: The Effect of Water. *Catal. Today* **2005**, *106* (1–4), 186–189. <https://doi.org/10.1016/j.cattod.2005.07.129>.
- (137) Sitthisa, S.; Pham, T.; Prasomsri, T.; Sooknoi, T.; Mallinson, R. G.; Resasco, D. E. Conversion of Furfural and 2-Methylpentanal on Pd/SiO₂ and Pd-Cu/SiO₂ Catalysts. *J. Catal.* **2011**, *280* (1), 17–27. <https://doi.org/10.1016/j.jcat.2011.02.006>.
- (138) Liu, S.; Wang, H.; Smith, K. J.; Kim, C. S. Hydrodeoxygenation of 2-Methoxyphenol over Ru, Pd, and Mo₂C Catalysts Supported on Carbon. *Energy and Fuels* **2017**, *31* (6), 6378–6388. <https://doi.org/10.1021/acs.energyfuels.7b00452>.
- (139) Banerjee, A.; Mushrif, S. H. Investigating Reaction Mechanisms for Furfural Hydrodeoxygenation on Ni and the Effect of Boron Doping on the Activity and Selectivity of the Catalyst. *J. Phys. Chem. C* **2018**, *122* (32), 18383–18394. <https://doi.org/10.1021/acs.jpcc.8b01301>.
- (140) Ma, Y.; Guan, G.; Hao, X.; Cao, J.; Abudula, A. Molybdenum Carbide as Alternative Catalyst for Hydrogen Production – A Review. *Renewable and Sustainable Energy Reviews*. Elsevier Ltd 2017, pp 1101–1129. <https://doi.org/10.1016/j.rser.2016.11.092>.
- (141) Sullivan, M. M.; Chen, C. J.; Bhan, A. Catalytic Deoxygenation on Transition Metal Carbide Catalysts. *Catalysis Science and Technology*. Royal Society of Chemistry 2016, pp 602–616. <https://doi.org/10.1039/c5cy01665g>.
- (142) Kitchin, J. R.; Nørskov, J. K.; Barteau, M. A.; Chen, J. G. Trends in the Chemical Properties of Early Transition Metal Carbide Surfaces: A Density Functional Study. *Catal. Today* **2005**, *105* (1 SPEC. ISS.), 66–73. <https://doi.org/10.1016/j.cattod.2005.04.008>.
- (143) Shi, Y.; Yang, Y.; Li, Y. W.; Jiao, H. Mechanisms of Mo₂C(101)-Catalyzed Furfural Selective Hydrodeoxygenation to 2-Methylfuran from Computation. *ACS Catal.* **2016**, *6* (10), 6790–6803. <https://doi.org/10.1021/acscatal.6b02000>.
- (144) Chen, C. J.; Lee, W. S.; Bhan, A. Mo₂C Catalyzed Vapor Phase Hydrodeoxygenation of Lignin-Derived Phenolic Compound Mixtures to Aromatics under Ambient Pressure. *Appl. Catal. A Gen.* **2016**, *510*, 42–48. <https://doi.org/10.1016/j.apcata.2015.10.043>.
- (145) Liu, S.; Wang, H.; Kim, C. S.; Smith, K. J. Jo Ur Na l P Of. *Applied Catal. A, Gen.* **2020**, 117628. <https://doi.org/10.1016/j.apcata.2020.117628>.
- (146) Stottlemeyer, A. L.; Kelly, T. G.; Meng, Q.; Chen, J. G. Reactions of Oxygen-Containing

- Molecules on Transition Metal Carbides: Surface Science Insight into Potential Applications in Catalysis and Electrocatalysis. *Surf. Sci. Rep.* **2012**, *67* (9–10), 201–232. <https://doi.org/10.1016/j.surfrep.2012.07.001>.
- (147) Smirnov, A. A.; Geng, Z.; Khromova, S. A.; Zavarukhin, S. G.; Bulavchenko, O. A.; Saraev, A. A.; Kaichev, V. V.; Ermakov, D. Y.; Yakovlev, V. A. Nickel Molybdenum Carbides: Synthesis, Characterization, and Catalytic Activity in Hydrodeoxygenation of Anisole and Ethyl Caprate. *J. Catal.* **2017**, *354*, 61–77. <https://doi.org/10.1016/j.jcat.2017.07.009>.
- (148) Yu, C. C.; Ramanathan, S.; Dhandapani, B.; Chen, J. G.; Oyama, S. T. Bimetallic Nb-Mo Carbide Hydroprocessing Catalysts: Synthesis, Characterization, and Activity Studies. *J. Phys. Chem. B* **1997**, *101* (4), 512–518. <https://doi.org/10.1021/jp9624966>.
- (149) Zhou, M.; Doan, H. A.; Curtiss, L. A.; Assary, R. S. Effect of Ni Dopant on Furan Activation over Mo₂C Surface: Insights from First-Principles-Based Microkinetic Modeling. *J. Phys. Chem. C* **2020**, *124* (10), 5636–5646. <https://doi.org/10.1021/acs.jpcc.9b10126>.
- (150) G. Kelly, T.; G. Chen, J. Controlling C–O, C–C and C–H Bond Scission for Deoxygenation, Reforming, and Dehydrogenation of Ethanol Using Metal-Modified Molybdenum Carbide Surfaces. *Green Chem.* **2014**, *16* (2), 777–784. <https://doi.org/10.1039/C3GC41259H>.
- (151) Kelly, T. G.; Stottlemeyer, A. L.; Ren, H.; Chen, J. G. Comparison of OAH, CAH, and CAO Bond Scission Sequence of Methanol on Tungsten Carbide Surfaces Modified by Ni, Rh, and Au. *J. Phys. Chem. C* **2011**, *115*, 6644–6650. <https://doi.org/10.1021/jp112006v>.
- (152) G. Kelly, T.; G. Chen, J. Metal Overlayer on Metal Carbide Substrate: Unique Bimetallic Properties for Catalysis and Electrocatalysis. *Chem. Soc. Rev.* **2012**, *41* (24), 8021–8034. <https://doi.org/10.1039/C2CS35165J>.
- (153) Wannakao, S.; Artrith, N.; Limtrakul, J.; Kolpak, A. M. Engineering Transition-Metal-Coated Tungsten Carbides for Efficient and Selective Electrochemical Reduction of CO₂ to Methane. *ChemSusChem* **2015**, *8* (16), 2745–2751. <https://doi.org/10.1002/CSSC.201500245>.
- (154) Wannakao, S.; Artrith, N.; Limtrakul, J.; Kolpak, A. M. Catalytic Activity and Product Selectivity Trends for Carbon Dioxide Electroreduction on Transition Metal-Coated Tungsten Carbides. *J. Phys. Chem. C* **2017**, *4*, 121. <https://doi.org/10.1021/acs.jpcc.7b05741>.
- (155) Eschrig, H.; Seifert, G.; Ziesche, P. Current Density Functional Theory of Quantum Electrodynamics. *Solid State Commun.* **1985**, *56* (9), 777–780. [https://doi.org/10.1016/0038-1098\(85\)90307-2](https://doi.org/10.1016/0038-1098(85)90307-2).
- (156) Kohn, W.; Sham, L. J. Self-Consistent Equations Including Exchange and Correlation Effects. *Phys. Rev.* **1965**, *140* (4A), A1133. <https://doi.org/10.1103/PHYSREV.140.A1133/FIGURE/1/THUMB>.
- (157) Kresse, G.; Furthmüller, J. Efficiency of Ab-Initio Total Energy Calculations for Metals and Semiconductors Using a Plane-Wave Basis Set. *Comput. Mater. Sci.* **1996**, *6* (1), 15–50. [https://doi.org/10.1016/0927-0256\(96\)00008-0](https://doi.org/10.1016/0927-0256(96)00008-0).
- (158) Kresse, G.; Furthmüller, J. Efficient Iterative Schemes for Ab Initio Total-Energy

- Calculations Using a Plane-Wave Basis Set. *Phys. Rev. B - Condens. Matter Mater. Phys.* **1996**, *54* (16), 11169–11186. <https://doi.org/10.1103/PhysRevB.54.11169>.
- (159) Blöchl, P. E. Projector Augmented-Wave Method. *Phys. Rev. B* **1994**, *50* (24), 17953–17979. <https://doi.org/10.1103/PhysRevB.50.17953>.
- (160) Birgersson, M.; Almladh, C.-O.; Borg, M.; Andersen, J. N. Density-Functional Theory Applied to Rh(111) and CO/Rh(111) Systems: Geometries, Energies, and Chemical Shifts. *Phys. Rev. B* **2003**, *67* (4), 045402. <https://doi.org/10.1103/PhysRevB.67.045402>.
- (161) Köhler, L.; Kresse, G. Density Functional Study of CO on Rh(111). *Phys. Rev. B* **2004**, *70* (16), 165405. <https://doi.org/10.1103/PhysRevB.70.165405>.
- (162) Bellafont, N. P.; Bagus, P. S.; Illas, F. Prediction of Core Level Binding Energies in Density Functional Theory: Rigorous Definition of Initial and Final State Contributions and Implications on the Physical Meaning of Kohn-Sham Energies. *J. Chem. Phys.* **2015**, *142* (21), 214102. <https://doi.org/10.1063/1.4921823>.
- (163) Trinh, Q. T.; Banerjee, A.; Yang, Y.; Mushrif, S. H. Sub-Surface Boron-Doped Copper for Methane Activation and Coupling: First-Principles Investigation of the Structure, Activity, and Selectivity of the Catalyst. *J. Phys. Chem. C* **2017**, *121* (2), 1099–1112. <https://doi.org/10.1021/ACS.JPCC.6B09236>.
- (164) Fajín, J. L. C.; Gomes, J. R. B.; Cordeiro, M. N. D. S. Mechanistic Study of Carbon Monoxide Methanation over Pure and Rhodium- or Ruthenium-Doped Nickel Catalysts. *J. Phys. Chem. C* **2015**, *119* (29), 16537–16551. <https://doi.org/10.1021/ACS.JPCC.5B01837>.
- (165) JK, N.; T, B.; J, R.; CH, C. Towards the Computational Design of Solid Catalysts. *Nat. Chem.* **2009**, *1* (1), 37–46. <https://doi.org/10.1038/NCHEM.121>.
- (166) Hammer, B.; Nørskov, J. K. Theoretical Surface Science and Catalysis—Calculations and Concepts. *Adv. Catal.* **2000**, *45* (C), 71–129. [https://doi.org/10.1016/S0360-0564\(02\)45013-4](https://doi.org/10.1016/S0360-0564(02)45013-4).
- (167) Tian-E Fan; Ilker Demiroglu; A. Hussein, H.; Tun-Dong Liu; L. Johnston, R. DFT Study of the Structure, Chemical Ordering and Molecular Adsorption of Pd–Ir Nanoalloys. *Phys. Chem. Chem. Phys.* **2017**, *19* (39), 27090–27098. <https://doi.org/10.1039/C7CP04811D>.
- (168) Ferrando, R.; Fortunelli, A.; Rossi, G. Quantum Effects on the Structure of Pure and Binary Metallic Nanoclusters. <https://doi.org/10.1103/PhysRevB.72.085449>.
- (169) CHRISTENSEN, A.; AN, C. A NEUTRON DIFFRACTION INVESTIGATION ON A CRYSTAL OF ALPHA -MO₂C. *A NEUTRON Diffr. Investig. A Cryst. ALPHA -MO₂C.* **1977**.
- (170) Dubois, J.; Epicier, T.; Esnouf, C.; Fantozzi, G.; Convert, P. Neutron Powder Diffraction Studies of Transition Metal Hemicarbides M₂C_{1-x}-I. Motivation for a Study on W₂C and Mo₂C and Experimental Background for an in Situ Investigation at Elevated Temperature. *Acta Metall.* **1988**, *36* (8), 1891–1901. [https://doi.org/10.1016/0001-6160\(88\)90292-1](https://doi.org/10.1016/0001-6160(88)90292-1).
- (171) Epicier, T.; Dubois, J.; Esnouf, C.; Fantozzi, G.; Metallurgica, P. C.-A.; 1988, undefined. Neutron Powder Diffraction Studies of Transition Metal Hemicarbides M₂C_{1-x}—II. In

Situ High Temperature Study on W₂C_{1-x} and Mo₂C_{1-x}. *Elsevier*.

- (172) Otani, S.; Ishizawa, Y. Preparation of Mo₂C Single Crystals by the Floating Zone Method. *J. Cryst. Growth* **1995**, *154* (1–2), 202–204. [https://doi.org/10.1016/0022-0248\(95\)00243-X](https://doi.org/10.1016/0022-0248(95)00243-X).
- (173) Venezia, A. M. X-Ray Photoelectron Spectroscopy (XPS) for Catalysts Characterization. *Catal. Today* **2003**, *77* (4), 359–370. [https://doi.org/10.1016/S0920-5861\(02\)00380-2](https://doi.org/10.1016/S0920-5861(02)00380-2).
- (174) Knop-Gericke, A.; Kleimenov, E.; Hävecker, M.; Blume, R.; Teschner, D.; Zafeiratos, S.; Schlögl, R.; Bukhtiyarov, V. I.; Kaichev, V. V.; Prosvirin, I. P.; Nizovskii, A. I.; Bluhm, H.; Barinov, A.; Dudin, P.; Kiskinova, M. Chapter 4 X-Ray Photoelectron Spectroscopy for Investigation of Heterogeneous Catalytic Processes. *Adv. Catal.* **2009**, *52* (C), 213–272. [https://doi.org/10.1016/S0360-0564\(08\)00004-7](https://doi.org/10.1016/S0360-0564(08)00004-7).
- (175) Trinh, Q. T.; Yang, J.; Lee, J. Y.; Saeys, M. Computational and Experimental Study of the Volcano Behavior of the Oxygen Reduction Activity of PdM@PdPt/C (M = Pt, Ni, Co, Fe, and Cr) Core-Shell Electrocatalysts. *J. Catal.* **2012**, *291*, 26–35. <https://doi.org/10.1016/J.JCAT.2012.04.001>.
- (176) Takahata, Y.; Marques, A. D. S. Accurate Core-Electron Binding Energy Shifts from Density Functional Theory. *J. Electron Spectros. Relat. Phenomena* **2010**, *178–179* (C), 80–87. <https://doi.org/10.1016/J.ELSPEC.2009.03.018>.
- (177) Todorova, M.; Lundgren, E.; Blum, V.; Mikkelsen, A.; Gray, S.; Gustafson, J.; Borg, M.; Rogal, J.; Reuter, K.; Andersen, J. N.; Scheffler, M. The Pd(100)–(5×5)R27°-O Surface Oxide Revisited. *Surf. Sci.* **2003**, *541* (1–3), 101–112. [https://doi.org/10.1016/S0039-6028\(03\)00873-2](https://doi.org/10.1016/S0039-6028(03)00873-2).
- (178) Bianchetin, L.; Baraldi, A.; Gironcoli, S. de; Vesselli, E.; Lizzit, S.; Comelli, G.; Rosei, R. Surface Core Level Shift: High Sensitive Probe to Oxygen-Induced Reconstruction of Rh(100). *J. Phys. Chem. C* **2009**, *113* (30), 13192–13198. <https://doi.org/10.1021/JP901223D>.
- (179) Trinh, Q. T.; Bholá, K.; Prince, #; Amaniampong, N.; Franç, ll; Jérô, J.; Mushrif, S. H. Synergistic Application of XPS and DFT to Investigate Metal Oxide Surface Catalysis. **2018**. <https://doi.org/10.1021/acs.jpcc.8b05499>.
- (180) Chun, H. J.; Lee, Y.; Kim, S.; Yoon, Y.; Kim, Y.; Park, S. C. Surface Termination of BaTiO₃(1 1 1) Single Crystal: A Combined DFT and XPS Study. *Appl. Surf. Sci.* **2022**, *578*, 152018. <https://doi.org/10.1016/J.APSUSC.2021.152018>.
- (181) Artyushkova, K.; Kiefer, B.; Halevi, B.; Knop-Gericke, A.; Schlögl, R.; Atanassov, P. Density Functional Theory Calculations of XPS Binding Energy Shift for Nitrogen-Containing Graphene -like Structures. *Chem. Commun.* **2013**, *49* (25), 2539–2541. <https://doi.org/10.1039/C3CC40324F>.
- (182) Golfetto, E.; Baraldi, A.; Pozzo, M.; Alfè, D.; Sala, A.; Lacovig, P.; Vesselli, E.; Lizzit, S.; Comelli, G.; Rosei, R. Determining the Chemical Reactivity Trends of Pd/Ru(0001) Pseudomorphic Overlayers: Core-Level Shift Measurements and DFT Calculations. *J. Phys. Chem. C* **2010**, *114* (1), 436–441. <https://doi.org/10.1021/JP908568V>.

- (183) Baraldi, A.; Bianchettin, L.; Gironcoli, S. de; Vesselli, E.; Lizzit, S.; Petaccia, L.; Comelli, G.; Rosei, R. Enhanced Chemical Reactivity of Under-Coordinated Atoms at Pt–Rh Bimetallic Surfaces: A Spectroscopic Characterization. *J. Phys. Chem. C* **2011**, *115* (8), 3378–3384. <https://doi.org/10.1021/JP110329W>.
- (184) Choi, J. S.; Bugli, G.; Djéga-Mariadassou, G. Influence of the Degree of Carburization on the Density of Sites and Hydrogenating Activity of Molybdenum Carbides. *J. Catal.* **2000**, *193* (2), 238–247. <https://doi.org/10.1006/JCAT.2000.2894>.
- (185) Hong, Y. K.; Lee, D. W.; Eom, H. J.; Lee, K. Y. The Catalytic Activity of Pd/WO_x/γ-Al₂O₃ for Hydrodeoxygenation of Guaiacol. *Appl. Catal. B Environ.* **2014**, *150–151*, 438–445. <https://doi.org/10.1016/j.apcatb.2013.12.045>.
- (186) Bui, V. N.; Laurenti, D.; Delichère, P.; Geantet, C. Hydrodeoxygenation of Guaiacol. Part II: Support Effect for CoMoS Catalysts on HDO Activity and Selectivity. *Appl. Catal. B Environ.* **2011**, *101* (3–4), 246–255. <https://doi.org/10.1016/j.apcatb.2010.10.031>.
- (187) Jongorius, A. L.; Jastrzebski, R.; Bruijninx, P. C. A.; Weckhuysen, B. M. CoMo Sulfide-Catalyzed Hydrodeoxygenation of Lignin Model Compounds: An Extended Reaction Network for the Conversion of Monomeric and Dimeric Substrates. *J. Catal.* **2012**, *285* (1), 315–323. <https://doi.org/10.1016/j.jcat.2011.10.006>.
- (188) Kushagra Agrawal; Alberto Roldan; Nanda Kishore; J. Logsdail, A. Hydrodeoxygenation of Guaiacol over Orthorhombic Molybdenum Carbide: A DFT and Microkinetic Study. *Catal. Sci. Technol.* **2022**. <https://doi.org/10.1039/D1CY01273H>.
- (189) Konadu, D.; Kwawu, C. R.; Tia, R.; Adei, E.; de Leeuw, N. H. Mechanism of Guaiacol Hydrodeoxygenation on Cu (111): Insights from Density Functional Theory Studies. *Catal. 2021, Vol. 11, Page 523* **2021**, *11* (4), 523. <https://doi.org/10.3390/CATAL11040523>.
- (190) Lee, K.; Gu, G. H.; Mullen, C. A.; Boateng, A. A.; Vlachos, D. G. Guaiacol Hydrodeoxygenation Mechanism on Pt(111): Insights from Density Functional Theory and Linear Free Energy Relations. *ChemSusChem* **2015**, *8* (2), 315–322. <https://doi.org/10.1002/CSSC.201402940>.
- (191) Liu, X.; An, W.; Wang, Y.; Turner, C. H.; Resasco, D. E. Hydrodeoxygenation of Guaiacol over Bimetallic Fe-Alloyed (Ni, Pt) Surfaces: Reaction Mechanism, Transition-State Scaling Relations and Descriptor for Predicting C–O Bond Scission Reactivity. *Catal. Sci. Technol.* **2018**, *8* (8), 2146–2158. <https://doi.org/10.1039/c8cy00282g>.
- (192) Zhou, J.; An, W. Unravelling the Role of Oxophilic Metal in Promoting the Deoxygenation of Catechol on Ni-Based Alloy Catalysts. *Catal. Sci. Technol.* **2020**, *10* (20), 6849–6859. <https://doi.org/10.1039/d0cy01361g>.
- (193) Chang, J.; Danuthai, T.; Dewiyanti, S.; Wang, C.; Borgna, A. Hydrodeoxygenation of Guaiacol over Carbon-Supported Metal Catalysts. *ChemCatChem* **2013**, *5* (10), 3041–3049. <https://doi.org/10.1002/cctc.201300096>.
- (194) Nanda, S.; Mohanty, P.; Pant, K. K.; Naik, S.; Kozinski, J. A.; Dalai, A. K. Characterization of North American Lignocellulosic Biomass and Biochars in Terms of Their Candidacy for Alternate Renewable Fuels. *Bioenergy Res.* **2013**, *6* (2), 663–677.

<https://doi.org/10.1007/s12155-012-9281-4>.

- (195) Ryymin, E. M.; Honkela, M. L.; Viljava, T. R.; Krause, A. O. I. Competitive Reactions and Mechanisms in the Simultaneous HDO of Phenol and Methyl Heptanoate over Sulphided NiMo/ γ -Al₂O₃. *Appl. Catal. A Gen.* **2010**, *389* (1–2), 114–121. <https://doi.org/10.1016/j.apcata.2010.09.010>.
- (196) Şenol, O. I.; Viljava, T. R.; Krause, A. O. I. Effect of Sulphiding Agents on the Hydrodeoxygenation of Aliphatic Esters on Sulphided Catalysts. *Appl. Catal. A Gen.* **2007**, *326* (2), 236–244. <https://doi.org/10.1016/j.apcata.2007.04.022>.
- (197) Laurent, E.; Delmon, B. Study of the Hydrodeoxygenation of Carbonyl, Carboxylic and Guaiacyl Groups over Sulfided CoMo/ γ -Al₂O₃ and NiMo/ γ -Al₂O₃ Catalyst. II. Influence of Water, Ammonia and Hydrogen Sulfide. *Appl. Catal. A, Gen.* **1994**, *109* (1), 97–115. [https://doi.org/10.1016/0926-860X\(94\)85005-4](https://doi.org/10.1016/0926-860X(94)85005-4).
- (198) Banerjee, A.; Mushrif, S. H. Reaction Pathways for the Deoxygenation of Biomass-Pyrolysis-Derived Bio-Oil on Ru: A DFT Study Using Furfural as a Model Compound. *ChemCatChem* **2017**, *9* (14), 2828–2838. <https://doi.org/10.1002/cctc.201700036>.
- (199) Lee, H.; Kim, H.; Yu, M. J.; Ko, C. H.; Jeon, J. K.; Jae, J.; Park, S. H.; Jung, S. C.; Park, Y. K. Catalytic Hydrodeoxygenation of Bio-Oil Model Compounds over Pt/HY Catalyst. *Sci. Rep.* **2016**, *6*, 1–8. <https://doi.org/10.1038/srep28765>.
- (200) Huynh, T. M.; Armbruster, U.; Pohl, M.-M.; Schneider, M.; Radnik, J.; Hoang, D.-L.; Phan, B. M. Q.; Nguyen, D. A.; Martin, A. Hydrodeoxygenation of Phenol as a Model Compound for Bio-Oil on Non-Noble Bimetallic Nickel-Based Catalysts. *ChemCatChem* **2014**, *6* (7), 1940–1951. <https://doi.org/10.1002/cctc.201402011>.
- (201) Wu, X.; Wang, Z.; Zhang, D.; Qin, Y.; Wang, M.; Han, Y.; Zhan, T.; Yang, B.; Li, S.; Lai, J.; Wang, L. Solvent-Free Microwave Synthesis of Ultra-Small Ru-Mo₂C@CNT with Strong Metal-Support Interaction for Industrial Hydrogen Evolution. *Nat. Commun.* **2021**, *12* (1), 1–10. <https://doi.org/10.1038/s41467-021-24322-2>.
- (202) Huang, Y.; Gong, Q.; Song, X.; Feng, K.; Nie, K.; Zhao, F.; Wang, Y.; Zeng, M.; Zhong, J.; Li, Y. Mo₂C Nanoparticles Dispersed on Hierarchical Carbon Microflowers for Efficient Electrocatalytic Hydrogen Evolution. *ACS Nano* **2016**, *10* (12), 11337–11343. <https://doi.org/10.1021/acsnano.6b06580>.
- (203) Huang, X.; Wang, J.; Bing Tao, H.; Tian, H.; Zhang, Z.; Xu, H. Unraveling the Oxide Layer on Mo₂C as the Active Center for Hydrogen Evolution Reaction. *J. Catal.* **2020**, *389*, 461–467. <https://doi.org/10.1016/j.jcat.2020.06.020>.
- (204) Zhang, Q.; Pastor-Pérez, L.; Gu, S.; Reina, T. R. Transition Metal Carbides (TMCS) Catalysts for Gas Phase CO₂ Upgrading Reactions: A Comprehensive Overview. *Catalysts* **2020**, *10* (9). <https://doi.org/10.3390/catal10090955>.
- (205) Porosoff, M. D.; Baldwin, J. W.; Peng, X.; Mpourmpakis, G.; Willauer, H. D. Potassium-Promoted Molybdenum Carbide as a Highly Active and Selective Catalyst for CO₂ Conversion to CO. *ChemSusChem* **2017**, *10* (11), 2408–2415. <https://doi.org/10.1002/cssc.201700412>.

- (206) Porosoff, M. D.; Yang, X.; Boscoboinik, J. A.; Chen, J. G. Molybdenum Carbide as Alternative Catalysts to Precious Metals for Highly Selective Reduction of CO₂ to CO. *Angew. Chemie - Int. Ed.* **2014**, *53* (26), 6705–6709. <https://doi.org/10.1002/anie.201404109>.
- (207) Brungs, A. J.; York, A. P. E.; Green, M. L. H. Comparison of the Group V and VI Transition Metal Carbides for Methane Dry Reforming and Thermodynamic Prediction of Their Relative Stabilities. *Catal. Letters* **1999**, *57* (1–2), 65–69. <https://doi.org/10.1023/a:1019062608228>.
- (208) Shi, C.; Zhang, A.; Li, X.; Zhang, S.; Zhu, A.; Ma, Y.; Au, C. Ni-Modified Mo₂C Catalysts for Methane Dry Reforming. *Appl. Catal. A Gen.* **2012**, *431–432*, 164–170. <https://doi.org/10.1016/j.apcata.2012.04.035>.
- (209) Tran, C.-C.; Mohan, O.; Banerjee, A.; Mushrif, S. H.; Kaliaguine, S. A Combined Experimental and DFT Investigation of Selective Hydrodeoxygenation of Guaiacol over Bimetallic Carbides. *Energy & Fuels* **2020**, *34* (12), 16265–16273.
- (210) Chen, C.-J.; Lee, W.-S.; Bhan, A. Mo₂C Catalyzed Vapor Phase Hydrodeoxygenation of Lignin-Derived Phenolic Compound Mixtures to Aromatics under Ambient Pressure. *Appl. Catal. A Gen.* **2016**, *510*, 42–48.
- (211) Zhang, W.; Zhang, Y.; Zhao, L.; Wei, W. Catalytic Activities of NiMo Carbide Supported on SiO₂ for the Hydrodeoxygenation of Ethyl Benzoate, Acetone, and Acetaldehyde. *Energy & Fuels* **2010**, *24* (3), 2052–2059.
- (212) Zhao, Z.; Yang, H.; Li, Y.; Guo, X. Cobalt-Modified Molybdenum Carbide as an Efficient Catalyst for Chemoselective Reduction of Aromatic Nitro Compounds. *Green Chem.* **2014**, *16* (3), 1274–1281. <https://doi.org/10.1039/C3GC42049C>.
- (213) Stankovikj, F.; Tran, C. C.; Kaliaguine, S.; Olarte, M. V.; Garcia-Perez, M. Evolution of Functional Groups during Pyrolysis Oil Upgrading. *Energy and Fuels* **2017**, *31* (8), 8300–8316. <https://doi.org/10.1021/acs.energyfuels.7b01251>.
- (214) He, R.; Ye, X. P.; English, B. C.; Satrio, J. A. Influence of Pyrolysis Condition on Switchgrass Bio-Oil Yield and Physicochemical Properties. *Bioresour. Technol.* **2009**, *100* (21), 5305–5311. <https://doi.org/10.1016/j.biortech.2009.02.069>.
- (215) Lohitharn, N.; Shanks, B. H. Upgrading of Bio-Oil: Effect of Light Aldehydes on Acetic Acid Removal via Esterification. *Catal. Commun.* **2009**, *11* (2), 96–99. <https://doi.org/10.1016/j.catcom.2009.09.002>.
- (216) Choi, Y. S.; Johnston, P. A.; Brown, R. C.; Shanks, B. H.; Lee, K. H. Detailed Characterization of Red Oak-Derived Pyrolysis Oil: Integrated Use of GC, HPLC, IC, GPC and Karl-Fischer. *J. Anal. Appl. Pyrolysis* **2014**, *110* (1), 147–154. <https://doi.org/10.1016/j.jaap.2014.08.016>.
- (217) Maduskar, S.; Maliekkal, V.; Neurock, M.; Dauenhauer, P. J. On the Yield of Levoglucosan from Cellulose Pyrolysis. *ACS Sustain. Chem. Eng.* **2018**, *6* (5), 7017–7025. <https://doi.org/10.1021/acssuschemeng.8b00853>.
- (218) Joubert, D. From Ultrasoft Pseudopotentials to the Projector Augmented-Wave Method.

- Phys. Rev. B - Condens. Matter Mater. Phys.* **1999**, *59* (3), 1758–1775. <https://doi.org/10.1103/PhysRevB.59.1758>.
- (219) Klime, J.; Bowler, D. R.; Michaelides, A. Van Der Waals Density Functionals Applied to Solids. *Phys. Rev. B - Condens. Matter Mater. Phys.* **2011**, *83* (19), 195131. <https://doi.org/10.1103/PhysRevB.83.195131>.
- (220) Kumar, A.; Phadke, S.; Bhan, A. Acetic Acid Hydrodeoxygenation on Molybdenum Carbide Catalysts. *Catal. Sci. Technol.* **2018**, *8* (11), 2938–2953. <https://doi.org/10.1039/C8CY00358K>.
- (221) Fang, H.; Roldan, A.; Tian, C.; Zheng, Y.; Duan, X.; Chen, K.; Ye, L.; Leoni, S.; Yuan, Y. Structural Tuning and Catalysis of Tungsten Carbides for the Regioselective Cleavage of C O Bonds. *J. Catal.* **2019**, *369*, 283–295. <https://doi.org/10.1016/j.jcat.2018.11.020>.
- (222) Fang, H.; Du, J.; Tian, C.; Zheng, J.; Duan, X.; Ye, L.; Yuan, Y. Regioselective Hydrogenolysis of Aryl Ether C-O Bonds by Tungsten Carbides with Controlled Phase Compositions. *Chem Commun* **2017**, *53* (74), 10295–10298. <https://doi.org/10.1039/c7cc05487d>.
- (223) Geißer, B.; Skrivanek, T.; Zimmermann, U.; Stufkens, D. J.; Alsfasser, R. Inductive Effects in Ruthenium-Modified Amino Acids. *Eur. J. Inorg. Chem.* **2001**, No. 2, 439–448. [https://doi.org/10.1002/1099-0682\(200102\)2001:2<439::aid-ejic439>3.0.co;2-v](https://doi.org/10.1002/1099-0682(200102)2001:2<439::aid-ejic439>3.0.co;2-v).
- (224) Dwiatmoko, A. A.; Seo, J.; Choi, J. W.; Suh, D. J.; Jae, J.; Ha, J. M. Improved Activity of a CaCO₃-Supported Ru Catalyst for the Hydrodeoxygenation of Eugenol as a Model Lignin-Derived Phenolic Compound. *Catal. Commun.* **2019**, *127*, 45–50. <https://doi.org/10.1016/J.CATCOM.2019.04.024>.
- (225) Sreenavya, A.; Sahu, A.; Sakthivel, A. Hydrogenation of Lignin-Derived Phenolic Compound Eugenol over Ruthenium-Containing Nickel Hydrotalcite-Type Materials. *Ind. Eng. Chem. Res.* **2020**, *59* (26), 11979–11990. https://doi.org/10.1021/ACS.IECR.0C01106/ASSET/IMAGES/LARGE/IE0C01106_0006.JPG.
- (226) Huš, M.; Bjelić, A.; Grilc, M.; Likozar, B. First-Principles Mechanistic Study of Ring Hydrogenation and Deoxygenation Reactions of Eugenol over Ru(0001) Catalysts. *J. Catal.* **2018**, *358*, 8–18. <https://doi.org/10.1016/j.jcat.2017.11.020>.
- (227) Deng, W.; Feng, Y.; Fu, J.; Guo, H.; Guo, Y.; Han, B.; Jiang, Z.; Kong, L.; Li, C.; Liu, H.; Nguyen, P. T. T.; Ren, P.; Wang, F.; Wang, S.; Wang, Y.; Wang, Y.; Wong, S. S.; Yan, K.; Yan, N.; Yang, X.; Zhang, Y.; Zhang, Z.; Zeng, X.; Zhou, H. Catalytic Conversion of Lignocellulosic Biomass into Chemicals and Fuels. *Green Energy Environ.* **2022**, No. xxxx. <https://doi.org/10.1016/j.gee.2022.07.003>.
- (228) Serrano-Ruiz, J. C.; Dumesic, J. A. Catalytic Routes for the Conversion of Biomass into Liquid Hydrocarbon Transportation Fuels. *Energy Environ. Sci.* **2011**, *4* (1), 83–99. <https://doi.org/10.1039/c0ee00436g>.
- (229) Lu, Q.; Chen, C.-J.; Luc, W.; Chen, J. G.; Bhan, A.; Jiao, F. Ordered Mesoporous Metal Carbides with Enhanced Anisole Hydrodeoxygenation Selectivity. *ACS Catal.* **2016**, *6* (6),

- 3506–3514. <https://doi.org/10.1021/acscatal.6b00303>.
- (230) Prasomsri, T.; Nimmanwudipong, T.; Román-Leshkov, Y. Effective Hydrodeoxygenation of Biomass-Derived Oxygenates into Unsaturated Hydrocarbons by MoO₃ Using Low H₂ Pressures. *Energy Environ. Sci.* **2013**, *6* (6), 1732–1738. <https://doi.org/10.1039/C3EE24360E>.
- (231) Oliveira, R. R.; Rocha, A. S.; Teixeira Da Silva, V.; Rocha, A. B. Investigation of Hydrogen Occlusion by Molybdenum Carbide. *Appl. Catal. A Gen.* **2014**, *469*, 139–145. <https://doi.org/10.1016/j.apcata.2013.09.031>.
- (232) Choi, Y.; Lee, J.; Shin, J.; Lee, S.; Kim, D.; Lee, J. K. Selective Hydroconversion of Naphthalenes into Light Alkyl-Aromatic Hydrocarbons. *Appl. Catal. A Gen.* **2015**, *492*, 140–150. <https://doi.org/10.1016/j.apcata.2014.12.001>.
- (233) Frauwallner, M. L.; López-Linares, F.; Lara-Romero, J.; Scott, C. E.; Ali, V.; Hernández, E.; Pereira-Almao, P. Toluene Hydrogenation at Low Temperature Using a Molybdenum Carbide Catalyst. *Appl. Catal. A Gen.* **2011**, *394* (1–2), 62–70. <https://doi.org/10.1016/j.apcata.2010.12.024>.
- (234) Choi, J. S.; Krafft, J. M.; Krzton, A.; Djéga-Mariadassou, G. Study of Residual Oxygen Species over Molybdenum Carbide Prepared During In Situ DRIFTS Experiments. *Catal. Lett.* **2002**, *81* (3), 175–180. <https://doi.org/10.1023/A:1016568804706>.
- (235) Lee, W.-S.; Wang, Z.; Wu, R. J.; Bhan, A. Selective Vapor-Phase Hydrodeoxygenation of Anisole to Benzene on Molybdenum Carbide Catalysts. *J. Catal.* **2014**, *319*, 44–53.
- (236) Likith, S. R. J.; Farberow, C. A.; Manna, S.; Abdulslam, A.; Stevanović, V.; Ruddy, D. A.; Schaidle, J. A.; Robichaud, D. J.; Ciobanu, C. V. Thermodynamic Stability of Molybdenum Oxycarbides Formed from Orthorhombic Mo₂C in Oxygen-Rich Environments. *J. Phys. Chem. C* **2018**, *122* (2), 1223–1233. <https://doi.org/10.1021/acs.jpcc.7b11110>.
- (237) Óvári, L.; Kiss, J.; Farkas, A. P.; Solymosi, F. Surface and Subsurface Oxidation of Mo₂C/Mo(100): Low-Energy Ion-Scattering, Auger Electron, Angle-Resolved X-Ray Photoelectron, and Mass Spectroscopy Studies. *J. Phys. Chem. B* **2005**, *109* (10), 4638–4645. <https://doi.org/10.1021/jp045693a>.
- (238) Blanco, E.; Díaz de León, J. N.; García-Fierro, J. L.; Escalona, N. Study of Supported Bimetallic MoRe Carbides Catalysts for Guaiacol Conversion. *Catal. Today.* **2021**, *367*, 290–296. <https://doi.org/10.1016/j.cattod.2020.03.031>.
- (239) Pang, J.; Sun, J.; Zheng, M.; Li, H.; Wang, Y.; Zhang, T. Transition Metal Carbide Catalysts for Biomass Conversion: A Review. *Applied Catalysis B: Environmental.* 2019. <https://doi.org/10.1016/j.apcatb.2019.05.034>.
- (240) Akmach, D.; Bathla, S.; Tran, C.-C.; Kaliaguine, S.; Mushrif, S. H. Transition Metal Carbide Catalysts for Upgrading Lignocellulosic Biomass-Derived Oxygenates: A Review of the Experimental and Computational Investigations into Structure-Property Relationships. *Catal. Today.* **2023**, *423*. <https://doi.org/10.1016/j.cattod.2023.114285>.
- (241) Ferna, M. Nanostructured Ti - W Mixed-Metal Oxides: Structural and Electronic Properties. **2005**, 6075–6083.

- (242) Védrine, J. C. Importance, Features and Uses of Metal Oxide Catalysts in Heterogeneous Catalysis. *Chinese J. Catal.* **2019**, *40* (11), 1627–1636. [https://doi.org/10.1016/S1872-2067\(18\)63162-6](https://doi.org/10.1016/S1872-2067(18)63162-6).
- (243) Ham, D.; Lee, J. Transition Metal Carbides and Nitrides as Electrode Materials for Low Temperature Fuel Cells. *Energies* **2009**, *2* (4), 873–899. <https://doi.org/10.3390/en20400873>.
- (244) Schaidle, J. A.; Lausche, A. C.; Thompson, L. T. Effects of Sulfur on Mo₂C and Pt/Mo₂C Catalysts: Water Gas Shift Reaction. *J. Catal.* **2010**, *272* (2), 235–245. <https://doi.org/10.1016/j.jcat.2010.04.004>.
- (245) Zhang, X.; Zhang, M.; Deng, Y.; Xu, M.; Artiglia, L.; Wen, W.; Gao, R.; Chen, B.; Yao, S.; Zhang, X.; Peng, M.; Yan, J.; Li, A.; Jiang, Z.; Gao, X.; Cao, S.; Yang, C.; Kropf, A. J.; Shi, J.; Xie, J.; Bi, M.; van Bokhoven, J. A.; Li, Y. W.; Wen, X.; Flytzani-Stephanopoulos, M.; Shi, C.; Zhou, W.; Ma, D. A Stable Low-Temperature H₂-Production Catalyst by Crowding Pt on α -MoC. *Nature* **2021**, *589* (7842), 396–401. <https://doi.org/10.1038/s41586-020-03130-6>.
- (246) Jain, A.; Montoya, J.; Dwaraknath, S.; Zimmermann, N. E. R.; Dagdelen, J.; Horton, M.; Huck, P.; Winston, D.; Cholia, S.; Ong, S. P.; Persson, K. *The Materials Project: Accelerating Materials Design Through Theory-Driven Data and Tools*; 2020. https://doi.org/10.1007/978-3-319-44677-6_60.
- (247) Regmi, Y. N.; Leonard, B. M. General Synthesis Method for Bimetallic Carbides of Group VIIIA First Row Transition Metals with Molybdenum and Tungsten. *Chem. Mater.* **2014**, *26* (8), 2609–2616. <https://doi.org/10.1021/cm500076v>.
- (248) Tehrani, A. M.; Oliynyk, A. O.; Rizvi, Z.; Lotfi, S.; Parry, M.; Sparks, T. D.; Brgoch, J. Atomic Substitution to Balance Hardness, Ductility, and Sustainability in Molybdenum Tungsten Borocarbide. *Chem. Mater.* **2019**, *31* (18), 7696–7703. <https://doi.org/10.1021/acs.chemmater.9b02596>.
- (249) Sholl, D. S.; Steckel, J. a. DFT Calculations for Simple Solids. *Density Funct. Theory* **2009**, 35–48. <https://doi.org/10.1002/9780470447710.ch2>.
- (250) A, C. L.; Krishnan, R.; L, D. J. Computational Thermochemistry. *Comput. Thermochem.* **1998**, *677* (3), 176–196. <https://doi.org/10.1021/bk-1998-0677.ch014>.
- (251) Kepp, K. P. A Quantitative Scale of Oxophilicity and Thiophilicity. *Inorg. Chem.* **2016**, *55* (18), 9461–9470. <https://doi.org/10.1021/acs.inorgchem.6b01702>.
- (252) Shi, Y.; Yang, Y.; Li, Y. W.; Jiao, H. Activation Mechanisms of H₂, O₂, H₂O, CO₂, CO, CH₄ and C₂H_x on Metallic Mo₂C(001) as Well as Mo/C Terminated Mo₂C(101) from Density Functional Theory Computations. *Appl. Catal. A Gen.* **2016**, *524*, 223–236. <https://doi.org/10.1016/j.apcata.2016.07.003>.
- (253) Hammer, B.; Hansen, L. B.; Nørskov, J. K. Improved Adsorption Energetics within Density-Functional Theory Using Revised Perdew-Burke-Ernzerhof Functionals. *Phys. Rev. B* **1999**, *59* (11), 7413. <https://doi.org/10.1103/PhysRevB.59.7413>.
- (254) Yoosuk, B.; Tumnantong, D.; Prasassarakich, P. Unsupported MoS₂ and CoMoS₂

- Catalysts for Hydrodeoxygenation of Phenol. *Chem. Eng. Sci.* **2012**, *79*, 1–7. <https://doi.org/10.1016/j.ces.2012.05.020>.
- (255) Mortensen, P. M.; Grunwaldt, J. D.; Jensen, P. A.; Jensen, A. D. Screening of Catalysts for Hydrodeoxygenation of Phenol as a Model Compound for Bio-Oil. *ACS Catal.* **2013**, *3* (8), 1774–1785. <https://doi.org/10.1021/cs400266e>.
- (256) De Souza, P. M.; Rabelo-Neto, R. C.; Borges, L. E. P.; Jacobs, G.; Davis, B. H.; Resasco, D. E.; Noronha, F. B. Hydrodeoxygenation of Phenol over Pd Catalysts. Effect of Support on Reaction Mechanism and Catalyst Deactivation. *ACS Catal.* **2017**, *7* (3), 2058–2073. <https://doi.org/10.1021/acscatal.6b02022>.
- (257) Mohan, O.; Xu, R.; Mushrif, S. H. Novel Nickel-Based Single-Atom Alloy Catalyst for CO₂ Conversion Reactions: Computational Screening and Reaction Mechanism Analysis. *J. Phys. Chem. C* **2021**, *125* (7), 4041–4055. <https://doi.org/10.1021/acs.jpcc.0c11578>.
- (258) Priya, B.; Bathla, S.; Kumar, A.; Singh, S. K.; Mushrif, S. H. Water-Assisted Hydrogenation of Aromatics under Ambient Conditions over Ru Catalyst: A Combined Experimental and Computational Investigation. *J. Catal.* **2024**, *434*, 115522. <https://doi.org/10.1016/j.jcat.2024.115522>.
- (259) Chen, L.; Liu, W.; Feng, H.; Ren, Y.; Chen, C.; Wang, S.; Yin, P.; Yang, Y.; Zhang, X.; Wei, M. Oxygen Binding Energy of Doped Metal: A Shortcut to Efficient Ni-Based Bimetallic Catalysts for the Hydrodeoxygenation Reaction. *Catal. Sci. Technol.* **2021**, *11* (13), 4376–4386. <https://doi.org/10.1039/d1cy00496d>.
- (260) Avanesian, T.; Gusmão, G. S.; Christopher, P. Mechanism of CO₂ Reduction by H₂ on Ru(0 0 0 1) and General Selectivity Descriptors for Late-Transition Metal Catalysts. *J. Catal.* **2016**, *343*, 86–96. <https://doi.org/10.1016/j.jcat.2016.03.016>.
- (261) Jia, X.; An, W.; Wang, Z.; Zhou, J. Effect of Doped Metals on Hydrodeoxygenation of Phenol over Pt-Based Bimetallic Alloys: Caryl-OH Versus AliphaticH-OH Bond Scission. *J. Phys. Chem. C* **2019**, *123* (27), 16873–16882. <https://doi.org/10.1021/acs.jpcc.9b04457>.
- (262) Abbasi, T.; Abbasi, S. A. Biomass Energy and the Environmental Impacts Associated with Its Production and Utilization. *Renew. Sustain. Energy Rev.* **2010**, *14* (3), 919–937. <https://doi.org/10.1016/j.rser.2009.11.006>.
- (263) Sasaki, H. Non-Renewable Resources and the Possibility of Sustainable Economic Development in an Economy with Positive or Negative Population Growth. *Bull. Econ. Res.* **2021**, *73* (4), 704–720. <https://doi.org/10.1111/boer.12276>.
- (264) Isikgor, F. H.; Becer, C. R. Lignocellulosic Biomass: A Sustainable Platform for the Production of Bio-Based Chemicals and Polymers. *Polym. Chem.* **2015**, *6* (25), 4497–4559. <https://doi.org/10.1039/c5py00263j>.
- (265) Li, C.; Zhao, X.; Wang, A.; Huber, G. W.; Zhang, T. Catalytic Transformation of Lignin for the Production of Chemicals and Fuels. *Chem. Rev.* **2015**, *115* (21), 11559–11624. <https://doi.org/10.1021/acs.chemrev.5b00155>.
- (266) Sun, Z.; Fridrich, B.; De Santi, A.; Elangovan, S.; Barta, K. Bright Side of Lignin Depolymerization: Toward New Platform Chemicals. *Chem. Rev.* **2018**, *118* (2), 614–678.

<https://doi.org/10.1021/acs.chemrev.7b00588>.

- (267) Mei, Q.; Shen, X.; Liu, H.; Han, B. Selectively Transform Lignin into Value-Added Chemicals. *Chinese Chem. Lett.* **2019**, *30* (1), 15–24. <https://doi.org/10.1016/j.ccllet.2018.04.032>.
- (268) Shen, X.; Zhang, C.; Han, B.; Wang, F. Catalytic Self-Transfer Hydrogenolysis of Lignin with Endogenous Hydrogen: Road to the Carbon-Neutral Future. *Chem. Soc. Rev.* **2022**, *51* (5), 1608–1628. <https://doi.org/10.1039/d1cs00908g>.
- (269) Agarwal, A.; Rana, M.; Park, J. H. Advancement in Technologies for the Depolymerization of Lignin. *Fuel Process. Technol.* **2018**, *181* (August 2018), 115–132. <https://doi.org/10.1016/j.fuproc.2018.09.017>.
- (270) Liu, C.; Wu, S.; Zhang, H.; Technology, R. X.-F. P.; 2019, undefined. Catalytic Oxidation of Lignin to Valuable Biomass-Based Platform Chemicals: A Review. *Elsevier*.
- (271) Mahmood, N.; Yuan, Z.; Schmidt, J.; Xu, C. Production of Polyols via Direct Hydrolysis of Kraft Lignin: Effect of Process Parameters. *Bioresour. Technol.* **2013**, *139*, 13–20. <https://doi.org/10.1016/j.biortech.2013.03.199>.
- (272) Zhang, J.; Sun, J.; Wang, Y. Recent Advances in the Selective Catalytic Hydrodeoxygenation of Lignin-Derived Oxygenates to Arenes. *Green Chem.* **2020**, *22* (4), 1072–1098. <https://doi.org/10.1039/c9gc02762a>.
- (273) Tu, R.; Lv, W.; Sun, Y.; Wu, Y.; Wu, Y.; Fan, X.; ... E. J.-C. E.; 2023, undefined. Ru-RuO₂-Nb₂O₅/H β Zeolite Catalyst for High-Active Hydrogenation of Lignin Derivatives at Room Temperature. *Elsevier*.
- (274) Cui, X.; Surkus, A. E.; Junge, K.; Topf, C.; Radnik, J.; Kreyenschulte, C.; Beller, M. Highly Selective Hydrogenation of Arenes Using Nanostructured Ruthenium Catalysts Modified with a Carbon-Nitrogen Matrix. *Nat. Commun.* **2016**, *7*, 1–8. <https://doi.org/10.1038/ncomms11326>.
- (275) Boronoev, M. P.; Shakirov, I. I.; Roldugina, E. A.; Kardasheva, Y. S.; Kardashev, S. V.; Maksimov, A. L.; Karakhanov, E. A. Hydrogenation of Guaiacol on Nanoscale Supported Ruthenium Catalysts: Influence of Support Particle Size and the Presence of Bio-Oil Oxygenates. *Russ. J. Appl. Chem.* **2022**, *95* (10), 1555–1563. <https://doi.org/10.1134/S1070427222100068>.
- (276) Patharkar, R. G.; Nandanwar, S. U.; Chakraborty, M. Synthesis of Colloidal Ruthenium Nanocatalyst by Chemical Reduction Method. *J. Chem.* **2013**, *2013*, 2–6. <https://doi.org/10.1155/2013/831694>.
- (277) Kumar, A.; Awasthi, M. K.; Sheet, N.; Kharde, T. A.; Singh, S. K. One-Pot Upcycling of Waste Plastics for Selective Hydrogen Production at Low-Temperature. *ChemCatChem* **2023**, *15* (18). <https://doi.org/10.1002/cctc.202300574>.
- (278) Banerjee, A.; Mushrif, S. H. Investigating Reaction Mechanisms for Furfural Hydrodeoxygenation on Ni and the Effect of Boron Doping on the Activity and Selectivity of the Catalyst. *J. Phys. Chem. C* **2018**, *122* (32), 18383–18394. <https://doi.org/10.1021/ACS.JPCC.8B01301>.

- (279) Analysis, D. M.-S. and I.; 2015, undefined. Resolving Ruthenium: XPS Studies of Common Ruthenium Materials. *Wiley Online Libr.* **2015**, *47* (11), 1072–1079. <https://doi.org/10.1002/sia.5852>.
- (280) Ma, Z.; Zhao, S.; Pei, X.; Xiong, X.; Technology, B. H.-C. S. &; 2017, undefined. New Insights into the Support Morphology-Dependent Ammonia Synthesis Activity of Ru/CeO₂ Catalysts. *pubs.rsc.org*.
- (281) Zawadzki, M.; Okal, J. Synthesis and Structure Characterization of Ru Nanoparticles Stabilized by PVP or γ -Al₂O₃. *Mater. Res. Bull.* **2008**, *43* (11), 3111–3121. <https://doi.org/10.1016/j.materresbull.2007.11.006>.
- (282) Cao, N.; Luo, W.; Cheng, G. One-Step Synthesis of Graphene Supported Ru Nanoparticles as Efficient Catalysts for Hydrolytic Dehydrogenation of Ammonia Borane. *Int. J. Hydrogen Energy* **2013**, *38* (27), 11964–11972. <https://doi.org/10.1016/j.ijhydene.2013.06.125>.
- (283) Yang, J.; Ye, F.; Liu, H.; Yang, J.; Cao, H. Morphology and Structure Controlled Synthesis of Ruthenium Nanoparticles in Oleylamine. *Dalt. Trans.* **2013**, *42* (34), 12309–12316. <https://doi.org/10.1039/c3dt51294k>.
- (284) Chakroune, N.; Viau, G.; Ammar, S.; Poul, L.; Veautier, D.; Chehimi, M. M.; Mangeney, C. Nanoparticles : XPS , XAS , and HRTEM Studies Edited by Foxit Reader. *Electronics* **2006**, *6796* (16), 6788–6796.
- (285) Iqbal, S.; Kondrat, S. A.; Jones, D. R.; Schoenmakers, D. C.; Edwards, J. K.; Lu, L.; Yeo, B. R.; Wells, P. P.; Gibson, E. K.; Morgan, D. J.; Kiely, C. J.; Hutchings, G. J. Ruthenium Nanoparticles Supported on Carbon: An Active Catalyst for the Hydrogenation of Lactic Acid to 1,2-Propanediol. *ACS Catal.* **2015**, *5* (9), 5047–5059. https://doi.org/10.1021/ACSCATAL.5B00625/ASSET/IMAGES/LARGE/CS-2015-00625E_0016.JPEG.
- (286) Methaapanon, R.; Geyer, S. M.; Lee, H. B. R.; Bent, S. F. The Low Temperature Atomic Layer Deposition of Ruthenium and the Effect of Oxygen Exposure. *J. Mater. Chem.* **2012**, *22* (48), 25154–25160. <https://doi.org/10.1039/c2jm35332f>.
- (287) Koopman, P. G. J.; Kieboom, A. P. G.; van Bekkum, H. Characterization of Ruthenium Catalysts as Studied by Temperature Programmed Reduction. *J. Catal.* **1981**, *69* (1), 172–179. [https://doi.org/10.1016/0021-9517\(81\)90139-1](https://doi.org/10.1016/0021-9517(81)90139-1).
- (288) Maximov, A. L.; Zolotukhina, A. V.; Mamedli, A. A.; Kulikov, L. A.; Karakhanov, E. A. Selective Levulinic Acid Hydrogenation in the Presence of Hybrid Dendrimer-Based Catalysts. Part I: Monometallic. *ChemCatChem* **2018**, *10* (1), 222–233. <https://doi.org/10.1002/cctc.201700691>.
- (289) Noël, S.; Madureira, A.; Léger, B.; Ponchel, A.; Sadjadi, S.; Monflier, É. Cyclodextrin-Assisted Catalytic Hydrogenation of Hydrophobic Substrates with Halloysite Immobilized Ruthenium NPs Dispersed in Aqueous Phase. *J. Indian Chem. Soc.* **2021**, *98* (3). <https://doi.org/10.1016/j.jics.2021.100034>.
- (290) Kong, X.; Gong, Y.; Mao, S.; Wang, Y. Selective Hydrogenation of Phenol. *ChemNanoMat*

- 2018**, 4 (5), 432–450. <https://doi.org/10.1002/cnma.201800031>.
- (291) Li, G.; Han, J.; Wang, H.; Zhu, X.; Ge, Q. Role of Dissociation of Phenol in Its Selective Hydrogenation on Pt(111) and Pd(111). *ACS Catal.* **2015**, 5 (3), 2009–2016. <https://doi.org/10.1021/cs501805y>.
- (292) Mao, S.; Wang, Z.; Chen, Z.; Wu, K.; Zhang, K.; Li, Q.; Yan, H.; Lü, G.; Huang, G.; Wang, Y. Towards the Selectivity Distinction of Phenol Hydrogenation on Noble Metal Catalysts. *Nano Mater. Sci.* **2023**, 5 (1), 91–100. <https://doi.org/10.1016/j.nanoms.2020.11.002>.
- (293) Wang, X.; ChemSusChem, R. R.-; 2012, undefined. Solvent Effects on the Hydrogenolysis of Diphenyl Ether with Raney Nickel and Their Implications for the Conversion of Lignin. *Wiley Online Libr.* **2012**, 5 (8), 1455–1466. <https://doi.org/10.1002/cssc.201200040>.
- (294) Feng, G.; Liu, Z.; Chen, P.; Lou, H. Influence of Solvent on Upgrading of Phenolic Compounds in Pyrolysis Bio-Oil. *RSC Adv.* **2014**, 4 (91), 49924–49929. <https://doi.org/10.1039/c4ra10891d>.
- (295) Zope, B. N.; Hibbitts, D. D.; Neurock, M.; Davis, R. J. During Selective Oxidation Catalysis. *Science (80-.)*. **2010**, 533 (OCTOBER), 74–79.
- (296) Tan, J.; Cui, J.; Deng, T.; Cui, X.; Ding, G.; Zhu, Y.; Li, Y. Water-Promoted Hydrogenation of Levulinic Acid to γ -Valerolactone on Supported Ruthenium Catalyst. *ChemCatChem* **2015**, 7 (3), 508–512. <https://doi.org/10.1002/cctc.201402834>.
- (297) Song, W.; He, Y.; Lai, S.; Lai, W.; Yi, X.; Yang, W.; Jiang, X. Selective Hydrodeoxygenation of Lignin Phenols to Alcohols in the Aqueous Phase over a Hierarchical Nb₂O₅-Supported Ni Catalyst. *Green Chem.* **2020**, 22 (5), 1662–1670. <https://doi.org/10.1039/c9gc03842f>.
- (298) Shu, R.; Zhang, Q.; Xu, Y.; Long, J.; Ma, L.; Wang, T.; Chen, P.; Wu, Q. Hydrogenation of Lignin-Derived Phenolic Compounds over Step by Step Precipitated Ni/SiO₂. *RSC Adv.* **2016**, 6 (7), 5214–5222. <https://doi.org/10.1039/c5ra23041a>.
- (299) Mironenko, A. V.; Vlachos, D. G. Conjugation-Driven “Reverse Mars-van Krevelen”-Type Radical Mechanism for Low-Temperature C-O Bond Activation. *J. Am. Chem. Soc.* **2016**, 138 (26), 8104–8113. <https://doi.org/10.1021/jacs.6b02871>.
- (300) Lu, J.; Heyden, A. Theoretical Investigation of the Reaction Mechanism of the Hydrodeoxygenation of Guaiacol over a Ru(0 0 0 1) Model Surface. *J. Catal.* **2015**, 321, 39–50. <https://doi.org/10.1016/j.jcat.2014.11.003>.
- (301) Gao, M.; Tan, H.; Zhu, P.; Zhang, J.; Wang, H.; Liu, X.; Zheng, Z. Why Phenol Is Selectively Hydrogenated to Cyclohexanol on Ru (0001): An Experimental and Theoretical Study. *Appl. Surf. Sci.* **2021**, 558 (January), 149880. <https://doi.org/10.1016/j.apsusc.2021.149880>.
- (302) Maier, S.; Stass, I.; Cerdá, J. I.; Salmeron, M. Unveiling the Mechanism of Water Partial Dissociation on Ru(0001). *Phys. Rev. Lett.* **2013**, 112 (12), 1–5. <https://doi.org/10.1103/PhysRevLett.112.126101>.
- (303) Demir, B.; Kropp, T.; Gilcher, E. B.; Mavrikakis, M.; Dumesic, J. A. Effects of Water on

- the Kinetics of Acetone Hydrogenation over Pt and Ru Catalysts. *J. Catal.* **2021**, *403*, 215–227. <https://doi.org/10.1016/J.JCAT.2021.03.013>.
- (304) Wu, Z.; Chin, Y. H. C. Catalytic Pathways and Mechanistic Consequences of Water during Vapor Phase Hydrogenation of Butanal on Ru/SiO₂. *J. Catal.* **2021**, *394*, 429–443. <https://doi.org/10.1016/j.jcat.2020.10.022>.
- (305) Sun, H.; Guo, W.; Zhou, X.; Chen, Z.; Liu, Z.; Liu, S. Progress in Ru-Based Amorphous Alloy Catalysts for Selective Hydrogenation of Benzene to Cyclohexene. *Chinese J. Catal.* **2011**, *32* (1–2), 1–16. [https://doi.org/10.1016/S1872-2067\(10\)60154-4](https://doi.org/10.1016/S1872-2067(10)60154-4).
- (306) Wang, J.; Wang, Y.; Xie, S.; Qiao, M.; Li, H.; Fan, K. Partial Hydrogenation of Benzene to Cyclohexene on a Ru–Zn/m-ZrO₂ Nanocomposite Catalyst. *Appl. Catal. A Gen.* **2004**, *272* (1–2), 29–36. <https://doi.org/10.1016/J.APCATA.2004.04.038>.
- (307) Ning, J.; Xu, J.; Liu, J.; Lu, F. Selective Hydrogenation of Benzene to Cyclohexene Over Colloidal Ruthenium Catalyst Stabilized by Silica. *Catal. Lett.* **2006**, *109* (3), 175–180. <https://doi.org/10.1007/S10562-006-0075-1>.
- (308) Fan, C.; Zhu, Y. A.; Zhou, X. G.; Liu, Z. P. Catalytic Hydrogenation of Benzene to Cyclohexene on Ru(0 0 1) from Density Functional Theory Investigations. *Catal. Today* **2011**, *160* (1), 234–241. <https://doi.org/10.1016/J.CATTOD.2010.03.075>.
- (309) Motagamwala, A. H.; Dumesic, J. A. Microkinetic Modeling: A Tool for Rational Catalyst Design. *Chem. Rev.* **2021**, *121* (2), 1049–1076. <https://doi.org/10.1021/acs.chemrev.0c00394>.
- (310) Mohan, O.; Shambhawi; Lapkin, A. A.; Mushrif, S. H. Investigating Methane Dry Reforming on Ni and B Promoted Ni Surfaces: DFT Assisted Microkinetic Analysis and Addressing the Coking Problem. *Catal. Sci. Technol.* **2020**, *10* (19), 6628–6643. <https://doi.org/10.1039/d0cy00939c>.
- (311) Shambhawi, N.; Mohan, O.; Choksi, T. S.; Lapkin, A. A. The Design and Optimization of Heterogeneous Catalysts Using Computational Methods. *Catal. Sci. Technol.* **2023**, *14* (3), 515–532. <https://doi.org/10.1039/d3cy01160g>.
- (312) Lym, J.; Gu, G. H.; Jung, Y.; Vlachos, D. G. Lattice Convolutional Neural Network Modeling of Adsorbate Coverage Effects. *J. Phys. Chem. C* **2019**, *123* (31), 18951–18959. <https://doi.org/10.1021/acs.jpcc.9b03370>.
- (313) Toyao, T.; Maeno, Z.; Takakusagi, S.; Kamachi, T.; Takigawa, I.; Shimizu, K. I. Machine Learning for Catalysis Informatics: Recent Applications and Prospects. *ACS Catal.* **2020**, *10* (3), 2260–2297. <https://doi.org/10.1021/acscatal.9b04186>.
- (314) Yang, Z.; Gao, W. Applications of Machine Learning in Alloy Catalysts: Rational Selection and Future Development of Descriptors. *Adv. Sci.* **2022**, *9* (12), 1–22. <https://doi.org/10.1002/advs.202106043>.

Appendices

Appendix A Computational Methods

A.1 Overview of Electronic Structure Calculations

The Schrödinger equation is a second order differential equation that forms the basis of quantum mechanics.¹ It can describe the spatial and temporal evolution of the wavefunction of a particle in a given potential. It is given as,

$$H\psi(r, t) = i\hbar \frac{\partial}{\partial t} \psi(r, t) \quad (\text{A-1})$$

Where \hbar is the reduced Planck's constant, ψ is the wavefunction and H is the Hamiltonian operator which is given as follows:

$$H = \left(\frac{\hbar^2}{2m} \nabla^2 + U(r) \right) \quad (\text{A-2})$$

The first term in the Hamiltonian operator is the kinetic energy operator and the second term is the potential energy operator. The wavefunction can be separated into the spatial and temporal parts on applying the separation of variables approach as follows:

$$\Psi(r, t) = \Psi(r)f(t) \quad (\text{A-3})$$

On substituting equation, A-3 into equation A-1, we get

$$\frac{1}{\Psi(r)} H\Psi(r) = \frac{1}{f(t)} i\hbar \frac{d}{dt} f(t) \quad (\text{A-4})$$

The left-hand side (L.H.S.) of equation (A-4) is only a function of space while the right-hand side (R.H.S.) is only a function of time. Since these two are completely independent variables, equation (A-4) can only be true when both the sides of the equation are constant, i.e.

$$\frac{1}{\Psi(r)} H\Psi(r) = E; H\Psi(r) = E\Psi(r) \quad (\text{A-5})$$

E is a constant in equation (A-5). Since the Hamiltonian is an energy operator, it is intuitive that the E is the energy of the system. We can solve for $f(t) = \exp\left(-\frac{iEt}{\hbar}\right)$ and after substituting $f(t)$ in equation (A-3), we get:

$$\Psi(r, t) = \Psi(r) \exp\left(-\frac{iEt}{\hbar}\right) \quad (\text{A-6})$$

Thus, the wavefunction can be written as a function of time and space with amplitude $\Psi(r)$ and phase $\exp\left(-\frac{iEt}{\hbar}\right)$. The time independent Schrodinger equation can be obtained after substituting equation (A-6) into equation (A-1),

$$H\Psi(r) = E\Psi(r) \quad (\text{A-7})$$

$$\left[-\frac{\hbar^2}{2m}\nabla^2 + U(r)\right]\Psi(r) = E\Psi(r) \quad (\text{A-8})$$

From now on, when we refer to the Schrodinger equation, we will be referring to the time-independent version of it.

A nucleus is significantly heavier than electrons, and this substantial mass difference implies that its velocity is much lower compared to that of the electrons. Consequently, nuclei display minimal quantum effects and can be approached using classical mechanics. Electrons, on the other hand, can promptly adapt to any alterations in the nuclear coordinates. It is possible to represent an atom or molecule as a collection of electrons (e) and nuclei (n). We can use the coordinates r_e and R_n to describe the positions of electrons and nuclei, respectively. Then, the Schrodinger equation can be written as follows;

$$H_{sys}\Psi_{sys}(r_e, R_n) = E_{sys}\Psi_{sys}(r_e, R_n) \quad (\text{A-9})$$

With the Hamiltonian defined by

$$H_{sys} = T_n + T_e + V_{ee}(r_e) + V_{en}(r_e, R_n) + V_m(R_n) = T_n + H_e \quad (\text{A-10})$$

T denotes the kinetic energy operator and V denotes the potential energy operator (columbic interactions between electron-electron, electron-nucleus and nucleus-nucleus). The total wavefunction of the system depends on the coordinates and velocities of the electrons and the nuclei. However, due to the separation of time scales between the electronic and nuclear motion (nuclei moving much slower than the electrons) it can be assumed that the nuclei are almost stationary with respect to the electrons. This is known as the Born-Oppenheimer approximation.

Using this approximation, the separation of electronic and nuclear motion in a system can be done as follows;

$$H_e \Psi_e(r_e, R_n) = E_e \Psi_e(r_e, R_n) \quad (\text{A-11})$$

Here the energy, E_e , and the wavefunction, Ψ_e , depend only on the nuclear coordinates and not on nuclear velocities. The total energy of the system then can be computed from the following equation.

$$(T_e + E_e) \Psi_n(R_n) = E_{sys} \Psi_n(R_n) \quad (\text{A-12})$$

Most of the electronic structure calculations are performed using this approximation (i.e. using equation (A-11) instead of equation (A-9) and all the electronic structure calculation methods described henceforth in this will be using the Born-Oppenheimer approximation.

A.2 Density Functional Theory (DFT)

A.2.1 Origin and Formulation

The rigorous developments of the density-functional theory were posed by Hohenberg, Kohn and Sham^{2,3} that legitimized the model intuitively established by Thomas, Fermi and Dirac. Comparing with the wave-function approach, DFT could describe the system by connecting the electron density with the energy of the system while the complexity and computational cost of a wave function increases exponentially with the size of a system. They overcome the overwhelming complexity of wavefunction by using electron density to calculate electronic energy which is the primary target. In the previous section, we discussed that the Schrodinger wave equation for an N electron system is given as

$$\left[\sum_i^N -\frac{1}{2} \nabla^2 - \sum_i^N \sum_j^N \frac{1}{r_{ij}} + \sum_i^N \frac{Z}{r_i} \right] \Psi = E \Psi \quad (\text{A-13})$$

The ground state electronic density of the system can be calculated as follows;

$$\rho(r_1) = N \int dx_1 dx_2 \dots dN \Psi^*(r_1, x_1, \dots, N) \Psi(r_1, x_1, \dots, N) \quad (\text{A-14})$$

For a given potential, it is possible to compute the ground state density using Equations (A-13) and (A-14) via the electronic wavefunction. However, Hohenberg and Kohn³ showed that there

exists an inverse mapping with which it is possible to obtain an external potential, if the ground state is known or provided. They also demonstrated that this inverse mapping can be employed to determine the ground state energy of a multielectron system using the variational principle, without needing to calculate the wavefunction. If the wavefunction is given as

$$\Psi = \Psi(v) \text{ and } v = (\rho) \quad (\text{A-15})$$

$$\Psi = (\rho) \quad (\text{A-16})$$

Using the variational principle, the energy of the system can be calculated as,

$$E = \min\langle\Psi|H|\Psi\rangle = \min\langle\Psi[\rho]|H|\Psi[\rho]\rangle = \langle\Psi[\rho]|T + v + V_{ee}|\Psi[\rho]\rangle \quad (\text{A-17})$$

Where $T = \left(-\frac{\nabla^2}{2}\right)$, $v = \left(-\frac{Z}{r}\right)$ and $V_{ee} = \frac{1}{r_{ee}}$

On rearranging equation (A-17), it can be re-written as follows;

$$E = \min\{\langle\Psi[\rho]|v + |\Psi[\rho]\rangle + \langle\Psi[\rho]|T + V_{ee}|\Psi[\rho]\rangle\} \quad (\text{A-18})$$

$$E = \min\{d^3r\rho(r)v(r) + F[\rho]\} \quad (\text{A-19})$$

The energy is thus minimized over the density and not over the wave function.

The inverse mapping of density on potential is also valid, by Thomas⁴ and Fermi⁵, provided a way to calculate the energy of a non-interacting system by replacing the wave function with electron density:

$$E = \sum_{i=1}^N \int d^3r \chi_i(\vec{r}) \left(-\frac{\nabla^2}{2}\right) \chi_i(\vec{r}) + \sum_{i=1}^N \int d^3r \chi_i(\vec{r}) \chi_i(\vec{r}) v(\vec{r}) \quad (\text{A-20})$$

$$= \sum_{i=1}^N \int d^3r \chi_i(\vec{r}) \left(-\frac{\nabla^2}{2}\right) \chi_i(\vec{r}) + \sum_{i=1}^N \int d^3r \rho(\vec{r}) v(\vec{r}) \quad (\text{A-21})$$

As shown in equation (A-21), Thomas-Fermi replaced the wave function with the electronic density. They also showed that the kinetic energy part of a homogenous electron gas is given as:

$$T_s = \frac{3}{10} (3\pi^2)^{\frac{2}{3}} \int d^3r \rho^{\frac{5}{3}}(\vec{r}) \quad (\text{A-22})$$

Hence according to Thomas-Fermi approach, the energy of the non-interacting system can be given in terms of the electron density as,

$$E(\rho) = \sum_{i=1}^N \frac{3}{10} (3\pi^2)^{\frac{2}{3}} \int d^3r \rho^{\frac{5}{3}}(\vec{r}) + \int d^3r \rho(\vec{r}) v(\vec{r}) \quad (\text{A-23})$$

This Thomas-Fermi approach of calculating the kinetic energy part of the non-interacting system of electrons is used to develop a scheme to evaluate the functional $F[\rho]$.

A.2.2 Kohn-Sham formulation

In 1965, Kohn and Sham² suggested that the electron kinetic energy should be calculated from an auxiliary set of orbitals used for representing the electron density. The main drawback of previous orbital-free DFT models is the poor representation of the kinetic energy, and Kohn-Sham density functional theory (KS-DFT) splits the kinetic energy functional into a term can be calculated exactly and a small correction term. KS-DFT introduces a fictitious non-interacting system which Hamiltonian can be given as:

$$h_{ks} = -\frac{1}{2}\nabla^2 + v_{ks}(\vec{r}) \quad (\text{A-24})$$

The first term in equation (A-24) represents the kinetic energy of the electrons and the second term represents the potential energy of electron-nucleus interactions. For such an orbital corresponding to the above Hamiltonian, is often referred as KS orbital, χ_{ks} . The kinetic energy of the non-interacting system is

$$T_S = \langle \chi_{ks} | T | \chi_{ks} \rangle \quad (\text{A-25})$$

For the actual wave function of the system, Ψ , the ground state electronic energy could be expressed as

$$E = \langle \Psi | T + v + V_{ee} | \Psi \rangle = \langle \Psi | T | \Psi \rangle + \int d^3r \rho(\vec{r}) v(\vec{r}) + \langle \Psi | V_{ee} | \Psi \rangle \quad (\text{A-26})$$

$$= T_S + \int d^3r \rho(\vec{r}) v(\vec{r}) + U[\rho] - E_{XC} \quad (\text{A-27})$$

where $U[\rho] = \frac{1}{2} \int d^3r d^3r' \frac{\rho(\vec{r})\rho(\vec{r}')}{|\vec{r}-\vec{r}'|}$ and $E_{XC} = T_K - T_S + \langle \Psi | V_{ee} | \Psi \rangle - U[\rho]$. As T_S is the kinetic energy which can be calculated using KS orbitals. The “exchange-correlation” functional term, E_{XC} , is the only undetermined functional of electronic density which needs to be approximated, and it is about 10% of the total energy. E_{XC} accounts for the difference between the actual electronic kinetic energy of the system and the KS non-interacting electronic kinetic energy, and the difference between exact electron-electron interaction energy and $U[\rho]$. Typically the kinetic energy correlation part is minimal and many functional do not compute the kinetic energy correction explicitly and some use empirical parameters for this correction. However, the electron-electron interaction correction is relatively significant.

The two common approximations for E_{XC} are the local density approximation (LDA) and the generalized gradient approximation (GGA). LDA treats the exchange correlation energy density at every point in a system will be the same as that exchange-correlation energy density of the interacting uniform electron gas of the same electron density as in that position. GGA is an improvement over LDA with the implementation of the gradient correction as

$$E_{XC}^{GGA} = \int d^3r g(\rho, \nabla\rho) \quad (\text{A-28})$$

Since Perdew-Burke-Ernzerhof (PBE) functional⁶ is used throughout this thesis, only the formulation of GGA will be discussed. In PBE functional, E_{XC} is given as is separated into exchange and correlation part and the correlation term is given as

$$E_C^{GGA} = \int \rho [\epsilon_c(r_s, \zeta) + H(r_s, \zeta, t)] d^3r \quad (\text{A-29})$$

Where t is the dimensionless density gradient given as $t = \frac{|\nabla\rho|}{2\phi k_s \rho}$, $\phi = \frac{(1+\zeta)^{\frac{2}{3}} + (1-\zeta)^{\frac{2}{3}}}{2}$, $\zeta = \frac{\rho_\alpha - \rho_\beta}{\rho_\alpha + \rho_\beta}$,

$$k_s = \sqrt{\frac{4(3\pi^2\rho)^{\frac{1}{3}}}{\pi(\frac{\hbar^2}{me^2})}}, H = \left(\frac{e^2}{\hbar^2}\right) 0.031091 \phi^3 \ln \left(1 + \frac{0.066725}{0.031091} t^2 \left[\frac{1+\bar{A}t^2}{1+\bar{A}t^2+\bar{A}^2t^4}\right]\right),$$

$$\bar{A} = \frac{0.066725}{0.031091} \left[\exp \left\{ \frac{-\epsilon_c}{\frac{e^2}{\hbar^2}} \right\} - 1 \right]^{-1}.$$

The exchange energy term is defined as

$$E_X^{GGA} = \int \rho \epsilon_x(\rho) F_X(s) d^3r \quad (\text{A-30})$$

Where s is another type of reduced density gradient given as $\left(\frac{r_s m e^2}{h^2}\right)^{0.5} \phi t / 1.2277$ and $F_X(s) = 1 + 0.0804 - \frac{0.804}{1 + \frac{0.2195s^2}{0.804}}$

When DFT is applied to repeated periodic system such as crystal and catalyst surface, periodic conditions to the unit cell can be used to reduce the computational cost. If the cell is defined by vector a_1, a_2 and a_3 , then its volume is $\Omega = a_1 \cdot (a_2 \times a_3)$, the general lattice vectors are integer multiples of these vectors as

$$\vec{L} = N_1 a_1 + N_2 a_2 + N_3 a_3 \quad (\text{A-31})$$

In such case, the effective potential also has periodicity which is

$$v_{eff}(\vec{r} + \vec{L}) = v_{eff}(\vec{r}) \quad (\text{A-32})$$

Such periodic potential can be expanded as a Fourier series. Due to the nature of the Fourier transformation, $v_{eff}(\vec{r})$ is transformed from a real space periodic potential into a Fourier space potential. Bloch's theorem states that if $v(\vec{r})$ is a periodic potential, then the wave function of a one electron Hamiltonian of the form $-\frac{1}{2}\nabla^2 + v(\vec{r})$ is given as planewave times a function with the same periodicity as the potential. Hence, the KS-DFT equations can be rewritten as

$$\left(-\frac{1}{2}\nabla^2 + v_{ks}(\vec{r})\right)\Psi_{\vec{k}}(\vec{r}) = \epsilon_{\vec{k}}\Psi_{\vec{k}}(\vec{r}) \quad (\text{A-33})$$

And the electron density is given as

$$\rho(\vec{r}) = 2 \frac{\Omega}{(2\pi^3)} \int |\Psi_{\vec{k}}(\vec{r})|^2 \delta(E_F - \epsilon_{\vec{k}}) d^3k \quad (\text{A-34})$$

Factor of 2 in equation (A-34) is to consider both the electron spins and δ is the step function which 1 for positive and 0 for negative function arguments. The integration in equation (A-34) is over the Brillouin zone, which means the primitive cell in the reciprocal space. Hence, only a small periodic cell is needed for an extended system with extended number of electrons. Since the electronic wave function at k-points close to each other will be similar, it is also possible to replace the above integral as a discrete sum over limited number of k-points. The error due to this approximation can be minimized by using large number of k-points. In this work, the convergence

tests regarding to the choice of k-point were performed and will be discussed later. For practical application of planewaves approach, a solution to the nodal structure of valence wave functions problem needs to be addressed. Therefore, pseudopotentials are used to replace the electron-nuclear potential. Since this pseudopotential eradicates the core electrons from the system, it is very important that the pseudopotential considers the electron-nucleus interaction as if shielded the core electrons and the electron-electron interaction between the valence and core electrons. Hence the pseudopotential is angular moment dependent as well. Also, the contribution of core electrons to chemical bonding is negligible and only the valence electrons play significant part in it. Outside a certain cut-off radius, the pseudopotential matches the true potential of the system, and the pseudo-wave function matches the true wave function of the system. The core electrons play an important part in the calculation of the total energy though and this implies that the removal of core electrons will also result in lower energy differences between different configurations, thereby reducing the costs in achieving the required accuracy. Ultra-soft pseudopotentials are used throughout this work.

Appendix B Supplementary Information to Chapter 2

B.1 Estimating Gibbs energy for elementary reaction steps

Given an elementary reaction step with transition state species AB^*



ΔG_a and ΔG_{rxn} is defined as

$$\Delta G_a = G_{AB^*} - G_a - G_B \quad (\text{B-1})$$

$$\Delta G_{rxn} = G_C + G_D - G_a - G_B \quad (\text{B-2})$$

The Gibbs energy (G_a) for a species is given as

$$G_a = E_{DFT} + E_{ZPE} + \Delta H_T(0 \rightarrow T) - T\Delta S \quad (\text{B-3})$$

where, E_{DFT} is the energy obtained from DFT, E_{ZPE} is the zero-point energy correction, ΔH_T is the temperature correction from 0 K to the reaction temperature T and $T\Delta S$ is the entropy correction. The zero-point energy correction is calculated as

$$E_{ZPE} = \sum_{i=1}^{num.of\ modes} \frac{N_A h \theta_i}{2} \quad (\text{B-4})$$

where, N_A is Avogadro's number, h is Planck's constant and θ_i is the frequency of the normal mode. However, temperature and entropy corrections are different for gaseous and surface species.

B.1.1 Gaseous species

These species have all of the translational, rotational and vibrational degrees of freedom active. Hence total enthalpy temperature correction ΔH_T at temperature T is given as sum of translational (H_{trans}), rotational (H_{rot}), and vibrational (H_{vib}) enthalpy corrections as;

$$\Delta H_T = H_{trans} + H_{rot} + H_{vib} \quad (\text{B-5})$$

Where,

$$H_{trans} = \frac{5}{2}RT \quad (\text{B-6})$$

$$H_{rot} = \frac{f}{2}RT \quad (\text{B-7})$$

f is equal to 2 for linear molecules and 3 for other cases

$$H_{vib} = \sum_i^{\text{num of modes}} \left(\frac{N_a h \nu_i \exp\left(-\frac{h \nu_i}{k_B T}\right)}{1 - \exp\left(-\frac{h \nu_i}{k_B T}\right)} \right) \quad (\text{B-8})$$

k_B is Boltzmann constant.

Similarly, the total entropy correction is given as the sum of translational (S_{trans}), rotational (S_{rot}), and vibrational (S_{vib}) entropy corrections as

$$\Delta S = S_{trans} + S_{rot} + S_{vib} \quad (\text{B-9})$$

The translational entropy correction is given as

$$S_{trans} = R \left[\ln \left(\frac{(2\pi m k_B T)^{\frac{3}{2}}}{h^3} \right) + \ln \left[\frac{V}{N_g} \right] + \frac{5}{2} \right] \quad (\text{B-10})$$

where m is the mass of the molecule and $\frac{V}{N_g}$ is the volume per molecule in the standard state. The rotational entropy correction for a non-linear molecule is given as

$$S_{rot} = R \left[\ln \left(\frac{8\pi^2 \left(8\pi^3 I_x I_y I_z (k_B T)^{\frac{3}{2}} \right)^{\frac{1}{2}}}{\sigma_r h^3} \right) + \frac{3}{2} \right] \quad (\text{B-12})$$

where I_x , I_y , and I_z are the three moments of inertia about the principal axes and σ_r is the rotational symmetry number. For linear molecules, however,

$$S_{rot,linear} = R \left[\ln \left(\frac{8\pi^2 I_{linear}(k_B T)}{\sigma_r h^2} \right) + 1 \right] \quad (\text{B-12})$$

where I_{linear} is the moment of inertia of a linear molecule. The vibrational entropy correction of a molecule is

$$S_{vib} = R \sum_i^{num\ of\ modes} \left(\frac{\frac{h\nu_i}{k_B T}}{\exp\left(\frac{h\nu_i}{k_B T}\right) - 1} - \ln \left(1 - \exp\left(\frac{h\nu_i}{k_B T}\right) \right) \right) \quad (\text{B-13})$$

B.2 Electronic Energy of All Reactions

Table B.1 Activation energies and reaction energies (in kJ/mol) for all the studied reaction pathways for guaiacol activation on Mo₂C (100) surfaces.

Reaction (R)	$\Delta E_a^*/\Delta G_a$	$\Delta E_{rxn}^*/\Delta G_{rxn}$
C² – O Scission		
1. (C ₆ H ₄)(OH)(OCH ₃) → (C ₆ H ₄)(OH) + OCH ₃	78/62	-148/-151
2. (C ₆ H ₄)(OH) + H → (C ₆ H ₅)(OH)	129/127	40/-76
3. (C ₆ H ₅)(OH) → (C ₆ H ₅) + OH	88/75	-82/-85
4. C ₆ H ₅ + H → C ₆ H ₆	105/101	-30/29
C⁷ – O Scission		
5. (C ₆ H ₄)(OCH ₃)(OH) → (C ₆ H ₄)(OCH ₃) + OH	73/60	-122/-123
6. (C ₆ H ₄)(OCH ₃) + H → (C ₆ H ₅)(OCH ₃)	108/99	-33/-15
7. (C ₆ H ₅)(OCH ₃) → (C ₆ H ₅) + OCH ₃	84/67	-142/-139
8. C ₆ H ₅ + H → C ₆ H ₆	115/101	12/29
C¹ – O scission		
9. (C ₆ H ₄)(OH)(OCH ₃) → (C ₆ H ₄)(OH)(O) + CH ₃	125/96	151
10. (C ₆ H ₄)(OH)(O) + H → (C ₆ H ₄)(OH)(OH)	199/101	29
11. (C ₆ H ₄)(OH)(OH) → (C ₆ H ₄)(OH) + OH	62/45	136
12. (C ₆ H ₄)(OH) + H → (C ₆ H ₅)(OH)	129/127	-80/-76
Ring Hydrogenation of Phenol		
13. (C ₆ H ₅)(OH) + H → (C ₆ H ₆)OH	115/113	100/114
14. (C ₆ H ₆)OH + H → (C ₆ H ₇)OH	106/104	39/86
15. (C ₆ H ₇)OH + H → (C ₆ H ₈)OH	125/131	72/119
16. (C ₆ H ₈)OH + H → (C ₆ H ₉)OH	143/145	65/73
17. (C ₆ H ₉)OH → (C ₆ H ₉) + OH	25/25	-162/-170

18. $(C_6H_9) + H \rightarrow C_6H_{10}$	86/90	39/91
Ring Hydrogenation of Anisole		
19. $(C_6H_5)(OCH_3) + H \rightarrow (C_6H_6)(OCH_3)$	109/135	105/123
20. $(C_6H_6)(OCH_3) + H \rightarrow (C_6H_7)(OCH_3)$	130/119	63/94
21. $(C_6H_7)(OCH_3) + H \rightarrow (C_6H_8)(OCH_3)$	111/146	128/134
22. $(C_6H_8)(OCH_3) + H \rightarrow (C_6H_9)(OCH_3)$	135/135	4/43
23. $(C_6H_9)(OCH_3) \rightarrow (C_6H_9) + OCH_3$	61/49	-162/-167
24. $(C_6H_9) + H \rightarrow C_6H_{10}$	125/118	38/90
Ring Hydrogenation of Catechol		
25. $(C_6H_4)(OH)(OH) + H \rightarrow (C_6H_5)(OH)(OH)$	134/139	132/136
26. $(C_6H_5)(OH)(OH) + H \rightarrow (C_6H_6)(OH)(OH)$	126/121	42/85
27. $(C_6H_6)(OH)(OH) + H \rightarrow (C_6H_7)(OH)(OH)$	85/92	47/84
28. $(C_6H_7)(OH)(OH) + H \rightarrow (C_6H_8)(OH)(OH)$	157/153	43/91
29. $(C_6H_8)(OH)(OH) \rightarrow (C_6H_8)(OH) + OH$	35/24	-180/-142
30. $(C_6H_8)OH + H \rightarrow (C_6H_9)OH$	108/112	77/81
Ring Hydrogenation of Guaiacol		
31. $(C_6H_4)(OH)(OCH_3) + H \rightarrow (C_6H_5)(OH)(OCH_3)$	126/135	93/117
32. $(C_6H_5)(OH)(OCH_3) + H \rightarrow (C_6H_6)(OH)(OCH_3)$	141/169	36/136
33. $(C_6H_6)(OH)(OCH_3) + H \rightarrow (C_6H_7)(OH)(OCH_3)$	134/160	123/160
34. $(C_6H_7)(OH)(OCH_3) + H \rightarrow (C_6H_8)(OH)(OCH_3)$	156/153	-9/64
35. $(C_6H_8)(OH)(OCH_3) \rightarrow (C_6H_8)(OH) + OCH_3$	25/14	-229/14
36. $(C_6H_8)OH + H \rightarrow (C_6H_9)OH$	107/112	71/81
Ring Hydrogenation of Benzene		
37. $C_6H_6 + H \rightarrow C_6H_7$	126/109	89/101
38. $C_6H_7 + H \rightarrow C_6H_8$	102/98	52/99
39. $C_6H_8 + H \rightarrow C_6H_9$	119/124	53/87
40. $C_6H_9 + H \rightarrow C_6H_{10}$	116/98	90/79
41. $C_6H_{10} + H \rightarrow C_6H_{11}$	108/109	89/98
42. $C_6H_{11} + H \rightarrow C_6H_{12}$	194/176	23/29
Ring Opening of Guaiacol		
43. $(C_7H_8O_2) \rightarrow (C_4H_8O_2)(C^2C^7)$	94/90	-16/-16
44. $(C_7H_8O_2) \rightarrow (C_6H_5O) + OC^1H_3$	27/15	-197/-205
45. $(C_6H_5O) + H \rightarrow C_6H_6O$	108/107	65/69
46. $C_6H_6O \rightarrow C_6H_5 + OH$	34/34	-173/-175
47. $C_6H_5 + H \rightarrow C_6H_6$	106/105	38/42
48. $(C_7H_8O_2) \rightarrow (C_7H_7O) + OH$	58/44	-179/-183
49. $(C_7H_7O) + H \rightarrow (C_7H_8O)$	107/104	43/55
50. $(C_7H_8O) \rightarrow (C_6H_5) + OC^1H_3$	32/32	-191/-190

51. $C_6H_5 + H \rightarrow C_6H_6$	105/105	60/60
52. $(C_7H_8O_2) + H \rightarrow C_7H_9O_2 (C^2H)$	151/149	84/84
53. $(C_7H_8O_2) + H \rightarrow C_7H_9O_2 (C^7H)$	139/142	106/106

* $\Delta E_a / \Delta E_{rxn}$ are calculated as the electronic energy differences between the transition state and reactant/product and reactant.

B.3 Transition State Configurations on Mo_2C

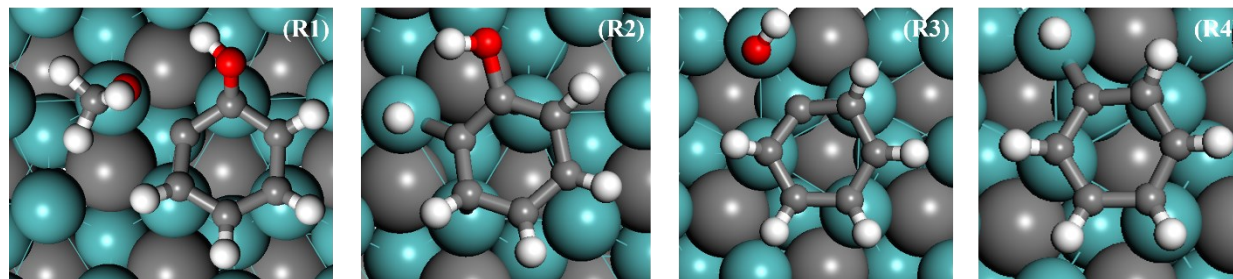


Figure B.1 Transition state geometries for C^2 -O dissociation pathway on Mo_2C surface (R1 to R4)

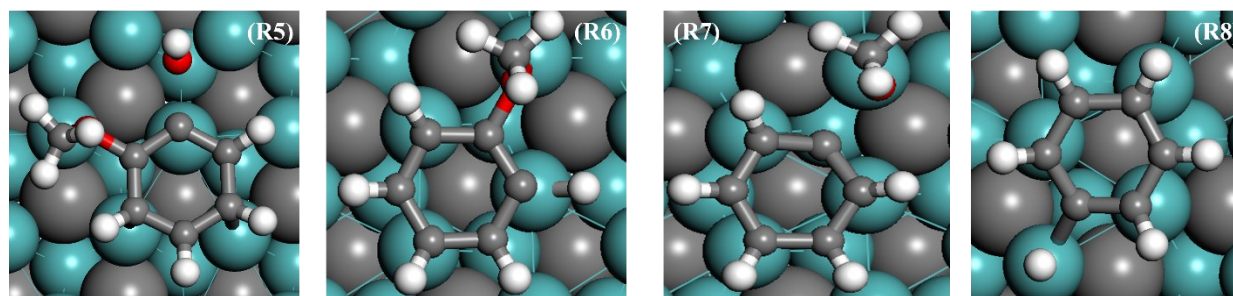


Figure B.2 Transition state geometries for C^7 -O dissociation pathway on Mo_2C surface (R5 to R8)

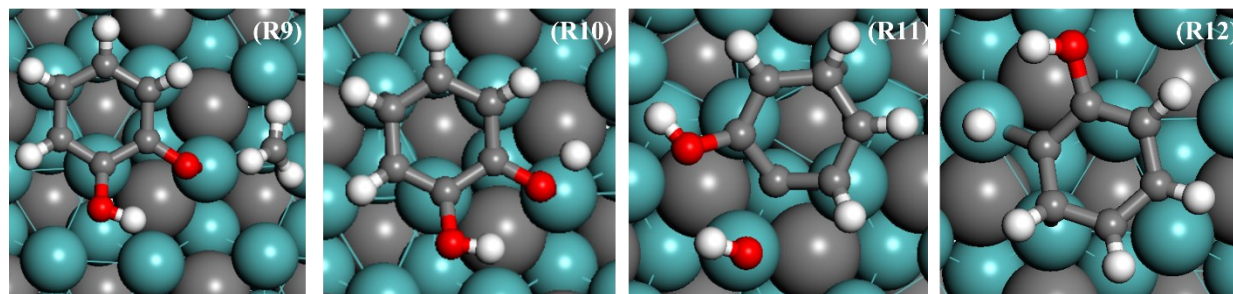


Figure B.3 Transition state geometries for C^1 -O dissociation pathway on Mo_2C surface (R9 to R12)

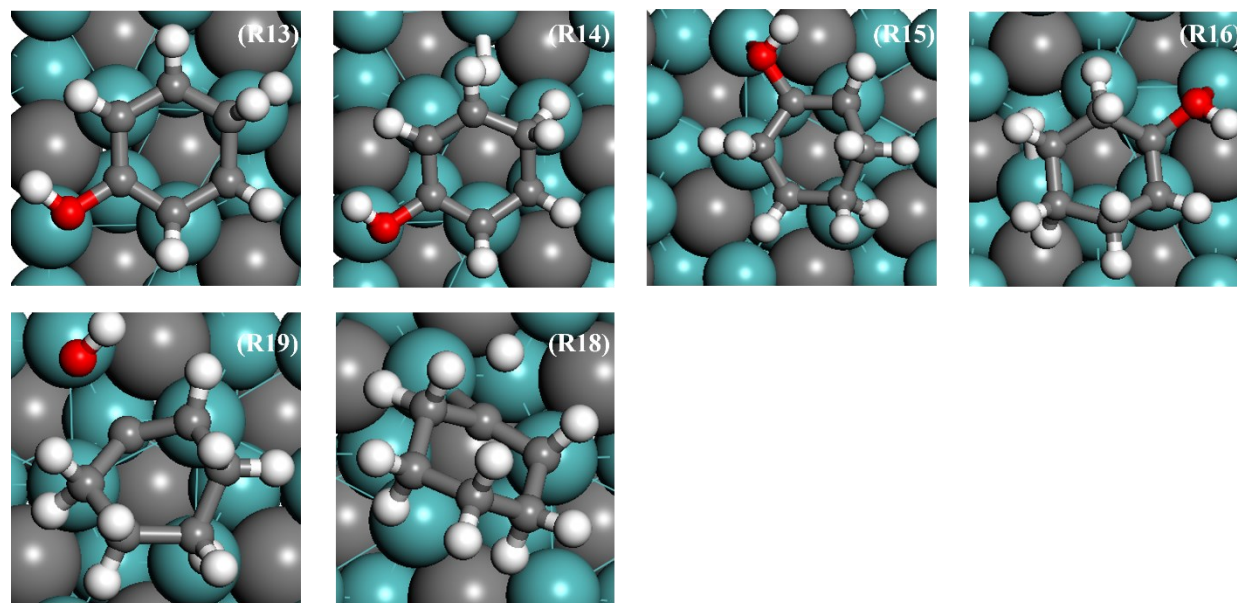


Figure B.4 Transition state geometries for phenol hydrogenation (HYD) pathway on Mo_2C surface (R13 to R18) to form cyclohexene.

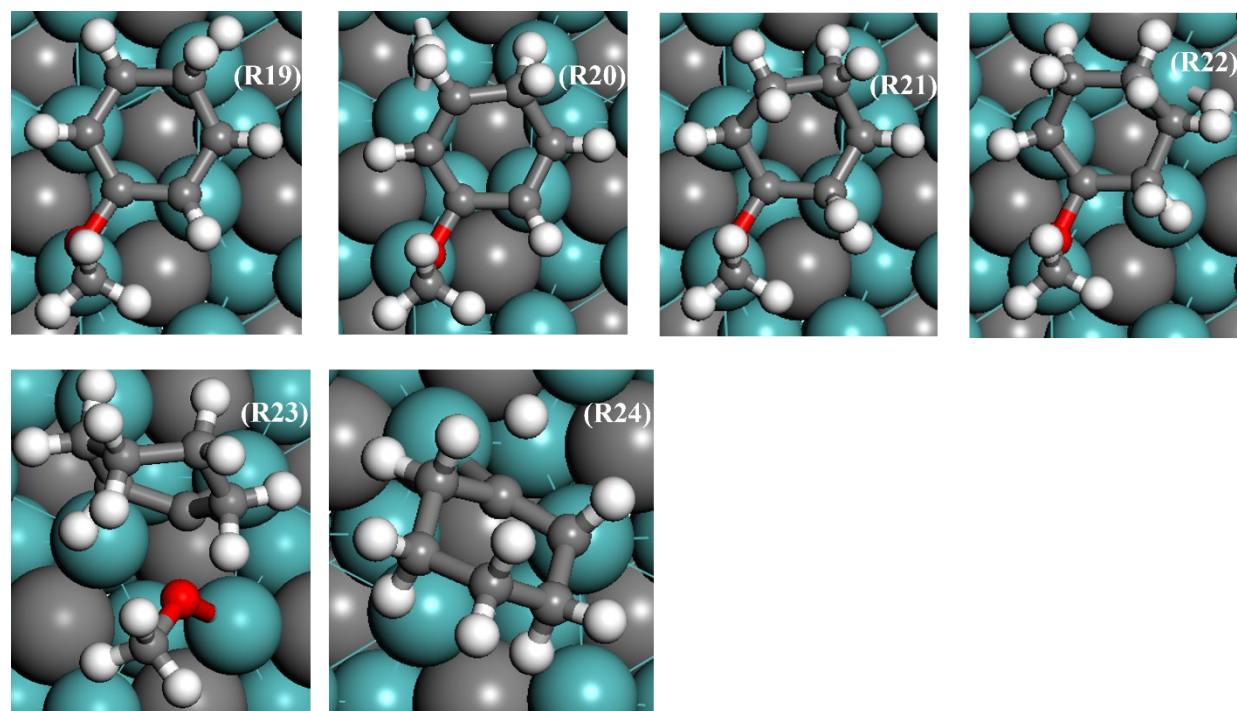


Figure B.5 Transition state geometries for anisole hydrogenation (HYD) pathway on Mo_2C surface (R19 to R24) to form cyclohexene.

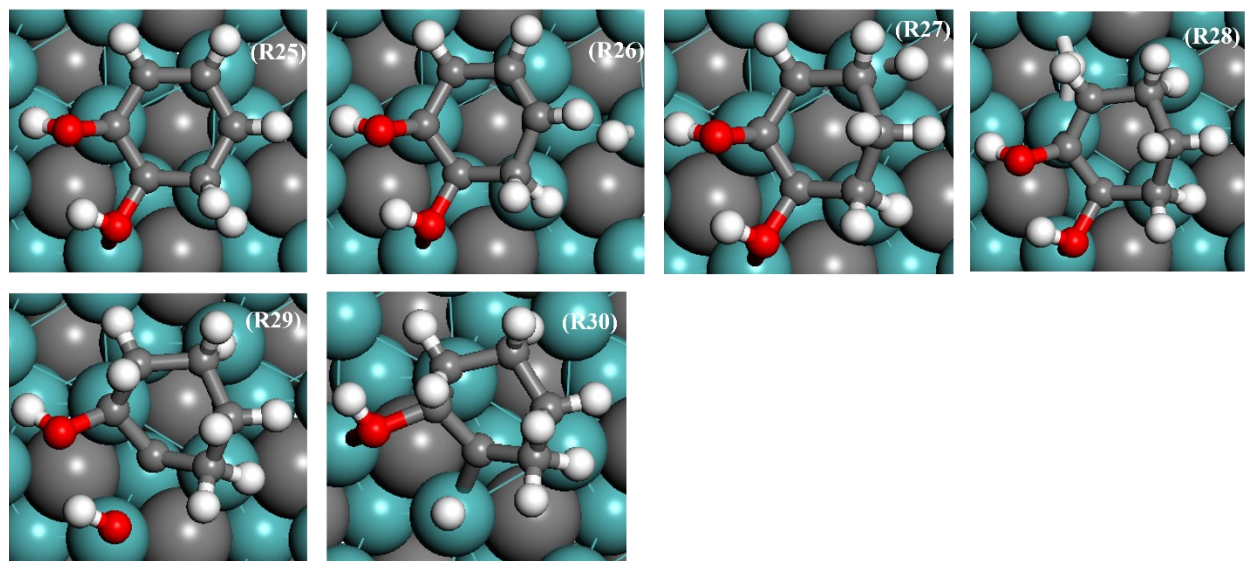


Figure B.6 Transition state geometries for catechol hydrogenation (HYD) pathway on Mo₂C surface (R25 to R30) to form cyclohexene.

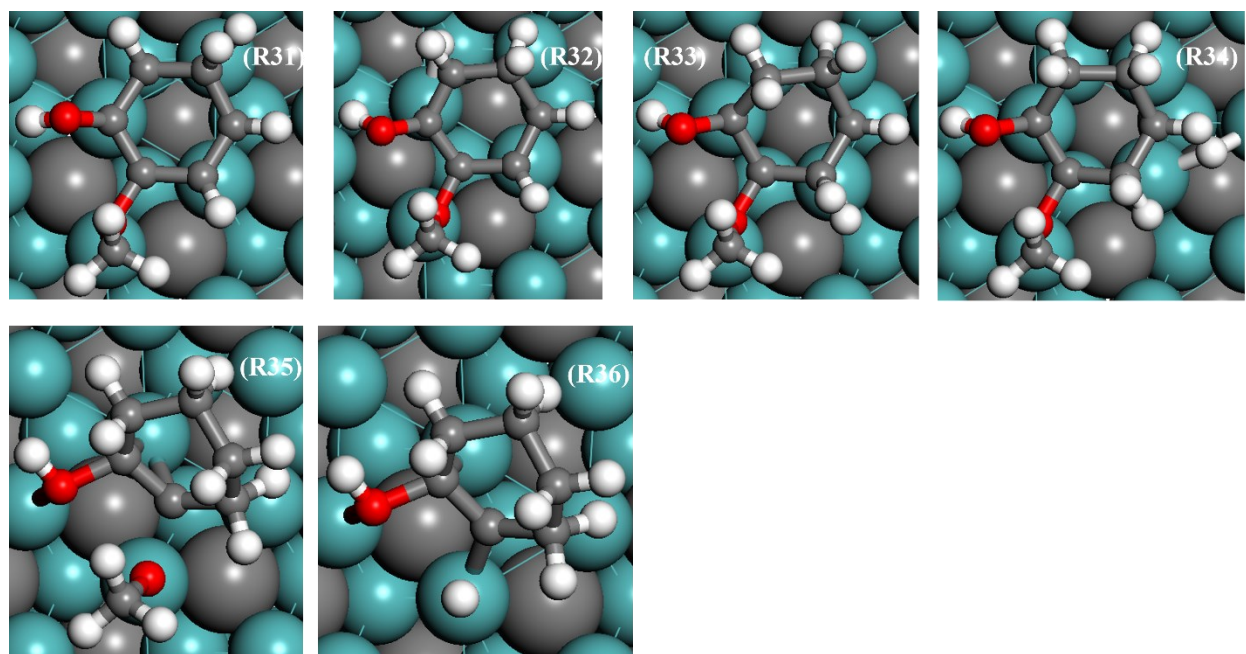


Figure B.7 Transition state geometries for guaiacol ring hydrogenation (HYD) pathway on Mo₂C surface (R31 to R36)

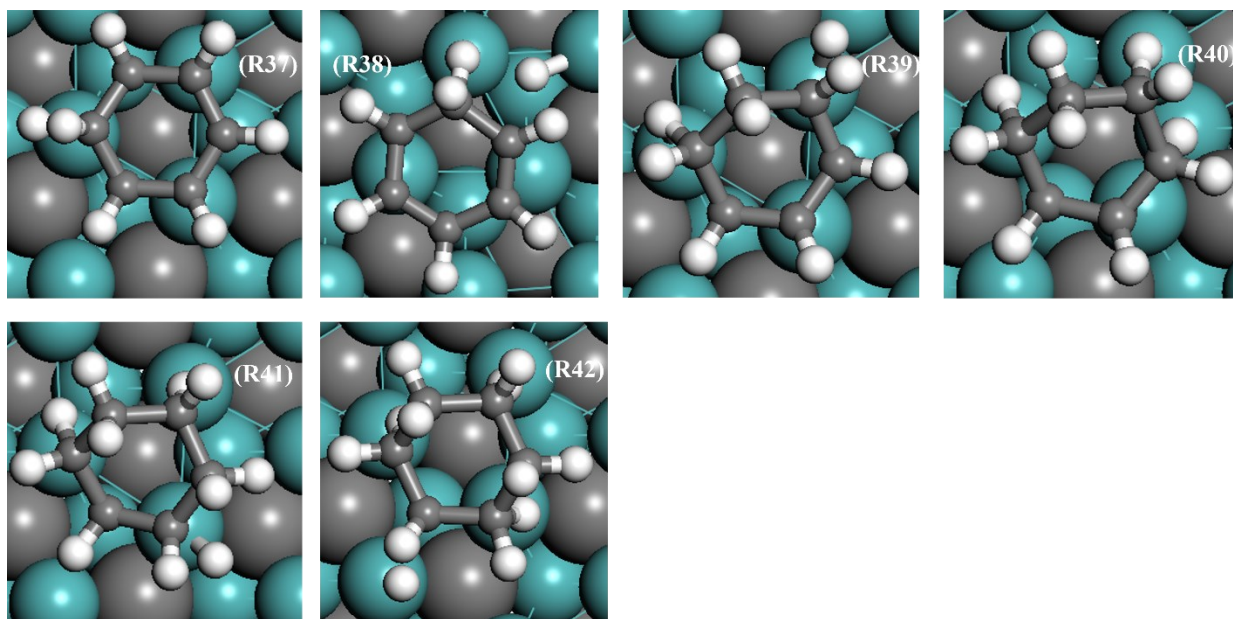


Figure B.8 Transition state geometries for benzene ring hydrogenation pathway on Mo₂C surface (R37 to R42)

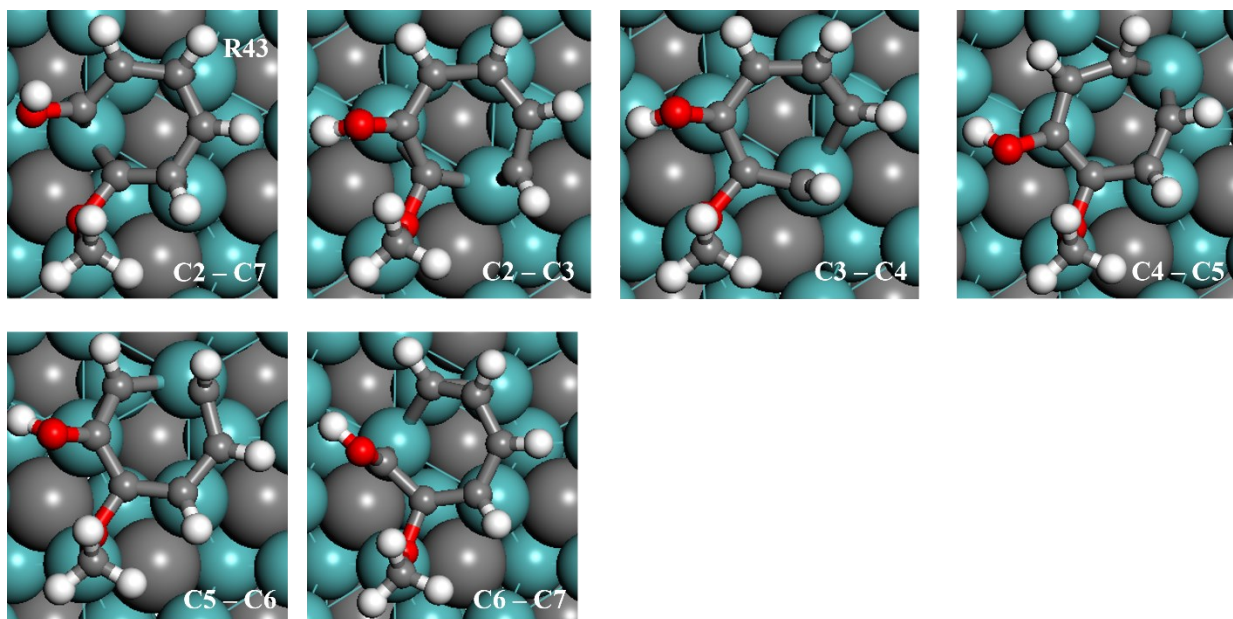


Figure B.9 Transition state geometries for the ring-opening possibility of guaiacol activation on Mo₂C (R43)

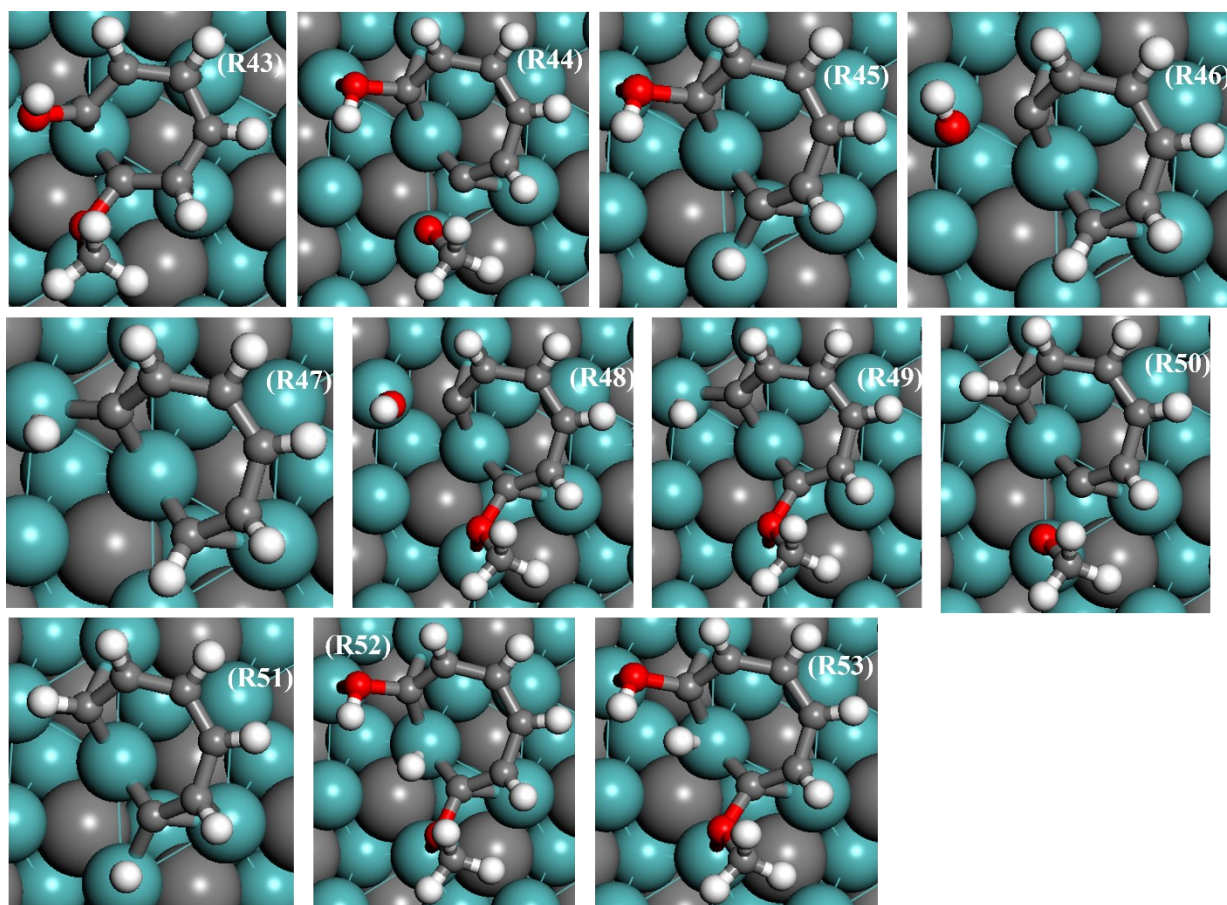
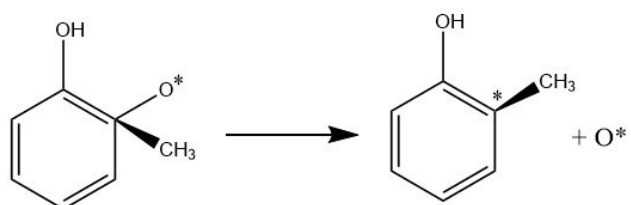


Figure B.10 Transition state geometries for the ring-opening of guaiacol pathway on Mo₂C (R43 to R53)



B.4 Transition State Configurations on MoWC

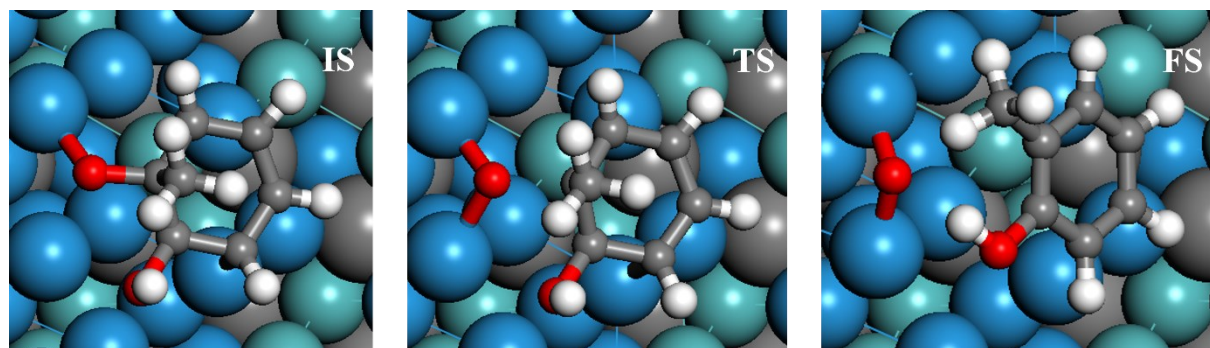


Figure B.11 Initial, Transition, and Final state configuration for guaiacol activation reaction (shown above) by C²-O scission on MoWC_{4W_W} surface

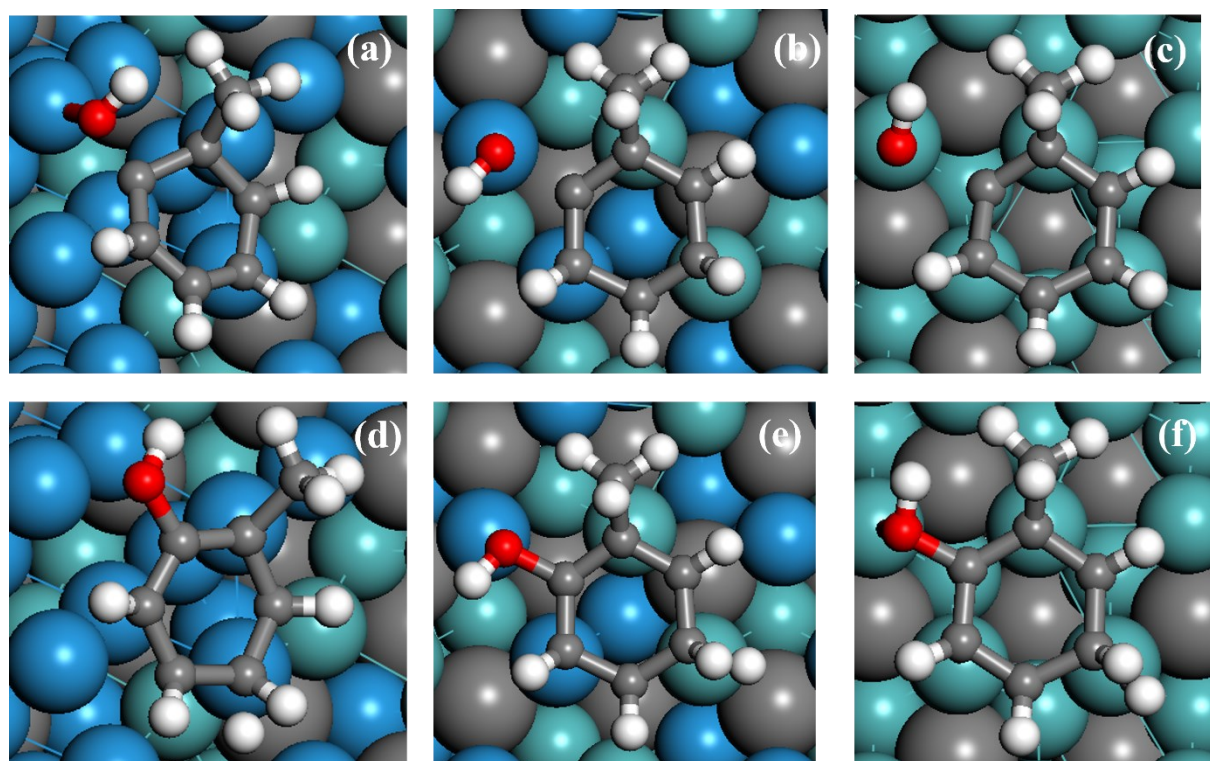


Figure B.12 Transition state configurations for (a, b, and c) Direct dehydroxylation reaction (d, e, and f) Ring hydrogenation of cresol among Mo₂C, MoWC, and MoWC_{bulk} catalyst surface.

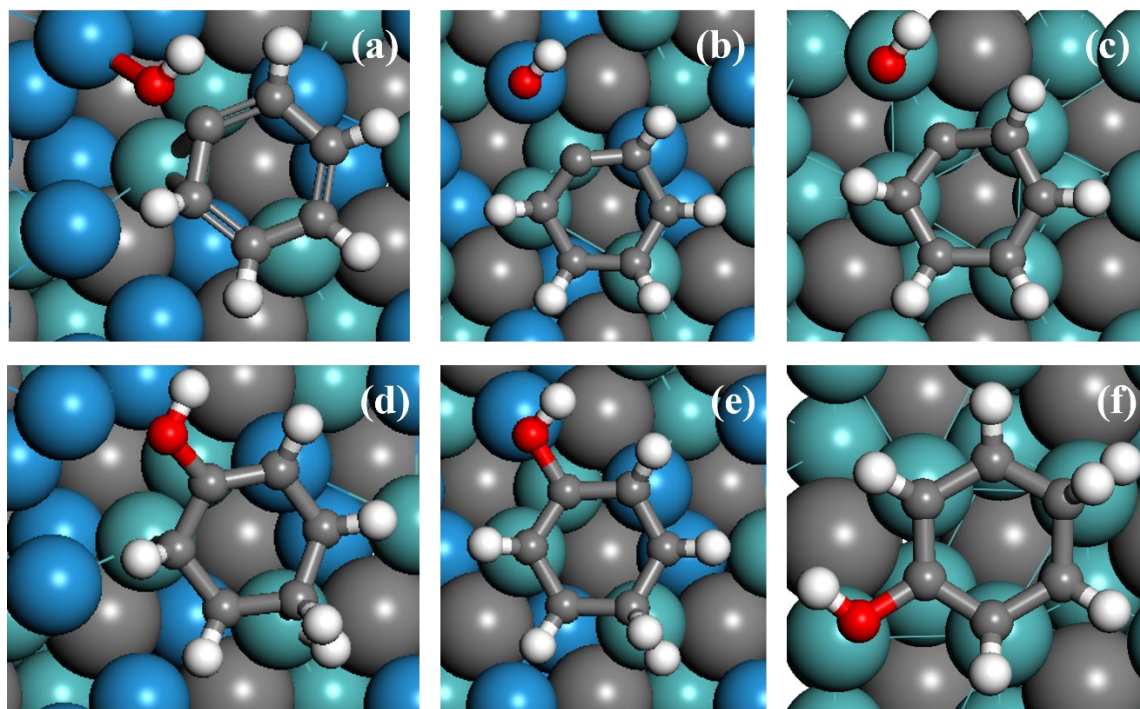


Figure B.13 Transition state configurations for Direct dehydroxylation reaction (a, b, and c), and Ring hydrogenation (d,e, and f) of phenol among Mo₂C, MoWC, and MoWC_bulk catalyst surface.

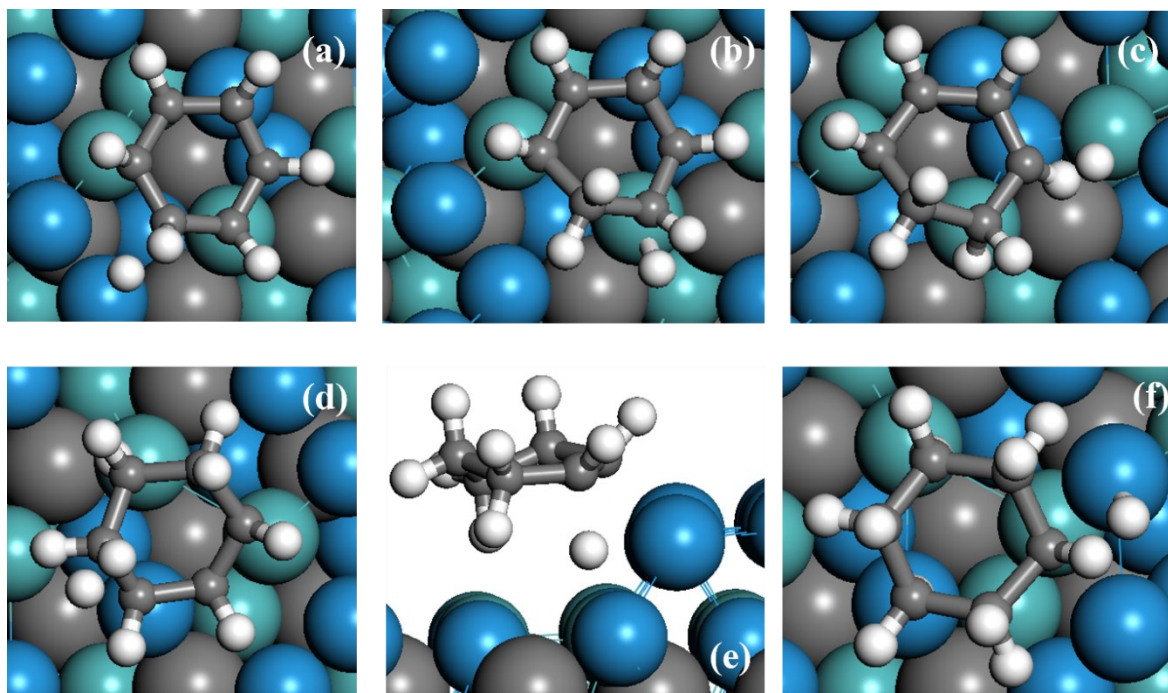


Figure B.14 Transition state geometries for benzene ring hydrogenation pathway on MoWC surface for 6 hydrogenation steps are shown from (a) to (f) forming cyclohexane.

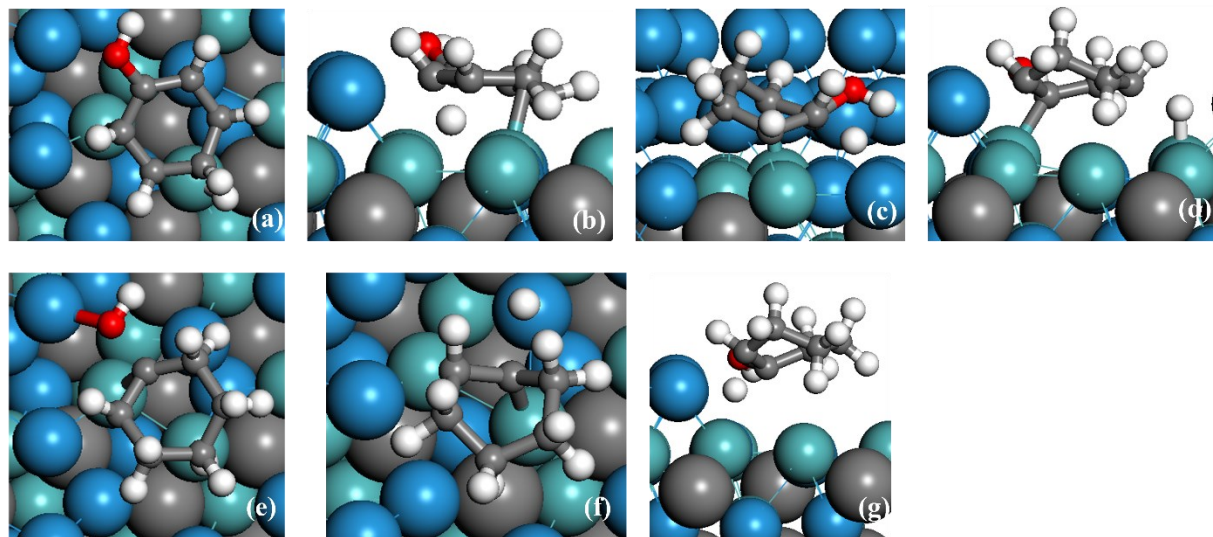


Figure B.15 Transition state geometries for phenol ring hydrogenation pathway (HYD) on MoWC surface are shown from (a) to (f) forming cyclohexene.

Table B.2 Gibbs Free Energy of Adsorption (in kJ/mol) of Major Guaiacol HDO Products on Mo₂C and MoWC Surfaces at 623 K and 1 bar.

Intermediate	G _{adsorption} (kJ/mol)(Mo ₂ C)	G _{adsorption} (kJ/mol)(MoWC)	d _{C-O} (Å)/Mo ₂ C	d _{C-O} (Å)/MoWC
Phenol	-84	-0.5		
Benzene	-110	-90	–	–
Anisole	-173	–	–	–
Guaiacol	-121	-169	1.43	1.49

B.5 Experimental Characterization Results

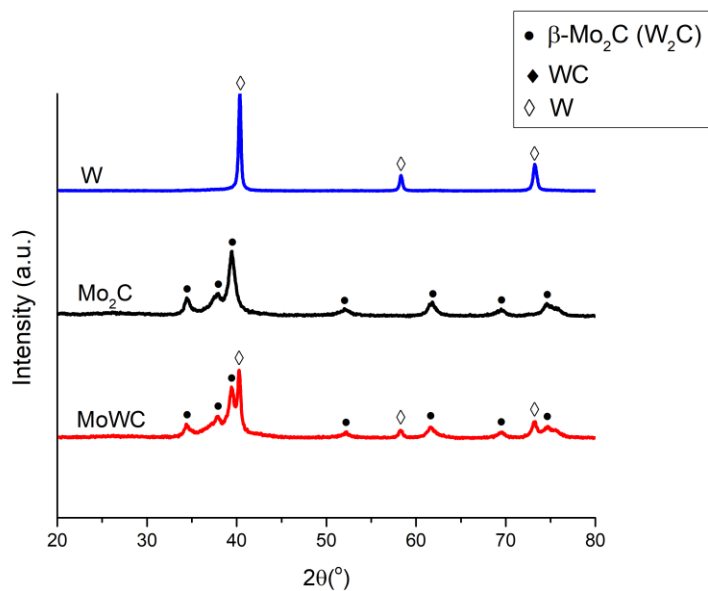


Figure B.16 X-Ray diffraction patterns of W, Mo₂C and the mixed metal carbide MoWC.

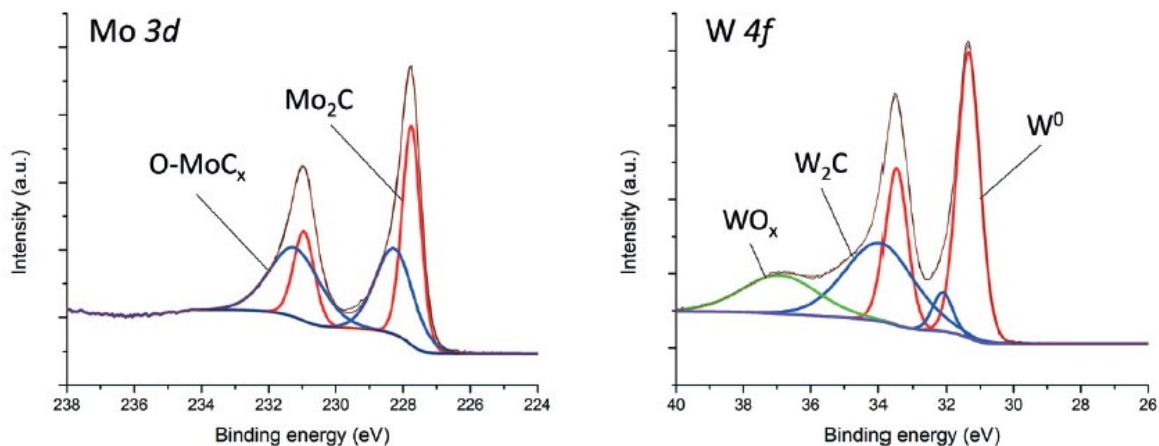


Figure B.17 Mo 3d and W 4f XPS spectra and the deconvolution of MoWC carbide.

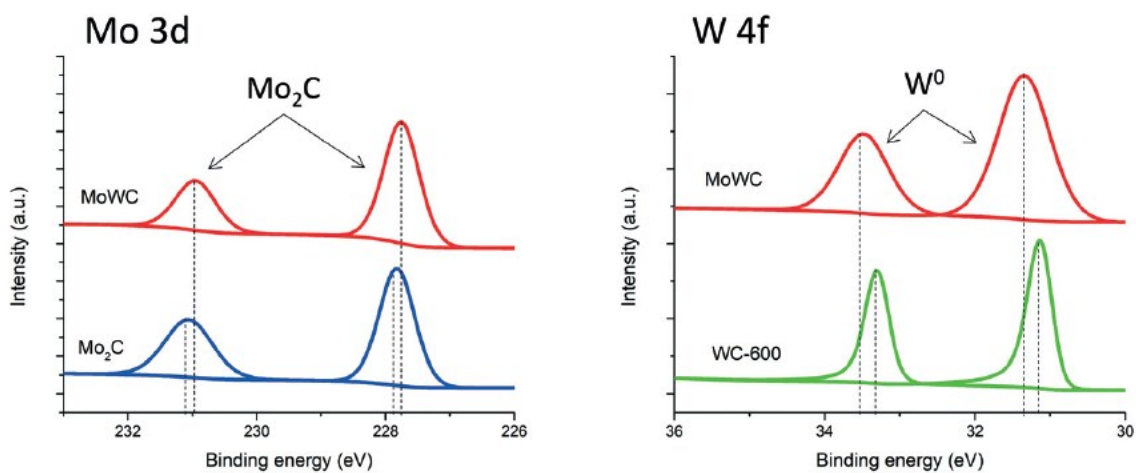


Figure B.18 Chemical shifts of the Mo₂C state and metallic W state for MoWC, Mo₂C, and WC samples.

Table B.3 Atomic ratios of the samples derived from peak deconvolution of the XPS spectra

Catalysts	C/Mo	C/W	C/(Mo + W)	Mo/W
Mo ₂ C	0.34	—	—	—
MoWC	0.97	0.87	0.54	0.6

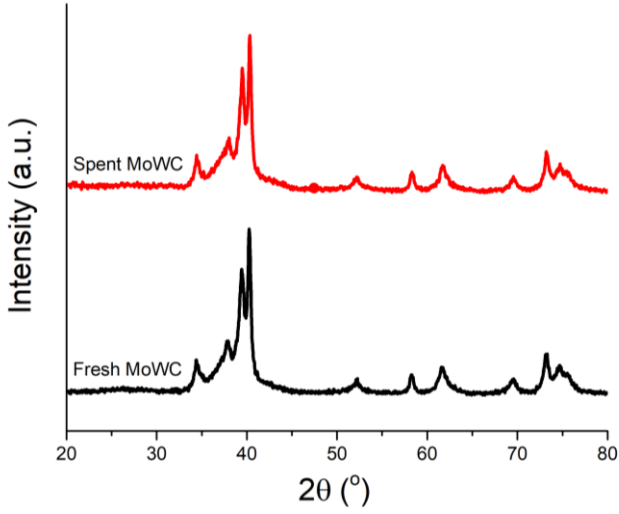


Figure B.19 XRD patterns of the fresh and spent carbide catalysts.

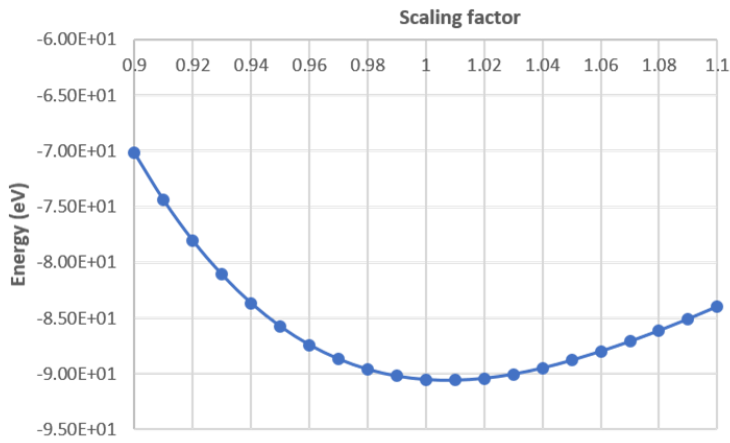


Figure B.20 Lattice Parameter Optimization of Mo₂C catalyst.

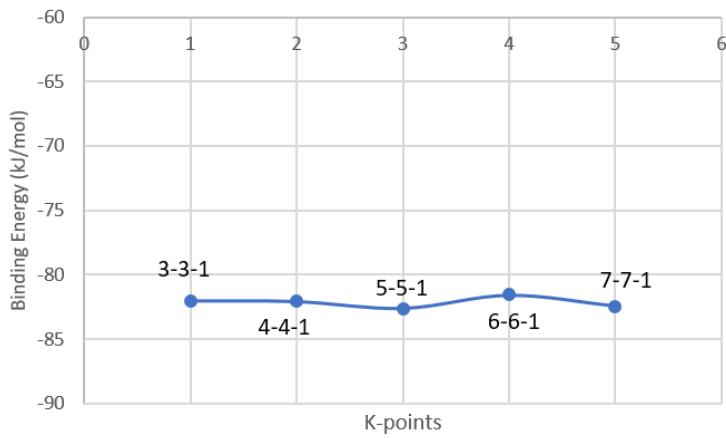


Figure B.21 Benchmarking of K-points

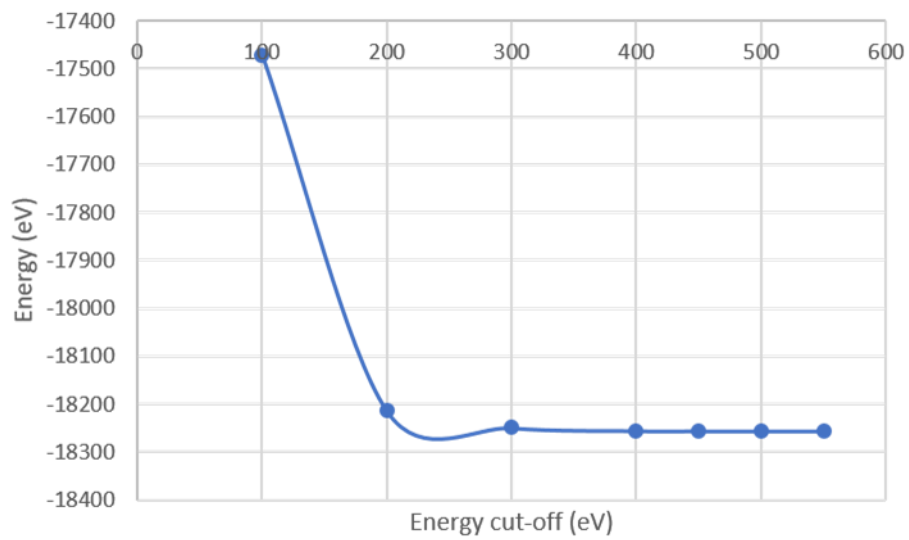


Figure B.22 Benchmarking of Energy Cut-off

Appendix C Supplementary Information to Chapter 3

C.1 Energy Barriers of All Reactions on Six Model Compounds

Table C.1 Energy barrier E_a (kJ/mol) and reaction energy E_r (kJ/mol) of six representative constituents of bio-oil considered for hydrodeoxygenation on the Mo_2C and MoWC surfaces

Reaction	$E_a(\text{Mo}_2\text{C}/\text{MoWC})$	$E_r(\text{Mo}_2\text{C}/\text{MoWC})$
5 - HMF		
1. $\text{C}^1 - \text{O}$ scission	99/107	-201/-146
2. $\text{C}^6 - \text{O}$ scission	39/spontaneous	-149/spontaneous
3. $\text{C}^2 - \text{O}$ scission	57/57	-92/-137
4. $\text{C}^5 - \text{O}$ scission	34/18	-20/-72
5. $\text{C}^5 - \text{C}^6$ scission	191/117	15/-72
6. $\text{C}^1 - \text{C}^2$ scission	180/200	4/16
7. $\text{C}^1 - \text{O}$ hydrogenation@O	193/320	147/160
$\text{C}^1 - \text{O}$ hydrogenation@C	148/166	127/20
8. C^{ring} hydrogenation	122/189	112/83
I - 1 (5 - HMF)		
9. $\text{C}^1 - \text{O}$ scission	105/107	-198/-147
10. $\text{C}^5 - \text{O}$ dissociation	8/18	-85/-72
11. $\text{C}^2 - \text{O}$ dissociation	44/58	-201/-137
12. $\text{C}^1 - \text{C}^2$ dissociation	176/200	14/-340
13. $\text{C}^1 - \text{O}$ hydrogenation@O	213/320	120/160
14. $\text{C}^1 - \text{O}$ hydrogenation@C	125/166	72/20
I - 2 (5 - HMF)		
15. $\text{C}^1 - \text{O}$ scission	101/104	-164/-142
16. $\text{C}^1 - \text{O}$ hydrogenation@O	216/219	114/185
17. $\text{C}^1 - \text{O}$ hydrogenation@C	103/130	-32/6
18. $\text{C}^2 - \text{O}$ dissociation	34/42	-223/-214
I - 3 (5 - HMF)		
19. $\text{C}^1 - \text{O}$ scission	125/61	-159/-232
20. $\text{C}^1 - \text{O}$ hydrogenation@O	160/229	80/134
21. $\text{C}^1 - \text{O}$ hydrogenation@C	123/93	26/-16
Methyl Glyoxal (MG)		
22. $\text{C}^1 - \text{C}^2$ scission	61/96	-72/59
23. $\text{C}^2 - \text{C}^3$ scission	127/174	-27/-52

24. $C^1 - O$ scission	76/28	-64/-177
25. $C^2 - O$ scission	33/34	-129/-113
26. $C^1 - O$ hydrogenation	157/271	93/2
27. $C^2 - O$ hydrogenation	230/259	126/182
Acetic Acid (AA)		
28. $C^1 - O$ dissociation	70/4	-154/-129
29. $C^1 - OH$ dissociation	12/32	-194/-33
30. $C^1 - C^2$ cleavage	84/114	-106/17
31. $C^1 - O$ hydrogenation	206/126	117/18
Levogluconan (LGA)		
32. $C^1 - O^6$ scission	45/98	-112/-85
33. $C^1 - O^1$ scission	108/36	-117/-15
34. $C^6 - O^6$ scission	116/spontaneous	-207/spontaneous
35. $C^5 - O^1$ scission	98/26	-171/-60
36. $C^2 - OH$	79/100	-178/-5
37. $C^4 - OH$ scission	79/38	-175/-2
Intermediate1&2 - LGA		
38. $C^2 - OH$	47/90	-98/-316
39. $C^3 - OH$	84	-185
40. $C^6 - OH$	143	-143
41. $C^1 - O^1$ scission	135/37	-152/5
42. $C^5 - O^1$ scission	52	-207
43. $C^5 - C^6$ scission	385	-152
44. $C^1 - C^2$ scission	297	8
Vanillin		
45. $C^1 - O$ scission	121/81	-127/-170
46. $C^2 - O$ scission	93/59	-171/-117
47. $C^7 - O$ scission	84/90	-146/-107
48. $C^8 - O$ scission	128/83	-171/-158
49. $C^4 - C^8$ scission	195/137	36/164
50. $C^8 - O$ hydrogenation@O	182/192	143/91
51. $C^8 - O$ hydrogenation@C	158/89	82/5
Eugenol		
52. $C^2 - O$ scission	80/6	-156/-146
53. $C^7 - O$ scission	97/66	-118/-210
54. C^9 hydrogenation	140/135	111/110

55. C^{10} hydrogenation	153/164	93/115
56. C^{ring} hydrogenation	126/132	104/99

C.2 Adsorption Characteristics of model compounds on Mo₂C and MoWC

Table C.2 Adsorption energies (kJ/mol) and bond distances (d, Å) of different bond types present in considered six representative constituents of bio-oil in their adsorption configuration on Mo₂C and MoWC surfaces

Bond Type Compound	Bond distances are reported for Mo ₂ C/MoWC in (Å)					
	5 - HMF	MG	AA	LGA	Vanillin	Eugenol
$C^1 - O^1$	1.361/1.396	1.377/1.473		1.451/1.487	1.45/1.486	1.469/1.482
$C^2 - O^2$	1.437/1.441	1.422/1.426	1.365/1.536			
$C^2 - O^1$					1.428/1.431	1.424/1.494
$C^1 - O^5$				1.473/1.500		
$C^1 - O^6$				1.428/1.399		
$C^2 - OH$			1.545/1.52	1.467/1.446		
$C^3 - OH$				1.449/1.452		
$C^4 - OH$				1.465/1.476		
$C^5 - O^2$	1.512/1.474					
$C^6 - O^6$	1.495			1.466		
$C^7 - O^7$					1.45/1.395	1.426/1.475
$C^8 - O^8$					1.369/1.413	
$C^5 - C^6$	1.499/1.458					
$C^1 - C^2$	1.428/1.37	1.485/1.513				
Adsorption Energy	-163/-478	-122/-333	58/-170	-29/-281	-156/-402	-162/-301

C.3 Transition state Configurations of 5-HMF

C.3.1 Mo₂C

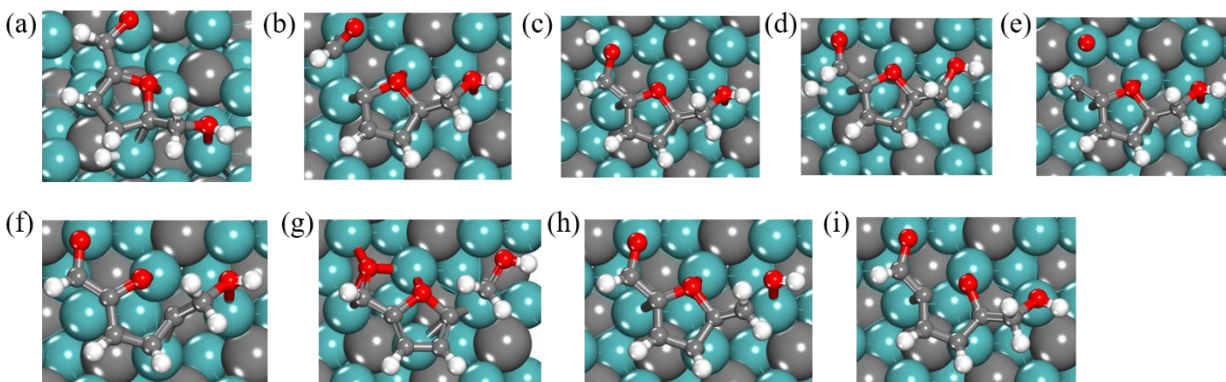


Figure C.1 Transition state geometries for first activation of 5-HMF on Mo₂C surface (R1 to R8). Dark cyan and blue spheres represent Mo and W atoms in the carbides, respectively. White, red, and gray spheres represent H, O, and C in the adsorbed guaiacol, respectively.

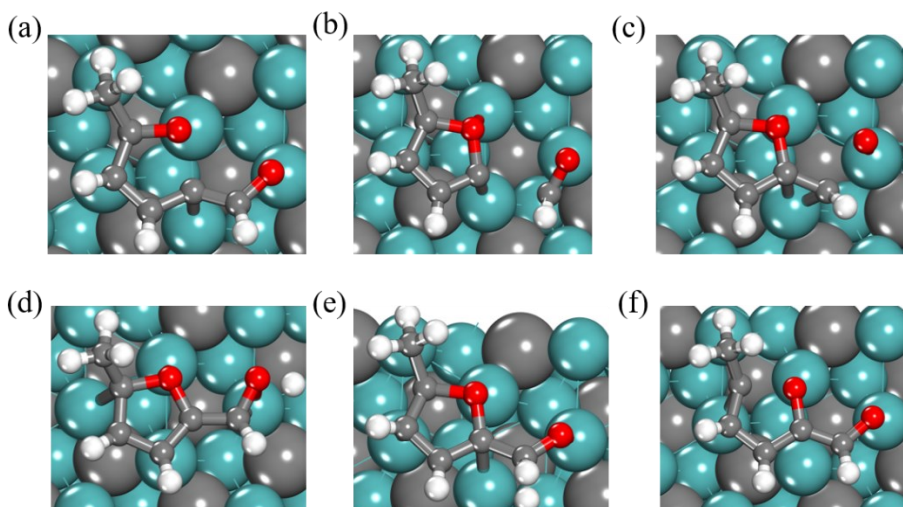


Figure C.2 Transition state geometries for 2nd activation of 5-HMF on Mo₂C surface (R9 to R14). Dark cyan and blue spheres represent Mo and W atoms in the carbides, respectively. White, red, and gray spheres represent H, O, and C in the adsorbed guaiacol, respectively.

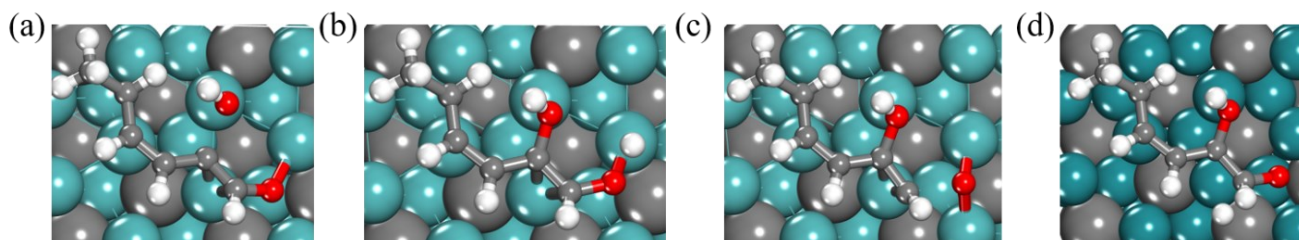


Figure C.3 Transition state geometries for 3rd activation of 5-HMF on Mo₂C surface (R15 to R18). Dark cyan and blue spheres represent Mo and W atoms in the carbides, respectively. White, red, and gray spheres represent H, O, and C in the adsorbed guaiacol, respectively.

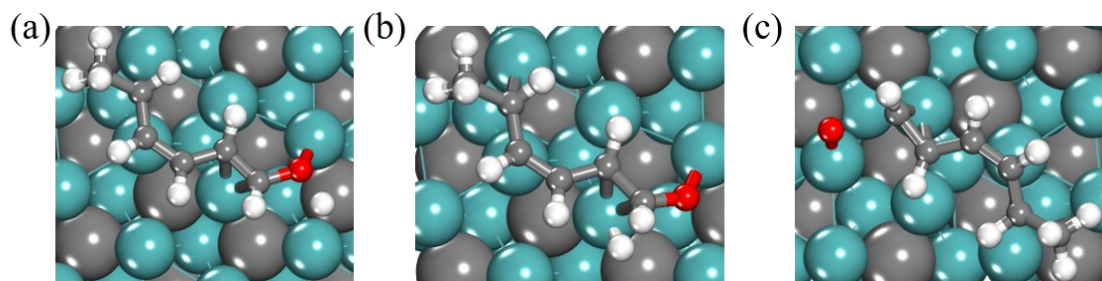


Figure C.4 Transition state geometries for final activation of 5-HMF on Mo₂C surface (R19 to R21). Dark cyan and blue spheres represent Mo and W atoms in the carbides, respectively. White, red, and gray spheres represent H, O, and C in the adsorbed guaiacol, respectively.

C.3.2 MoWC

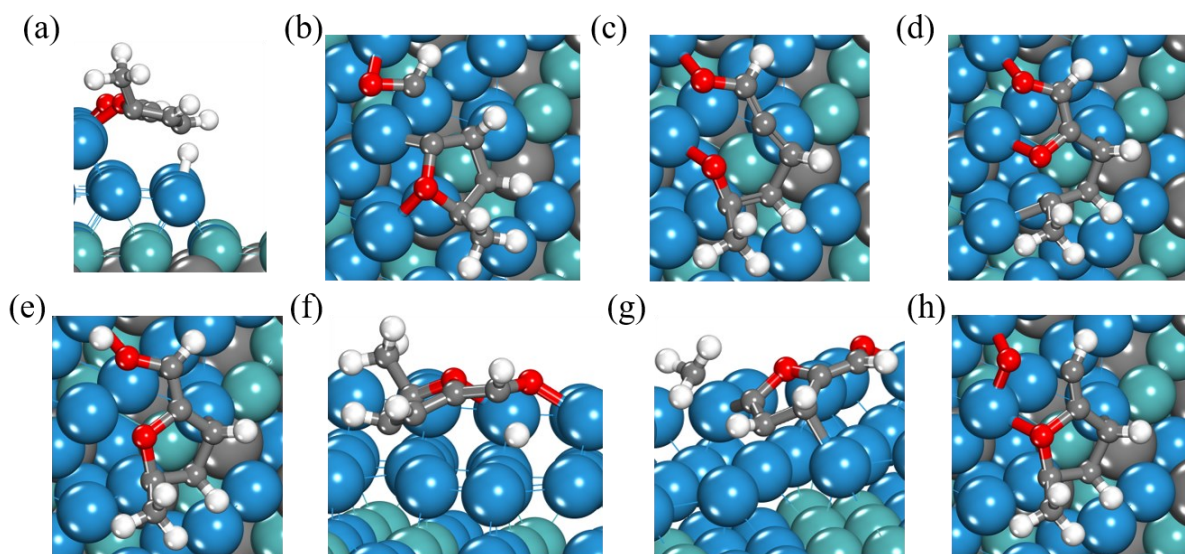


Figure C.5 Transition state geometries for first activation of 5-HMF on MoWC surface (R1 to R8). Dark cyan and blue spheres represent Mo and W atoms in the carbides, respectively. White, red, and gray spheres represent H, O, and C in the adsorbed guaiacol, respectively.

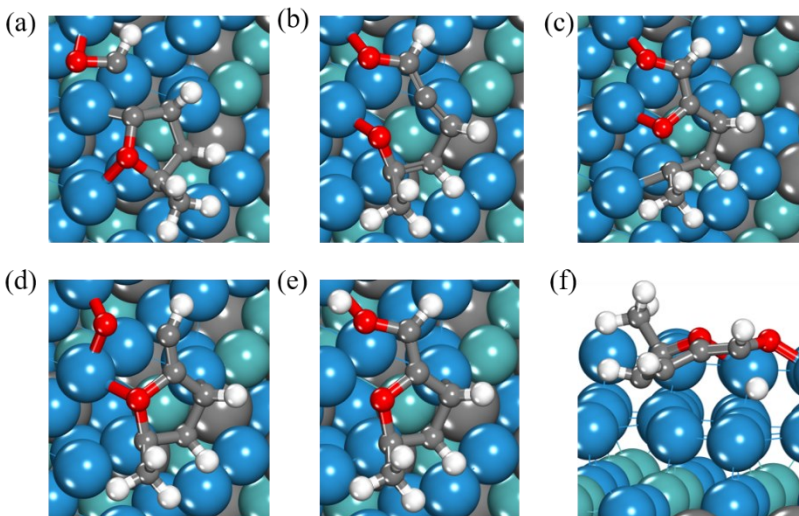


Figure C.6 Transition state geometries for 2nd activation of 5-HMF on MoWC surface (R9 to R14). Dark cyan and blue spheres represent Mo and W atoms in the carbides, respectively. White, red, and gray spheres represent H, O, and C in the adsorbed guaiacol, respectively.

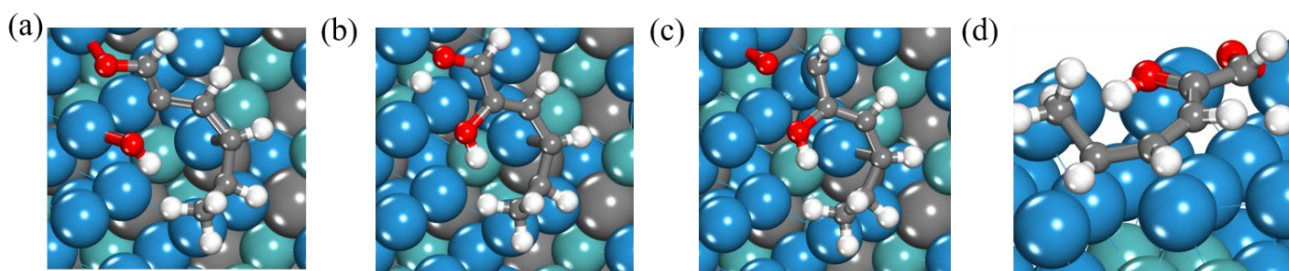


Figure C.7 Transition state geometries for 3rd activation of 5-HMF on MoWC surface (R15 to R18). Dark cyan and blue spheres represent Mo and W atoms in the carbides, respectively. White, red, and gray spheres represent H, O, and C in the adsorbed guaiacol, respectively.

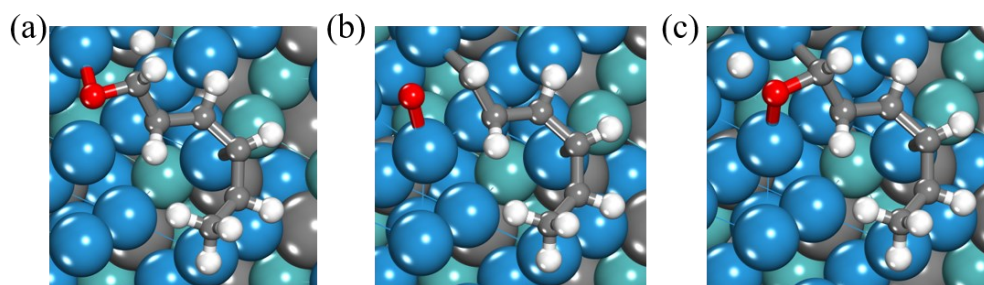


Figure C.8 Transition state geometries for final activation of 5-HMF on MoWC surface (R19 to R21). Dark cyan and blue spheres represent Mo and W atoms in the carbides, respectively. White, red, and gray spheres represent H, O, and C in the adsorbed guaiacol, respectively.

C.4 Transition state Configurations of Methyl Glyoxal

C.4.1 Mo₂C

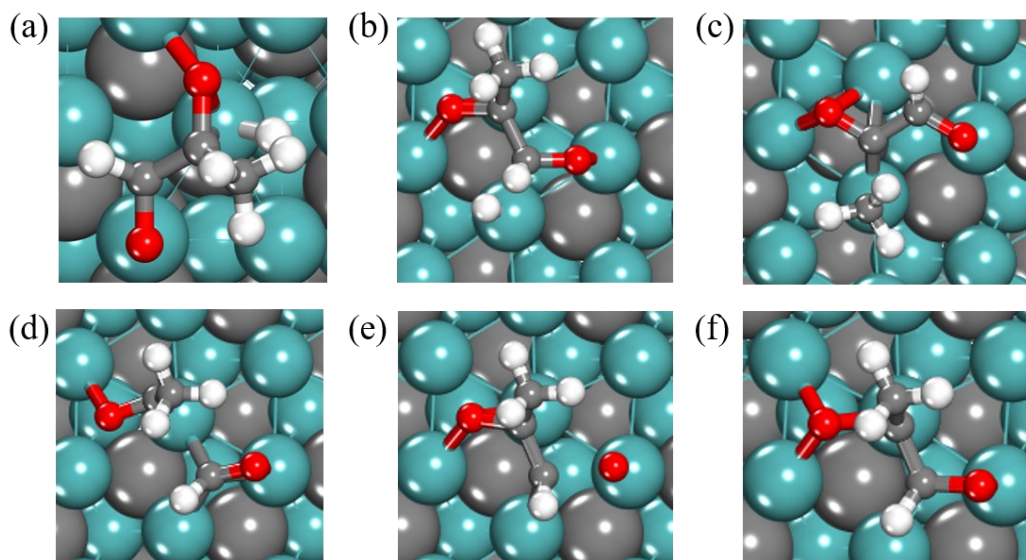


Figure C.9 Transition state geometries for final activation of methyl glyoxal on Mo₂C surface (R22 to R27). Dark cyan and blue spheres represent Mo and W atoms in the carbides, respectively. White, red, and gray spheres represent H, O, and C in the adsorbed guaiacol, respectively.

C.4.2 MoWC

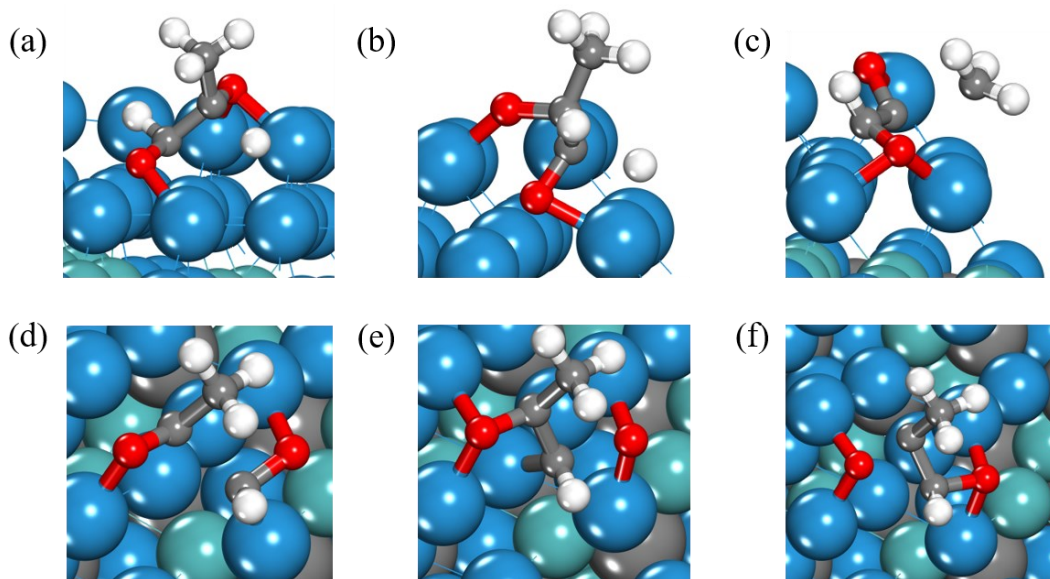


Figure C.10 Transition state geometries for final activation of methyl glyoxal on MoWC surface (R22 to R27). Dark cyan and blue spheres represent Mo and W atoms in the carbides, respectively. White, red, and gray spheres represent H, O, and C in the adsorbed guaiacol, respectively.

C.5 Transition state Configurations of Acetic Acid

C.5.1 Mo₂C

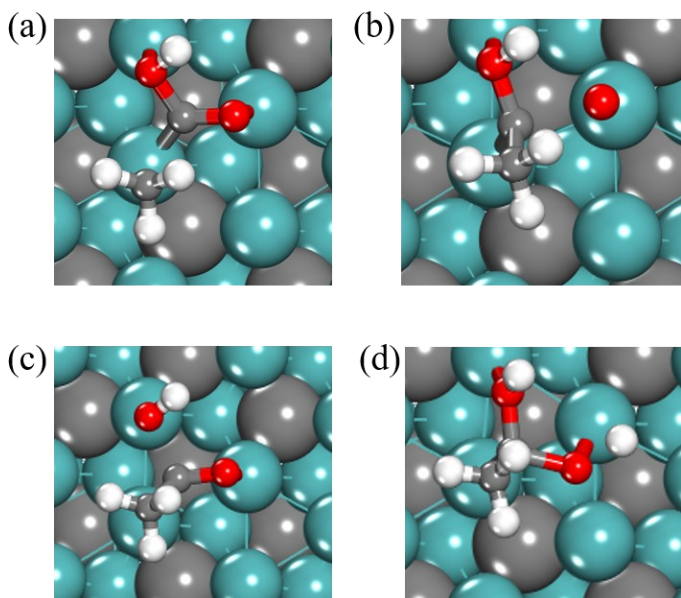
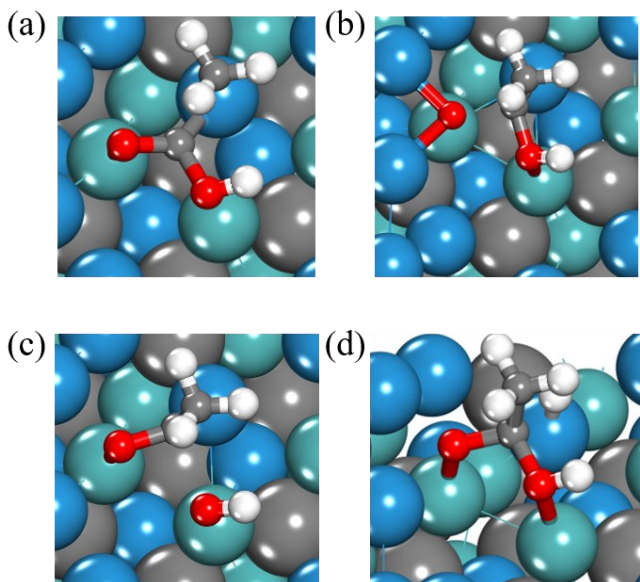


Figure C.11 Transition state geometries for final activation of acetic acid on Mo₂C surface (R28 to R31). Dark cyan and blue spheres represent Mo and W atoms in the carbides, respectively. White, red, and gray spheres represent H, O, and C in the adsorbed guaiacol, respectively.

C.5.2 MoWC



Figure_Apx C.12 Transition state geometries for final activation of acetic acid on MoWC surface (R28 to R31). Dark cyan and blue spheres represent Mo and W atoms in the carbides,

respectively. White, red, and gray spheres represent H, O, and C in the adsorbed guaiacol, respectively.

C.6 Transition state Configurations of LGA

C.6.1 Mo₂C

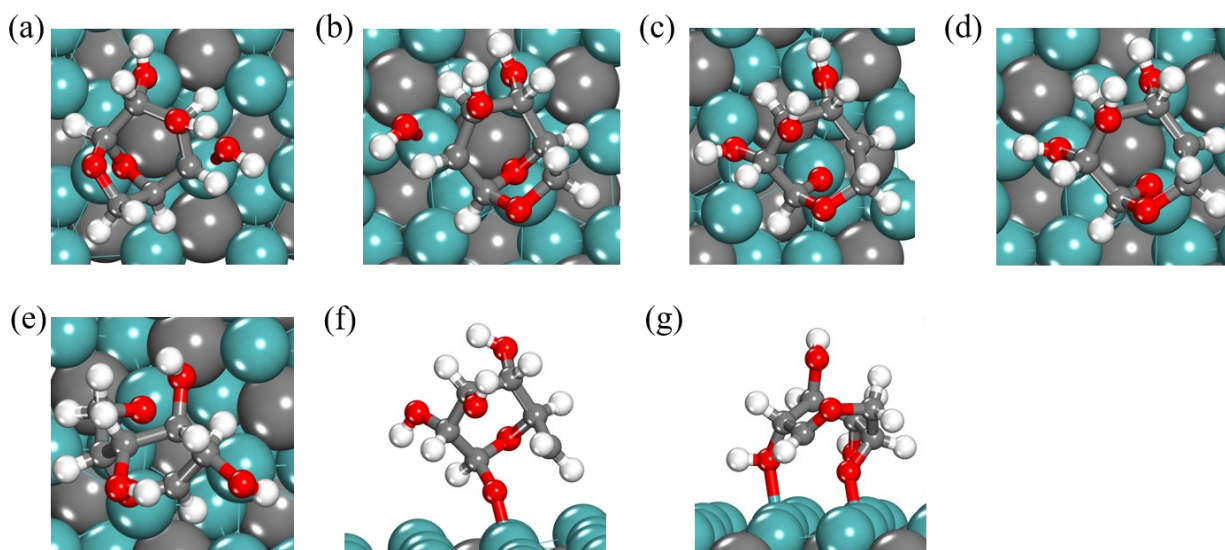


Figure C.13 Transition state geometries for final activation of LGA on Mo₂C surface (R32 to R37). Dark cyan and blue spheres represent Mo and W atoms in the carbides, respectively. White, red, and gray spheres represent H, O, and C in the adsorbed guaiacol, respectively.

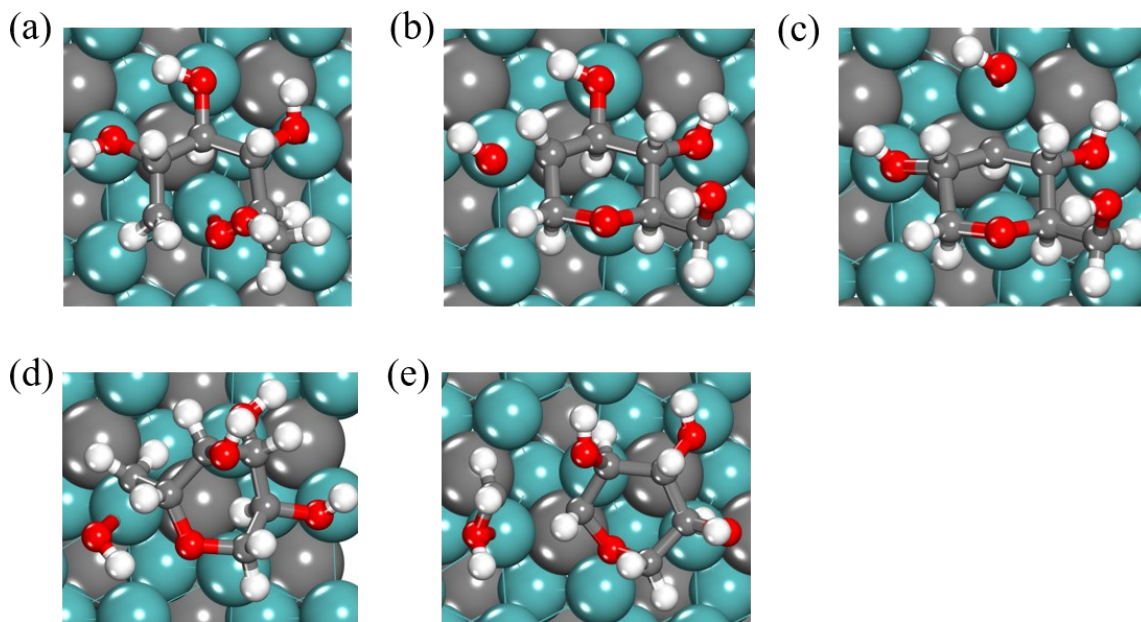


Figure C.14 Transition state geometries for final activation of LGA on Mo₂C surface (R38 to R43). Dark cyan and blue spheres represent Mo and W atoms in the carbides, respectively. White, red, and gray spheres represent H, O, and C in the adsorbed guaiacol, respectively.

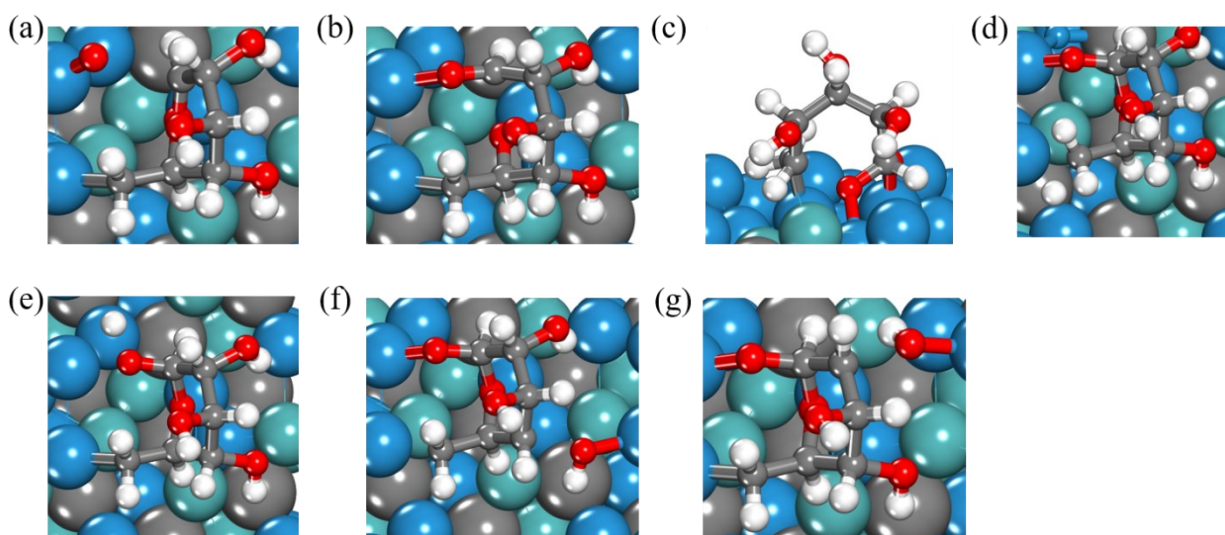


Figure C.15 Transition state geometries for first activation of LGA on MoWC surface (R32 to R37). Dark cyan and blue spheres represent Mo and W atoms in the carbides, respectively. White, red, and gray spheres represent H, O, and C in the adsorbed guaiacol, respectively.

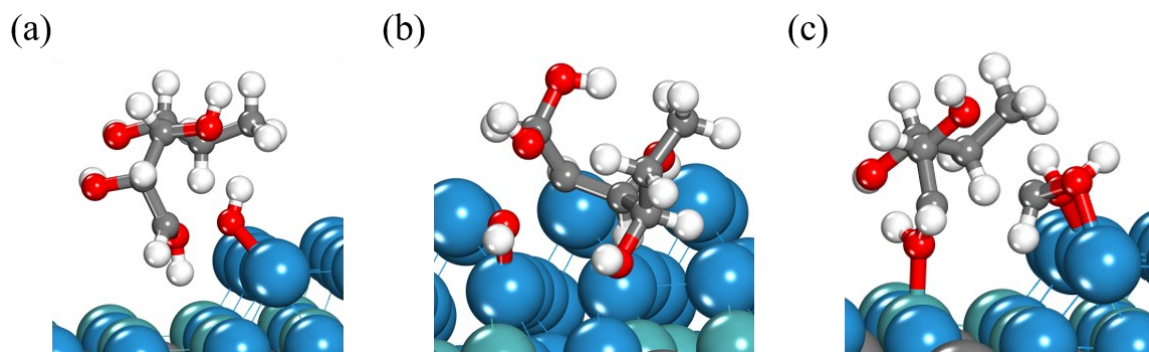


Figure C.16 Transition state geometries for 2nd activation of LGA on MoWC surface (R38, R41, and R44). Dark cyan and blue spheres represent Mo and W atoms in the carbides, respectively. White, red, and gray spheres represent H, O, and C in the adsorbed guaiacol, respectively.

C.7 Transition state Configurations of Vanillin

C.7.1 Mo₂C

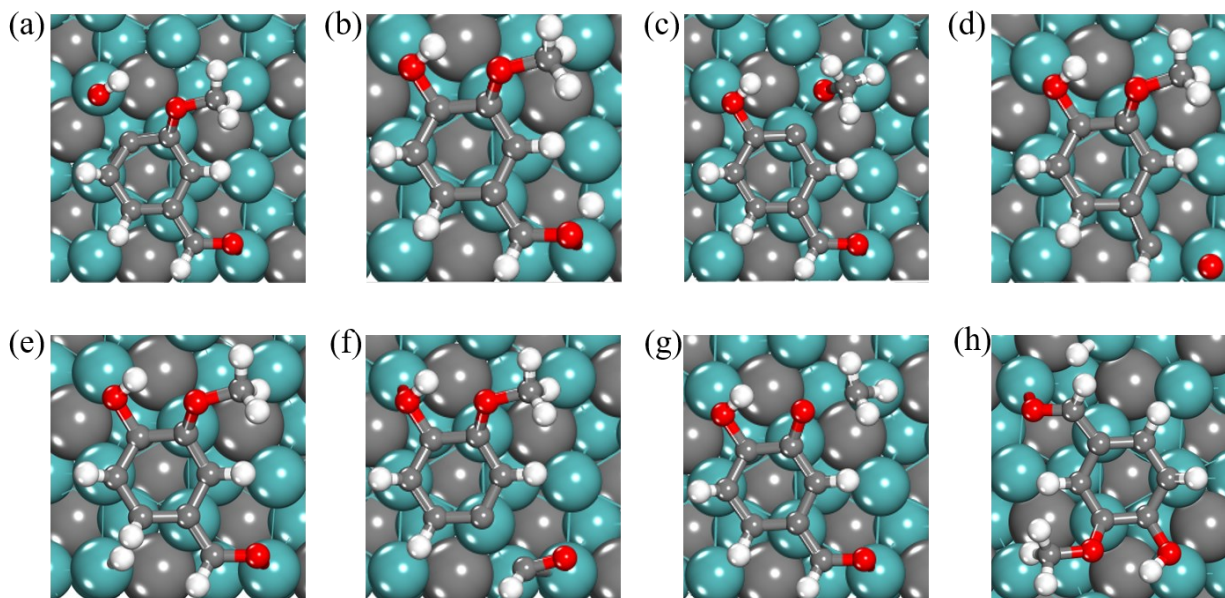


Figure C.17 Transition state geometries for first activation of Vanillin on Mo₂C surface (R45 to R51). Dark cyan and blue spheres represent Mo and W atoms in the carbides, respectively. White, red, and gray spheres represent H, O, and C in the adsorbed guaiacol, respectively.

C.7.2 MoWC

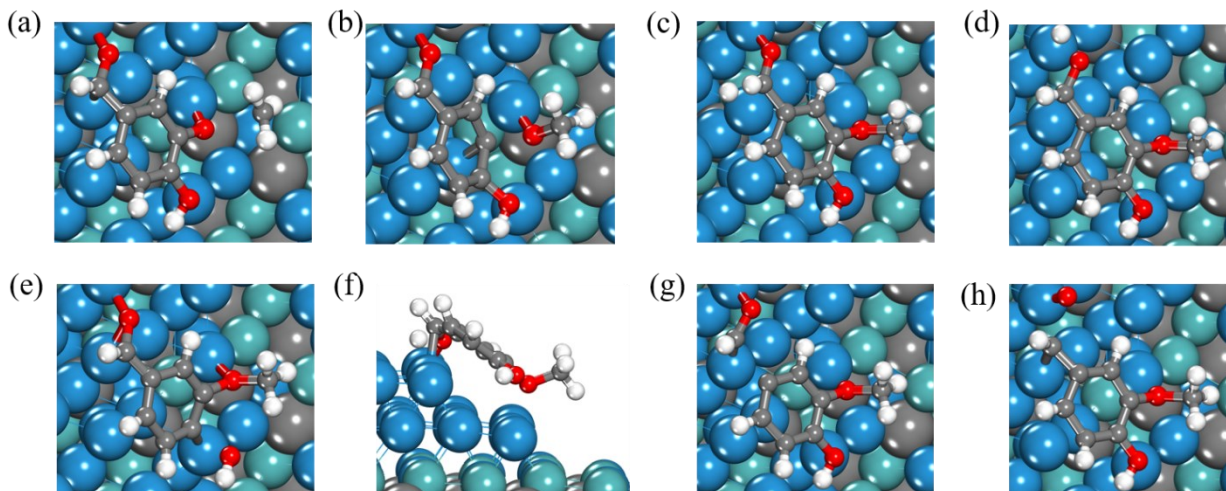


Figure C.18 Transition state geometries for first activation of Vanillin on MoWC surface (R45 to R51). Dark cyan and blue spheres represent Mo and W atoms in the carbides, respectively. White, red, and gray spheres represent H, O, and C in the adsorbed guaiacol, respectively.

C.8 Transition state Configurations of Eugenol

C.8.1 Mo₂C

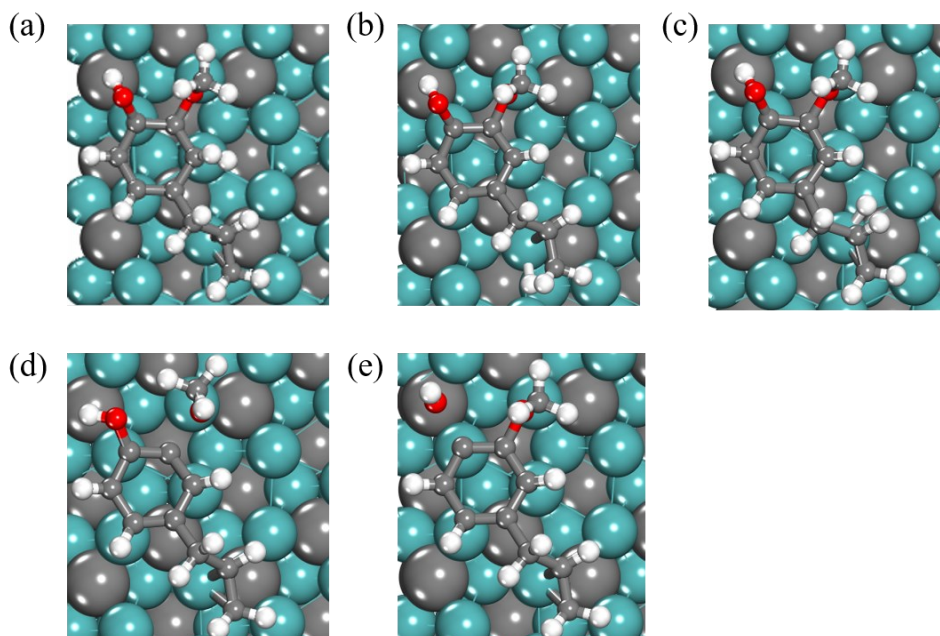


Figure C.19 Transition state geometries for first activation of Eugenol on Mo₂C surface (R52 to R56). Dark cyan and blue spheres represent Mo and W atoms in the carbides, respectively. White, red, and gray spheres represent H, O, and C in the adsorbed guaiacol, respectively.

C.8.2 MoWC

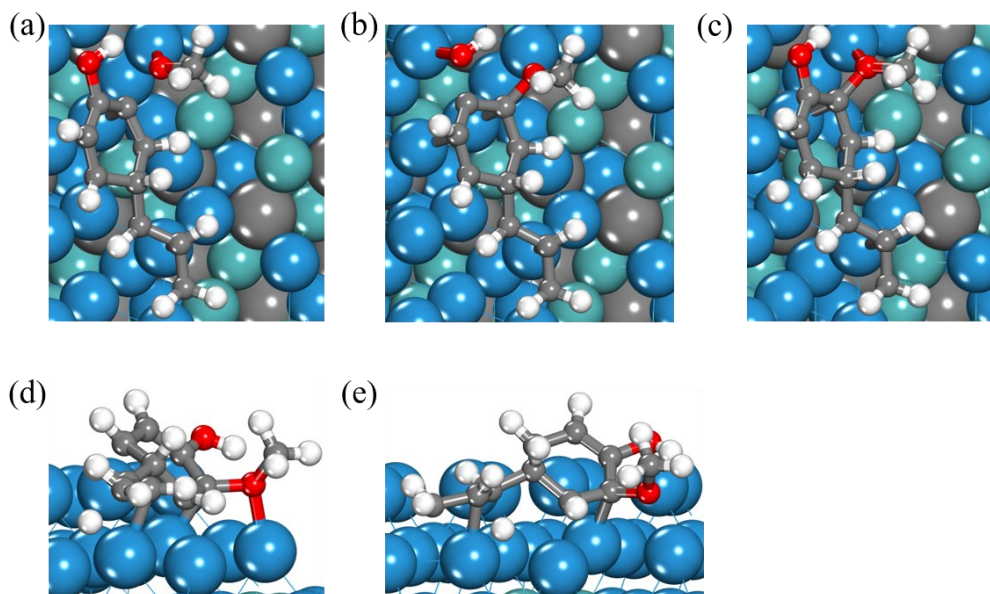


Figure C.20 Transition state geometries for first activation of Eugenol on MoWC surface (R52 to R56). Dark cyan and blue spheres represent Mo and W atoms in the carbides, respectively. White, red, and gray spheres represent H, O, and C in the adsorbed guaiacol, respectively.

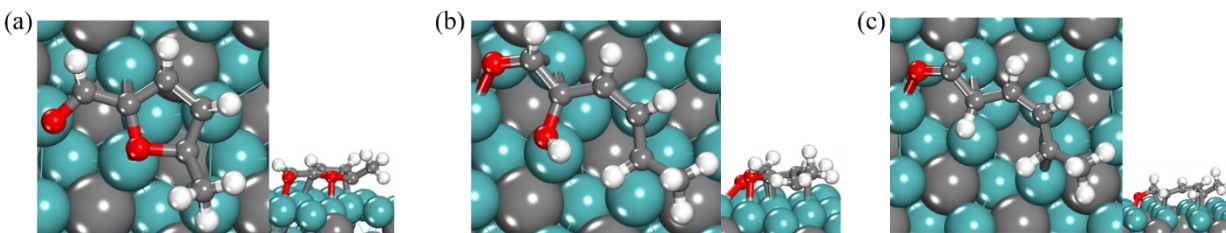


Figure C.21 Optimized adsorption configurations for intermediates obtained (a) first activation (I – 1), (b) 2nd activation (I – 2), (c) 3rd activation (I – 3) of 5-HMF on Mo₂C surface. Dark cyan and blue spheres represent Mo and W atoms in the carbides, respectively. White, red, and gray spheres represent H, O, and C in the adsorbed guaiacol, respectively.

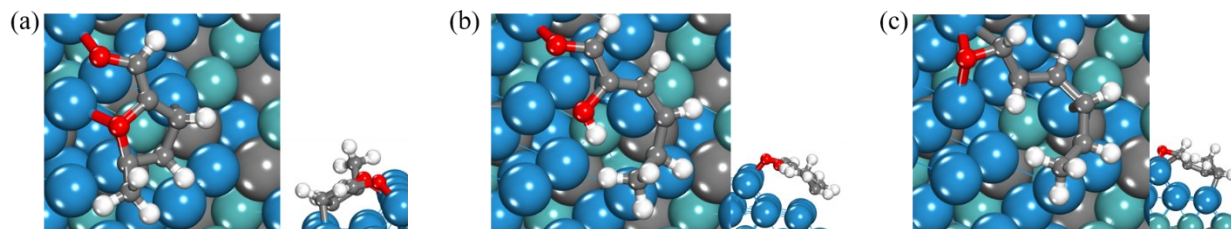


Figure C.22 Optimized adsorption configurations for intermediates obtained (a) first activation (I – 1), (b) 2nd activation (I – 2), (c) 3rd activation (I – 3) of 5-HMF on MoWC surface. Dark cyan and blue spheres represent Mo and W atoms in the carbides, respectively. White, red, and gray spheres represent H, O, and C in the adsorbed guaiacol, respectively.

Appendix D Supplementary Information to Chapter 4

D.1 Surface Energy Calculations

Surface energy calculations were performed with a method developed by Tian et al.⁷, which we refer to as the cleavage energy method. This method determines the energy contributions of A- and B-terminations via the following process. First, the relaxation energy of a slab is calculated as the difference between the surface energy of the frozen slab and the surface energy of the slab with either the A- or B-termination relaxed,

$$E_{\text{relax}}(\text{A}) = \frac{E_{\text{frozen}} - \eta E_{\text{bulk}}}{A} - \frac{E_{\text{A-relax}} - \eta E_{\text{bulk}}}{A} \quad (\text{D-1})$$

$$E_{\text{relax}}(\text{B}) = \frac{E_{\text{frozen}} - \eta E_{\text{bulk}}}{A} - \frac{E_{\text{B-relax}} - \eta E_{\text{bulk}}}{A} \quad (\text{D-2})$$

where E_{frozen} is the energy of a slab with both terminations frozen, and $E_{\text{A-relax}}$ and $E_{\text{B-relax}}$ are the energies of the slab with A and B relaxed respectively. Next, the cleavage energy is determined as an approximation of the energy of a frozen surface,

$$E_{\text{cleave}} = \frac{E_{\text{frozen}} - \eta E_{\text{bulk}}}{2A} \quad (\text{D-3})$$

Finally, the relaxed surface energies of each termination, γ_{A} and γ_{B} , are obtained as the difference of the cleavage and relaxation energies,

$$\gamma_{\text{A}} = E_{\text{cleave}} - E_{\text{relax}}(\text{A}) \quad (\text{D-4})$$

$$\gamma_{\text{B}} = E_{\text{cleave}} - E_{\text{relax}}(\text{B}) \quad (\text{D-5})$$

It must be noted, however, that although the cleavage energy method provides the surface energies for the individual relaxed terminations, it nonetheless assumes, somewhat inaccurately, that the energy contributions of the frozen terminations are the same in asymmetric slabs.

D.2 Lattice Parameter Optimization

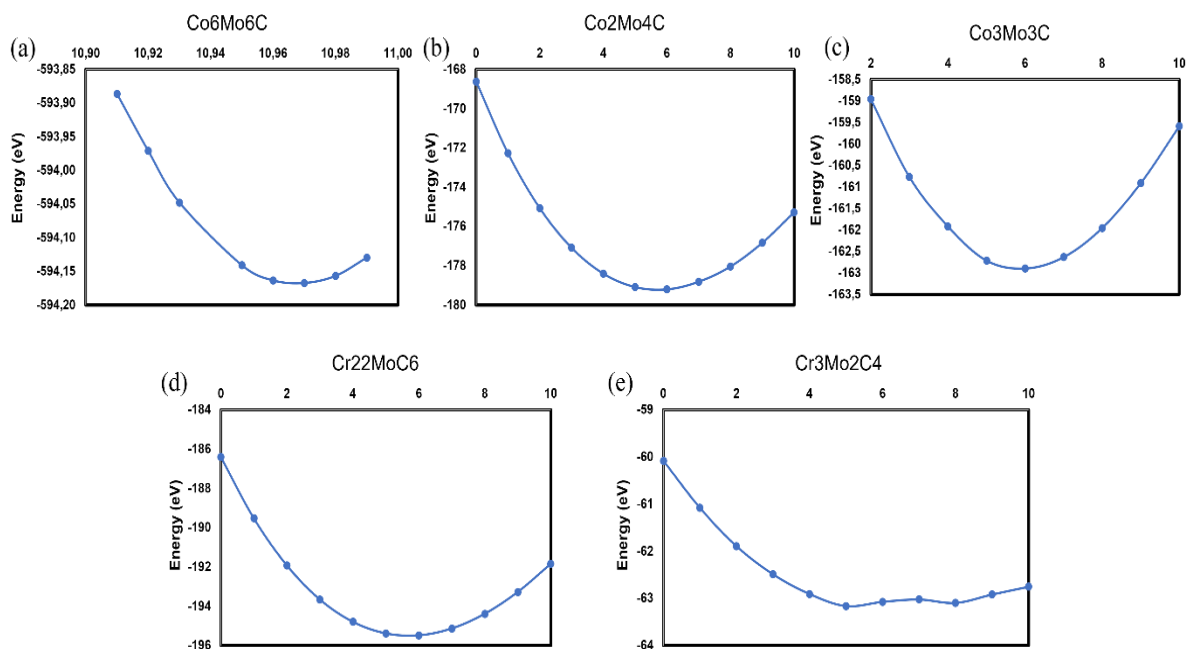


Figure D.1 Lattice parameter optimisation for (a) $\text{Co}_6\text{Mo}_6\text{C}$, (b) $\text{Co}_2\text{Mo}_4\text{C}$, (c) $\text{Co}_3\text{Mo}_3\text{C}$, (d) $\text{Cr}_{22}\text{MoC}_6$ and (e) $\text{Cr}_3\text{Mo}_2\text{C}_4$ catalysts.

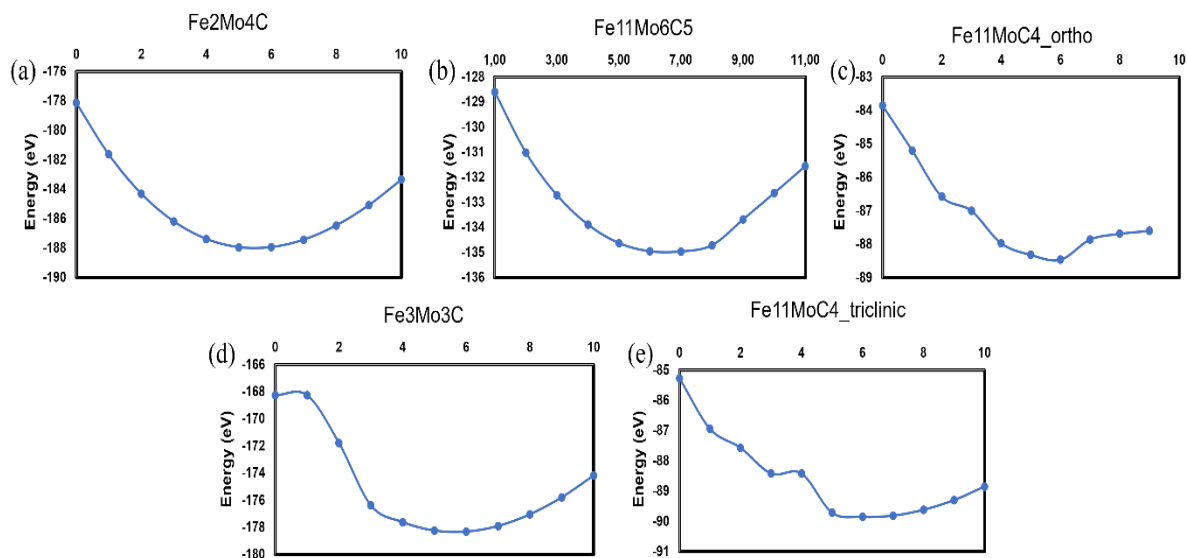


Figure D.2 Lattice parameter optimisation for (a) $\text{Fe}_2\text{Mo}_4\text{C}$, (b) $\text{Fe}_{11}\text{Mo}_6\text{C}_5$, (c) $\text{Fe}_{11}\text{MoC}_4$ (orthorhombic), (d) $\text{Fe}_3\text{Mo}_3\text{C}$ and (e) $\text{Fe}_{11}\text{MoC}_4$ (triclinic) catalysts.

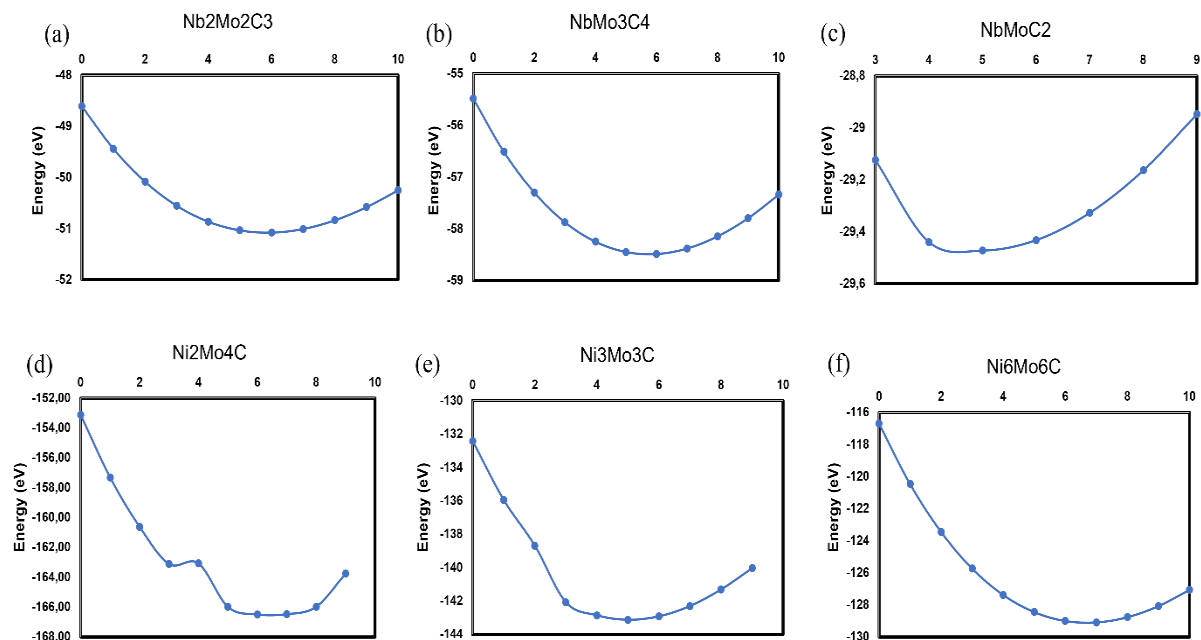


Figure D.3 Lattice parameter optimisation for (a) $\text{Nb}_2\text{Mo}_2\text{C}_3$, (b) NbMo_3C_4 , (c) NbMoC_2 , (d) $\text{Ni}_2\text{Mo}_4\text{C}$, (e) $\text{Ni}_3\text{Mo}_3\text{C}$ and (f) $\text{Ni}_6\text{Mo}_6\text{C}$ catalysts.

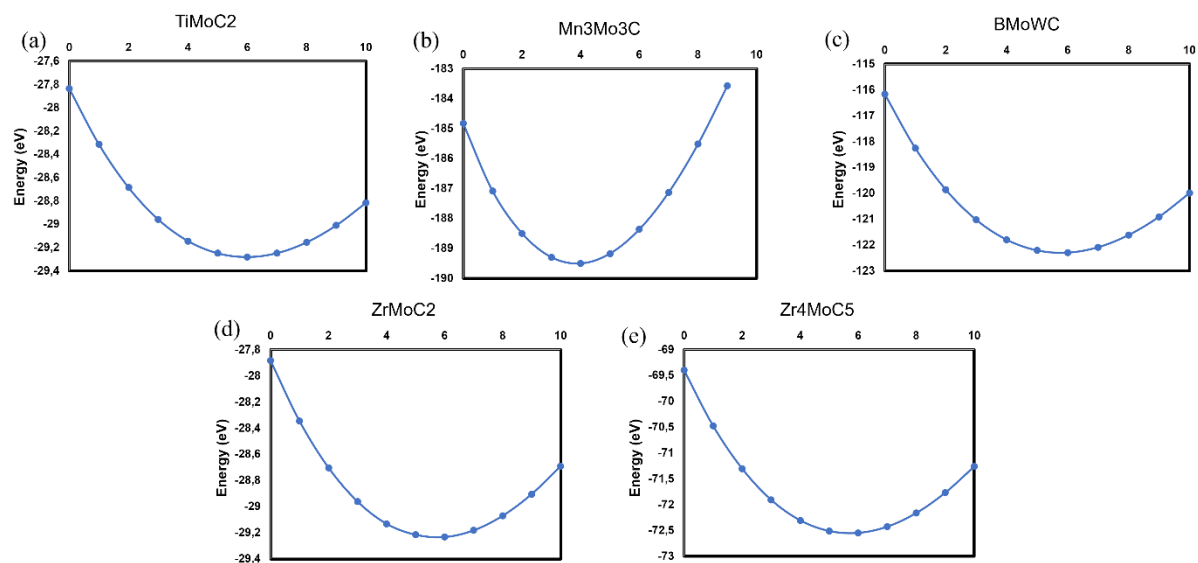


Figure D.4 Lattice parameter optimisation for (a) TiMoC_2 , (b) $\text{Mn}_3\text{Mo}_3\text{C}$, (c) BMoWC , (d) ZrMoC_2 and (e) Zr_4MoC_5 catalysts.

D.3 Surface energy tables

Table D.1 Surface energy for lower miller indices for $\text{Co}_2\text{Mo}_4\text{C}$, $\text{Co}_3\text{Mo}_3\text{C}$, and $\text{Co}_6\text{Mo}_6\text{C}$ catalyst surfaces.

	$\text{Co}_2\text{Mo}_4\text{C}$	$\text{Co}_3\text{Mo}_3\text{C}$	$\text{Co}_6\text{Mo}_6\text{C}$
Facet	Energy (J/m^2)	Energy (J/m^2)	Energy (J/m^2)
001	1.72	2.13	2.02
010	2.63	2.13	2.01
100	2.63	2.27	2.00
101	2.41	2.53	2.20
110	3.00	2.44	2.21
111	1.92	2.21	2.00

Table D.2 Surface energy for lower miller indices for $\text{Cr}_{22}\text{MoC}_6$ and $\text{Cr}_3\text{Mo}_2\text{C}_4$ catalyst surfaces

	$\text{Cr}_{22}\text{MoC}_6$	$\text{Cr}_3\text{Mo}_2\text{C}_4$
Facet	Energy (J/m^2)	Energy (J/m^2)
001	2.46	1.63
010	2.50	1.60
100	2.42	1.60
101	2.96	2.09
110	2.59	1.98
111	2.39	1.61

Table D.3 Surface energy for lower miller indices for $\text{Fe}_2\text{Mo}_4\text{C}$, $\text{Fe}_3\text{Mo}_3\text{C}$, $\text{Fe}_{11}\text{Mo}_6\text{C}_5$, Orthorhombic- $\text{Fe}_{11}\text{MoC}_4$, and Triclinic- $\text{Fe}_{11}\text{MoC}_4$ catalyst surfaces.

	$\text{Fe}_2\text{Mo}_4\text{C}$	$\text{Fe}_3\text{Mo}_3\text{C}$	$\text{Fe}_{11}\text{Mo}_6\text{C}_5$	$\text{Fe}_{11}\text{MoC}_4$ orthorhombic	$\text{Fe}_{11}\text{MoC}_4$ triclinic
Facet	Energy (J/m^2)	Energy (J/m^2)	Energy (J/m^2)	Energy (J/m^2)	Energy (J/m^2)
001	2.10	2.14	1.75	2.13	2.21
010	2.10	2.00	2.00	2.03	1.96
100	2.10	1.88	2.12	2.17	2.08
101	2.32	2.24	1.94	1.69	2.91
110	2.32	2.23	1.94	1.14	2.19
111	2.08	2.81	1.91	1.62	1.97

Table D.4 Surface energy for lower miller indices for Ni₂Mo₄C, Ni₃Mo₃C, and Ni₆Mo₆C catalyst surfaces.

Facet	<i>Ni₂Mo₄C</i>	<i>Ni₃Mo₃C</i>	<i>Ni₆Mo₆C</i>
	<i>Energy (J/m²)</i>	<i>Energy (J/m²)</i>	<i>Energy (J/m²)</i>
001	1.98	2.02	1.94
010	2.65	2.02	1.94
011	2.62	2.46	2.51
100	2.65	2.02	1.94
101	2.62	2.46	2.20
110	2.62	2.46	2.51
111	2.38	1.52	2.10

Table D.5 Surface energy for lower miller indices for Nb₂Mo₂C₃, NiMo₃C₄, and NbMoC₂ catalyst surfaces.

Facet	<i>Nb₂Mo₂C₃</i>	<i>NbMo₃C₄</i>	<i>NbMoC₂</i>
	<i>Energy (J/m²)</i>	<i>Energy (J/m²)</i>	<i>Energy (J/m²)</i>
001	1.66	1.89	2.12
010	1.58	1.17	1.19
011	2.84	0.45	2.51
100	1.58	1.17	1.19
101	2.84	0.45	2.03
110	1.67	0.73	2.03
111	2.01	1.17	1.11

Table D.6 Surface energy for lower miller indices for ZrMoC₂, and Zr₄MoC₅ catalyst surfaces.

Facet	<i>ZrMoC₂</i>	<i>Zr₄MoC₅</i>
	<i>Energy (J/m²)</i>	<i>Energy (J/m²)</i>
001	3.67	3.78
010	1.57	1.87
011	2.37	2.68
100	1.57	1.79
101	2.37	2.68
110	2.37	2.68
111	1.57	1.80

Table D.7 Surface energy for lower miller indices for Mn_3Mo_3C , $TiMoC_2$, and $BMoWC$ catalyst surfaces.

Facet	Mn_3Mo_3C	$TiMoC_2$	$BMoWC$
	Energy (J/m^2)	Energy (J/m^2)	Energy (J/m^2)
001	1.96	2.37	2.77
010	1.96	1.63	1.92
100	1.96	1.63	2.73
101	2.75	3.27	1.78
110	2.75	3.86	2.72
111	2.79	1.63	1.77

D.4 Catalyst Models

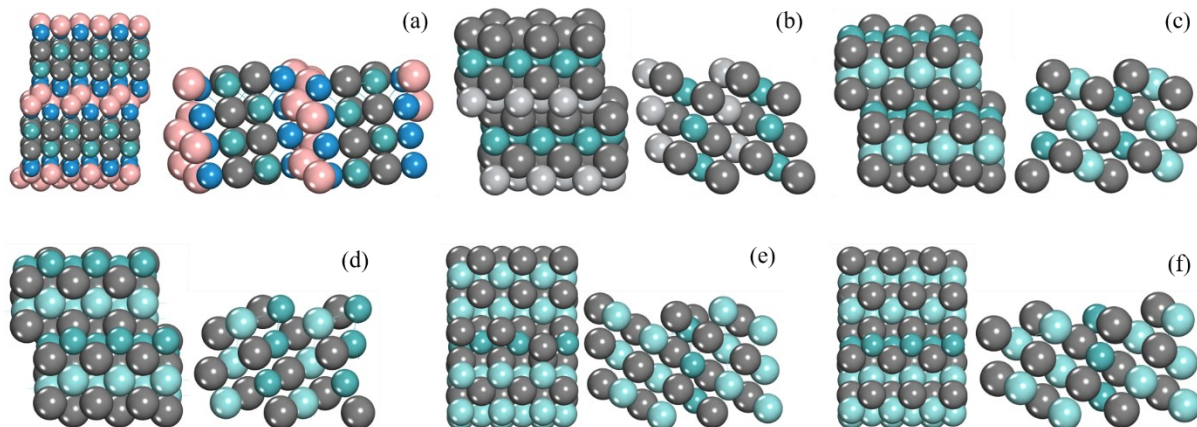


Figure D.5 Optimised configurations of pristine catalyst surfaces of (a) $BMoWC$, (b) $TiMoC_2$, (c) Zr_A , (d) Zr_B , (e) Zr_{4A} and (f) Zr_{4B} . The dark grey spheres represent C. In (a), the pink, green and blue spheres represent B, Mo and W respectively. In (b), the green and light grey spheres represent Mo and Ti respectively. In (c)-(f), the darker teal and lighter turquoise spheres represent Mo and Zr respectively.

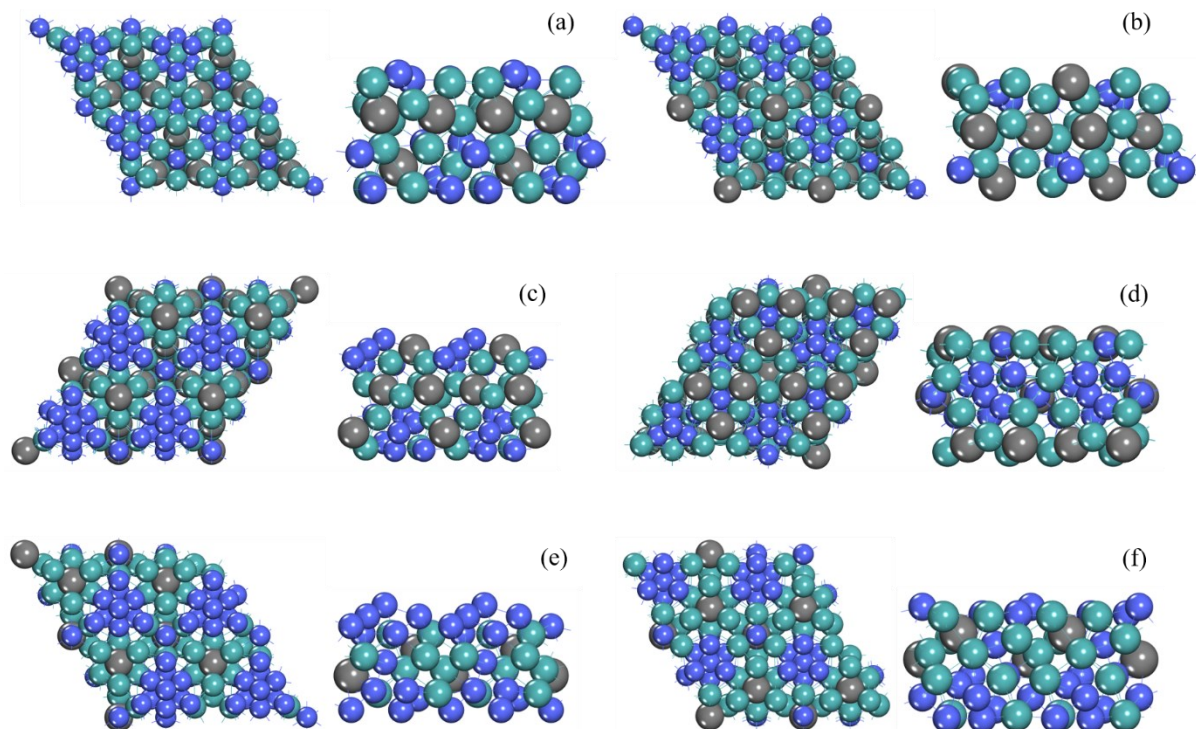


Figure D.6 Optimised configurations of pristine catalyst surfaces of (a) Co_2A , (b) Co_2B , (c) Co_3A , (d) Co_3B , (e) Co_6A and (f) Co_6B . The grey spheres represent C. The green and blue spheres represent Mo and Co respectively.

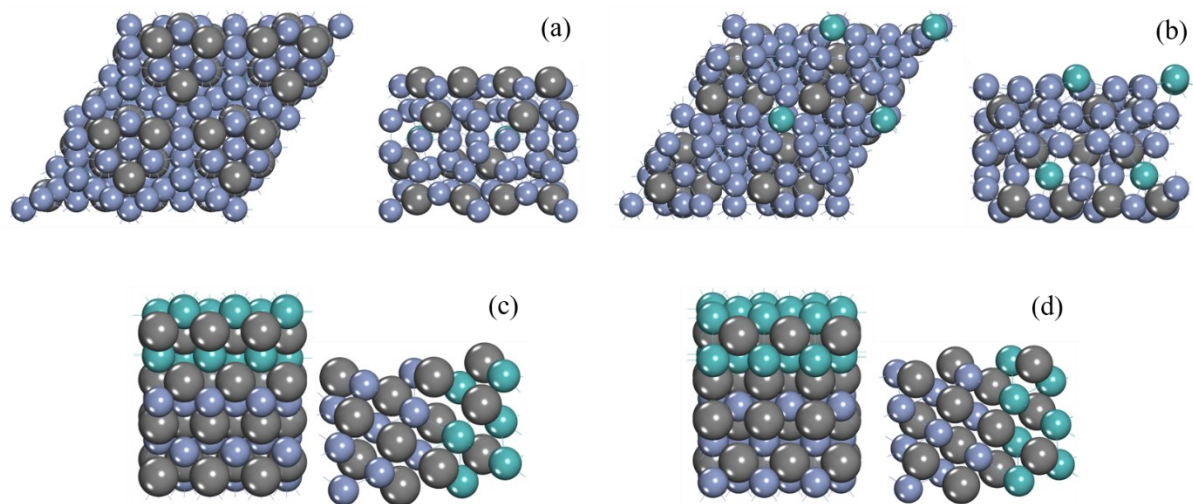


Figure D.7 Optimised configurations of pristine catalyst surfaces of (a) Cr_{22}A , (b) Cr_{22}B , (c) Cr_3A and (d) Cr_3B . The grey spheres represent C. The green and pastel blue spheres represent Mo and Cr respectively.

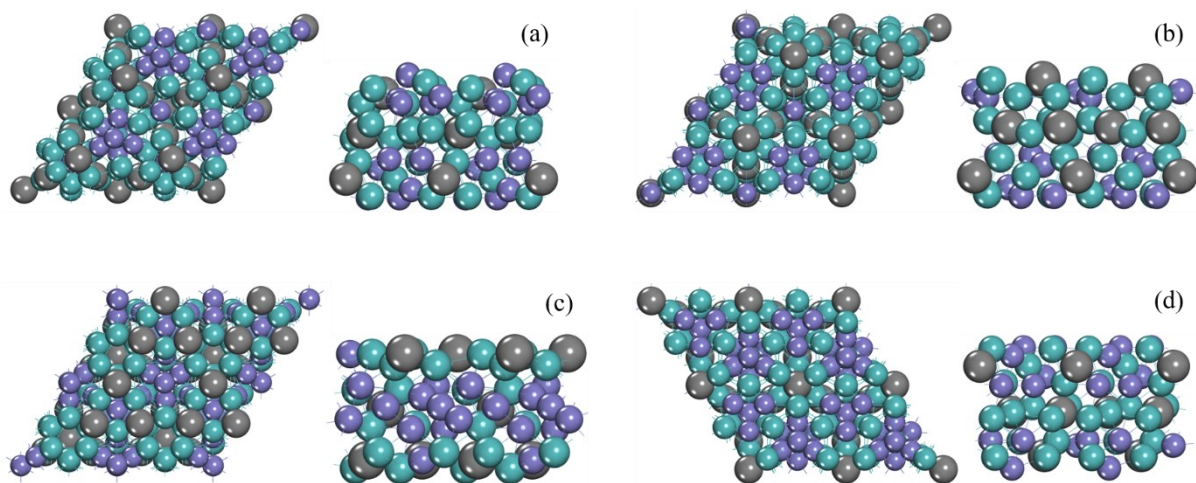


Figure D.8 Optimised configurations of pristine catalyst surfaces of (a) $\text{Fe}_{2\text{A}}$, (b) $\text{Fe}_{2\text{B}}$, (c) $\text{Fe}_{3\text{B}}$ and (d) $\text{Fe}_{3\text{C}}$. The grey spheres represent C. The green and purple spheres represent Mo and Fe respectively.

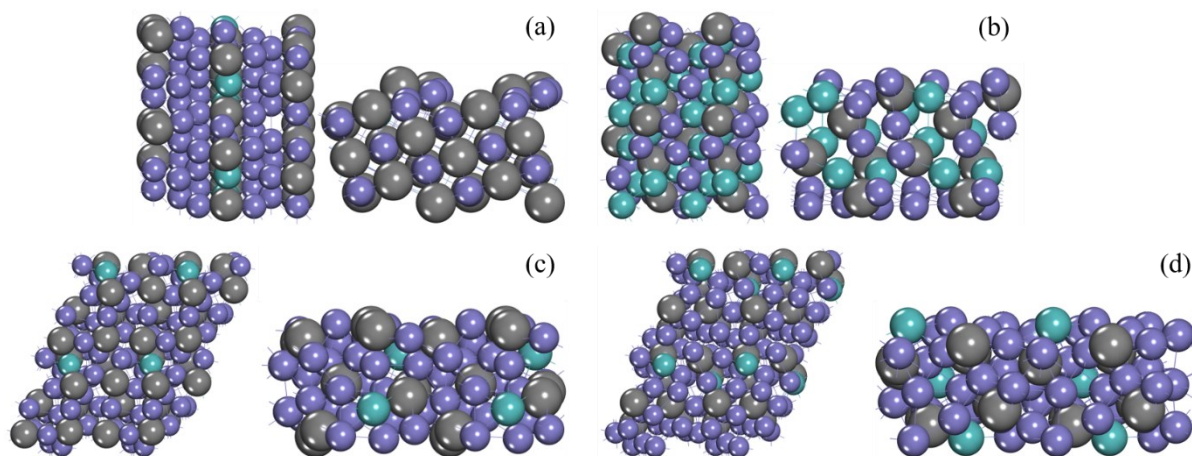


Figure D.9 Optimised configurations of pristine catalyst surfaces of (a) $\text{Fe}_{11\text{O}_\text{A}}$, (b) $\text{Fe}_{11\text{O}_\text{C}}$, (c) $\text{Fe}_{11\text{T}_\text{A}}$ and (d) $\text{Fe}_{11\text{T}_\text{B}}$. The grey spheres represent C. The green and purple spheres represent Mo and Fe respectively.

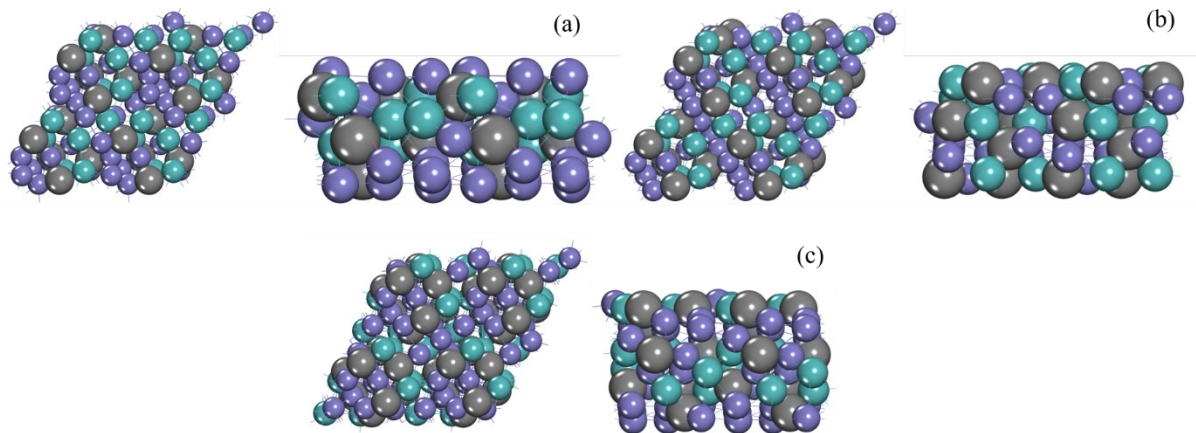


Figure D.10 Optimised configurations of pristine catalyst surfaces of (a) $\text{Fe}_{11\text{A}}$, (b) $\text{Fe}_{11\text{B}}$ and (c) $\text{Fe}_{11\text{C}}$. The grey spheres represent C. The green and purple spheres represent Mo and Fe respectively.

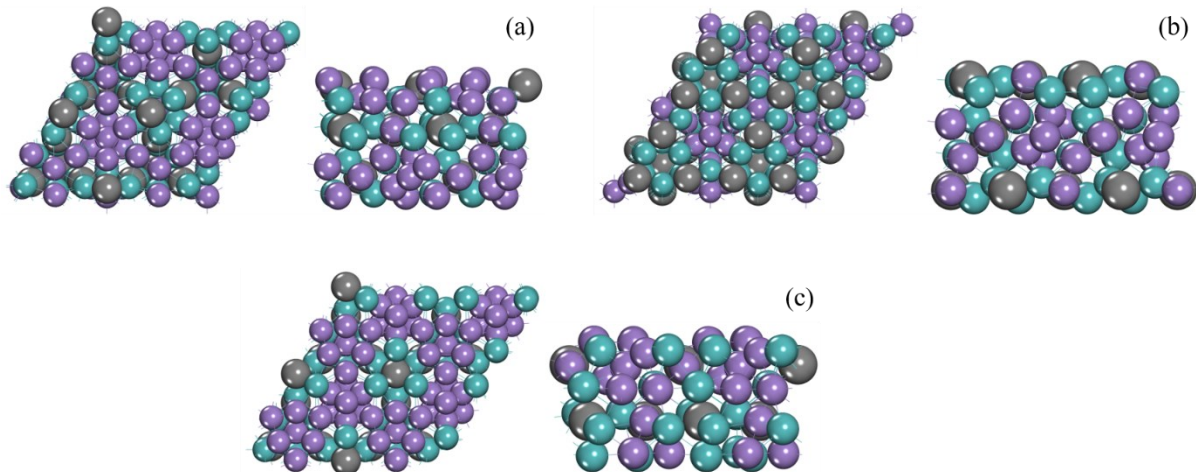


Figure D.11 Optimised configurations of pristine catalyst surfaces of (a) Mn_{A} , (b) Mn_{B} and (c) Mn_{C} . The grey spheres represent C. The green and purple spheres represent Mo and Mn respectively.

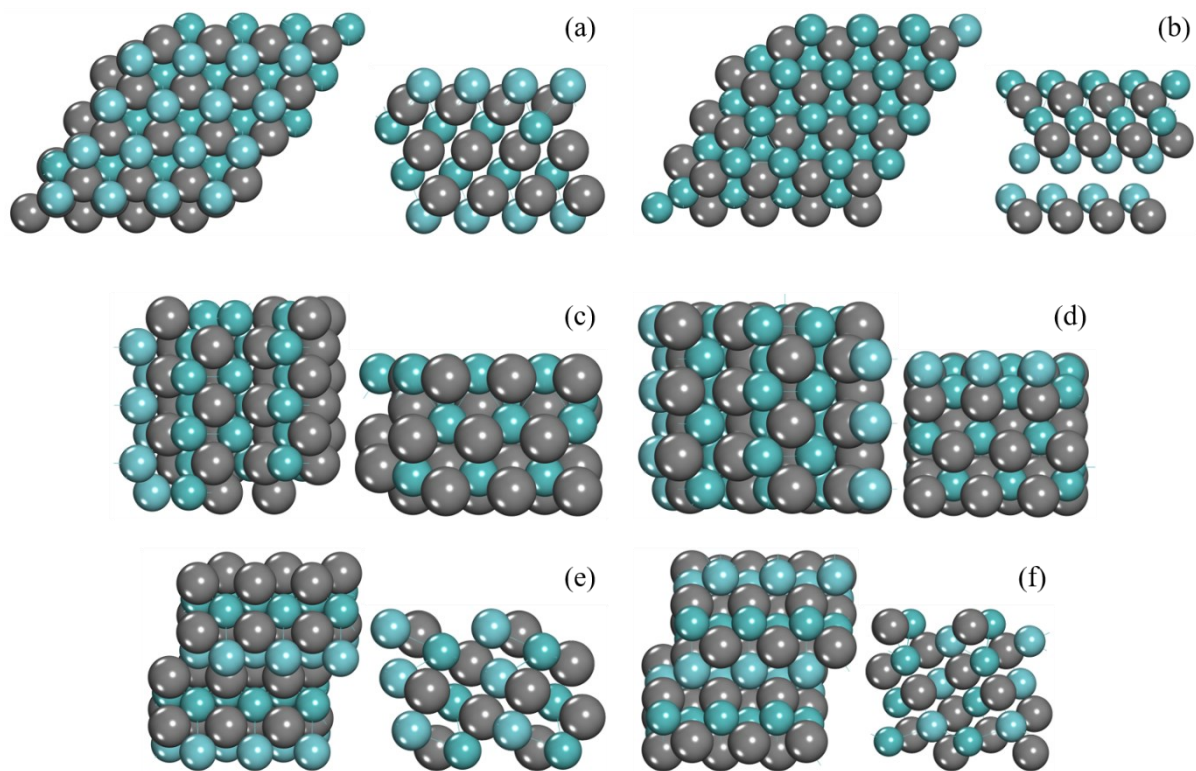


Figure D.12 Optimised configurations of pristine catalyst surfaces of (a) $\text{Nb}_{2\text{A}}$, (b) $\text{Nb}_{2\text{B}}$, (c) $\text{NbMo}_{3\text{B}}$, (d) $\text{NbMo}_{3\text{C}}$, (e) NbMo_{A} and (f) NbMo_{B} . The grey spheres represent C. The darker and lighter green spheres represent Mo and Nb respectively.

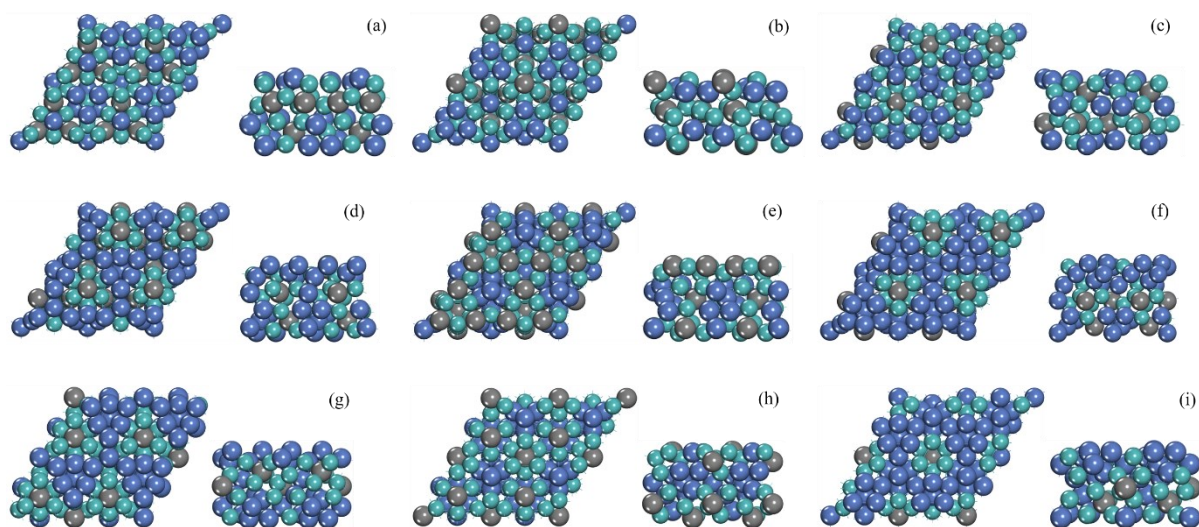


Figure D.13 Optimised configurations of pristine catalyst surfaces of (a) Ni_{2A}, (b) Ni_{2B}, (c) Ni_{2C}, (d) Ni_{3A}, (e) Ni_{3B}, (f) Ni_{3C}, (g) Ni_{6A}, (h) Ni_{6B} and (i) Ni_{6C}. The grey spheres represent C. The green and blue spheres represent Mo and Ni respectively.

D.5 Optimized stable adsorption configuration of H adatom on catalyst surfaces

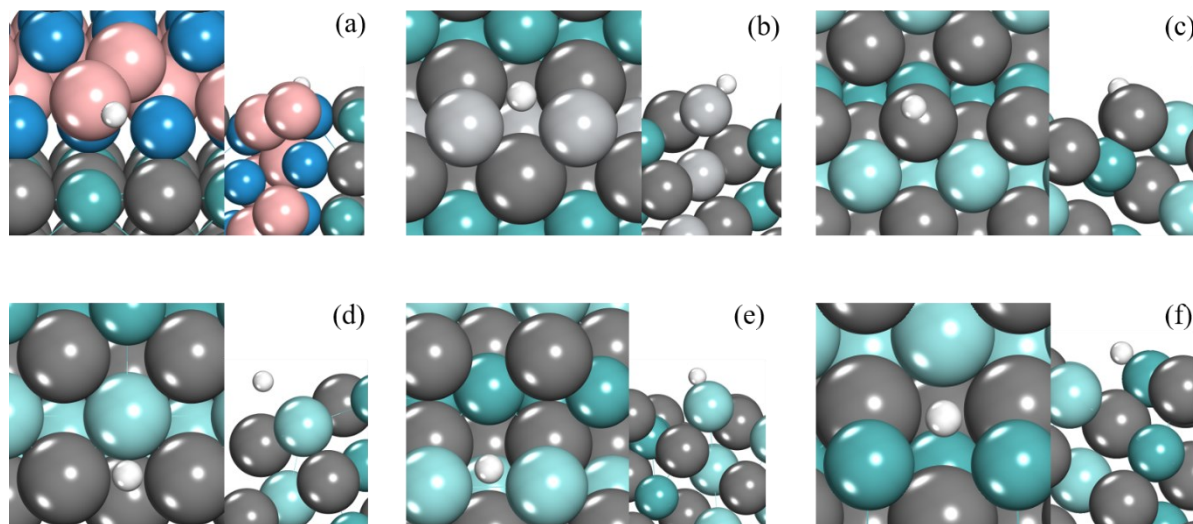


Figure D.14 Optimised configurations of H* adsorption on (a) BMoWC, (b) TiMoC₂, (c) Zr_A, (d) Zr_B, (e) Zr_{4A} and (f) Zr_{4B}. The white sphere represents H. In (a), the pink, green and blue spheres represent B, Mo and W respectively. In (b), the green and light grey spheres represent Mo and Ti respectively. In (c)-(f), the darker teal and lighter turquoise spheres represent Mo and Zr respectively.

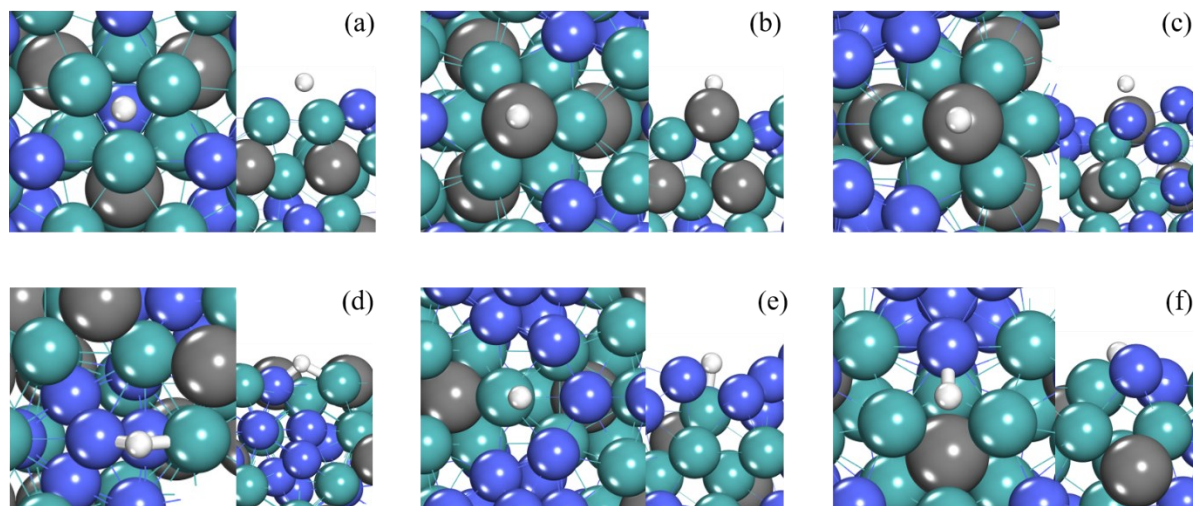


Figure D.15 Optimised configurations of H* adsorption on (a) Co₂A, (b) Co₂B, (c) Co₃A, (d) Co₃B, (e) Co₆A and (f) Co₆B. The white sphere represents H. The green and blue spheres represent Mo and Co respectively.

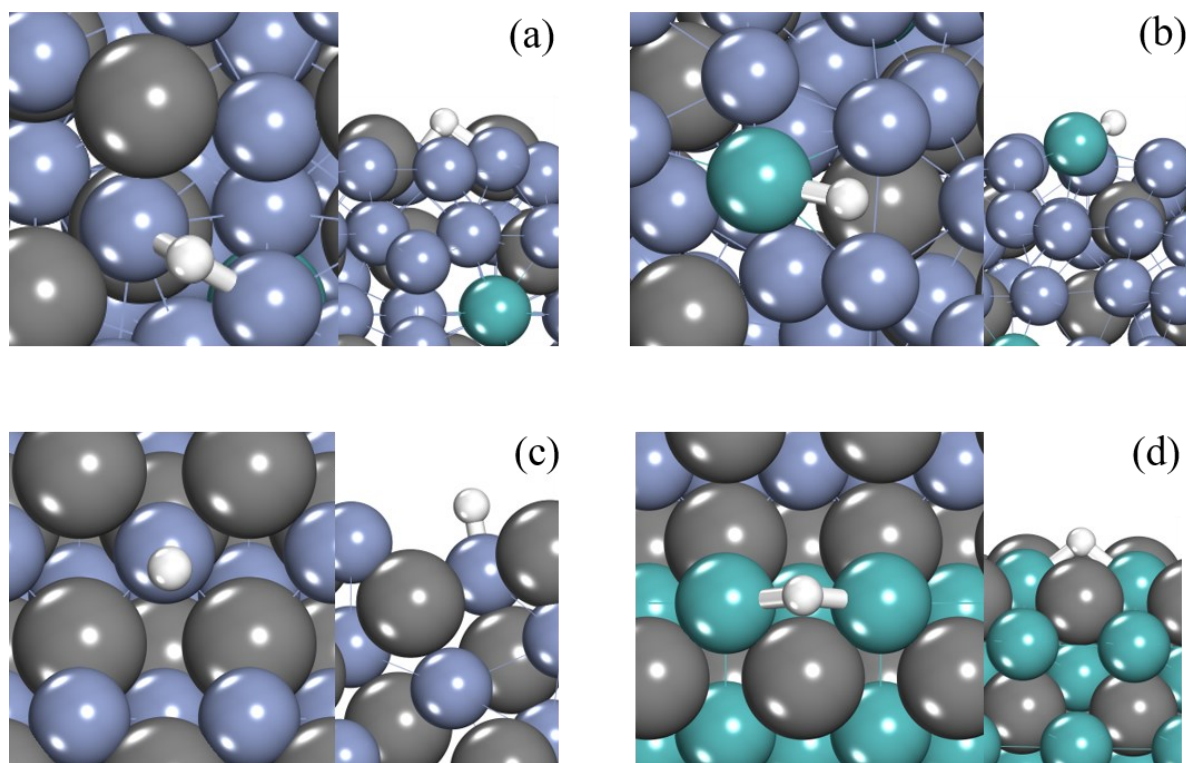


Figure D.16 Optimised configurations of H* adsorption on (a) Cr₂₂A, (b) Cr₂₂B, (c) Cr₃A and (d) Cr₃B. The white sphere represents H. The green and pastel blue spheres represent Mo and Cr respectively.

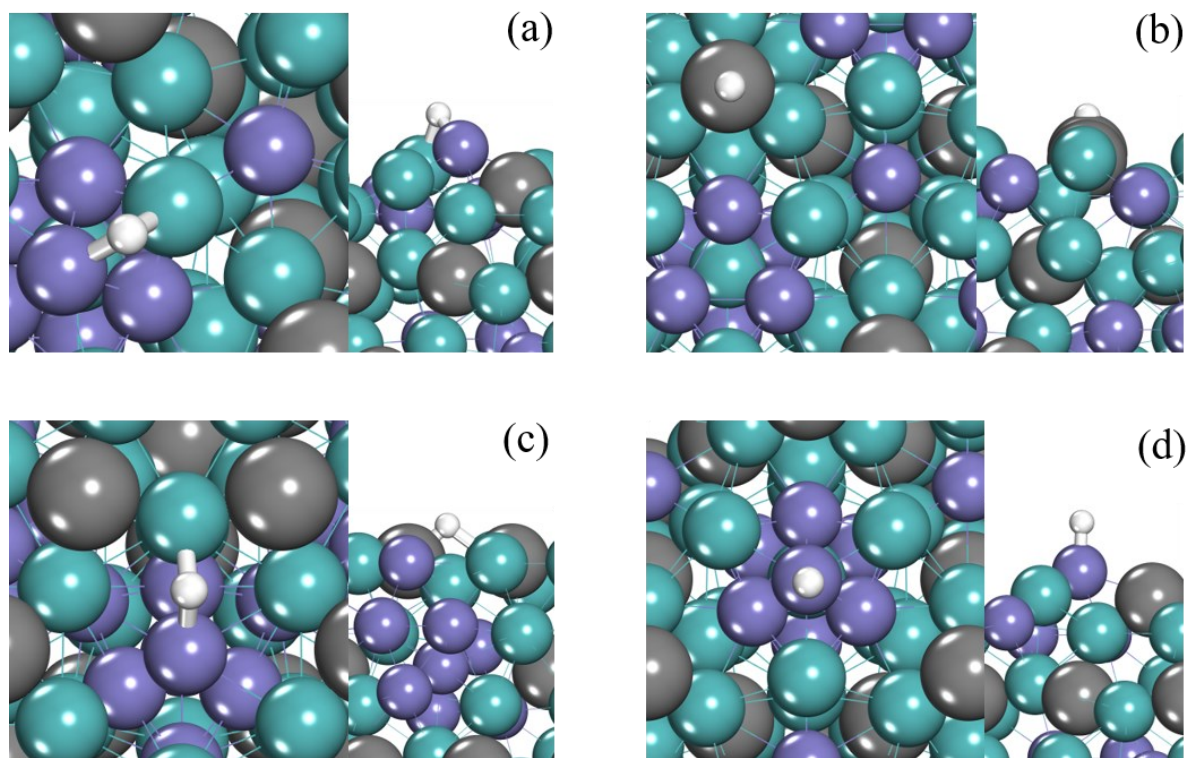


Figure D.17 Optimised configurations of H* adsorption on (a) Fe_{2A}, (b) Fe_{2B}, (c) Fe_{3B} and (d) Fe_{3C}. The white sphere represents H. The green and purple spheres represent Mo and Fe respectively.

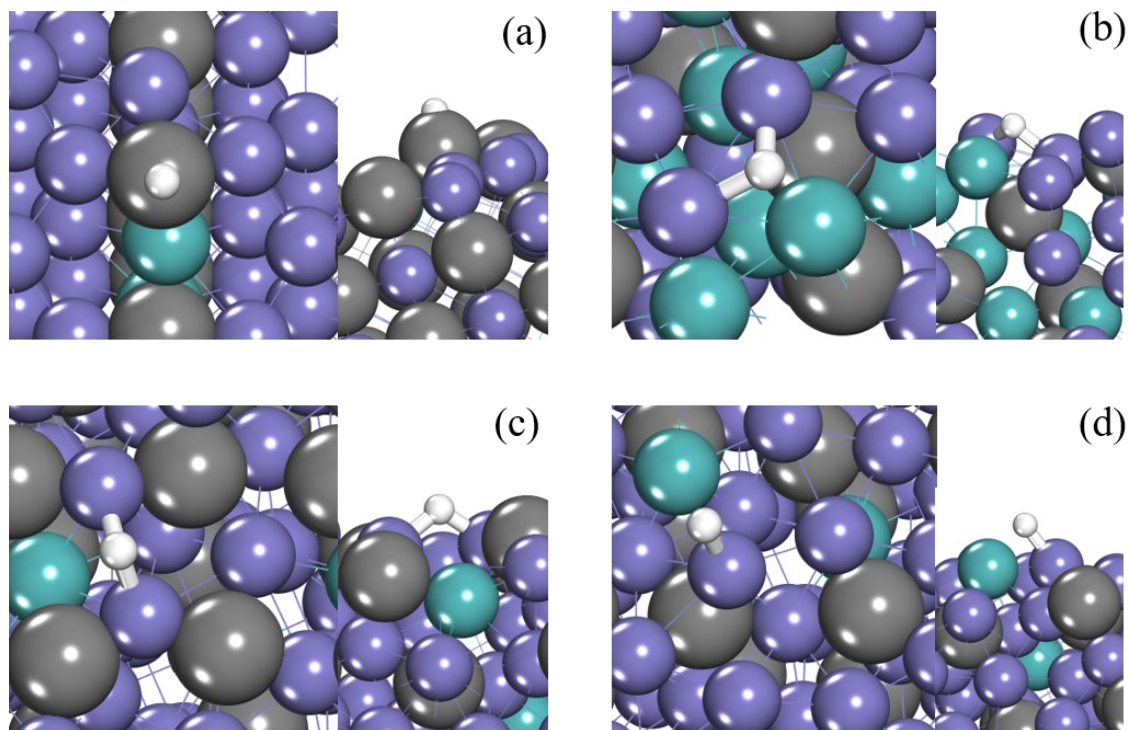


Figure D.18 Optimised configurations of H* adsorption on (a) Fe₁₁O_A, (b) Fe₁₁O_C, (c) Fe₁₁T_A and (d) Fe₁₁T_B. The white sphere represents H. The green and purple spheres represent Mo and Fe respectively.

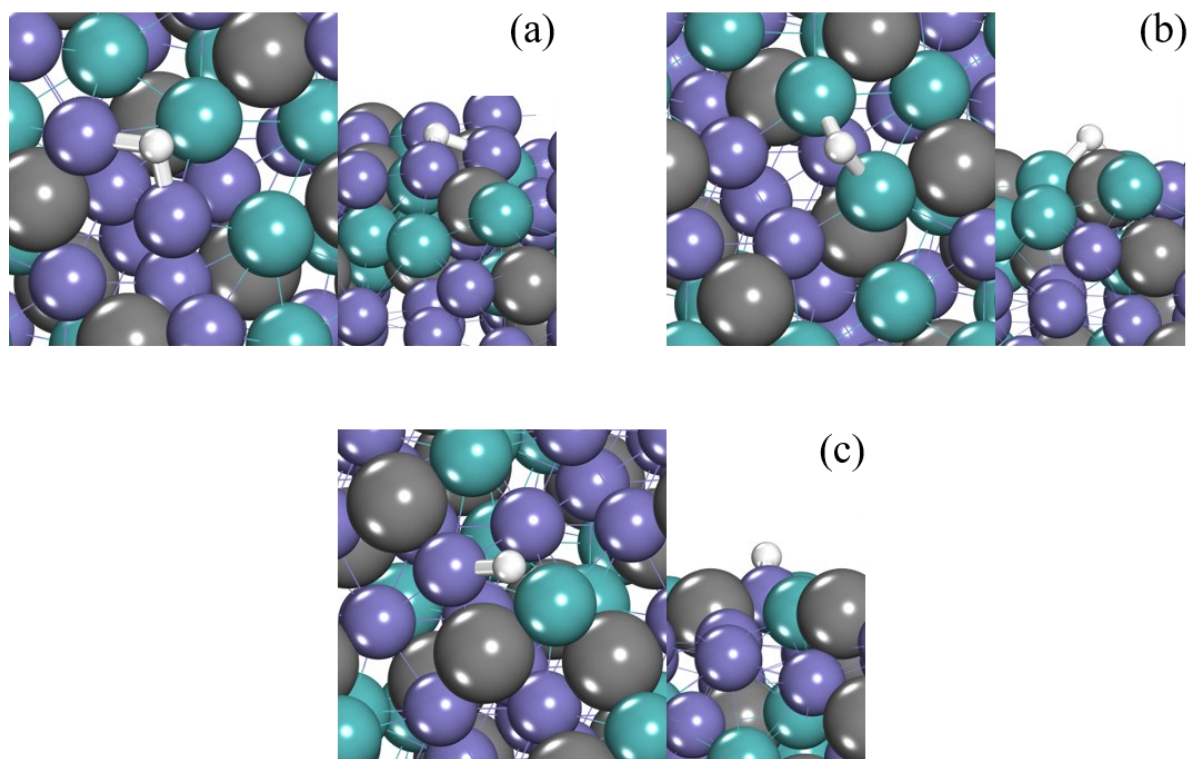


Figure D.19 Optimised configurations of H* adsorption on (a) Fe_{11A}, (b) Fe_{11B} and (c) Fe_{11C}. The white sphere represents H. The green and purple spheres represent Mo and Fe respectively.

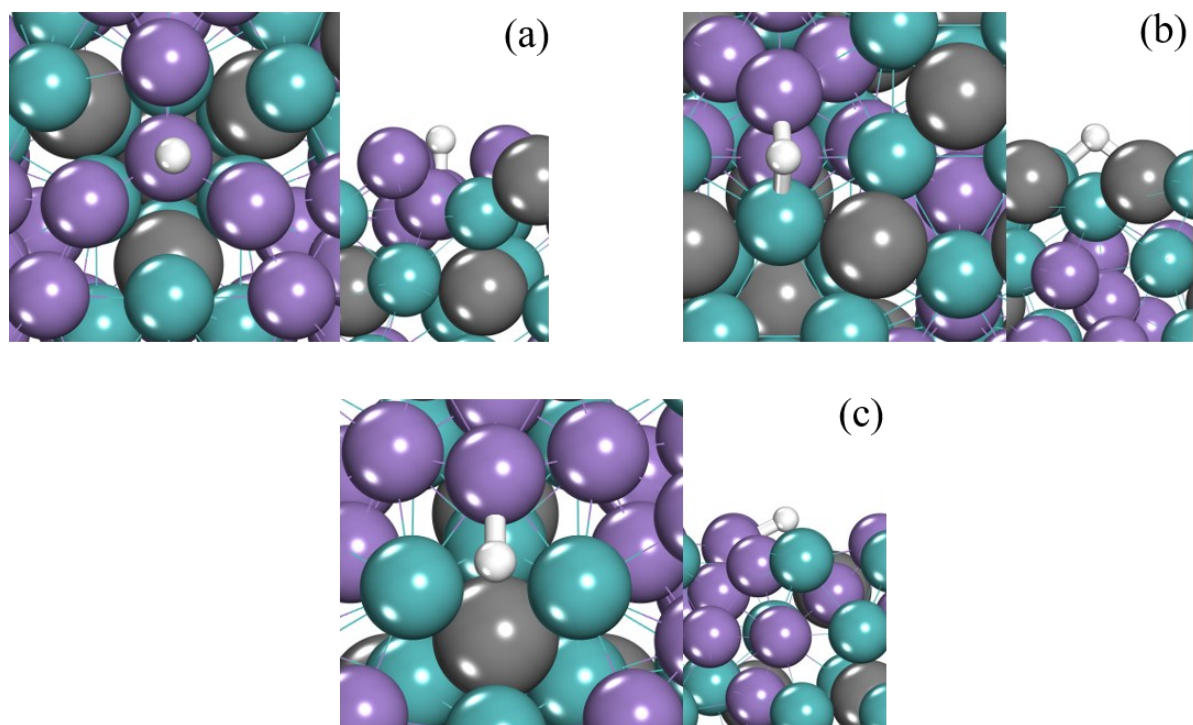


Figure D.20 Optimised configurations of H^* adsorption on (a) Mn_A , (b) Mn_B and (c) Mn_C . The white sphere represents H. The green and purple spheres represent Mo and Mn respectively.

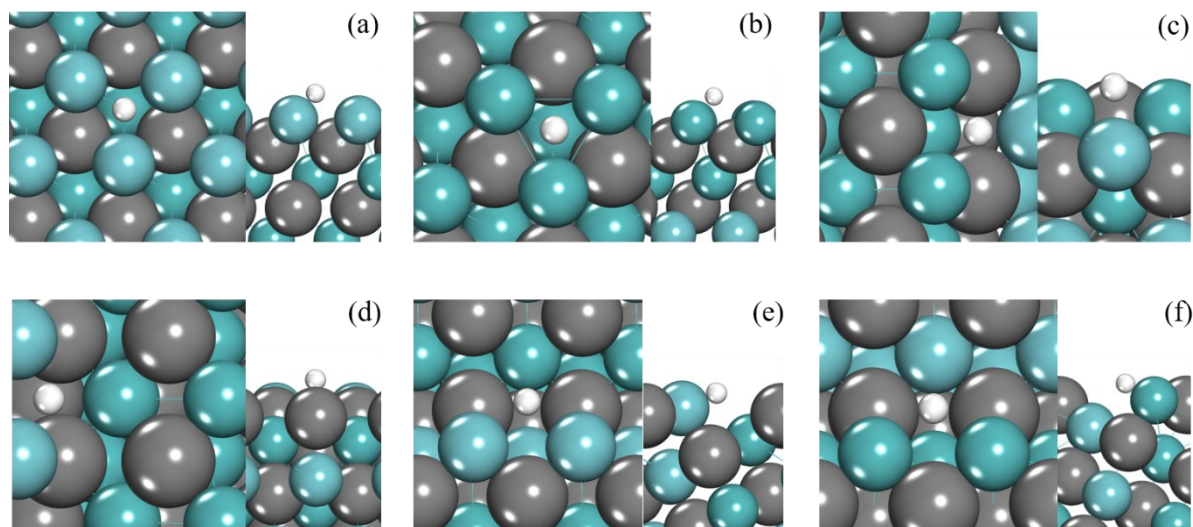


Figure D.21 Optimised configurations of H^* adsorption on (a) Nb_{2A} , (b) Nb_{2B} , (c) $NbMo_{3B}$, (d) $NbMo_{3C}$, (e) $NbMo_A$ and (f) $NbMo_B$. The white sphere represents H. The darker and lighter green spheres represent Mo and Nb respectively.

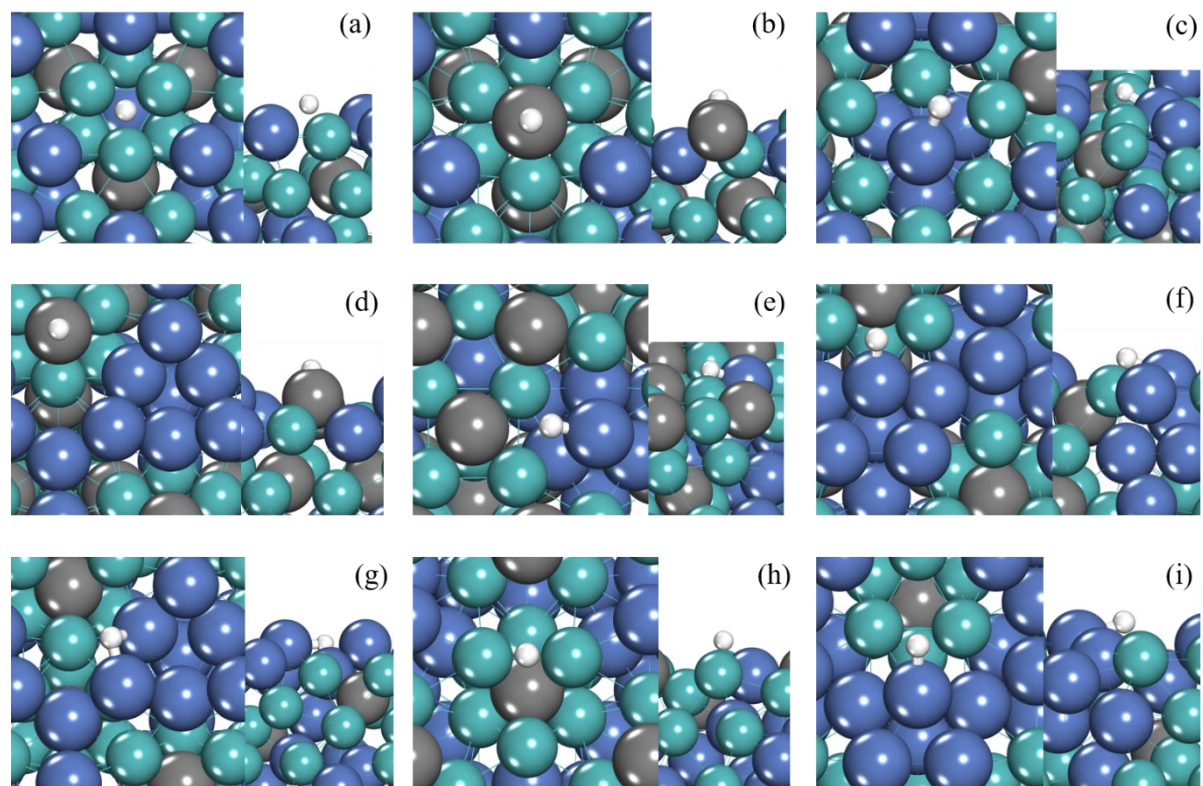


Figure D.22 Optimised configurations of H^* adsorption on (a) Ni_{2A} , (b) Ni_{2B} , (c) Ni_{2C} , (d) Ni_{3A} , (e) Ni_{3B} , (f) Ni_{3C} , (g) Ni_{6A} , (h) Ni_{6B} and (i) Ni_{6C} . The white sphere represents H. The green and blue spheres represent Mo and Ni respectively.

D.6 Optimized stable adsorption configuration of OH fragment on catalyst surfaces

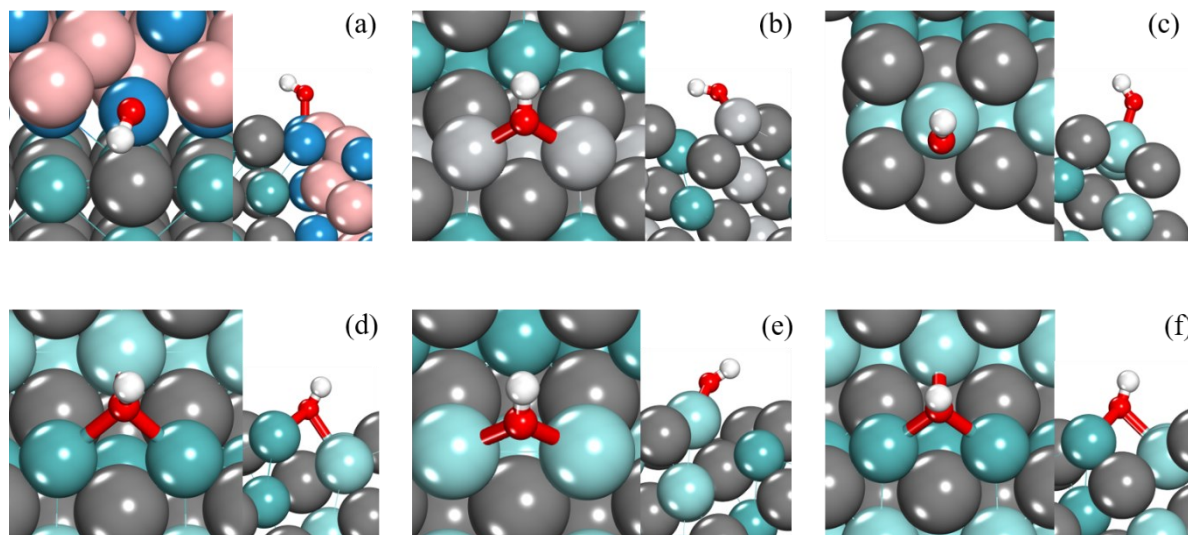


Figure D.23 Optimised configurations of OH* adsorption on (a) BMoWC, (b) TiMoC₂, (c) Zr_A, (d) Zr_B, (e) Zr_{4A} and (f) Zr_{4B}. The red and white spheres represent O and H respectively. In (a), the pink, green and blue spheres represent B, Mo and W respectively. In (b), the green and light grey spheres represent Mo and Ti respectively. In (c)-(f), the darker teal and lighter turquoise spheres represent Mo and Zr respectively.

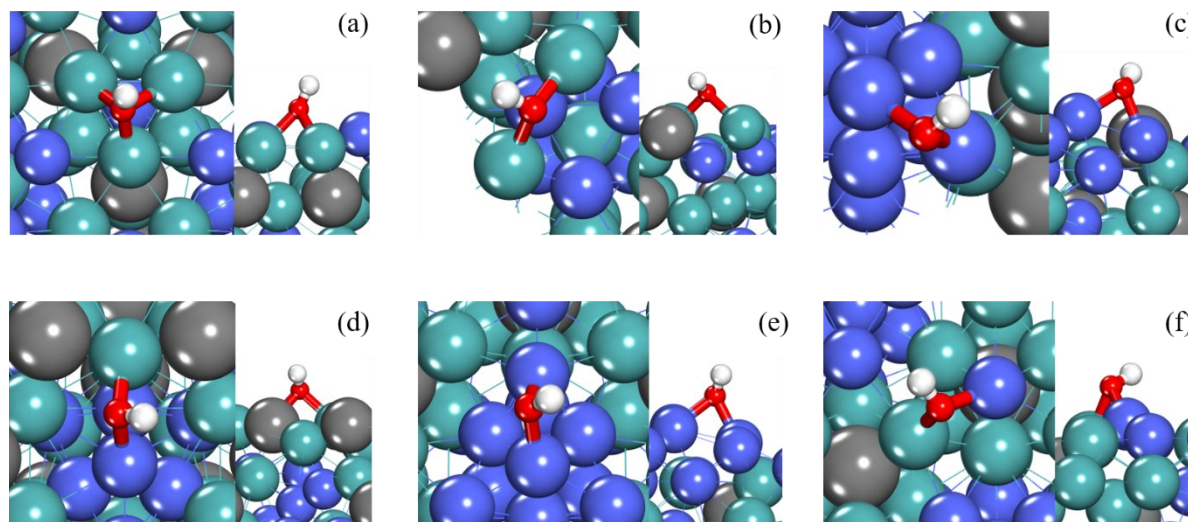


Figure D.24 Optimised configurations of OH* adsorption on (a) Co_{2A}, (b) Co_{2B}, (c) Co_{3A}, (d) Co_{3B}, (e) Co_{6A} and (f) Co_{6B}. The red and white spheres represent O and H respectively. The green and blue spheres represent Mo and Co respectively.

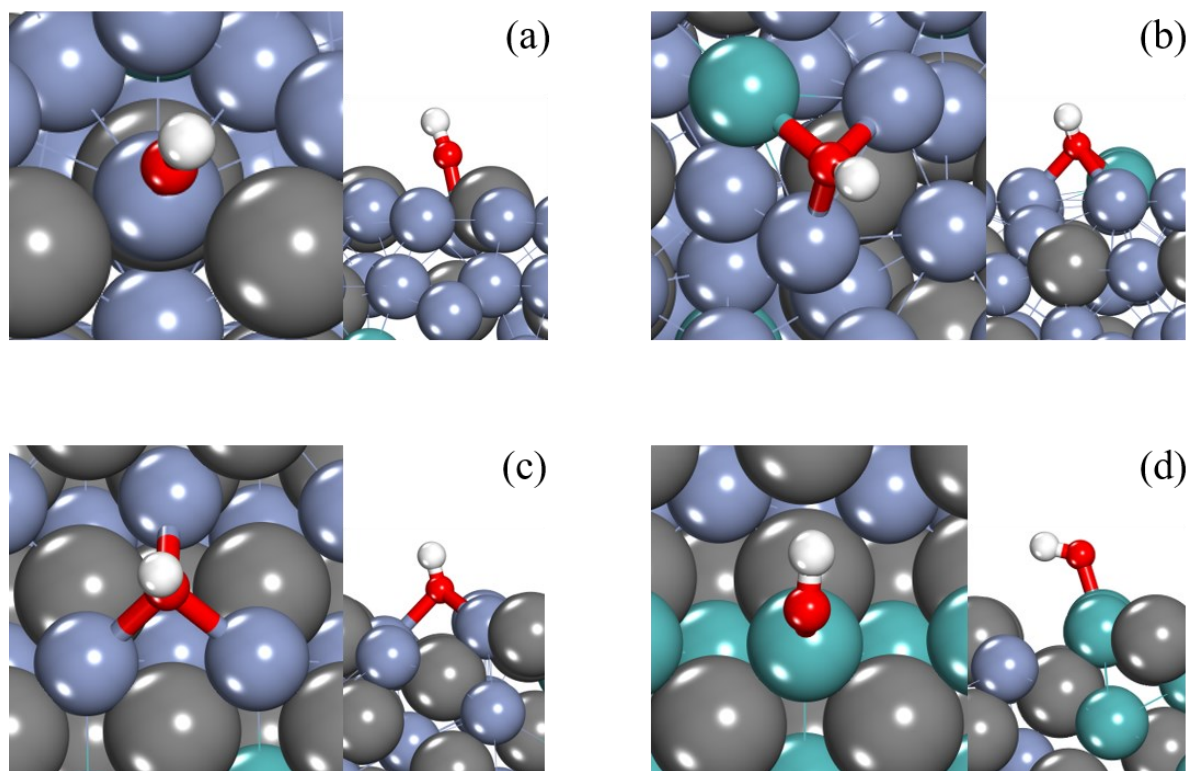


Figure D.25 Optimised configurations of OH* adsorption on (a) Cr_{22A}, (b) Cr_{22B}, (c) Cr_{3A} and (d) Cr_{3B}. The red and white spheres represent O and H respectively. The green and pastel blue spheres represent Mo and Cr respectively.

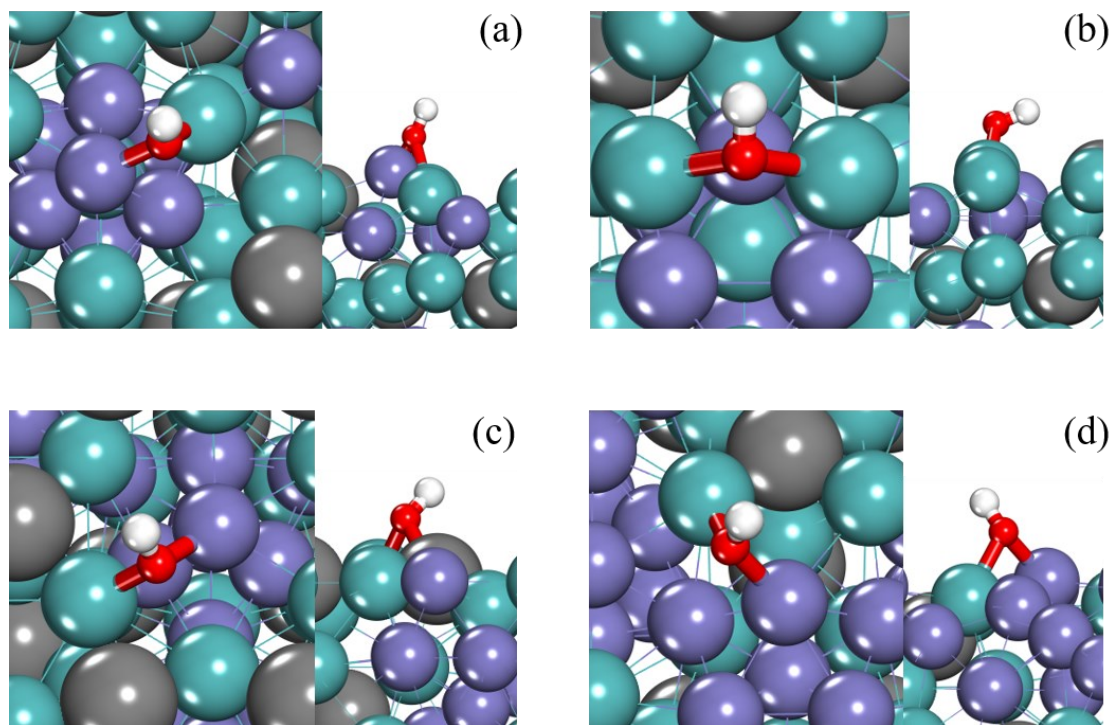


Figure D.26 Optimised configurations of OH* adsorption on (a) Fe_{2A}, (b) Fe_{2B}, (c) Fe_{3B} and (d) Fe_{3C}. The red and white spheres represent O and H respectively. The green and purple spheres represent Mo and Fe respectively.

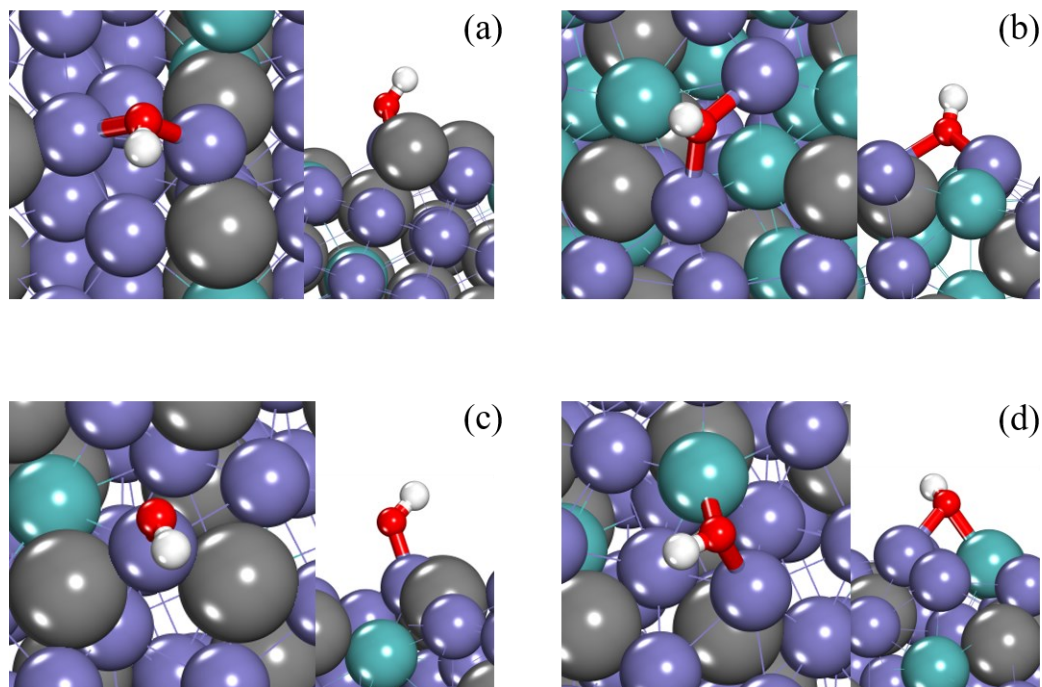


Figure D.27 Optimised configurations of OH* adsorption on (a) Fe₁₁O_A, (b) Fe₁₁O_C, (c) Fe₁₁T_A and (d) Fe₁₁T_B. The red and white spheres represent O and H respectively. The green and purple spheres represent Mo and Fe respectively.

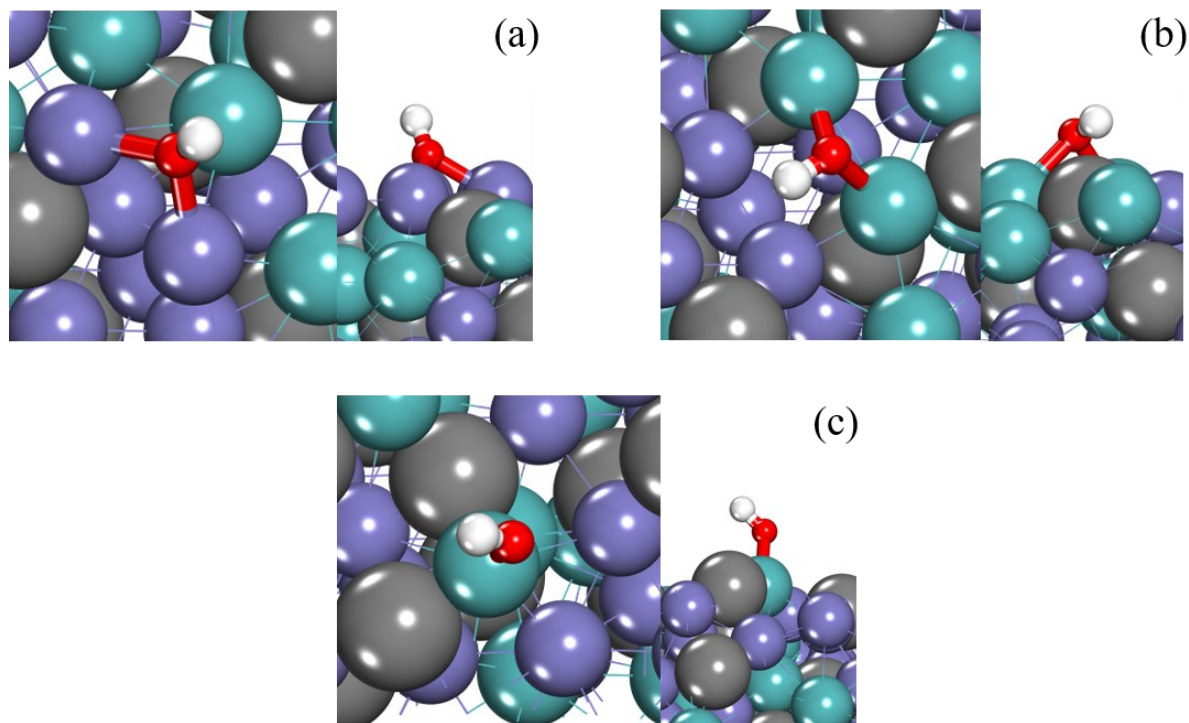


Figure D.28 Optimised configurations of OH* adsorption on (a) Fe₁₁A, (b) Fe₁₁B and (c) Fe₁₁C. The red and white spheres represent O and H respectively. The green and purple spheres represent Mo and Fe respectively.

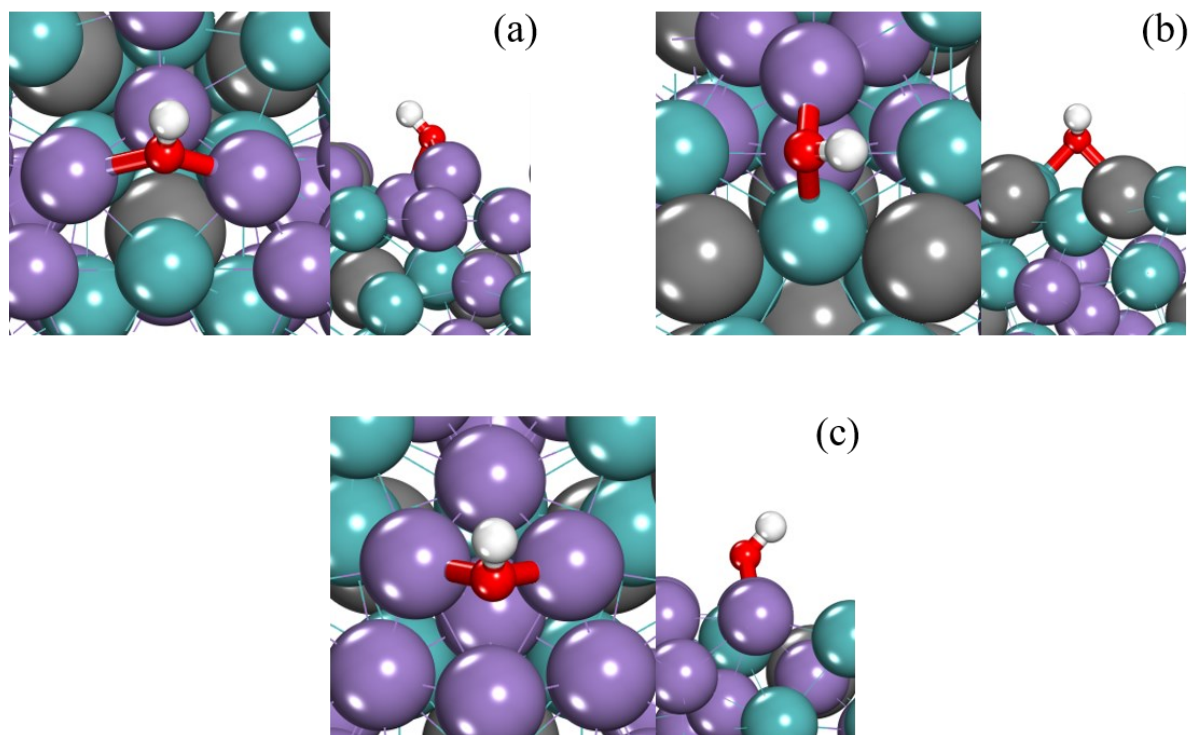


Figure D.29 Optimised configurations of OH* adsorption on (a) Mn_A, (b) Mn_B and (c) Mn_C. The red and white spheres represent O and H respectively. The green and purple spheres represent Mo and Mn respectively.

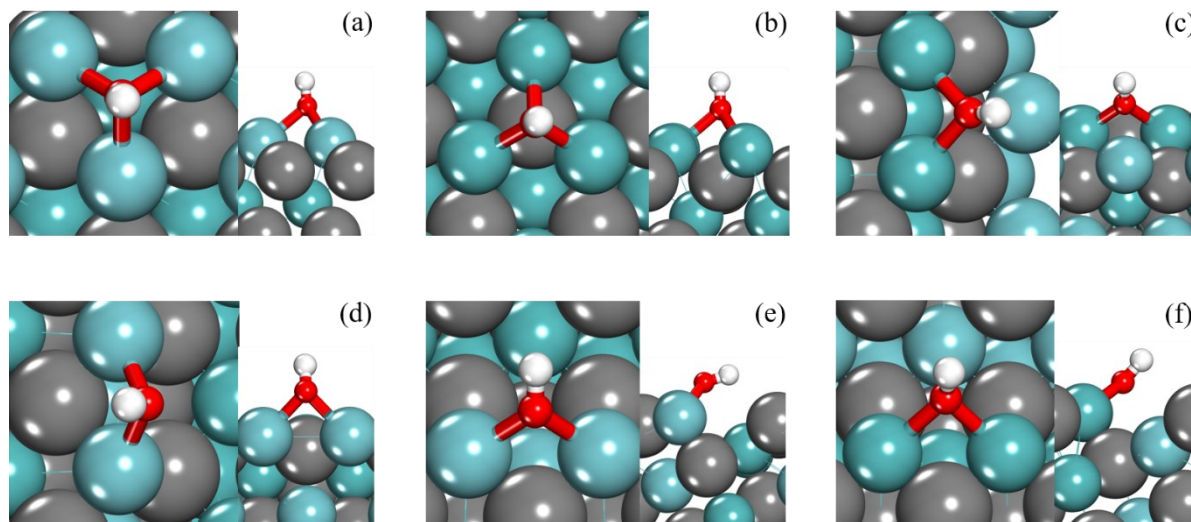


Figure D.30 Optimised configurations of OH* adsorption on (a) Nb_{2A}, (b) Nb_{2B}, (c) NbMo_{3B}, (d) NbMo_{3C}, (e) NbMo_A and (f) NbMo_B. The red and white spheres represent O and H respectively. The darker and lighter green spheres represent Mo and Nb respectively.

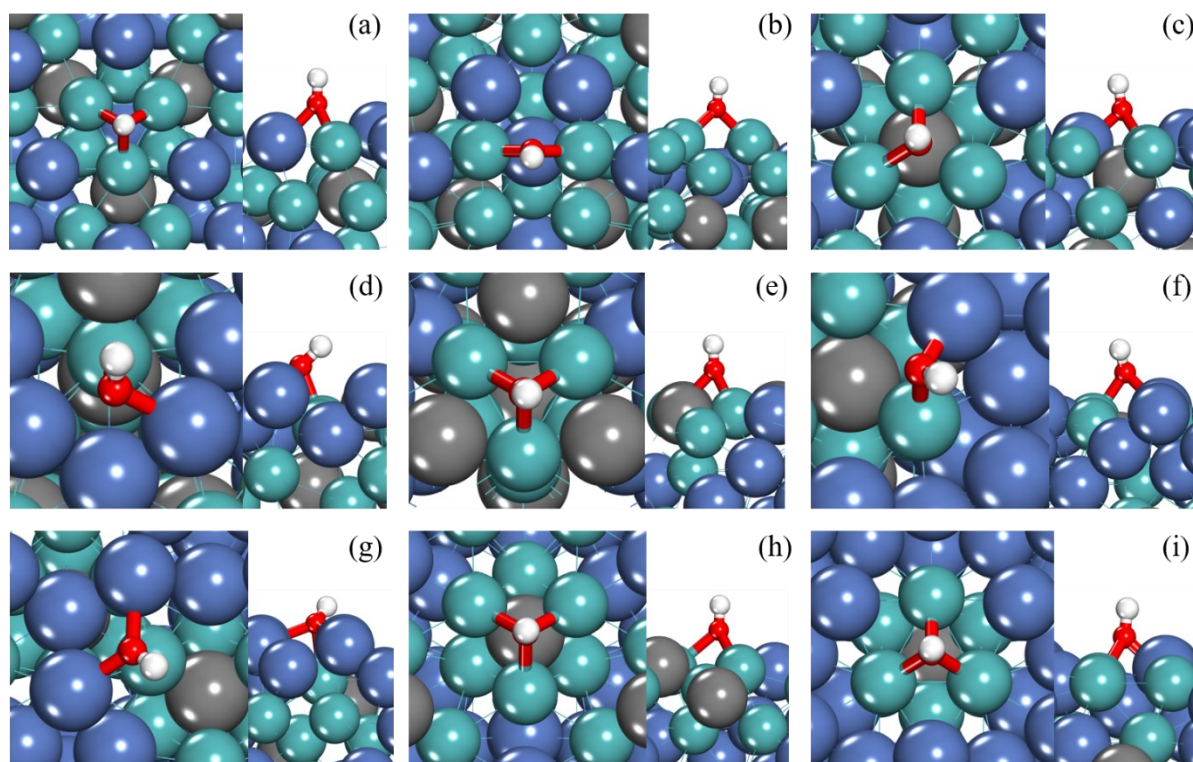


Figure D.31 Optimised configurations of OH* adsorption on (a) Ni_{2A}, (b) Ni_{2B}, (c) Ni_{2C}, (d) Ni_{3A}, (e) Ni_{3B}, (f) Ni_{3C}, (g) Ni_{6A}, (h) Ni_{6B} and (i) Ni_{6C}. The red and white spheres represent O and H respectively. The green and blue spheres represent Mo and Ni respectively.

D.7 Hydrogen Binding Energy (HBE) and Oxygen Binding Energy (OBE) Plots

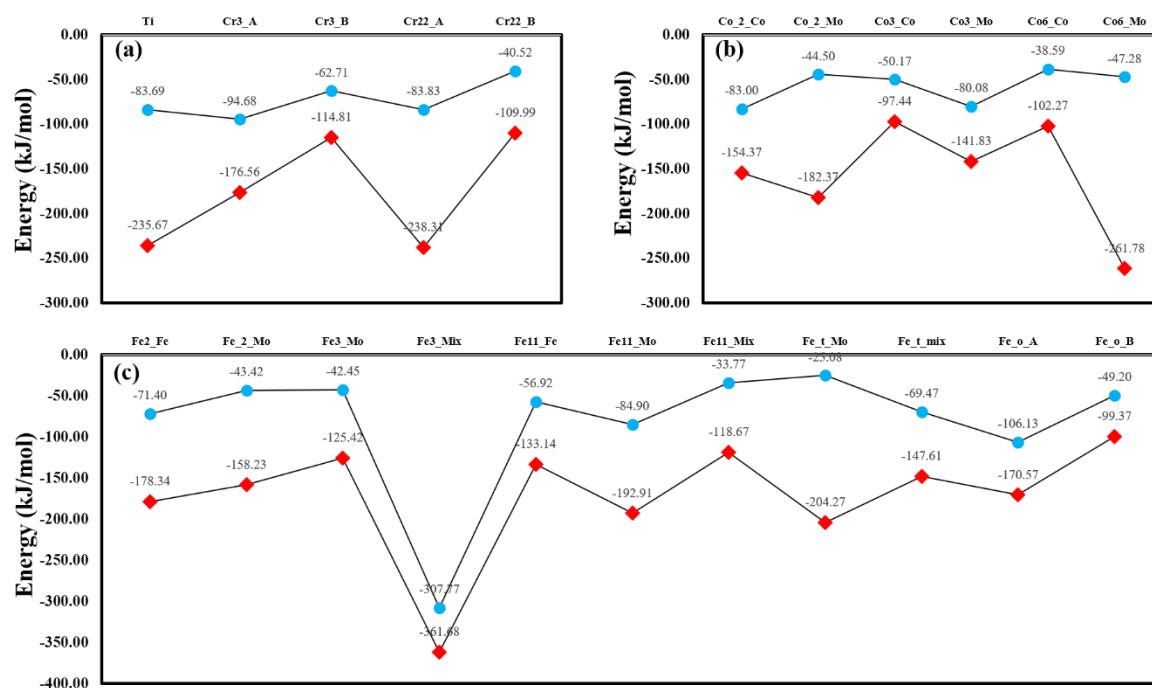


Figure D.32 Hydrogen binding energies (HBE) and oxygen binding energies (OBE), represented by blue circles and red diamonds respectively, on (a) Co-doped, (b) Cr-doped and Ti-doped, and (c) Fe-doped bimetallic carbides.

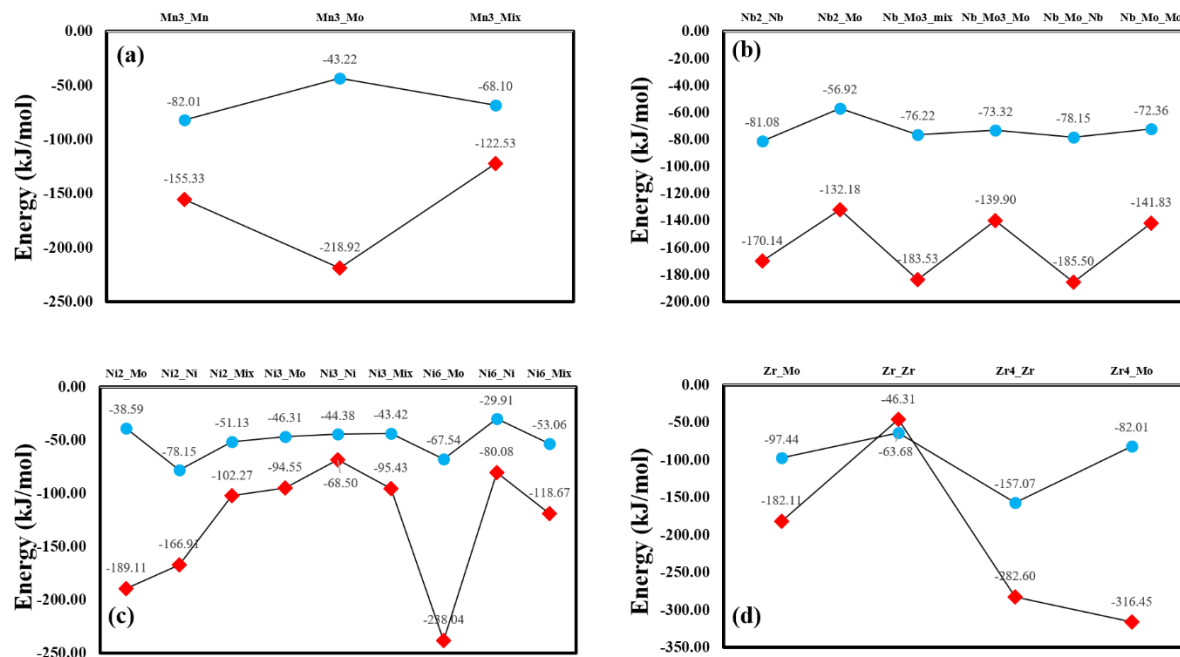


Figure D.33 Hydrogen binding energies (HBE) and oxygen binding energies (OBE), represented by blue circles and red diamonds respectively, on (a) Mn-doped, (b) Nb-doped, (c) Ni-doped and (d) Zr-doped bimetallic carbides.

Table D.8 Values of oxygen binding energies (OBE), hydrogen binding energies (HBE) and the metal-OH* bond length in adsorbed phenol on 47 catalyst surfaces. Energies and lengths are reported in kJ/mol and Å respectively.

Catalyst	OBE (kJ/mol)	HBE (kJ/mol)	M-OH* bond length	Catalyst	OBE (kJ/mol)	HBE (kJ/mol)	M-OH* bond length
BMoW	-93	-34	1.945	Mo ₂ C	-155	-82	
C				MoWC	-191	-99	
Co ₂ A	-154	-83	2.176 ^a	Nb ₂ A	-170	-81	2.330 ^a
Co ₂ B	-182	-44	2.206 ^a	Nb ₂ B	-132	-57	2.298 ^a
Co ₃ A	-97	-50	1.961 ^a	NbMo ₃ B	-140	-73	2.264 ^a
Co ₃ B	-142	-80	2.085 ^a	NbMo ₃ C	-183	-76	2.245 ^a
Co ₆ A	-102	-39	1.951 ^a	NbMo ₄ A	-185	-78	2.247 ^a
Co ₆ B	-261	-47	2.054 ^a	NbMo ₄ B	-142	-72	2.265 ^a
Cr ₂₂ A	-110	-41	1.977	Ni ₂ A	-167	-78	2.272 ^a
Cr ₂₂ B	-238	-84	2.183 ^a	Ni ₂ B	-189	-39	2.160 ^a
Cr ₃ A	-177	-95	2.196 ^a	Ni ₂ C	-102	-51	2.317 ^a
Cr ₃ B	-115	-63	1.983	Ni ₃ A	-68	-44	2.137 ^a
Fe ₁₁ A	-133	-57	2.118 ^a	Ni ₃ B	-95	-46	2.274 ^a
Fe ₁₁ B	-193	-85	2.155 ^a	Ni ₃ C	-95	-43	2.063 ^a
Fe ₁₁ C	-119	-34	1.959				

Fe ₁₁ O _A	-171	-106	2.005 ^a	Ni ₆ A	-80	-30	2.173 ^a
Fe ₁₁ O _C	-99	-49	2.085 ^a	Ni ₆ B	-238	-68	2.307 ^a
Fe ₁₁ T _A	-148	-69	1.833	Ni ₆ C	-119	-53	2.239 ^a
Fe ₁₁ T _B	-204	-25	2.073 ^a	TiMoC ₂	-235	-84	2.123 ^a
Fe ₂ A	-178	-71	2.045 ^a	Zr _A	-46	-64	1.996
Fe ₂ B	-158	-43	2.212 ^a	Zr _B	-182	-97	2.327 ^a
Fe ₃ B	-125	-42	2.084 ^a	Zr ₄ A	-283	-157	2.241 ^a
Fe ₃ C	-362	-308	2.078 ^a	Zr ₄ B	-316	-82	2.310 ^a
Mn _A	-155	-82	2.170 ^a				
Mn _B	-219	-43	2.093 ^a				
Mn _C	-122	-68	1.999 ^a				

^a Average value of the bond length is presented.

Table D.9 Values of phenol adsorption energies (E_{ads}) and activation barriers and reaction energies for R1 (C-O dissociation), R2 (water formation) and R3 (ring hydrogenation) on 35 catalyst surfaces. All values are reported in units of kJ/mol.

Catalyst	E_{ads} of phenol	R1 barrier	R1 E_{rxn}	R2 barrier	R2 E_{rxn}	R3 barrier	R3 E_{rxn}
BMoWC	-101	197	83	107	30	257	134
Co ₂ A	-148	99	-57	175	125	110	60
Co ₂ B	-166	136	-119	142	104	170	42
Co ₃ A	-80	176	-139	295	111	151	86
Co ₃ B	-198	56	-74	143	71	165	118
Co ₆ A	-84	146	-88	174	106	135	84
Co ₆ B	-290	167	-112	184	118	94	79
Cr ₂₂ A	-77	140	-87	172	99	300	160
Cr ₃ A	-112	79	59	204	130	166	14
Cr ₃ B	-371	55	-141	163	98	156	66
Fe ₁₁ A	-97	95	-125	214	159	129	35
Fe ₁₁ B	-154	132	-139	267	161	91	74
Fe ₁₁ C	-115	155	-60	150	77	220	30
Fe ₁₁ O _A	-204	164	-235	257	190	299	180
Fe ₁₁ O _C	-180	159	127	178	111	153	-41
Fe ₁₁ T _A	-251	239	36	233	6	83	56
Fe ₁₁ T _B	-123	106	87	301	157	46	-31
Fe ₂ A	-227	57	-165	287	53	141	91
Fe ₂ B	-173	125	-123	282	164	183	42

Fe _{3B}	-92	120	-42	101	92	225	87
Fe _{3C}	-426	82	-76	203	129	117	80
Mn _A	-185	72	-80	127	121	108	15
Mn _B	-169	169	113	187	126	193	157
Mo _{2C}	-197	77	-82	259	196	111	96
MoWC	-133	34	-144	237	193	106	100
Nb _{2B}	-229	95	-131	187	152	125	120
NbMo _{3B}	-87	100	-122	188	134	344	192
NbMo _B	-114	124	-116	217	165	132	89
Ni _{2C}	-169	80	-85	148	87	136	94
Ni _{3A}	-112	79	-76	127	69	104	20
Ni _{3B}	-71	165	105	225	105	280	164
Ni _{3C}	-153	95	-80	210	96	77	48
Ni _{6A}	-285	91	-58	141	100	47	-7
Ni _{6C}	-149	72	-87	187	138	101	68
Zr _A	-101	183	77	74	53	147	36

D.8 Adsorption configurations of Phenol

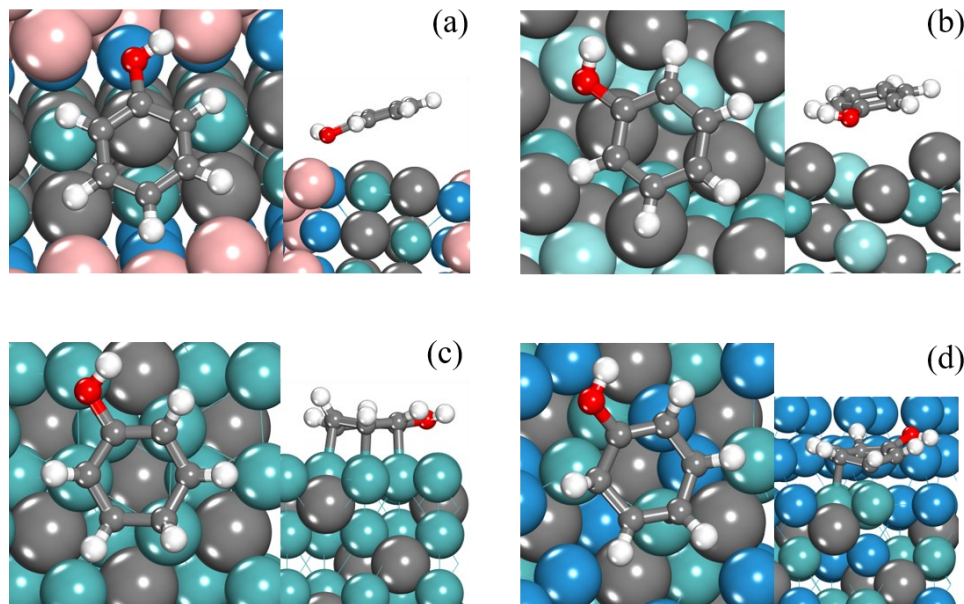


Figure D.34 Optimised adsorption configurations of phenol on (a) BMoWC, (b) ZrA, (c) Mo_{2C} and (d) MoWC. The grey, red and white spheres represent C, O and H respectively. In (a), (c) and (d), the pink, green and blue spheres represent B, Mo and W respectively. In (b), the darker teal and lighter turquoise spheres represent Mo and Zr respectively.

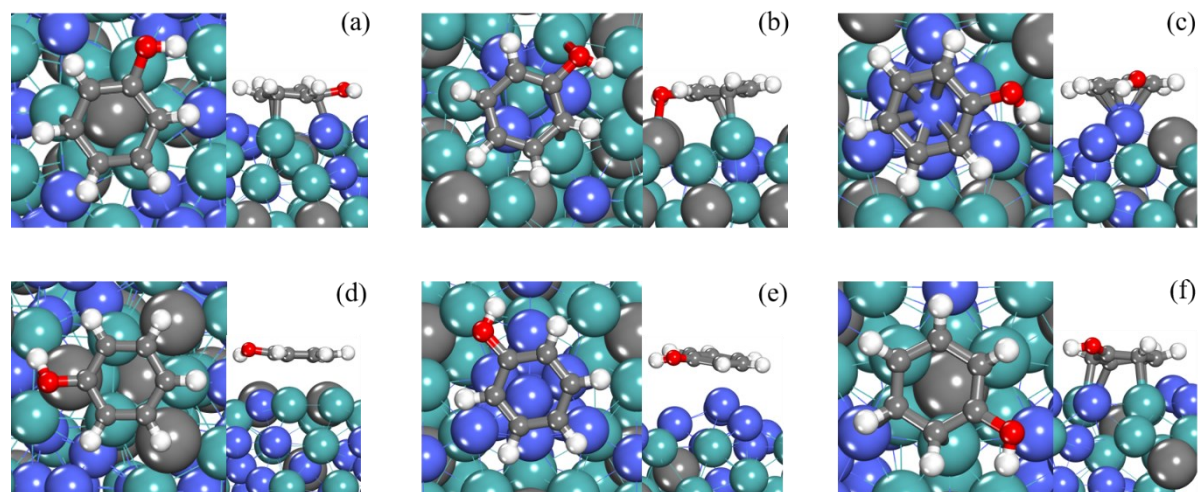


Figure D.35 Optimised adsorption configurations of phenol on (a) Co_{2A}, (b) Co_{2B}, (c) Co_{3A}, (d) Co_{3B}, (e) Co_{6A} and (f) Co_{6B}. The green and blue spheres represent Mo and Co respectively. The grey, red and white spheres represent C, O and H respectively.

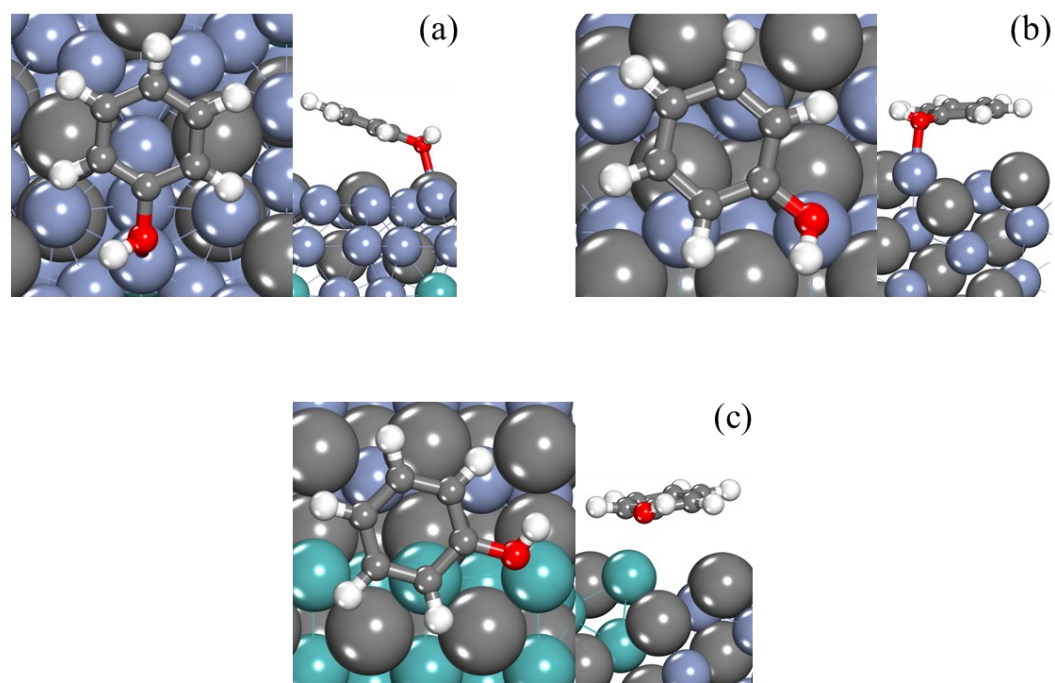


Figure D.36 Optimised adsorption configurations of phenol on (a) Cr_{22A}, (b) Cr_{3A} and (c) Cr_{3B}. The green and pastel blue spheres represent Mo and Cr respectively. The grey, red and white spheres represent C, O and H respectively.

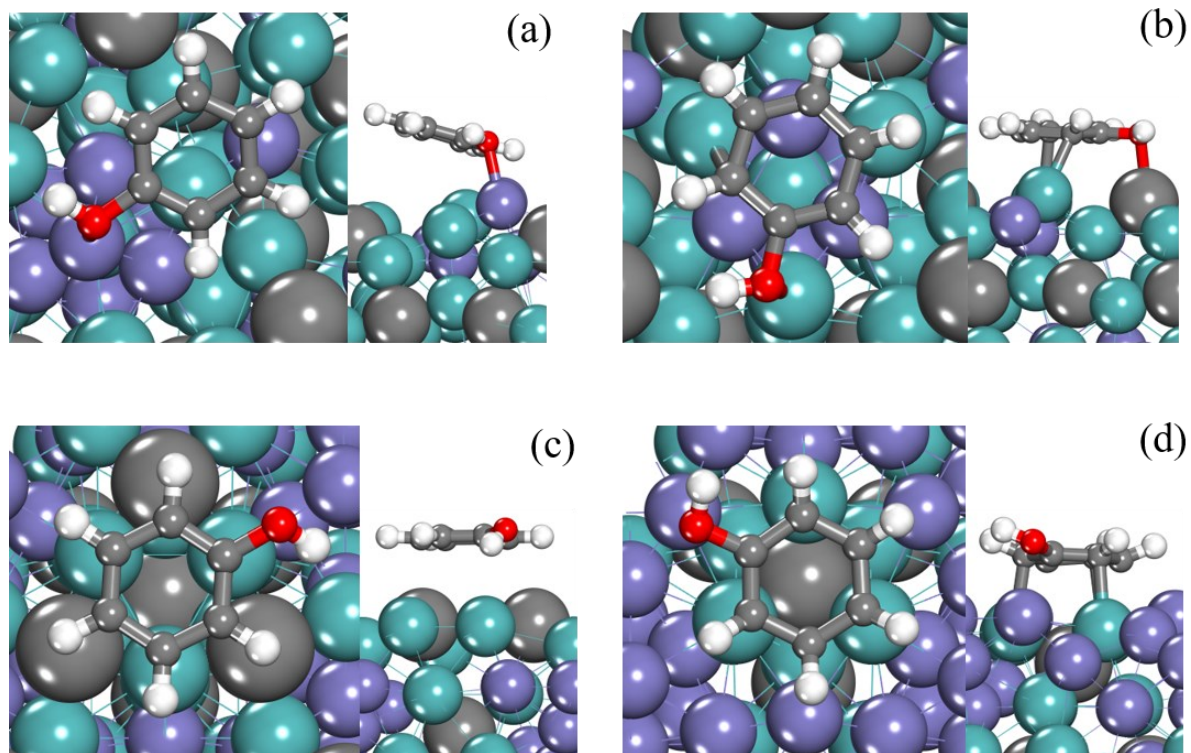


Figure D.37 Optimised adsorption configurations of phenol on (a) Fe_{2A}, (b) Fe_{2B}, (c) Fe_{3B} and (d) Fe_{3C}. The green and purple spheres represent Mo and Fe respectively. The grey, red and white spheres represent C, O and H respectively.

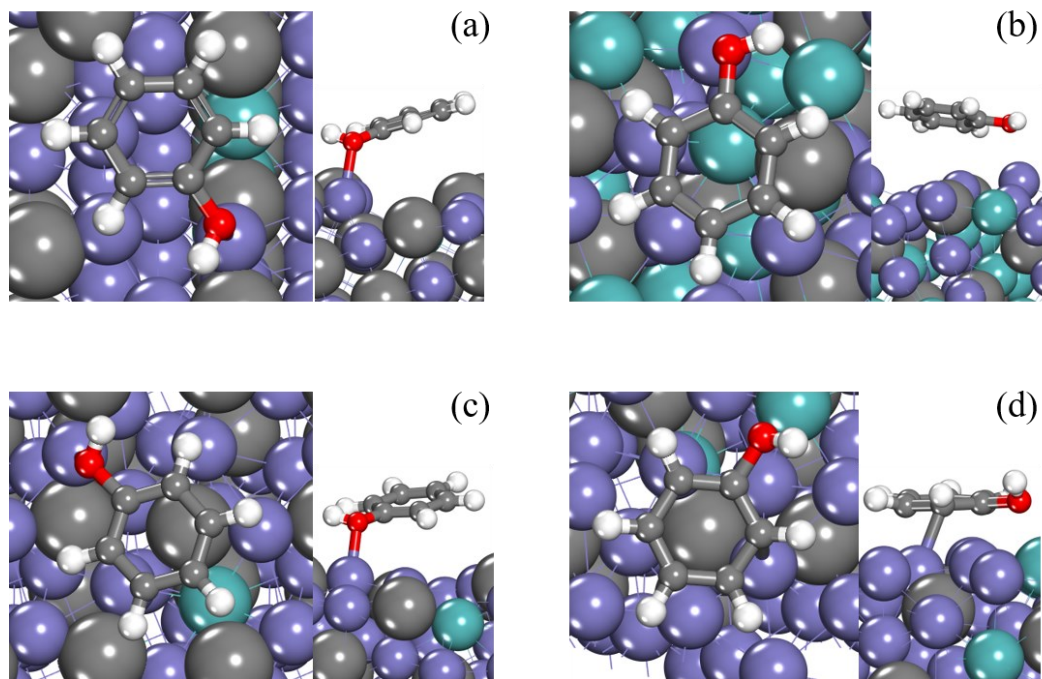


Figure D.38 Optimised adsorption configurations of phenol on (a) Fe_{11}O_A , (b) Fe_{11}O_C , (c) Fe_{11}T_A and (d) Fe_{11}T_B . The green and purple spheres represent Mo and Fe respectively. The grey, red and white spheres represent C, O and H respectively.

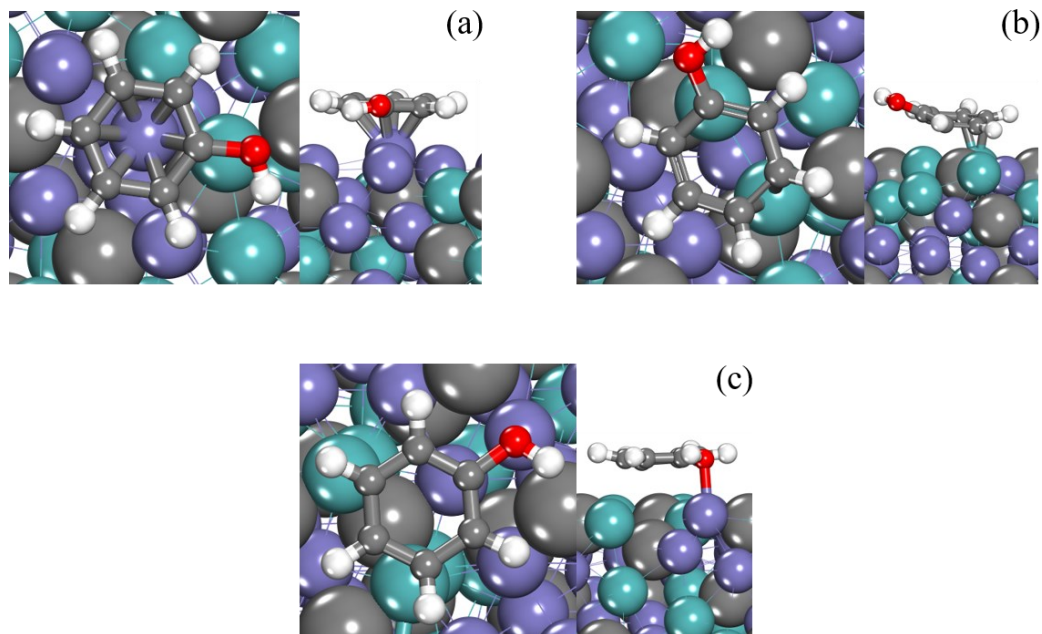


Figure D.39 Optimised adsorption configurations of phenol on (a) Fe_{11A} , (b) Fe_{11B} and (c) Fe_{11C} . The green and purple spheres represent Mo and Fe respectively. The grey, red and white spheres represent C, O and H respectively.

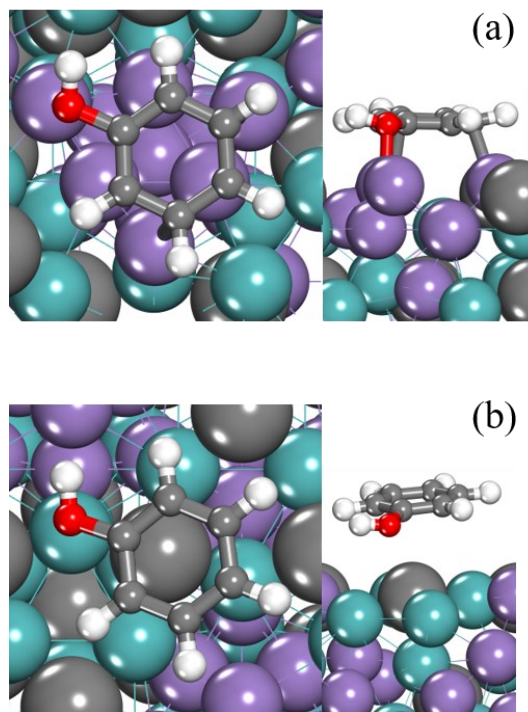


Figure D.40 Optimised adsorption configurations of phenol on (a) Mn_A and (b) Mn_B . The green and purple spheres represent Mo and Mn respectively. The grey, red and white spheres represent C, O and H respectively.

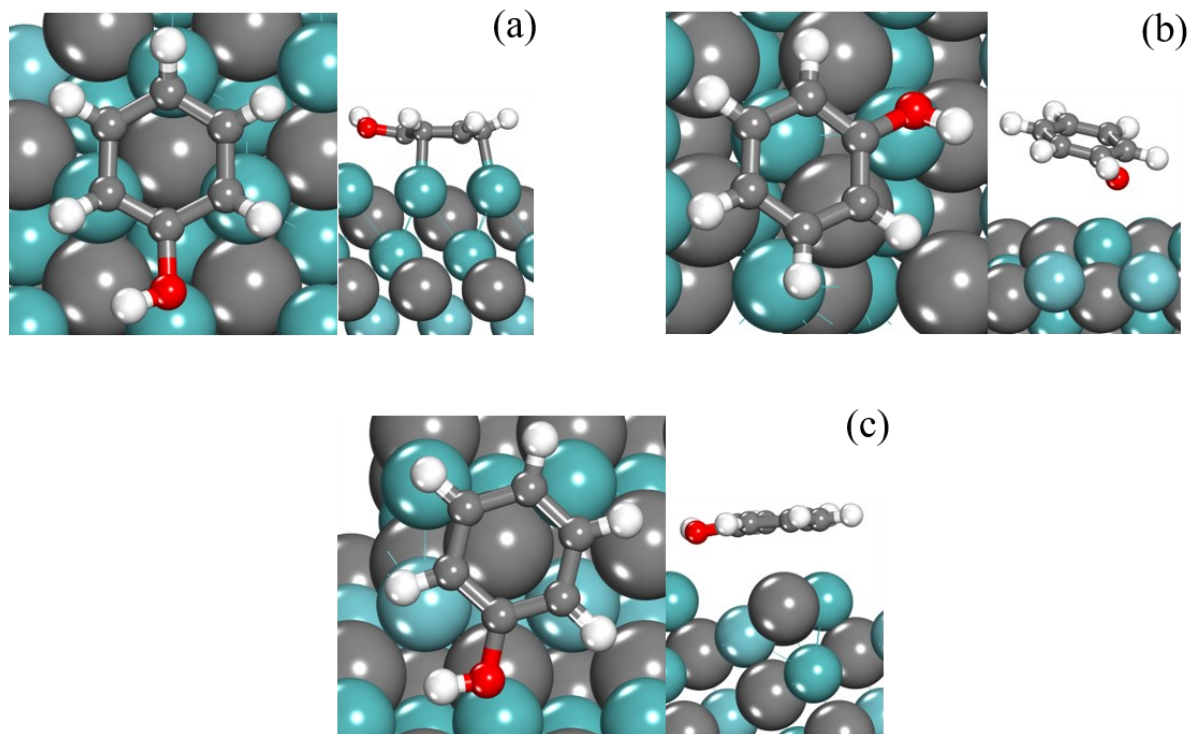


Figure D.41 Optimised adsorption configurations of phenol on (a) Nb₂B, (b) NbMo₃B and (c) NbMoB. The darker and lighter green spheres represent Mo and Nb respectively. The grey, red and white spheres represent C, O and H respectively.

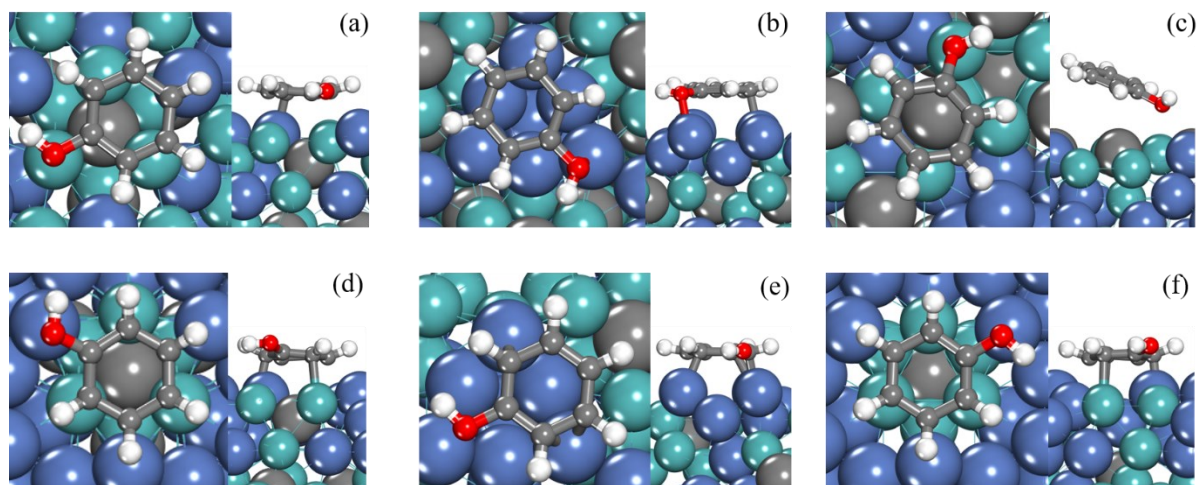


Figure D.42 Optimised adsorption configurations of phenol on (a) Ni₂C, (b) Ni₃A, (c) Ni₃B, (d) Ni₃C, (e) Ni₆A and (f) Ni₆C. The green and blue spheres represent Mo and Ni respectively. The grey, red and white spheres represent C, O and H respectively.

D.9 Transition State Configurations of C-O dissociation (R1) reaction

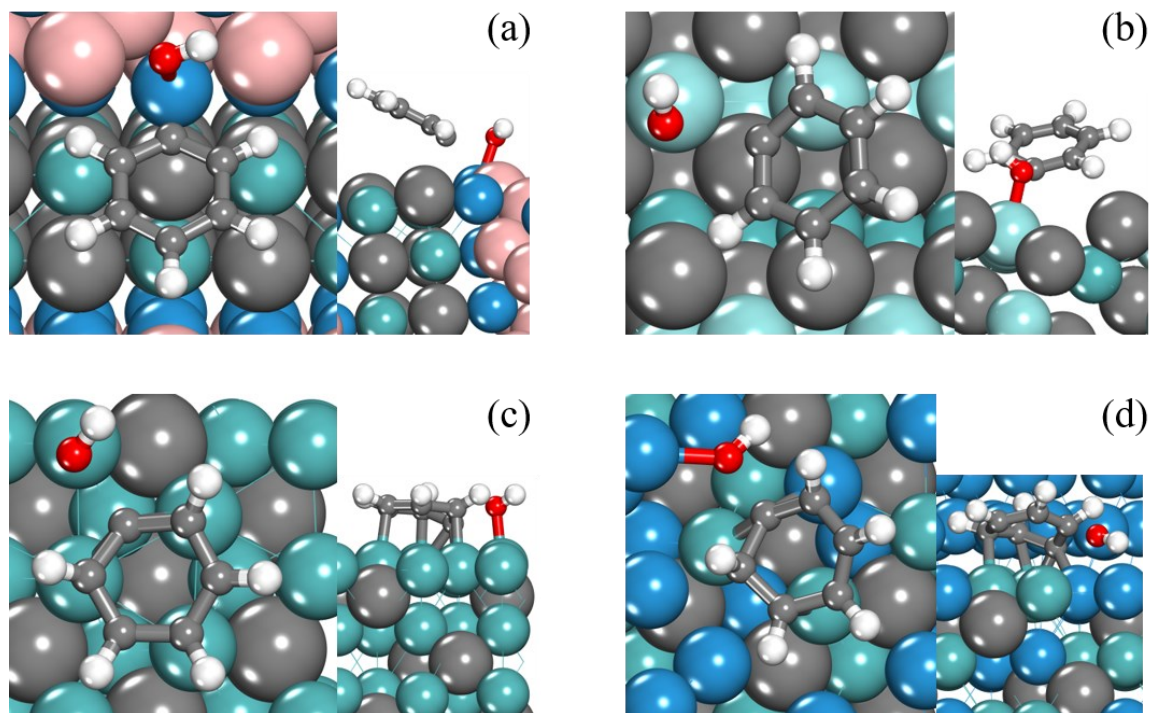


Figure D.43 Optimised transition state configurations of R1 (C-O dissociation) on (a) BMoWC, (b) ZrA, (c) Mo₂C and (d) MoWC. The grey, red and white spheres represent C, O and H respectively. In (a), (c) and (d), the pink, green and blue spheres represent B, Mo and W respectively. In (b), the darker teal and lighter turquoise spheres represent Mo and Zr respectively.

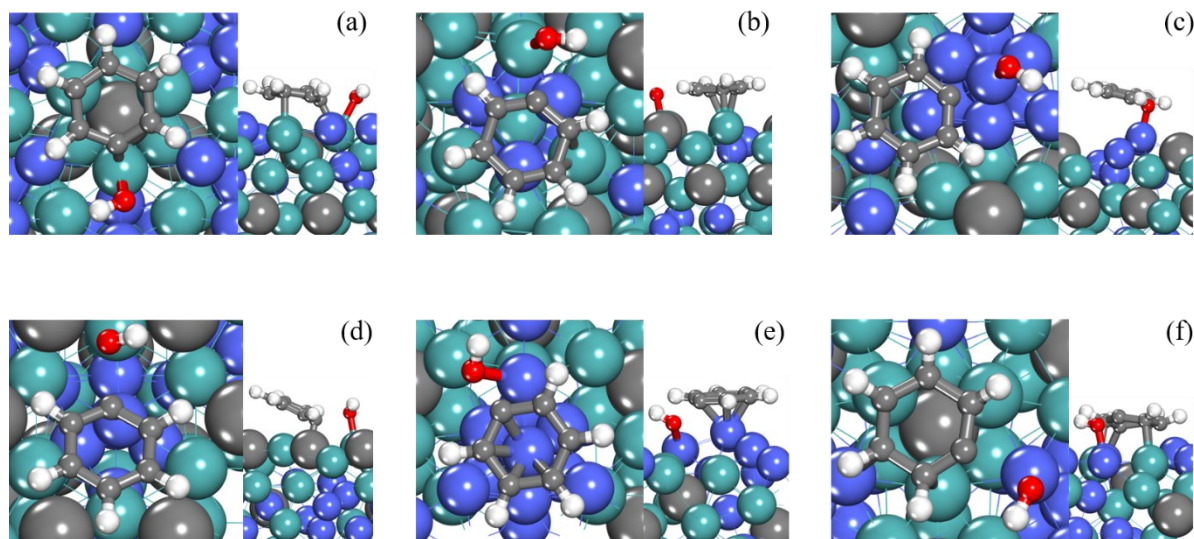


Figure D.44 Optimised transition state configurations of R1 (C-O dissociation) on (a) Co_{2A}, (b) Co_{2B}, (c) Co_{3A}, (d) Co_{3B}, (e) Co_{6A} and (f) Co_{6B}. The green and blue spheres represent Mo and Co respectively. The grey, red and white spheres represent C, O and H respectively.

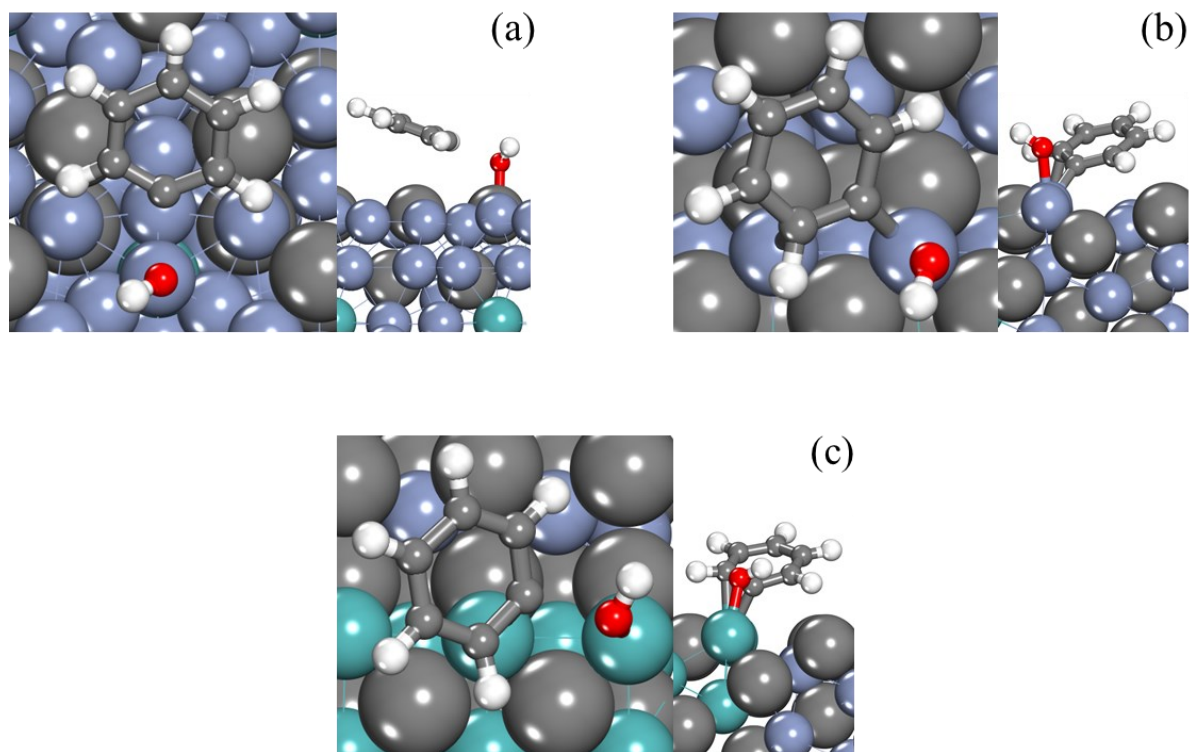


Figure D.45 Optimised transition state configurations of R1 (C-O dissociation) on (a) Cr_{22A}, (b) Cr_{3A} and (c) Cr_{3B}. The green and pastel blue spheres represent Mo and Cr respectively. The grey, red and white spheres represent C, O and H respectively.

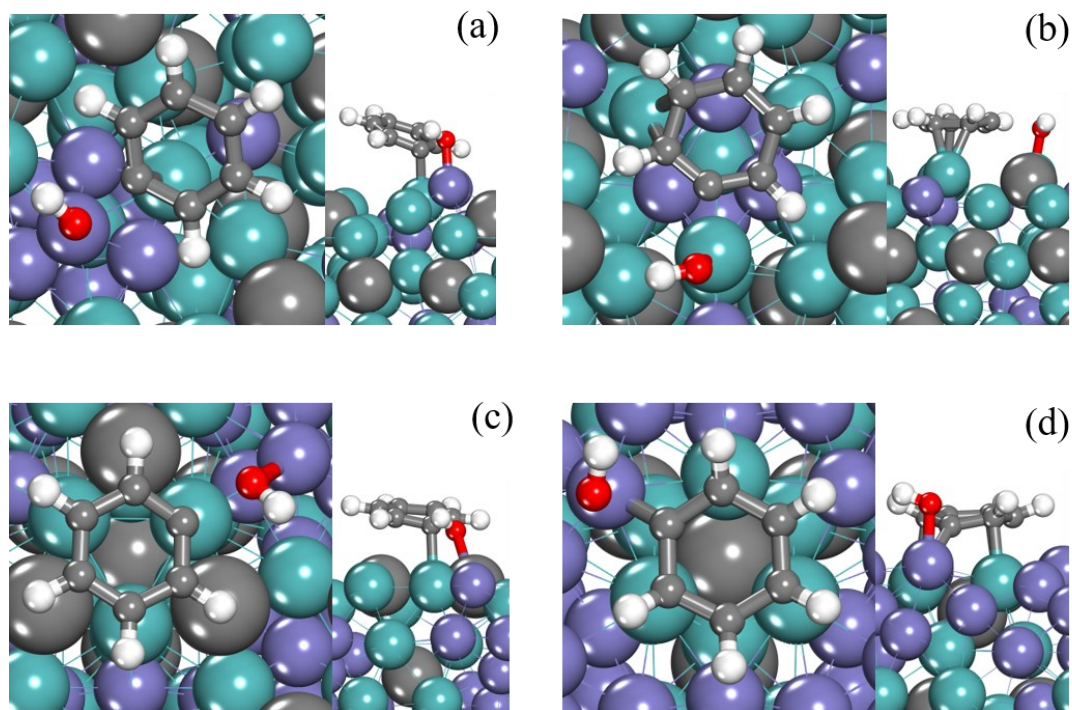


Figure D.46 Optimised transition state configurations of R1 (C-O dissociation) on (a) Fe_{2A}, (b) Fe_{2B}, (c) Fe_{3B} and (d) Fe_{3C}. The green and purple spheres represent Mo and Fe respectively. The grey, red and white spheres represent C, O and H respectively.

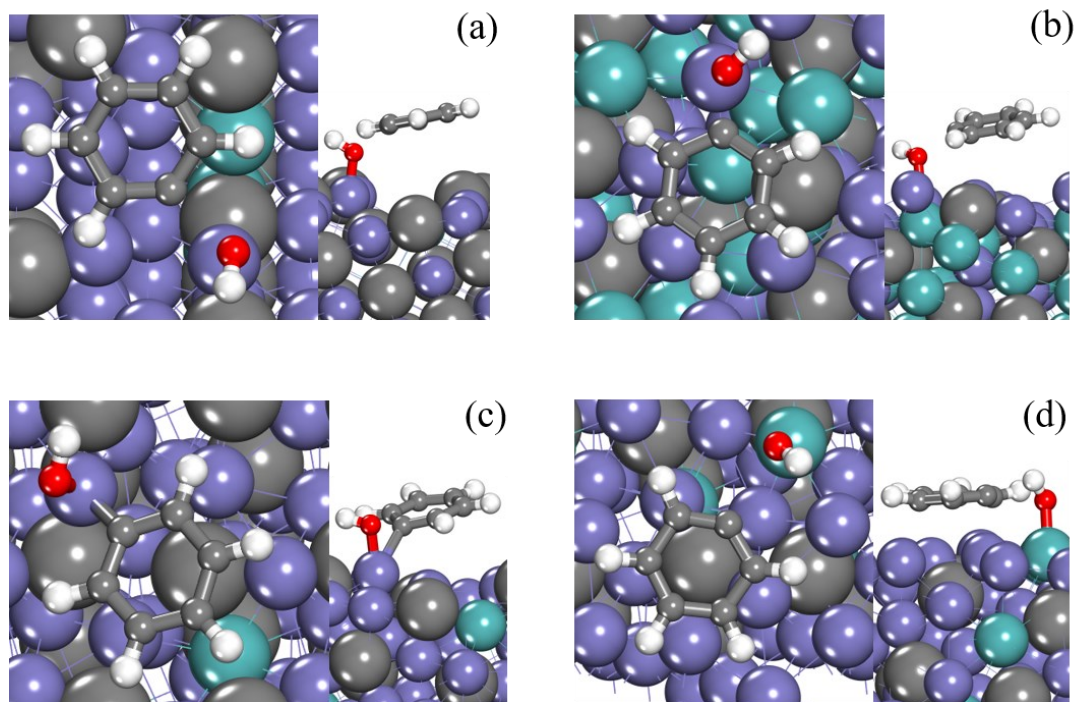


Figure D.47 Optimised transition state configurations of R1 (C-O dissociation) on (a) Fe_{11}O_A , (b) Fe_{11}O_C , (c) Fe_{11}T_A and (d) Fe_{11}T_B . The green and purple spheres represent Mo and Fe respectively. The grey, red and white spheres represent C, O and H respectively.

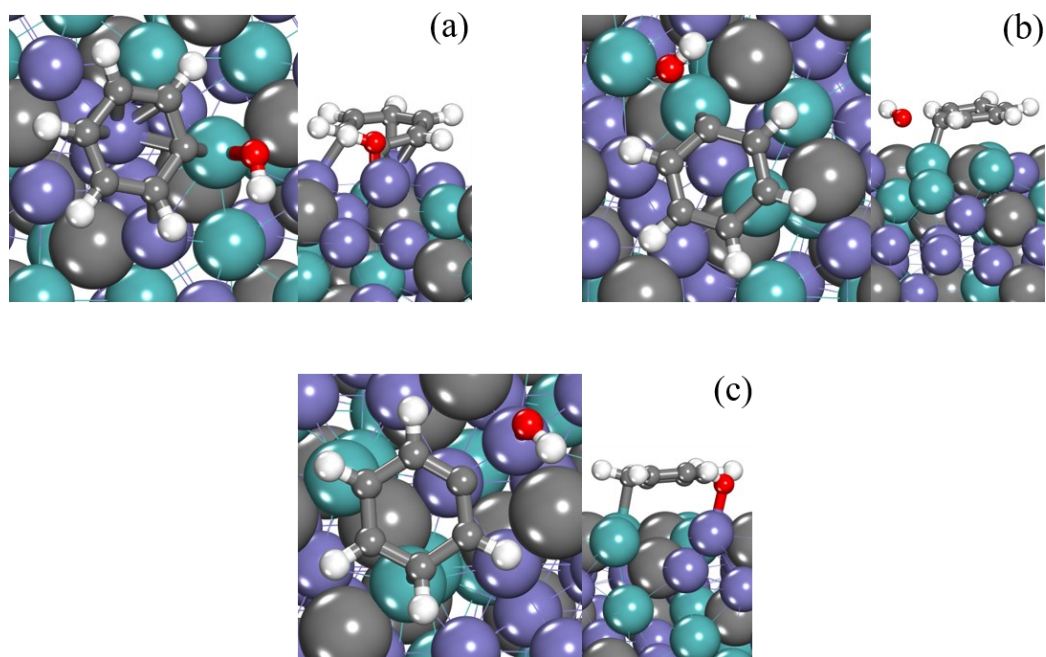


Figure D.48 Optimised transition state configurations of R1 (C-O dissociation) on (a) Fe_{11}I_A , (b) Fe_{11}I_B and (c) Fe_{11}I_C . The green and purple spheres represent Mo and Fe respectively. The grey, red and white spheres represent C, O and H respectively.

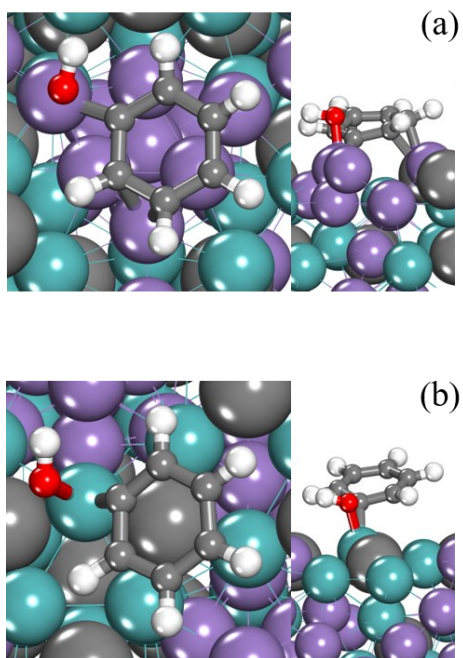


Figure D.49 Optimised transition state configurations of R1 (C-O dissociation) on (a) Mn_A and (b) Mn_B . The green and purple spheres represent Mo and Mn respectively. The grey, red and white spheres represent C, O and H respectively.

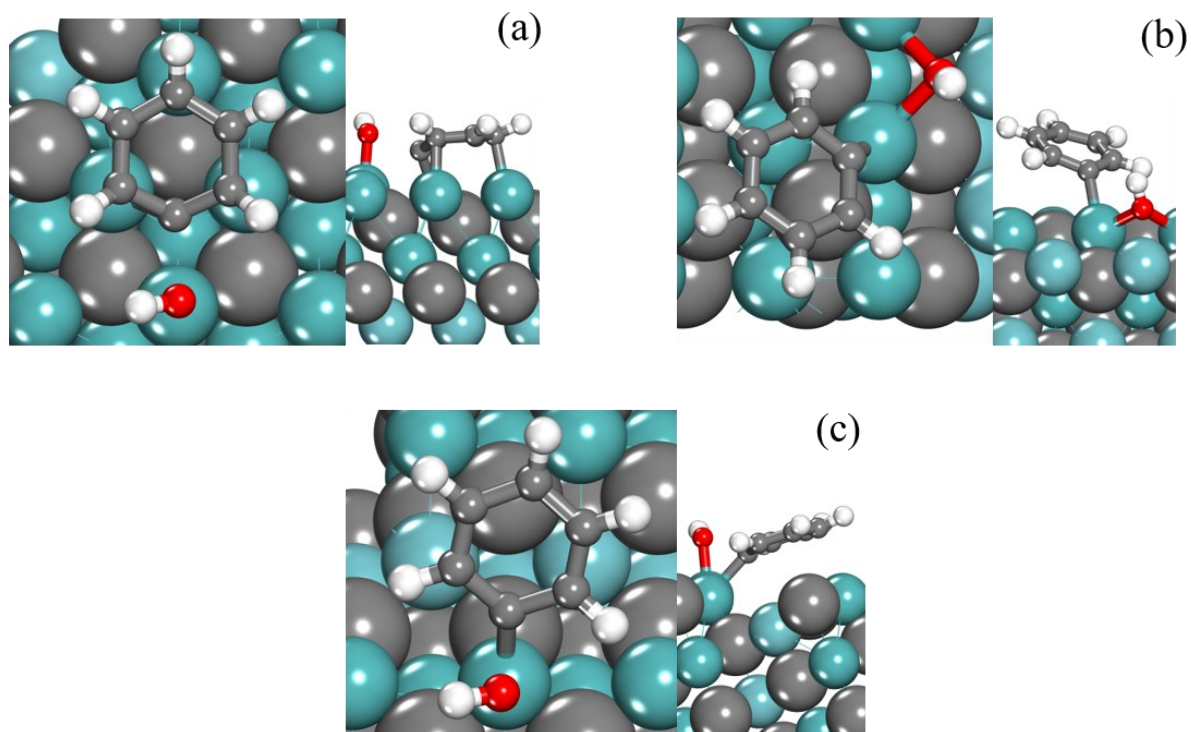


Figure D.50 Optimised transition state configurations of R1 (C-O dissociation) on (a) Nb₂B, (b) NbMo₃B and (c) NbMoB. The darker and lighter green spheres represent Mo and Nb respectively. The grey, red and white spheres represent C, O and H respectively.

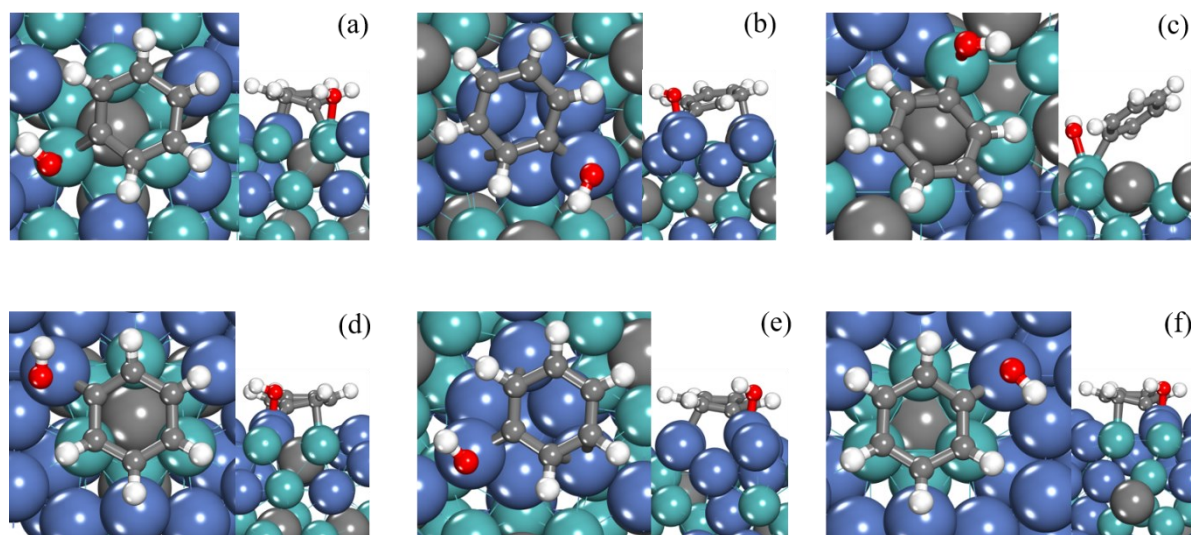


Figure D.51 Optimised transition state configurations of R1 (C-O dissociation) on (a) Ni₂C, (b) Ni₃A, (c) Ni₃B, (d) Ni₃C, (e) Ni₆A and (f) Ni₆C. The green and blue spheres represent Mo and Ni respectively. The grey, red and white spheres represent C, O and H respectively.

D.10 Transition State Configurations for O* removal (R3) Reaction

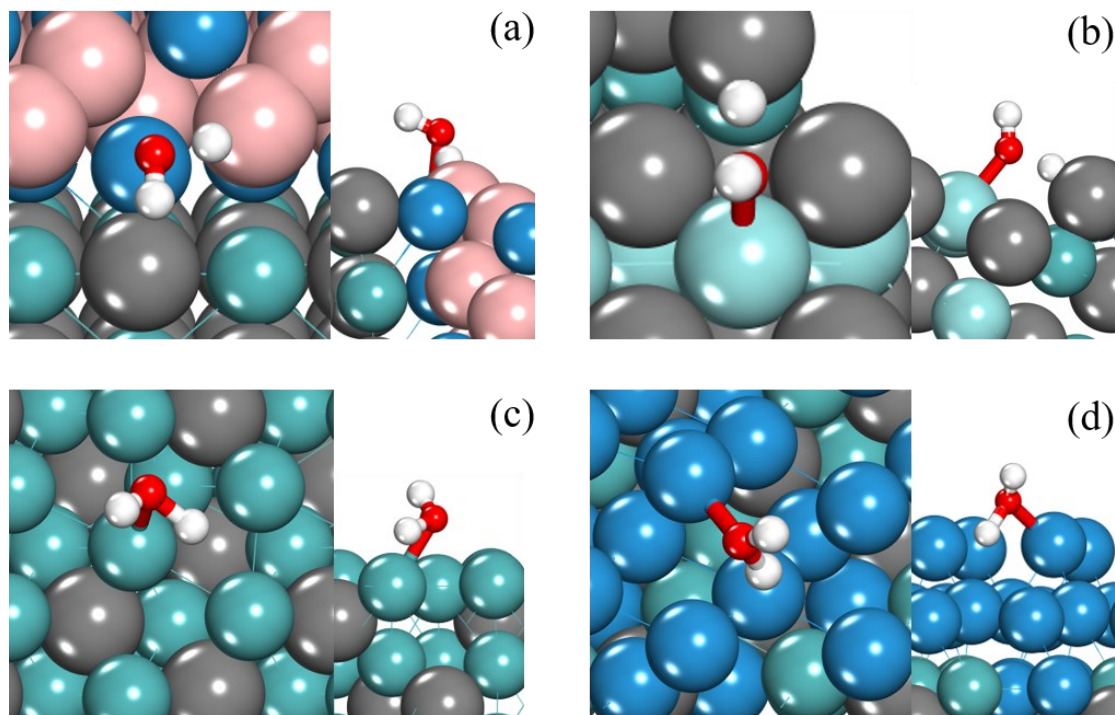


Figure D.52 Optimised transition state configurations of R2 (water formation) on (a) BMoWC, (b) ZrA, (c) Mo₂C and (d) MoWC. The grey, red and white spheres represent C, O and H respectively. In (a), (c) and (d), the pink, green and blue spheres represent B, Mo and W respectively. In (b), the darker teal and lighter turquoise spheres represent Mo and Zr respectively.

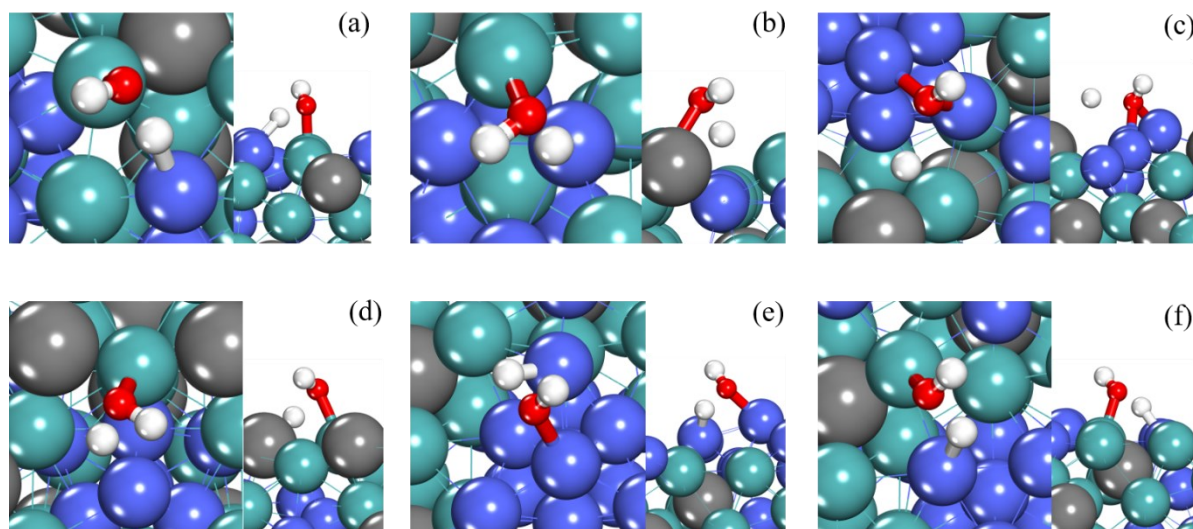


Figure D.53 Optimised transition state configurations of R2 (water formation) on (a) Co₂A, (b) Co₂B, (c) Co₃A, (d) Co₃B, (e) Co₆A and (f) Co₆B. The green and blue spheres represent Mo and Co respectively. The grey, red and white spheres represent C, O and H respectively.

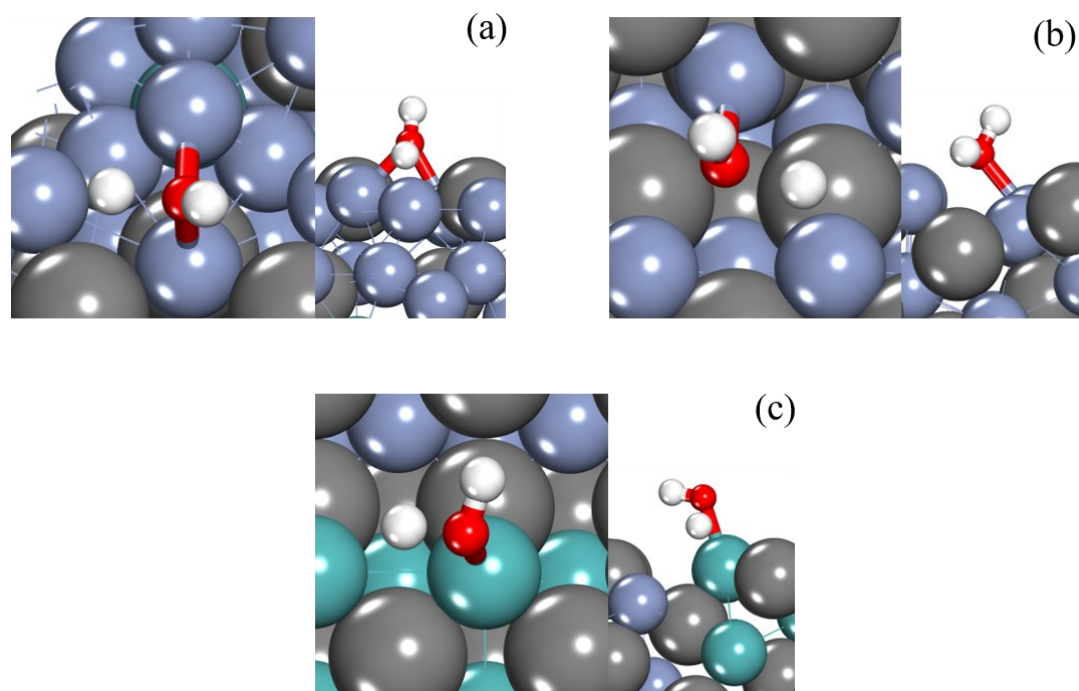


Figure D.54 Optimised transition state configurations of R2 (water formation) on (a) Cr_{22A}, (b) Cr_{3A} and (c) Cr_{3B}. The green and pastel blue spheres represent Mo and Cr respectively. The grey, red and white spheres represent C, O and H respectively.

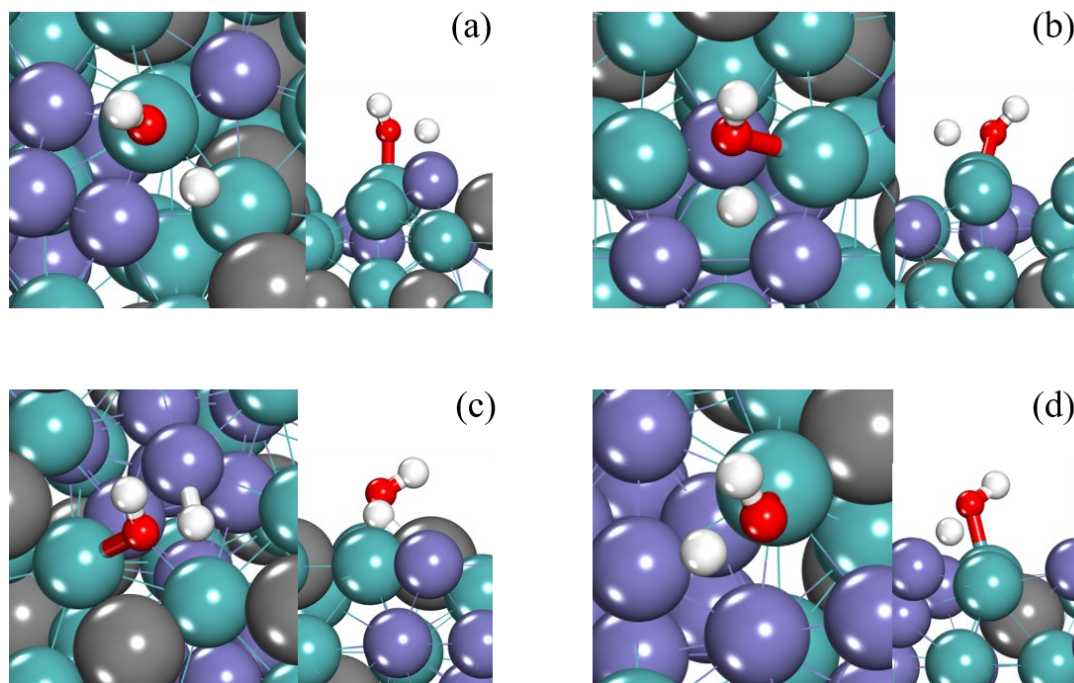


Figure D.55 Optimised transition state configurations of R2 (water formation) on (a) Fe_{2A}, (b) Fe_{2B}, (c) Fe_{3B} and (d) Fe_{3C}. The green and purple spheres represent Mo and Fe respectively. The grey, red and white spheres represent C, O and H respectively.

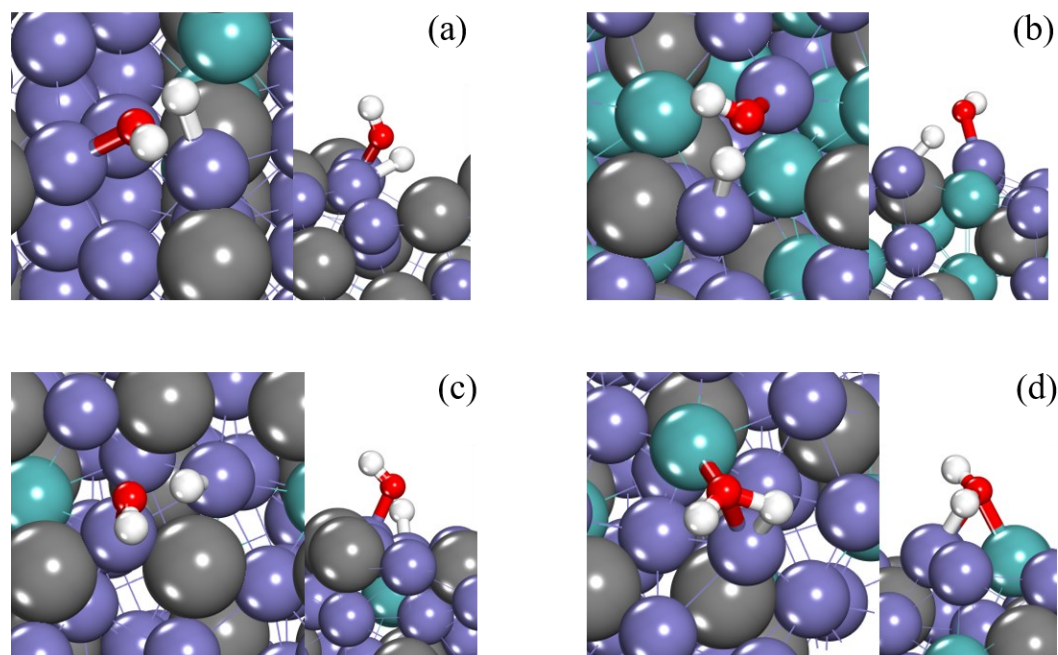


Figure D.56 Optimised transition state configurations of R2 (water formation) on (a) Fe_{11}O_A , (b) Fe_{11}O_C , (c) Fe_{11}T_A and (d) Fe_{11}T_B . The green and purple spheres represent Mo and Fe respectively. The grey, red and white spheres represent C, O and H respectively.

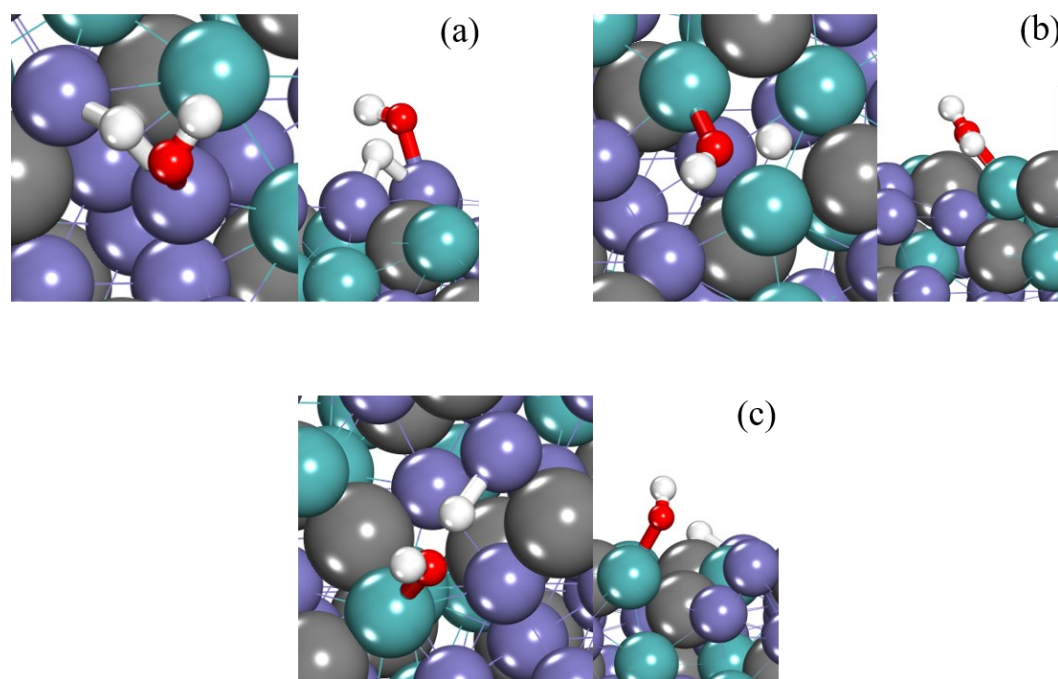


Figure D.57 Optimised transition state configurations of R2 (water formation) on (a) Fe_{11A} , (b) Fe_{11B} and (c) Fe_{11C} . The green and purple spheres represent Mo and Fe respectively. The grey, red and white spheres represent C, O and H respectively.

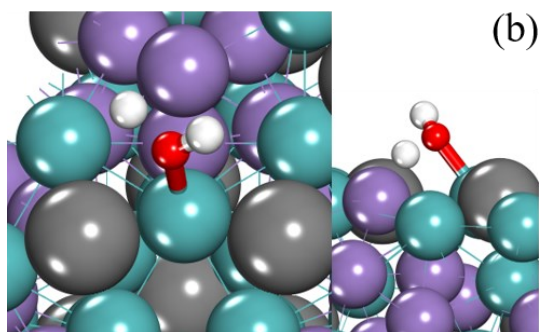
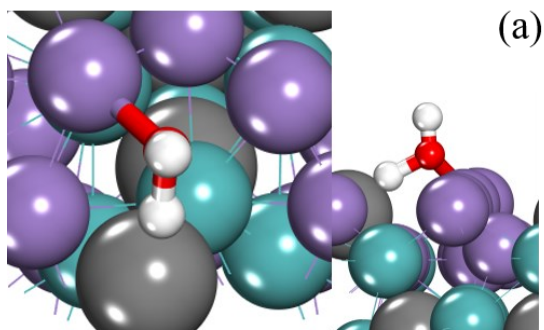


Figure D.58 Optimised transition state configurations of R2 (water formation) on (a) Mn_A and (b) Mn_B . The green and purple spheres represent Mo and Mn respectively. The grey, red and white spheres represent C, O and H respectively.

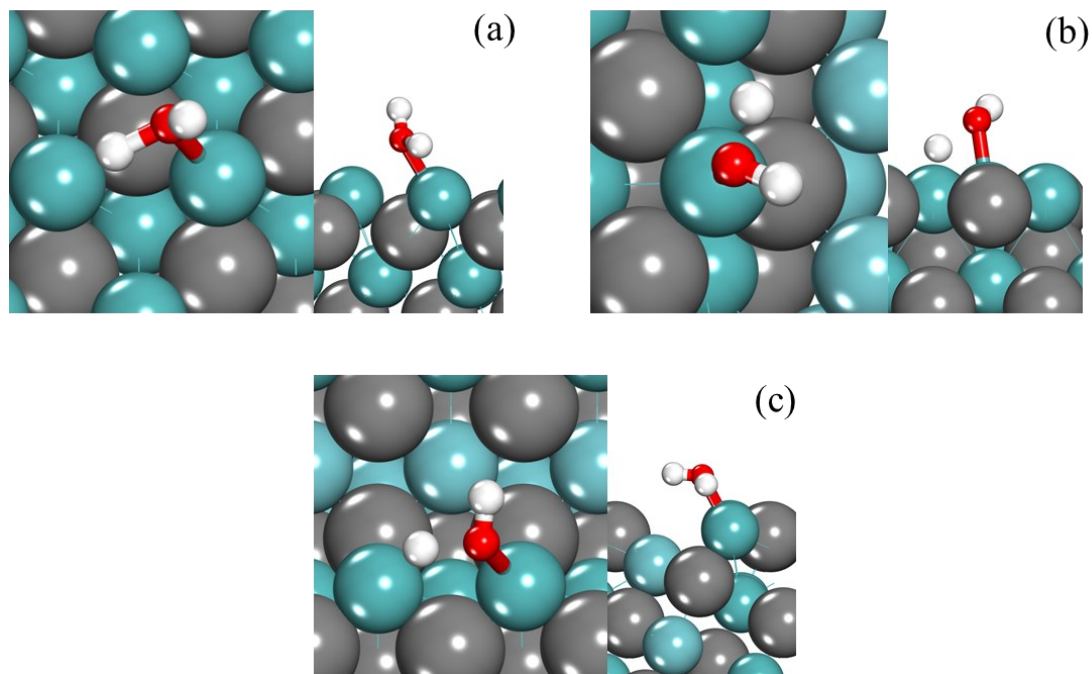


Figure D.59 Optimised transition state configurations of R2 (water formation) on (a) Nb₂B, (b) NbMo₃B and (c) NbMoB. The darker and lighter green spheres represent Mo and Nb respectively. The grey, red and white spheres represent C, O and H respectively.

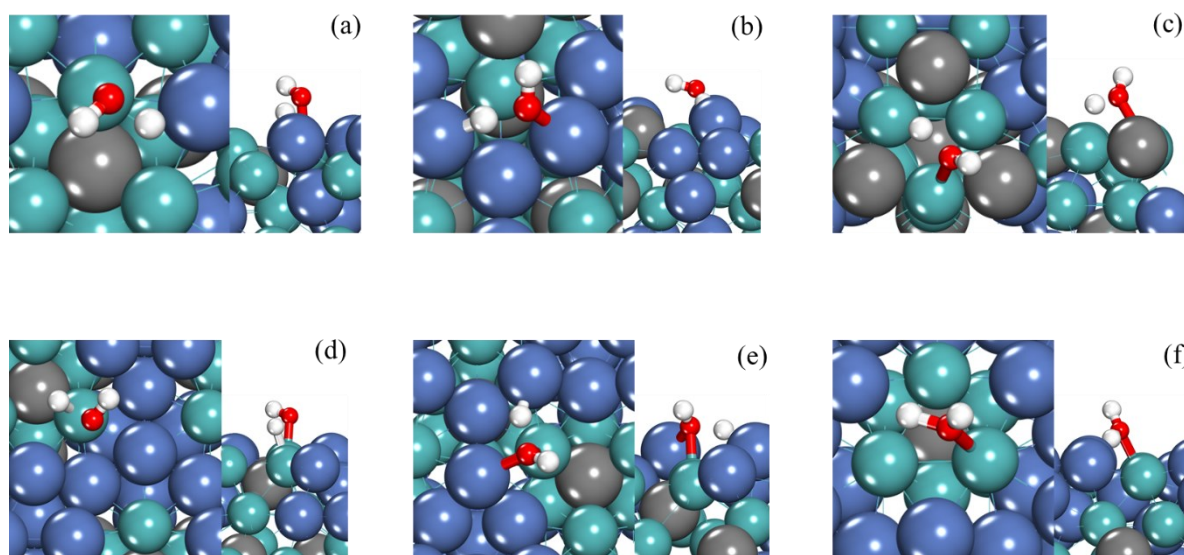


Figure D.60 Optimised transition state configurations of R2 (water formation) on (a) Ni₂C, (b) Ni₃A, (c) Ni₃B, (d) Ni₃C, (e) Ni₆A and (f) Ni₆C. The green and blue spheres represent Mo and Ni respectively. The grey, red and white spheres represent C, O and H respectively.

D.11 Transition State Configurations for Ring Hydrogenation (R3) Reaction

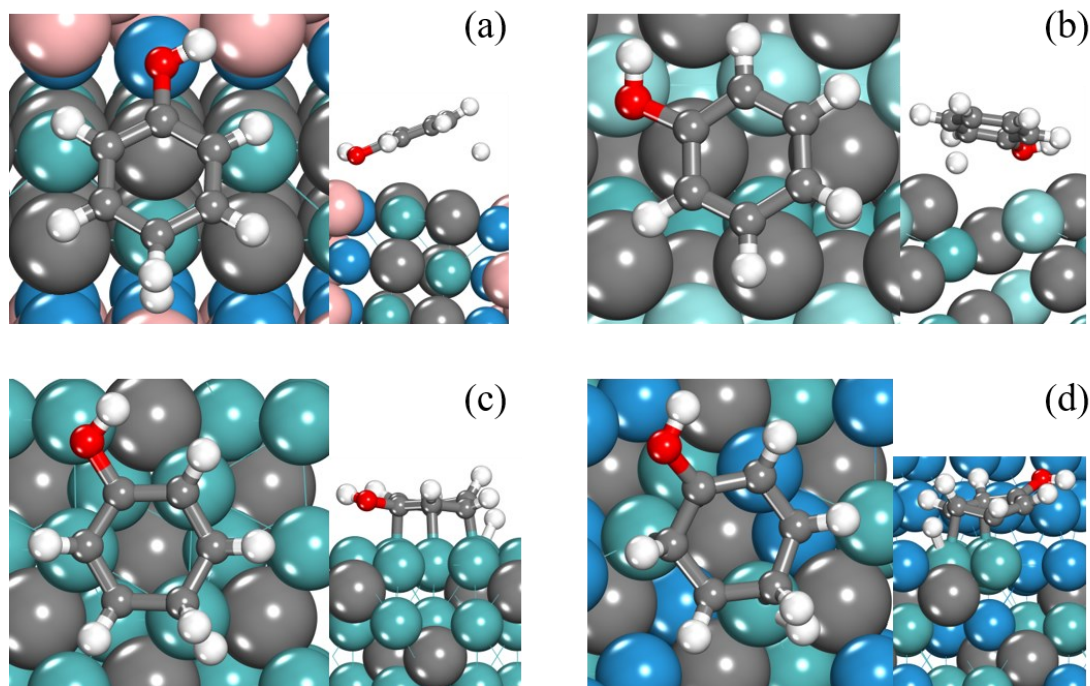


Figure D.61 Optimised transition state configurations of R3 (ring hydrogenation) on (a) BMoWC, (b) ZrA, (c) Mo₂C and (d) MoWC. The grey, red and white spheres represent C, O and H respectively. In (a), (c) and (d), the pink, green and blue spheres represent B, Mo and W respectively. In (b), the darker teal and lighter turquoise spheres represent Mo and Zr respectively.

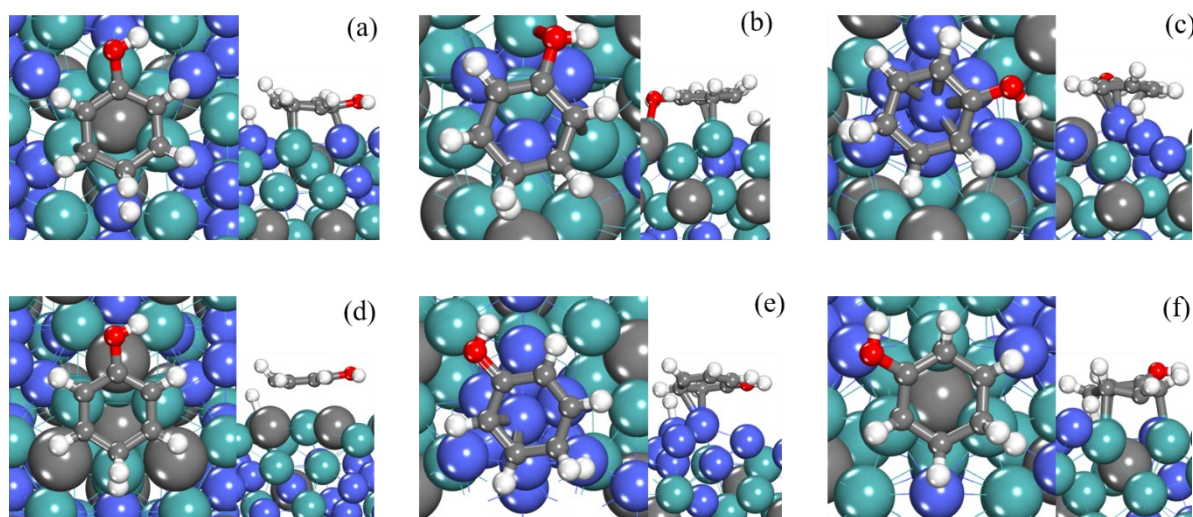


Figure D.62 Optimised transition state configurations of R3 (ring hydrogenation) on (a) Co_{2A}, (b) Co_{2B}, (c) Co_{3A}, (d) Co_{3B}, (e) Co_{6A} and (f) Co_{6B}. The green and blue spheres represent Mo and Co respectively. The grey, red and white spheres represent C, O and H respectively.

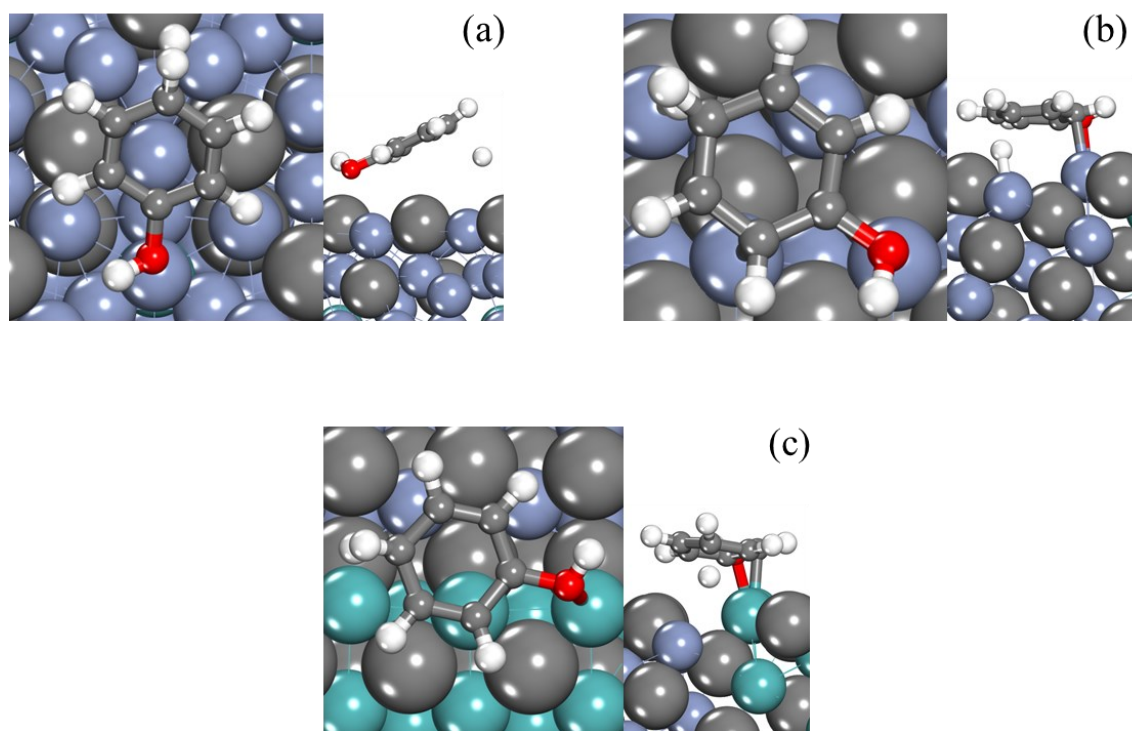


Figure D.63 Optimised transition state configurations of R3 (ring hydrogenation) on (a) $\text{Cr}_{22\text{A}}$, (b) $\text{Cr}_{3\text{A}}$ and (c) $\text{Cr}_{3\text{B}}$. The green and pastel blue spheres represent Mo and Cr respectively. The grey, red and white spheres represent C, O and H respectively.

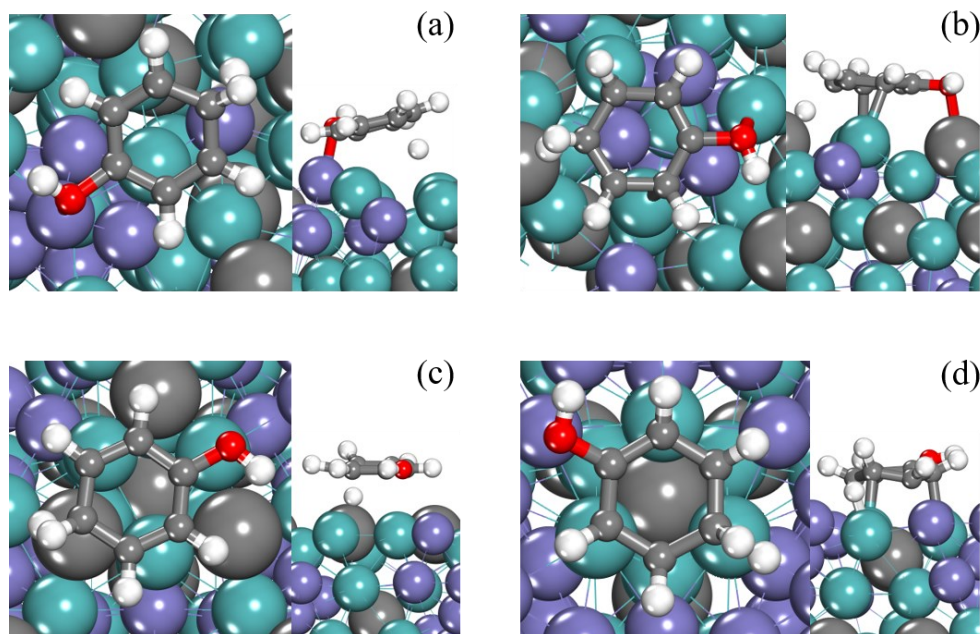


Figure D.64 Optimised transition state configurations of R3 (ring hydrogenation) on (a) Fe_{2A}, (b) Fe_{2B}, (c) Fe_{3B} and (d) Fe_{3C}. The green and purple spheres represent Mo and Fe respectively. The grey, red and white spheres represent C, O and H respectively.

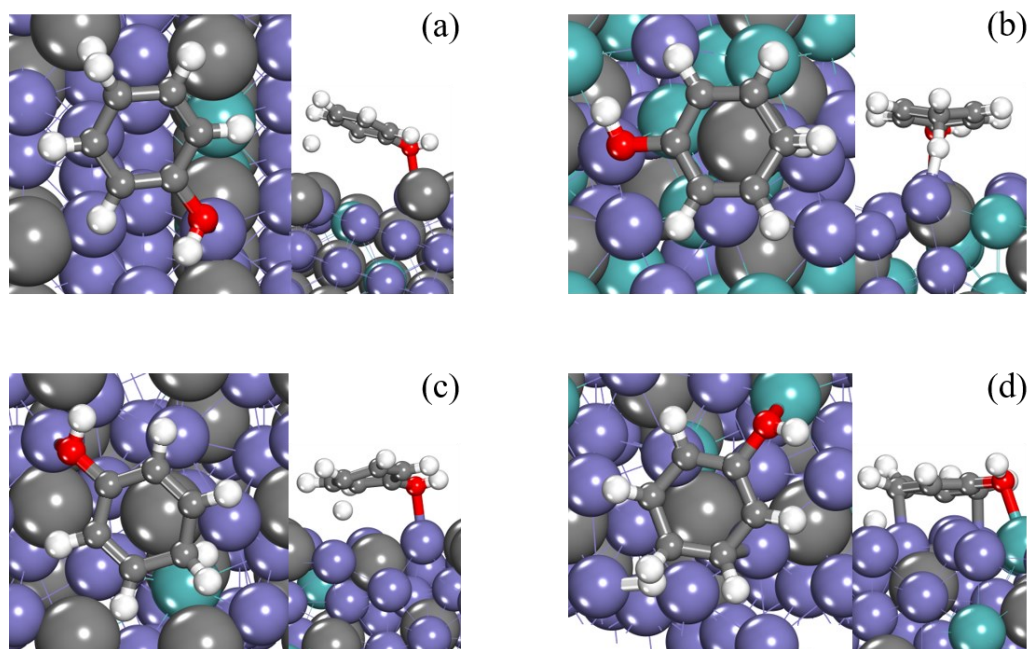


Figure D.65 Optimised transition state configurations of R3 (ring hydrogenation) on (a) Fe_{11OA}, (b) Fe_{11OC}, (c) Fe_{11TA} and (d) Fe_{11TB}. The green and purple spheres represent Mo and Fe respectively. The grey, red and white spheres represent C, O and H respectively.

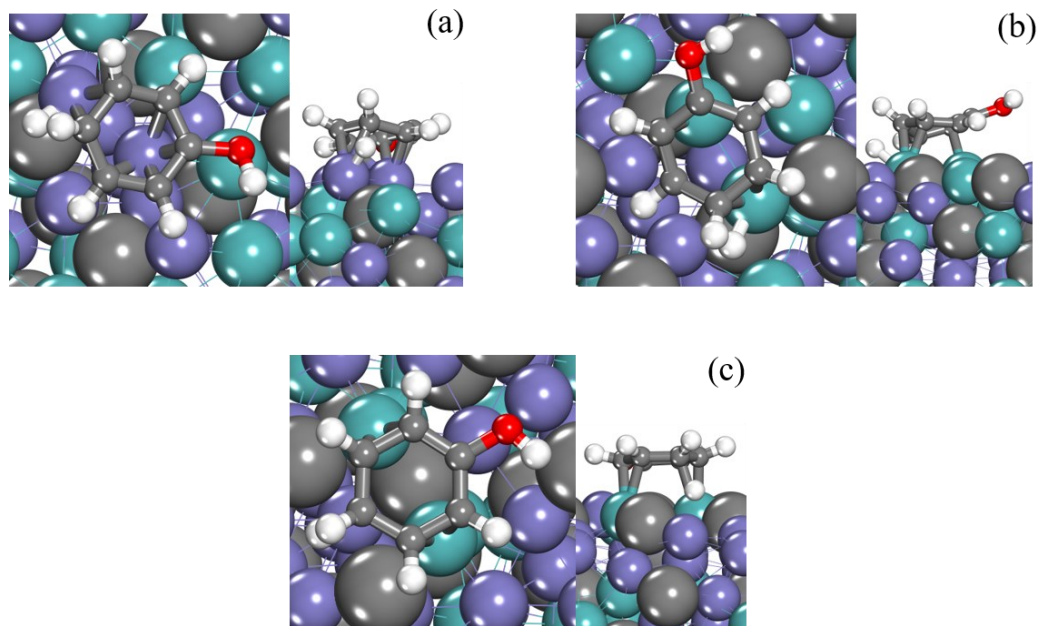


Figure D.66 Optimised transition state configurations of R3 (ring hydrogenation) on (a) Fe_{11A}, (b) Fe_{11B} and (c) Fe_{11C}. The green and purple spheres represent Mo and Fe respectively. The grey, red and white spheres represent C, O and H respectively.

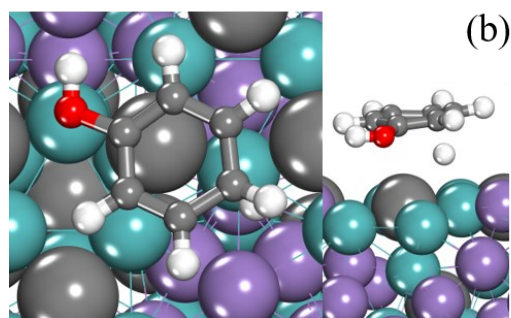
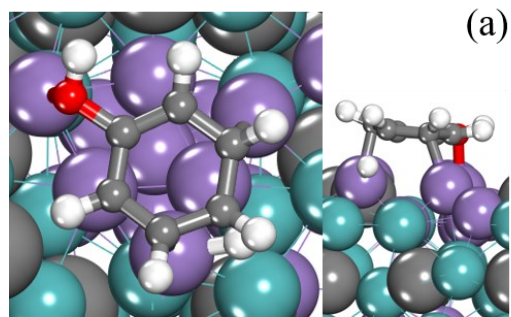


Figure D.67 Optimised transition state configurations of R3 (ring hydrogenation) on (a) Mn_A and (b) Mn_B . The green and purple spheres represent Mo and Mn respectively. The grey, red and white spheres represent C, O and H respectively.

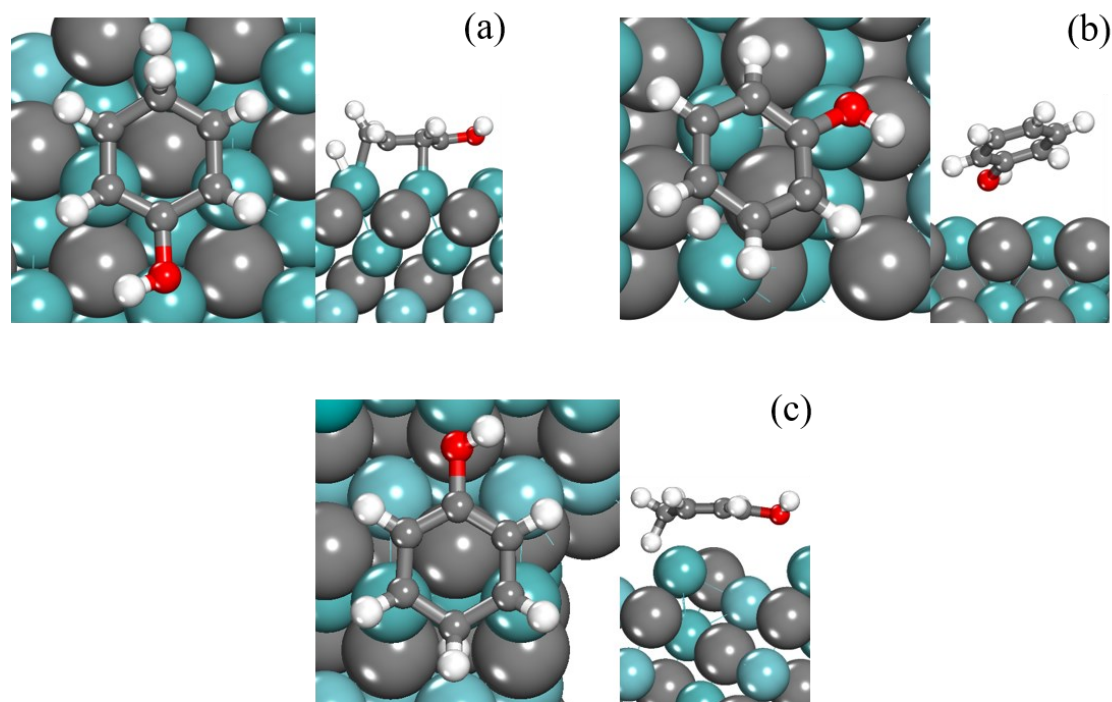


Figure D.68 Optimised transition state configurations of R3 (ring hydrogenation) on (a) Nb_2B , (b) NbMo_3B and (c) NbMoB . The darker and lighter green spheres represent Mo and Nb respectively. The grey, red and white spheres represent C, O and H respectively.

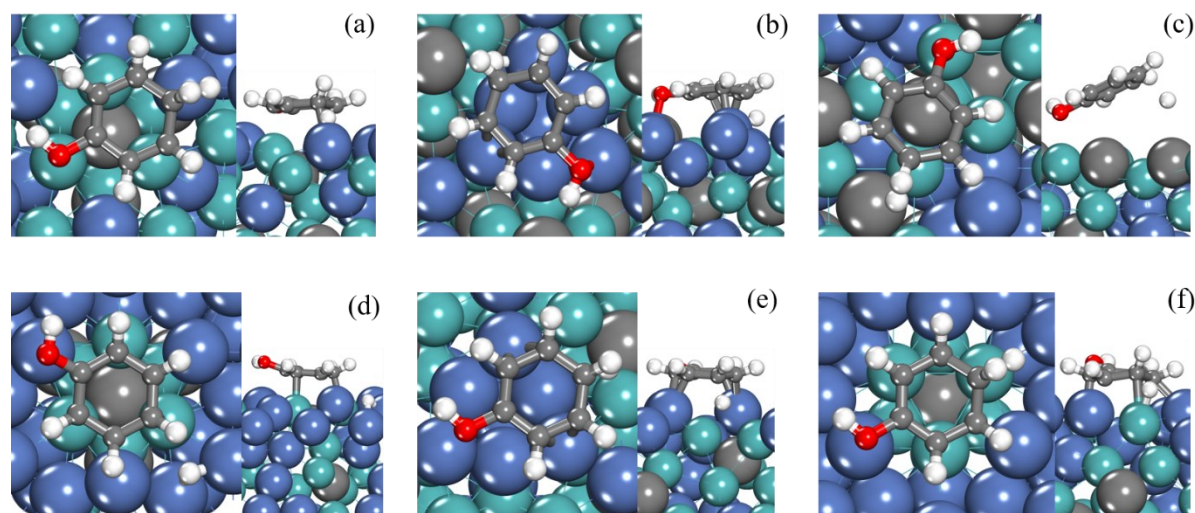


Figure D.69 Optimised transition state configurations of R3 (ring hydrogenation) on (a) Ni_2C , (b) Ni_3A , (c) Ni_3B , (d) Ni_3C , (e) Ni_6A and (f) Ni_6C . The green and blue spheres represent Mo and Ni respectively. The grey, red and white spheres represent C, O and H respectively.

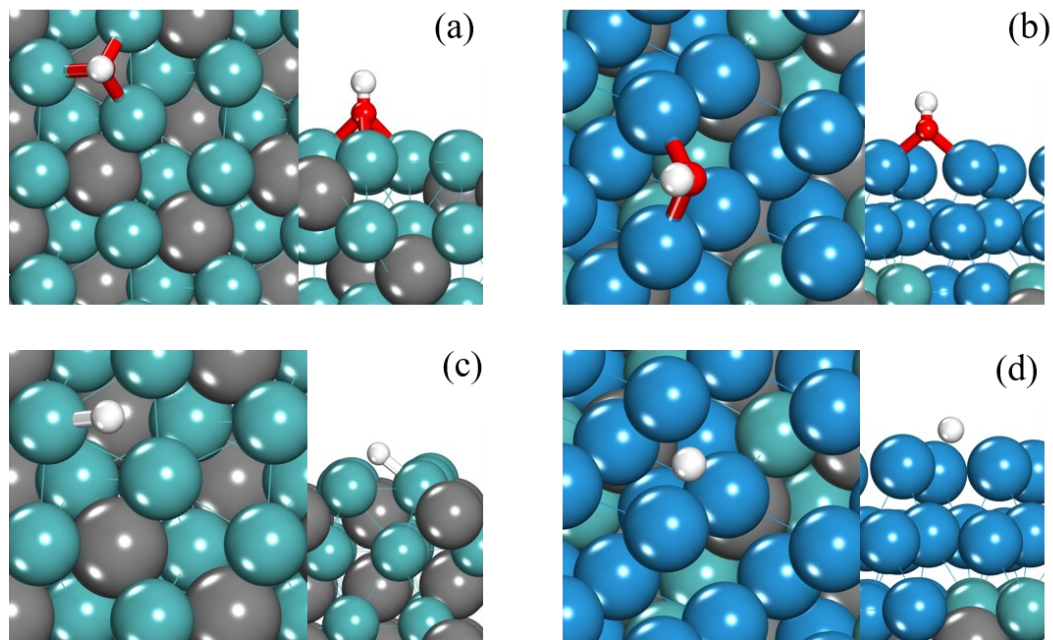


Figure D.70 Optimised configurations of (a) OH* adsorption on Mo₂C, (b) OH* adsorption on MoWC, (c) H* adsorption on Mo₂C and (d) H* adsorption on MoWC. The red and white spheres represent O and H respectively. The green, blue and grey spheres represent Mo, W and C respectively.

Appendix E Supplementary Information to Chapter 5

E.1 Experimental Results

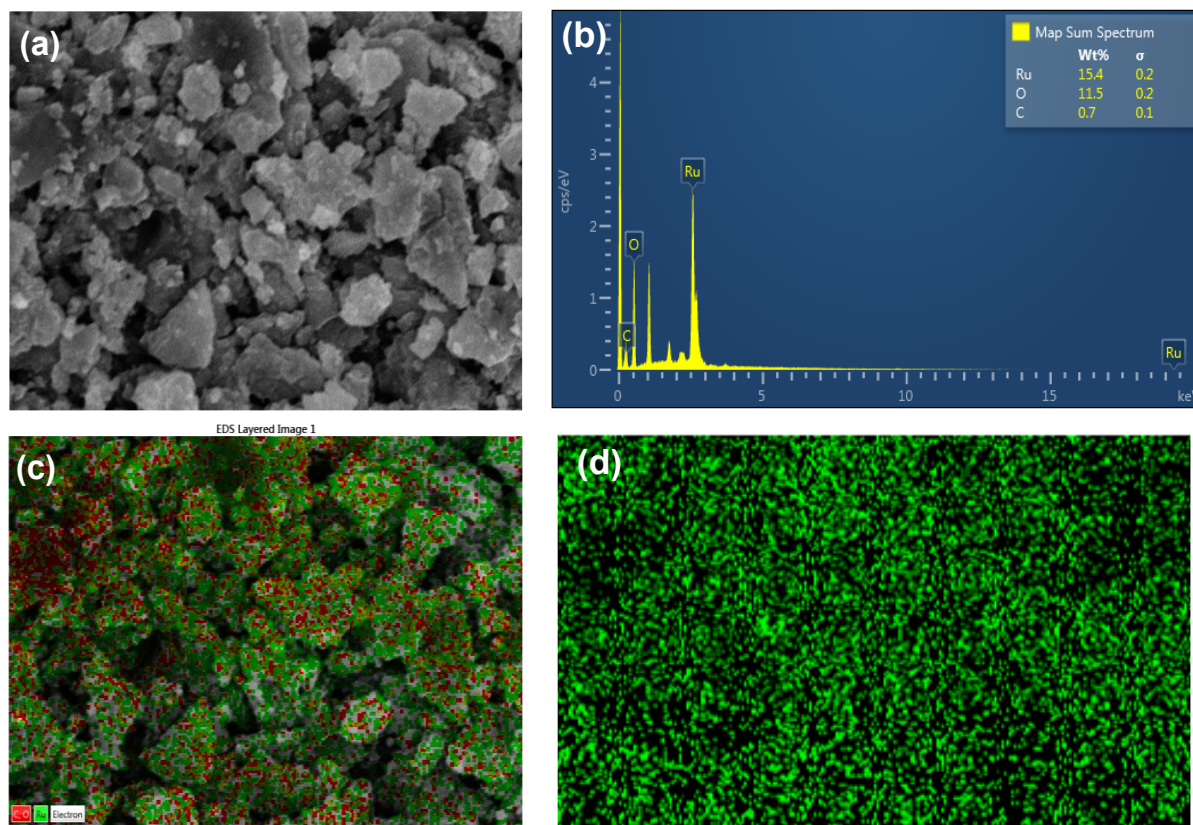


Figure E.1 (a) SEM image, (scale - 5 μm) and corresponding (b) EDX spectra, (c) elemental mapping, and (d) elemental mapping showing presence of Ru (green) in catalyst.

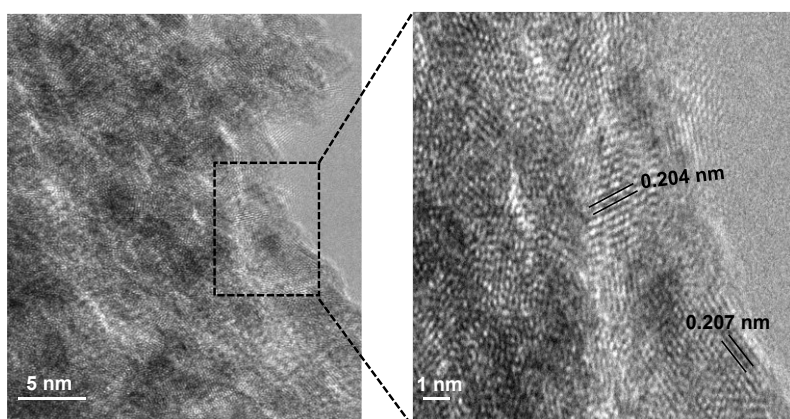


Figure E.2 HR-TEM image for Ru catalyst.

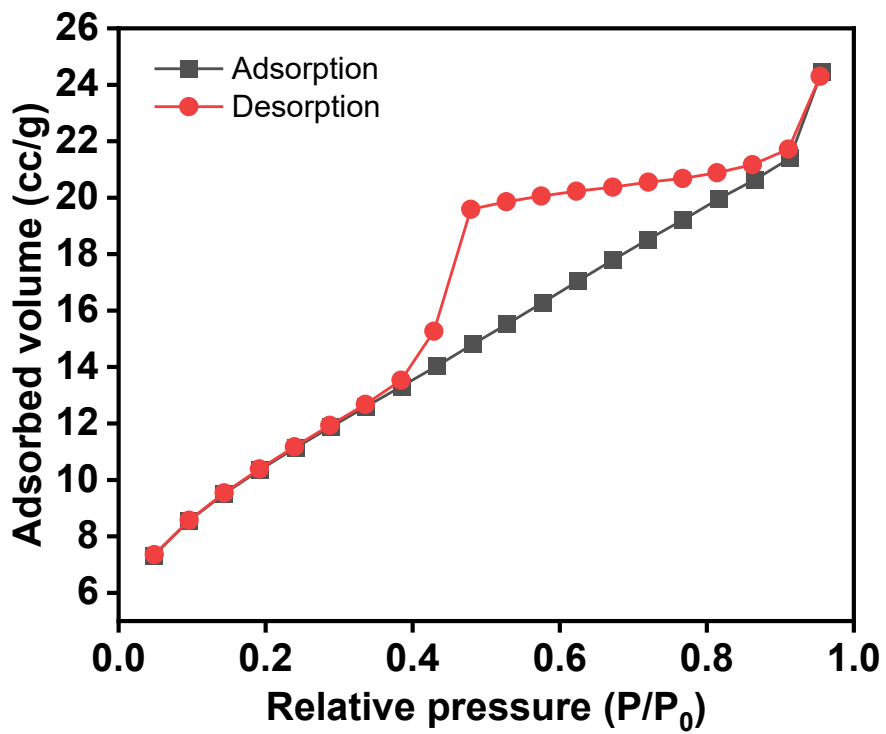


Figure E.3 N₂ adsorption-desorption isotherm for Ru nanoparticles.

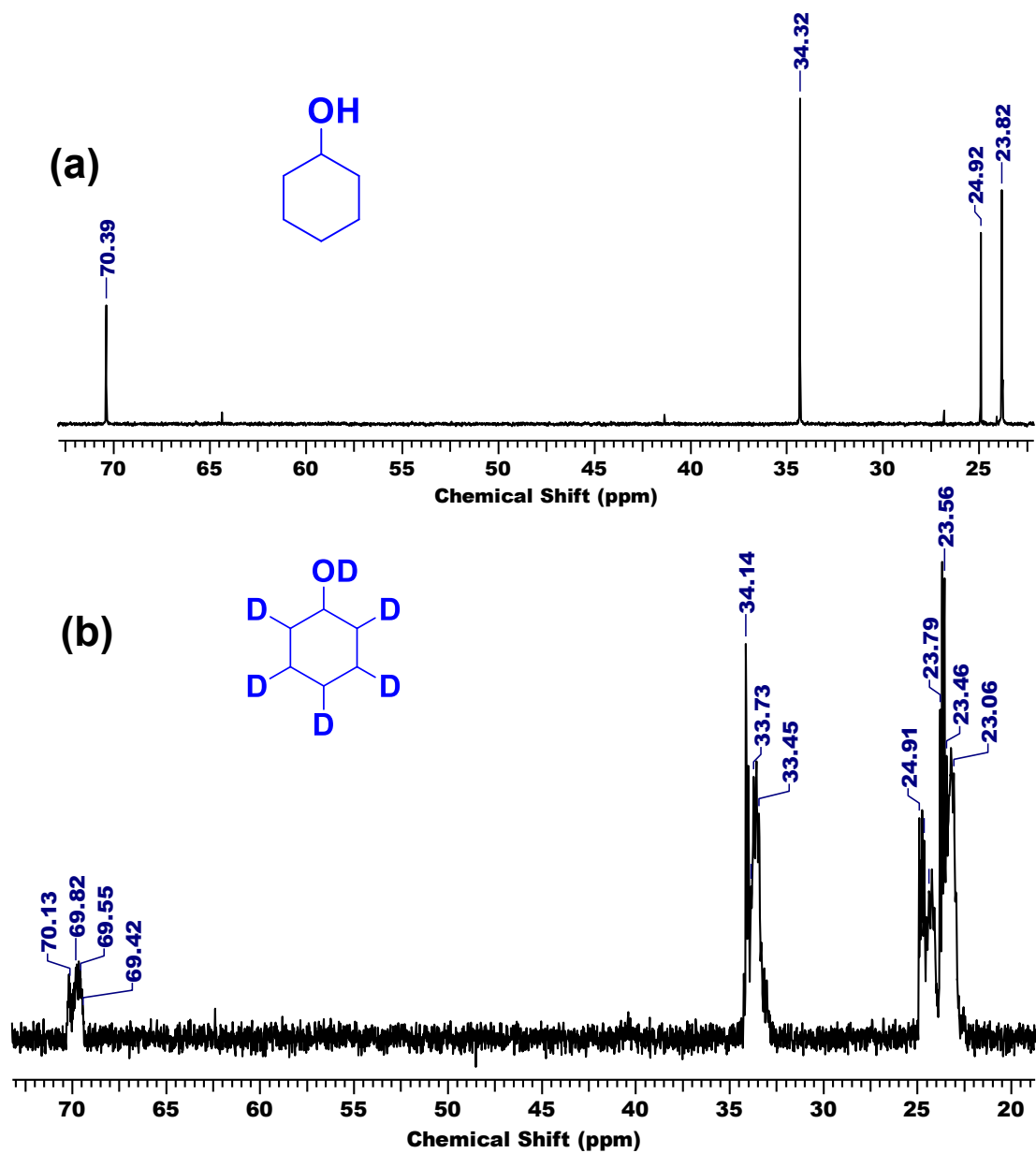


Figure E.4 (a) ^{13}C NMR of reaction performed in H_2O . (b) ^{13}C NMR of reaction performed in D_2O . Reaction conditions : Ru catalyst (0.04 mmol), Phenol (1 mmol), solvent (10 mL), H_2 (1 bar), room temperature, 75 min.

Table E.1 Optimization of reaction conditions for hydrogenation of guaiacol.^a

Entry	Time (h)	Conv. (%)	Selectivity of 2a (%)	Selectivity of 1a (%)	Selectivity of 2b (%)
1	1	52	84	13	3
2	2	61	83	14	3
3	3	69	80	18	2
4	4	80	84	16	-
5	5	91	83	17	-
6	6	>99	81	19	-
7 ^b	6	n.r.	-	-	-

^aReaction conditions: Ru catalyst (0.04 mmol), guaiacol (1 mmol), water (10 mL), H₂ (1 bar), room temperature, t h, ^b2-methoxycyclohexanol used as substrate.

Table E.2 Content of Ru in reaction aliquot as determined by ICP-AES analysis.

Entry	Amount of Ru (in ppm)
1	0.58

E.2 Leaching experiment.

Leaching experiment was conducted to further investigate the stability of the Ru catalyst. For leaching experiments, the hydrogenation of phenol was performed over the Ru catalyst under optimized reaction conditions. After 45 min, the catalyst was recovered by centrifugation (6000 rpm for 10 min) and the obtained supernatant was divided into two parts. One part was analysed using ¹H NMR spectroscopy (54% conversion), while the other part was continued to stir for another 30 min under the optimized reaction conditions (Figure E.5). ¹H NMR analysis of the second part exhibited no remarkable increment in the conversion of phenol, which depicts the heterogeneous nature of the Ru catalyst during the catalytic hydrogenation reaction (Figure E.5). Moreover, the ICP-AES analysis of the reaction mixture reveals no significant leaching of Ru catalyst (<0.1 ppm).

E.3 Hg poisoning experiment.

Additionally, catalyst poisoning experiment was performed with elemental Hg, exhibiting a noteworthy quenching in the catalytic activity of the Ru catalyst, which also reinforces the heterogeneity of the catalytic hydrogenation reaction (Figure E.5). In this experiment, an excess of elemental mercury (100 mg) was accurately weighed and placed in a 50 mL flask. To this flask, an aqueous suspension of Ru nanoparticles (0.04 mmol in 10 mL) was added and stirred for 2 hours at room temperature. Subsequently, the contents of the flask were transferred to a reactor, and 1 mmol of phenol was introduced. The reactor was pressurized with H₂ gas, and the reaction mixture was stirred for 75 minutes at room temperature to facilitate the catalytic reaction. Upon completion of the reaction, the catalyst and Hg were separated by centrifugation at 8500 rpm for 15 minutes. The supernatant liquid was then tested for the conversion of phenol. Proper disposal procedures were followed for the mercury waste in compliance with regulations, and extreme care was taken throughout the experiment to minimize the risk of exposure to mercury.

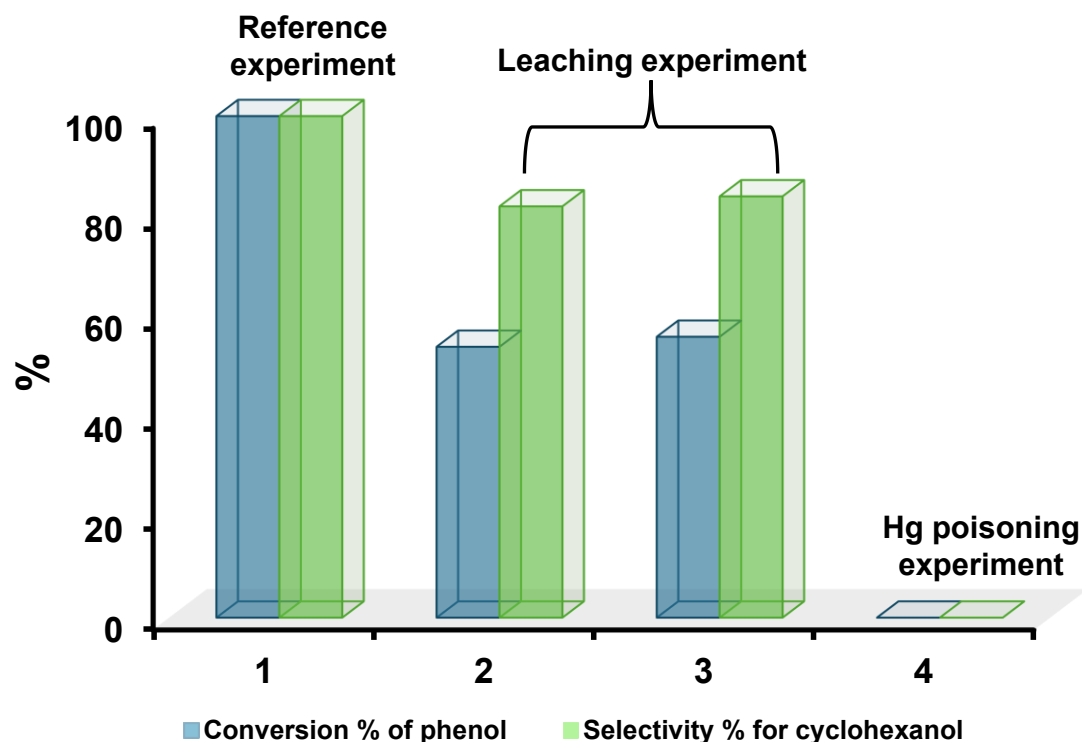


Figure E.5 Reference experiment: (1) Catalytic hydrogenation of phenol over Ru catalyst at 30 °C in 75 min under the optimized reaction conditions. Leaching experiments: (2) Catalytic

hydrogenation of phenol over Ru in 30 min and subsequently (3) catalyst was recovered from the reaction mixture by centrifugation and supernatant was again stirred at room temperature for another 45 min in presence of H₂. (4) Hg poisoning experiment: Catalytic hydrogenation of phenol over Ru catalyst in the presence of an excess of elemental Hg at 30 °C and 1 bar H₂.

E.4 Catalyst stability and reusability.

Furthermore, the studied Ru catalyst also displayed high stability in water as well as under the employed reaction conditions. The recyclability experiments for the Ru catalyst were carried out for the catalytic hydrogenation of phenol to cyclohexanol under the optimized reaction conditions for ten consecutive catalytic runs (Figure E.6). In the first six runs, there was no loss in the conversion but selectivity to cyclohexanol was decreased to 93%, and in the tenth cycle 81% conversion of phenol was achieved with 80% selectivity for cyclohexanol. P-XRD spectra of used catalyst did not change significantly after reaction (Figure E.7a). So, the decrease in catalyst activity could be attributed to the increase in the oxide layer on the Ru nanoparticles, which can hinder the accessibility of reactants to the active sites, leading to reduced catalytic performance (Figure E.7b). Additionally, the particle size in used catalyst was found to be increased (3.5-4 nm) than fresh catalyst (2.5-3 nm) which could also affect the catalytic activity, as smaller nanoparticles typically exhibit higher surface area and more active sites (Figure E.8). Loss of the catalyst during the recovery process could further contribute to the decrease in the overall activity. All these factors collectively contribute to decrease in the activity of the catalyst over multiple catalytic runs.

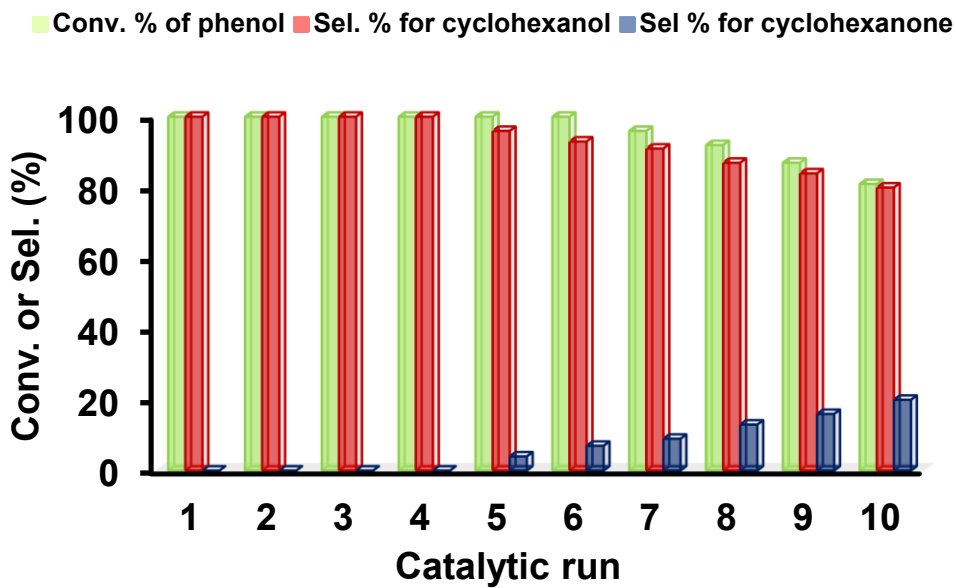


Figure E.6 Recyclability experiment for the phenol hydrogenation over Ru catalyst under optimized reaction conditions.

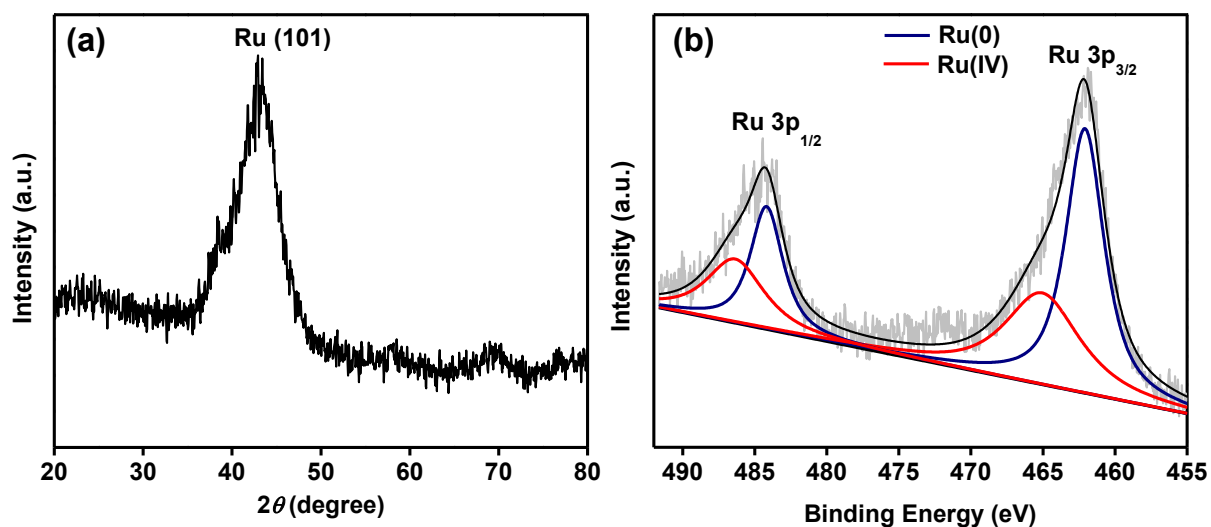


Figure E.7 (a) P-XRD pattern, and (b) XPS spectra of 3p core levels for spent Ru nanoparticles.

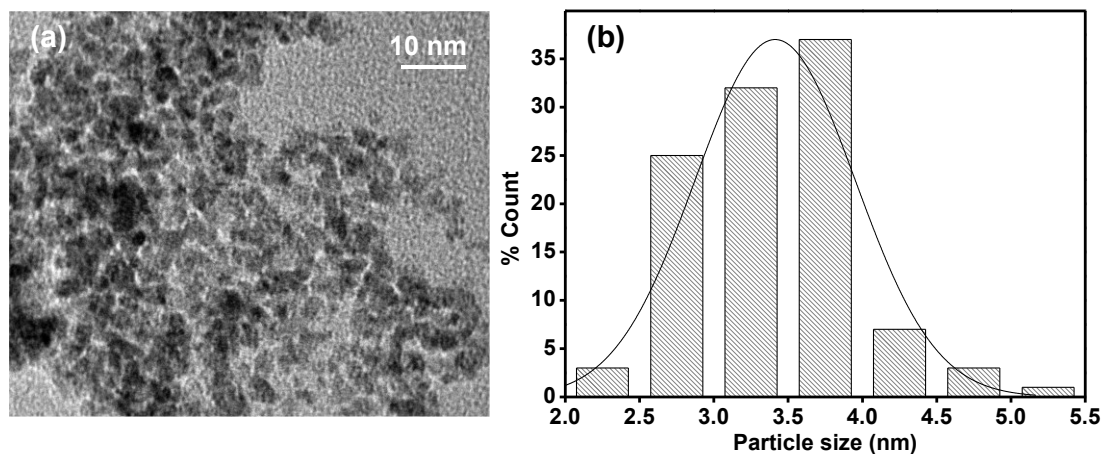


Figure E.8 (a) TEM image, and (b) corresponding particle size distribution curve for spent Ru nanoparticles.

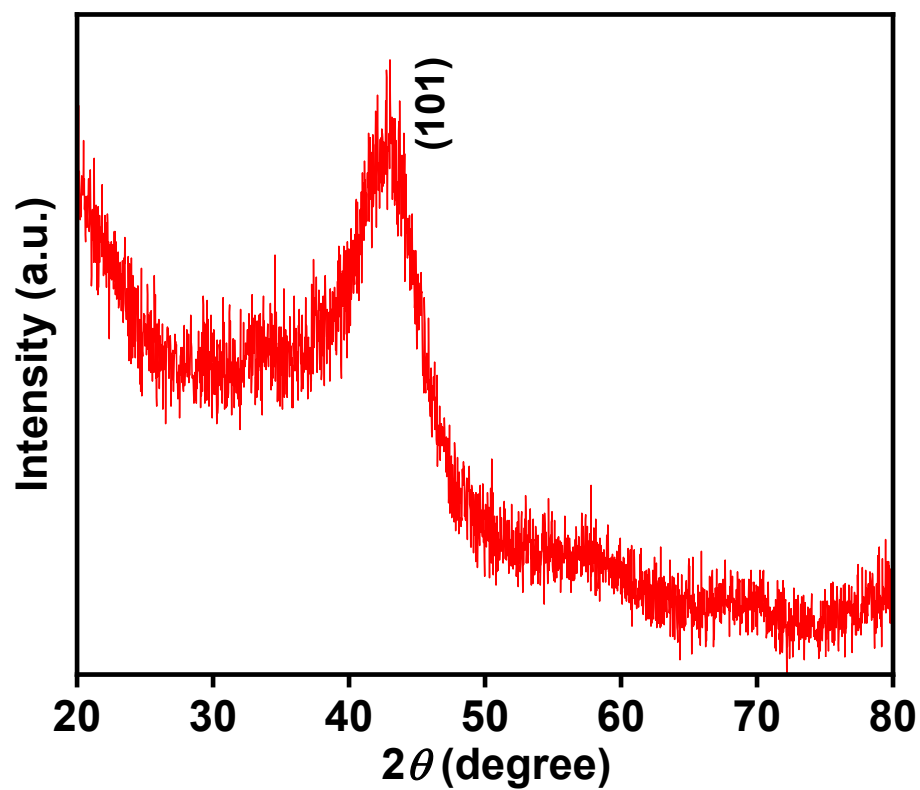
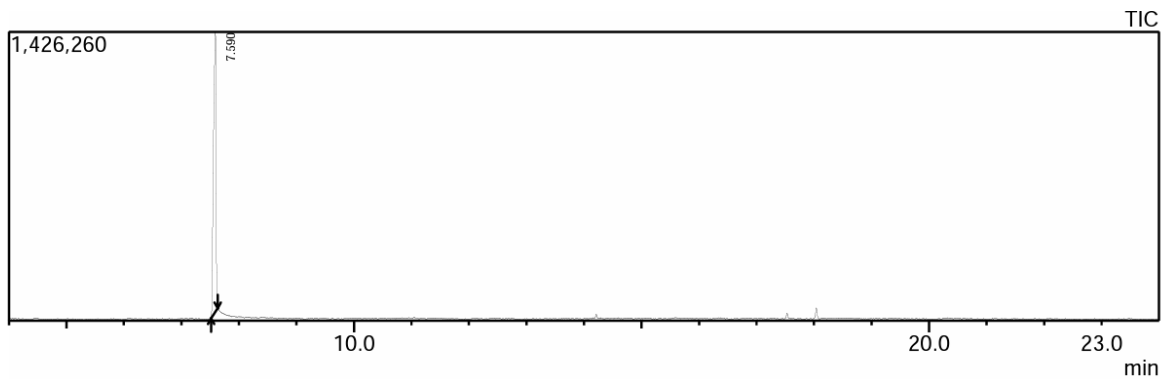


Figure E.9 PXRD of Ru catalyst (after reaction).



Peak Report TIC

Peak#	R. Time	Area	Area%	Height	Height%	A/H	Name
1	7.590	4336382	100.00	1381726	100.00	3.14	Cyclohexanol
		4336382	100.00	1381726	100.00		

Line#:1 R.Time:7.590(Scan#:719)
 MassPeaks:241
 RawMode:Averaged 7.585-7.595(718-720) BasePeak:57(370605)
 BG Mode:Calc. from Peak Group 1 - Event 1 Scan

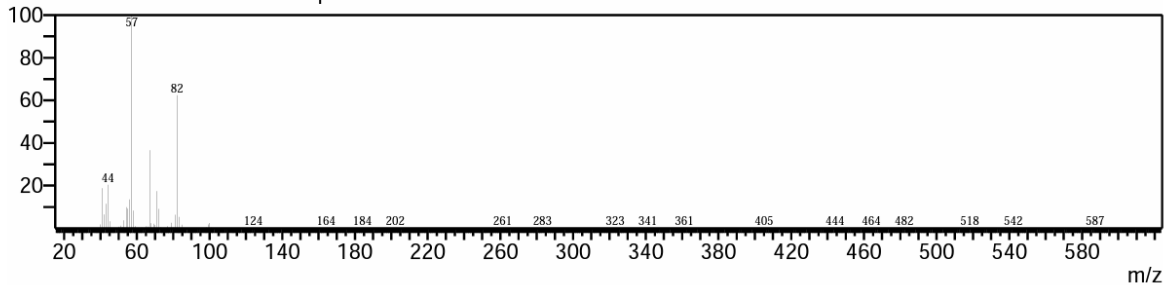
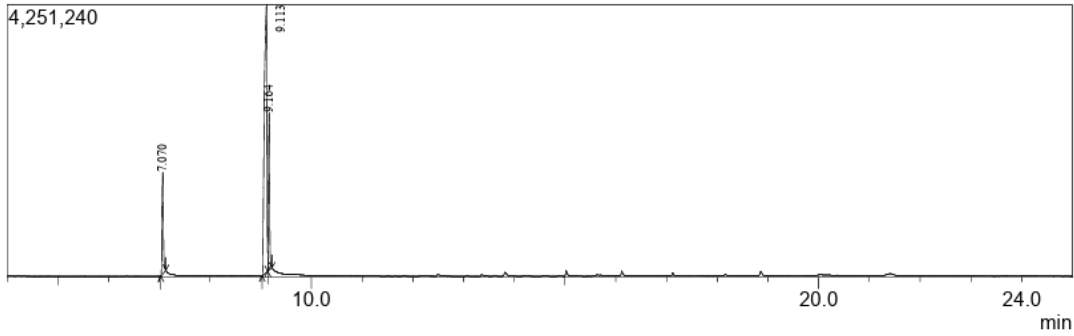


Figure E.10 GC-MS for entry 6 of table 1.



Peak Report TIC

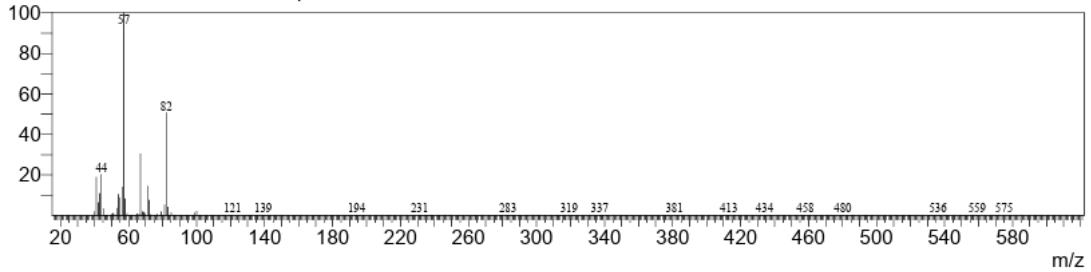
Peak#	R. Time	Area	Area%	Height	Height%	A/H	Name
1	7.070	3045530	13.71	1583960	19.29	1.92	Cyclohexanol
2	9.113	5246668	68.65	4171459	50.81	3.65	Cyclohexanol, 4-methoxy-
3	9.164	3918429	17.64	2455006	29.90	1.60	Cyclohexanol, 4-methoxy-
		22210627	100.00	8210425	100.00		

Line#1 R.Time:7.070(Scan#:615)

MassPeaks:257

RawMode:Averaged 7.065-7.075(614-616) BasePeak:57(446535)

BG Mode:Calc. from Peak Group 1 - Event 1 Scan

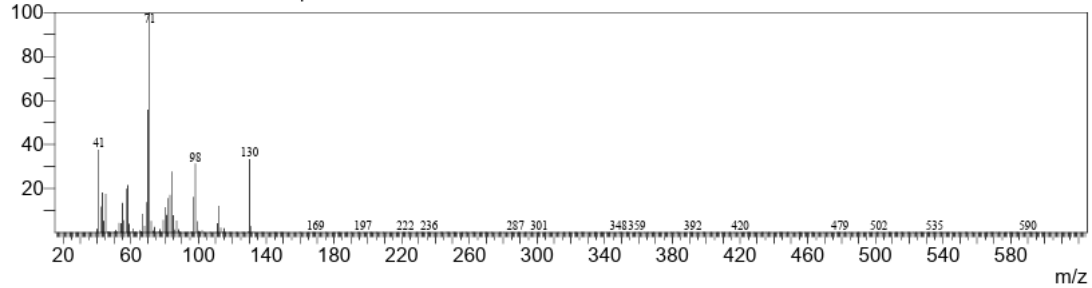


Line#2 R.Time:9.115(Scan#:1024)

MassPeaks:321

RawMode:Averaged 9.110-9.120(1023-1025) BasePeak:71(660433)

BG Mode:Calc. from Peak Group 1 - Event 1 Scan



Line#3 R.Time:9.165(Scan#:1034)

MassPeaks:336

RawMode:Averaged 9.160-9.170(1033-1035) BasePeak:71(367926)

BG Mode:Calc. from Peak Group 1 - Event 1 Scan

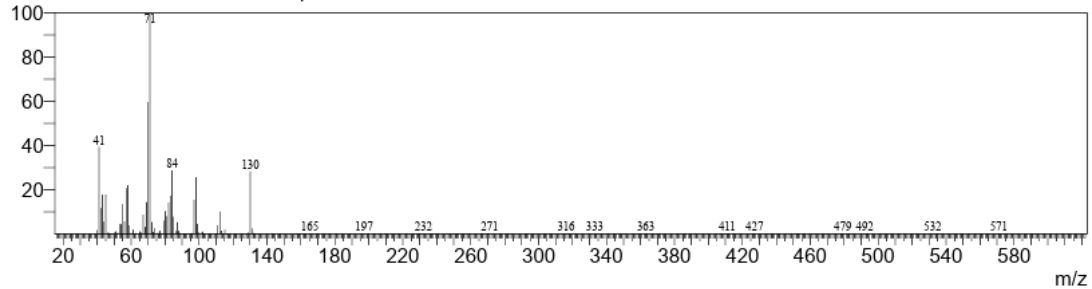
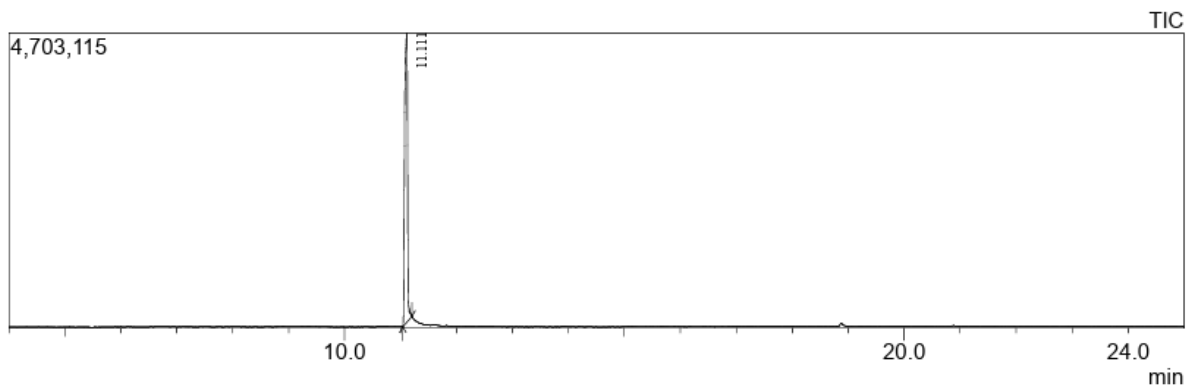


Figure E.11 GC-MS for entry 6 of table E1.



Peak Report TIC

Peak#	R.Time	Area	Area%	Height	Height%	A/H	Name
1	11.111	6537990	100.00	4605176	100.00	3.59	Cyclohexanepropanol-
		6537990	100.00	4605176	100.00		

Line#:1 R.Time:11.110(Scan#:1423)

MassPeaks:332

RawMode:Averaged 11.105-11.115(1422-1424) BasePeak:82(660075)

BG Mode:Calc. from Peak Group 1 - Event 1 Scan

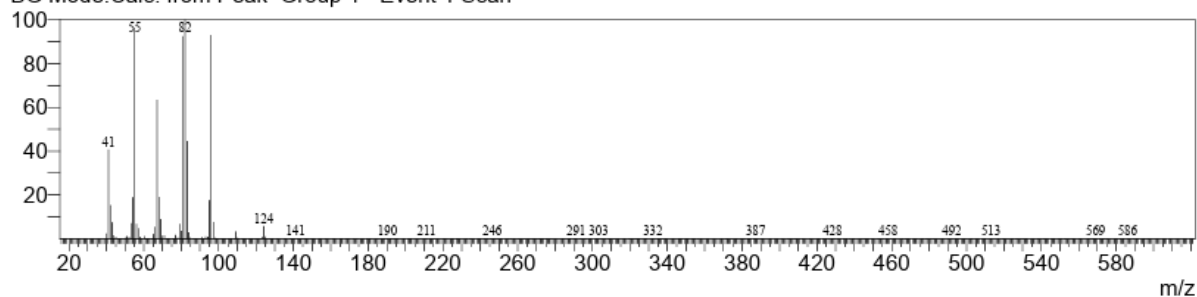
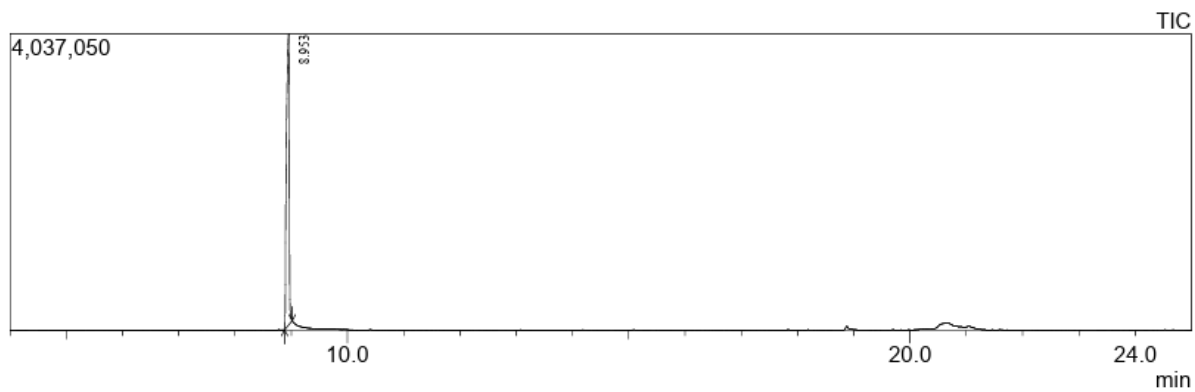


Figure E.12 GC-MS for entry 1 of table 2.



Peak Report TIC

Peak#	R. Time	Area	Area%	Height	Height%	A/H	Name
1	8.953	3299104	100.00	3957187	100.00	3.36	Cyclohexanemethanol
		3299104	100.00	3957187	100.00		

Line#:1 R. Time:8.955(Scan#:992)

MassPeaks:250

RawMode:Averaged 8.950-8.960(991-993) BasePeak:55(920364)

BG Mode:Calc. from Peak Group 1 - Event 1 Scan

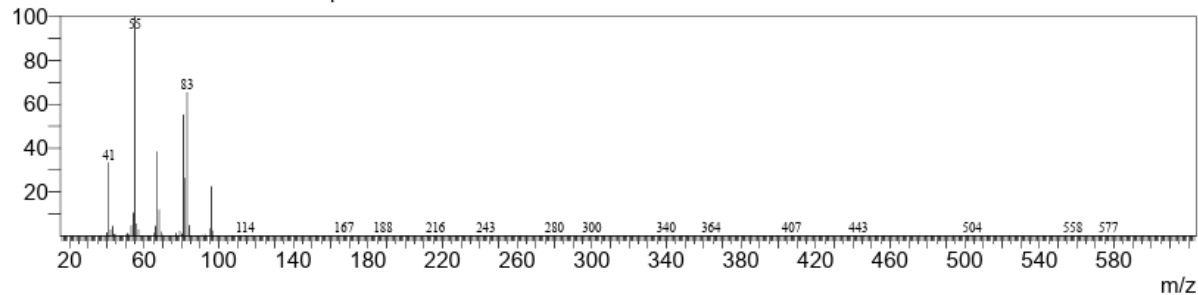
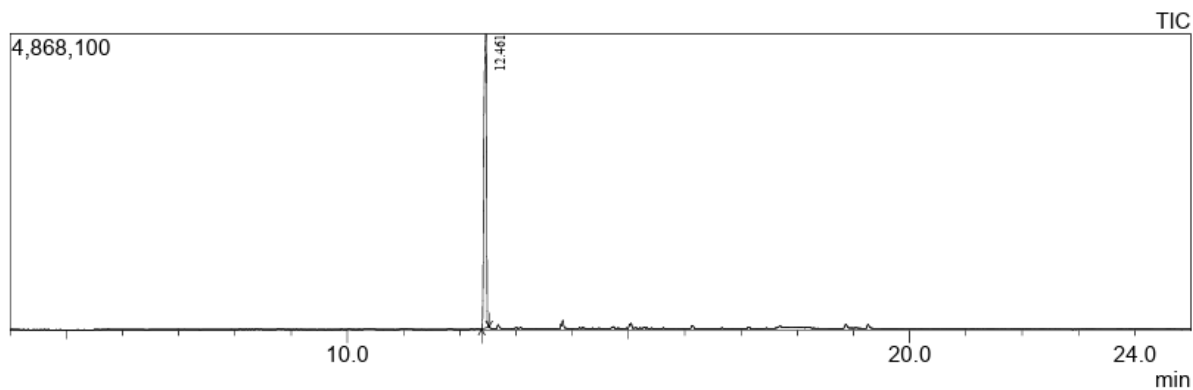


Figure E.13 GC-MS for entry 2 of table 2.



Peak Report TIC

Peak#	R.Time	Area	Area%	Height	Height%	A/H	Name
1	12.461	5113985	100.00	4819915	100.00	3.14	Cyclohexane, 1,1'-methylenebis-
		5113985	100.00	4819915	100.00		

Line#:1 R.Time:12.460(Scan#:1693)

MassPeaks:275

RawMode:Averaged 12.455-12.465(1692-1694) BasePeak:82(878022)

BG Mode:Calc. from Peak Group 1 - Event 1 Scan

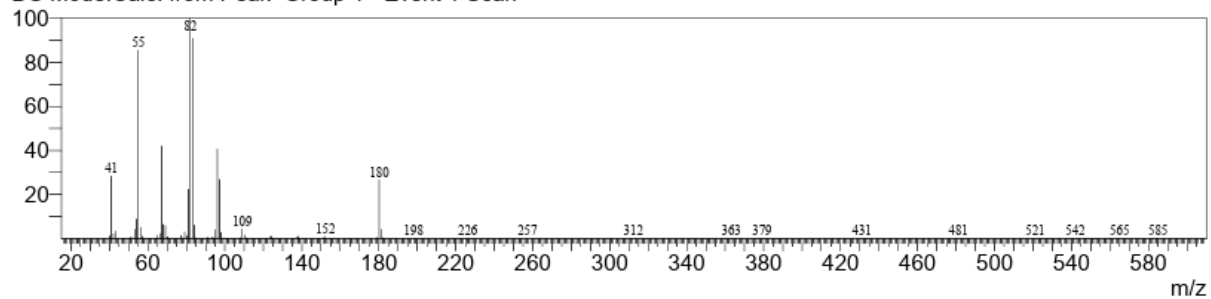
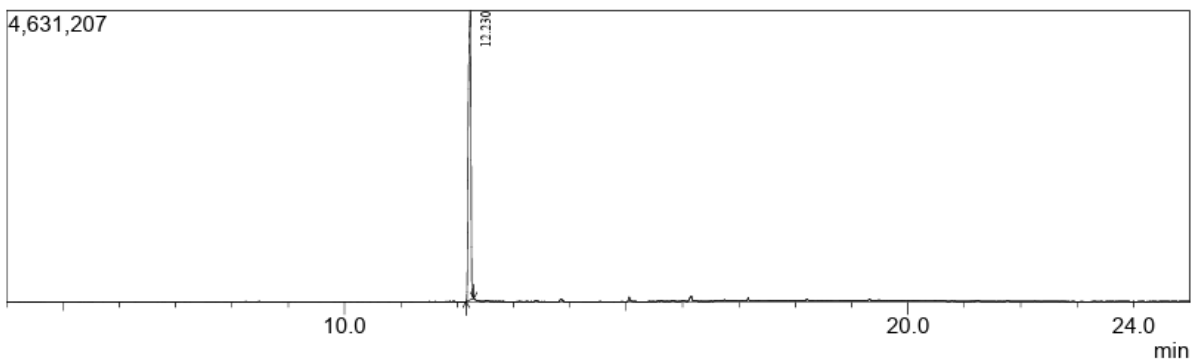


Figure E.14 GC-MS for entry 3 of table 2.



Peak Report TIC

Peak#	R.Time	Area	Area%	Height	Height%	A/H	Name
1	12.230	4122966	100.00	4587756	100.00	3.08	Cyclohexane, 1,1'-oxybis-
		4122966	100.00	4587756	100.00		

Line#:1 R.Time:12.230(Scan#:1647)

MassPeaks:349

RawMode:Averaged 12.225-12.235(1646-1648) BasePeak:100(784426)

BG Mode:Calc. from Peak Group 1 - Event 1 Scan

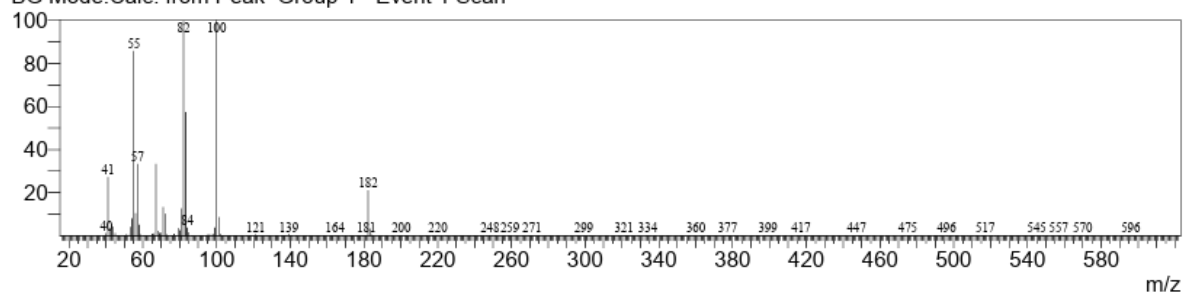
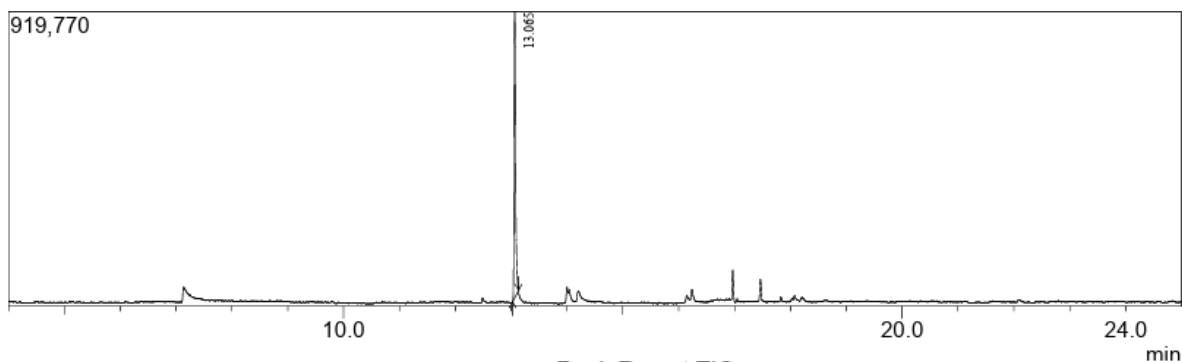


Figure E.15 GC-MS for entry 4 of table 2



Peak Report TIC

Peak#	R.Time	Area	Area%	Height	Height%	A/H	Name
1	13.065	1568946	100.00	892973	100.00	1.76	cyclohexylmethoxy cyclohexane
		1568946	100.00	892973	100.00		

Line#:1 R.Time:13.065(Scan#:1814)

MassPeaks:280

RawMode:Averaged 13.060-13.070(1813-1815) BasePeak:55(160277)

BG Mode:Calc. from Peak Group 1 - Event 1 Scan

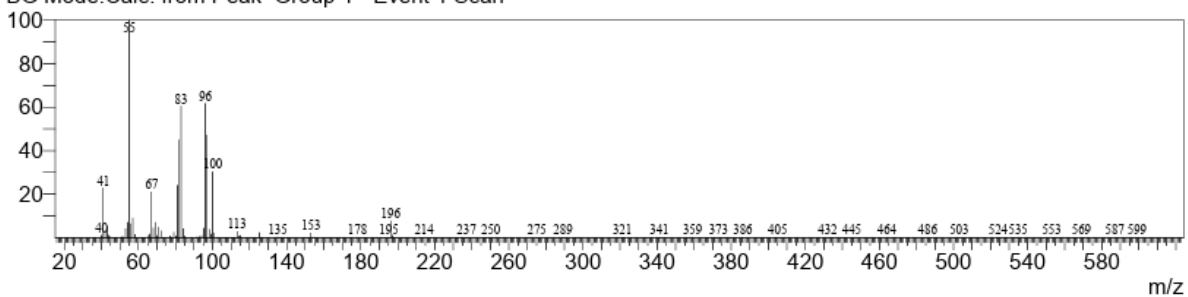
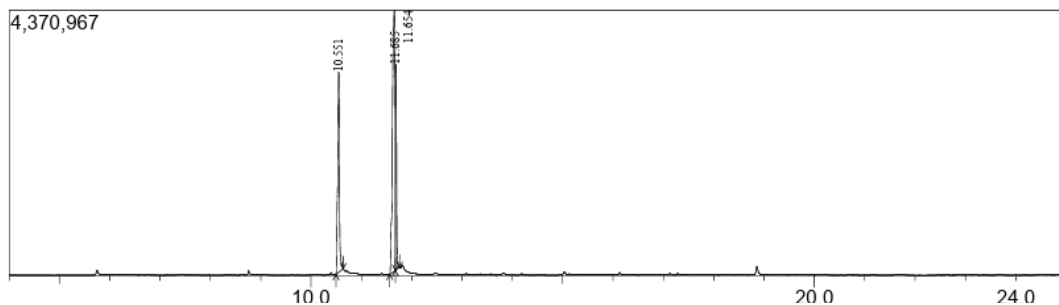


Figure E.16 GC-MS for entry 5 of table 2.



Peak Report TIC

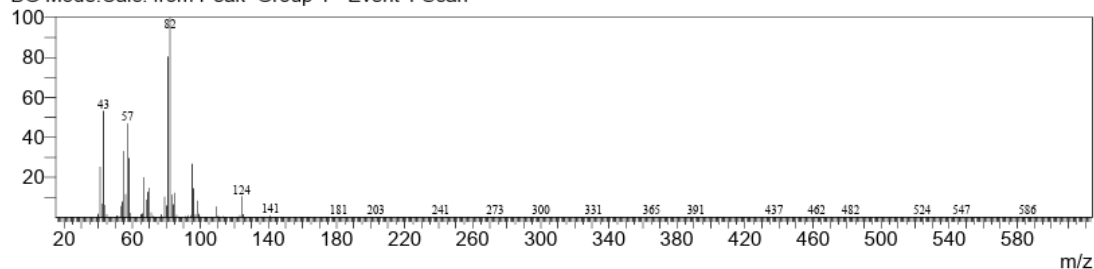
Peak#	R.Time	Area	Area%	Height	Height%	A/H	Name
1	10.551	8167151	29.36	3293846	30.06	2.48	Cyclohexanol, (4-propyl)
2	11.654	5376232	55.28	4285681	39.12	3.59	2-methoxy, 4-propyl cyclohexanol
3	11.685	4273171	15.36	3376663	30.82	1.27	2-methoxy, 4-propyl cyclohexanol
		7816554	100.00	10956190	100.00		

Line#:1 R.Time:10.550(Scan#:1311)

MassPeaks:281

RawMode:Averaged 10.545-10.555(1310-1312) BasePeak:82(530874)

BG Mode:Calc. from Peak Group 1 - Event 1 Scan

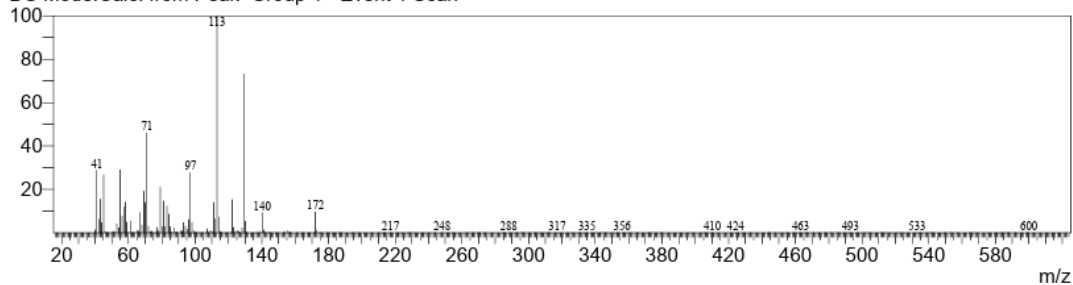


Line#:2 R.Time:11.655(Scan#:1532)

MassPeaks:311

RawMode:Averaged 11.650-11.660(1531-1533) BasePeak:113(321493)

BG Mode:Calc. from Peak Group 1 - Event 1 Scan



Line#:3 R.Time:11.685(Scan#:1538)

MassPeaks:379

RawMode:Averaged 11.680-11.690(1537-1539) BasePeak:113(138186)

BG Mode:Calc. from Peak Group 1 - Event 1 Scan

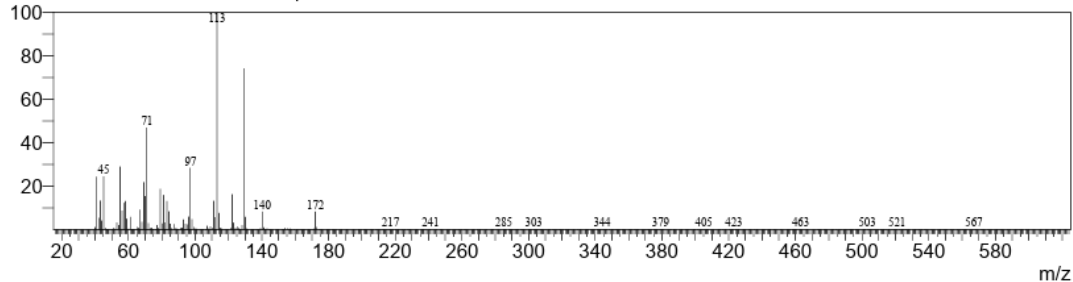


Figure E.17 GC-MS for entry 6 of table 2.

E.5 Computational Data – Transition State and Adsorption Configurations

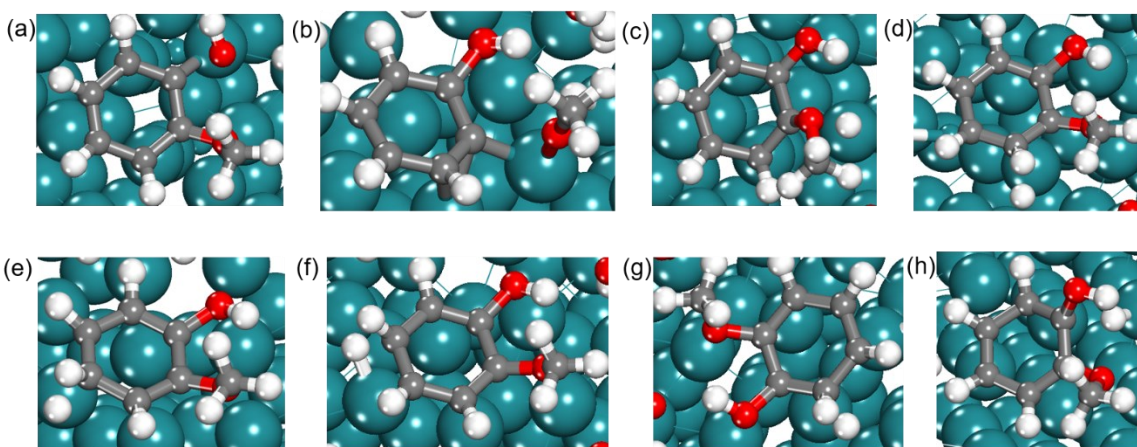


Figure E.18 Optimized geometries of transition state structures for first activation of guaiacol for considered reactions on the Ru (101) surface in the presence of co-adsorbed partially dissociated water molecules (a) C^7 -O dissociation, (b) C^2 -O dissociation, (c) hydrogenation at C^2 carbon, (d) hydrogenation at C^3 carbon, (e) hydrogenation at C^4 carbon, (f) hydrogenation at C^5 carbon, (g) hydrogenation at C^6 carbon, and (h) hydrogenation at C^7 carbon. The atoms in the adsorbed guaiacol is represented by white, red, and grey spheres for H, O, and C, respectively and Ru atoms are shown in green color.

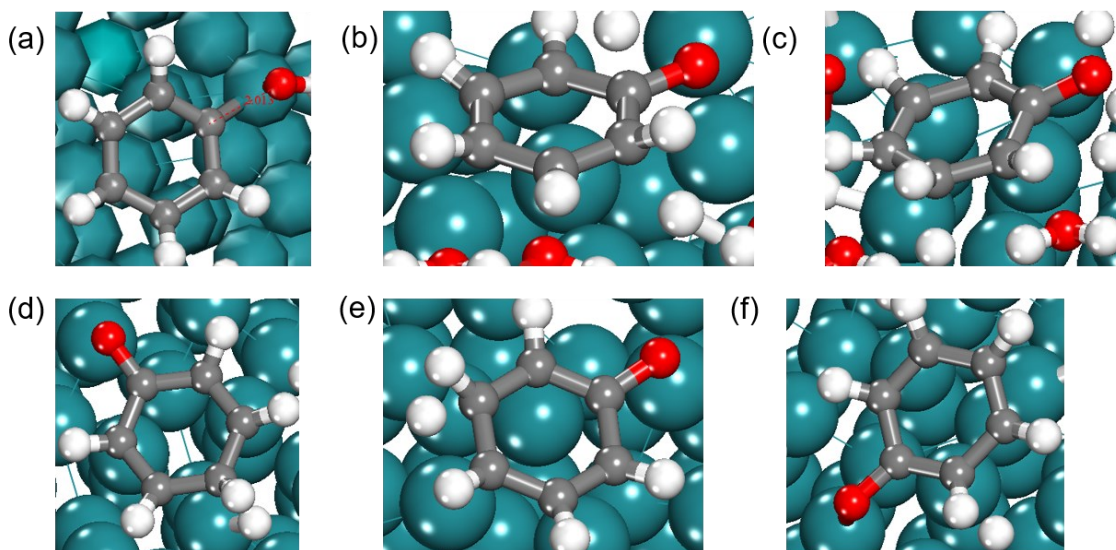


Figure E.19 Optimized geometries of transition state structures for first activation of phenol for considered reactions on the Ru (101) surface in the presence of co-adsorbed partially dissociated water molecules (a) C^7 - O dissociation, (b) hydrogenation at C^2 carbon, (c) hydrogenation at C^3 carbon, (d) hydrogenation at C^4 carbon, (e) hydrogenation at C^5 carbon, and (f) hydrogenation at C^6 carbon. The atoms in the adsorbed phenol is represented by white, red, and grey spheres for H, O, and C, respectively and Ru atoms are shown in green color.

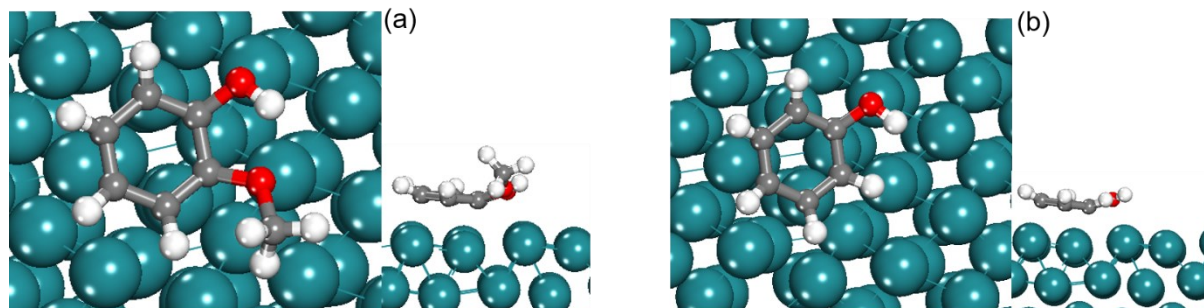


Figure E.20 Optimized geometries of adsorption configuration of (a) guaiacol, and (b) phenol on the Ru (101) surface in the absence of co-adsorbed partially dissociated water molecules. The atoms in the adsorbed guaiacol and phenol is represented by white, red, and grey spheres for H, O, and C, respectively and Ru atoms are shown in green color.

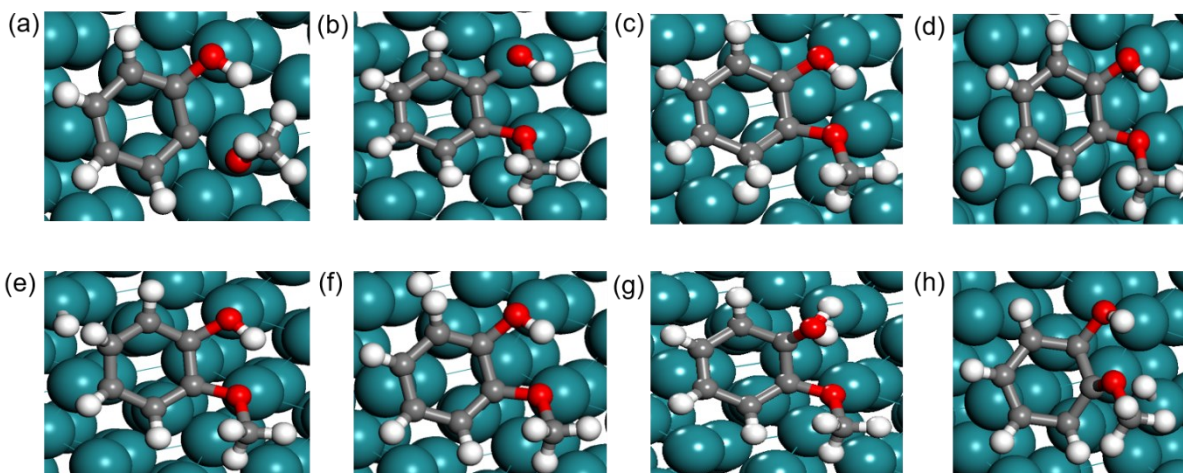


Figure E.21 Optimized geometries of transition state structures for first activation of guaiacol for considered reactions on the Ru (101) surface in the absence of co-adsorbed partially dissociated water molecules (a) C^2-O dissociation, (b) C^7-O dissociation, (c) hydrogenation at C^3 carbon, (d) hydrogenation at C^4 carbon, (e) hydrogenation at C^5 carbon, (f) hydrogenation at C^6 carbon, (g) hydrogenation at C^7 carbon, and (h) hydrogenation at C^2 carbon. The atoms in the adsorbed guaiacol are represented by white, red, and grey spheres for H, O, and C, respectively and Ru atoms are shown in green color.

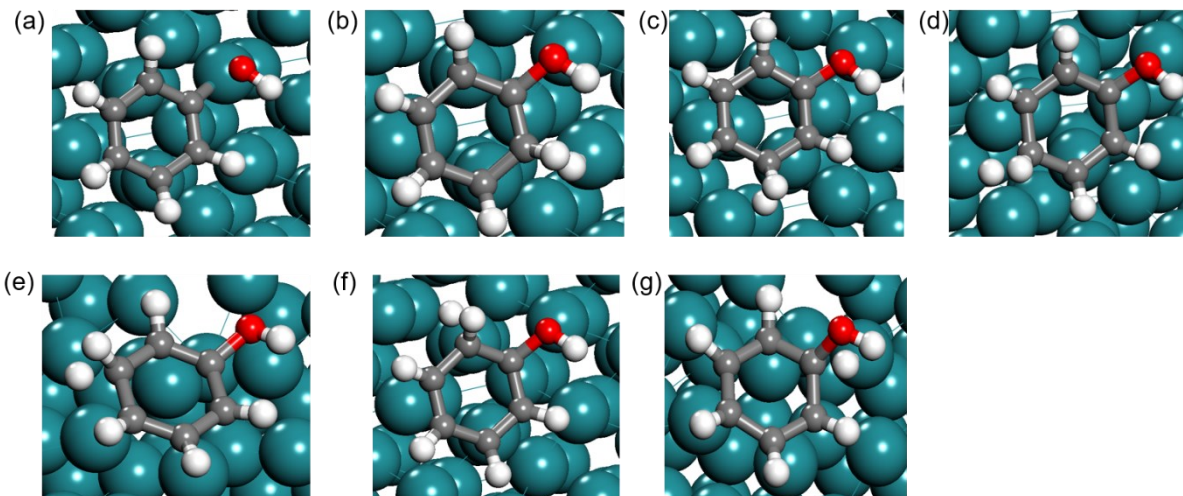


Figure E.22 Optimized geometries of transition state structures for first activation of phenol for considered reactions on the Ru (101) surface in the absence of co-adsorbed partially dissociated water molecules (a) C^7-O dissociation, (b) hydrogenation at C^2 carbon, (c) hydrogenation at C^3 carbon, (d) hydrogenation at C^4 carbon, (e) hydrogenation at C^5 carbon, (f) hydrogenation at C^6 carbon, and (g) hydrogenation at C^7 carbon. The atoms in the adsorbed phenol are represented by white, red, and grey spheres for H, O, and C, respectively and Ru atoms are shown in green color.

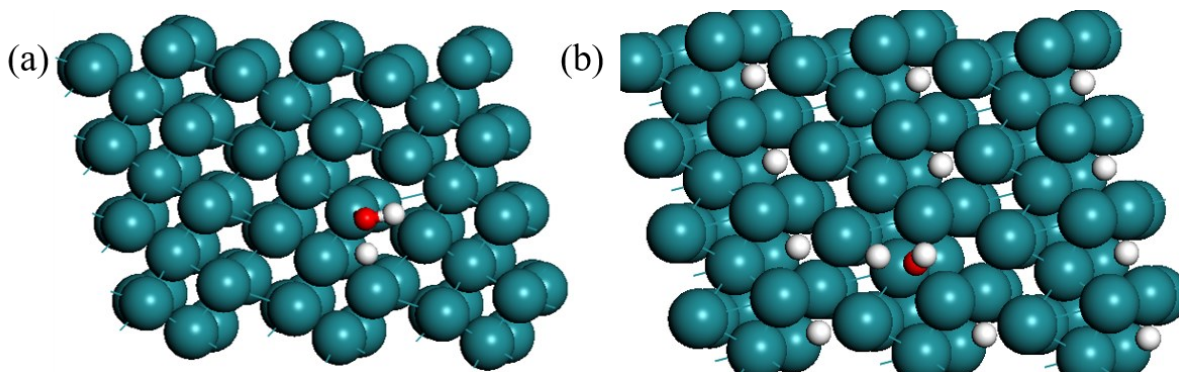


Figure E.23 Optimized geometries of transition state structures for water dissociation ($H_2O \rightarrow H^* + OH^*$) on the Ru (1 0 1) surface (a) in the absence of co-adsorbed hydrogen (b) on the H-pre-covered Ru surface. The atoms in the adsorbed water are represented by white, red, spheres for H, and O, respectively and Ru atoms are shown in green color.

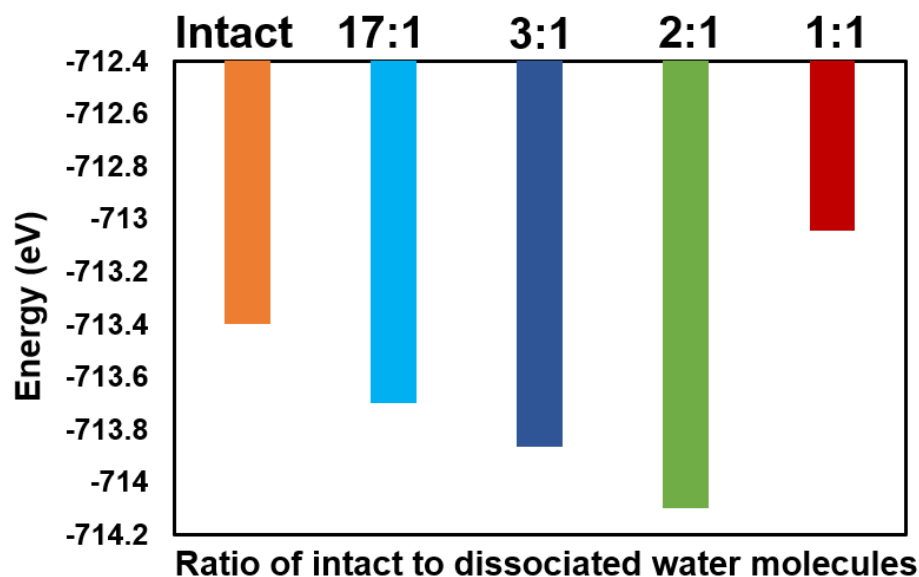


Figure E.24 Comparison of relative stability of five configurations with different ratios of intact water molecules to partially dissociated water molecules on the Ru (101) surface.

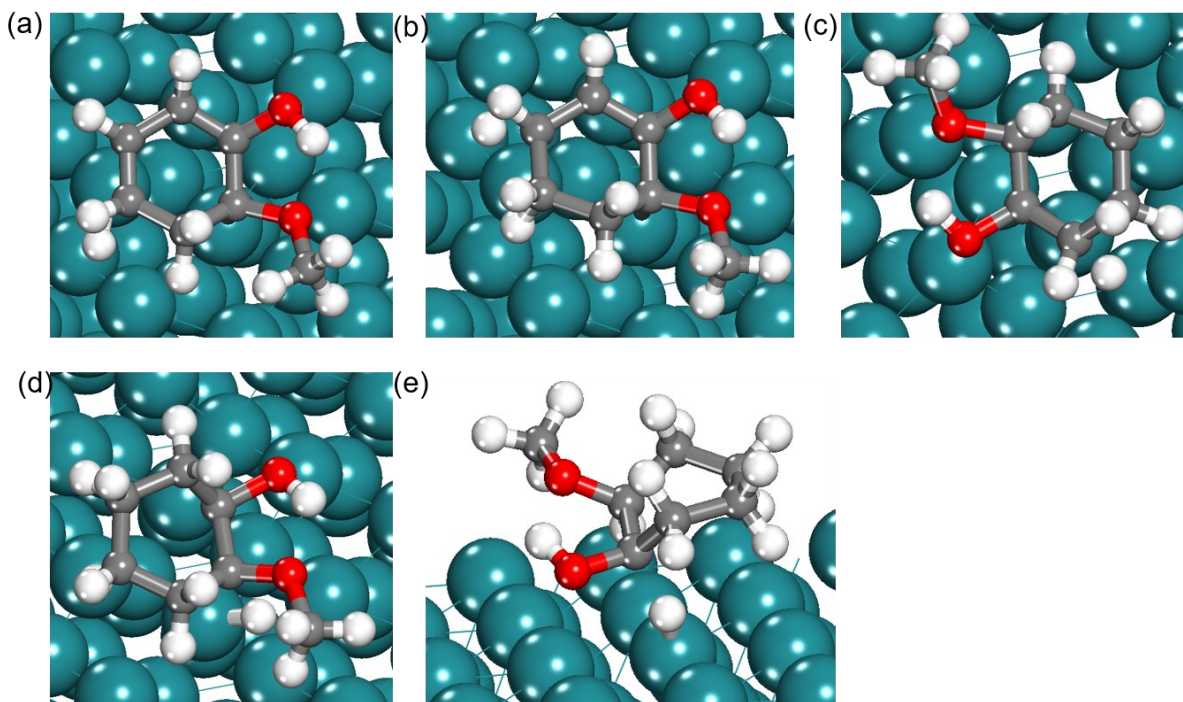


Figure E.25 Optimized geometries of transition state structures for subsequent of guaiacol for considered reactions on the Ru (101) surface in the absence of co-adsorbed partially dissociated water molecules (a) 2nd hydrogenation step, (b) 3rd hydrogenation step, (c) 4th hydrogenation step, (d) 5th hydrogenation, (e) 6th hydrogenation step. The atoms in the adsorbed phenol are represented by white, red, and grey spheres for H, O, and C, respectively and Ru atoms are shown in green color.

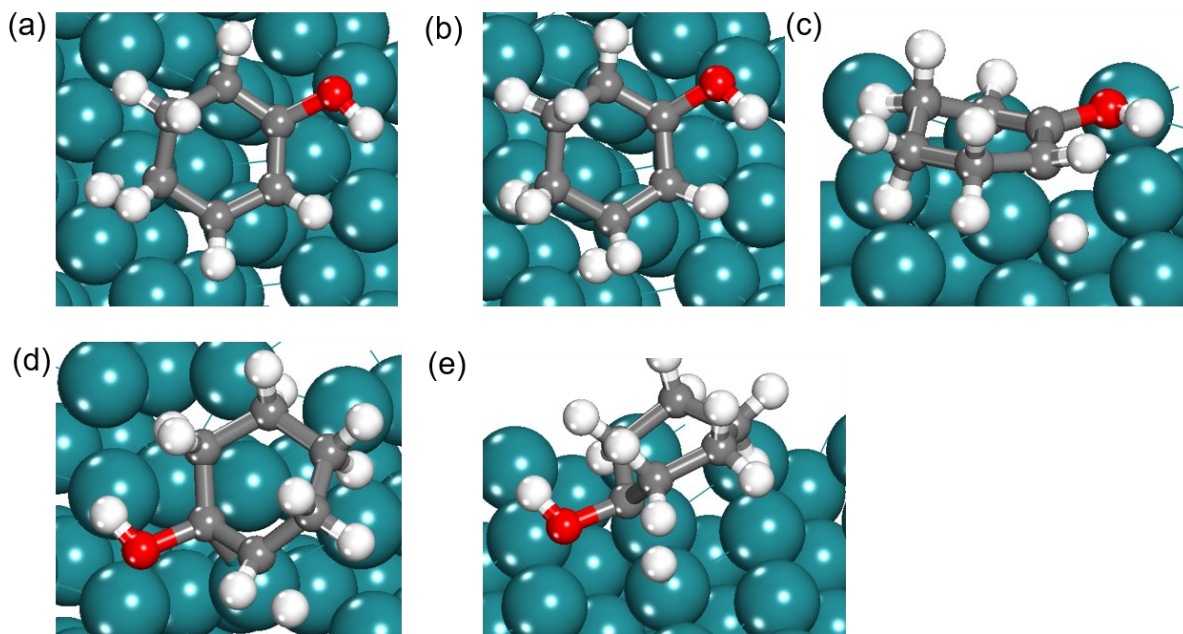


Figure E.26 Optimized geometries of transition state structures for subsequent of phenol for considered reactions on the Ru (101) surface in the absence of co-adsorbed partially dissociated water molecules (a) 2nd hydrogenation step, (b) 3rd hydrogenation step, (c) 4th hydrogenation step, (d) 5th hydrogenation, (e) 6th hydrogenation step. The atoms in the adsorbed phenol are represented by white, red, and grey spheres for H, O, and C, respectively and Ru atoms are shown in green color.

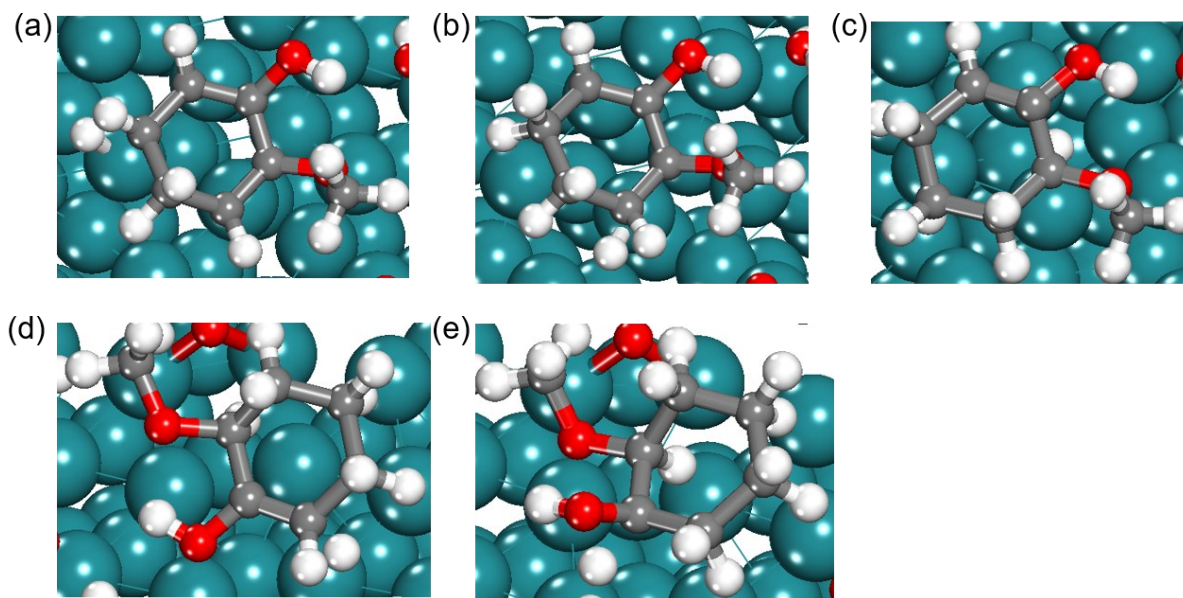


Figure E.27 Optimized geometries of transition state structures for subsequent of guaiacol for considered reactions on the Ru (101) surface in the presence of co-adsorbed partially dissociated water molecules (a) 2nd hydrogenation step, (b) 3rd hydrogenation step, (c) 4th hydrogenation step, (d) 5th hydrogenation, (e) 6th hydrogenation step. The atoms in the adsorbed guaiacol are

represented by white, red, and grey spheres for H, O, and C, respectively and Ru atoms are shown in green color.

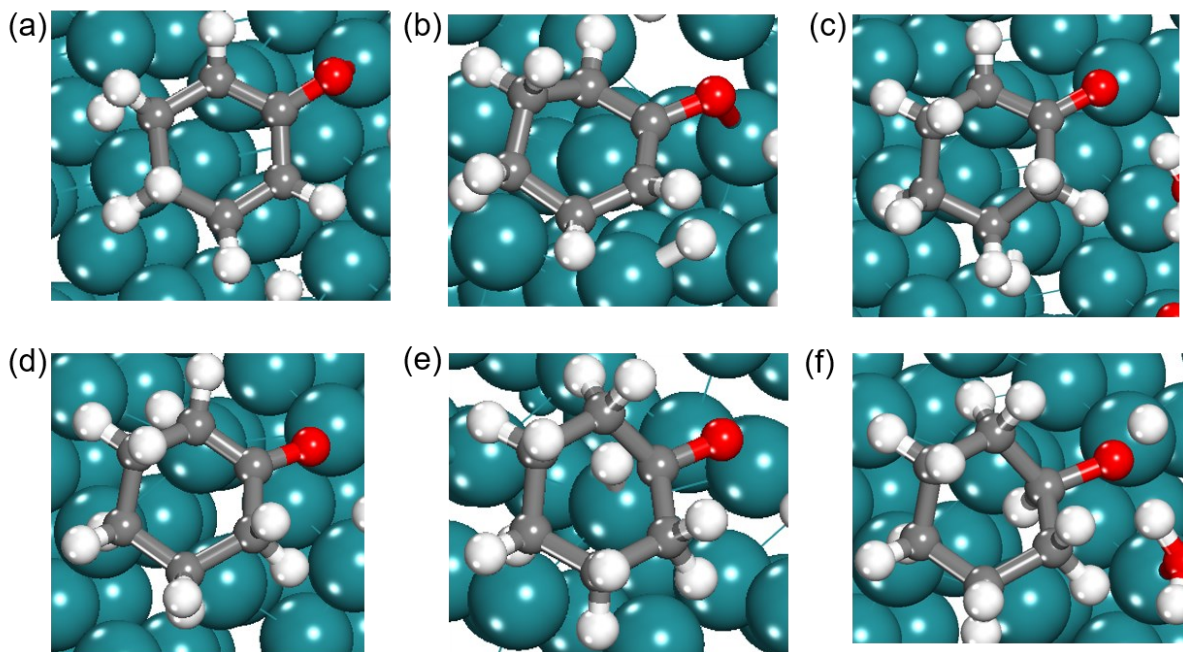
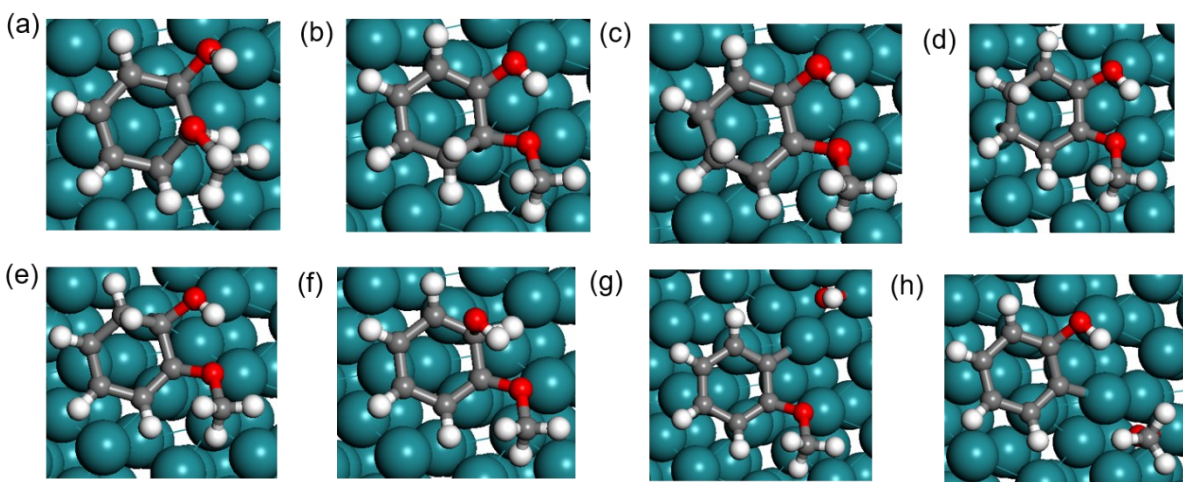


Figure E.28 Optimized geometries of transition state structures for subsequent of phenol for considered reactions on the Ru (101) surface in the presence of co-adsorbed partially dissociated water molecules (a) 2nd hydrogenation step, (b) 3rd hydrogenation step, (c) 4th hydrogenation step, (d) 5th hydrogenation, (e) 6th hydrogenation step, and (f) cyclohexanol formation reaction step. The atoms in the adsorbed phenol are represented by white, red, and grey spheres for H, O, and C, respectively and Ru atoms are shown in green color.



Figure_Apx E.29 Optimized geometries of intermediates obtained for first activation of guaiacol for considered reactions on the Ru (101) surface in the absence of co-adsorbed partially dissociated water molecules (a) hydrogenation at C² carbon, (b) hydrogenation at C³ carbon, (c)

hydrogenation at C⁴ carbon, (d) hydrogenation at C⁵ carbon, (e) hydrogenation at C⁶ carbon, (f) hydrogenation at C⁷ carbon, (g) C⁷-O dissociation, and (h) C²-O dissociation. The atoms in the adsorbed phenol are represented by white, red, and grey spheres for H, O, and C, respectively and Ru atoms are shown in green color.

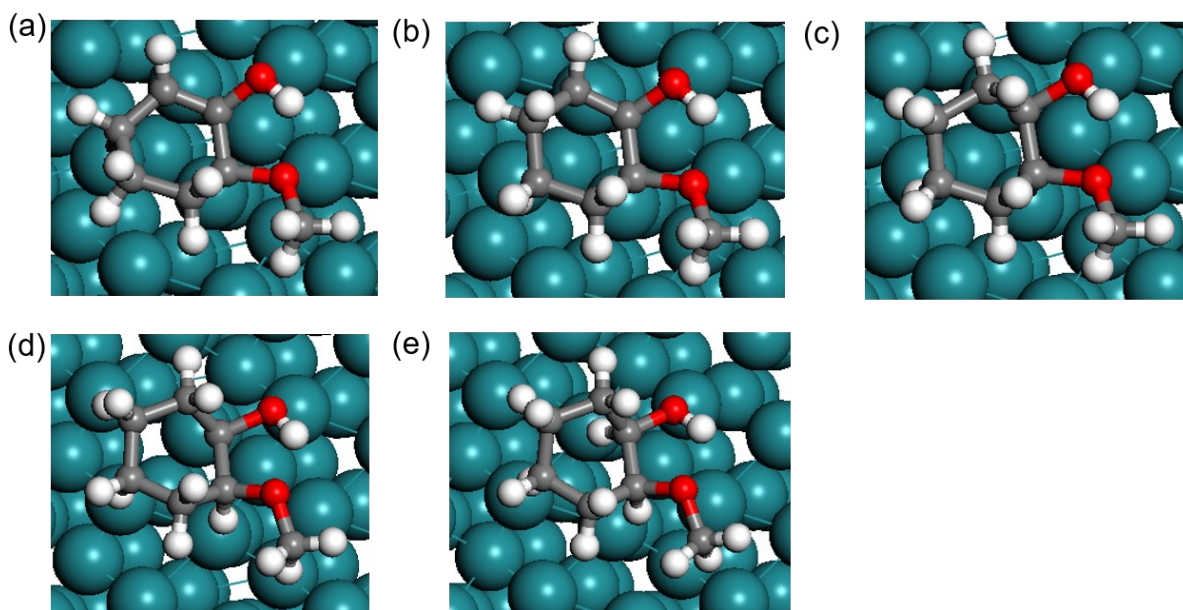


Figure E.30 Optimized geometries of intermediates for subsequent of guaiacol for considered reactions on the Ru (101) surface in the absence of co-adsorbed partially dissociated water molecules (a) 2nd hydrogenation step, (b) 3rd hydrogenation step, (c) 4th hydrogenation step, (d) 5th hydrogenation, (e) 6th hydrogenation step. The atoms in the adsorbed guaiacol are represented by white, red, and grey spheres for H, O, and C, respectively and Ru atoms are shown in green color.

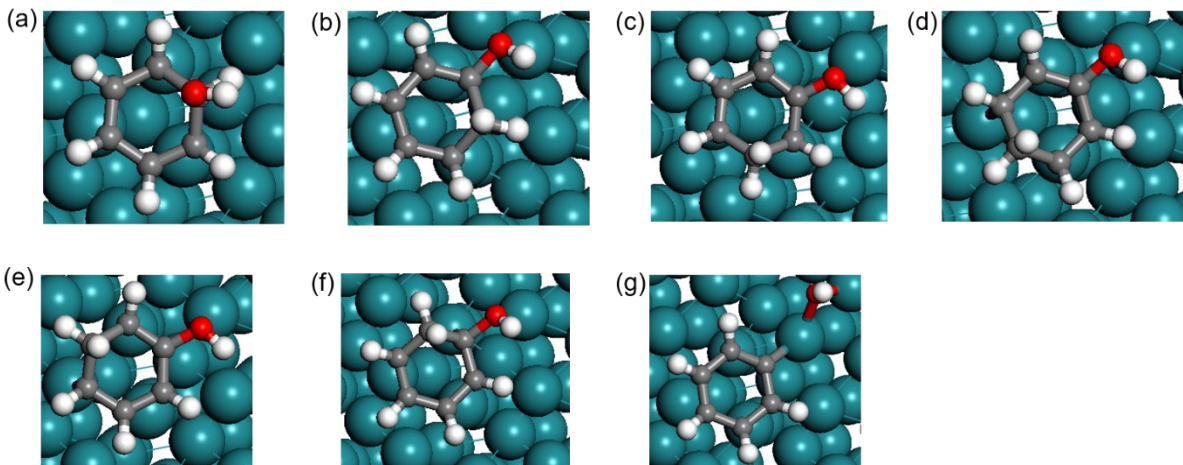


Figure E.31 Optimized geometries of intermediates for first activation of phenol for considered reactions on the Ru (101) surface in the absence of co-adsorbed partially dissociated water molecules (a) hydrogenation at C1 carbon, (b) hydrogenation at C2 carbon, (c) hydrogenation at C3 carbon, (d) hydrogenation at C4 carbon, (e) hydrogenation at C5 carbon, (f) hydrogenation at C6 carbon, and (g) C7–O dissociation. The atoms in the adsorbed phenol are represented by white, red, and grey spheres for H, O, and C, respectively and Ru atoms are shown in green color.

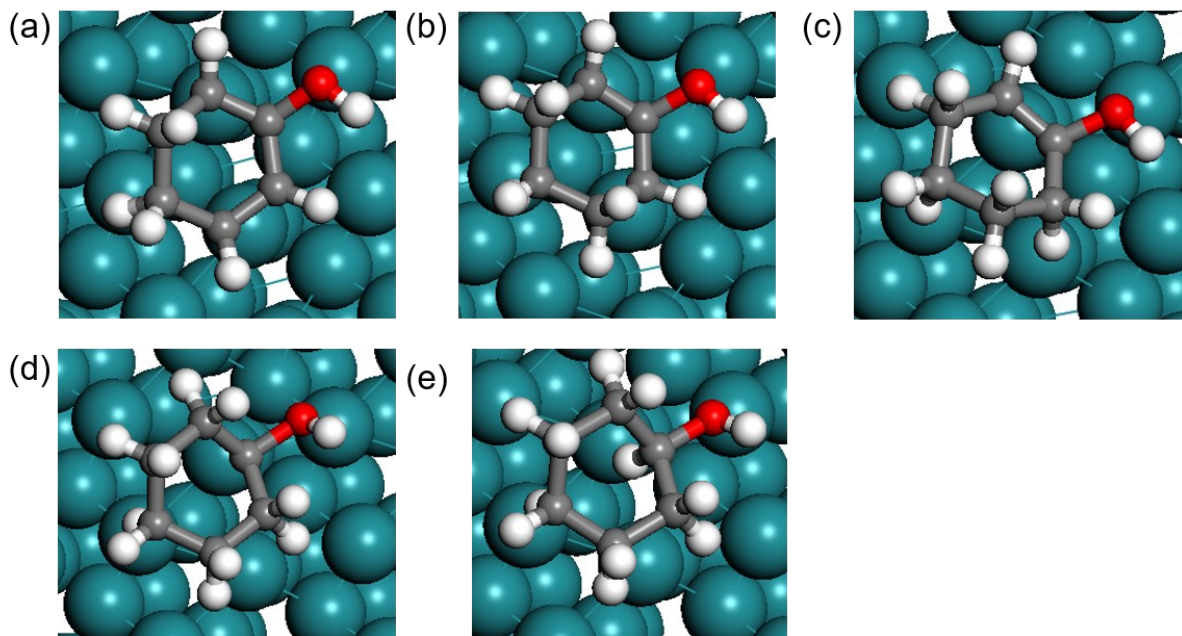


Figure E.32 Optimized geometries of intermediates for subsequent of phenol for considered reactions on the Ru (101) surface in the absence of co-adsorbed partially dissociated water molecules (a) 2nd hydrogenation step, (b) 3rd hydrogenation step, (c) 4th hydrogenation step, (d) 5th hydrogenation, (e) 6th hydrogenation step. The atoms in the adsorbed phenol are represented by white, red, and grey spheres for H, O, and C respectively and Ru atoms are shown in green color.

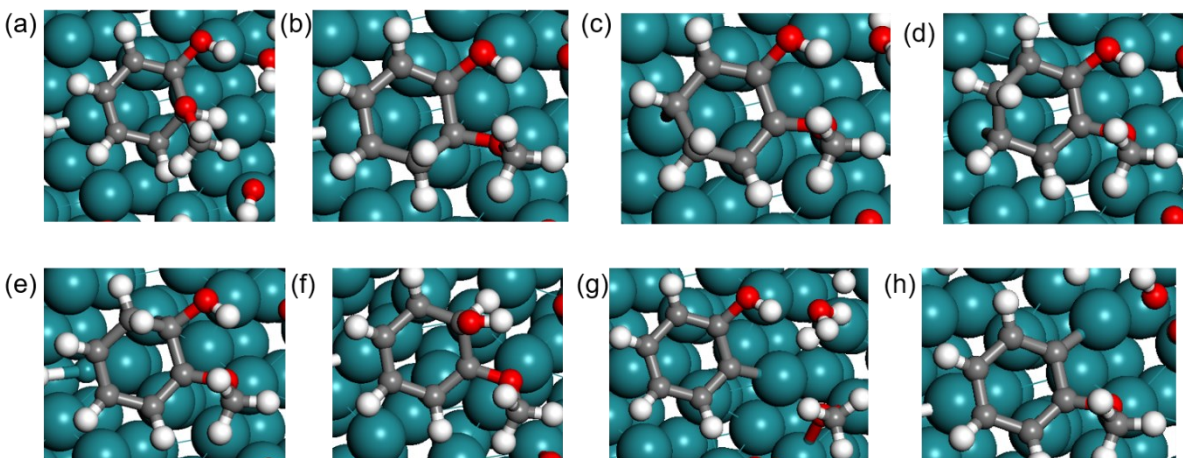


Figure E.33 Optimized geometries of intermediates obtained for first activation of guaiacol for considered reactions on the Ru (101) surface in the presence of co-adsorbed partially dissociated water molecules (a) hydrogenation at C² carbon, (b) hydrogenation at C³ carbon, (c) hydrogenation at C⁴ carbon, (d) hydrogenation at C⁵ carbon, (e) hydrogenation at C⁶ carbon, (f) hydrogenation at C⁷ carbon, (g) C⁷-O dissociation, and (h) C²-O dissociation. The atoms in the adsorbed phenol are represented by white, red, and grey spheres for H, O, and C, respectively and Ru atoms are shown in green color.

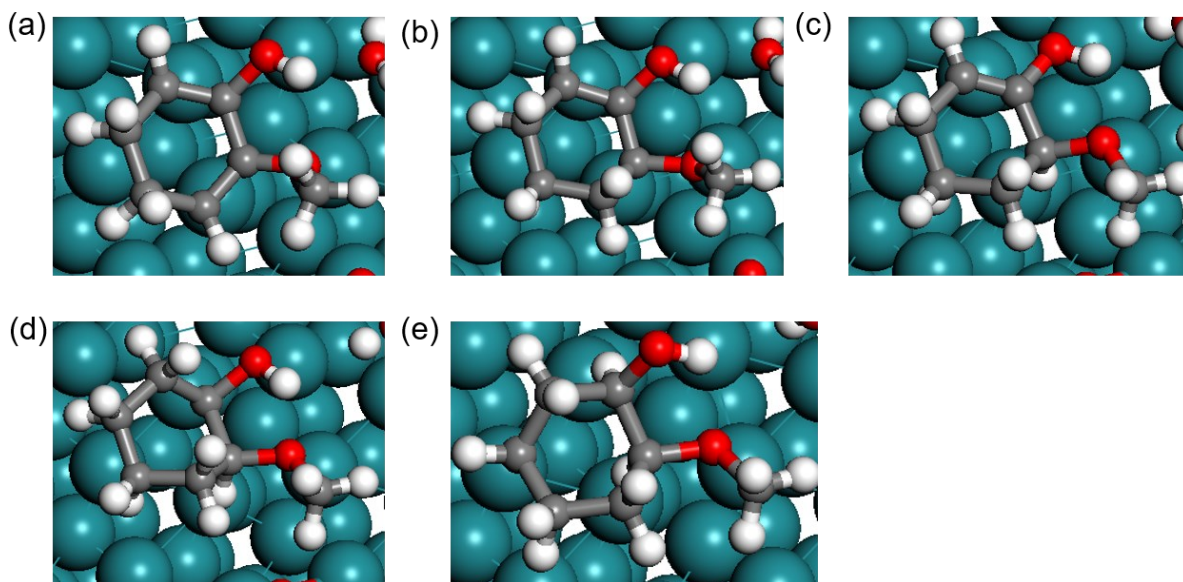


Figure E.34 Optimized geometries of intermediates for subsequent of guaiacol for considered reactions on the Ru (101) surface in the presence of co-adsorbed partially dissociated water molecules (a) 2nd hydrogenation step, (b) 3rd hydrogenation step, (c) 4th hydrogenation step, (d) 5th hydrogenation, (e) 6th hydrogenation step. The atoms in the adsorbed guaiacol are represented by white, red, and grey spheres for H, O, and C, respectively and Ru atoms are shown in green color.

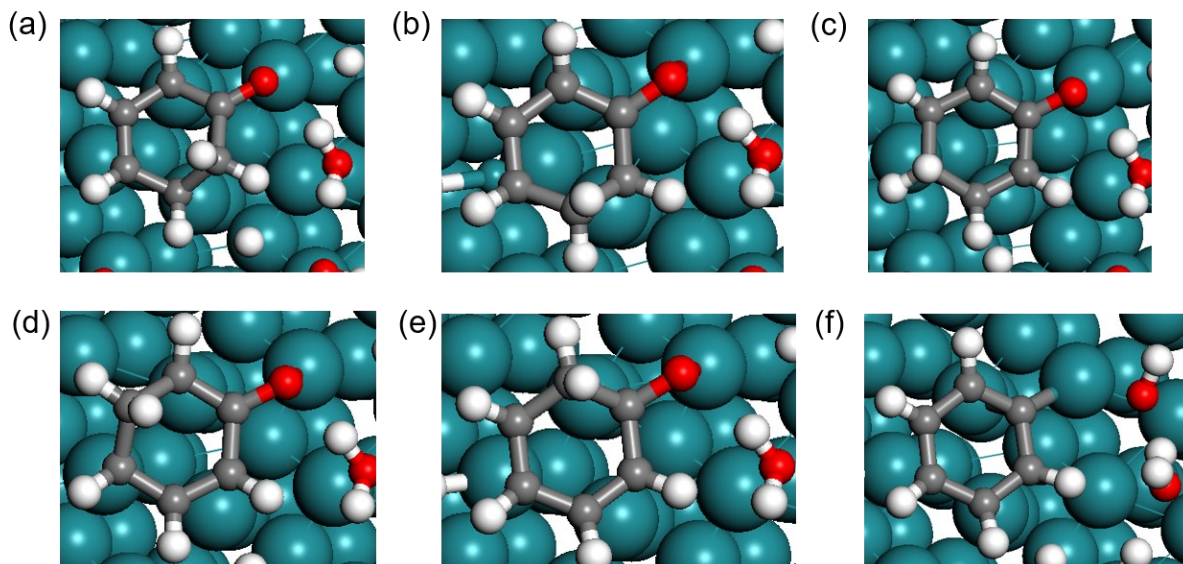


Figure E.35 Optimized geometries of intermediates for first activation of phenol for considered reactions on the Ru (101) surface in the presence of co-adsorbed partially dissociated water molecules (a) hydrogenation at C^1 carbon, (b) hydrogenation at C^2 carbon, (c) hydrogenation at

C³ carbon, (d) hydrogenation at C⁴ carbon, (e) hydrogenation at C⁵ carbon, (f) hydrogenation at C⁶ carbon, and (g) C⁷-O dissociation. The atoms in the adsorbed phenol are represented by white, red, and grey spheres for H, O, and C, respectively and Ru atoms are shown in green color.

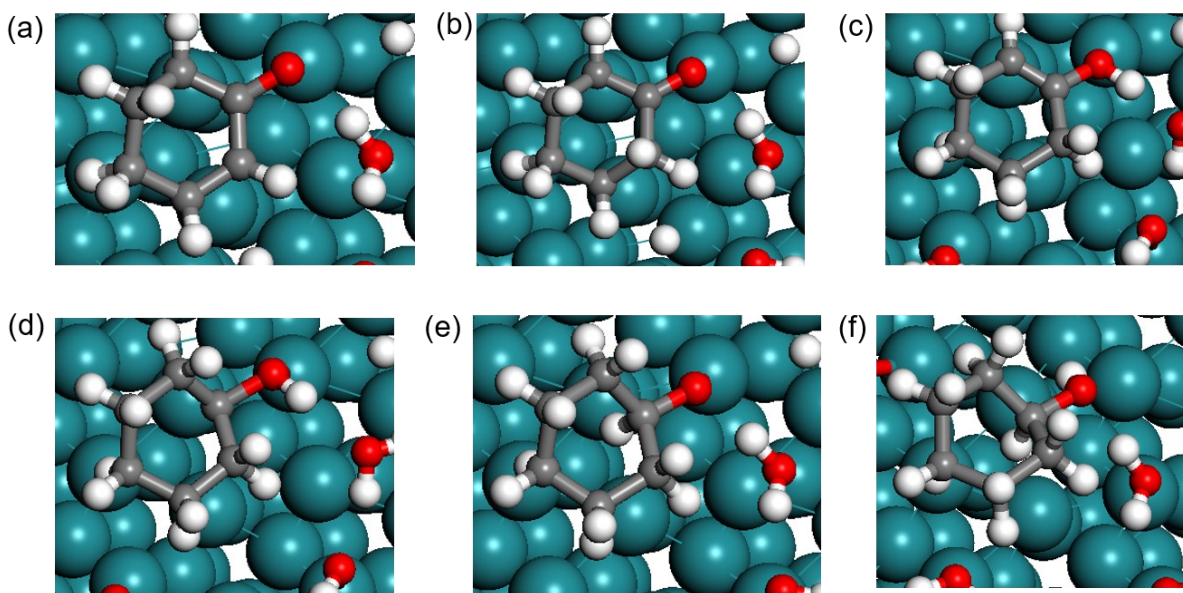


Figure E.36 Optimized geometries of intermediates for subsequent of phenol for considered reactions on the Ru (101) surface in the absence of co-adsorbed partially dissociated water molecules (a) 2nd hydrogenation step, (b) 3rd hydrogenation step, (c) 4th hydrogenation step, (d) 5th hydrogenation, (e) 6th hydrogenation step. The atoms in the adsorbed phenol are represented by white, red, and grey spheres for H, O, and C, respectively and Ru atoms are shown in green color.

Bibliography

- (1) Schrödinger, E. An Undulatory Theory of the Mechanics of Atoms and Molecules. *Phys. Rev.* **1926**, 28 (6), 1049–1070. <https://doi.org/10.1103/PhysRev.28.1049>.
- (2) Kohn, W.; Sham, L. J. Self-Consistent Equations Including Exchange and Correlation Effects. *Phys. Rev.* **1965**, 140 (4A), A1133. <https://doi.org/10.1103/PHYSREV.140.A1133/FIGURE/1/THUMB>.
- (3) Hohenberg, P.; Kohn, W. Inhomogeneous Electron Gas. *Phys. Rev.* **1964**, 136 (3B). <https://doi.org/10.1103/PhysRev.136.B864>.
- (4) Thomas, L. H. The Calculation of Atomic Fields. *Math. Proc. Cambridge Philos. Soc.* **1927**, 23 (5), 542–548. <https://doi.org/10.1017/S0305004100011683>.
- (5) Fermi, E., Un Metodo Statistico per La Determinazione Di Alcune Priorieta Dell'atomo. *Rend Accad Naz Lincei* 1927, 6, 602-607.
- (6) Perdew, J. P.; Burke, K.; Ernzerhof, M. Generalized Gradient Approximation Made Simple. *Phys. Rev. Lett.* **1996**, 77 (18), 3865. <https://doi.org/10.1103/PhysRevLett.77.3865>.
- (7) Tian, X.; Wang, T.; Fan, L.; Wang, Y.; Lu, H.; Mu, Y. A DFT Based Method for Calculating the Surface Energies of Asymmetric MoP Facets. *Appl. Surf. Sci.* **2018**, 427, 357–362. <https://doi.org/10.1016/j.apsusc.2017.08.172>.